Study on Structural, Optical and Dielectric Properties of few Double ($AB'B''O_3$) and Triple ($AB'B''B'''O_3$) Perovskites

Thesis Submitted for the Degree of Doctor of Philosophy (Science)

Jadavpur University

2023

By

Arpita Barua

Registration No: SOPHY1303516

Index No: 35/16/Phys./24

Department of Physics, Jadavpur University, Kolkata-700032

যাদবপুর বিশ্ববিদ্যালয়
কলকাতা-৭০০০৩২, ভারত

JADAVPUR UNIVERSITY
KOLKATA-700032, INDIA

FACULTY OF SCIENCE : DEPARTMENT OF PHYSICS

Dr. Sanjay Kumar
Professor
Department of Physics
Email: kumar_dsa@yahoo.com, sanjay.kumar@jadavpuruniversity.in

Ref No.: 24/2023
Date: 24/03/2023

CERTIFICATE FROM THE SUPERVISOR

This is to certify that the thesis entitled " **Study on Structural, Optical and Dielectric Properties of few Double ($AB'B''O_3$) and Triple ($AB'B''B'''O_3$) Perovskites"** submitted by Smt. **Arpita Barua (Registration no.: SOPHY1303516, Index no.: 35/16/Phys./24)** who got her name registered on **15/04/16** for the award of Ph.D (Science) degree of Jadavpur University, is absolutely based upon her own work under the supervision of **Prof. Sanjay Kumar, Department of Physics, Jadavpur University, Kolkata-700032** and that neither this thesis nor any part of it has been submitted for either any degree / diploma or any other academic award anywhere before.

Sanjay Kumar
24.03.2023
(Signature of the Supervisor date with official seal)

Dr. SANJAY KUMAR
Professor
Department of Physics
Jadavpur University
Kolkata - 700032, India

যাদবপুর বিশ্ববিদ্যালয়
কলকাতা-৭০০০৩২, ভারত

JADAVPUR UNIVERSITY
KOLKATA-700032, INDIA

FACULTY OF SCIENCE : DEPARTMENT OF PHYSICS

Dr. Sanjay Kumar
Professor
Department of Physics
Email: kumar_dsa@yahoo.com, sanjay.kumar@jadavpuruniversity.in

Ref No.: 24/2023
Date: 24/03/2023

Certificate of similarity check for plagiarism verification

This is to certify that the plagiarism checking for this thesis authored by Arpita Barua has been performed using professional plagiarism prevention software iThenticate. According to the report generated by iThenticate there is 08 % similarity in this thesis, which is in category 'Level 0' (minor similarities) as per 'Promotion of Academic Integrity and Prevention of Plagiarism in Higher Education Institutions Regulations, 2018' of University Grant Commission (UGC) of India. All sentences written/rewritten by providing proper references (treated as quoted work), references (bibliography), table of contents, preface, acknowledgements, generic terms used in the subject area of the present thesis, a common knowledge or coincidental terms up to 12 (twelve) consecutive words (as prescribed in the above said UGC Regulation up to 14 (fourteen) terms for such common knowledge or coincidental terms can be excluded) and own works of the candidate published in peer reviewed journals (Physica B 649 (2023) 414449; Journal of Alloys and Compounds 854 (2021) 157217; Physica B 583 (2020) 412057; AIP Conference Proceedings 1942 (2018) 110033; Ionics 23 (2017) 471–483; these papers are attached in the Appendix of the thesis) are excluded from similarity checking. It is certified that the present thesis submitted by Arpita Barua is plagiarism free and she has followed standard norms of academic integrity and scientific ethics.

Sanjay Kumar 24.03.2023

(Signature of the Supervisor)

DR. SANJAY KUMAR
Professor
Department of Physics
Jadavpur University
Kolkata - 700032, India

(Signature of Head, Department of Physics)

Prof. Kalyan Kr. Chakrabarti
Professor and Head
Department of Physics
Jadavpur University
Kolkata – 700 032

24.3.23

Declaration

I hereby declare that the work embodied in the present thesis titled '**Study on Structural, Optical and Dielectric Properties of few Double ($AB'B''O_3$) and Triple ($AB'B''B'''O_3$) Perovskites**' has been carried out by me in the Department of Physics, Jadavpur University, Kolkata-700032, India. Neither this thesis nor any part of it has been submitted for any degree elsewhere.

Date: 24/03/23

Arpita Barua

Arpita Barua
Research Scholar
Department of Physics
Jadavpur University
Kolkata- 700032, India

Dedicated to my parents

Acknowledgement

I would like to acknowledge a number of people without whom this thesis would not have been possible. First of all, I am eternally thankful to my supervisor Prof. Sanjay Kumar, Professor, Department of Physics, Jadavpur University for providing me the opportunity to pursue Ph.D in the fascinating field of material science. I would also like to thank him for his guidance, understanding and insight over the years. Frequent discussions with him regarding the analysis of different experimental results had made my work easier. His immense knowledge in the field of material science keeps me updated regarding the current developments in my field and he has always mentored me by giving responses to my different queries related to my work as and when required. Without his dynamic support it would not have been possible for me to perform different experiments and achieve excel in writing research papers. It is his belief in me that has made me a more confident person today. I am very lucky to have such an inspiring guide and mentor. He has not only guided me through this research but also provided many valuable life lessons. I am thankful to all the faculty members of Department of Physics, Jadavpur University for allowing me to avail the experimental facilities for my research.

I am extremely grateful to the professors of Department of Physics Jadavpur University; Prof. Joydeep Chowdhury, Prof. Partha Pratim Ray and Prof. Sukhen Das for helping me with the experimental facilities. I would like to thank professors of Department of Chemistry, Jadavpur University; Prof. Debajyoti Ghosal, Prof. Kausikisankar Pramanik, Prof. Saurabh Das and Prof. Arup Gayen for allowing me to access their laboratory. I would like to thank Prof. Chandan Mazumdar and Dr. Papri Dasgupta of Saha Institute of National Physics for different measurements. I would like to thank the FIST and PURSE program of Jadavpur University for providing us with the instrumental facilities.

I am immensely grateful to my senior lab mate Dr. Sanjay Kumar Dey for his extensive help throughout my research. I would like to thank my seniors Mr. Sumit Maity, Dr. S. k Sabyasachi and Dr. Monwar Haque for their help. I would also like to thank Dr. Rajat Saha, Dr. Subhrajyoti Dey, Dr. Sumit Majumdar and Mr. Somen Goswami for their useful advises. I would especially like to thank Dr. Soumen

Singha for his intellectual discussions throughout the research. I would also like to thank Dr. Rituparna Mondal for helping me throughout my research. I would like to thank Koyel Sarkar for helping me with the research. I would also like to thank Dr. Subhayan Saha and Dr. Snehal Mandal for their help. I would also like to thank my juniors Ms. Moisili Dutta, Mr. Nirmal Mondal and Mr. Bhaskar Khanra.

I would like to thank all my teachers whose teaching and encouragement has inspired me to pursue scientific research. I am also thankful to all my colleagues of Presidency University for their support. Finally, I would like to thank my family members and friends who have kept me motivated throughout this journey. This degree would have not been possible without the support of my parents and in-laws. I am grateful to my husband for his continuous encouragement and support. Lastly, I am thankful to God for providing me the strength to undertake this research work and enabling me to its completion.

Arpita Barua

Preface

The present thesis entitled '**Study on Structural, Optical and Dielectric Properties of few Double ($AB'B''O_3$) and Triple ($AB'B''B'''O_3$) Perovskites'** consists of eight chapters.

The significance of perovskite materials along with their various technological applications have been discussed in **Chapter 1**. The genesis and definition of the problem along with different types of perovskite oxides are discussed here. The methods of analysis of different dielectric parameters are included here. Objective and scope of the thesis have been discussed here.

Chapter 2 consists of different experimental techniques for the synthesis of perovskite oxides. Different experimental tools used to characterize the samples like X-ray diffractometer, Field emission scanning electron microscope, energy dispersive X-ray spectrometer, Fourier transform infrared spectrometer, Raman spectrometer and LCR meter along with the underlying theory of these techniques have been discussed.

Chapter 3 deals with the synthesis of double perovskite Ba_2YbTaO_6 and the characterization of its physical properties. The results obtained from XRD, FESEM, UV, PL and FTIR spectroscopy have been discussed. The dielectric parameters like the complex impedance, dielectric permittivity, loss tangent and ac conductivity exhibited by the sample have been elaborately discussed for understanding of its dielectric behaviour. The work reported in this chapter is based on the paper published in Physica B (Physica B 583 (2020) 412057).

Chapter 4 describes the formation of a nanocomposite of Ba_2YbSbO_6-$BaCO_3$ due to the mechanical milling of bulk Ba_2YbSbO_6 under normal atmospheric conditions. The structural, microstructural, Raman and FTIR characteristics of both the bulk and the

nanocomposite samples have been elaborately discussed. The dielectric parameters like the complex impedance, dielectric permittivity, loss tangent, ac conductivity and electrical modulus exhibited by the samples have been discussed in detail. The anomalous dielectric behaviour exhibited by the nanocomposite due to release of surface adsorbed CO_2 and H_2O have also been discussed. The work reported in this chapter is based on the paper published in Physica B (Physica B 649 (2023) 414449).

In **Chapter 5** the synthesis of perovskite oxides Sr_2YbNbO_6 and Sr_2YbSbO_6 have been discussed. Their structural and microstructural characteristics have been reported. The results obtained from UV, PL, Raman and FTIR spectroscopy have been discussed. Their dielectric properties in the permittivity, loss tangent and ac conductivity formalism have been discussed for understanding their dielectric behaviour. A portion of the work reported in this chapter is based on the paper published in AIP Conference Proceedings (AIP Conference Proceedings 1942 (2018) 110033).

Chapter 6 comprises of the synthesis techniques of triple perovskite $Ba_3NiTaNbO_9$ and $Ba_3NiTaSbO_9$. Their structural, microstructural, Raman and FTIR characteristics have been elaborately discussed. The dielectric parameters like the complex impedance, dielectric permittivity, loss tangent and ac conductivity exhibited by the samples have been discussed in detail for understanding the changes in their dielectric behaviour due to their B-site doping with three different cations. The work reported in this chapter is based on the paper published in Journal of alloys and compounds (Journal of Alloys and Compounds 854 (2021) 157217).

Chapter 7 comprises of the synthesis techniques of perovskite oxide $BaCo_{1/3}Nb_{2/3}O_3$ and $BaCo_{1/3}Sb_{2/3}O_3$. Their structural, microstructural, Raman and FTIR characteristics have been elaborately discussed. The dielectric parameters like the complex impedance, dielectric permittivity, loss tangent and ac conductivity exhibited by the samples have been discussed in

detail to examine the different dielectric properties exhibited by different B-site cation. A portion of the work reported in this chapter is based on the paper published in Ionics (Ionics 23 (2017) 471–483).

Chapter 8 describes the conclusion of the works performed in this thesis. The inferences drawn from the obtained results have been discussed here. The future scope of work has also been discussed.

Date: 24/03/23

Arpita Barua
Arpita Barua
Research Scholar
Department of Physics
Jadavpur University
Kolkata- 700032, India

Contents

Chapter - 1

Introduction

1.1. Genesis and definition of the problem

Perovskite oxides with general formula ABO_3 have been widely studied due to their widespread applications in chemical and technological industry. In chemical industry they are used as sensors and catalysts. Perovskites in the form of resonators capacitors and filters have widespread technological application in wireless communication system, global positioning systems, cell phones and memory devices [1–17]. Understanding the relationship between their structural and electrical properties is very important for developing new materials having high dielectric constant and low dielectric loss. Size dependent dielectric properties have also attracted major interest owing to the large demand for device miniaturization. Perovskite oxides exhibit different structures having unique magnetic and dielectric properties.

The unit cell of perovskite oxide having ABO_3 structure consists of oxygen atoms making a cubic lattice of octahedra where each octahedra consist of B-site cations at the centre and are 6-fold coordinated with oxygen atoms. A-site cations form another interpenetrating cubic sublattice and are 12-fold coordinated with oxygen atoms. The size of A-site cations is comparatively larger than that of B-site cations. Only few perovskite oxides have the highly symmetric cubic structure while most of them have lower symmetry like tetragonal, orthorhombic, monoclinic and rhombohedral structures. In case of ideal cubic structure, the radius of the A, B and O ions; r_A, r_B and r_O, follows the relation: $r_A + r_O = \sqrt{2}\,(r_B + r_O)$. The variation from the cubic structure can be determined from the Goldsmith tolerance [18] factor $t = (r_A + r_O) / \sqrt{2}\,(r_B + r_O)$. The value of t usually lies between 0.75–1.10 in case of perovskite oxide [19–21]. For cubic structure t =1 whereas the value of t decreases due to the misfit of the ionic radii of the A and B cations. In order to compensate the misfit of the ionic

radii of the constituent atoms, octahedral tilting and rotational distortion occurs making the crystal structure triclinic. When $t < 0.95$ the crystal structure is monoclinic and if $0.95 < t < 1$ the structure is orthorhombic. For $t > 1.06$ the crystal structure is hexagonal. The crystal structure of perovskite oxide is mainly determined by the ionic radii and the nature of its constituent A and B cations. The structural distortions like octahedral tilting, rotation and elongation of the octahedra highly effects the physical properties of perovskite oxides. More than simple perovskite the complex perovskite like $A_2B'B''O_6$ and $A_3B'B''O_9$ have more technological application.

If the B-site of a perovskite consists of two different cations they are known as double perovskite (DP) oxide. The substitution of B-site is done in such a way that the overall charge and the total atoms in ABO_3 unit cell remains same. DP oxide has the chemical structure $A_2B'B''O_6$ where B' and B" cations are arranged alternatively in lattice having rock salt like structure. The crystal structure and physical properties of DP oxides can be easily manipulated by changing the B-site cations. The B-site cations when replaced by transitional metal ions exhibit interesting semiconducting properties. Owing to their diverse physical properties DP oxide have various applications in the field of telecommunication, microelectronics, superconductors, fuel cells, memory and charge storage devices, spintronics and integrated circuits [22–31]. The tolerance factor in case of DP oxide is given by $t = (r_A + r_O) / \sqrt{2}\ (\langle r_B \rangle + r_O)$ where $\langle r_B \rangle$ is the average radius of the constituent B-site cations [32–33]. If the B-site cation has charge difference equal to two or more than their arrangement will be either ordered, partially ordered or disordered based on their ionic radii [34]. If the ratio $(r_{B'} - r_{B''})/r_{B''} \geq 0.09$, where the ionic radii of B' is $r_{B'}$ and B" is $r_{B''}$, then the B-site atoms follow ordered arrangement [35]. As the heterovalent perovskite $AB'_xB''_{1-x}O_3$

possess disordered arrangement of B-site cations, they exhibit variety of crystal structure and high dielectric constant [9–17].

The triple perovskite with general formula $A_3B'B''_2O_9$ and $A_3B'B''B'''O_9$ possesses variety of structure and have many technological applications [36–43]. Ba based triple perovskite exhibit multiferroicity, photocatalytic activity and high dielectric properties [44–47]. They can accommodate cations of different sizes in the A-site and lanthanide and d-block elements in the B-sites [48–57]. It has been reported that $A_3B'B''_2O_9$ (B'= Mg, Ni and B''=Nb, Ta) exhibit 2:1 ordering of B-site cations but $Pb_3MgNb_2O_9$ and $Ba_3ZnNb_2O_9$ exhibit 1:1 ordering of B-site cations [36, 58–59]. Ordering of B-site cations can also be varied by changing the concentration of atoms present in the B-site as reported in case of $A_3Ca_{1+x}Nb_{2-x}O_{9-\delta}$, A= Ba, Sr [40]. Large amount of work has been carried out on examining the crystal structure of Ba based triple perovskite oxide by employing Rietveld refinement [36–38, 43].

Perovskites having non cubic structure when heated to a very high temperature transforms to cubic structure. This transition occurs through several intermediate distorted phases. Perovskite oxides exhibits different types of crystal structure and varied physical properties, a detailed study of the structural and dielectric properties of different types of perovskite oxides is very important for understanding the relationship between their crystal structure and physical properties. In this background the aim of the present thesis is to study the structural, microstructural, optical and dielectric properties of some double (Ba_2YbTaO_6, Sr_2YbSbO_6, Sr_2YbNbO_6, Ba_2YbSbO_6) and triple ($Ba_3NiTaNbO_9$, $Ba_3NiTaSbO_9$, $BaCo_{1/3}Nb_{2/3}O_3$ and $BaCo_{1/3}Sb_{2/3}O_3$) perovskite oxides; and also, a nanocomposite (Ba_2YbSbO_6 – $BaCO_3$) of perovskite oxide with the goal to understand the impacts of structural and microstructural properties on their dielectric behaviour.

1.2. Theoretical background

1.2.1. Dielectric material

Dielectrics are insulating material having application in filter, capacitor, actuator, sensor and memory devices. A materials dielectric property usually describes its electrical charge storage, energy transfer and dissipation capabilities. Dielectric polarization gives rise to its ability to store electrical charge. During polarization the molecular dipoles are either displaced or rearranged with respect to the electric field. Charge dissipation or dielectric loss arises from the dielectric relaxation, electrical charge transport or conduction, non-linear dielectric effects and resonant transition. The loss of electrical energy is associated with the conversion, radiation or scattering of energy in the form of thermal energy. As the electromagnetic wave propagates through a dielectric media it transfers energy and its propagation velocity is determined by the dielectric permittivity of the medium. Dielectric materials have widespread applications from satellite communication to radio transmission. The demand for device miniaturization has led to the need of developing new and improved dielectric materials.

1.2.2. Dielectric polarization in dc electric field

The dipolar relaxation and the motion of charge carriers inside the material determines its dielectric properties. The dielectric constant decreases as the frequency is increased and a relaxation peak is observed at a particular frequency. The bound charges present in the dielectric material gives rise to electronic, ionic and orientational polarization. Electronic polarization occurs due to the displacement of the negative electron cloud with respect to its positive atomic core when an electric field is applied. Ionic polarization occurs due to the lattice displacement of constituent atoms with respect to each other on application

of electric field. Materials with permanent dipole moment gives rise to orientational polarization as the dipoles align themselves in the direction of the applied electric field. The mobile and the trapped charges present inside the dielectric material also gives rise to hopping and space charge polarization. The motion of localized charges like the electrons and holes or ions and vacancies by hopping from one local site to another and getting trapped in some localized state gives rise to hopping polarization. This hopping mechanism can be seen in ionic crystals and amorphous semiconductors where the motion of charge carriers takes place through the hopping process. When the charge carriers get trapped in the bulk grain or grain boundary interface, they give rise to space charge polarization. The dielectric constant of a material having permanent electric dipole is dependent on its polarizability. Dielectric material when placed in between parallel plate capacitor and a static field is applied across it than the dipoles align along the field direction. As the dielectric material gets polarized charges are induced in the plates (Fig. 1).

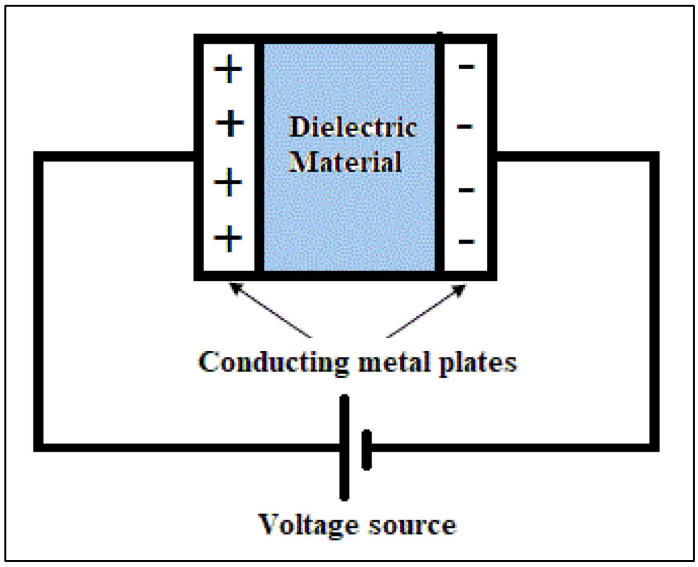

Fig. 1: *Charges induced on the plates after the dielectric material gets polarized.*

1.2.3. Dielectric polarization in an ac electric field

The structural information and the dielectric properties of a material can be better analysed by studying its dielectric response in an ac field. The ac response of a dielectric material can be either analysed using the time domain approach or frequency domain approach. In time domain analysis we study the variation of polarization with respect to time when an electric field is applied or the decay of polarization (dielectric relaxation) from a constant value when the polarizing field is removed. In frequency domain analysis we study the dielectric constant at different frequencies when an ac field is applied. Both the methods give same results. In this thesis we have performed our analysis in the frequency domain approach.

A parallel plate capacitor having unit area and 'd' distance between the plates when placed in an ac electric field than the total current is

$$C_t = C + \frac{dD}{dt} = C + \varepsilon_0 \varepsilon^* \frac{dE}{dt} \quad (1)$$

where C denotes conduction current, D is the vector representing electric displacement, ε_0 is the permittivity of the free space and ε^* is the complex dielectric constant. The complex dielectric constant $\varepsilon^* = \varepsilon' + i\,\varepsilon''$, where ε' denotes the dielectric permittivity and ε'' arises due to the dielectric losses. If the applied ac field is $E = E_m e^{i\omega t}$ where ω is the angular frequency than the equation 1 can be written as

$$C_t = \sigma E + i\omega\varepsilon_0(\varepsilon' + i\,\varepsilon'')\,E \quad (2)$$

$$C_t = \sigma E + \omega\varepsilon_0\varepsilon'' E + i\omega\varepsilon_0\varepsilon' E \quad (3)$$

where σ denotes the electrical conductivity of the sample. The first term is associated with the losses due to the scattering of mobile charge carriers after collision with obstacles during their motions. The second term again denotes losses due to the resistance associated with the

orientation and polarization of electric dipoles which increases with the increase in angular frequency. The displacement current is denoted by the third term. The value of ε' is obtained from the ratio of the capacitance of a parallel plate capacitor with and without the dielectric material. When a varying electric field is applied across a dielectric material there exists a lag between the change in the electric field and the change in the polarization due to the resistance faced by the atoms in the dielectric during their motion. This lag is represented by the phase difference Φ or the loss angle $\delta = 90 - \Phi$. Sin δ represents the power factor and tan δ represents the dissipation factor. The product of the power factor and the dielectric constant gives the loss factor. The loss tangent $\tan \delta = (\varepsilon' / \varepsilon'')$.

Overall polarization of a dielectric material involves electronic, ionic and orientational polarization and the time required for each polarization process is different. The electronic or ionic polarization and their depolarization occurs in a fraction of seconds. This polarization process is known as the resonance process as it involves resonance of vibration modes of the system when the natural frequency of the system and the frequency of the excitation field becomes equal. The orientational polarization and their depolarization takes longer time dependent on the type of the dielectric material. As there is a relaxation time involved this process is known as the relaxation process.

The polarization of a dielectric material is given by $P(t) = P_0 e^{-t/\tau}$, where P_0 is the dipole moment and τ is the relaxation time dependent on the type of material. The physical properties involving the relaxation time usually follows the Debye model. As per the Debye model the frequency dependent complex dielectric constant can be written as

$$\varepsilon^*(\omega) = \varepsilon_\infty + \frac{P_0\tau(1+i\omega\tau)}{1+(\omega\tau)^2};\ P_0\tau = \Delta\varepsilon' = \varepsilon_0 - \varepsilon_\infty \quad (4)$$

The frequency at which the real part of the permittivity decreases by Δε', a peak can be observed in the ε" curve indicating dielectric loss (Fig. 2). The peak in the ε" curve represents the dielectric relaxation [60] mechanism present in the sample.

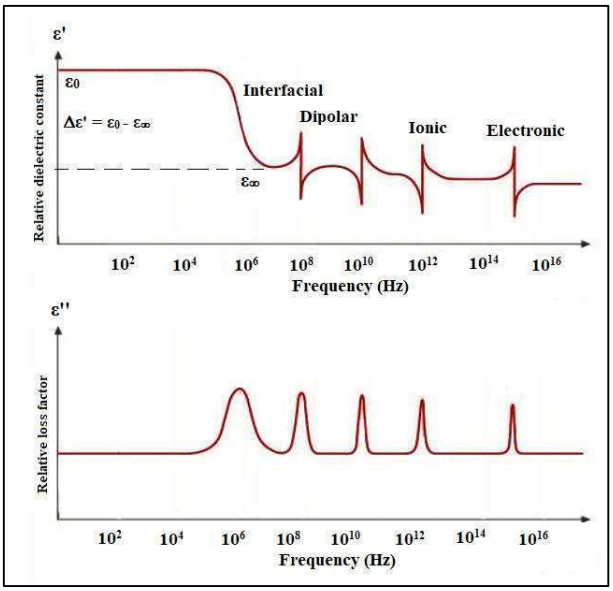

Fig. 2: *Frequency dependence of ε' and ε'' along with various polarization processes.*

1.2.4. Dielectric relaxation behaviour

The dielectric study of the sample provides information about the dipole moments of the molecules and correlate the relaxation behaviour with the dynamics of its molecules as well as its structure [61,62]. The relaxation behaviour of a material is associated with the reorientation of its electric dipoles when placed in an electric field. Dipoles in non-polar materials are induced only when an electric field is applied. Due to the presence of permanent dipole moments in polar materials they exhibit various relaxation processes. The frequency at which the relaxation occurs is known as the characteristic relaxation frequency ω_m and

strength of the relaxation is denoted by $\Delta\varepsilon'$. Dielectrics with single relaxation time follows the Debye model [60]

$$\varepsilon^*(\omega) = \varepsilon_\infty + \frac{\varepsilon_S - \varepsilon_\infty}{1+i\omega\tau}; \varepsilon' = \varepsilon_\infty \text{ when } \omega >> \omega_m \quad (5)$$

The contribution of permanent dipoles to dielectric permittivity is negligible at high frequencies.

The frequency dependent dielectric behaviour of a sample obtained experimentally usually do not follow the exponential behaviour and exhibit more than one relaxation time [63–65]. Such non-Debye type of dielectric behaviour follows either Cole-Cole [66] or Davidson-Cole [67, 68] or Havriliak Nigami [69, 70] model. The frequency dependent complex dielectric response defined using these models are:

Cole Cole: $$\varepsilon^*(\omega) = \varepsilon_\infty + \frac{\varepsilon_S - \varepsilon_\infty}{1+(i\omega\tau)^{\alpha}}; \quad (6)$$

Davidson Cole: $$\varepsilon^*(\omega) = \varepsilon_\infty + \frac{\varepsilon_S - \varepsilon_\infty}{(1+i\omega\tau)^{\alpha}}; \quad (7)$$

Havriliak Nigami: $$\varepsilon^*(\omega) = \varepsilon_\infty + \frac{\varepsilon_S - \varepsilon_\infty}{[1+(i\omega\tau)^{\alpha}]^{\beta}}; \quad (8)$$

1.2.5. Complex plane method of analysis

The information about the electrical microstructure of dielectric materials and their charge transport mechanism can be obtained using alternating current impedance spectroscopy (ACIS) [71]. The relaxation frequency intrinsic for a given dielectric material at a particular temperature can be determined using ACIS technique. Dielectric measurements over a range of frequencies including the relaxation frequency gives more precise results as compared to those measured at discrete frequencies. Any errors arising from the stray frequencies can be removed during impedance measurements.

The complex impedance of a sample consists of real and imaginary part ($Z^*(\omega) = Z' - i\,Z''$) and are usually depicted in the form of a complex plane plot known as the Nyquist plot. The complex impedance in terms of the other complex dielectric parameters:

$$\varepsilon^*(\omega) = \varepsilon' - i\,\varepsilon'' = \frac{1}{i\omega C_0 Z^*} \text{ (Complex dielectric permittivity)} \quad (9)$$

$$Y^*(\omega) = Y' + i\,Y'' = \frac{1}{Z^*(\omega)} \text{ (Complex admittance)} \quad (10)$$

$$M^*(\omega) = M' + i\,M'' = \frac{1}{\varepsilon^*} = i\omega C_0 Z^* \text{ (Complex modulus)} \quad (11)$$

$$C_0 = \frac{\varepsilon_0 A}{t} \quad (12)$$

where A is the sample pellet's area, t is the pellet thickness ε_0 is the permittivity of the free space. Using the above expressions one can analyse different dielectric spectra like ε' or M' vs log ω (dispersion spectra), ε'' or Z'' or M'' vs log ω (loss spectra), Z'' vs Z' (complex impedance spectra). The complex impedance in case of polycrystalline materials consists of both grain and grain boundary resistances. The bulk grain resistance is very small as compared to the grain boundary resistance and in some cases grain boundary resistance masks the bulk grain's contribution in the Nyquist plots. Z^* in terms of resistance R and capacitance C can be written as:

$$Z^* = \left(\frac{1}{R} + j\omega C\right)^{-1} = \left\{\frac{R}{1+(\omega\tau)^2} - \frac{jR^2\omega C}{1+(\omega\tau)^2}\right\};\ \tau = RC \quad (13)$$

The above expression can also be written as [72]

$$(Z' - R/2)^2 + Z''^2 = R^2/4 \quad (14)$$

Equation 14 represents a circle centred at (R/2, 0) and radius R/2. Thus, the complex impedance plots of Z' vs Z'' represents a semicircle. Such plots can also be obtained for ε' *vs* ε'', M' *vs* M'' and Y' *vs* Y'' (Fig. 3). The complex plane plots may have more than one semi-

circle indicating different relaxation phenomena present in a sample owing to the contribution of grain, grain boundary and interfacial polarization.

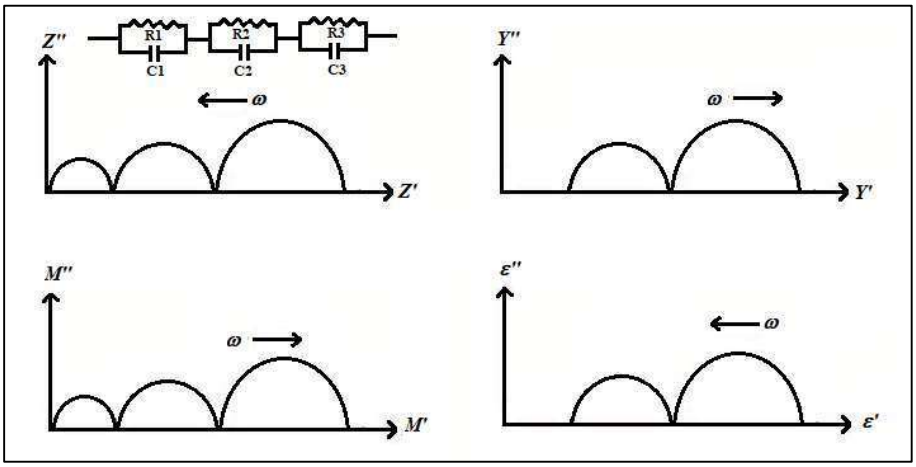

Fig. 3: *Complex plane impedance plot with its electrical equivalent circuit and the complex plots of other dielectric parameters.*

When the dielectric relaxation is ideal Debye type than a semi-circular arc having centre in the x axis is observed in the Nyquist plot [60, 73]. In case of non-Debye type of relaxation origin of the semi-circular arc lies below the x axis in the Nyquist plot [74]. The amount of deformation of the semi-circular arc was first shown by Cole-Cole [66] as $d = \frac{\phi}{\frac{\pi}{2}}$ where the depression angle ϕ is the angle between the centre of the semi-circle and its intercept with x axis (Fig. 4). Thus, the parameter of depression can be rewritten as $d = \frac{2\phi}{\pi}$. The parameter $\alpha = 1\text{-}d$ ($0 \leq \alpha \leq 1$) in the above equations (6–8) can be used to signify the deviation from Debye type relaxation. In case of ideal Debye relaxation $\phi \rightarrow 0°$ and $\alpha \rightarrow 1$ and for non-Debye behaviour $\phi \rightarrow 90°$ and $\alpha \rightarrow 0$. It has been observed that some complex plane

plots consist of depressed semi-circle along with semi-circular arc. Some materials are found to satisfy the Davidson-Cole equation where β is the depression parameter representing the deformed semi-circular arc [67,68]. In this response semi-circular arc does not indicate any specific centre so the peak portion of the curve does not signify the time constant ωτ =1.

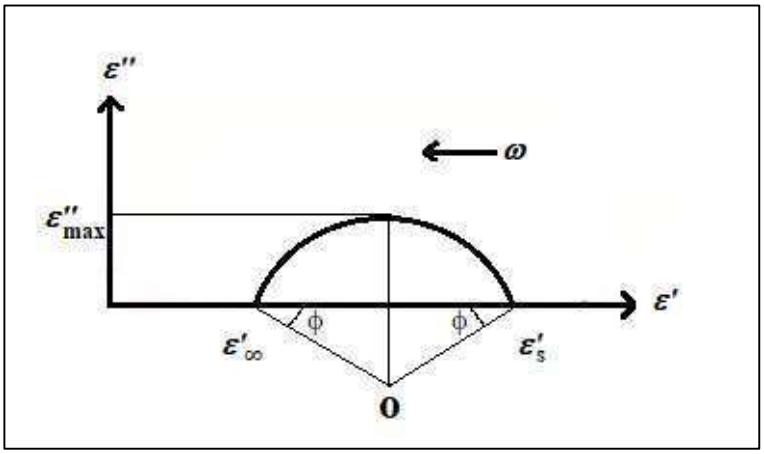

Fig. 4: *The Cole-Cole plot of dielectric permittivity.*

It has been reported by Havriliak et al. that the dielectric dispersion at high frequencies is linear and at low frequencies they assume circular shape [69,70]. Using this function one can represent both Cole-Cole and Davidson-Cole function by varying the depression parameters. The dielectric parameters using this model has identical counterpart as in Cole-Cole model. The equation 6, 7 and 8 can also be used for Z^* as Z^* follows the same anti clockwise direction with varying frequency as in ε^*. The real and imaginary part of Z^* can be written in terms of phase angle (P) and experimentally measured impedance (Z) as:

$$Z' = Z\,Cos\,(P) \text{ and } Z'' = Z\,Sin\,(P) \quad (15)$$

The resistance (R) and capacitance (C) values of a crystal is obtained by simulating the experimental complex impedance plots with a parallel R-C element [75]. For bulk crystals the

presence of interfacial boundary layers gives rise to two semi-circular arcs in the complex impedance plots, the experimental curves can therefore be simulated using a series circuit consisting of two parallel RC elements. Two arcs in the impedance plots are due to the grain and grain boundary's contribution to the total impedance. The arc associated with the grain arises at a greater value of frequency than grain boundary. The relaxation frequency (f_r) associated with the peak of each semi-circle can be calculated using

$\omega_{max}\tau = 1$

$\Rightarrow \omega_{max} RC = 1$

$\Rightarrow 2\pi f_r RC = 1$

$$\Rightarrow f_r = \frac{1}{2\pi RC} \text{ and } \tau = \frac{1}{2\pi f_r} \quad (16)$$

The impedance data can also be used to calculate other dielectric parameters using the relations:

dielectric permittivity: $$\varepsilon' = \frac{Ct}{\varepsilon_0 A} = \frac{Z'}{\omega C_0 (Z'^2 + Z''^2)} \quad (17)$$

loss tangent: $$tan\ \delta = \frac{\varepsilon'}{\varepsilon''} = \frac{Z'}{Z''} \quad (18)$$

ac conductivity: $$\sigma_{ac} = \frac{Z't}{A(Z'^2 + Z''^2)} \quad (19)$$

1.2.6. Brief review on the recent works on different types of perovskite oxides:

In the last few decades, the progress of electronics as well as electrical technology is based on the continuous effort to develop smart and eco-friendly materials. Lead being a toxic material, other alternatives like lead free dielectric materials are being developed [76–80]. Perovskite oxides have been widely used in the field of microwave communication systems in the form of resonators and filters [81]. They have been widely explored due to

their tuneable physical properties which are dependent on their composition and their crystal structure. An extensive survey of the literature on ytterbium based double perovskite oxides shows that, the temperature dependent ac electrical properties of very few are reported. The structural properties of Ba_2LnTaO_6 (where Ln is a trivalent lanthanide) in between 82 K and 723 K temperature have been reported by Hammink et al. [82]. Konopka et al. [83] have reported the dielectric permittivity of Ba_2YbTaO_6 in the microwave frequency range and its magnetic susceptibilities and the electron paramagnetic resonance measured between 5 K and room temperature have been reported by Taria et al. [84]. Dielectric analysis of $Ba(Ni_{1/3}Ta_{2/3})O_3$ has been reported by Hoque et al. [85]. A series of rare earth-based perovskite oxide having catalytic, optical, magnetic and electrical applications have been reported by Du et al. [86]. Dielectric properties of Sr-based double perovskite oxides have been reported by Sinha et al. [87,88].

In recent past a large amount of research have been carried out on triple perovskites having general formula $A_3(B'B''B''')O_9$ because of their structural diversity and technologically important physical properties. Barium based triple perovskites have been reported to exhibit multiferroicity, better dielectric properties and photocatalytic properties [89–92]. Triple perovskites usually have hexagonal, orthorhombic, monoclinic and trigonal symmetries as they can accommodate varied sized cations in the A-site and any lanthanide or any d-block element in the B-sites [93–102]. This structure can easily accommodate different elements, which allows us to substitute different cations in order to obtain the desired physical properties. The dielectric permittivity arises due to the combination of electronic and ionic polarization [103]. The lattice vibrations affect the ionic polarization but the electronic polarization is constant for a specified ion [104, 105]. So, by incorporating different ions in the B-site of triple perovskites one can obtain a range of dielectric properties. Mani et. al.

have reported the structural and bonding properties of $Ba_3M^{II}M^{IV}WO_9$ (M^{II} = Ca, Zn; M^{IV} = Ti, Zr) Perovskite Oxides [106]. J. B. Philipp et al. have reported the room temperature dielectric properties of $Ba_3M^{III}TiM^{V}O_9$ (where, M^{III} = Ga, Y, Lu; M^{V} = Nb, Ta) and $Ba_3M^{III}TiSbO_9$ (where, M^{III} = Fe, Ga) [107]. The structural and dielectric properties of $Ba_3ZnTa_{2-x}Nb_xO_9$ and $Ba_3MgTa_{2-x}Nb_xO_9$ have been reported by Ganguli et al. [108]. Sharma et al. have shown the application of triple perovskite oxides as advanced pseudocapacitive material [109]. Lee et al. have reported the application of triple perovskites as an electrocatalyst for oxygen evolution reaction [110].

Nowadays there is a huge demand of nanometric materials having high dielectric constant and low dielectric loss for use in high performance miniaturized microwave, radio frequency and energy storage devices. They also have applications in the development of multi-layer capacitors and dynamic random-access memory in smaller structures [111–113]. Research in the area of developing nanometric dielectric materials has been rapidly flourishing in the recent years. In past two decades, the nanometric materials having applications in microwave electronic circuits, optical storage devices, piezoelectric sensors, sonars, transducers and multilayer ceramic capacitors have been developed [111–115]. From application point of view, $BaTiO_3$ is an excellent perovskite oxide. The dielectric properties of nanosized $BaTiO_3$ synthesized by both chemical and high energy ball milling method have been elaborately investigated [111–113,115]. The nanosized perovskites are known to have applications in the sensing of NO_2 (using $LaFeO_3$), CO (using $LaCoO_3$), alcohols (using $SrFeO_3$), hydrocarbons (using $LnFeO_3$), H_2O_2 and glucose (using$LaNiO_3$). They are also used in dopamine detection (using $LaFeO_3$), solid oxide fuel cells (using $NdFeO_3$) and as catalysts (using $LaFeO_3$) for hydrogen evolution and oxygen reduction reactions [116–124]. In the recent past, the size dependent dielectric properties of nanosized $BaTiO_3$ have been

extensively studied due to its high permittivity values and widespread applications in the electronic industry [111–115,125–127]. The nanosized $BaTiO_3$ and $LaCoO_3$ (synthesized by high energy ball milling method) and nanometric $LaFeO_3$ (prepared by sol-gel method) have shown to adsorb gases like CO_2, CO, NO_2 etc. [116, 117,128,129].

1.3. Objective and scope of the thesis:

The objective and scope of this thesis has been discussed below:

1. Synthesis of 1:1 ordered double perovskites Sr_2YbSbO_6, Ba_2YbTaO_6 and Sr_2YbNbO_6 and to investigate their structural, microstructural and optical properties.
2. Analysis of the dielectric behaviour of the 1:1 ordered double perovskites Sr_2YbSbO_6, Ba_2YbTaO_6 and Sr_2YbNbO_6 in dielectric permittivity, dielectric loss, ac conductivity and impedance formalism in the framework of the modified Cole-Cole model.
3. Study of the effects of mechanical milling of Ba_2YbSbO_6 leading to a nanocomposite formation (Ba_2YbSbO_6-CO_3) and investigation of their structural, optical and dielectric properties.
4. Synthesis of triple perovskites $Ba_3NiTaNbO_9$ and $Ba_3NiTaSbO_9$ and investigation on their structural, microstructural and optical properties.
5. Analysis of the dielectric behaviour of the triple perovskites $Ba_3NiTaNbO_9$ and $Ba_3NiTaSbO_9$ in dielectric permittivity, dielectric loss, ac conductivity and impedance formalism in the framework of the modified Cole-Cole model.
6. Synthesis of 1:2 ordered perovskites $BaCo_{1/3}Nb_{2/3}O_3$ and $BaCo_{1/3}Sb_{2/3}O_3$ for investigation of their structural, microstructural and bonding properties.

7. Analysis of 1:2 ordered perovskites $BaCo_{1/3}Nb_{2/3}O_3$ and $BaCo_{1/3}Sb_{2/3}O_3$ in dielectric permittivity, dielectric loss, ac conductivity and impedance formalism in the framework of the modified Cole-Cole model.

References

[1] M. S. Fu, X. Q. Liu, X. M. Chen, Y.W. Zeng, J. Am. Ceram. Soc. 93 (2010) 787–795.

[2] M. R. Shah, A. K. M. Akther Hossain, J. Mater. Sci. Technol. 29 (2013) 323–329.

[3] C. T. Chen, C. Y. Huang, Y. M. Lin, C. T. Lee, Jpn. J. Appl. Phys. 50 (2011) 091503.

[4] A. Belous, O. Ovchar, O. Kramarenko, D. Mischuk, B. Jancar, M. Spreitzer, D. Suvorov, G. Annino, D. Grebennikov, P. Mascher, Ferroelectrics 387 (2009) 36–45.

[5] O. Ovchar, A. Belous, O. Kramarenko, D. Mischuk, B. Jancar, M. Spreitzer, D. Suvorov, G. Annino, D. Grebennikov, P. Mascher, Ferroelectrics 387 (2009)189–196.

[6] Z. Yang, Y. Zhang, G. You, K. Zhang, R. Xiong, J. Shi, J. Mater. Sci. Technol. 28 (2012) 1145–1150.

[7] T. Hungr, M. Alguero, A. Castro, J. Am. Ceram. Soc. 90 (2007) 2122–2127.

[8] H. Lu, L. Zhu, J. P. Kim, S. H. Son, J. H. Park, J. Mater. Sci. Technol. 28 (2012) 654–660.

[9] L. Agrawal, A. Dutta, S. Shannigrahi, B.P. Singh, T. P. Sinha, Physica B. 406 (2011) 1081–1087.

[10] V. Prakash, A. Dutta, S. N. Choudhary, T. P. Sinha, Mater. Sc. and Eng. B 142 (2007) 98–105.

[11] P. K. Bajpai, K. N. Singh, Physica B 406 (2011) 1226–1232.

[12] P. K. Bajpai, M. Pastor, K. N. Singh, J. Appl. Phys. 109 (2011) 014114.

[13] A. Dutta, C. Bharti, T. P. Sinha, Physica B 403 (2008) 3389–3393.

[14] A. Dutta, T. P. Sinha, Physica B 405 (2010) 1475–1479.

[15] A. Dutta, C. Bharti, T. P. Sinha, Mater. Res. Bull. 43 (2008) 1246–1254.

[16] Md. M. Hoque, A. Dutta, S. Kumar, T. P. Sinha, Physica B 407 (2012) 3740–3748.

[17] Md. M. Hoque, A. Dutta, S. Kumar, T. P. Sinha, J. Mater. Sci. Technol. 30 (2014) 311–320.

[18] Goldschmidt, V. M. Skr. Nor. Viedenk.-Akad., Kl. I: Mater.- Naturvidensk. Kl. No. 8 (1926).

[19] R. M. Hazen, Sci. Am. 258 (1988) 74.

[20] T. Yagi, H. K. Mao, P. M. Bell, Phys. Chem. Miner. 3 (1978) 97.

[21] T. Ishihara (Ed.), Perovskite Oxide for Solid Oxide Fuel Cells, Springer (2009).

[22] R. H. Mitchel, Perovskites Modern and Ancient, Almaz Press, Ontario (2000).

[23] L. G. Tejuca, J. L. G. Fierro, Properties and Applications of Perovskite Type Oxides, Marcel Decker, New York (1993).

[24] S. N. Putilin, E. V. Antipov, O. Chmaissem, M. Marezio, Nature 362 (1993) 226.

[25] S. Jin, T. H. Tiefel, M. McCormack, R. A. Fastnacht, R. Ramesh, L. H. Chen, Science 264 (1994) 413.

[26] C. G. Zhong, J. H. Fang, Q. Jiang, J. Phys. Condens. Matter. 16 (2004) 9059.

[27] M. Vazquez, A. Hernando, J. Phys. D: Appl. Phys. 29 (1996) 939.

[28] J. P. Wang, Nat. Mater. 4 (2005) 191.

[29] G. Reiss, A. Hutten, Nat. Mater. 4 (2005) 725.

[30] X. Li, K. Terabe, H. Hatano, H. Zeng, K. Kitamura, J. Appl. Phys. 100 (2006) 106103.

[31] Y. H. Xie, Y. Y. Lin, T. A. Tang, Integr. Ferroelectr. 67 (2004) 255.

[32] V. M. Goldschmidt, Skrifter Nordske Videnskaps-Akad. Oslo I, Mat-Naturvidensk Kl., 8 (1926) 2.

[33] Y. Teraoka, M. D. Wei, S. Kagawa, J. Mater. Chem. 8 (1998) 2323.

[34] G. King, P. M. Woodward, J. Mater. Chem. 20 (2010) 5785.

[35] L. A. Khalam, M. T. Sebastian, J. Am. Ceram. Soc. 90[5] (2007) 1467.

[36] M. W. Lufaso, Chem. Mater. 16 (2004) 2148.

[37] R. Mani, P. Selvamani, J. E. Joy, J. Gopalakrishnan, Inorg. Chem. 46 (2007) 6661.

[38] I. Levin, J. Y. Chan, R. G. Geyer, J. E. Maslar, T. A. Vanderah, J. Solid State Chem. 156 (2001) 122.

[39] M. Bieringer, S. M. Moussa, L. D. Noailles, A. Burrows, C. J. Kiely, M. J. Rosseinsky, R. M. Ibberson, Chem. Mater. 15 (2003) 586.

[40] Y. Du, A. S. Nowick, J. Am. Ceram. Soc. 78 (1995) 3033.

[41] M. Thirumal, A. K. Ganguli, Bull. Mater. Sci. 25 (2002) 259.

[42] M. Thirumal, A. K. Ganguli, Prog. Cryst. Growth Charact. Mater. 44 (2002) 147.

[43] H. Vincent, Ch. Perrier, Ph. I'heritier, M. Labeyrie, Mat. Res, Bull. 28 (1993) 951.

[44] M. Lee, E.S. Choi, X. Huang, J. Ma, C.R. Dela Cruz, M. Matsuda, W. Tian, Z.L. Dun, S. Dong, H.D. Zhou, Phys. Rev. B 90 (2014) 224402.

[45] J. Hwang, E. S. Choi, F. Ye, C. R. Dela Cruz, Y. Xin, H. D. Zhou, P. Schlottmann, Phys. Rev. Lett. 109 (2012) 257205.

[46] I. Molodetsky, P. K. Davies, J. Eur. Ceram. Soc. 21 (2001) 2587–2591.

[47] B. Xu, F. Zhang, X. Y. Liu, J. H. Ye, W. H. Zhang, L. Shi, X. G. Wan, J. Yin, Z. G. Liu, Phys. Rev. B 76 (2007) 125109.

[48] Y. Doi, Y. Hinatsu, J. Mater. Chem. 12 (2002) 1792–1795.

[49] S. J. Kim, M. D. Smith, J. Darriet, H. C. zur Loye, J. Solid State Chem. 177 (2004) 1493–1500.

[50] Y. Doi, Y. Hinatsu, J. Phys. Condens. Matter 16 (2004) 2849–2860.

[51] J. G. Zhao, L. X. Yang, Y. Yu, F. Y. Li, R. C. Yu, C. Q. Jin, J. Solid State Chem. 182 (2009) 327–330.

[52] V. U. Treiber, S. Kemmler-Sack, A. Ehmann, Z. Anorg, Allg. Chem. 487 (1982) 198.

[53] P. Lightfoot, P. D. Battle, J. Solid State Chem. 89 (1990) 174–183.

[54] J. C. Albornoz, D. A. Landinez Tellez, J. Roa-Rojas, J. A. Munevar, E. Baggio-Saitovich, J. Supercond. Nov. Magnetism 26 (2013) 2313–2317.

[55] P. Beran, S. A. Ivanov, P. Nordblad, S. Middey, A. Nag, D. D. Sarma, S. Ray, R. Mathieu, Solid State Sci 50 (2015) 58–64.

[56] F. Casallas, E. Vera, D. Landinez, C. Parra, J. Roa, J. Phys.: Conf. Ser. 687 (2016) 012047.

[57] T. Ferreira, D. Carone, A. Huon, A. Herklotz, S.A. Stoian, S.M. Heald, G. Morrison, M.D. Smith, H.C. zur Loye, Inorg. Chem. 57 (2018) 7362–7371.

[58] J. Chen, H. M. Chan, M. P. Harmer, J. Am. Ceram. Soc. 72 (1989) 593.

[59] M. P. Harmer, J. Chen, P. Peng, H. M. Chan, D. M. Smyth, Ferroelectrics 97 (1989) 263.

[60] P. Debye, Polar Molecules, Chemical Catalogue Company, New York (1929).

[61] C. R. Smyth, Dielectric Behaviour and Structure, McGraw Hill, New York (1955).

[62] K. S. Cole, R. H. Cole, J. Chem. Phys. 9 (1941) 341.

[63] K. C. Kao, Dielectric Phenomena in Solids Elsevier Academic Press, London (2004).

[64] A. K. Jonscher, Universal Relaxation Law, Chelsea Dielectric Press, London (1996).

[65] J. Kakalios, R. A. Street, W. B. Jackson, Phys. Rev. Lett. 59 (1987) 1037.

[66] K. S. Cole, R. H. Cole, J. Chem. Phys. 10 (1942) 98.

[67] D. W. Davidson, R. H. Cole, J. Chem. Phys. 18 (1950) 1417.

[68] D. W. Davidson, R. H. Cole, J. Chem. Phys. 19 (1951) 1484.

[69] S. Havriliak, S. Negami, J. Polym. Sci.: Part C 14 (1966) 99.

[70] S. Havriliak, S. Negami, Polymer 8 (1967) 161.

[71] A. K. Jonscher, Dielectric Relaxation in Solids, Chelsea Dielectrics Press, London, (1983).

[72] A. R. West, Solid State Chemistry and Its Application, John Wiley and Sons, (1987).

[73] A. R. von. Hippel, Dielectric and Waves, Wiely, New York (1954).

[74] R. H. Cole, J. Phys. Chem. 23 (1955) 493.

[75] S. Saha, T. P. Sinha, J. Appl. Phys. 99 (2006) 014109

[76] S. Priya, A. Ando, Y. Sakebe, J. Appl. Phys. 94 (2003) 1171.

[77] I. Levin, J. Y. Chan, J. E. Maslar, T. A. Vanderah, J. Appl. Phys. 90 (2001) 904.

[78] R. Zurmuhlen, J. Petzett, S. Kamba, V. V. Voitsekhovskii, E. Colla, N. Setter, J. Appl. Phys. 77 (1995) 5341.

[79] R. Zurmuhlen, J. Petzelt, S. Kamba, G. Kozlov, A. Volkov, B. Gorshunov, D. Dube, A. Tagantsev, N. Setter, J. Appl. Phys. 77 (1995) 5351.

[80] S. Saha, T. P. Sinha, J. Phys. Condens. Matter 14 (2002) 249.

[81] S. N. Putilin, E. V. Antipov, O. Chmaissem, M. Marezio, Nature 362 (1993) 226–228.

[82] T. S. Hammink, W. T. Fu, D. J. W. IJdo, J. Solid State Chem. 184 (2011) 848–851.

[83] J. Konopka, R. Jose, M. Wołcyrz, Physica C 435 (2006) 53–58.

[84] N. Taira, Y. Hinatsu, J. Solid State Chem. 150 (2000) 31–35.

[85] M. M. Hoque, A. Dutta, S. Kumar, T. P. Sinha, Physica B. 407 (2012) 3740–3748.

[86] X. Chen, J. Xu, Y. Xu, F. Luo, Y. Du, Inorg. Chem. Front. 6 (2019) 2226–2238.

[87] C. Bharti, T. P. Sinha, Solid State Sci. 12 (2010) 498–502.

[88] C. Bharti, T. P. Sinha, Physica B 406 (2011) 624–627.

[89] M. Lee, E. S. Choi, X. Huang, J. Ma, C. R. Dela Cruz, M. Matsuda, W. Tian, Z. L. Dun, S. Dong, H. D. Zhou, Phys. Rev. B 90 (2014) 224402.

[90] J. Hwang, E. S. Choi, F. Ye, C. R. Dela Cruz, Y. Xin, H. D. Zhou, P. Schlottmann, Phys. Rev. Lett. 109 (2012) 257205.

[91] I. Molodetsky, P. K. Davies, J. Eur. Ceram. Soc. 21 (2001) 2587–2591.

[92] B. Xu, F. Zhang, X. Y. Liu, J. H. Ye, W. H. Zhang, L. Shi, X. G. Wan, J. Yin, Z. G. Liu, Phys. Rev. B 76 (2007) 125109.

[93] Y. Doi, Y. Hinatsu, J. Mater. Chem. 12 (2002) 1792–1795.

[94] S. J. Kim, M. D. Smith, J. Darriet, H. C. zur Loye, J. Solid State Chem. 177 (2004) 1493–1500.

[95] Y. Doi, Y. Hinatsu, J. Phys. Condens. Matter 16 (2004) 2849–2860.

[96] J. G. Zhao, L. X. Yang, Y. Yu, F. Y. Li, R. C. Yu, C. Q. Jin, J. Solid State Chem. 182 (2009) 327–330.

[97] V. U. Treiber, S. Kemmler-Sack, A. Ehmann, Z. Anorg, Allg. Chem. 487 (1982) 198.

[98] P. Lightfoot, P. D. Battle, J. Solid State Chem. 89 (1990) 174–183.

[99] J. C. Albornoz, D. A. Landinez Tellez, J. Roa-Rojas, J. A. Munevar, E. Baggio Saitovich, J. Supercond. Nov. Magnetism 26 (2013) 2313–2317.

[100] J.Bijelić, A. Stanković, M. Medvidović-Kosanović, B. Marković, P. Cop, Y. Sun, S. Hajra, M. Sahu, J. Vukmirović, D. Marković, Á. Kukovecz, Z. Jagličić, B. M. Smarsly, I. Djerdj, J. Phys. Chem. C 124 (2020) 12794–12807.

[101] F. Casallas, E. Vera, D. Landinez, C. Parra, J. Roa, J. Phys.: Conf. Ser. 687 (2016) 012047.

[102] T. Ferreira, D. Carone, A. Huon, A. Herklotz, S. A. Stoian, S. M. Heald, G. Morrison, M. D. Smith, H. C. zur Loye, Inorg. Chem. 57 (2018) 7362–7371.

[103] R. D. Shannon, J. Appl. Phys. 73 (1993) 348.

[104] H. Tamura, D. A. Sagala, K. Wakino, Jpn. J. Appl. Phys. 25 (1986) 787.

[105] I. M. Reaney, I. Qazi, W. E. Lee, J. Appl. Phys. 88 (2000) 6708.

[106] R. Mani, P. Selvamani, J. E. Joy, J. Gopalakrishnan, Inorg. Chem. 46 (2007) 6661–6667.

[107] J. B. Philipp, P. Majewski, L. Alff, A. Erb, R. Gross, T. Graf, M. S. Brandt, J. Simon, T. Walther, W. Mader, D. Topwal, D. D. Sarma, Phys. Rev. B 68 (2003) 144431.

[108] M. Thirumal, G. S. Murugan, K. B. R. Varma, A. K. Ganguli, Mater. Res. Bull. 35, (2000) 2423–2430.

[109] A. K. Tomar, A. Joshi, G. Singh, R. K. Sharma, J. Mater. Chem. A 8 (2020) 24013–24023.

[110] A. K. Tomar, U. N. Pan, N. H. Kim, J. H. Lee, ACS Energy Lett. 8 (2023) 565–573.

[111] X. Wang, H. Wen, R. Chen, H. Zhou, L. Li, IEEE Int. Ultrasonics, Ferroelectrics, and Frequency Control Joint 50th Anniversary Conf, Canada, Montreal, (2004).

[112] T. Hoshina, J. Ceram. Soc. Jpn. 121 (2) (2013) 156.

[113] Y. Kobayashi, A. Nishikata, T. Tanase, M. Konno, J. Sol. Gel Sci. Technol. 29 (2004) 49.

[114] S. Mukherjee, S. Ghosh, C. Ghosh, M.K. Mitra, J. Inst. Eng. India Ser. D 94 (2013) 57.

[115] R. Ashiri, RSC Adv. 6 (2016) 1713.

[116] A. Benali, S. Azizi, M. Bejar, E. Dhahri, M. F. P. Graça, Ceram. Int. 40 (9) (2014) 14367.

[117] M. Ghasdi, H. Alamdari, Sensor. Actuator. B Chem. 148 (2010) 478.

[118] Y. Wang, J. Chen, X. Wu, Mater. Lett. 49 (2001) 361.

[119] H. T. Giang, H. T. Duy, P. Q. Ngan, G. H. Thai, D. T. A. Thu, D. T. Thu, N. N. Toan, Sensor. Actuator. B Chem. 158 (2011) 246.

[120] B. Wang, S. Gu, Y. Ding, Y. Chu, Z. Zhang, X. Ba, Q. Zhang, X. Li, Analyst 138 (2013) 362.

[121] G. Wang, J. Sun, W. Zhang, S. Jiao, B. Fang, Microchim. Acta 164 (2009) 357.

[122] C. Tongyun, S. Liming, L. Feng, Z. Weichang, Z. Qianfeng, C. Xiangfeng, J. Rare Earths 30 (2012) 1138.

[123] A. Galal, N. F. Atta, S. M. Ali, Electrochim. Acta 56 (2011) 5722.

[124] S. M. Ali, Y. M. Abd Al-Rahman, A. Galal, J. Electrochem. Soc. 159 (2012) 600.

[125] M. H. Frey, Z. Xu, P. Han, D. A. Payne, Ferroelectrircs 206 (1998) 337.

[126] M. Vigneswari, K. Sakthipandi, S. Sankarrajan, IJERT 3 (2014) 2278.

[127] V. Buscaglia, C. A. Randall, J. Eur. Ceram. Soc. 40 (2020) 3744.

[128] S. Neogi, U. Chowdhury, A. K. Chakraborty, J. Ghosh, Micro & Nano Lett. 10 (2015) 109.

[129] J. Ghosh, S. Bysakh, S. Mazumder, Phil. Trans. 87 (2014) 325.

Chapter – 2

Experimental Techniques

2.1. Experimental

The study of structural, microstructural, optical, thermal and dielectric properties of a material are performed in order to understand their physical properties. Various experimental techniques have been employed in order to examine their physical properties. In this chapter the sample preparation and the experimental techniques employed have been discussed in detail.

2.2. Sample preparation:

2.2.1. Materials Prepared:

We have synthesized the following perovskite oxides: Ba_2YbTaO_6, Sr_2YbSbO_6, $Ba_3NiTaNbO_9$, $Ba_3NiTaSbO_9$, Sr_2YbNbO_6, $BaCo_{1/3}Nb_{2/3}O_3$, $BaCo_{1/3}Sb_{2/3}O_3$ and Ba_2YbSbO_6 by solid state ceramic method. The reagent grade powders of the respective oxides and carbonates were used for the synthesis.

2.2.2. Solid state synthesis:

The Ceramic materials are usually prepared using this method due to their lower production cost. In this process the stoichiometric amount of the starting reagents (usually oxides or carbonates) is mixed together in presence of acetone using a motor pestle for 10 hours to form a homogeneous mixture. Then the mixture is sintered at a very high temperature around 1200–1500˚ C with a controlled heating rate for initial phase formation. Again, the obtained mixture is annealed at a high temperature about 50˚ C above the sintering temperature for 10–15 hours to obtain the desired compound. This process is based on the kinetic and the thermodynamic factor [1]. The thermodynamic factor predicts the possibility of the reaction to take place and the rate of the reaction is determined by the kinetic factor [2,3]. Thus, for obtaining a required phase using solid state ceramic method, different

parameters like temperature, pressure, atmospheric condition and reaction time must be maintained accordingly. The phase formation of the sample is confirmed using X-ray diffraction.

2.2.2.1. Stoichiometric mixing:

In order to synthesize perovskite oxide with a desired chemical formula the calculation and weighing of the stoichiometric amount of the reagent powders is very important. At first the total molecular weight of the desired compound (M_t) is calculated. In order to prepare M_n gram of the desired sample, the amount of each element that should be present in M_n gram of the sample is calculated using: $(mM_n)/M_t$, where m is the total molecular weight of the respective element present in the desired sample. Now as the reagent are in the form of oxides, the molecular weight of the corresponding oxides (M_o) is noted. The oxides of each sample required for synthesis is calculated using: $(mM_n\ M_o)/m_oM_t$, where m_o is amount of each element present in its respective oxides. Obtaining a homogeneous mixture is very important as it affects the properties of ceramic materials. For obtaining a homogeneous mixture, the oxides are mixed for about 10 hours in presence of acetone.

2.2.2.2. Calcination and sintering:

Calcination is an endothermic reaction in which the decomposition of carbonates and nitrates takes place emitting gaseous products and leaving behind the solid product. During calcination the particle size, its distribution, surface morphology and defects like porosity are created. It is usually performed in order to remove undesired volatile impurities, carbon dioxide, nitrogen oxide and water of hydration. During this process the desired sample is obtained by the thermo-chemical reaction. By controlling the calcination temperature, the particle size can be manipulated.

The calcined samples are grinded again using motor pestle to obtain a homogeneous mixture and to remove the intergranular voids. The sample is than mixed with polyvinyl alcohol (5% of the weight of the sample) which acts as a binder to form a compact mass of granules. This binder is expelled during the sintering process due to heating. The samples are then pelletized into discs using a high pressure of 14 MPa using a hydraulic press. The pellets are then fired at a very high temperature but below its melting point. The crystal bonding between two adjacent atoms is increased at the contact interface as a result of diffusion of constituent atoms at the particle surface due to surface energy. This firing makes the ceramic denser and removes porosity and is known as sintering. During sintering the average grain sizes of the particle are increased which leads to the decrease in the total surface area. Sintering also creates the grain boundaries by eliminating the solid interfaces making the sample denser.

Initially the contact area between the particle increases by neck growth which increases its relative density (Fig. 1). The density further increases by the diffusion of atoms and reduction of voids. In the final stage the pores are almost eliminated with the formation of well-defined grain boundary. By controlling the sintering temperature, the physical properties of the ceramics can be controlled. The fine grain powders have large surface free energy which is reduced during sintering with reduction of particle surface. Sintering rate is affected by temperature, particle size and distribution, presence of impurities, non-stoichiometry and the samples atmospheric conditions. The grains, grain boundaries and pores present in the sample after sintering greatly affects its physical properties. The grain shape and size of a sample are finalized during sintering [4].

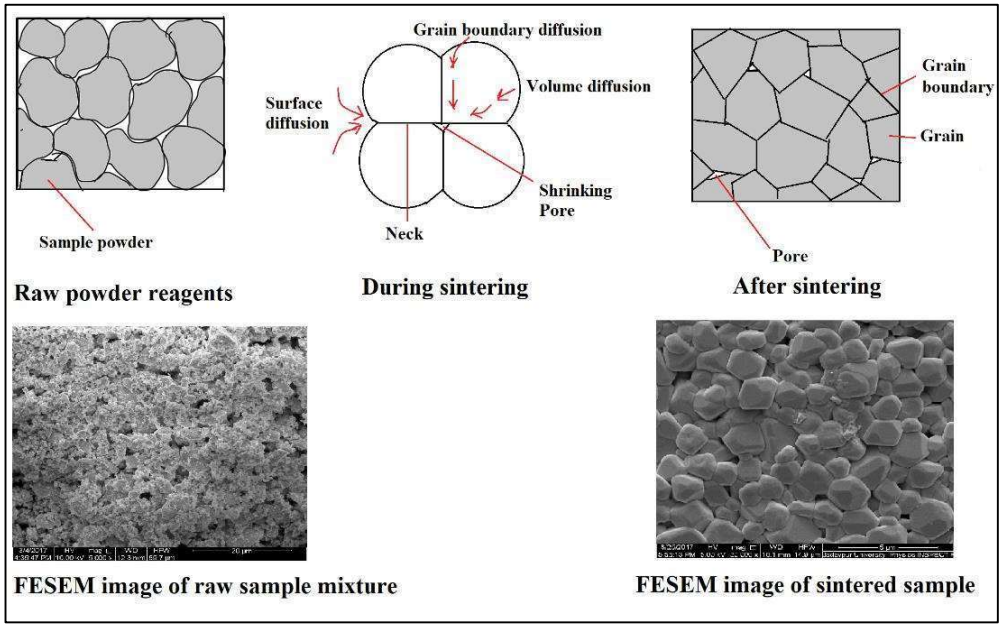

Fig. 1: *Grain and grain boundary formation due to sintering.*

2.2.2.3. Electrodes

In order to perform the dielectric measurements, the sintered pellets are polished with fine emery paper and electrodes are developed on the flat surfaces. Electrodes are usually created with conducting materials like silver and gold. The electrode material should be chosen in such a way that it adheres to the sample, its contact resistance is zero, forms a thin layer over the sample surface and it should be durable. If the electrode material does not stick properly to the sample surface the gap acts as a low value of capacitance in series with the sample's capacitance which lowers the effective capacitance of the sample. Voltage drop occurs in the gap which affects its operation.

2.3. Material Characterization:

2.3.1. X-ray diffraction (XRD):

XRD analysis is a non-destructive method for obtaining the chemical composition and the crystallographic structure of a given material. Various crystallographic parameters such as crystal structure, crystallite size, micro strain, macro stress and the phases present in a sample can be determined using XRD. The incident X-rays on interacting with the electrons of an atom gives rise to the diffraction patterns. According to Bragg's law when the two diffracted rays have a path difference which is an integral multiple of wavelength than constructive interference between the scattered rays takes place [5,6].

$$n\lambda = 2d \sin\theta \quad (1)$$

where n is an integer, X-ray's wavelength is λ, d is the inter planer spacing and the diffraction angle is denoted by θ. X-ray diffraction occurs when its wavelength is comparable with the distances between its scattering centers (Fig. 2).

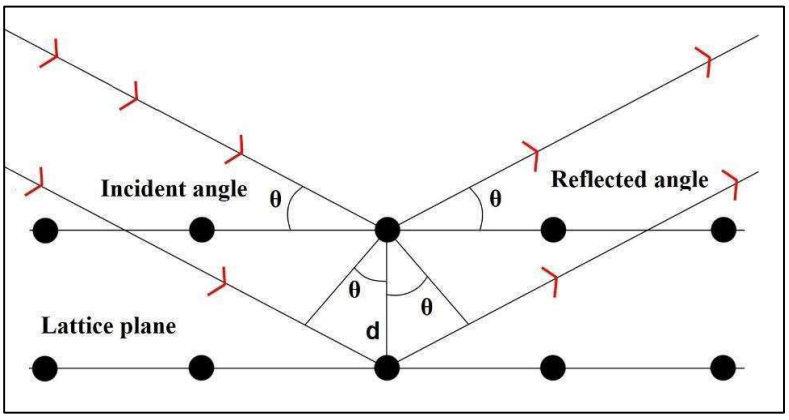

Fig. 2: *Bragg's law of reflection.*

For the XRD analysis the intensity of the diffracted ray is plotted as a function of diffraction angle 2θ. Using Bragg's law (equation 1) one can determine the interplanar spacing d of the crystal. The reflections from the lattice planes helps in determining the structure of the sample. Crystals with lower symmetry has larger number of atomic planes as compared to high symmetry crystals which have fewer atomic planes. As the wavelength of X-ray is of Å order, the inter atomic distance in crystals, so using XRD analysis one can determine the atomic arrangement [7–9]. Crystal structure is usually defined by its unit cell which is repeated in all direction forming atomic planes at regular interval. The interplanar spacing d is related to its unit cell parameters (Table 1).

Table 1: The relationship between d spacing between adjacent planes and unit cell parameters.

Crystal Structure	d-spacing ($1/d^2$)	Cell volume
Monoclinic	$1/\sin^2(\beta)[(h^2/a^2)+(\sin^2(\beta) k^2/b^2)+(l^2/c^2)-(2hl\cos(\beta)/ac)]$	$abc \sin(\beta)$
Cubic	$(h^2 + k^2 + l^2)/ a^2$	a^3
Tetragonal	$(h^2 + k^2)/ a^2+(l^2/ c^2)$	a^2c
Orthorhombic	$(h^2/a^2)+(k^2/ b^2)+(l^2/ c^2)$	abc
Hexagonal	$4/3(h^2+hk + k^2)/ a^2+(l^2/ c^2)$	$(\sqrt{3}a^2c)/2$

The schematic diagram of X-ray diffractometer is depicted in Fig. 3. X-rays incident on the sample gets diffracted and falls on the detector after passing through a filter. The sample holder rotates in such a way that the angle between the incident beam and the diffracting planes is θ and the detector is kept at equivalent angle 2θ. Thus, the detector records the intensity of the diffracted beam as a function of 2θ. Every material has its characteristic XRD pattern using which we can recognize them [10]. We can also confirm the phase formation of a reported sample by comparing its XRD patterns to the ICDD file. We have used Rigaku Miniflex II powder x-ray diffractometer and Bruker D8 advanced diffractometer to analyze the samples reported in this thesis. The diffraction peaks of all the samples were recorded in between $10^{\circ} \leq 2\theta \leq 120^{\circ}$ using Cu Kα (λ=1.54184 Å) radiation at room temperature. The step size was kept at 0.02° and the scan rate was fixed at 2° min^{-1}. The voltage of the X-ray generator was fixed at 35 kV and the current to 35 mA and their structural parameters were determined using two Rietveld based software GSAS with EXPGUI interface [11] and FULLPROF program [12]

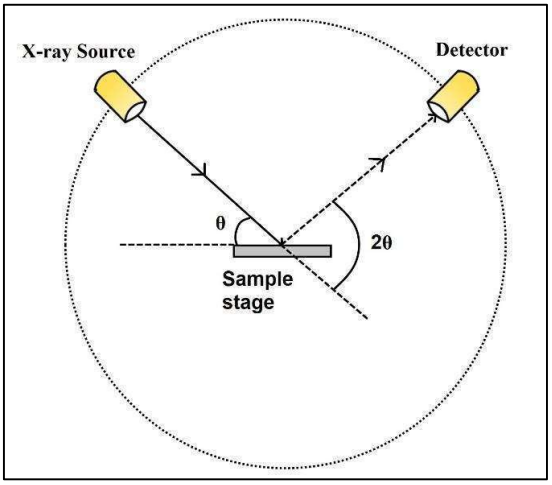

Fig. 3: *Schematic diagram of X-ray powder diffractometer.*

2.3.2. Rietveld refinement:

In 1967 Hugo Rietveld formulated a method for characterizing the crystalline materials. The structural and other parameters affecting the diffraction pattern are refined using this method. During the refinement a calculated diffraction profile is created by refining lattice parameters, peak shape, peak width and preferred orientation. The calculated diffraction profile is matched with the experimentally obtained diffraction peaks. The calculated pattern is then refined using least square method to match the experimental and calculated patterns. The diffraction pattern is plotted as intensity values (I_i) at each of several thousand equal steps (i) with scattering angle (2θ). The least square fit of each I_i gives the best fit curve. The quantity to be minimized during the least square refinement (S_y) is expressed as

$$S_y = \Sigma R_i [I_i - I_{ci}]^2 \quad (2)$$

where $R_i = 1/I_i$, I_i is the experimentally obtained intensity value at the i^{th} step, I_{ci} is the theoretically determined intensity value at the i^{th} step and the summation is performed over entire data points. During the refinement the refinable parameters are adjusted so that S_y of equation 2 becomes minimum for obtaining a best fit between calculated and experimental patterns. Refinable parameters are composed of structural and profile parameters. Structural parameters include atomic coordinates, site occupancy and temperature factors whereas profile parameters include the zero position of the diffractometer and peak shape.

Factors determining a successful refinement is based on the minimum values of R factors defined as [13]:

$$R_p = \left[\frac{\Sigma \left|Yi\ (Observed) - \left(\frac{1}{c}\right) Yi(Calculated)\right|}{\Sigma\ Yi\ (Observed)}\right] \quad (3)$$

$$R_{wp} = \left[\frac{\Sigma Wi\ (Yi\ (Observed) - \left(\frac{1}{c}\right) Yi(Calculated))^2}{\Sigma Wi\ (Yi\ (Observed))^2}\right] \quad (4)$$

$$R_{exp} = \left[\frac{(n+p+c)}{\Sigma Wi\,(Yi\,(Observed))^2}\right]^{1/2} \quad (5)$$

where R_p denotes profile factor, R_{wp} is the weighted profile factor, R_{exp} is the expected profile factor, c is the number of constraints, p is the number of variables and n is the number of observations. For successful refinement $1 < R_{wp} = 2\ R_{exp}$. The ratio of R_{wp} and R_{exp} is denoted by χ (equation 6) and is used as a quality of fit

$$\chi^2 = (R_{wp} / R_{exp})^2 \quad (6)$$

The Rietveld refinement in this thesis is using GSAS with EXPGUI interface and FULLPROF program. Using this software one can perform the refinement of both X-ray and Neutron diffraction data.

2.3.3. Field emission scanning electron microscopy (FESEM)

FESEM is used extensively to study the morphology of the surface of any material. The image produced has a three-dimensional appearance. The micrographs obtained are due to the atomic number difference and the topological variations present in the sample. Using FESEM we can obtain detailed information about the shape and uniformity of its grains, its surface topology, particle size and regularity of pattern arrays [14–16].

FESEM consists of electron generated from a field emission source. Using a high electrical field gradient electrons are accelerated. Inside a high vacuum tube, a high energy focused electron beam is obtained by passing it through a series of magnetic lenses. This focused beam strikes the sample and releases secondary electrons. The surface morphology of the material is determined by the velocity and the angle with which the secondary electrons are emitted. The secondary electrons are received by detector which counts and amplifies it to obtain the electronic signal. The electronic signal is amplified and converted into a video scan-image visible on a monitor (Fig. 4). The electron beam is moved over the

surface of the specimen using a set of scanning coils in order to acquire the image of the surface under investigation. The image can be magnified from 10 to 3000000 times using FESEM. The surface morphology of the samples in this research have been analysed using FEI INSPECT F50 scanning electron microscope. The average grain size of the samples reported in this thesis were calculated by measuring the grains in different regions and taking their average.

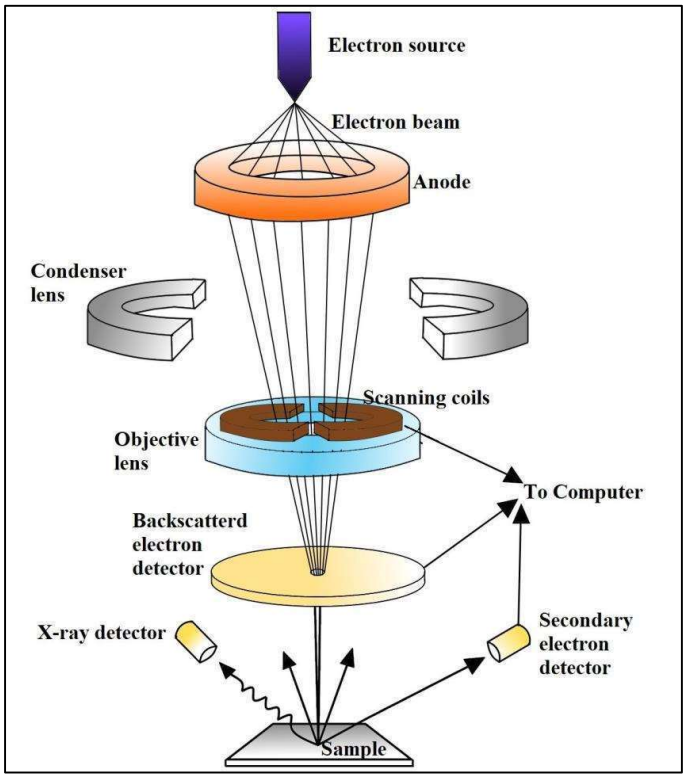

Fig. 4: *Schematic diagram of FESEM.*

2.3.4. Energy dispersive spectroscopy (EDAX):

In EDAX a low count energy dispersive X-ray spectrum is produced which provides the elemental composition of each point of measurement. In EDAX the atoms are

excited by a narrow beam of electron which produce X-rays distinctive of elements present. As the atomic structure of every element is unique so the X-rays emitted by each element can be distinguished from one another. Electrons occupy discrete energy levels inside an atom. If the incident beam has enough energy, it may excite an electron from inner shell which gets ejected from the shell leaving behind a hole in its position. Electron from any higher energy shell may occupy the hole that was produced releasing the difference in the energy in the form of X-rays. The emitted X-rays can be analysed using energy dispersive spectrometer. For every element the X-rays are distinct owing to their different atomic structure, so the elemental composition of the sample can be studied from the X-rays that are produced. The relative concentration of each element present at the point of measurement is calculated from the total intensity of obtained X-rays. The EDX measurement of the samples reported in this thesis were performed using BRUKER EDS system attached with FEI INSPECT F50 scanning electron microscope.

2.3.5. Fourier transform infrared spectroscopy (FTIR):

The FTIR spectroscopy is based on the phenomena of vibration of chemical bonds present in a sample as a result of the interaction between the sample and electromagnetic radiation in the infrared (IR) region. If the IR energy incident on the sample is in resonance with the energy of its chemical bonds than the energy couples with that of the sample. The variation in the incident beam intensity is recorded before and after its interaction with the sample. Either reflection or transmission experiments are used to detect the incident radiation. In the IR spectrum the variation of intensity with frequency is recorded. As the infrared spectrum is unique for every molecular structure so FTIR can be used to characterize materials, study its molecular structure, its molecular surroundings. The transmittance or the absorption peaks in the FTIR spectrum is associated with the frequency of vibration of atomic

bonds present in the sample. Presence of different functional groups in the sample can be investigated from the peaks obtained in the FTIR spectrum.

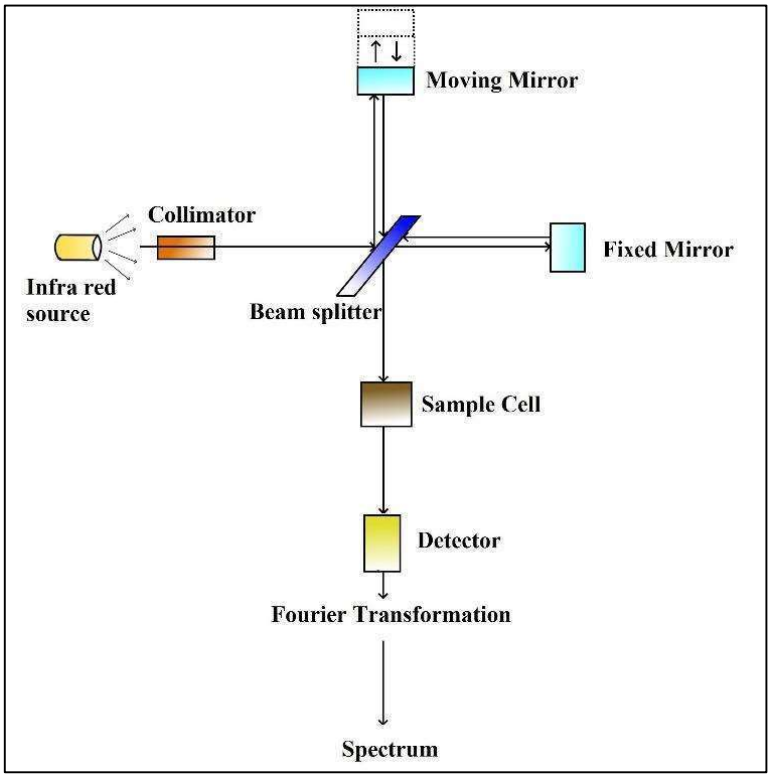

Fig. 5: *Schematic diagram of FTIR instrument.*

The main part of the FTIR instrument is the Michelson type interferometer. IR radiations from the source are collimated and made to fall on the beam splitter (Fig. 5). Ideally half of the radiation is transmitted by the beam splitter to a moving mirror and it refracts the remaining half of the radiation to a stationary mirror. The radiations from both the mirror are reflected back to the beam splitter. The beams reflected from the stationary and the moving mirror has optical path difference which causes interference on recombining at the beam splitter. The optical path difference created by the moving mirror is twice the

displacement of the mirror. The recombined beam then falls on the sample and passes on to the detector. An interferogram is obtained by the detector where the interference signal is measured as a function of optical path difference. Fourier transform of the interferogram is performed by a computer to obtain the spectrum for quantitative analysis. The FTIR spectrums of the samples in the present work were recorded in room temperature using KBr pellet technique in between wavelengths 450 to 1400 cm^{-1} with Perkin-Elemer FT-IR instrument.

2.3.6. Raman Spectroscopy:

The basic principle of Raman spectroscopy is the inelastic scattering of monochromatic light by the sample, resulting in the change in its photon frequency. Laser source emits a monochromatic light which falls on the sample. Some of the photons from this incident light are absorbed by the sample before being emitted again. The emitted photon frequency is either shifted up or down in comparison to the frequency of the incident photons and is termed as the Raman effect. This change in the photon frequency is associated with the material's rotational, vibrational and low frequency modes. Raman effect usually occurs in the ultraviolet to visible region of the energy spectrum. When a monochromatic beam having frequency f_0 is incident on the sample, two types of scattering take place which are Raman and Rayleigh scattering. Raman scattering is weaker than the incident beam and has frequency $f_0 \pm f_m$, where f_m frequency of vibration of the molecule. Rayleigh scattering being elastic has the same frequency as the incident beam. Raman scattering consists of Stokes line having frequency $f_0 - f_m$ and anti-Stokes line having frequency $f_0 + f_m$ [17]. During Raman scattering electrons moves to virtual energy state lying below E_1 (excited electronic state). In Stokes line the transition of electrons takes place from lower vibrational energy state in comparison to anti- Stokes line. As the lower energy level 0 has a greater number of electrons

as compared to energy level 1 so the intensity of Stokes lines is more as compared to anti-Stokes lines (Fig. 6). In the Raman Spectra the Stoke lines are usually reported.

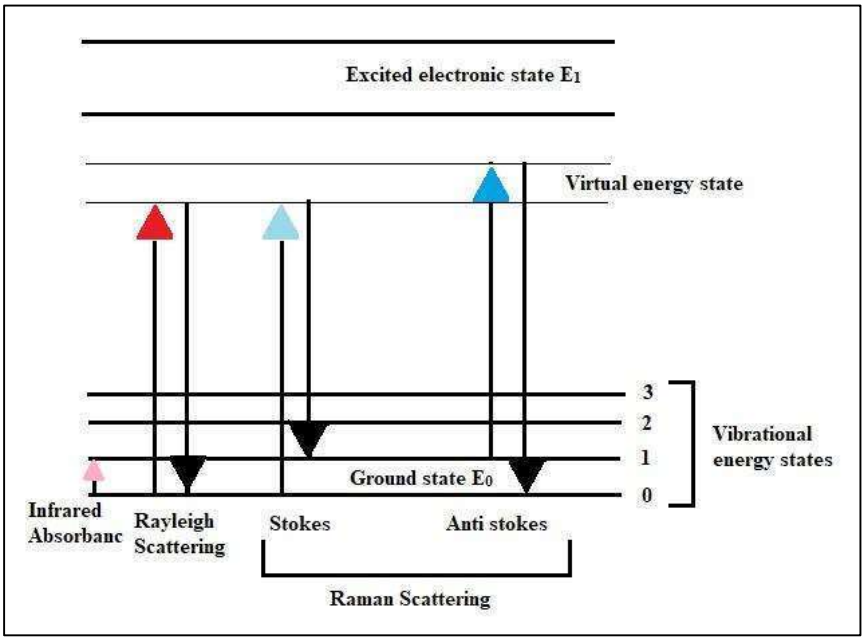

Fig. 6: *Different types of scattering in Raman spectroscopy*.

In a crystal or a molecule, the atomic bonds are not rigid. Change in the susceptibility of the medium due to vibrations gives rise to the Raman effect. Vibrations are associated with the material and inelastic scattering which involves coupling of incident photons and excitation of quasiparticle present in the sample (electronic single particle, magnons and phonons). In solids crystals the phonons give rise to the Raman effect. The number of Raman modes present depends on the crystal symmetry of the material. Crystal orientation of an anisotropic crystal can be determined from the Raman spectroscopy. A unit cell of a crystal having *n* number of atoms contain *3n* number of lattice vibrational modes from which *3* modes are acoustic and *3n–3* modes are optical. The optical modes consist of IR, Raman and

silent modes. Raman spectroscopy is complementary to Infrared spectroscopy as variation in the dipole moment of a molecule is associated with IR spectroscopy whereas variation in the polarizability of the molecule is associated with Raman spectroscopy. IR spectroscopy is associated with the change in the electron's vibrational state within a given energy state. As per the exclusion principle for centrosymmetric structure a given mode cannot be both IR and Raman active. The lattice vibration modes present in a sample can be determined from its group factor analysis depending on the Wyckoff sites of the atoms present in the sample [18]. The Raman spectra of the samples reported here have been recorded using WITEC alpha 300 R instrument.

2.3.7. Optical absorption and emission study:

The optical properties of the samples have been investigated with the help of UV (PerkinElmer UV-vis spectrometer) and Photoluminescence (Shimadzu RF-5301PC) spectroscopic analysis. The experimental band gap of the samples has been calculated with the help of its optical absorption spectrum in the UV region. The UV vis spectrum arises from the absorption of electromagnetic waves in the visible and ultraviolet region by the sample. The PL spectra in perovskites arises due to the electron transition from the valence band (composed of the 2p orbitals occupied by the oxides) to the conduction band (containing empty d orbitals present in the transition metals) by absorption of photon. The transition from the ground to the excites state is non radiative whereas the reverse transition from excited to ground state is radiative in nature i.e. luminescence. As the energy is provided by the photons it is termed as photoluminescence.

2.3.8. Alternating Current Impedance Spectroscopy (ACIS):

ACIS technique is widely employed for studying the material's dielectric properties [19–21]. It can be used to investigate the motion of mobile or bound charges in the grain or

grain boundary regions of various solids like semiconductors, ionic solids and dielectrics. The basic parameters measured by this technique are capacitance (C), conductance (G), impedance (Z) and phase angle (ϕ) at different frequency range for any given temperature. From these measured parameters one can calculate the dielectric functions like dielectric permittivity, loss tangent, complex impedance and ac conductivity. For the dielectric measurement the samples are pelletized into discs using a high pressure of 140 MPa. The discs are then polished and electrodes are developed on the two flat surfaces by applying silver paste and drying it. The disc is than placed in the sample holder of the LCR meter connected with a temperature controller (Eurotherm 2216 e) to perform the dielectric measurement. The ACIS measurements of the samples were performed using Hioki 3532 LCR meter. The measurements were carried out in the frequency range of 40 Hz to 5 MHz and at discrete temperatures between 333 to 573 K.

Different types of relaxation process exist in perovskite oxides as a result of different energy barriers present in them. These energy barriers exist in the sample due to the formation of point defects during the processing of the samples. Thus, the relaxation mechanism deviates from the ideal Debye model arising from the dipole-dipole interaction [22]. In case of insulators and semiconducting materials the dielectric relaxation mechanism consists of conductivity relaxation mechanism and dipolar relaxation mechanism. In case of dipolar relaxation arising from the dipole motion, it can be described using either of the models: Debye, Cole-Cole, Havriliak-Negami, Davidson-Cole depending on their relaxation mechanism [23–28]. The dielectric data in this work has been analysed using Cole-Cole and Havriliak-Negami model in the framework of impedance, dielectric permittivity, electric modulus and ac conductivity formalism [24,27,28] as discussed in the previous chapter. The conductivity relaxation follows the Jonscher's Power law [29]:

$$\sigma(\omega) = \sigma_{dc}\,[1+ (\omega/\omega_h)^n] \quad (7)$$

where σ is real part of conductivity, σ_{dc} is dc conductivity, ω angular frequency, ω_h hopping frequency and n is a constant having values between 0 to 1.

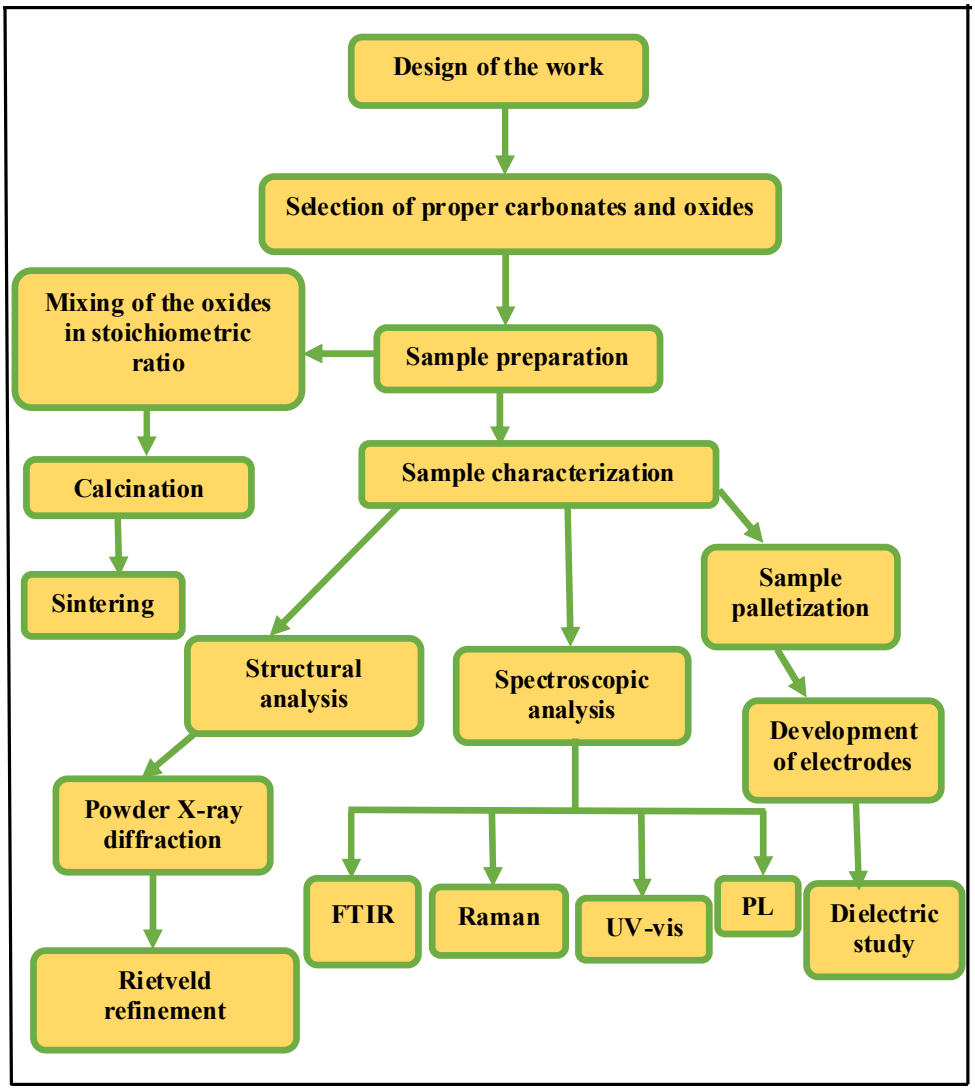

Flow chart of the methodology scheme adapted.

Reference

[1] R. R. Chromik, W. K. Neils, E. J. Cotts, J. Appl. Phys. 86 (1999) 4273–4281.

[2] H. Yokokawa, N. Sakai, T. Kawada, M. Dokiya, Solid State Ion. 52 (1992) 43–56.

[3] J. Šesták, G. Berggren, Thermochim. Acta 3 (1971) 1–12.

[4] K. Uchino, Manufacturing Methods for Piezoelectric Ceramic Materials, Woodhead Publishing in Materials (2017) 385–421.

[5] Charles Kittel, Introduction to Solid State Physics, John Wiley Sons. Inc., New York (1997).

[6] H. P. Klung, L. E. Alexander, X-ray diffraction procedures, John Wiley Sons. Inc., New York (1954).

[7] A. R. West, Solid State Chemistry and Its Applications, Wiley, UK (1991).

[8] R. E. Dinnebier, S. J. L. Billinge, Principles of Powder Diffraction: Theory and Practice, The Royal Society of Chemistry, UK (2008).

[9] R. Jenkins, X-Ray Techniques: Overview, John Wiley & Sons, USA (2006).

[10] V. K. Pecharsky, P. Y. Zavalij, Fundamentals of Powder Diffraction and Structural Characterization of Materials, Springer, US (2009).

[11] A. C. Larson, R. B. Von Dreele, General Structure Analysis System (GSAS), Los Alamos National Laboratory, Report LAUR (2000) 86–784.

[12] J. Rodriguez-Carvaja, Physica B 192 (1993) 55–69.

[13] R. A. Young, The Rietveld Method International Union of Crystallography, Oxford University Press (1993).

[14] J. R. Jurado, M. T. Colomer, J. R. Frade, J. Am. Ceram. Soc. 83 (2000) 2715.

[15] F. D. Morrison, D. C. Sinclair, A. R. West, J. Appl. Phys. 86 (1999) 6355.

[16] S. Ananta, N. W. Thomas, J. Eur. Ceram. Soc. 19 (1999) 2917.

[17] J. R. Ferraro, K. Nakamoto, C. W. Brown, Introductory Raman Spectroscopy, Academic Press, New York (2003).

[18] D. L. Rousseau, R. P. Bauman, S. P. S. Porto, J. Raman Spectrosc. 10 (1981) 253.

[19] J. R. Macdonald, Impedance Spectroscopy emphasizing solid materials and systems, John Wiley and sons, New York (1987).

[20] A. Dutta, C. Bharti, T. P. Sinha, Physica B. 403 (2008) 3389.

[21] A. Dutta, C. Bharti, T. P. Sinha, Mater. Res. Bull. 43 (2008) 1246.

[22] A. K. Jonscher, J. Phys. D: Appl. Phys. 13 (1980) 89.

[23] P. Debye, Polar Molecules, Chemical Catalogue Company, New York (1929).

[24] K. S. Cole, R. H. Cole, J. Chem. Phys. 10 (1942) 98.

[25] D. W. Davidson, R. H. Cole, J. Chem. Phys. 18 (1950) 1417.

[26] D. W. Davidson, R. H. Cole, J. Chem. Phys. 19 (1951) 1484.

[27] S. Havriliak, S. Negami, J. Polym. Sci.: Part C 14 (1966) 99.

[28] S. Havriliak, S. Negami, Polymer 8 (1967) 161.

[29] A. K. Jonscher, Universal Relaxation Law, Chelsea Dielectric Press, London (1996).

Chapter – 3

Structural, optical and electrical characterization of Ba_2YbTaO_6

3.1. Introduction:

Double perovskite oxides are the most promising functional material in the field of electronics as well as electrical technology as they can have different types of chemical composition, various crystal structure and their dependent physical properties [1–3]. Amalgamation of different physical properties in a single material is the most exigent task for material scientists and perovskite oxides have given this opportunity [4]. However, most binary, ternary or quaternary compounds contain lead which is extremely toxic by nature. In the last few decades, the progress of electronics as well as electrical technology is based on the continuous effort to develop smart and eco-friendly materials. Lead being a toxic material, other alternatives like lead free dielectric materials are need to be developed [5–9]. The conventional chemical formula of the double perovskite oxides is $A_2B'B''O_6$ [10].

An extensive survey of the literature on ytterbium based double perovskite oxides shows that, the ac electrical properties of very few are reported. The structural properties of Ba_2LnTaO_6 (where Ln is a trivalent lanthanide) in temperature between 82 K and 723 K have been reported by Hammink et al. [11]. Konopka et al. [12] have reported the dielectric permittivity of Ba_2YbTaO_6 in the microwave frequency range and its magnetic susceptibilities and the electron paramagnetic resonance measured between 5 K and room temperature have been reported by Taria et al. [13]. However, the detailed analysis of the variation of the electrical parameters like dielectric permittivity, loss tangent, impedance and conductivity with temperature and frequency of 'Barium Ytterbium Tantalum Oxide' (Ba_2YbTaO_6, BYT) has not yet been reported in the low frequency region.

Here we have used the solid-state reaction route to synthesize the BYT sample. The structural, optical, vibrational and electrical properties of BYT have been reported in this

paper. Alternating Current Impedance Spectroscopy (ACIS) technique was utilized for measuring the dielectric properties of BYT which was measured using the frequency between 42 Hertz and 1 Megahertz and temperatures between 303 K and 623 K.

3.2. Experimental:

Stoichiometric amount of Barium Carbonate (Ba_2CO_3, Loba, Extra pure), Ytterbium oxide (Yb_2O_3, Sigma-Aldrich, 99.9%) and Tantalum Pentoxide (Ta_2O_5, 99.9%) were mixed using acetone (Merck) in an agate motor for 12 hours and then placed in a Platinum crucible and calcined at 1500° C for about 8 hours. The mixture was then cooled at a rate of 100° C/h and brought down to 30° C. The palletization of the powdered mixture was done after mixing it with a small amount of polyvinyl alcohol which acts as a binding agent. The sintering of the pelletized disc, having 7.46 mm diameter and 1.4 mm thickness, was done at 1550° C for 12 hours. The sintered sample was then brought down to 30° C by cooling it at a rate of 1° C/min.

The powder x-ray diffraction (PXRD) pattern was obtained by keeping the Bragg's angle between $10^o \leq 2\theta \leq 120^o$ and by using Cu-Kα radiation. The PXRD data was recorded at room temperature with step scanning size of 0.02. The surface morphology and homogeneity of BYT was studied with a scanning electron microscope (SEM). For the dielectric measurement, the disc of the sample was polished and a conductive silver electrode on each side of the sample disc were developed and then fired. In order to perform the dielectric measurements LCR meter (HIOKI-3532, Japan) was used.

3.3. Results:

3.3.1. Structural investigation:

The tolerance factor t of BYT has been calculated using $t = \frac{rA+r0}{\sqrt{2}\,(rB+r0)}$, where, r_A, $r_{B\,[=(r_{B'}+r_{B''})/2]}$ and r_0 are the ionic radii of the constituent A, B and O site ions, respectively [14]. The calculation has been made considering the Shannon ionic radii [15]. The tolerance factor t for BYT is 0.99. This value of t agrees well with that of the cubic structure which has no driving force to deform them to a lower symmetry thus no octahedral tilt is expected in the system. The Rietveld refinement of the PXRD pattern of BYT (Fig. 1) was performed using the FULLPROF program [16]. The refined PXRD profile has been denoted by the continuous line in Fig. 1 whereas the experimental data are represented by the scattered symbols and their difference is represented by the blue line at the bottom. The Bragg's positions are depicted within first bracket corresponding to each peak position. The flat nature of the difference between the refined PXRD profile and the experimental data suggests the phase formation with cubic phase and $Fm\bar{3}m$ $\left(O_h^5\right)$ space group.

Fig. 2 shows the crystal structure of BYT with YbO_6 and TaO_6 octahedra being represented in different colours. The PXRD fitting, structural parameters and Yb–O–Ta bond angle is given in Table 1. From Fig. 2 it can be clearly seen that no tilt is present in both the YbO_6 and TaO_6 octahedra. For BYT the average grain size is 7.609 μm which has been determined by the Debye-Scherrer's equation: $D_{hkl} = K\lambda/\beta\cos\theta$. The inset of Fig. 1 depicts the SEM image of BYT having average grain size of 7.78 μm. It can thus be concluded that our calculated result agrees well with the experimental data. The compactness of the grains in the SEM image points toward the high density of the prepared sample. The theoretical density of the sample is 8.165 g cc^{-1}. The density of BYT pellet measured using the

Archimedes principle is 8.092 g cc^{-1}, indicating negligible amount of porosities present in the sample disc. The chemical constituents of BYT have been depicted in the EDAX spectrum [the inset of Fig. 3].

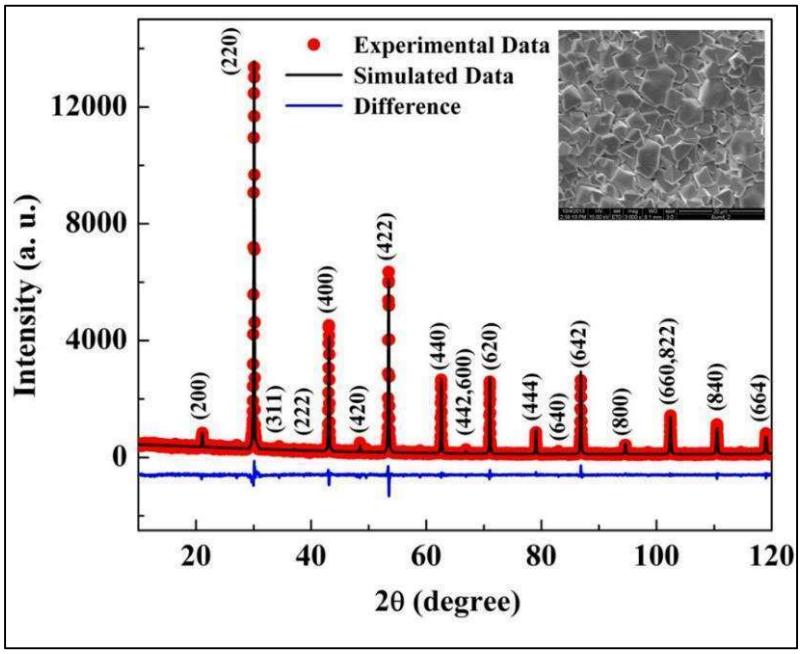

Fig. 1: *Rietveld refinement plot of BYT where the experimental points are represented by symbols and the line represents the simulated PXRD data. SEM micrograph is in the inset.*

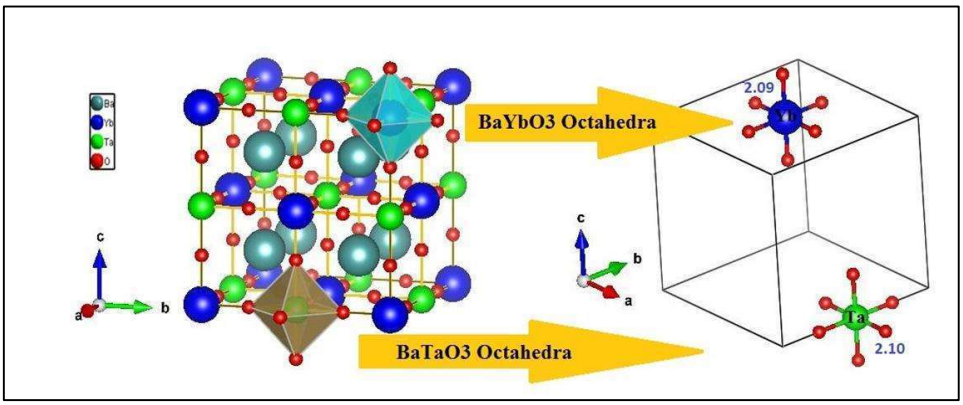

Fig. 2: *The structure of BYT obtained from the Rietveld refinement.*

Table 1. XRD fitting and structural parameters.

Atom	Wyckoff position	x	y	z	B	Bond length (Å)	BVS
Ba	8c	0.25	0.25	0.25	0.090	Ba–O(×4)=2.96463(3)	1.912
Yb	4a	0.0	0.0	0.0	0.074	Ba-O(×8)=2.96(7)	1.912
Ta	4b	0.5	0.5	0.5	0.774	Yb-O(×4)=2.08789(3)	3.642
O	24e	0.25(1)	0.0	0.0	1.000	Yb-O(× 2)=2.09(9)	
						Ta-O(× 4)=2.10466	
						Ta-O(×2)=2.10(9)	

Cell parameters: a = b = c = 8.38510(14) Å; Rwp = 15.2; Rexp = 8.87; Rp = 15.6; χ^2 = 2.95, (Yb-O-Ta)= 180° (4)

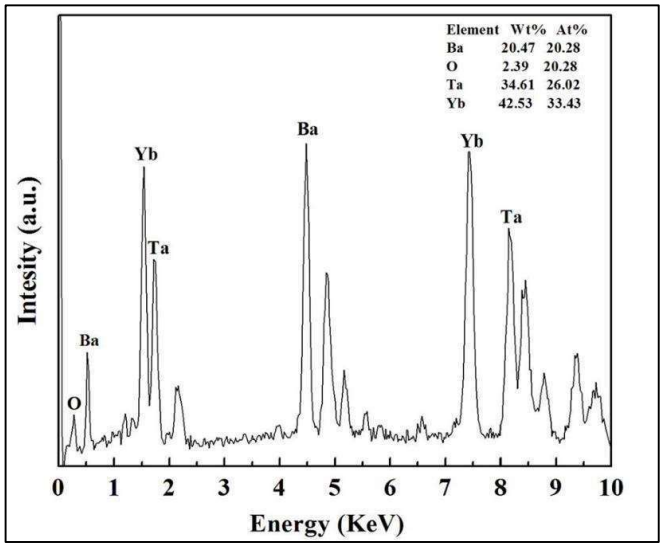

Fig. 3: *EDAX spectrum of BYT.*

3.3.2. UV-visible Spectroscopic analysis:

Fig. 4 demonstrates the UV-visible absorption spectrum of BYT from which the optical band gap (E_g) of BYT has been determined using the Tauc's relation [17]

$$[F(R) * h\upsilon] = C [h\upsilon - E_g]^n \quad (1)$$

where the Kubelka-Munk function is represented by F(R), hυ is the incident photon's energy, C is a constant, and n indicates the nature of the sample transition. The optical absorbance of a sample can be calculated from its reflectance by using F(R): $F(R) = \frac{(1-R)^2}{2R}$, where R is the reflectance %. At the linear absorption edge a tangent is drawn in the graph and from the intersection of the tangent with the abscissa the value of E_g for BYT is calculated to be 3.95 eV.

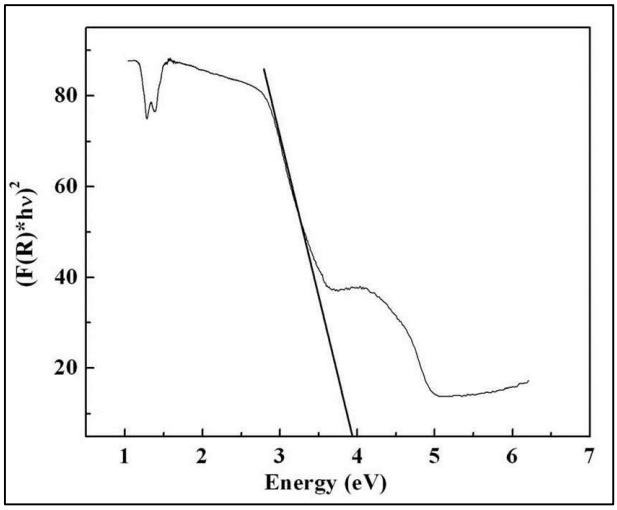

Fig. 4: *The UV-visible absorption spectrum of BYT.*

3.3.3. Photoluminescence Spectroscopic Study:

The photoluminescence (PL) emission spectrum was obtained by keeping the excitation wavelength fixed at 316 nm and is shown in Fig. 5. From the PL spectra we

observe a strong, intense peak at around 414 nm which arises due to the direct transition of electron to conduction band (CB) from the valance band (VB). Another shoulder hump at around 438 nm is due to the dangling bonds associated with the BYT microstructure. These dangling bonds may increase the surface states within the band gap of the material. The electrons originating from the bulk BYT fill up the mid-gap states till the Fermi level. The charge accumulation at the surface creates a depletion region resulting in the development of an electric field which causes the bending of the edges of valance band and conduction band. Trap levels are created by these types of band structures and the electron goes from VB to CB via this trap level. The peak at around 438 nm is due to trap related recombination of electron that originates from the structural defects. Photoluminescence excitation (PLE) measurement has been performed keeping the emission wavelength fixed at 414 nm, which is shown in Fig. 6. In the PLE spectra it is observed that the exitonic peak is at 316 nm which is very close to the excitonic peak of the UV -Vis spectra.

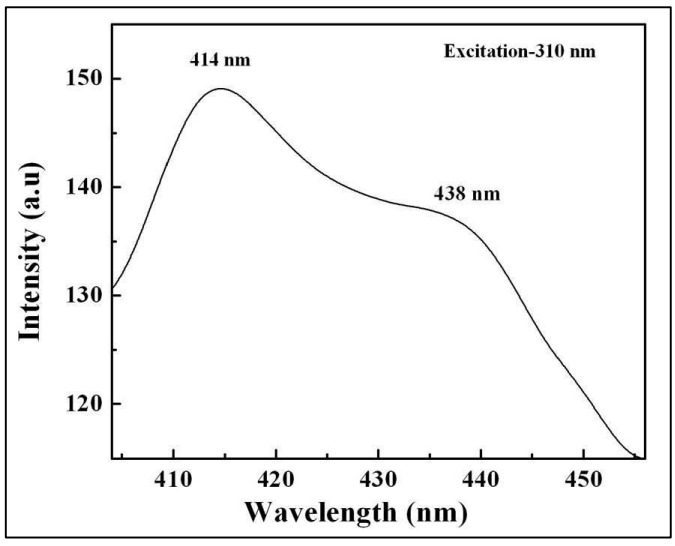

Fig. 5: *The photoluminescence emission spectra of BYT.*

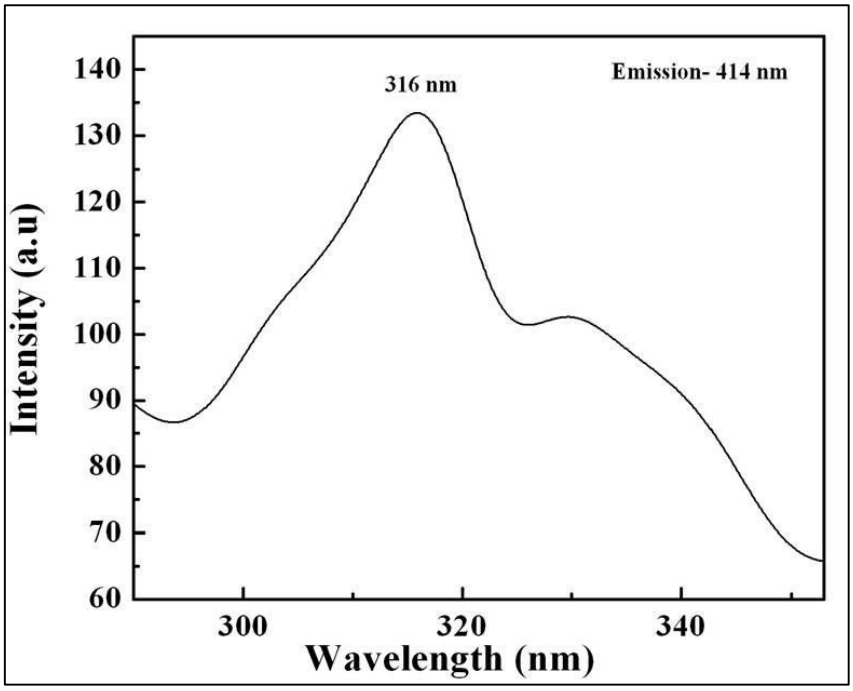

Fig. 6: *The photoluminescence excitation spectra of BYT.*

3.3.4. FTIR analysis:

In order to study the chemical bonding present in BYT we have performed the Fourier transform infrared (FTIR) spectroscopy (Fig. 7) where three bands are detected at 577 cm^{-1}, 1440 cm^{-1} and 1642 cm^{-1}. The results agree well with the predictions of group theory for a cubic perovskite structure [18]. The absorption peaks represent the vibrational coupling between various coordination polyhedral present in BYT. The asymmetric stretching vibration of TaO_6 octahedral is indicated by a strong peak at about 577 cm^{-1} [19]. The FTIR bands matches well with that reported for cubic $A_2B'B''O_6$ type perovskites [20–24]. The weak band at about 1440 cm^{-1} is due to the overtones of the fundamental vibrations present within BYT and small bands around 1642 cm^{-1} arises because of the carrier KBr $(H_2O)_n$.

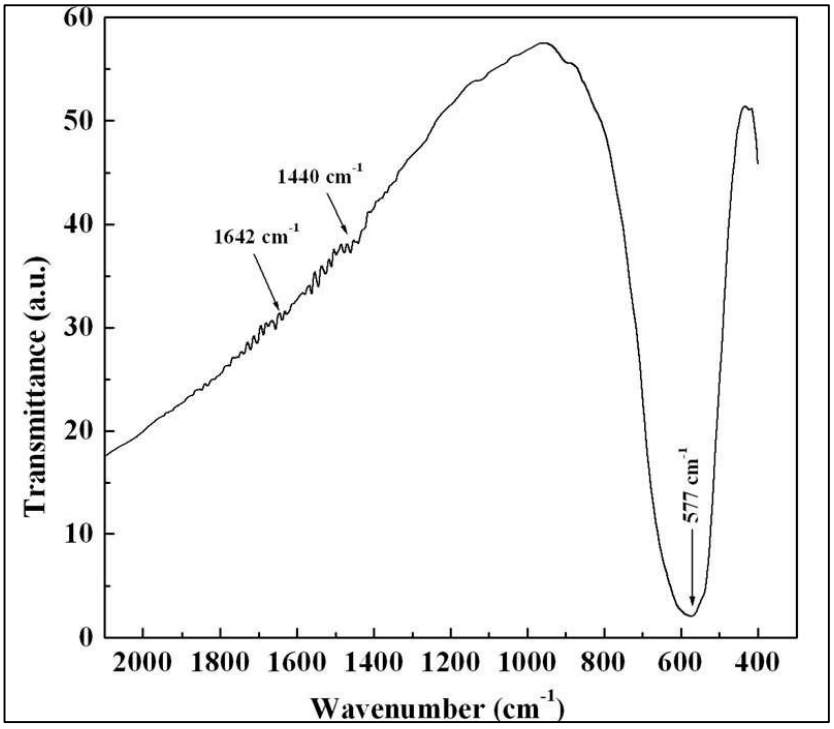

Fig. 7: *FTIR spectrum of BYT.*

3.3.5. Impedance analysis:

Fig. 8 illustrates the impedance formalism at temperatures 453 K and 483 K which has been analysed for understanding the relaxation behaviour of BYT. Two deformed semi-circular arcs are present in the complex impedance plot for each temperature. The smaller semi-circular arc is detected in higher frequency side whereas the larger semi-circular arc is detected in lower frequency side which point towards the role of both grain boundary (lower frequency side) and grain (higher frequency side) in contributing to the total impedance. The depressed or deformed semi-circular arc in the Nyquist plot is due to the non-Debye type relaxation mechanism which is attributed to the possibility of polydispersive nature of BYT.

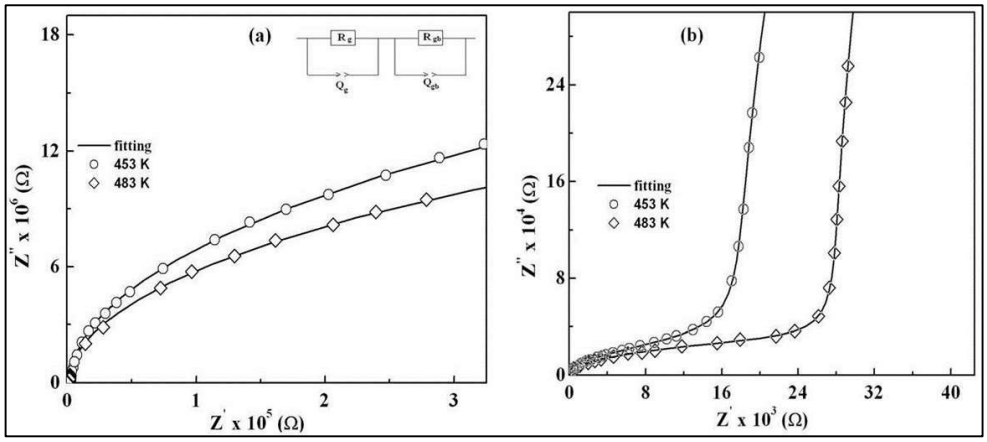

Fig. 8: *The complex impedance plane plots between Z'' and Z' for BYT.*

The Debye type relaxation has only one relaxation process with definite relaxation time whereas non-Debye type relaxation involves multiple relaxation processes having different relaxation time, which leads to a distribution in the relaxation times of the dipoles present in the sample. This polydispersive nature can be probed from the Nyquist plot of the sample. In case of Debye type relaxation, the semi-circular arc's centre is located in the Z′ axis whereas for the relaxation of non-Debye type as in case of our sample the centre lies well below the Z′ axis [25]. Thus, the relaxation phenomena that our sample exhibits is polydispersive in nature. Here the non-Debye relaxation process arises due to the charge carriers that are distributed in-homogeneously around grain-boundaries causing local variation of resistances in those regions [26].

The experimental curve has been simulated using a comparable circuit consisting of two parallel resistor-capacitor (RC) components joined together in series. By definition the total impedance consists of real ($Z^{'}$) and imaginary ($Z^{''}$) parts which can be written as [27, 28]:

$$Z' = \frac{R_g}{1+(\omega R_g C_g)^2} + \frac{R_{gb}}{1+(\omega R_{gb} C_{gb})^2} \quad (2)$$

$$Z'' = R_g\left[\frac{\omega R_g C_g}{1+(\omega R_g C_g)^2}\right] + R_{gb}\left[\frac{\omega R_{gb} C_{gb}}{1+(\omega R_{gb} C_{gb})^2}\right] \quad (3)$$

Here R_g and C_g denotes the grain's contribution to the resistance and the capacitance whereas R_{gb} and C_{gb} denotes the grain-boundary's contribution to the resistance and the capacitance. According to this model the phase angle $\tan\theta = Z''/Z'$, is not constant and is frequency dependent. In the complex Z-plane plot of our sample, it has been observed that at lower frequency side (Fig. 8 (b)) it is almost straight line (independent of frequency) which means that the phase is constant. So, there exist a discrepancy between the Cole-Cole model and the Nyquist plot of our present sample and some modifications are required in the Cole-Cole model. The pure capacitor cannot explain this vagueness thus in the Cole-Cole equation the pure capacitor has to be substituted using a constant phase element (CPE). From the theory of CPE, the capacitance is written as $C=Q^{1/n}\,R^{[(1-n)/n]}$, where Q and R are the constant phase element and the resistance associated with the grain boundaries (R_{gb}, Q_{gb}) and the grains (R_g, Q_g). The deviance from ideal capacitive behaviour is denoted by n. For n = 0 the behaviour is purely resistive and for n = 1 the behaviour is purely capacitive in nature. The modified Cole-Cole equation in terms of CPE is as follows:

$$Z' = \frac{R_g}{1+\left[\omega(R_g Q_g)^{\frac{1}{n_g}}\right]^2} + \frac{R_{gb}}{1+\left[\omega(R_{gb} Q_{gb})^{\frac{1}{n_{gb}}}\right]^2} \quad (4)$$

$$Z'' = R_g\left[\frac{\omega(R_g Q_g)^{\frac{1}{n_g}}}{1+\left[\omega(R_g Q_g)^{\frac{1}{n_g}}\right]^2}\right] + R_{gb}\left[\frac{\omega(R_{gb} Q_{gb})^{\frac{1}{n_{gb}}}}{1+\left[\omega(\ _{gb} Q_{gb})^{\frac{1}{n_{gb}}}\right]^2}\right] \quad (5)$$

The experimental data has been fitted using equations (4) & (5) and is denoted by solid lines as shown in Fig. 8. In Table 2 the different fitting parameters for 453 K and 483 K are tabulated. The Nyquist plots have been fitted considering CPE instead of pure capacitance of the electrical circuit. The experimental and the fitted curves agrees well with each other

confirming the non-ideal nature of the capacitance which results from the multiple relaxation processes for a given relaxation time [29]. The value of 'n' in the fitted parameters as seen in Table 2, indicates the deviation from the ideal Debye process. The RC equivalent circuit for the complex impedance has been shown in the inset of Fig. 8 (a). The Nyquist plot of BYT confirms the involvement of both grain boundary and grain to the overall impedance, each having different values of resistances which gives rise to non - Debye type relaxation process. The presence of polycrystalline grains and their grain boundaries are well observed in the SEM image of BYT.

Table 2. The various fitted parameters of the impedance circuit

Temp.(K)	R_g (10^4 Ω)	Q_g (10^{-10} F/Ω)	n_g	R_{gb} (10^7 Ω)	Q_{gb} (10^{-10}F/Ω)	n_{gb}
453	2.8	29	0.72	5	10	0.64
483	1.8	68	0.65	3.6	7.86	0.57

3.3.6. Dielectric formalism:

The Fig. 9 (a) & (b) illustrates the angular frequency (ω) dependent dielectric permittivity (ε') and loss tangent (tan δ) curves. The relaxation of ε' is associated with the dipole′s oscillation in an ac field which can be examined using Debye theory [30]. From Fig. 9 (a) it has been observed that for ε', two distinct regions of dispersion are present. The interfacial polarization is responsible for dispersion when the frequency is low [31]. Dielectric properties are strongly dependent upon the grain size and the interfacial polarization. In the low frequency region, the dielectric value is dependent upon the conductivity of grain boundaries. If the sizes of the grain boundaries are large, they give rise to large dielectric values. The dielectric permittivity value decreases as the frequency increases as the charge exchange are unable to follow the applied field. The change in

dielectric permittivity is almost negligible when the frequency is high as the electronic and the atomic polarization governing the dielectric permittivity values are independent of the variations in temperature and frequency. The dielectric permittivity increases with temperature when the frequency is low as the interfacial and dipolar polarization are dependent on temperature. Thus, the dielectric dispersion in the sample is due to the existence of the grain and grain boundary interface.

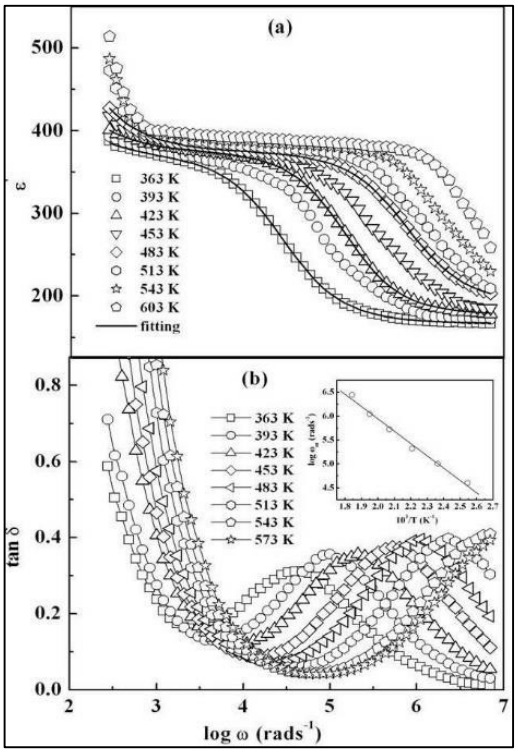

Fig.9. (a) *Frequency dependence of ε' (a) and tan δ (b) of BYT at various temperatures, where the solid lines are the Cole-Cole fit to the experimental data which are represented by symbols. Arrhenius plot of most probable relaxation time is shown in the inset of (b).*

It can be seen from Fig. 9 (a), that at lower frequencies the dipoles trail the applied alternating field and $\varepsilon' = \varepsilon_s$ whereas on increasing the frequency the dipoles start lagging behind the field and the ε' value decreases. The characteristic frequency where $\omega = (1/\tau)$, the ε' value suddenly decreases signifying a relaxation process. On increasing the frequency to a very high value the dipoles cannot trail the field and ε' attains a constant value $\varepsilon' \approx \varepsilon_\infty$. At low frequencies the ε' varies considerably with temperature. In the region of dispersion for ε' a relaxation peak is observed in the loss tangent curve. On increasing the temperature, the peak in the loss tangent curve starts shifting towards higher frequency region because more polarization occurs at higher temperature and eventually leading to relaxation at higher frequency. This shifting of tan δ peak with temperature point towards a temperature dependency of the dielectric relaxation of BYT. In our sample the existence of dc conductivity (σ_{dc}) is indicated by the dramatic change in tan δ at the low frequencies. According to ideal Debye relaxation process a kink is expected to appear in tan δ which is attributed to the monodispersive relaxation process. But in our present sample the broad nature of the loss tangent peaks points towards a polydispersive behaviour of the relaxation process.

In the loss tangent curve, the peak position gives the value of the relaxation time τ_m (= $1/\omega_m$). It is observed that ω_m satisfies the Arrhenius law,

$$\omega_m = \omega_0 \exp\left[-\frac{E_a}{K_B T}\right] \quad (6)$$

Here E_a represents the activation energy and ω_0 is a constant. The inset of Fig. 9 (b) is a plot between log ω_m and 1000/T, where the experimental data are represented by the symbols and the straight line denotes the least squares fit of the experimental data points. The value of E_a = 0.51 eV as calculated from the Arrhenius plot suggests that the hopping of p-type polaron is responsible for the conduction mechanism of BYT [32–35]. It can be seen from the Table 2

for the fitted parameters of the impedance spectra that the resistance for the grain boundaries is very large in comparison to that of the grains. Thus, the grain boundaries provide a barrier to the charge transport acting as a trap for the charge carriers [29]. The oxygen anions surrounding the cations can be considered isolated from one another as the overlapping of the charged clouds is very small. This localization leads to the formation of polaron. The charge transport occurs between the nearest neighbour sites by hopping of charged particles in between the localized sites. The occupancy of the trap centres decreases as the frequency increases endorsing the hopping of the charge carriers which leads to the increase in the conductivity. In our case the behaviour of the grain boundaries as the trap centres leads to the conduction process by polaron hopping. The Cole-Cole model has been utilized for examining the polydispersive behaviour of the relaxation process of BYT as illustrated in Fig.10 [36]

$$\varepsilon^* = \varepsilon' - i\varepsilon'' = \varepsilon_\infty + \frac{\varepsilon_s - \varepsilon_\infty}{[1+(i\omega)^{1-\alpha}]} \quad (7)$$

Here ε_s denotes the low frequency quasi-static value and ε_∞ denotes the high frequency value of dielectric permittivity, the difference $(\varepsilon_s - \varepsilon_\infty)$ gives the dielectric relaxation strength, τ denotes relaxation time and α gives the variation of relaxation times having values amid 0 and 1. When α value is 0 it signifies ideal Debye relaxation and when $\alpha > 0$ it signifies a deviation from ideal Debye relaxation having different relaxation times. Equating real and imaginary parts of equation (7), [37]

$$\varepsilon' = \varepsilon_\infty + \left(\frac{\varepsilon_s - \varepsilon_\infty}{2}\right) \times \left\{1 - \frac{\sinh((1-\alpha)\ln(\omega\tau))}{(\cosh((1-\alpha)\ln(\omega\tau)) + \cos((1-\alpha)\frac{\pi}{2}))}\right\} \quad (8)$$

$$\varepsilon'' = \left(\frac{\varepsilon_s - \varepsilon_\infty}{2}\right) \times \left\{1 - \frac{(\sinh((1-\alpha)\frac{\pi}{2}))}{(\cosh((1-\alpha)\ln(\omega\tau)) + \cos((1-\alpha)\frac{\pi}{2}))}\right\} \quad (9)$$

A sharp increase is observed in both ε' and ε" at low frequencies which arises due to contribution of electrical conduction. Thus, a contribution term for the electrical conductivity needs to be added to the Cole-Cole equation which becomes

$$\varepsilon^* = \varepsilon_\infty + \left(\frac{\varepsilon_s - \varepsilon_\infty}{1+(i\omega\tau)^{1-\alpha}}\right) - j\frac{\sigma^*}{\varepsilon_0\omega^s} \quad (10)$$

where s represents a constant quantity having values between 0 and 1 and σ* ($\sigma^*=\sigma_1+\sigma_2$) represents the complex electrical conductivity with σ_1 as dc conductivity and σ_2 as the conductivity for the space charges. Dividing equation (10) into real and imaginary parts,

$$\varepsilon' = \varepsilon_\infty + \frac{(\varepsilon_s-\varepsilon_\infty)\,[1+(\omega\tau)^{1-\alpha}\,\sin(\alpha\frac{\pi}{2})]}{1+2(\omega\tau)^{1-\alpha}\,\sin(\alpha\frac{\pi}{2})+(\omega\tau)^{2-2\alpha}} + \frac{\sigma_2}{\varepsilon_0\omega^s} \quad (11)$$

$$\varepsilon'' = \varepsilon_\infty + \frac{[(\varepsilon_s-\varepsilon_\infty)\,(\omega\tau)^{1-\alpha}\,\cos(\alpha\frac{\pi}{2})]}{1+2(\omega\tau)^{1-\alpha}\,\sin(\alpha\frac{\pi}{2})+(\omega\tau)^{2-2\alpha}} + \frac{\sigma_1}{\varepsilon_0\omega^s} \quad (12)$$

From equation (11) and (12) it is clear that ε' is associated with the space charge conductivity (σ_2) and ε" is associated with the dc conductivity (σ_1). In Fig. 9 (a) and Fig. 10 solid lines represent the fitted curve which has been obtained with the help of equations (11) and (12) for temperatures 363 K, 423 K and 483 K. The parameters utilized for fitting are presented in Table 3.

The characteristic relaxation time can be calculated by $\tau_m = \omega_m^{-1}$. The variation of ω_m of ε" with temperature (inset of Fig. 10) follows the Arrhenius law from which the value of E_a is found to be 0.50 eV, which is nearly equal to that calculated from the Arrhenius plot for tan δ. In Fig. 11 the scaling behaviour of ε" is depicted where ε" is scaled by ε''_m and ω by ω_m. Here ε''_m is the peak value of the ε" versus log ω curve. The coinciding curves indicate that same mechanism is followed for relaxation process at different temperatures. In the scaled curves the overlapping does not occur at low frequencies because the dipoles can trail the field applied at low frequencies.

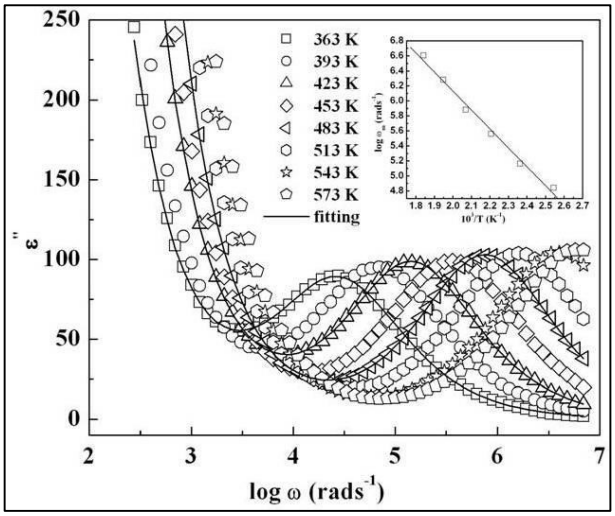

Fig. 10: *Frequency dependence of ε" at various temperatures for BYT where the solid lines are the Cole-Cole fit to the experimental data which are represented by symbols. Arrhenius plot of most probable relaxation time is shown in the inset.*

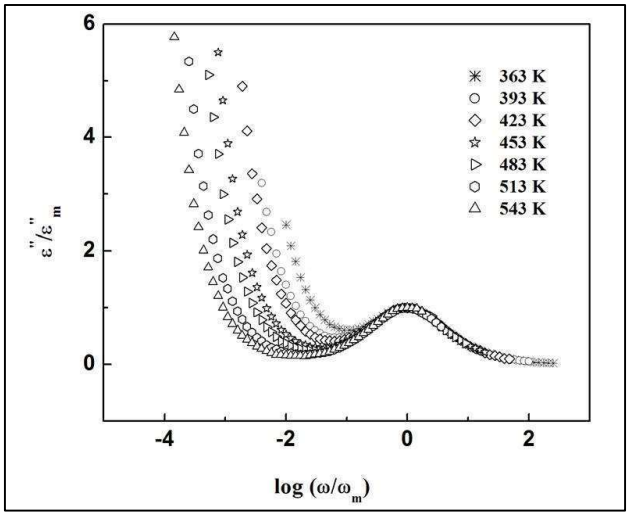

Fig. 11: *Scaling behaviour of ε" at various temperatures.*

Table 3. The various fitting parameters of modified Cole–Cole equation.

Temp. (K)	$\varepsilon_s - \varepsilon_\alpha$	ω_m (KHz)	α	σ_1 (Sm^{-1})	n
363	251	27.54	0.15	4.3×10^{-8}	0.95
393	185	69.38	0.15	5.6×10^{-7}	0.95
423	225	145.21	0.14	8.7×10^{-7}	0.96
453	290	363.65	0.13	1.06×10^{-6}	0.95
483	300	765.50	0.15	1.31×10^{-6}	0.95
513	303	1591.72	0.15	1.67×10^{-9}	0.94
543	299	3999.86	0.14	1.99×10^{-6}	0.95
573	267	5782.51	0.15	2.36×10^{-6}	0.95

Electronic and ionic polarization together plays the key role in determining the dielectric property of the material. For a given ion, electronic polarization is constant but the ionic polarization depends on the crystal structure as ionic polarization occurs due to the lattice vibrations. There exists a correlation between the bond valence sum (BVS) and the dielectric property of a cubic perovskite. The correlation of the dielectric property with the BVS of the B-site cation has been reported by Lufaso et al. [38]. The ions with smaller BVS gives rise to larger ionic polarization as for the ions with longer and weaker bonds polarization can be achieved easily. The BVS values of BYT are mentioned in Table 1. It may be noted that the BVS values of BYT is comparatively smaller than its Niobium based counterpart Ba_2YbNbO_6 as reported by Maity et al. [35] as the Ta-O bond length is comparatively larger than Nb-O bond length. The dielectric permittivity values for BYT are significantly large as compared to that reported by Maity et al. as the Ta-O bond length being

weaker; the polarization can be easily achieved. In this way the lattice vibrations associated with the crystal structure strongly affect the dielectric permittivity values.

3.3.7. Conductivity formalism:

Fig. 12 depicts the angular frequency variation of ac conductivity of BYT at several temperatures and it consists of two plateaus indicative of two processes involved in the bulk conduction behaviour. It can be observed in Fig. 12 (a) that as the frequency is decreased the conductivity becomes constant at a certain value called the dc conductivity (σ_{dc}). At low frequency the periodicity of the electric field is very low as a result the accumulation of charge carriers takes place which contributes to the dc conductivity (σ_{dc}) [39]. The spectra of conductivity versus frequency follows Jonscher power law [40]

$$\sigma = \sigma_{dc}\left[1 + \left(\frac{\omega}{\omega_H}\right)^n\right] \quad (13)$$

here ω_H is the frequency of hopping of charge carriers, n is a frequency exponent and σ_{dc} is the dc conductivity. The changeover from the slow rise of conductivity (σ_{dc}) at lower frequency region to sudden change in the conductivity at higher frequency region suggests the onset of conductivity relaxation process.

Table 4. The various fitting parameters of conductivity spectra.

Temp. (K)	Low frequency plateau			High frequency plateau		
	σ_{dc} (Sm^{-1})	ω_H (rad s^{-1})	n	σ_{dc} (Sm^{-1})	ω_H (rad s^{-1})	n
363	2.702×10^{-8}	530	1.98	1.21×10^{-4}	268600	0.6
483	10.502×10^{-8}	4000	1.98	4.00×10^{-3}	2563454	0.67

This ac conductivity behaviour of the present sample can be easily analysed using jump relaxation model [41]. When $\omega < \omega_H$ the charge carriers travel very slowly throughout the crystal lattice so they can hop between one site to another resulting in the dc conductivity (σ_{dc}). Again, at high frequency ($\omega > \omega_H$) power law becomes $\sigma(\omega) \propto \omega^n$ which causes a sharp rise in the conductivity value. Fig. 12 (b) illustrates the fitted conductivity spectra of BYT at 363 K and 483 K which has been fitted using equation (13). The value of n in the low frequency region lies between $1 < n < 2$ whereas n lies between $0 < n < 1$ in the high frequency region as shown in Table 4.

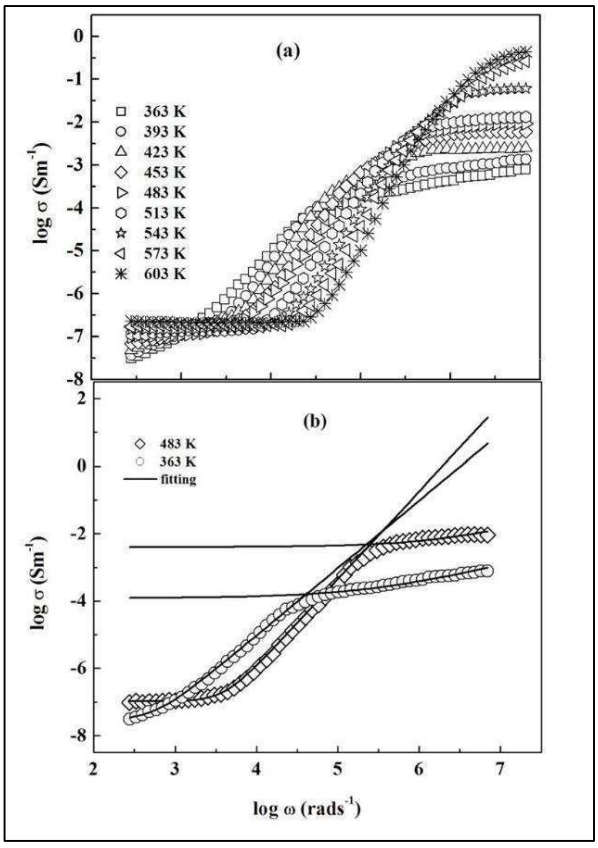

Fig. 12:*(a) Frequency dependence of the conductivity (σ) for BYT at various temperature and the fittings (b) of power law for the same at 363 K and 483 K has been shown by solid lines.*

The frequency variation of conductivity results from the hopping of charged particles trough trap sites separated by different potential barriers. The conductivity variation becomes independent of frequency when a charge carrier moves along a lattice comprised of similar potential well. The conductivity value increases with frequency and finally saturates at high frequency when the charge carrier hops back and forth in a double well having infinite barrier on each side. A system consisting of potential well with different barrier height as in case of our sample, the conductivity spectra show a step like nature on increasing the temperature. The varied potential barrier heights arise due to the existence of both the grain boundary and the grain.

3.4. Conclusions:

The ceramic method has been employed to synthesize BYT at 1500° C. The analysis of the PXRD pattern of BYT suggests the cubic structure with $Fm\bar{3}m$ space group. The cubic phase of BYT is further confirmed by the three bands obtained in the FTIR spectra which is associated with the $Fm\bar{3}m$ space group. The average grain size of BYT obtained from SEM is 7.78 μm. EDAX shows the uniformity of the sample. The optical band gap of BYT is 3.95 eV which was calculated by means of the UV–visible absorption spectrum. A relaxation behavior is detected in all the temperature region. The presence of two arcs in the Nyquist plot points towards the role of both grain boundary and grain in contributing to the total impedance. The broad nature of the loss tangent peaks points towards the polydispersive nature of the relaxation process. The activation energy value of 0.5 eV as obtained from the Arrhenius plot of the relaxation time indicates that the conductivity and the dielectric relaxation at different temperature is due to the p-type polaron hopping. The existence of two

plateaus in the conductivity plot indicates that in the bulk conduction behaviour two processes are involved for the contribution of both grain and grain boundary.

References

[1] S. N. Putilin, E. V. Antipov, O. Chmaissem, M. Marezio, Nature. 362 (1993) 226–228.

[2] S. Jin, T. H. Tiefel, M. McCornack, R. A. Fastnacht, L. H Chen, Science. 264 (1994) 413– 415.

[3] C. G. Zhong, J. H. Fang, Q. Jiang, J. Phys. Condens. Matter. 16 (2004) 9059–9068.

[4] A.S. Bhalla, R. Guo, R. Roy, Mat Res Innovat. 4 (2000) 3–26.

[5] S. Priya, A. Ando, Y. Sakebe, J. Appl. Phys. 94 (2003) 1171.

[6] I. Levin, J.Y. Chan, J.E. Maslar, T.A. Vanderah, J. Appl. Phys. 90 (2001) 904.

[7] R. Zurmuhlen, J. Petzett, S. Kamba, V. V. Voitsekhovskii, E. Colla, N. Setter, J. Appl. Phys. 77 (1995) 5341.

[8] R. Zurmuhlen, J. Petzelt, S. Kamba, G. Kozlov, A. Volkov, B. Gorshunov, D. Dube, A. Tagantsev, N. Setter, J. Appl. Phys. 77 (1995) 5351.

[9] S. Saha, T.P. Sinha, J. Phys. Condens. Matter. 14 (2002) 249.

[10] A. W. Sleight, R. Ward, J. Am. Chem. Soc. 83 (1961) 1088–1090.

[11] T.S. Hammink, W.T. Fu, D.J.W. IJdo, J. Solid State Chem. 184 (2011) 848–851.

[12] J. Konopka, R. Jose, M. Wołcyrz, Physica C. 435 (2006) 53–58.

[13] N. Taira, Y. Hinatsu, J. Solid State Chem. 150 (2000) 31–35.

[14] V. M. Goldschmidt, Naturwissenschaften. 14 (1926) 477–485.

[15] Shannon RD, Acta Crystallogr. A 32 (1976) 751–767.

[16] J. Rodriguez-Carvaja, Physica B. 192 (1993) 55–69.

[17] J. Tauc, R. Grigorovici, A. Vancu, Phts. Stat. Sol. 15 (1966) 627.

[18] M. Licheron, F. Gervais, J. Coutures, J. Choisnet, Solid State Commun. 75 (1990) 759–763.

[19] R. Ratheesh, H. Sreemoolanadhan, M.T. Sebastian, J. Solid State Chem. 2 (1997) 131.

[20] A.E. Lavat, M.C. Grasselli, E.J. Baran, R.C. Mercader, Mater. Lett. 47 (2001) 194.

[21] A.F. Corsmit, H.E. Hoefdraad, G. Blasse, J. Inorg. Nucl. Chem. 34 (1972) 3401.

[22] G. Blasse, A.F. Corsmit, J. Solid State Chem. 6 (1973) 513.

[23] W. Zheng, W. Pang, G. Meng, Mater. Lett. 37 (1998) 276.

[24] A. Dutta, T.P. Sinha, Integr. Ferroelectr. 116 (2010) 41.

[25] A. Mishra, S. N. Choudhary, R. N. P. Choudhary, V. R. K. Murthy, K. Prasad, J. Mater. Sci: Mater Electron 23 (2012) 185–192.

[26] R. C. Da, Y. G. Yan, Electron. Elements. Mater. 1 (1982) 25.

[27] M. M. Hoque, A. Barua, A. Dutta, S. K. Dey, T. P. Sinha, S. Kumar, Ionics 23 (2017) 471–483

[28] R. Gerhardt, J. Phys. Chem. Solids. 55 (1994) 1491.

[29] S. Halder, Md. Seikh, B. Ghosh, T. P. Sinha, Ceram. Int. 43 (2017) 11097–11108.

[30] P. Debye, Polar Molecules, Chemical Catalogue Company, New York, 1929.

[31] D. N. Singh, D. K. Mahato, T. P. Singha, Physica B, 550 (2018) 400–406.

[32] A. Barua, S. Maity, R. Mondal, S. Kumar, AIP Conference Proceedings 1942 (2018) 110033.

[33] W. H. Jung, J. Appl. Phys. 90 (2001) 2455.

[34] M. Idrees, M. Nadeem, M.M. Hassan, J. Phys. D 43 (2010) 155401.

[35] S. K. Maity, A. Dutta, S. Kumar, T P Sinha, Phys. Scr. 88 (2013) 065702.

[36] K. S. Cole, R. H. Cole, J. Chem. Phys. 9 (1941) 341.

[37] K. Majhi, B. S. Prakash, K. B. R. Varma, J. Phys. D. Appl. Phys. 40 (2007) 7128–7135.

[38] M. W. Lufaso, Chem. Mater. 16 (2004) 2148–2156.

[39] A. S. A. Khiar, R. Puteh, A. K. Arof, Physica B. 373 (2006) 23–27.

[40] A. K. Jonscher: Dielectric Relaxation in solids, Chelsea Dielectrics Press, London, (1983).

[41] K. Funke, Solid State Ionics 94 (1997) 27.

Chapter – 4

Influences of crystal structure, microstructure and adsorbed CO_2 on dielectric properties of Ba_2YbSbO_6-$BaCO_3$ formed by mechanical activation of Ba_2YbSbO_6

4.1. Introduction

Perovskite oxide is one of the fabulous dielectric materials having widespread commercial application in microwave oscillator, radio frequency oscillator, resonator, filter and communication devices [1–8]. However, nowadays there is a huge demand of nanometric materials having high dielectric constant and low dielectric loss for use in high performance miniaturized microwave, radio frequency and energy storage devices. They also have applications in the development of multi-layer capacitors and dynamic random-access memory in smaller structures [9–11]. Research in the area of developing nanometric dielectric materials has been rapidly flourishing in the recent years. In past two decades, the nanometric materials having applications in microwave electronic circuits, optical storage devices, piezoelectric sensors, sonars, transducers and multilayer ceramic capacitors have been developed [9–13]. From application point of view, $BaTiO_3$ is an excellent perovskite oxide. The dielectric properties of nanosized $BaTiO_3$ synthesized by both chemical and high energy ball milling method have been elaborately investigated [9–11, 13]. It may be noted that mechanical milling has been largely employed for the production of nanosized counterparts of bulk samples [14–16]. The strain induced by ball milling creates crystalline defects and surface disorder in nanometric samples synthesized by high energy mechanical milling [17–20]. The dielectric properties of nanosized perovskite oxides prepared by high energy ball milling differs from their bulk counterparts [16, 21–24]. Very few works have been reported on the dielectric properties of nanocomposites of double perovskite oxides synthesized by high energy ball milling method. In this context, we have reported the dielectric properties of Ba_2YbSbO_6 (BYSB) synthesized by solid state ceramic method and a nanocomposite of Ba_2YbSbO_6-$BaCO_3$ (BYSN) synthesized by high energy ball milling of

BYSB. We have shown how the nanocomposite Ba_2YbSbO_6-$BaCO_3$ is formed when Ba_2YbSbO_6 is mechanically activated by high energy ball milling. Further, the effects of crystalline defects, surface disorder and adsorbed CO_2 present in BYSN on its physical properties have been examined.

The nanosized perovskites are known to have applications in the sensing of NO_2 (using $LaFeO_3$), CO (using $LaCoO_3$), alcohols (using $SrFeO_3$), hydrocarbons (using $LnFeO_3$), H_2O_2 and glucose (using $LaNiO_3$). They are also used in dopamine detection (using $LaFeO_3$), solid oxide fuel cells (using $NdFeO_3$) and as catalysts (using $LaFeO_3$) for hydrogen evolution and oxygen reduction reactions [25–33]. In the recent past, the size dependent dielectric properties of nanosized $BaTiO_3$ have been extensively studied due to its high permittivity values and widespread applications in the electronic industry [9–15, 21–23]. The rare earth based double perovskites Ba_2RASbO_6 (where RA is a rare earth element) exhibit interesting dielectric properties [34–37]. The nanosized $BaTiO_3$ and $LaCoO_3$ (synthesized by high energy ball milling method) and nanometric $LaFeO_3$ (prepared by sol-gel method) have shown to adsorb gases like CO_2, CO, NO_2 etc. [14, 15, 25, 26]. There are few reports on crystal structure and dielectric properties of Ba_2YbSbO_6 [38–40]. It is may be noted that the dielectric property of this sample has been investigated at room temperature only. The bulk Ba_2YbSbO_6 synthesized by solid state ceramic method: (i) crystalizes in *R-3* space group with lattice parameter a = 5.9104 Å and α = 59.99°, (ii) exhibits semiconducting behaviour with optical band gap of 3.62 eV and electrical band gap of 2.3 eV (theoretical) and (iii) its room temperature dielectric constant is 14 at 10 KHz [40]. On the other hand, the values of room temperature dielectric constant and loss tangent of nanosized Ba_2YbSbO_6 (of size 20–50 nm) synthesized by combustion method belongs to $Fm\bar{3}m$ space group (a = 8.4618 Å) are its 11.3 and 1.5×10^{-3}, respectively, at 5 MHz [38, 39]. It can be seen from the previous

reports that room temperature dielectric properties of bulk Ba_2YbSbO_6 and its nanometric counterpart differ drastically [38–40]. In this background, we have studied the physical properties of BYSB and BYSN in order to identify the changes in their dielectric properties arising from mechanically induced crystalline defects and surface disorder. Herein, we have reported the (i) crystal structure of BYSB and BYSN, (ii) relaxation mechanism governing their dielectric behaviour and (iii) influence of adsorbed atmospheric gases in determining the physical character and dielectric property of mechanically activated nanosized Ba_2YbSbO_6.

4.2. Experimental

BYSB has been synthesized by the solid-state ceramic method following the standard protocol depicted in literature [41], where the reagent grade (~ 99.9 % pure) powders of $BaCO_3$, Yb_2O_3 and Sb_2O_5 were used. The calcination temperature was 1798 K and the sample was heated for 10 h. The calcined powder was then sintered at 1848 K for 12 h to obtain BYSB. The nanosized BYSN sample was prepared at room temperature (300 K) by high energy ball milling of BYSB for 15 h with the help of Fritsch Planetary Mono Mill (pulverisette 6). Tungsten carbide vials and balls were used where ball to mass ratio was 16:1 and the rotational speed of the mill was 330 rpm.

The X-ray diffraction (XRD) patterns of the samples have been recorded by using Bruker D8 advanced diffractometer in order to confirm the phase purity and obtain the crystal structure of BYSB and BYSN. Both BYSB and BYSN have been thoroughly characterized by field emission scanning electron microscopy (FSEM, FEI Inspect 50), energy dispersive x-ray spectroscopy (EDS), high resolution transmission electron microscopy (TEM, Jeol 2100), FTIR (Perkin Elmer), TGA (Mettler Toledo TG-DTA 85) and Raman spectrometry (WITEC alpha 300 R Raman spectrometer). To carry out the dielectric measurements the pellets of the

samples were prepared using hydraulic press with 140 MPa pressure. For BYSB thickness and diameter of the pellets were 11.92 mm and 1.95 mm, respectively. For BYSN thickness and diameter of the pellets were 8.8 mm and 1.50 mm, respectively. Both the pellets were polished and coated with silver paint on each side. The pellets were then heated at 523 K in order to develop the electrodes for the dielectric measurements. The dielectric measurements were performed using LCR meter (Agilent) at discrete temperatures between 303 K to 663 K and in the frequency range of 40 Hz to 5 MHz. The amplitude of the oscillating voltage was kept at 50 mV during the dielectric measurements.

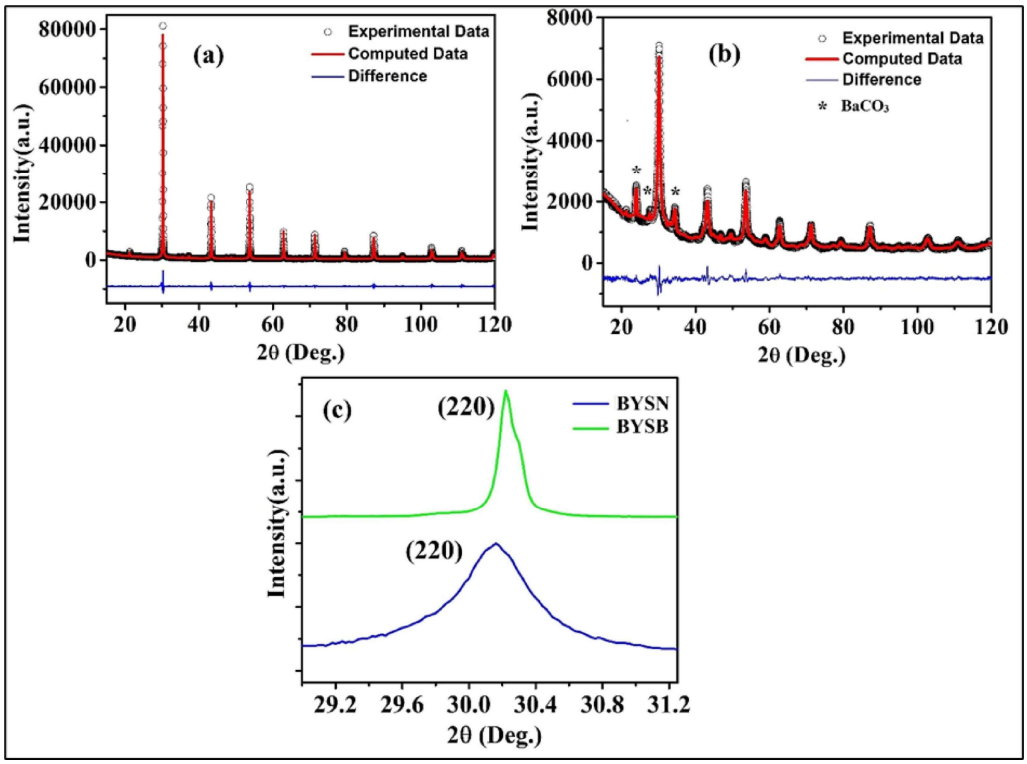

Fig. 1: *Rietveld refinement plots of XRD patterns of (a) BYSB, (b) BYSN and (c) the peak broadening and the shift of (220) peak in the BYSN.*

4.3. Results

4.3.1. Structural study

The XRD pattern of BYSB (Fig. 1(a)) agrees well with that reported earlier [39]. In the XRD pattern of BYSN (Fig. 1(b)) few extra peaks other than the Ba_2YbSbO_6 phase have been observed. It is noteworthy that some extra XRD peaks other than its perovskite phase may appear in Ba containing nanosized perovskite oxides synthesized by high energy ball milling technique [14, 15]. This extra phase arises due to the formation of orthorhombic $BaCO_3$ phase. The extra peaks observed in the XRD patterns of BYSN (Fig.1(b)) other than that of the Ba_2YbSbO_6 phase matches well with the orthorhombic $BaCO_3$ phase. Thus, the XRD pattern of BYSN (Fig.1(b)) indicates the presence of an additional orthorhombic $BaCO_3$ phase in it. The Rietveld refinement of the XRD patterns have been performed using the GSAS software [42]. The crystal structure of Ba_2YbSbO_6 [39] has been chosen as model structure for BYSB. The XRD pattern of BYSN has been analysed by superposing the XRD patterns of Ba_2YbSbO_6 [39] and $BaCO_3$ [14] phases.

The refined and the experimental patterns of both BYSB and BYSN are shown in Fig. 1(a) and Fig. 1(b), respectively. It can be observed from the figures that the experimental patterns match well with the calculated ones. The abundance (weight %) of Ba_2YbSbO_6 (Phase 1) and $BaCO_3$ (Phase 2) in BYSN sample has been determined with the help X'Pert Highscore Plus software using the crystallographic information file generated by the GSAS program [43]. The crystal structure refinement parameters of both the samples are presented in Table 1. The Wyckoff positions and the atomic coordinates of BYSB and BYSN (both Ba_2YbSbO_6 and $BaCO_3$ phases) are given in Table 2 and Table 3, respectively.

Table 1: The Rietveld refinement parameters of BYSB and BYSN.

Parameters	BYSB	BYSN	
		Phase 1 (Ba_2YbSbO_6)	Phase 2 ($BaCO_3$)
Crystal system	Cubic	Cubic	Orthorhombic
Space group	$Fm\bar{3}m$	$Fm\bar{3}m$	*P mcn*
Lattice Parameters (Å)	a = 8.361509(23)	a = 8.37809(25)	a = 5.3038 (11) b = 9.0039 (22) c = 6.5136 (13)
Volume ($Å^3$)	584.593(5)	588.08(5)	311.06 (11)
$\alpha = \beta = \gamma(^o)$	90	90	90
R_{wp}	0.0438	0.0397	
R_p	0.0653	0.0555	
GOF(σ)	2.10	1.71	
Microstrain	2.1800462×10^{-5}	1.3066313×10^{-4}	
Crystallite size (nm)	201.82	19.16	18.73

According to the results of the Rietveld refinement, BYSB is single phase cubic perovskite oxide of $Fm\bar{3}m$ space group with structural formula Ba_2YbSbO_6. On the other hand, BYSN is a nanocomposite composed of two phases: 86.4 % Ba_2YbSbO_6 belonging to $Fm\bar{3}m$ space group and 13.6 % $BaCO_3$ belonging to *Pmcn* space group. The unit cell and the

coordination environment of the constituent cations of BYSB sample are pictorially depicted in Fig. 2 (a) and Fig. 2 (b).

Table 2: The Wyckoff positions and atomic coordinates of BYSB.

Atom	site	x (Å)	y (Å)	z (Å)	B (Å^2)
Ba	8c	0.25	0.25	0.25	0.00687
Yb	4a	0.0	0.0	0.0	0.01255
Sb	4b	0.5	0.5	0.5	0.00183
O	24e	0.2662(11)	0.0	0.0	0.01631

Table 3: The Wyckoff positions and atomic coordinates of BYSN

Atom	site	x (Å)	y (Å)	z (Å)	B (Å^2)
			Phase 1		
Ba	8c	0.25	0.25	0.25	0.00687
Yb	4a	0.0	0.0	0.0	0.01255
Sb	4b	0.5	0.5	0.5	0.00183
O	24e	0.2542(44)	0.0	0.0	0.01631
			Phase 2		
Ba	4c	0.25	0.416	0.756	0.008
C	4c	0.25	0.745	-0.069	0.031
O1	4c	0.25	0.90	-0.076	0.031
O2	8d	0.46610	0.68140	-0.0779	0.031

The unit cell of BYSB consists of 8 Ba^{2+} (at 8c position), 4 Yb^{3+} (at 2a position), 4 Sb^{5+} (at 2b position) and 24 O^{2-} (at 24e position) ions. In the unit cell of BYSB (Fig 2 (a)), A sites are occupied by Ba^{2+} ions and B sites are composed of YbO_6 and SbO_6 octahedra. From Fig. 2 (b) it can be seen that Ba cations are coordinated with 12 oxygen anions and Yb and Sb cations are coordinated with 6 oxygen anions, respectively. The unit cell of BYSB is built up with two pseudocells. Further, it is evident from Fig. 2(c) that the Yb and Sb ions of the B

site are distributed along the (101) plane with repetitive stacking arrangement of Yb–Sb–Yb–Sb ions along the crystallographic c-axis. Thus, BYSB is a 1:1 ordered double perovskite.

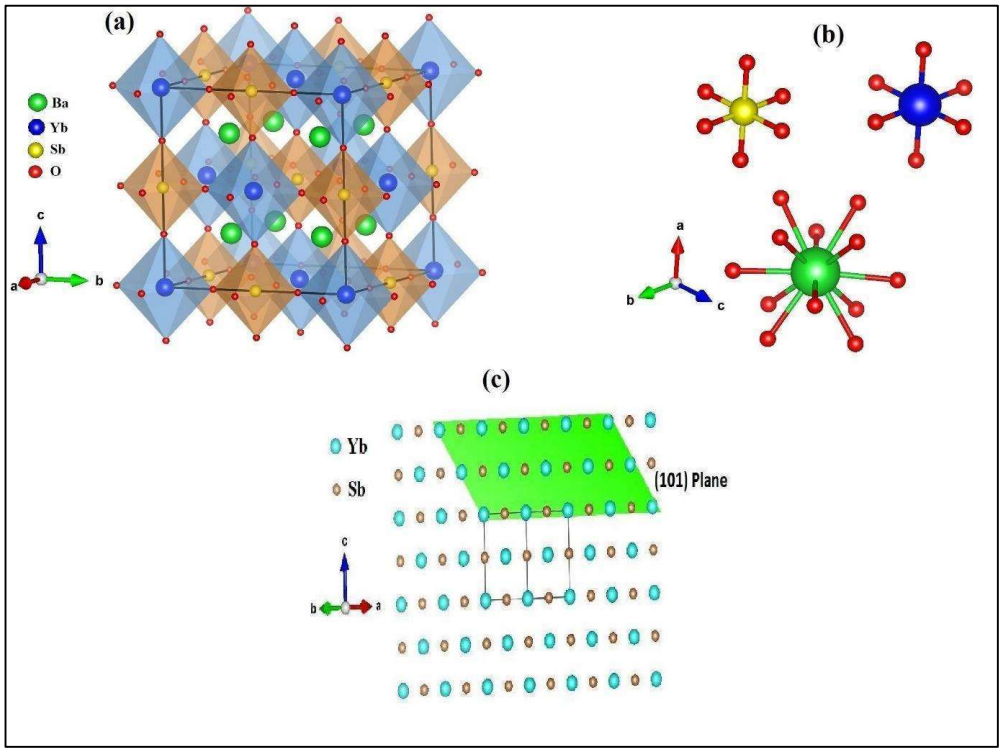

Fig. 2: *(a) Unit cell, (b) coordination environments of Ba^{2+}, Yb^{3+} and Sb^{5+} of BYSB sample and (c) ordering sequences of octahedral B site cations of BYSB along the crystallographic c axis.*

The unit cell and the coordination environment of Ba_2YbSbO_6 phase (Phase 1) of BYSN is similar to that of BYSB (Fig. 3). The unit cell and the coordination environment of the Ba^{2+} ion of $BaCO_3$ phase (Phase 2) of BYSN are depicted in Fig. 4. Each Ba cations are coordinated with 9 oxygen anions. The unit cell of $BaCO_3$ consists of 4 Ba^{2+} (at 4c position), 4 C^{4+} (at 4c position) and 12 O^{2-} ions (4 at 4c and 8 at 8d position). The Ba–O1, Ba–O2, C–

O1 and C–O2 bond lengths for $BaCO_3$ phase of BYSN are 2.726, 2.904, 1.3989 and 1.2812 Å, respectively. In case of BYSB the Ba–O, Yb–O and Sb–O bond lengths are 2.9593 Å, 2.226 Å and 1.955 Å, respectively. For the Phase 1 of BYSN the Ba–O, Yb–O and Sb–O bond lengths are 2.9623 Å, 2.23 Å and 2.06 Å, respectively (Table 4). It is evident that there is a stretching of bond lengths in case of Ba_2YbSbO_6 phase of BYSN as compared to BYSB resulting in the lattice elongation in BYSN as compared to BYSB.

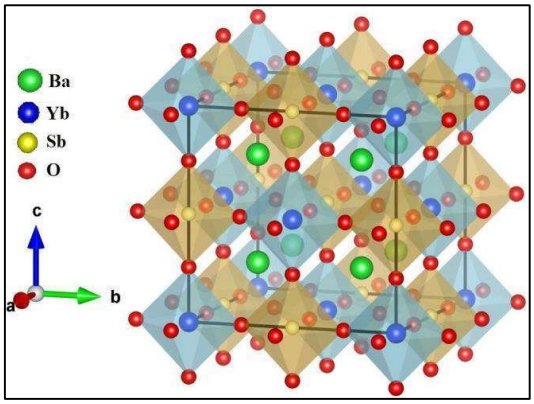

Fig. 3: *Unit cell of phase 1 (Ba_2YbSbO_6) of BYSN.*

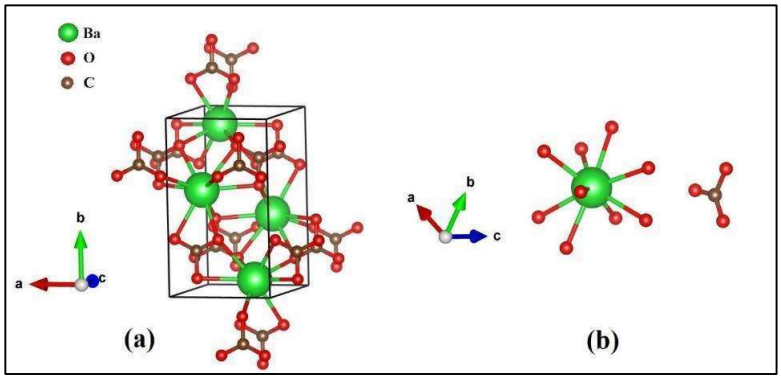

Fig. 4: *(a) Unit cell of Phase 2 ($BaCO_3$) of BYSN, (b) coordination environment of constituent ions.*

Table 4: Metal oxygen bond length of BYSB and Ba_2YbSbO_6 phase of BYSN.

Bond	BYSB Length (Å)	BYSN Length (Å)
Ba – O	2.9593 (5)	2.9623 (5)
Yb – O	2.226 (10)	2.13 (4)
Sb – O	1.955 (10)	2.06 (4)

High energy ball milling reduces particle size significantly, introduces crystalline defects and lattice disorder at the grain boundary of the sample. This leads to the increase in the internal tensile strain in the sample for the elongation or the contraction of its the crystal lattice [44]. As a result of which the XRD peaks of nanometric samples become broadened and gets shifted as compared to its bulk counterparts [44]. For example, the 220 peak of Ba_2YbSbO_6 phase (Phase 1) of BYSN has been broadened appreciably and has shifted towards lower 2θ angle (from 30.22 to 30.16 º) with respect to BYSB (Fig. 1 (c)). This point towards the presence of higher degree of internal tensile strain caused by crystalline defects and surface disorder in Phase 1 of BYSN [44, 45]. The peak broadening also indicates that the crystallites of Phase 1 of BYSN are smaller than BYSB. Thus, as a whole the characteristic peak broadening and reduction in intensity of the XRD peaks of BYSN as compared to BYSB can be ascribed to its nanometric size and stress induced enhancement of its lattice strain caused by high energy ball milling. It may be noted that some amount of energy gets transferred during the milling process from the milling balls to the sample being produced. This energy is responsible for the plastic deformation in nanosized samples leading to various crystalline defects like vacancies, stacking defects and dislocations [46]. It may therefore be inferred that in the present case the crystallite size has been reduced and the

lattice has been substantially elongated in case of Phase 1 of BYSN (Table 1) as a result of high energy ball milling. This agrees with the results of earlier reports on similar samples [47–49]. Moreover, the higher value of micro strain and elongation of lattice volume for Phase 1 of BYSN compared to BYSB (Table 1) confirms that in case of BYSN the lattice has been substantially deformed. In Phase 1 of BYSN, atoms in its lattice sites have been dislocated and plastic defects have been created at the surface of its constituent particles due to high energy ball milling [47, 48]. Similarly, the large broadening and slight shifting of the XRD peaks of $BaCO_3$ phase (Phase 2) in BYSN compared to bulk $BaCO_3$ suggest that the crystallite size of this phase of BYSN has been reduced and plastic defects has been created at its surface. Thus, the crystallites in BYSN are nanometric in size and have crystalline defects and plastic deformations at its surface.

For Ba containing mechanically activated nanosized perovskite oxide, there is a high chance of $BaCO_3$ formation owing to the spontaneous chemical reaction between the sample and the atmospheric CO_2 adsorbed at its surface [14, 15]. In general, the nanometric samples exhibits higher reactivity compared to their bulk counterparts due to their higher surface to volume ratio. Moreover, mechanically activated nanosized sample produced by high energy ball milling tends to exhibit surface phenomena like adsorption of atmospheric gases [15, 16]. Formation of high degree of surface defect prone to chemical reaction is the characteristic feature of the mechanically activated nanosized sample [50]. These features are not usually found in nanometric sample prepared by chemical route. It may therefore be concluded that the nanometric Ba_2YbSbO_6 sample synthesized by ball milling, adsorbs atmospheric CO_2. Further, this sample has active sites prone to chemical reactions due to which a part of Ba present in it reacts with surface adsorbed CO_2 and is converted into $BaCO_3$ when kept in normal atmospheric condition.

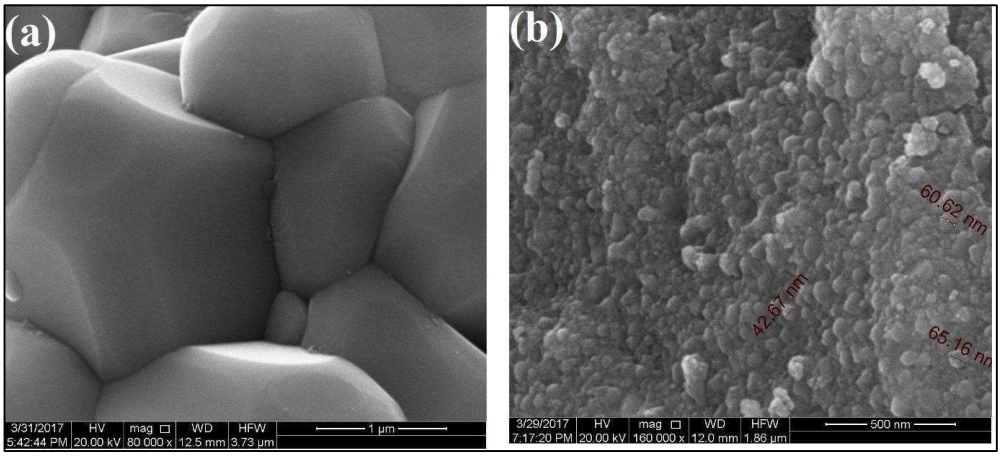

Fig. 5: *The scanning electron micrograph of (a) BYSB and (b) BYSN.*

4.3.2. Microstructural study

The FESEM images of BYSB and BYSN are shown in Fig. 5 (a) and Fig. 5 (b), respectively. The FESEM image of BYSB (Fig. 5 (a)) indicates that the particles in it are nearly hexagonal in shape with well-defined grain and grain boundaries. The particles in BYSB are of assorted size with average grain size of 1.92 μm. It can be seen from the FESEM image of BYSN (Fig. 5 (b)) that the particles in it are irregular shape and assorted size, which are the characteristic features of mechanically milled nanometric samples [50, 51]. The average grain size of BYSN is ~ 50 nm. It may be noted that we have recorded the TEM (Fig. 6) morphograph of a selective single particle of BYSN in order to visualize the lattice fringes and the presence of surface defects in it. In the TEM morphograph of BYSN the lattice fringes and crystalline defects are clearly visible.

The EDS spectra showing the constituent elements of BYSB and BYSN is illustrated in Fig. 7 (a) and Fig. 7 (b), respectively. The presence of carbon in BYSN is quite evident from Fig. 7 (b) whereas no such peak of carbon has been detected in BYSB. The theoretical mass % of Ba, Yb and Sb in BYSB has been calculated using Ba_2YbSbO_6 as its structural

formula (as determined from the results of XRD study) whereas the same for BYSN has been determined considering the ratio of its constituent phases (86.4 % Ba_2YbSbO_6 and 13.6 % $BaCO_3$ as determined from the results of XRD study). As the quantity of lighter elements like oxygen and carbon in a species cannot be accurately determined by EDS, therefore we have compared the theoretical and the experimental mass % of Ba, Yb and Sb only. The experimental and the theoretical values of mass % of Ba, Yb and Sb agree well with each other (Table 5).

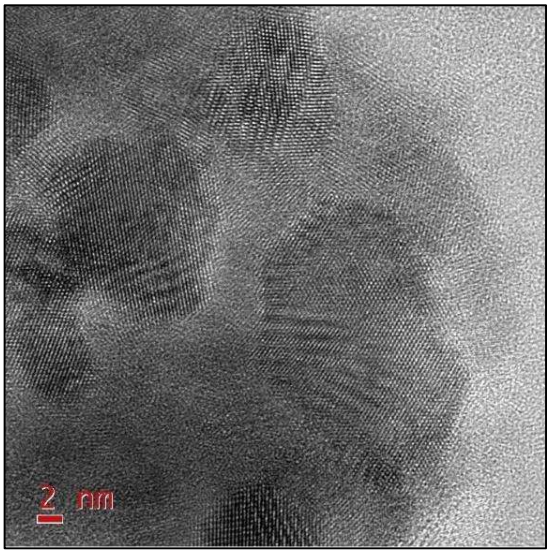

Fig. 6: *TEM image of BYSN.*

Table 5. EDX results of BYSB and BYSN.

Element	BYSB Theoretical mass %	BYSB Experimental mass %	BYSN Theoretical mass %	BYSN Experimental mass %
Ba	41.27	42.05	45.13	44.40
Yb	26	26.15	22.47	23.02
Sb	18.30	17.50	15.81	16.79

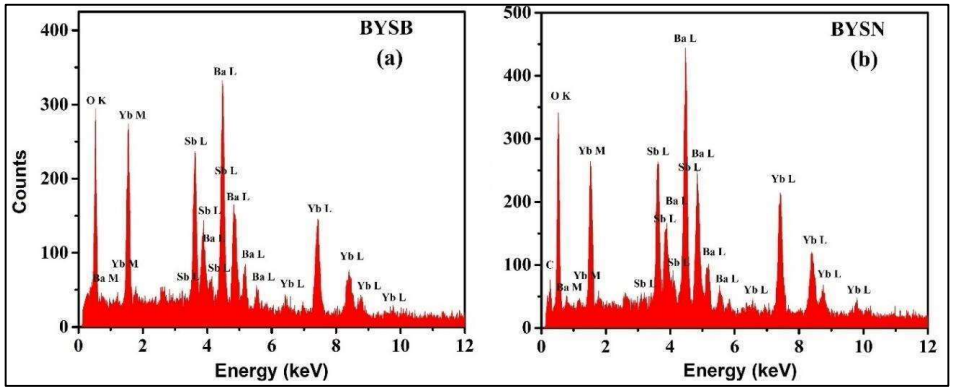

Fig. 7: *EDS spectra of (a) BYSB and (b) BYSN.*

4.3.3. FTIR study

The FTIR spectra of both BYSB and BYSN are illustrated in Fig. 8 (a) and Fig. 8 (b), respectively. The FTIR spectrum of BYSB is in consonance with that of Ba_2YbSbO_6 as reported earlier [38]. In the FTIR spectrum of BYSN some additional peaks for $BaCO_3$ phase have been observed along with the peaks for Ba_2YbSbO_6 phase. For both the samples, the bands for the BO_6 octahedra have been obtained in between 400–600 cm^{-1}. For both BYSB and BYSN the band obtained at around 460 cm^{-1} is associated with the asymmetric bending modes of the Yb–O and Sb–O bonds belonging to SbO_6 and YbO_6 octahedra, respectively. For both the samples the asymmetric stretching modes of the Yb–O bond of YbO_6 octahedra and Sb–O bond of SbO_6 octahedra gives rise to the intense band at around 614 cm^{-1}. The band centred around 772 cm^{-1} in the spectra of both the samples can be ascribed to the symmetric stretching mode of the SbO_6 octahedra [52]. The six Yb–O bonds of YbO_6 octahedra and six Sb–O bonds of SbO_6 octahedra differ slightly in length due to which the FTIR absorption peaks associated with these bonds appear in close proximity. As a result of this the bands due to Yb–O and Sb–O bonds are broad in nature.

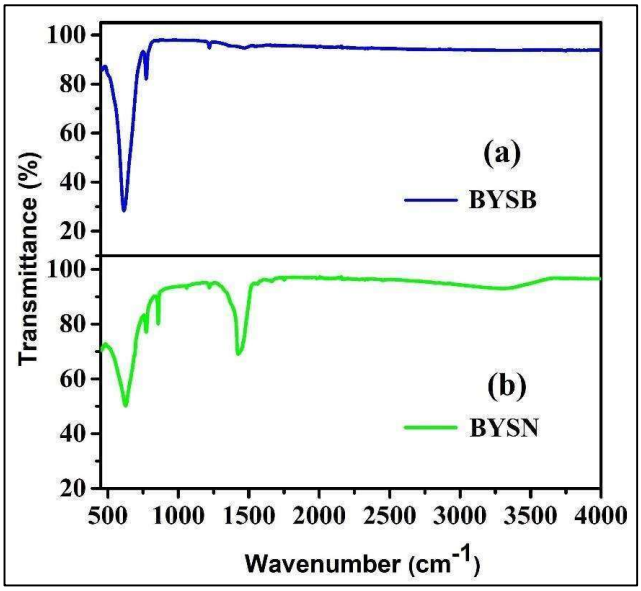

Fig. 8: *The FTIR spectrum of (a) BYSB and (b) BYSN.*

In the FTIR spectrum of BYSN in addition to the bands due to Ba_2YbSbO_6 phase some extra bands have been observed at around 857(s), 1059 (s), 1422 (s) and 3315 (w) cm^{-1}. It may be noted that the XRD and EDS studies have revealed that BYSN is a nanocomposite of Ba_2YbSbO_6-$BaCO_3$. In the FTIR spectrum of BYSN the wavelength of the extra peaks matches well with those of pure $BaCO_3$ [53]. Further, according to the theoretical calculation $BaCO_3$ gives rise to the peaks at ~ 892 and 1010 cm^{-1} due to vibrational modes [54]. Therefore, for BYSN the peaks at about 857 and 1059 cm^{-1} can be attributed to the presence of $BaCO_3$ in it. This further corroborates the results of the XRD and EDS studies. The weak and broad band at around 3315 cm^{-1} arises due to the surface adsorbed CO_2 [55]. The band observed at ~ 1422 cm^{-1} in BYSN can be attributed to the bending mode of the surface adsorbed H_2O and CO_2 [54]. These results indicate that the nanometric Ba_2YbSbO_6 prepared by high energy ball milling method adsorbs arial CO_2 and H_2O [54]. Further, the surface adsorbed CO_2 reacts with a part of Ba of nanometric Ba_2YbSbO_6 to form a nanocomposite of

Ba_2YbSbO_6 and $BaCO_3$. In the milled nanometric sample the existence of large surface area and active sites favours the formation of $BaCO_3$ [54]. Thus, the results of the FTIR study confirms the formation of a nanocomposite of Ba_2YbSbO_6-$BaCO_3$ from mechanically activated nanosized Ba_2YbSbO_6, which corroborates the results of the XRD study.

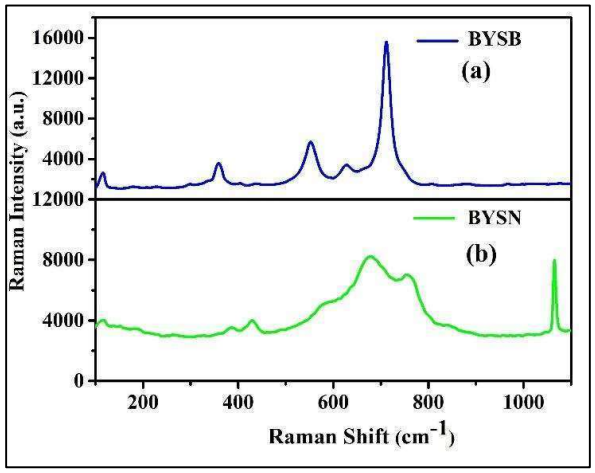

Fig. 9: *The Raman spectra of (a) BYSB and (b) BYSN.*

4.3.4. Raman study

The room temperature Raman spectra of BYSB and BYSN are shown in Fig. 9 (a) and Fig. 9 (b), respectively, and their corresponding Lorentzian peak analysis is illustrated in Fig. 10 (a) and Fig. 10 (b), respectively. The peak positions and the full width at half maxima (FWHM) as obtained from the Lorentzian fitting are presented in Table 6. The spectrum of BYSB is dominated by four strong bands centered at 117, 385, 597 and 772 cm^{-1} along with other weaker bands. These four prominent bands of BYSB matches well with those reported for analogous cubic perovskite oxides like Ba_2YbNbO_6, Ba_2ErSbO_6 and Ba_2YbTaO_6 [56–58]. The Raman modes of BYSB as listed in Table 6 are in consonance with the earlier reports on similar systems [56–58]. The lattice vibrational modes of BYSB have been determined with the help of the group factor analysis using the Wykoff sites of the atoms obtained from the

XRD study (Table 7). The expected phonon modes for BYSB having $Fm\bar{3}m$ space group (O_h^5) are: $\Gamma = A_{1g} + E_g + F_{1g} + 2F_{2g} + 5F_{1u} + F_{2u}$, where the four modes viz., A_{1g}, E_g, $2F_{2g}$ are Raman active, four F_{1u} modes are IR active, F_{1u} is acoustic mode and F_{1g} and F_{2u} are silent modes.

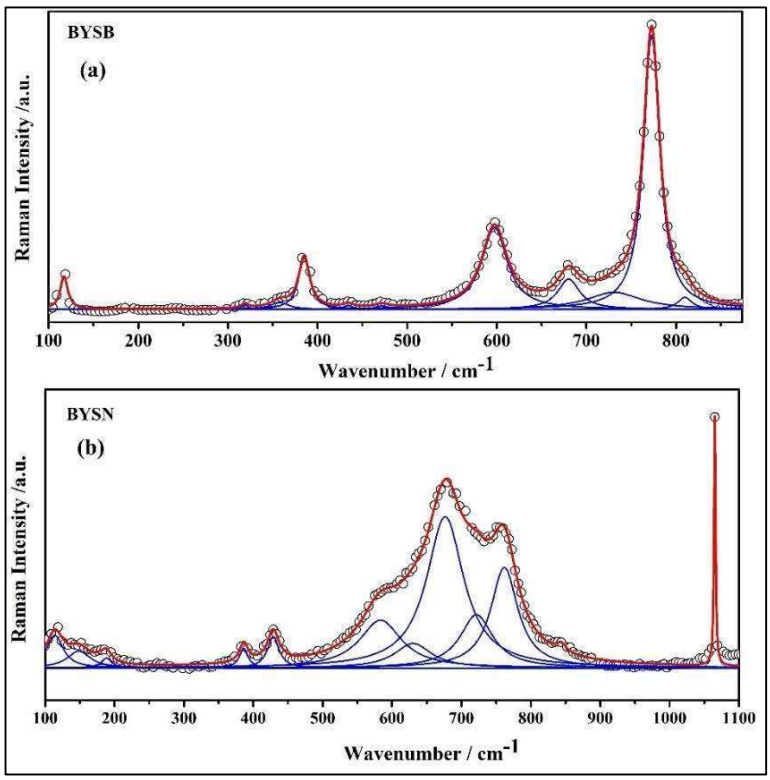

Fig. 10: *The Lorentzian fitting profiles of Raman spectra of (a) BYSB and (b) BYSN.*

The intense peaks at 772 cm^{-1} and 597 cm^{-1} appears due to the vibration of O ions along the Yb–O–Sb bond axis. The peak at around 772 cm^{-1} arises due to the symmetric stretching vibration of SbO_6 octahedra and it corresponds to the A_{1g} mode. The antisymmetric stretching vibration of the SbO_6 octahedra gives rise to the E_g mode at 597 cm^{-1}. The symmetric bending vibration of SbO_6 octahedra corresponding to the F_{2g} mode is obtained at

~ 385 cm^{-1}. The peak at around 117 cm^{-1} corresponds to the F_{2g} mode and arises due to the vibrations of the Ba ions. The weaker bands in the Raman spectra of the samples may be attributed to the second-ordered features [57].

Table 6. Experimental Raman active modes.

Peak No.	BYSB		BYSN	
	Frequency (cm^{-1})	FWHM (cm^{-1})	Frequency (cm^{-1})	FWHM (cm^{-1})
1	117.19936	10.08201	114.0711	29.41374
2	319.11887	9.98758	148.73972	40.88322
3	357.85036	24.13656	181.42688	25.3368
4	385.07184	15.21006	188.6309	18.22145
5	434.03625	13.78611	386.33556	15.13371
6	471.76312	17.07898	428.76496	20.33834
7	597.44298	34.37726	583.41594	73.40917
8	680.31262	29.60329	630.35296	64.69664
9	730.92477	73.53594	676.55511	65.17666
10	772.8061	22.0445	721.80107	57.66746
11	809.97301	19.43274	761.82933	47.39736
12			843.86522	17.42211
13			1065.16	2.66322

Comparing the obtained Raman modes of BYSB with those of Ba_2YbNbO_6 (BYN) and Ba_2YbTaO_6 (BYT) reported earlier [56, 58], it is found that the low frequency modes associated with the vibration of B-site atoms of BYSB are observed at higher wavelength than those of BYT but at lower wavelength than those of BYN. It may be noted that all the

B"-site ions of BYSB, BYN and BYT are pentavalent and their ionic mass is in the order Ta > Sb > Nb. Thus, the shifting of Raman modes of these three samples can be attributed to the difference of ionic mass of their B"-site atoms. The difference in the interatomic forces of BYSB, BYN and BYT are also responsible for the difference in the wavelength of the Raman modes of these samples having analogous structure. The cubic double perovskite is usually characterized by the intense A_{1g} mode whereas the lower symmetry perovskites are usually characterized by the splitting of the F_{2g} modes [58]. There is no splitting of the F_{2g} modes of BYSB which confirms its cubic structure.

Table 7. Distribution of modes for cubic BYSB.

Atom	Wyckoff Site	Symmetry	Distribution of modes
Ba	8c	T_d	$F_{1u} + F_{2g}$
Yb	4a	O_h	F_{1u}
Sb	4b	O_h	F_{1u}
O	24e	C_{4v}	$A_{1g} + F_{2g} + E_g + 2F_{1u} + F_{2u} + F_{1g}$
Γ_{TOTAL}			$A_{1g} + E_g + F_{1g} + 2F_{2g} + 5F_{1u} + F_{2u}$
$\Gamma_{ACOUSTIC}$			$1F_{1u}$
Γ_{RAMAN}			$A_{1g} + E_g + 2F_{2g}$
Γ_{IR}			$4F_{1u}$
Γ_{SILENT}			$F_{1g} + F_{2u}$

In the Raman spectrum of BYSN all the characteristic Raman modes of BYSB are present but their intensity has been significantly reduced due to the lowering of crystallite

size. In case of BYSN besides the peak for Ba_2YbSbO_6 phase, two extra peaks have been obtained around 630 cm^{-1} and 1065 cm^{-1} due to the presence of $BaCO_3$ in it. The wavelength of these peaks agrees well with the Raman spectra of single phase $BaCO_3$ reported in literature [53]. Thus, the results of Raman spectroscopic study are in full agreement with the findings of XRD, EDS and FTIR studies of BYSB and BYSN.

4.3.5. Thermogravimetric study

The thermogravimetric analysis of BYSB and BYSN samples have been carried out in the temperature range of 303–973 K in order to study their thermal stability. The TGA curves of BYSB and BYSN are illustrated in Fig. 11 (a) and Fig. 11 (b), respectively. From the TGA and its derivative curve of BYSB (Fig. 11 (a)) it is evident that the sample releases adsorbed atmospheric moisture at 340 K beyond which no appreciable weight loss has been observed up to 973 K (the highest temperature of measurement). This indicates that BYSB remains chemically stable up to 973 K.

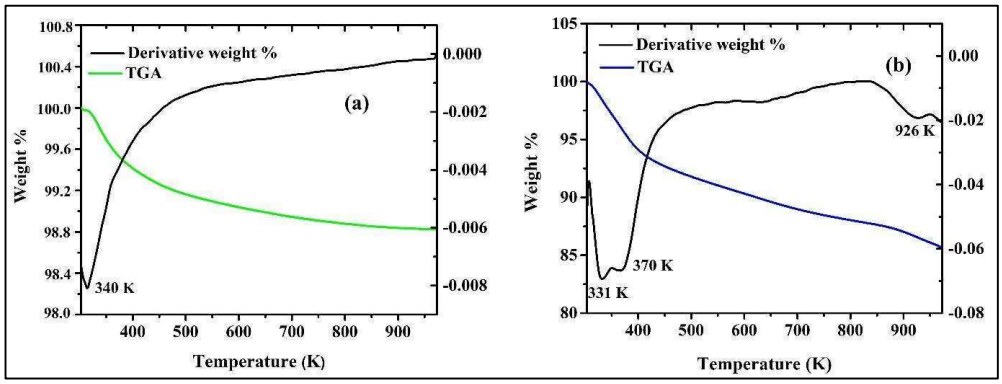

Fig. 11: *The TGA curves of (a) BYSB and (b) BYSN.*

For BYSN the initial weight loss at 331 K can be attributed to the loss of surface adsorbed moisture and the weight loss in the temperature range of 370 to 800 K can be ascribed to the release of surface adsorbed CO_2 (Fig. 11 (b)). It can be seen from the TGA

and its derivative curve of BYSN (Fig. 11 (b)) that a significant weight loss has occurred at 926 K due to the decomposition of $BaCO_3$ present in it. It may be noted that decomposition temperature of pillar like nanosized $BaCO_3$ (having diameter 20–40 nm and length 40–80 nm) is ~ 1073 K [59]. However, the decomposition temperature of $BaCO_3$ in BYSN having 50 nm size and irregular shape differs from its pure pillar like counterpart as they are morphologically different and in case of BYSN it is present in a nanocomposite form. Thus, the results of TGA study commensurate with those of XRD, EDS, FTIR and Raman studies.

4.3.6. Dielectric study

The variation of the dielectric constant (ε′) and the loss tangent (tan δ) with logarithmic angular frequency (log ω) at different temperatures are plotted in Fig. 12 (a) and Fig. 13 (a) for BYSB and BYSN, respectively. In case of BYSB, the value of ε′ increases with increase in temperature. The ε′ values for both the samples decreases with increase in frequency. The dipoles in the sample direct themselves along the applied field when the frequency is low and contributes to the total polarization. This results in the high value of ε′ at low frequency. At high frequency the dipoles are unable to align themselves along the applied field as the field changes rapidly. Due to this the values of ε′ becomes low and almost independent of temperature at high frequencies. Thus, all the ε′ versus log ω curves of BYSB merges together at higher frequencies (Fig. 12 (a)). As shown in the Fig. 12 (a) and Fig. 13 (a), the value of ε′ decreases with the increase in the frequency and in the dispersion region of the ε′, a relaxation peak in the tan δ (= ε''/ε') curve can be observed. In BYSB the value of ε′ increases with temperature indicating that the rate of polarization is higher at higher temperatures (Fig. 12 (b)). Thus, the relaxation peaks shift towards higher frequencies with increase in temperature (Fig. 12 (a)). The broad nature of the tan δ curve indicates polydispersive nature of the dielectric relaxation in these samples. In the low frequency

region, the tan δ values of BYSB shows a slight increasing trend while for BYSN the tan δ values increases sharply. This indicates that dc conductivity influences the dielectric response of BYSB (slightly) and BYSN (strongly) [60]. Thus, we have examined the dielectric relaxation process occurring in these samples with the help of the modified Cole-Cole model taking into account the effect of dc conductivity [61–63]. According to modified Cole-Cole model the complex dielectric permittivity (ε^*) is given by:

$$\varepsilon^* = \varepsilon_\infty + \frac{\varepsilon_s - \varepsilon_\infty}{1+(i\omega\tau)^{1-\alpha}} - i\frac{\sigma^*}{\varepsilon_0\omega^n} \quad (1)$$

where σ* is the complex conductivity (σ*= ($\sigma_1 + i\sigma_2$)) with σ_1 denoting the dc conductivity and σ_2 denoting the conductivity for the localized charges. As $\varepsilon^* = \varepsilon' - i\varepsilon''$, theabove equation (1) can be written in terms of the real and the imaginary part as,

$$\varepsilon' = \varepsilon_\infty + \frac{(\varepsilon_s - \varepsilon_\infty)\left[1+(\omega\tau)^{1-\alpha} sin\frac{1}{2}\alpha\pi\right.}{1+2(\omega\tau)^{1-\alpha} sin\frac{1}{2}\alpha\pi+(\omega\tau)^{2(1-\alpha)}} - \frac{\sigma_2}{\varepsilon_0\omega^n} \quad (2)$$

$$\varepsilon'' = \frac{(\varepsilon_s - \varepsilon_\infty)(\omega\tau)^{1-\alpha} cos\frac{1}{2}\alpha\pi}{1+2(\omega\tau)^{1-\alpha} sin\frac{1}{2}\alpha\pi \quad (\omega\tau)^{2(1-\alpha)}} + \frac{\sigma_1}{\varepsilon_0\omega^n} \quad (3)$$

where ε_s and ε_∞ are the low and the high frequency values of the dielectric permittivity, τ represents the relaxation time, the distribution of the relaxation time is represented by the parameter α and the term n denotes the frequency exponent. The equation (3) represents dielectric loss where the first term arises due to the relaxation of permanent dipoles and the second term arises due to the losses associated with the movement of charge carriers. The equations (2) and (3) have been utilized to fit the experimental ε′ verses log ω and tan δ verses log ω curves of both BYSB and BYSN. The fitted curves are shown by black lines in Fig. 12 (a) and Fig. 13 (a) and the parameters obtained from fitting are given in Table 8. It can be observed from Table 8 that the value of α is non zero indicating a dispersal of the

relaxation time. Thus, the relaxation mechanism of both BYSB and BYSN are polydispersive in nature and non-Debye type (α value is zero for Debye type relaxation) [60].

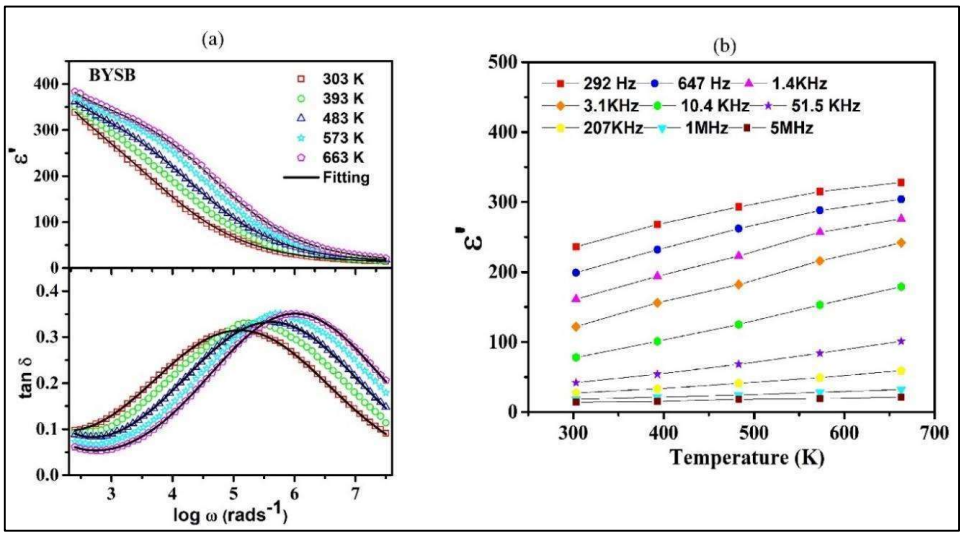

Fig 12: *(a) The variation of ε′ and tan δ with log ω and (b) the variation of ε′ with temperature for BYSB.*

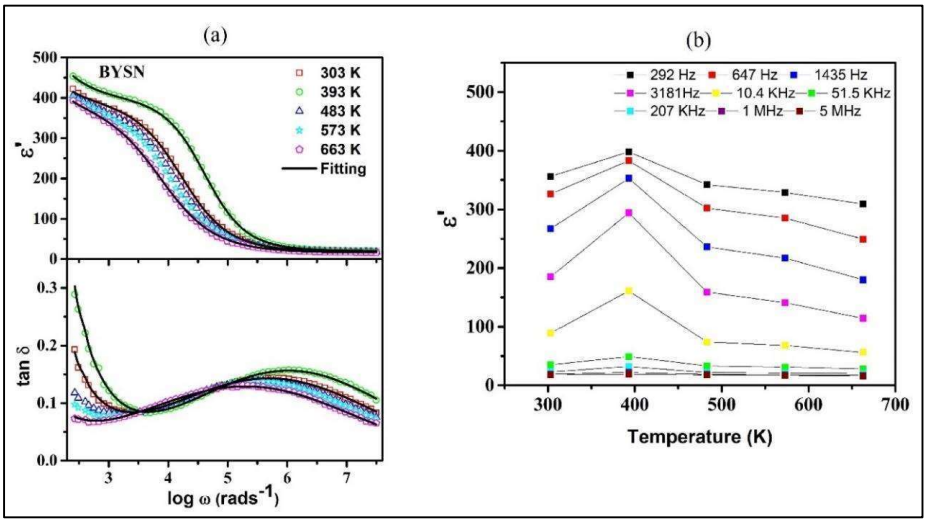

Fig 13: *(a) The variation of ε′ and tan δ with log ω and (b) the variation of ε′ with temperature for BYSN.*

Table 8. The Cole-Cole fitting parameters of BYSB and BYSN.

Temperature(K)	ε_s	ε_∞	ω_m (Hz)	α	n	σ_1 (Sm^{-1})	σ_2 (Sm^{-1})
BYSB							
303	350	12	5500	0.46	0.8	0.1×10^{-7}	0.3×10^{-7}
393	358	12.5	19500	0.45	0.85	0.2×10^{-7}	0.3×10^{-7}
663	366	13	51520	0.44	0.9	0.2×10^{-7}	0.4×10^{-7}
BYSN							
303	390	18	16755	0.55	0.94	0.1×10^{-6}	5×10^{-8}
393	400	20	41241	0.54	0.95	0.2×10^{-6}	8×10^{-8}
663	380	16	5522	0.56	0.92	0.2×10^{-7}	4×10^{-8}

The ε' verses log ω curves of BYSN exhibits a strong hump at 393 K and above this temperature the values of ε' values start decreasing as temperature increases (Fig. 13 (a) and Fig. 13 (b)). The peak in the tan δ verses log ω curves of BYSN shifts towards higher frequency region with increase in temperature till 393 K and above it the peak shifts towards lower frequency region with increase in temperature. Thus, BYSN exhibits drastically different dielectric response below and above 393 K. This anomalous behavior has not been observed for BYSB. It is noteworthy that the results of FTIR study suggests the presence of adsorbed CO_2 in BYSN. The TGA study suggests that BYSN releases adsorbed CO_2 between 370 K and 800 K. Thus, the anomalous dielectric behavior shown by BYSN above 393 K can be attributed to the continuous release of surface adsorbed atmospheric CO_2 as temperature increases beyond 393 K. This further confirms the presence of CO_2 in BYSN below 393 K while BYSB does not have any trapped CO_2 as has been revealed by their XRD, EDS, FTIR,

Raman and TGA studies. The decrease in the ε′ values after 393 K is indicative of the decrease in the amount of the charge carriers in BYSN above this temperature [64]. Thus, it can be inferred that CO_2 present in BYSN contributes to the charge carrier production and with its reduction above 393 K leads to the decrease in ε' with increase in temperature. Therefore, BYSN exhibits anomalous dielectric behavior above 393 K as CO_2 adsorbed by it starts escaping above this temperature.

The ε′ verses temperature (T) plots of both BYSB and BYSN at some discrete frequencies are shown in Fig. 12 (b) and Fig.13 (b), respectively. For BYSB it can be observed that as temperature increases ε' increases (Fig. 12 (b)) and the increase is much more prominent at lower frequencies (between 292 Hz to 207 KHz). In case of BYSB mainly the Maxwell- Wagner polarization around the grain boundaries gives rise to its high value of ε' at low frequencies [65]. Further, Schottky barrier layer with high contact capacitance and resistance is formed between the sample and electrode where charge accumulation takes place, which may also contribute to the high value of ε' at low frequencies [65,66]. The capacitance of BYSB becomes almost independent of temperature at higher frequencies and the slight increase in ε' with increase of temperature between 1 to 5 MHz results from the ion migration [67]. The ε′ verses T curves of BYSN exhibits a peak at 393 K up to 207 KHz frequency. At higher frequencies (1 and 5 MHz) the ε′ values of BYSN remains almost constant with increase in temperature as observed in case of BYSB. These indicates that BYSN exhibits anamolous dielectric response above 393 K as has been noticed in its frequency dependent dielectric response at discrete temperatures.

For BYSB and BYSN the variation of log ω_m (the frequency at which the peak in the tan δ verses log ω curves have been observed) with the inverse of temperature has been depicted in Fig. 14 (a) and Fig. 14 (b), respectively. We have plotted log ω_m vs. 1000/T curve

of BYSN in the temperature range of 303 to 393 K as it exhibits anomalous dielectric behaviour above this temperature. The log ω_m vs. 1000/T plots of both BYSB and BYSN follows the Arrhenius equation $\omega_m = \omega_0 \exp\left[-\frac{E_A}{K_B T}\right]$. The value of activation energy E_A is found to be 0.23 eV for BYSB and 0.21 eV for BYSN. The activation energy values indicates that electrical transport mechanism in both the samples is associated with hopping of p-type polarons [68, 69].

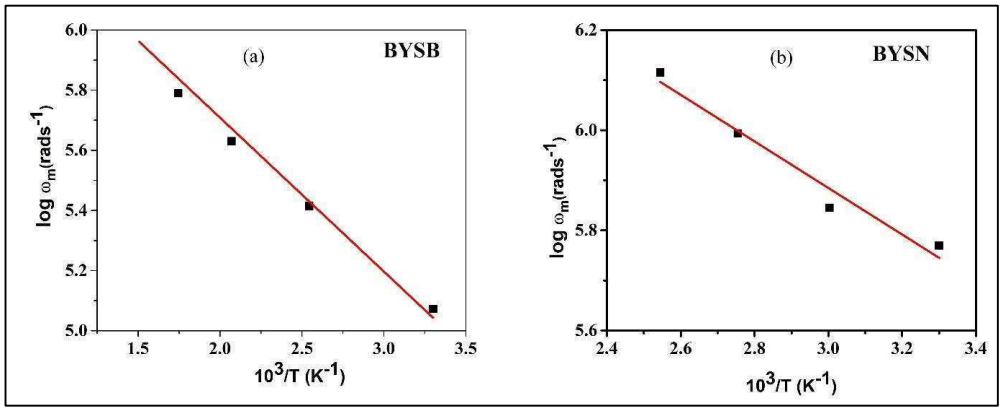

Fig 14: *Arrhenius plot of the most probable relaxation time ω_m for (a) BYSB and (b) BYSN.*

4.3.7. Impedance study

The complex impedance plane plots of both BYSB and BYSN at room temperature have been depicted in Fig. 15 (a) and Fig. 15 (b), respectively. The overall contribution of the grain and the grain boundary to the total impedance is evident from the presence of two distinct depressed semi-circular arc in the Nyquist plots of both BYSB and BYSN [60]. The well-defined grains and the grain boundaries are found in the FESEM images of both BYSB and BYSN. In the impedance plots the grain effect is manifested by the high frequency arc whereas the grain boundary effect is represented by the low frequency arc.

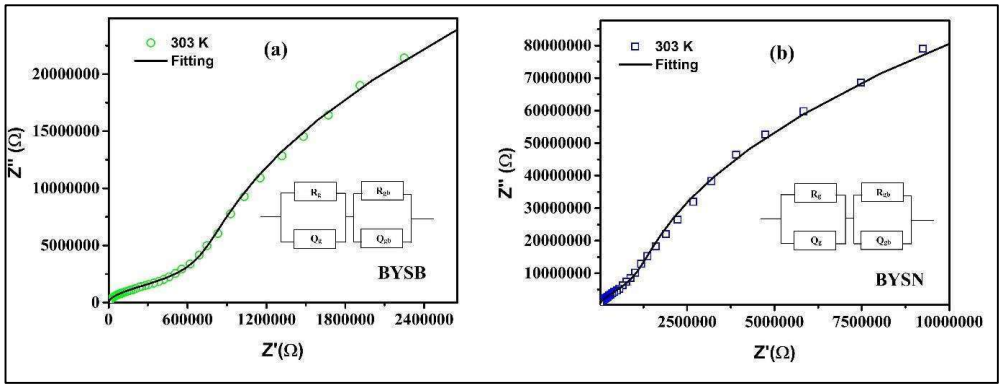

Fig. 15: *Complex impedance plane plots of (a) BYSB and (b) BYSN.*

The samples possessing polydispersive type of relaxation exhibit deformed semi-circular arc having centre below the Z′ axis as seen in our samples [70–74]. In order to separate the grain and the grain boundary contributions, the experimental impedance plots have been fitted with equivalent electrical circuit comprising of two parallel resistor-capacitor elements connected together in series as shown in the inset of Fig. 15 (a) and Fig. 15 (b). To account for the polydispersive nature of the relaxation process exhibited by the samples we have used a constant phase element (Q) in the model circuit in place of the capacitor element. C_p is the capacitance of constant phase element and is given by $C_p = Q^{1/c} R^{(1-c)/c}$, where the constant c accounts for the non-ideal behaviour of the sample. The value of c is 1 for ideal capacitance and 0 for ideal resistance. The impedance plots have been fitted using the formula:

$$Z' = \frac{R_g}{1+\left[\omega(R_gQ_g)^{\frac{1}{c_g}}\right]^2} + \frac{R_{gb}}{1+\left[\omega(R_{gb}Q_{gb})^{\frac{1}{c_{gb}}}\right]^2} \quad (4)$$

$$\text{and } Z'' = R_g\left[\frac{\omega(R_gQ_g)^{\frac{1}{c_g}}}{1+\left[\omega(R_gQ_g)^{\frac{1}{c_g}}\right]^2}\right] + R_{gb}\left[\frac{\omega(R_{gb}Q_{gb})^{\frac{1}{c_{gb}}}}{1+\left[\omega(R_{gb}Q_{gb})^{\frac{1}{c_{gb}}}\right]^2}\right] \quad (5)$$

where R and Q denotes the resistance and the constant phase element with suffix g and gb for the grain and the grain boundary contributions, respectively. The results have been summarized in Table 9.

It can be observed from Table 9 that the grain boundaries are comparatively more insulating than the grains because of the inhomogeneous distribution of the charge carriers around the grain boundaries [75]. The grain boundaries behaving like a trap to the moving charge carriers results in its high impedance values [76]. As BYSN has a greater number of grain boundaries owing to its nanometric size, it offers more barrier to the charge transport. This results in the impedance values of BYSN to be greater than that of BYSB.

Table 9: The fitted parameters for the impedance plots for BYSB and BYSN at room temperature.

	Temp. (K)	R_g (Ω)	Q_g (10^{-10} F/Ω)	c_g	R_{gb} (10^7 Ω)	Q_{gb} (10^{-11}F/Ω)	c_{gb}
BYSB	303	750000	7	0.8	30	9.5	0.85
BYSN	303	1200000	9	0.82	75	6.8	0.88

4.3.8. Conductivity study

The frequency dependence of the ac conductivity at different temperatures for both BYSB and BYSN has been illustrated in Fig. 16 (a) and Fig. 17(a), respectively. Two plateaus can be observed in the conductivity plots of both the samples which are representative of two processes responsible for the bulk conduction. At low frequency the conductivity tends towards a constant value which is termed as the dc conductivity (σ_{dc}) [77]. At low frequency the periodicity of the field is low, which causes the accumulation of charge

carriers giving rise to the dc conductivity [60]. In the higher frequency region, the rapid change in the conductivity is due to the commencement of conductivity relaxation process.

As per the results of the dielectric property study, the p-type polaron hopping caused by electric field governs the dielectric behaviour of the samples. Further, the difference in the potential energies at grains and grain boundaries creates trap sites, which acts as potential barriers towards the charge carriers [60]. Again, the higher value of grain boundary resistance as compared to that of its gain (as has been observed in the impendence study) results in transport of polaron by hopping from one site to another [60]. Thus, the conductivity of the samples increases with increase in frequency. However, in the high frequency region the conductivity value becomes constant as the polarons get trapped in sites having infinite barrier on each side and they start moving back and forth locally [78].

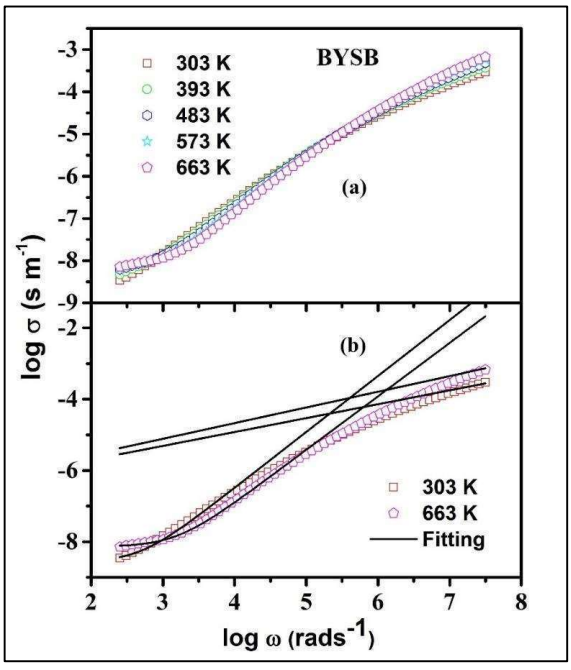

Fig. 16: *(a) The variation of ac conductivity with log ω and (b) power law fitting of conductivity spectra for BYSB.*

The variation of the conductivity with frequency can be examined with the help of the power law $\sigma(\omega) = \sigma_{dc} + A\,\omega^n$, where the A and n are the constants dependent on temperature and frequency [79]. We have fitted the conductivity spectra of both the samples recorded at all the temperatures. However, in Fig. 16 (b) and Fig. 17 (b) we have only shown two representative fitted curves at two distinct temperatures for each of the samples for the sake of clarity. We have provided the fitting parameters for all the temperatures in Table 10. The parameter A corresponds to the strength of polarizability of the sample and n is related to the degree of interaction between the moving charge carriers and its surrounding lattice [80]. The parameters A and n are temperature dependent. The value of n = 0 when the carriers are free to move through the sample. In the low frequency region, the values of n of both BYSB and BYSN are greater than 1 (Table 10) signifying the charge hopping is localized. On the other hand, for both BYSB and BYSN n is less than 1 in high frequency region indicating translational motion of charge carriers [81].

The temperature variation of n1 (the values of n at low frequency region) and n2 (the values of n at high frequency region) for both BYSB and BYSN have been shown in Fig. 18 (a) and Fig. 18 (b), respectively. For BYSB, n1 decreases with temperature which agrees with the correlated barrier hopping model (CBH) and n2 increases with temperature which is in agreement with the non-overlapping small polaron tunnelling model (NSPT) [64]. According to CBH model conduction occurs due to the hopping of charge carriers from one defect site to another separated by coulomb barrier [82]. As per NSPT model small polaron formation takes place due to the lattice distortions caused by the accumulation of charge carriers at the lattice site [82]. In BYSN the values n1 and n2 increase initially till 393 K and then they decrease between 393 and 483 K. Such anomalous behaviour of BYSN above 393 K has also been observed in its dielectric response and this can be attributed to the continuous release of

CO_2 above 393 K. It may be noted that for BYSN the values of n1 and n2 are independent of temperature beyond 483 K indicating a decrease in the interaction among the charge carriers. This corroborates the finding that amount of charge carrier in BYSN decreases above 393 K as seen in the dielectric study.

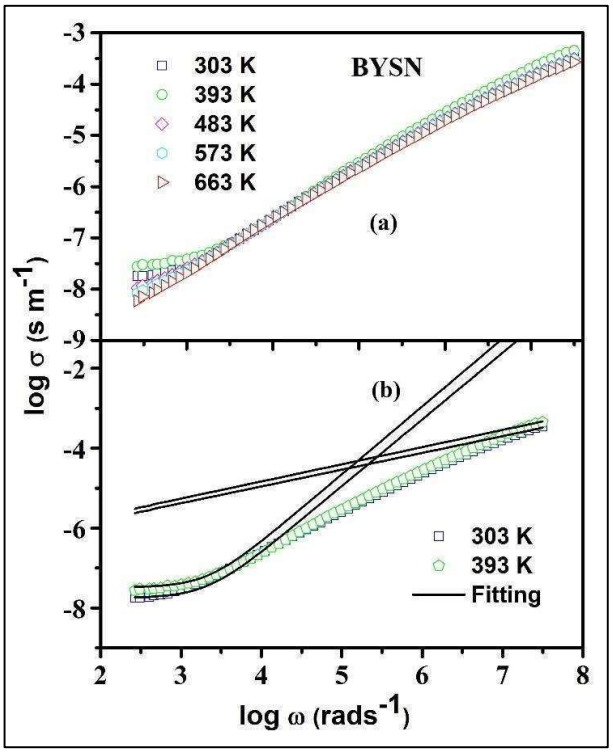

Fig. 17: *a) The variation of ac conductivity with log ω and (b) power law fitting of conductivity spectra for BYSN.*

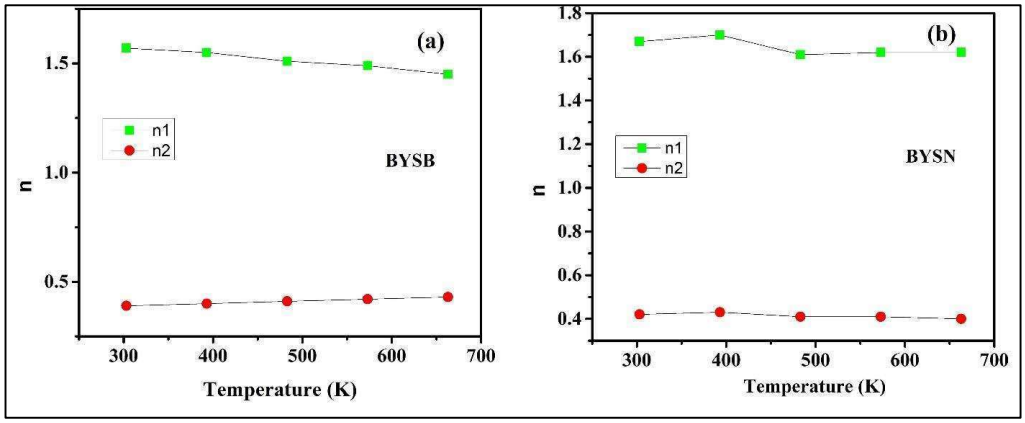

Fig. 18: *Temperature dependence of n1(low frequency) and n2 (high frequency) for (a) BYSB and (b) BYSN.*

Table 10: The parameters obtained from the fitting of the conductivity spectra for BYSB and BYSN.

Sample	Temperature (K)	σ_{dc} (Sm^{-1})	A1 (at low frequency)	n1 (at low frequency)	A2 (at high frequency)	n2 (at high frequency)
BYSB	303	2.7×10^{-9}	1.7×10^{-13}	1.57	3.3×10^{-7}	0.39
	393	4.1×10^{-9}	1.8×10^{-13}	1.55	3.6×10^{-7}	0.40
	483	5.8×10^{-9}	1.9×10^{-13}	1.51	3.8×10^{-7}	0.41
	573	6×10^{-9}	2×10^{-13}	1.49	4×10^{-7}	0.42
	663	6.7×10^{-9}	2.1×10^{-13}	1.45	4.05×10^{-7}	0.43
BYSN	303	1.8×10^{-8}	0.5×10^{-13}	1.67	2.3×10^{-7}	0.42
	393	3.3×10^{-8}	0.7×10^{-13}	1.7	2.8×10^{-7}	0.43
	483	1×10^{-8}	1.9×10^{-13}	1.61	2.5×10^{-7}	0.41
	573	0.7×10^{-8}	2×10^{-13}	1.62	2.4×10^{-7}	0.41
	663	0.5×10^{-8}	2.1×10^{-13}	1.62	2.4×10^{-7}	0.40

The temperature variation of A1 (the values of A in low frequency region) and A2 (the values of A in high frequency region) for BYSB and BYSN have been shown in Fig. 19 (a) and Fig. 19 (b), respectively. For BYSB the values of A1 and A2 increase with increase in temperature indicating an enhancement in its polarizability [83]. For BYSN, A1 increases rapidly up to 483 K and above this temperature it increases very slowly. The A2 verses T curve of BYSN shows a peak at 393 K indicative of maximum polarizability at this temperature. This anomalous behaviour observed for temperature dependence of A1 and A2 of BYSN also corroborates with the results of its dielectric study.

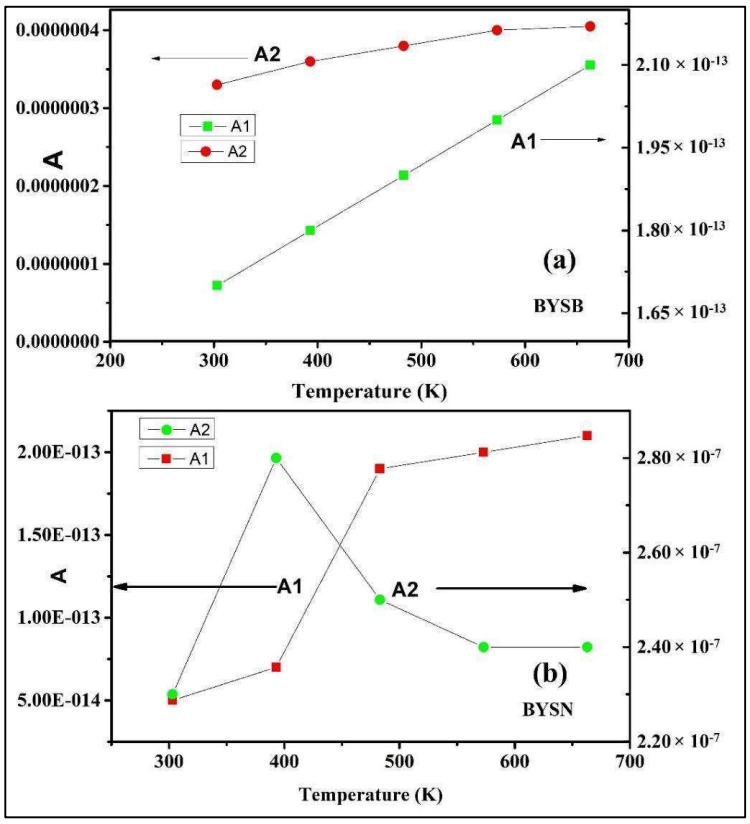

Fig. 19: *Temperature dependence of A1(low frequency) and A2 (high frequency) for (a) BYSB and (b) BYSN.*

4.3.9. Electrical modulus study

The linear frequency (f) dependence of M' and M" of BYSB are shown in in Fig. 20 (a) and Fig. 20 (b), respectively. Fig. 21 (a) and Fig. 21 (b) display the linear frequency dependence of M' and M" of BYSN, respectively. The value of M' decreases with decrease in frequency and approaches zero at all temperatures indicating that the electrode polarization is absent in the samples [84]. The dispersion observed in the M' curves arises due to the conductivity relaxation. The presence of short-range charge carriers is evident from the sigmoid nature of the M' curves [85]. At high frequencies M' tends to saturate due to the absence of any restoring force controlling the movement of charge carriers in the induced electric field [86,87]. Under these circumstances, the charge carriers can migrate over long distances indicating existence of long-range charge carriers [88]. The saturation of M' curves at high frequencies also indicates the discharging of space charge polarization [86].

M" verses f plots of both the samples exhibit prominent peaks (Fig. 20 (b) and Fig. 21 (b)) which are broad and asymmetric in nature pointing towards non-Debye relaxation in the samples [87]. This nature of M" spectrum also indicates that charge carriers in the samples are transported predominantly by hopping mechanism [88]. This corroborates the results of the dielectric study that charge conduction in the samples takes place by hopping of p type polaron. Further, with increase in temperature the peak in the M" curves of both the samples shifts towards higher frequency indicating the charge carriers are thermally activated and their relaxation rate increases with increase in temperature.

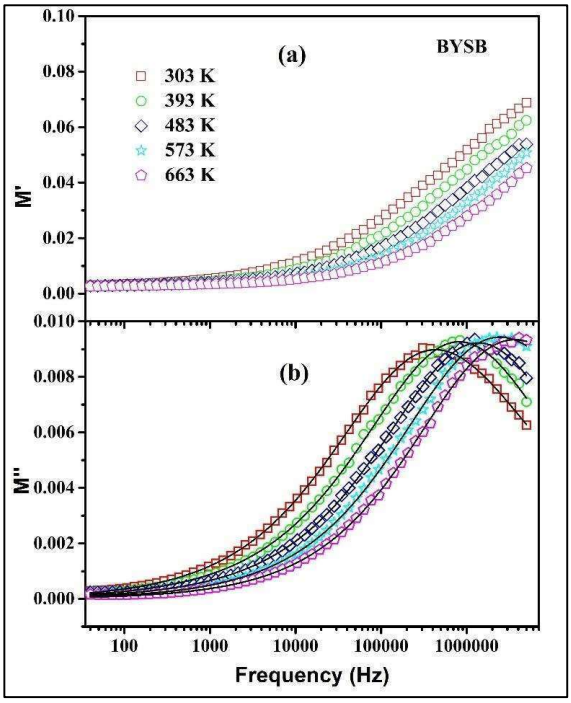

Fig. 20: *The variation of (a) M' and (b) M'' with frequency at different temperatures for BYSB.*

We have tried to fit the electric modulus spectra of BYSB and BYSN using Cole-Cole model but that lead to unsatisfactory results. On contrary, the dielectric spectra have been successfully analysed by the Cole-Cole model. In this context, it is noteworthy that generally, three angular frequency ($\omega = 2\pi f$) dependent functions viz., complex permittivity: $\varepsilon^*(\omega) = \varepsilon'(\omega) - i\,\varepsilon''(\omega)$, complex electric modulus: $M^*(\omega) = M'(\omega) + i\,M''(\omega)$ and complex conductivity: $\sigma^*(\omega) = \sigma'(\omega) + i\,\sigma''(\omega)$ are used to describe and assess the dielectric behaviour of materials [89]. They are interrelated to each other according to the equation: $M^*(\omega) = 1/\varepsilon^*(f\,\omega) = i\omega\varepsilon_0/\sigma^*(\omega)$ but emphasize different aspects of the same process [89]. Physically, M* is connected to the electric field (**E**) relaxation inside the material when the dielectric displacement (**D**) remains constant and it describes the actual relaxation. The ε* is associated

with the relaxation of **D** when **E** remains constant and it accounts for the dielectric retardation [90, 91]. The details which are not explicitly manifested in one formalism may be noticed in the spectra of other two formalisms [91].

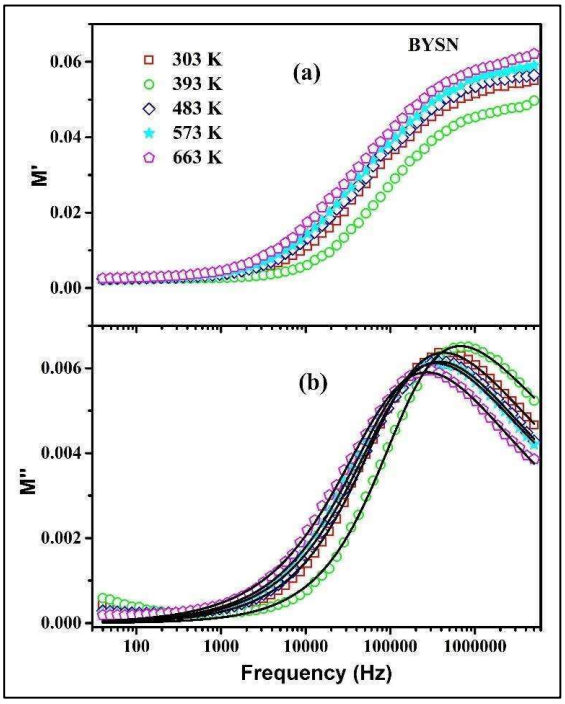

Fig. 21: *The variation of (a) M' and (b) M'' with frequency at different temperatures for BYSN.*

The dc conductivity (σ_{dc}) significantly influences the dielectric and conductivity spectrum but its effect remains masked in the electric modulus spectrum [90, 91]. In the dielectric loss spectra, the tan δ tends to increase at low frequency region due the influence of σ_{dc} (as in the present case), which suppresses the structural relaxation process. In such cases, customarily the electric modulus formalism is adopted to examine the dielectric relaxation of the sample. The relaxation time determined from electric modulus corresponds to

microscopic relaxation times [89, 92]. For non-Debye type relaxation, the relaxation time determined from modulus formalism (τ_m) is supposed to be more accurate than that determined from dielectric permittivity (τ_ε) and $\tau_m > \tau_\varepsilon$ [91].

For the present case tan δ increases (slightly for BYSB and sharply for BYSN) in the low frequency region (Fig. 12 (a) and Fig.13 (a)) due the influence of σ_{dc} whereas in M'' spectrum (Fig. 20 (b) and Fig. 21 (b)) only sharp peaks have been observed. Thus, the above mentioned discussion has insisted us to fit M'' spectra of BYSB and BYSN using Havriliak-Negami (HN) function: $F^*_{HN} = \frac{1}{[1+(i\omega\ _{HN})^{\beta}]^{\gamma}}$, where β and γ are fractional shape parameters representing symmetric and asymmetric broadening of the complex dielectric function. τ_{HN} is the characteristic relaxation time and $\beta\gamma = \beta_{kww}$ is the stretching parameter associated with the relaxation peak. The values of β and γ lies in the range of $0 < \beta \leq 1$ and $0 < \beta\gamma < 1$. At first tan δ verses log ω curves of BYSB and BYSN were fitted using the HN function excluding the low frequency region of those curves. It has been found that for tan δ spectra of both the samples the values of $\gamma \approx 1$, for which the HN function is equivalent to the Cole-Cole function. This justifies the proper fitting of tan δ verses log ω curves of the samples by Cole-Cole model. The M'' spectra are well fitted by HN function and γ lies between 0.58–0.95 for BYSB and 0.23–0.39 for BYSN. This reveals that the relaxation peaks of M'' for both the samples is asymmetric in nature and the asymmetry in BYSN is more prominent than BYSB. The effect of σ_{dc} is much more prominent in BYSN than BYSB which can be seen from the sharp increase of tan δ values of BYSN as compared to slow increase of tan δ in BYSB in the low frequency region (Fig. 12 (a) and Fig.13 (a)). It can therefore be concluded that the asymmetry masked in the relaxation peak of tan δ due to the presence of σ_{dc} is manifested in the M'' spectra.

The type of relaxation (Debye or non-Debye type) present in the sample can be confirmed using the stretched exponent parameter β_{kww} [93]. The value of $\beta_{kww} = 1$ where there is no interaction among the dipoles and $\beta_{kww} < 1$ where there is a significant interaction among the dipoles. The values of β_{kww} for BYSB lies between 0.45–0.81and for BYSN it lies between 0.26–0.35 indicating that the relaxation in both the sample is non-Debye type. For BYSN the value β_{kww} is lowest at 393 K which once again confirms the fact that it exhibits anomalous dielectric behaviour above 393 K due to release of surface adsorbed CO_2 by it as has been observed in its dielectric response in other formalisms.

4.4. Discussion:

The reported value of room temperature permittivity of bulk Ba_2YbSbO_6 (same as our BYSB sample) prepared by solid state ceramic method (belonging to *R-3* space group with lattice parameter a = 5.9104 Å and α = 59.99°) is 14 at 10 KHz [40] and the value of the same for BYSB (belonging to $Fm\bar{3}m$ space group with lattice a = 8.361509 and α = β = γ = 90°) is 14 at 5 MHz. To the best of our knowledge there is no report on temperature dependent dielectric response of Ba_2YbSbO_6. It may be noted that for Ba_2YbNbO_6 room temperature dielectric permittivity and loss tangent values are ~ 250 and ~ 0.28, respectively at 1.75 KHz [56]. The room temperature the values of dielectric permittivity and loss tangent of Ba_2HoSbO_6 are ~ 300 and 0.25, respectively, at 1.75 KHz [94]. At room temperature and 1.75 KHz the value of dielectric permittivity of BYSB (~168) is found to be less than that of its analogous systems like Ba_2YbNbO_6 and Ba_2HoSbO_6 but its loss tangent (~0.09) is better than those of its analogous systems. The values of room temperature dielectric permittivity and loss tangent of BYSB matches well with the reported values of these parameters for bulk Ba_2YbSbO_6 sample. On the other hand, the dielectric behaviour of BYSB and its analogous

system is significantly different. It may be noted that crystal structure has the direct influence on microscopic structural relaxation of dielectric materials [91]. Thus, the similarity in dielectric behaviour of BYSB with bulk Ba_2YbSbO_6 prepared by ceramic method can be attributed to structural similarity of these two systems. The difference in the microscopic structural relaxation between BYSB and its other analogous systems leads to the change in their dielectric properties. From the above discussion it can be inferred that the crystal structure which determines the microscopic structural relaxation has a key role in determining the dielectric property of perovskite oxides.

The reported values of dielectric constant and loss tangent of nanosized Ba_2YbSbO_6 (synthesized by combustion method and having particle size 20–50 nm) are 11.3 and 0.01, respectively, at 5 MHz frequency [38, 39]. However, there is no report on dielectric property of Ba_2YbSbO_6-$BaCO_3$ nanocomposite. The values of dielectric constant and loss tangent of BYSN is 18 and 0.08, respectively, at 5 MHz. It is noteworthy that both the single phase Ba_2YbSbO_6 sample mentioned above and the present Ba_2YbSbO_6-$BaCO_3$ nanocomposite are nanometric in size. Due to the difference in the microscopic structural relaxation owing to difference in the crystal structure of nanometric Ba_2YbSbO_6 and the nanocomposite BYSN their microscopic structural relaxation will be different. Moreover, BYSN has surface adsorbed CO_2. It can therefore be inferred that the presence of two crystalline phases and surface adsorbed CO_2 in BYSN is responsible for the difference in the dielectric response of BYSN and nanosized Ba_2YbSbO_6.

The influence of surface adsorbed CO_2 on the dielectric relaxation dynamics and conduction mechanism of BYSN has been discussed elaborately in the ‘Results’ section of this paper. Apart from this the difference in the crystal structure and microstructure of BYSB and BYSN can influence the dielectric relaxation and conduction mechanism of these

samples. At any particular temperature the ε' verses log ω and tan δ verses log ω curves of BYSN (Fig. 11 (a)) follows the same trend as seen in BYSB (Fig. 10 (a)). At any given temperature and frequency, the value of ε' for BYSN is higher than that of BYSB. The values of tan δ of BYSN are comparatively higher than BYSB at low frequency (up to ~1 KHz) owing to the presence of pronounced dc conductivity in it. The values of tan δ of BYSN is less than that of BYSB above 1 KHz. It may be noted that BYSB (Ba_2YbSbO_6) is a single-phase double perovskite while BYSN is a nanocomposite composed of Ba_2YbSbO_6 and $BaCO_3$ phases along with surface adsorbed CO_2. Thus, the difference of microscopic structural relaxation of pure Ba_2YbSbO_6 and Ba_2YbSbO_6-$BaCO_3$ nanocomposite along with the difference of particle size leads to the enhancement of dielectric constant and reduction of loss tangent of BYSN compared to that of BYSB. The dielectric behaviour of a palettized sample is strongly dependent on the presence of grain and grain boundary interface [60]. Due to its nanometric size the number of grains and grain boundary interfaces in the pelletized sample of BYSN are higher than BYSB. The grain size and the grain boundary interface have also contributed to the enhancement of dielectric permittivity and reduction of loss tangent in case of BYSN as compared to BYSB.

If the power law fitting parameter of the conductivity spectra, $n = 0$ then the charge carriers can move freely through the material. When $n \neq 0$, the motion of charge carriers takes place due to conduction as well as polarization [83]. This phenomenon is usually observed for samples with grain boundary disorder creating localized polarons [83]. The motion of the polaron takes place due to induced polarizations [94, 95]. Interaction between the mobile charge carriers and the lattice increases as the sample becomes more disordered. If the localized charge states are randomly distributed then hopping of charge carriers becomes faster. This motion of charge carriers increases conduction as well as polarizations. This

behaviour has been reported for samples having grain boundary disorder and localized polarons [96, 97]. It can be seen that the values of dc conductivity of BYSN at same frequency and temperature is higher than those of BYSB (Table 10). According to power law fitting of conductivity spectra, the values of n1 for BYSB and BYSN lie in the range of 1.45–1.57 and 1.67–1.7, respectively (Table 10). The values of n2 for BYSB and BYSN lie in the range of 0.30–0.43 and 0.40–0.42, respectively (Table 10). Thus, the nonzero values of n1 and n2 reveal the presence of grain boundary disorder (which is usual for palletized sample and has been observed in the FESEM images Fig. 3(a) and Fig. 3(b)) and localized polarons in both BYSB and BYSN. Moreover, the values of n1 for BYSN is greater than those of BYSB, which indicates presence more defects in BYSN. It is well known that mechanical milling induces crystalline defects and disorder mainly at the surface of the samples [17–20]. BYSN has been synthesized by ball milling method and it is nanometric in size while BYSB is synthesized by ceramic method and it is a bulk sample with large particle size. Therefore, BYSN should have more grain boundary disorder than BYSB. Thus, the microstructural (particle size and grain boundary defects) difference between BYSB and BYSN plays a key role in determining their conductivity.

The value of the parameter β_{kww} obtained from analysis of dielectric data in modulus formalism is lower for peaks which are broader and more asymmetric in nature and it also decreases with decrease in particle size [87, 91]. Thus, the β_{kww} values of BYSN which are less than those of BYSB [Table 11] results from the particle size effect. Moreover, in BYSN the number of energy barriers arising from the local defects are more owing to its nanometric size resulting in broader distribution of its relaxation time as compared to BYSB [87]. This phenomenon also contributes to the lowering of β_{kww} values of BYSN as compared to those of BYSB. For BYSB β_{kww} value increases with temperature and approaches 1 at higher

temperatures. It can therefore be inferred that the relaxation in BYSB tends towards Debye type process at higher temperatures.

Table 11: The parameters obtained from M" spectra.

Temperature (K)	BYSB		BYSN	
	β_{kww}	τ_{HN}	β_{kww}	τ_{HN}
303	0.45	4.186×10^{-6}	0.29	9.67×10^{-6}
393	0.57	1.319×10^{-6}	0.26	6.798×10^{-6}
483	0.64	9.027×10^{-7}	0.32	9.758×10^{-6}
573	0.77	8.47×10^{-7}	0.32	1.097×10^{-5}
663	0.81	6.78×10^{-7}	0.35	1.223×10^{-5}

4.5. Conclusion

Herein, we have reported the structural, microstructural, thermal, optical and temperature dependent dielectric properties of BYSB synthesized by solid state ceramic method and a nanocomposite BYSN synthesized by high energy ball milling of BYSB. The grain size of BYSB is ~ 1.92 μm and the particle size of BYSN is ~ 50 nm. Previously, the presence of orthorhombic $BaCO_3$ phase in mechanically activated nanometric $BaTiO_3$ has been detected by Rietveld refinement of XRD pattern only without any supportive spectroscopic evidence [14, 15]. In this endeavour, for the first time we have shown that the nanosized Ba_2YbSbO_6 prepared by ball milling of BYSB adsorbs atmospheric CO_2 leading to the formation of BYSN.

The samples have been characterized by XRD, FESEM, EDS, FTIR and Raman spectroscopy. BYSB possess $Fm\bar{3}m$ space group whereas BYSN is a nanocomposite

composed of 86.4 % Ba_2YbSbO_6 and 13.6 % $BaCO_3$ phases with surface adsorbed CO_2. The samples exhibit non-Debye type relaxation governed by polaron hopping. BYSN exhibits better dielectric behaviour than BYSB. Above 393 K BYSN sample exhibits anomalous dielectric and electrical properties due to the release of adsorbed CO_2. It has been shown that crystal structure, grain size, grain boundary contribution and surface adsorbed CO_2 strongly influence the dielectric relaxation dynamics and conduction mechanism of the samples. Moreover, due to their high dielectric constant and low loss tangent at room temperature both BYSB and the nanocomposite BYSN may be utilized for fabrication of radio frequency oscillator, resonator, filter and communication devices.

References

[1] M.W. Lufaso, Chem. Mater. 16 (2004) 2148.

[2] R. Mani, P. Selvamani, J.E. Joy, J. Gopalakrishnan, Inorg. Chem. 46 (2007) 6661.

[3] I. Levin, J.Y. Chan, R.G. Geyer, J.E. Maslar, T.A. Vanderah, J. Solid State Chem. 156 (2001) 122.

[4] M. Bieringer, S.M. Moussa, L.D. Noailles, A. Burrows, C.J. Kiely, M.J. Rosseinsky, R.M. Ibberson, Chem. Mater. 15 (2003) 586.

[5] Y. Du, A.S. Nowick, J. Am. Ceram. Soc. 78 (1995) 3033.

[6] M. Thirumal, A.K. Ganguli, Bull. Mater. Sci. 25 (2002) 259.

[7] M. Thirumal, A.K. Ganguli, Prog. Cryst. Growth Charact. Mater. 44 (2002) 147.

[8] H. Vincent, Ch Perrier, Ph I'heritier, M. Labeyrie, Mater. Res. Bull. 28 (1993) 951.

[9] X. Wang, H. Wen, R. Chen, H. Zhou, L. Li, IEEE Int. Ultrasonics, Ferroelectrics, and Frequency Control Joint 50th Anniversary Conf., Montreal, Canada, August 2004.

[10] T. Hoshina, J. Ceram. Soc. Jpn. 121 (2) (2013) 156.

[11] Y. Kobayashi, A. Nishikata, T. Tanase, M. Konno, J. Sol-Gel Sci. Technol. 29 (2004) 49.

[12] S. Mukherjee, S. Ghosh, C. Ghosh, M. K. Mitra, J. Inst. Eng. India Ser. D 94 (2013) 57.

[13] R. Ashiri, RSC Adv. 6 (2016) 1713.

[14] S. Neogi, U. Chowdhury, A. K. Chakraborty, J. Ghosh, Micro Nano Lett. 10 (2015) 109.

[15] J. Ghosh, S. Bysakh, S. Mazumder, Ph. Transit. 87 (2014) 325.

[16] V. R. Mudinepalli, L. Feng, W. C. Lin, B. S. Murty, J. Adv. Ceram. 4 (2015) 46.

[17] S. D. Shenoy, P. A. Joy, M. R. Anantharaman, J. Magn. Magn. Mater. 269 (2004) 217.

[18] A. Verma, K. Biswas, C. S. Tiwary, A. K. Mondal, K. Chattopadhyay, Metall. Mater. Trans. A. 42 (2011) 1127.

[19] M. M. Vijatovic Petrovic, J. D. Bobic, A. M. Radojkovic, J. Banys, B.D. Stojanovic, Ceram Int. 38 (2012) 5347.

[20] O. P. Thakur, A. Feteira, B. Kundys, D. C. Sinclair, J. Eur. Ceram. Soc. 27 (2007) 2577.

[21] M. H. Frey, Z. Xu, P. Han & D. A. Payne, Ferroelectrircs 206 (1998) 337.

[22] M. Vigneswari, K. Sakthipandi, S. Sankarrajan, IJERT. 3 (2014) 2278.

[23] V. Buscaglia, C. A. Randall, J. Eur. Ceram. Soc. 40 (2020) 3744.

[24] A. Prasatkhetragarn, S. Kaowphong, R. Yimnirun, Appl. Phys. A.107 (2012) 117.

[25] A. Benali, S. Azizi, M. Bejar, E. Dhahri, MFP. Graça, Ceram. Int.40(9) (2014) 14367.

[26] M. Ghasdi, H. Alamdari, Sens. Actuators B Chem. 148 (2010) 478.

[27] Y. Wang, J. Chen, X. Wu, Mater. Lett., 49 (2001) 361.

[28] H. T. Giang, H. T. Duy, P. Q. Ngan, G. H. Thai, D. T. A. Thu, D. T. Thu, N. N. Toan, Sens. Actuators B Chem. 158 (2011) 246.

[29] B. Wang, S. Gu, Y. Ding, Y. Chu, Z. Zhang, X. Ba, Q. Zhang, X. Li, Analyst. 138 (2013) 362.

[30] G. Wang, J. Sun, W Zhang, S. Jiao, B. Fang, Microchim. Acta. 164 (2009) 357.

[31] C. Tongyun, S. Liming, L. Feng, Z. Weichang, Z. Qianfeng, C. Xiangfeng, J. Rare Earths, 30 (2012) 1138.

[32] A. Galal, N. F. Atta, S. M. Ali, Electrochim. Acta. 56 (2011) 5722.

[33] S. M. Ali, Y. M. Abd Al-Rahman, A. Galal, J. Electrochem. Soc. 159 (2012) 600.

[34] W. T. Fu, S. Akerboom, D. J. W. Ijdo, J. Alloys Compd. 476 (2009) 11.

[35] W. T. Fu, D. J. W. Ijdo, J. Solid State Chem. 178 (2005) 2363.

[36] H. Karunadasa, Q. Huang, B. G. Ueland, P. Schiffer, R. J. Cava, Proceedings of the National Academy of Sciences of the United States of America 100 (2003) 8097.

[37] P. J. Saines, B. J. Kennedy, M. M. Elcombe, J. Solid State Chem. 180 (2007) 401.

[38] P. R. S. Wariar, V. R. Kumar, V. M. Nair, M. M. Yusoff, R. Jose, J. Koshy, Adv. Mater. Res. 545 (2012) 27.

[39] V. Manikantan Nair, L. Jacob, P. R. S. Wariar, R. Jose, IJESIT 3 (2014) 720.

[40] L. A. Carrero Bermúdez, R. Moreno Mendoza, R. Cardona, D. A. Landínez Téllez, J. Roa-Rojas, J. Exp. Theo. Nanotechnology 3 (2017) 161.

[41] M. M. Hoque, A. Barua, A. Dutta, S. K. Dey, T. P. Sinha, S. Kumar, Ionics 23 (2017) 471.

[42] Larson, A.C., Von Dreele, R.B.: General structure analysis system (GSAS). Los Alamos National Laboratory Report LAUR 86 (2004) 748.

[43] B. PANalytical, X'Pert HighScore Plus, Lelyweg, Almelo, Netherlands, 2 (2002).

[44] D. Shidqi Khaerudini, Arham, S. Alva, Adv. Nat. Sci.: Nanosci. Nanotechnol. 11 (2020) 015013.

[45] B Amitava, R Gupta, K Balani, J. Mater. Sci. 50 (2015) 6349.

[46] A. Banerjee, R. Gupta, K. Balani, J. Mater. Sci. 50 (2015) 6349.

[47] S. Alleg, F. Z. Bentayeb, R. Bensalem, C. Djebbari, L. Bessais, J. M. Greneche, Phys. Status. Solidi. A 205(2008)1641.

[48] N. Bensebaa, S. Alleg, J. M. Greneche, J. Alloys Compd. 393 (2005)194.

[49] A. S. Bolokang, M. Phasha, Mater. Lett. 64 (2010) 1894.

[50] S. Dey, S. K. Dey, B. Ghosh, V. R. Reddy, S. Kumar, Mater. Chem. Phys. 138 (2013) 833.

[51] R. Mondal, S. Dey, S. Majumder, A. Poddar, P. Dasgupta, S. Kumar, J. Magn. Magn. Mater. 448 (2018) 135.

[52] A. Barua, S. K. Dey, S. K. Sabyasachi, S. Kumar, J. Alloys Compd. 854 (2021) 157217.

[53] P. Pasierb, S Komorniki, M Rokita, M Rekas, J. Mol. Struct. 596 (2001) 151.

[54] P. Galhotra, J. G. Navea, S. C. Larsena, V. H. Grassian, Energy Environ. Sci. 2 (2009) 401.

[55] B. Bonelli, B. Civalleri, B. Fubini, P. Ugliengo, C. O. Arean, E. Garrone, J. Phys. Chem. B 104 (2000) 10978.

[56] S. K. Maity, A. Dutta, S. Kumar, T. P. Sinha, Phys. Scr. 88 (2013) 065702.

[57] R. Mukherjee, S. Saha, A. Dutta, T. P. Sinha, J. Alloys Compd. 651 (2015) 222.

[58] D. Rout, G. S. Babu, V. Subramanian, Int. J. Appl. Ceram. Technol. 5 (2008) 522.

[59] C. Zeng, P. Li, H. B. Xu, Z. F. Xu, H. H. Li, Y. Zhang, Ceram. Int. 37 (2011) 1215.

[60] A. Barua, S. Maity, S. Kumar, A. Dutta, T.P. Sinha, Physica B 583 (2020) 412057.

[61] K. S. Cole, R. H. Cole, J. Chem. Phys. 9 (1941) 341.

[62] K. S. Cole, R. H. Cole, J. Chem. Phys. 10 (1942) 98.

[63] R. Coelho, Physics of Dielectrics, Elsevier, New York, 1978.

[64] S. Singha, S. K. Maity, S. Biswas, R. Saha, S. Kumar, Inorganica Chim. Acta 453 (2016) 321.

[65] S. A. Fatima, R. Shaheen, K. Shahzad, Appl. Phys. A 127 (2021) 466.

[66] I. Ahmad, M. J. Akhtar, M. Younas, J. Solid State Electr. 21 (2017) 3093.

[67] U. Ahmadu, S. Tomas, S. A. Jonah, A. O. Musa, N. Rabiu, Adv. Mater. Lett. 4 (2013) 185.

[68] M. Idrees, M. Nadeem, M. M. Hassan, J. Phys. D Appl. Phys. 43 (2010) 155401.

[69] W. H. Jung, J. Appl. Phys. 90 (2001) 2455.

[70] L. Liu, H. Fan, L. Wang, X. Chen, P. Fang, Phil. Mag. 88 (2008) 537.

[71] L. Liu, H. Fan, P. Fang, L. Jin, Solid State Commun. 142 (2007) 573.

[72] L. Liu, H. Fan, P. Fang, X. Chen, Mater. Res. Bull. 43 (2008) 1800.

[73] R. Gerhardt, J. Phys. Chem. Solid. 55 (1994) 1491.

[74] M. C. H. Mckubre, J. R. Macdonald, in: J.R. Macdonald (Ed.), Wiley, New York, (1987) 191.

[75] R. C. Da, Y. G. Yan, Electron. Elem. Mater. 1 (1982) 25.

[76] S. Halder, Md. Seikh, B. Ghosh, T. P. Sinha, Ceram. Int. 43 (2017) 11097.

[77] A. S. A. Khiar, R. Puteh, A.K. Arof, Physica B 373 (2006) 23.

[78] Y. Tsuji, A. Kan, H. Ogawa, S. Ishihara, J. Eur. Ceram. Soc. 25 (2005) 2883.

[79] A. K. Jonscher, Universal Relaxation Law, London: Chelsea Dielectrics Press, (1996).

[80] A. Dhahri, E. Dhahri, E. K. Hlil, RSC Adv. 8 (2018) 9103.

[81] L. Biswal, P. R. Das, B. Behera, J. Adv. Ceram. 3 (2014) 215.

[82] A. Oueslati, Ionics 23 (2017) 857.

[83] D. K. Pradhan, S. Kumari, V. S. Puli, P. T. Das, D. K. Pradhan, A. Kumar, J. F. Scott, R. S. Katiyar, Phys. Chem. Chem. Phys. 19 (2017) 210.

[84] R. K. Parida, B. N. Parida, R. K. Bhuyan, S. K. Parida, Ferroelectrics 571 (2021) 162.

[85] S. Manzoor, S. Husain, A. Somvanshi, M. Fatem, J. Appl. Phys. 128 (2020) 064101.

[86] S. Mishra, R. N. P. Choudhary, S. K. Parida, J. Mol. Struct. 1265 (2022) 133353.

[87] N. H. Vasoya, P. K. Jha, K. G. Saija, S. N. Dolia, K. B. Zankat, K. B. Modi, J. Electron. Mater. 45 (2016) 2.

[88] R. Mukherjee, B. Ghosh, S. Saha, C. Bharti, T. P. Sinha, J. Rare Earths. 32 (2014) 334.

[87] S. N. Tripathy, Z. Wojnarowska, J. Knapik, H. Shirota, R. Biswas, M. Paluch, J. Chem. Phys. 142 (2015) 184504.

[88] S. Sharma, K. Shamim, A. Ranjan, R. Rai, P. Kumari, S. Sinha, Ceram. Int. 41 (2015) 7713.

[89] F. Kremer, A. Schoenhals, Broadband Dielectric Spectroscopy, Springer: Berlin, 2003.

[90] S. N. Tripathy, K. K. Satpathy, R. Palai, D. K. Pradhan, Ferroelectrics 589 (2022) 103.

[91] Z. Wojnarowska, J. Knapik, M. Díaz, A. Ortiz, I. Ortiz, M. Paluch, Macromolecules 47 (2014) 4056.

[92] A. Molak, M. Paluch, S. Pawlus, Phys. Rev. B. 78 (2008) 134207.

[93] M.H. Bhat, M. Ganguli, J. Rao, Bull. Mater. Sci. 26 (2003) 407.

[94] D. G. Chen, X. G. Tang, J. B. Wu, W. Zhang, Q. X. Liu, Y. P. Jiang, J. Magn. Magn. Mater. 323 (2011) 1717.

[95] H. Zheng, W. Weng, G. Han, P. Du, J. Phys. Chem. C 117 (2013) 12966.

[96] S. R. Elliot, Adv. Phys. 36 (1987) 135.

[97] N. Ortega, A. Kumar, P. Bhattacharya, S. B. Majumder, R. S. Katiyar, Phys. Rev. B Condens. Matter. 77 (2008) 014111.

Chapter – 5

Temperature dependent dielectric mechanism of lead-free double perovskites Sr_2YbNbO_6 and Sr_2YbSbO_6

5.1. Introduction:

Research in the field of double perovskite oxide with high dielectric constants have grabbed the interest of many researchers because of their diverse physical properties and their wide variety of technological applications. They find application in the manufacturing of filters, capacitors, resonators and oscillators [1–6]. There is a demand for the development of lead-free perovskite oxides due to the ecological constraint of using toxic lead. The volatile nature of lead oxide at high temperatures leads to environmental pollution and creates instability in its composition. Further the lead-based devices cannot be recycled. In the recent years lead free double perovskite oxides have grabbed the interest of the researchers due to their diverse crystal structure and unique dielectric property which are largely affected by their constituent cations [7,8]. Double perovskite oxide based on strontium have been reported to have applications in the field of telecommunication networks as microwave dielectric resonators [9-18]. Also, double perovskites based on niobium have been reported to have good mechanical and electrical properties for uses in electronic industries [19-22].

The structural and room temperature permittivity values of Strontium Ytterbium Niobium Oxide (Sr_2YbNbO_6) have been reported in literature [23,24] but the temperature dependent dielectric relaxation behaviour of SYN has not yet been reported. The crystal structure of Sr_2YbSbO_6 (SYS) has been thoroughly investigated by using neutron diffraction and powder x-ray diffraction techniques [8] but the temperature dependent dielectric relaxation behaviour of SYS has not yet been reported. As the dielectric properties of perovskites are highly dependent on temperature so it is important to investigate the variation in its dielectric parameters with change in temperature in order to understand its polarization mechanism. The signal carrying capacity and propagation swiftness of a device is dependent

on the dielectric constant and dielectric loss of the material, so understanding the dielectric behaviour is important for developing new materials for technological applications. So, in this context we have thoroughly investigated the dielectric permittivity, dielectric loss, ac conductivity of SYN and SYS and shown how their behaviour changes with temperature. We have also reported their crystal structure, surface morphology and optical properties.

5.2. Experimental:

The solid-state ceramic processing technique has been employed for the synthesis of SYN and SYS polycrystalline sample. The reagent grade powders of respective carbonates and oxides were taken in stoichiometric amounts along with acetone and grinded together with the help of agate-mortar for 14 h for SYN and 10 h for SYS. The mixed SYN sample was than calcined in normal atmospheric condition for 12 h at 1350° C which was then cooled at the rate of 100° C/ h till room temperature was reached. SYS sample was calcined in normal atmospheric condition for 8 h at 1500° C which was then cooled at the rate of 100° C/ h till room temperature was reached. The phase of the sample was obtained by powder X-ray diffraction analysis (XRD). The calcined SYN sample were then pelletized into discs (thickness = 1.20×10^{-3} m and diameter = 8×10^{-3} m) using polyvinyl alcohol as binder and applying pressure of 2×10^{6} N/m^2. The calcined SYS sample were then pelletized into discs (thickness = 1.90 mm and diameter = 12.92 mm) using polyvinyl alcohol as binder and applying pressure of 137 MPa. The prepared SYN disc was sintered for 10 h at 1370° C and SYS disc was sintered for 12 h at 1550° C followed by natural cooling. For the electrical measurements silver paste was applied on the two flat edges of the discs in order to develop the electrodes which were then dried at 200° C for 5 h.

The XRD patterns were obtained using CuKα radiation by step scanning at 0.02° per step and over a range of Bragg's angle $20^{o} \leq 2\theta \leq 120^{o}$. The microstructural analysis of the sample was performed using FEI Quanta 200 scanning electron microscope (SEM). The Fourier transform infrared spectra (FTIR) of SYN was recorded from 450 – 1400 cm^{-1} using Perkin-Elemer FT-IR instrument. The Raman measurement of SYN were carried out in between 100 – 900 cm^{-1} using the Raman spectrometer WITEC alpha 300 R. The dielectric measurements of SYN were performed by varying the frequency from 50 Hz to 1 MHz at discrete temperatures (303 – 513 K) using Hioki 3532 LCR meter whereas for SYS the measurements were performed by varying the frequency from 40 Hz to 5 MHz at discrete temperatures (303 – 663 K). During the dielectric measurements the temperature of the sample was increased at the rate of 0.5° C/min using a temperature-controlled oven.

5.3. Results and Discussion:

5.3.1. Structural and microstructural studies:

Fig. 1 (a) and (b) shows the XRD patterns of SYN and SYS, respectively at room temperature whose Rietveld refinement have been performed using GSAS software. The continuous line in Fig. 1 (a) and (b) represents the calculated patterns as obtained from the Rietveld refinement. The refinement parameters and Wykoff positions of SYN and SYS are listed in Table 1 and 2, respectively. SYN crystallizes in monoclinic $P2_1/n$ space group as suggested by Yang et al. [23]. SYS also crystallizes in monoclinic $P2_1/n$ space group. The schematic diagram of the monoclinic unit cell of SYN and SYS are shown in Fig. 2 and Fig. 3, respectively. Each B-site atoms Yb^{3+} and Nb^{5+} are coordinated with six O^{2-} ions forming the YbO_6 and NbO_6 octahedra which are arranged alternatively in the SYN unit cell. The B-site atoms Yb^{3+} and Sb^{5+} are coordinated with six O^{2-} ions forming the YbO_6 and SbO_6

octahedra and are arranged alternatively in the SYS unit cell. It can be observed from Table 3 and Table 4 that the bond lengths of the B-site cations with oxygen are different and there is a difference in the volume of the octahedra associated with each B-site cation. This difference in the bond lengths and volume arises from the ionic size difference and different valency of the constituent B-site cations. The octahedral volume difference associated with each B-site cation is responsible for the octahedral distortions in the samples. The presence of octahedral tilt can be easily observed in Fig. 4 and Fig. 5 for SYN and SYS, respectively. The anti-phase tilting angles of YbO_6 and NbO_6 of SYN are about 7˚ and 9˚ respectively, while their in-phase tilting angles are 1˚ greater than their anti-phase values. In SYS the anti-phase tilting angles of YbO_6 and SbO_6 are about 9˚ and 10˚ respectively, while their in-phase tilting angles are 1˚ greater than their anti-phase values.

Table 1: The parameters obtained from the Rietveld structural refinement.

	SYN	SYS
Crystal system	monoclinic	monoclinic
Space group	$P2_1/n$	$P2_1/n$
A	5.79644(16) (Å)	5.79 (5) Å
B	5.76612(6) (Å)	5.79 (12) Å
C	8.15671(18) (Å)	8.19 (11) Å
Volume	584.593(5) ($Å^3$)	596.42 (5) ($Å^3$)
$\alpha = \gamma$ (º)	90	90
β (º)	90.5109(28)	90.136°
R_{wp}	0.0438	0.079
R_p	0.0504	0.08
GOF(σ)	2.90	1.45

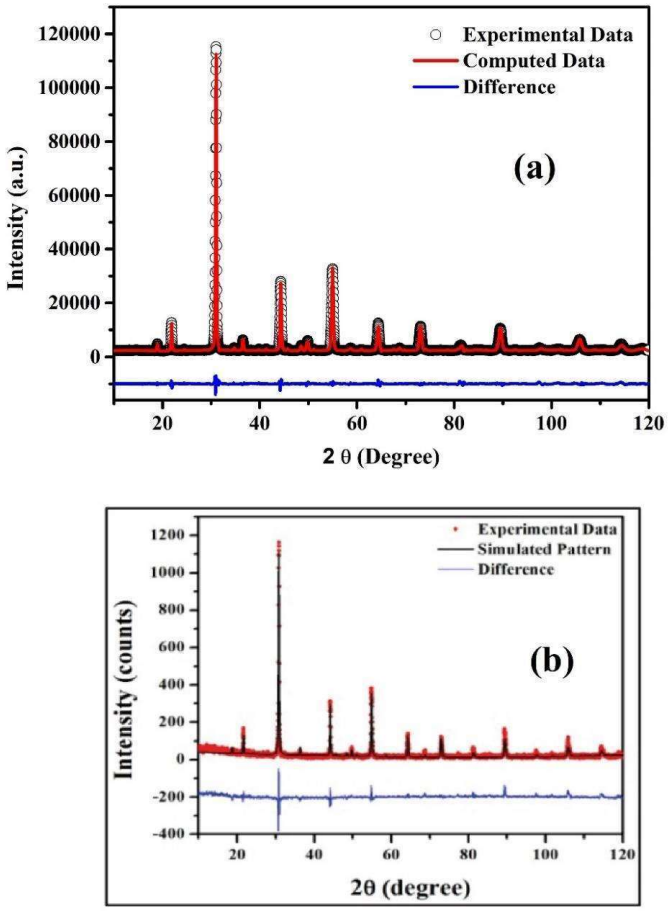

Fig. 1: *The XRD refinement plots of (a) SYN and (b) SYS.*

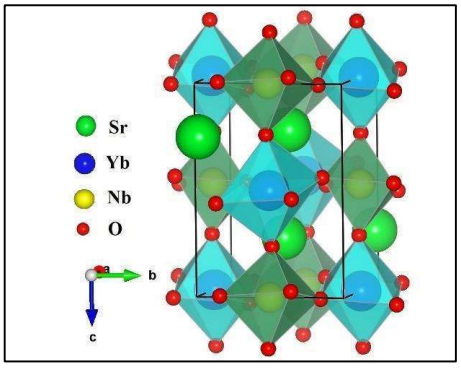

Fig. 2: *Unit cell of SYN*

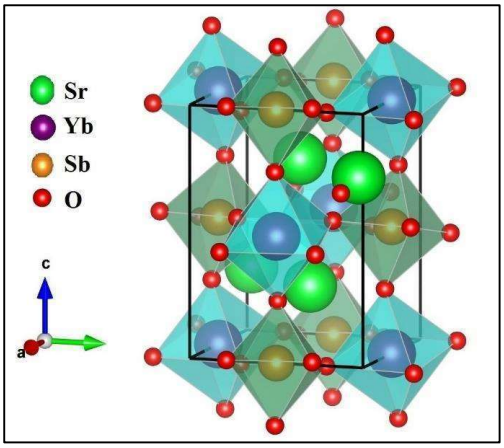

Fig. 3: *Unit cell of SYS*

Table 2: Special Wyckoff sites of the atoms and refined atomic coordinates of SYN and SYS.

SYN					
Atom	Site	x (Å)	y (Å)	z (Å)	B (Å^2)
Sr	4e	0.0050(4)	0.02059(33)	0.25214(19)	0.0208(4)
Yb	2d	0.5	0.0	0.0	0.0266(5)
Nb	2c	0.0	0.5	0.0	0.0269(7)
O1	4e	0.2346(21)	0.7856(15)	0.0211(15)	0.0010(29)
O2	4e	0.2450(19)	0.3019(14)	-0.9539(15)	0.0073(35)
O3	4e	0.4458(12)	0.0034(24)	-0.2644(10)	0.0210(25)
SYS					
Sr	4e	0.0047 (5)	0.0243 (2)	0.2484 (4)	0.51 (2)
Yb	2d	0.5	0.0	0.0	0.10
Sb	2c	0.0	0.5	0.0	0.10
O1	4e	0.2988 (4)	0.2831 (5)	0.0375 (4)	0.55 (8)
O2	4e	0.2771 (5)	0.2832 (5)	0.3646 (4)	0.60 (7)
O3	4e	0.96310 (4)	0.4565 (4)	0.1360 3()	0.07 (4)

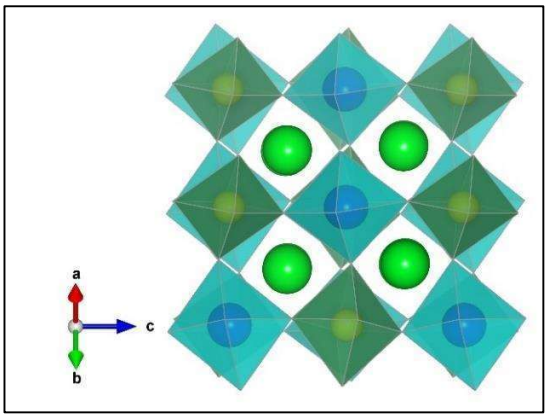

Fig. 4: *Octahedral tilt in SYN.*

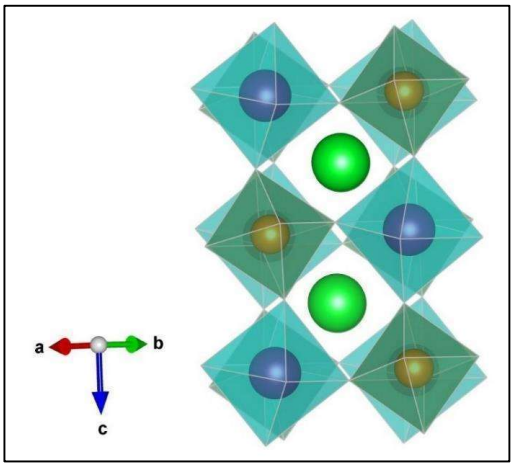

Fig. 5: *Octahedral tilt in SYS*

Table 3. Bond lengths and bond angles of different atoms in YbO_6 and NbO_6 octahedra of SYN.

NbO_6 octahedra		YbO_6 octahedra	
Bond lengths (Å)			
$Nb\text{-}O1^{i}$, $Nb\text{-}O1^{ii}$	1.950(9)	$Yb\text{-}O1^{i}$, $Yb\text{-}O1^{ii}$	2.177(9)
$Nb\text{-}O2^{iii}$, $Nb\text{-}O2^{iv}$	2.142(11)	$Yb\text{-}O2^{i}$, $Yb\text{-}O2^{ii}$	1.982(11)
$Nb\text{-}O3^{v}$, $Nb\text{-}O3^{vi}$	1.858(11)	$Yb\text{-}O3^{i}$, $Yb\text{-}O3^{ii}$	2.317(10)
Bond angles (°)			
$O1^{i}\text{-}Nb\text{-}O1^{ii}$, $O2^{iii}\text{-}Nb\text{-}O2^{iv}$, $O3^{v}\text{-}Nb\text{-}O3^{vi}$	180	$O1^{i}\text{-}Yb\text{-}O1^{ii}$, $O2^{i}\text{-}Yb\text{-}O2^{ii}$, $O3^{i}\text{-}Yb\text{-}O3^{ii}$	180
$O2^{iii}\text{-}Nb\text{-}O1^{i}$, $O2^{iv}\text{-}Nb\text{-}O1^{ii}$	87.9(5)	$O1^{ii}\text{-}Yb\text{-}O3^{i}$, $O3^{ii}\text{-}Yb\text{-}O1^{i}$	86.1(5)
$O2^{iii}\text{-}Nb\text{-}O1^{ii}$, $O1^{i}\text{-}Nb\text{-}O2^{iv}$	92.1(5)	$O3^{i}\text{-}Yb\text{-}O1^{i}$, $O1^{ii}\text{-}Yb\text{-}O3^{ii}$	93.9(5)
$O3^{iv}\text{-}Nb\text{-}O2^{iii}$, $O2^{iv}\text{-}Nb\text{-}O3^{iii}$	91.6(5)	$O3^{i}\text{-}Yb\text{-}O2^{ii}$, $O3^{ii}\text{-}Yb\text{-}O2^{i}$	92.4(4)
$O2^{iii}\text{-}Nb\text{-}O3^{iii}$, $O2^{iv}\text{-}Nb\text{-}O3^{iv}$	88.4(5)	$O3^{ii}\text{-}Yb\text{-}O2^{ii}$, $O3^{i}\text{-}Yb\text{-}O2^{i}$	87.6(4)
$O1^{i}\text{-}Nb\text{-}O3^{iii}$, $O3\text{-}Nb\text{-}O1^{iv}$	94.4(5)	$O1^{ii}\text{-}Yb\text{-}O2^{i}$, $O2^{ii}\text{-}Yb\text{-}O1^{i}$	90.8(5)
$O1^{i}\text{-}Nb\text{-}O3^{iv}$, $O1^{iii}\text{-}Nb\text{-}O3^{ii}$	85.6(5)	$O2^{i}\text{-}Yb\text{-}O1^{i}$, $O1^{ii}\text{-}Yb\text{-}O2^{ii}$	89.2(5)
Volume of octahedron ($Å^3$)	10.307	Volume of octahedron ($Å^3$)	13.2832
Quadratic elongation	1.0097	Quadratic elongation	1.0104

Symmetry codes: i. (x, y, z), ii. (-x, -y, -z), iii. (-x+1/2, y+1/2, -z+1/2), iv. (x+1/2, -y+1/2, z+1/2), v. (x+1/2, -y+1/2, z+1/2), vi. (-x+1/2, y+1/2, -z+1/2)

Table 4. Bond lengths and bond angles of different atoms in YbO_6 and SbO_6 octahedra of SYS.

SbO_6 octahedra		YbO_6 octahedra	
Bond lengths (Å)			
Sb-O1^{i}, Sb-O1^{ii}	1.984(0)	Yb-O1^{i}, Yb-O1^{ii}	2.208(3)
Sb-O2^{iii}, Sb-O2^{iv}	1.968(2)	Yb-O2^{i}, Yb-O2^{ii}	2.219(3)
Sb-O3^{v}, Sb-O3^{vi}	1.993(3)	Yb-O3^{i}, Yb-O3^{ii}	2.191(4)
Bond angles (°)			
O1^{i}-Sb-O1^{ii}, O2^{iii}-Sb-O2^{iv}, O3^{v}-Sb-O3^{vi}	180	O1^{i}-Yb-O1^{ii}, O2^{i}-Yb-O2^{ii}, O3^{i}-Yb-O3^{ii}	180
O2^{iii}-Sb-O1^{i}, O2^{iv}-Sb-O1^{ii}	89.27(11)	O1^{ii}-Yb-O3^{i}, O3^{ii}-Yb-O1^{i}	89.2(11)
O2^{iii}-Sb-O1^{ii}, O1^{i}-Sb-O2^{iv}	90.72(11)	O3^{i}-Yb-O1^{i}, O1^{ii}-Yb-O3^{ii}	90.7(11)
O3^{iv}-Sb-O2^{iii}, O2^{iv}-Sb-O3^{iii}	89.27(9)	O3^{i}-Yb-O2^{ii}, O3^{ii}-Yb-O2^{i}	90.39(9)
O2^{iii}-Sb-O3^{iii}, O2^{iv}-Sb-O3^{iv}	89.60(9)	O3^{ii}-Yb-O2^{ii}, O3^{i}-Yb-O2^{i}	89.6(9)
O1^{i}-Sb-O3^{iii}, O3-Sb-O1^{iv}	90.7(7)	O1^{ii}-Yb-O2^{i}, O2^{ii}-Yb-O1^{i}	90.4(7)
O1^{i}-Sb-O3^{iv}, O1^{iii}-Sb-O3^{ii}	89.75(7)	O2^{i}-Yb-O1^{i}, O1^{ii}-Yb-O2^{ii}	89.5(7)
Volume of octahedron (Å^3)	10.38	Volume of octahedron (Å^3)	14.31
Quadratic elongation	1.0001	Quadratic elongation	1.0003

From the SEM image of SYN and SYS (Fig. 6) it can be observed that the polycrystalline grains (size ~ 2.38 μm for SYN and 0.5 to 2.4 μm for SYS) having well defined grains and grain boundaries are uniformly distributed throughout the sample.

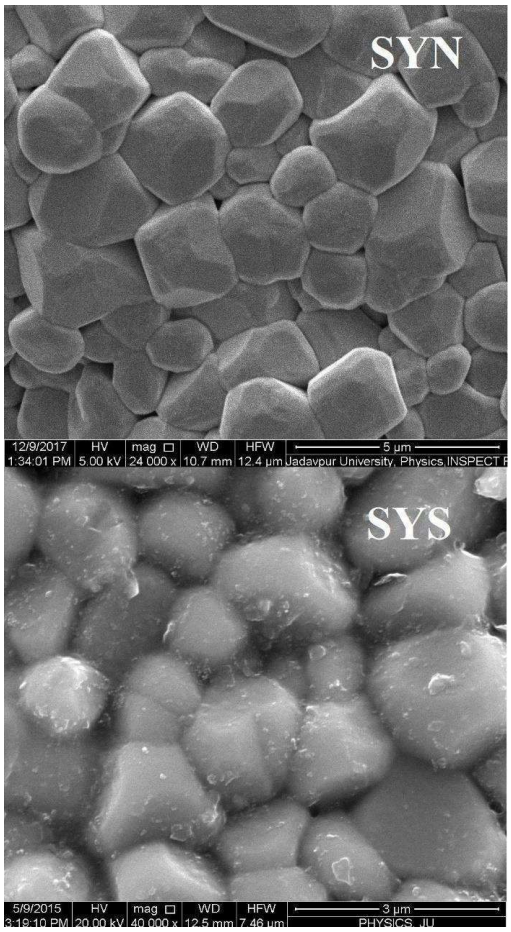

Fig. 6: *The SEM image of SYN and SYS.*

5.3.2. Raman Analysis:

The observed Raman spectra of SYN is given in Fig. 7 (a) and the Lorentzian peak fitting of the obtained experimental spectra are illustrated in Fig. 7 (b) and 7 (c). The Lorentzian peak fitting of the obtained experimental spectra of SYS is illustrated in Fig. 8. The obtained Raman spectra of SYN and SYS agrees well with their analogous systems

having $P2_1/n$ space group [7,25]. The peak positions and the full width half maxima as obtained from fitting are tabulated in Table 5.

The group theoretical analysis based on the atoms present in the Wykoff position have been performed in order to estimate the number of modes present in the Raman spectra (Table 6). The splitting of Raman peaks in the lower wavenumber side agrees well with the monoclinic structure of the samples as obtained from the XRD analysis. It can be seen that for monoclinic crystal with $P2_1/n$ space group, 24 modes are Raman active, 33 modes are IR active and 3 are acoustic modes. The obtained Lorentzian peaks of SYN agrees well with the 24 Raman active modes as calculated from the group theoretical analysis. In case of SYS 17 Raman modes are obtained and the lesser number of modes results from the overlapping of modes present in close proximity.

For SYN the peak centred around 818 cm^{-1} is associated with the NbO_6 octahedra due to the symmetric stretching vibration of the oxygen atom along the Yb-O-Nb axis [25]. The peak centred around 611 and 730 cm^{-1} arises due to the oxygen present in Yb-O-Nb as a result of its asymmetric stretching vibration along the axis. The peak centred around 416 cm^{-1} arises as a result of the oxygen bending motion in the octahedra. The translations of Sr cation give rise to the modes in the range of 110 - 300 cm^{-1} [26,27] as seen in case of both SYN and SYS. The lattice modes 336 and 362 cm^{-1} arise due to the rotation of the Sr cation [28]. For SYS peak around 422 cm^{-1} arises as a result of the oxygen bending motion in the octahedra. The asymmetric bending mode of SbO_6 octahedra is associated with the peak around 410 cm^{-1}. The peak centred around 800 cm^{-1} is associated with the symmetric stretching vibration of the SbO_6 octahedra. The peaks from 637 to 747 cm^{-1} arises due to the oxygen present in Yb-O-Sb as a result of its asymmetric stretching vibration along the axis [25].

Table 5. The experimentally obtained Raman modes of SYN and SYS.

Peak No.	SYN		SYS	
	Frequency (cm^{-1})	FWHM (cm^{-1})	Frequency (cm^{-1})	FWHM (cm^{-1})
1	110.2008	7.07386	115.48604	19.27038
2	128.51294	8.877	135.3251	12.88668
3	141.39116	12.21815	152.21126	19.93674
4	165.0593	12.9296	176.87099	22.88806
5	181.32052	25.32243	217.41972	12.96247
6	223.8383	29.35113	245.51857	21.30001
7	244.49817	16.74165	260.52867	16.51851
8	260.08837	14.68493	347.1244	7.6678
9	300.88907	30.42473	410.35191	22.02594
10	336.13334	20.99071	422.35664	11.68328
11	362.52812	25.30198	449.36573	11.27225
12	399.51069	18.31047	692.86486	131.47424
13	416.60965	19.92099	581.01045	21.43655
14	446.41831	10.30443	637.56166	0.5
15	532.8278	43.7371	747.58964	42.55122
16	560.73332	31.94242	765.33438	19.00128
17	577.83441	22.63165	800.90293	19.86821
18	596.1208	14.01845		
19	611.19178	18.53529		
20	630.48892	38.6828		
21	730.37607	19.31161		
22	764.67128	23.65405		
23	798.36005	22.11283		
24	818.51463	24.03372		

Table 6. Distribution of modes for the monoclinic SYN and SYS crystal with $P2_1/n$ space group.

Atom	Site		Distribution of modes
Sr	4e		$3A_g + 3A_u + 3B_g + 3B_u$
Yb	2b		$3A_u + 3B_u$
Nb	2d		$3B_u + 3A_u$
O_1	4e		$3B_g + 3B_u + 3A_g + 3A_u$
O_2	4e		$3B_g + 3B_u + 3A_g + 3A_u$
O_3	4e		$3B_g + 3B_u + 3A_g + 3A_u$
Modes for the atoms in their Wykoff site:		Γ_{TOTAL}	$12B_g + 18B_u + 12A_g + 18A_u$
		$\Gamma_{ACOUSTIC}$	$A_u + 2B_u$
		Γ_{RAMAN}	$12A_g + 12B_g$
		Γ_{IR}	$17A_u + 16B_u$

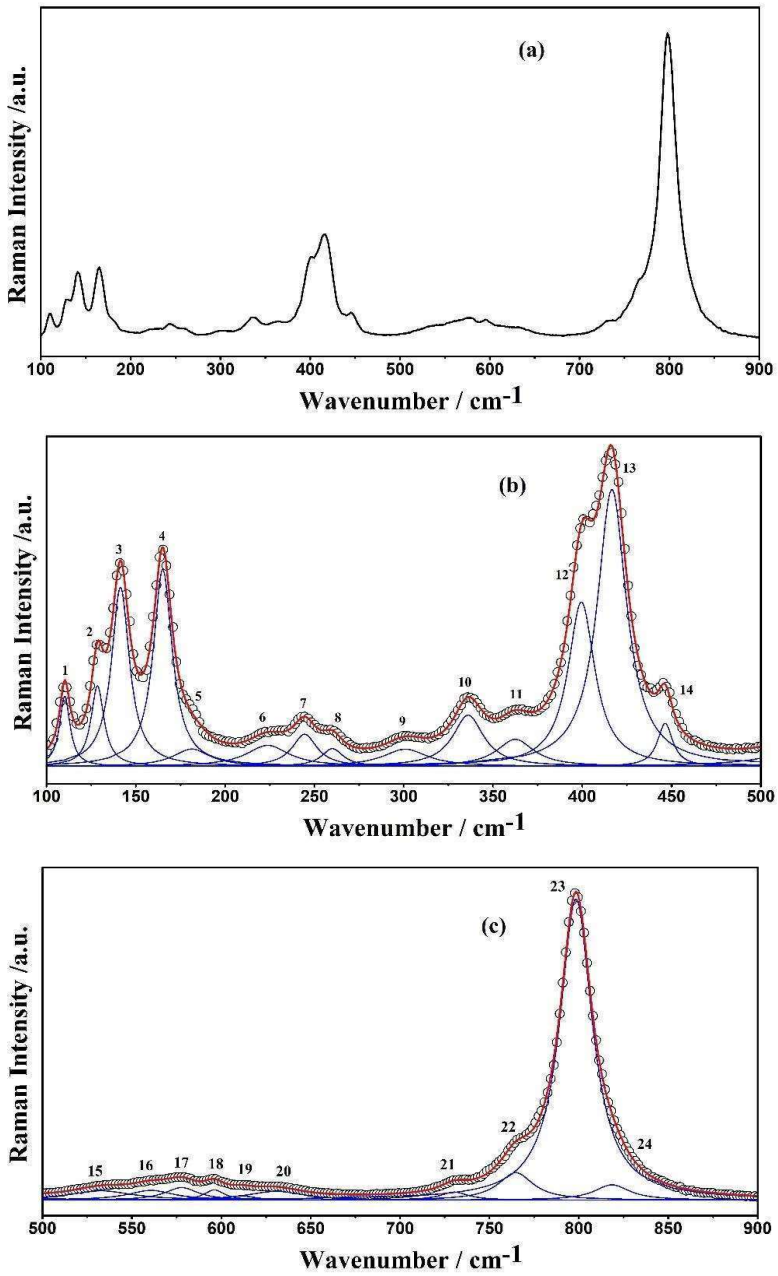

Fig. 7: *(a) The Raman spectra of SYN, (b) and (c) fitted Lorentzian curve represented by red line and experimental data represented by symbols.*

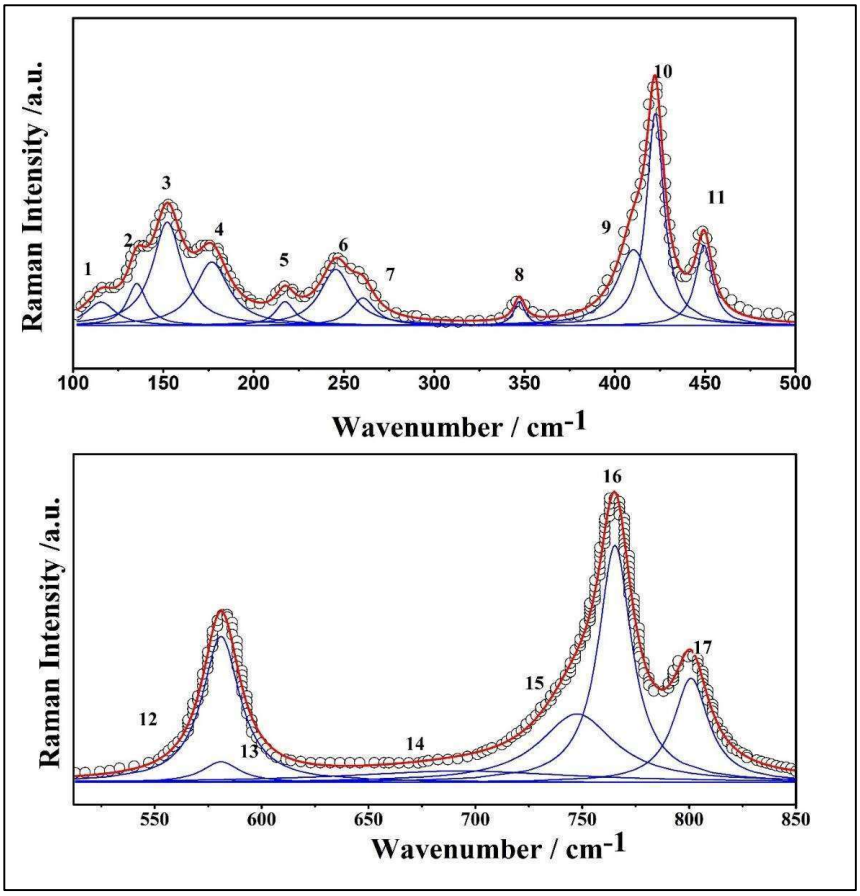

Fig. 8: *The Raman spectra of SYS with fitted Lorentzian curve represented by red line and experimental data represented by symbols.*

5.3.3. FTIR Analysis:

The FTIR spectrum of SYN and SYS are shown in Fig. 8 and 9, respectively. The bands below 500 cm^{-1} arises due to bending mode of the polyhedra associated with the B-site atoms [28]. For the NbO_6 octahedra its asymmetric bending mode gives rise to the band around 470 cm^{-1} and for SbO_6 it is obtained at 459 cm^{-1}. The bands around 548 to 700 cm^{-1} arises due to the octahedra associated with the B-site atoms. For the asymmetric stretching

mode of YbO_6 the band arises at 548 cm^{-1} for SYN and 570 cm^{-1} for SYS. For NbO_6 the band arises at 634 cm^{-1} in SYN and for SbO_6 the band arises at 688 cm^{-1}. The broad nature of the bands is due to the overlapping of the vibrational modes associated with YbO_6 and NbO_6 in SYN whereas the overlapping of the vibrational modes of YbO_6 and SbO_6 gives rise to the broad bands in SYS. The symmetric stretching mode of the NbO_6 octahedra in SYN also gives rise to the weak band around 861 cm^{-1} [27]. The symmetric stretching mode of the SbO_6 octahedra in SYS gives rise to the weak band around 855 cm^{-1}. Similar spectral patterns having two well defined bands in the range of 450 to 650 cm^{-1} have been reported for several $A_2B'B''O_6$ double perovskite oxide [29-34].

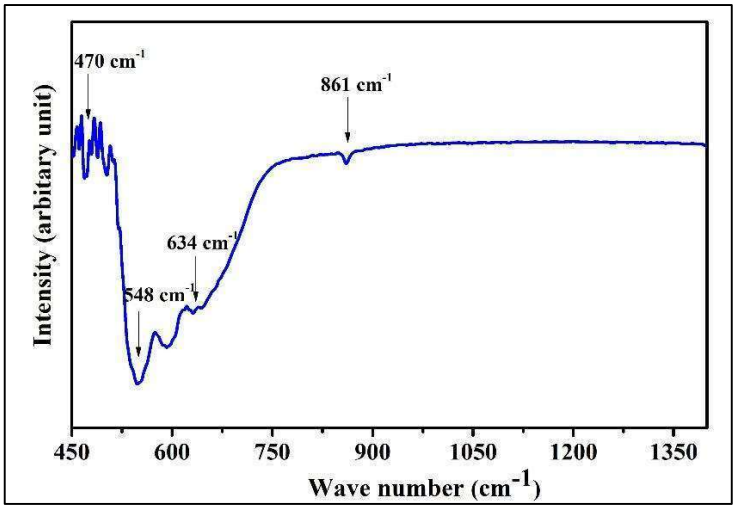

Fig. 8: *The FTIR spectrum of SYN.*

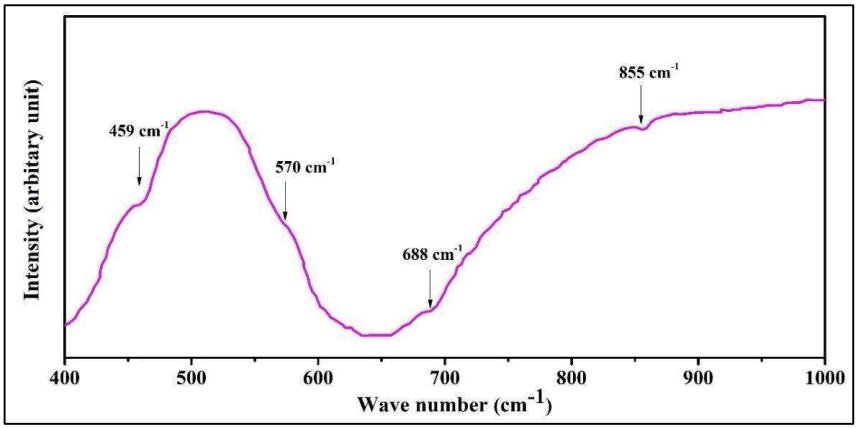

Fig 9: *The FTIR spectrum of SYS.*

5.3.4. Optical absorption and emission study:

The presence of crystalline defects and compositional ordering in a sample along with its electronic properties strongly effects its optical properties. The optical properties of SYN and SYS have been investigated with the help of UV and Photoluminescence spectroscopic analysis. The experimental band gap of SYN and SYS has been calculated with the help of the optical absorption spectrum in the UV region and shown in Fig. 10 and 11, respectively. The value of E_g has been calculated by extrapolating the linear absorption edge and it is found to be 3.08 eV for SYN and 3.65 eV for SYS. Due to this high value of band gap the SYN and SYS sample may find applications in high frequency optoelectronic devices as such materials works well in the UV spectral region [36,37].

The Photoluminescence (PL) spectra of SYN and SYS are illustrated in Fig. 12 and 13, respectively. In the B cation octahedra (YbO_6, NbO_6 and SbO_6) the displacement of the oxygen ions from their symmetric positions induces PL in SYN and SYS [38]. In the PL spectra of SYN an intense peak at about 367 nm can be observed which arises due to the electron transition from the valence band (composed of the 2p orbitals occupied by the oxide)

to the conduction band (containing empty d orbitals present in the transition metals) whereas for SYS this peak is obtained at 403 nm. The crystalline defects present in the microstructure gives rise to a small peak in the PL spectra at about 404 nm for SYN and 466 nm for SYS. The broad nature of the PL spectrum is either due to the presence localized states of defects and impurities or due to the states resulting from electron phonon coupling like self-trapped excitations or polarons [39].

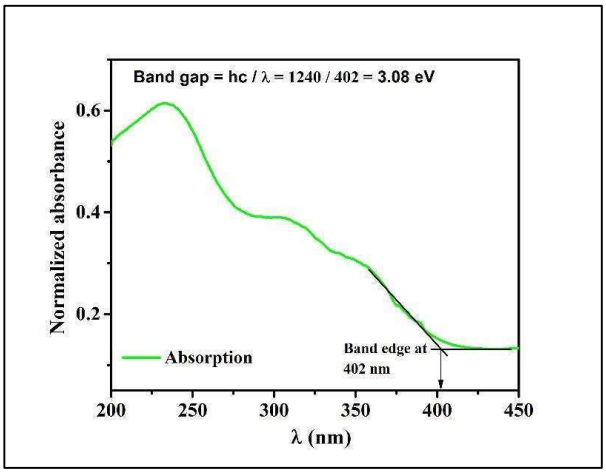

Fig. 10: *The optical absorption spectra of SYN.*

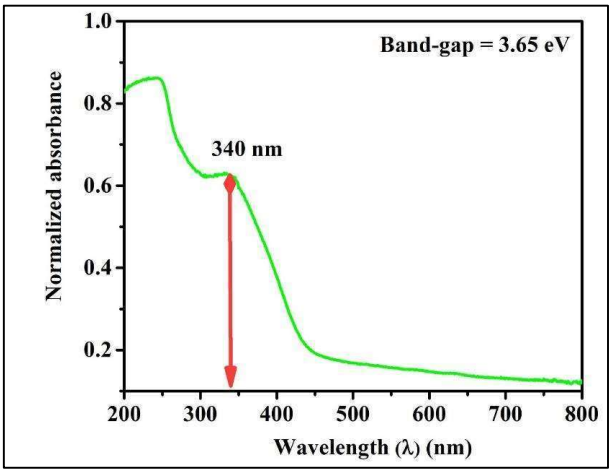

Fig. 11: *The optical absorption spectra of SYS.*

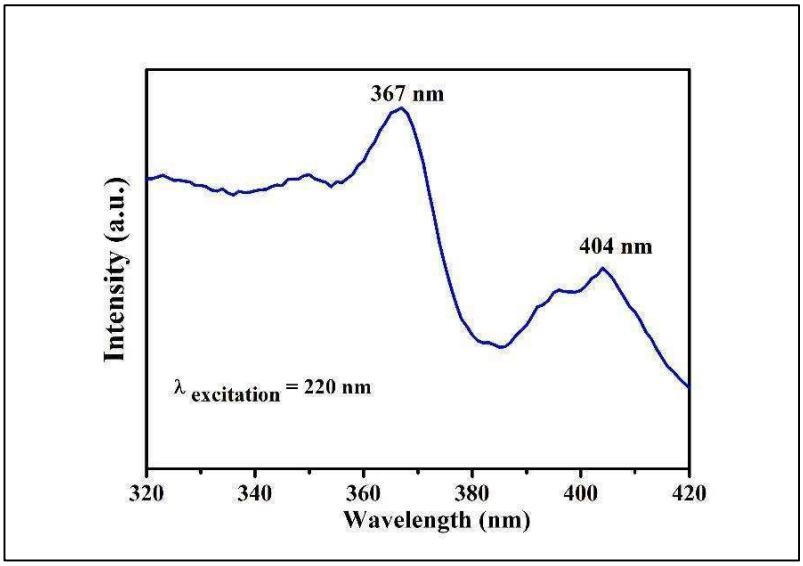

Fig. 12: *The PL spectra of SYN.*

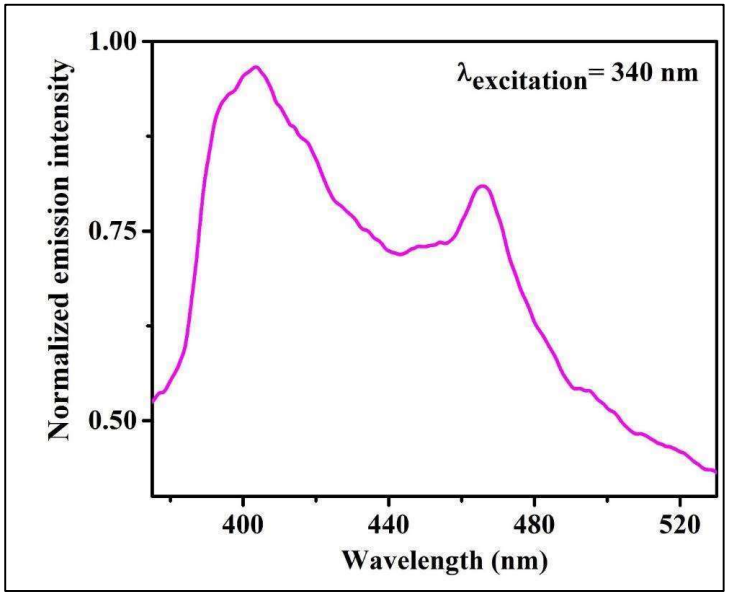

Fig. 13: *The PL spectra of SYS.*

5.3.5. Dielectric analysis:

The angular frequency (ω) and temperature dependence of ε' and ε'' which are the real and the imaginary part of the complex dielectric permittivity (ε*) for SYN are shown in Fig. 14 (a) and (b), respectively. For SYS the angular frequency and temperature dependence of ε' and loss tangent (tan δ) are shown in Fig. 15 (a) and (b), respectively. The orientational polarization associated with frequency governs the relaxation behaviour of the material. The variation of ε' with frequency and the relaxation peak in the frequency dependent ε'' or tan δ curve points towards Debye type relaxation. The dielectric permittivity arising from the oscillations of the free dipoles in presence of the alternating field can be analysed using the Debye equation [40].

At any given temperature if the frequency of the applied alternating field is low the dipoles will be fully polarized whereas if a high frequency field is applied it gets reversed even before the dipole polarization takes place. Thus, the magnitude of polarization decreases beyond a certain frequency resulting in the decrease of its ε' value [Fig. 14]. When the temperature is high more polarization of dipoles occurs due to which the relaxation occurs at higher value of frequency which can be observed in Fig. 14 and 15. When the low frequency field is applied charge migration of the free charge carriers is obstructed by the grain boundaries causing them to accumulate near the barrier which results in the localized polarization inside the grains [41]. This localized polarization is responsible for the high ε' values at low frequencies. At low frequency the ε'' value is high due to the presence of dc conductivity in SYN which becomes negligible at higher frequencies.

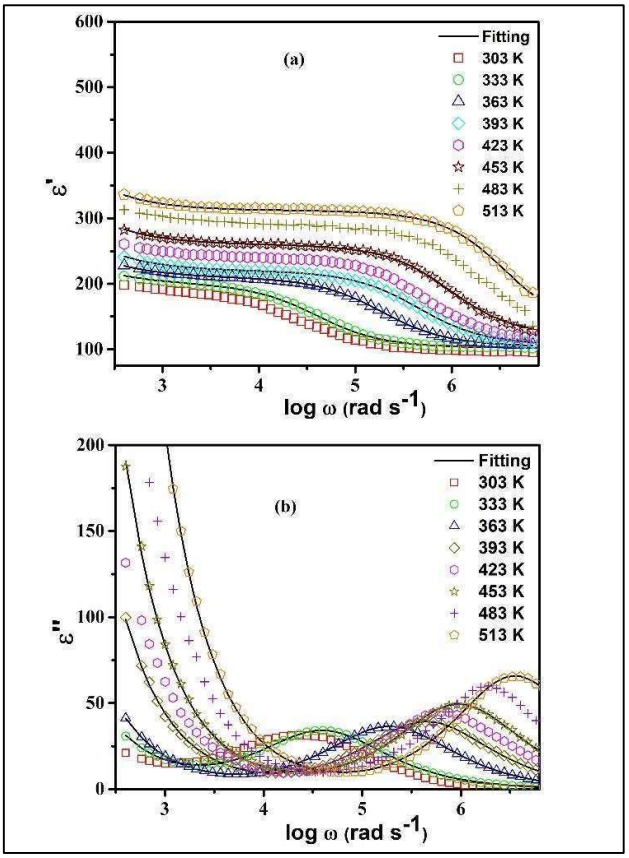

Fig. 14: *The variation of (a) ε′ and (b) ε″ with frequency at different temperatures for SYN.*

The dielectric permittivity can be analysed with the help of the Cole-Cole relaxation equation [42, 43]

$$\varepsilon * = \varepsilon' - i\varepsilon'' = \varepsilon_\infty + \frac{\varepsilon_s - \varepsilon_\infty}{1+(i\omega\tau)^{1-\alpha}} \quad (1)$$

where ε_s is the constant and ε_∞ is the high frequency values of ε*, τ is the average relaxation time and α is Cole-Cole parameter ($0 \leq \alpha \geq 1$). In case of ideal Debye type monodispersive relaxation α is 0 but $\alpha > 0$ for non-Debye type polydispersive relaxation. In the Cole-Cole equation conductivity term needs to be incorporated as dc conductivity dominates in the low frequency region [44,45]

$$\varepsilon * = \varepsilon_\infty + \frac{\varepsilon_s - \varepsilon_\infty}{1+(i\omega\tau)^{1-\alpha}} - i\frac{\sigma*}{\varepsilon_0\omega^n} \quad (2)$$

where complex conductivity $\sigma^* = (\sigma_1 + i\,\sigma_2)$ where σ_1 is dc conductivity, σ_2 is the conductivity associated with the charges that are localized and n is a constant ($0 < n < 1$). The equation 2 can be written in terms of its real and imaginary parts

$$\varepsilon' = \varepsilon_\infty + \frac{(\varepsilon_s - \varepsilon_\infty)\left[1+(\omega\tau)^{1-\alpha}sinsin\frac{1}{2}\alpha\pi\right]}{1+2(\omega\tau)^{1-\alpha}sinsin\frac{1}{2}\alpha\pi+(\omega\tau)^{2(1-\alpha)}} - \frac{\sigma_2}{\varepsilon_0\omega^n} \quad (3)$$

$$\varepsilon'' = \frac{(\varepsilon_s - \varepsilon_\infty)(\omega\tau)^{1-\alpha}coscos\frac{1}{2}\alpha\pi}{1+2(\omega\tau)^{1-\alpha}sinsin\frac{1}{2}\alpha\pi+(\omega\tau)^{2(1-\alpha)}} + \frac{\sigma_1}{\varepsilon_0\omega^n} \quad (4)$$

the dielectric loss can also be written as $\tan\delta = \varepsilon''/\varepsilon'$ (5)

The curves in Fig. 14 have been fitted using equation 3 and 4 and the fitted parameters have been provided in Table 7.

Since the effect of dc conductivity is not that evident in the loss spectra of SYS, we have fitted Fig. 15 neglecting the contribution of dc conductivity while using equations 3, 4 and 5. The fitting parameters for SYS have been provided in Table 8. The dielectric relaxation in SYN and SYS is polydispersive in nature ($\alpha > 0$ in Table 7 and 8) with distribution of relaxation time. Dipolar and conductivity relaxation together contributes to the overall dielectric relaxation in SYN whereas for SYS dipolar relaxation dominates the overall dielectric relaxation process [46-48]. The relaxation of the permanent dipole orientation is linked with the first term in equation 4 whereas the loses arising from the long-range movement of the charge carriers is associated with its second term. The accumulation of charge carriers in the interfaces and defect sites is linked to σ_2 and has a large contribution to the ε' values whereas σ_1 linked with the movement of the free charge carriers contributes to ε''.

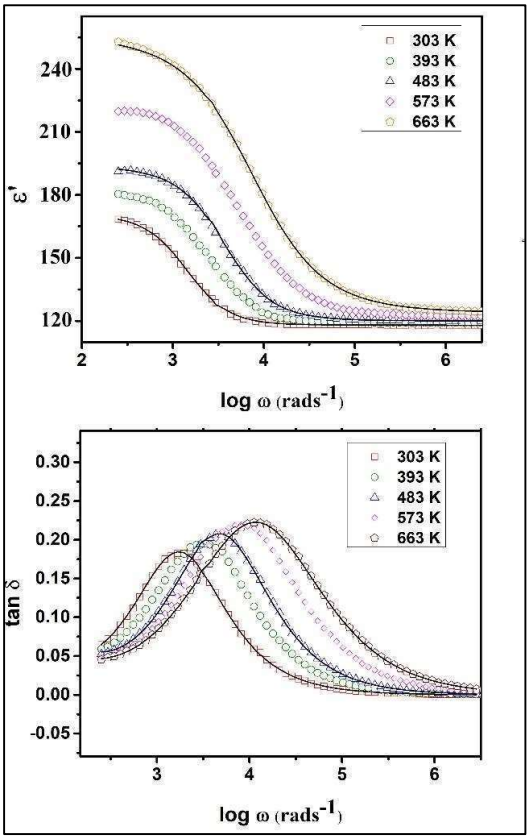

Fig. 15: *The variation of (a) ε' and (b) tan δ with frequency at different temperatures for SYS.*

Table 7. The Cole-Cole fitting parameters of the dielectric spectra of SYN.

Temperature (K)	ε_s	ε_∞	ω_m (Hz)	α	n	σ_1 (Sm^{-1})	σ_2 (Sm^{-1})
333	200	102	40219	0.15	0.86	0.45×10^{-7}	0.2×10^{-7}
363	210	104	190259	0.15	0.88	0.70×10^{-7}	0.3×10^{-7}
393	220	106	451668	0.15	0.89	1.8×10^{-7}	0.4×10^{-7}
453	260	120	958226	0.14	0.90	3.7×10^{-7}	0.45×10^{-7}
513	312	130	3552661	0.13	0.91	9.9×10^{-7}	0.48×10^{-7}

Table 8. The Cole-Cole fitting parameters of the dielectric spectra of SYS.

Temperature (K)	ε_s	ε_∞	ω_m (rads^{-1})	α
303	16.83	11.6	1433	0.02
483	19.22	12	3703	0.06
663	25.14	12.4	7525	0.19

5.3.6. Conductivity analysis:

The frequency dependent ac conductivity has been studied at different temperatures in order to analyse the effect of conductivity on the dielectric properties. Considering the dielectric loss at any given temperature is due to the conductivity, then the real part of the conductivity (σ) can be expressed as $\sigma = \omega \varepsilon_o \varepsilon''$ [29]. The plot of log of ac conductivity and log of frequency at different temperature is illustrated in Fig. 16 for SYN and Fig. 17 for SYS. The plot for SYN consists of two plateaus where the low frequency region is associated with the dc conductivity (σ_{dc}) arising from the accumulation of charge carriers [49] and the high frequency plateau is due to the grain's contribution to the total conductivity. Thus, two process are associated with the bulk conduction behaviour of SYN. In SYS only one plateau is evident indicating only the grain's contribution to the total conductivity. At low frequency the conductivity is independent of frequency as the charge carriers diffuse randomly by hopping between different localized sites.

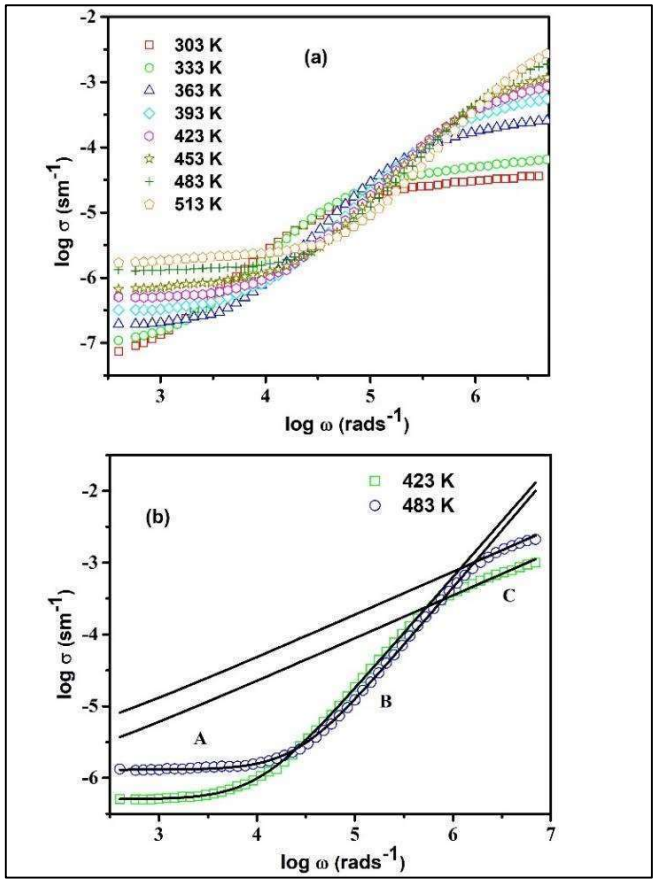

Fig. 16: *The temperature dependence of dc conductivity for SYN.*

At high frequencies the conductivity curves exhibit dispersion. The conductivity spectra have been fitted using the Jonscher power law [50,51]:

$$\sigma(\omega) = \sigma_{dc}\left[1+ \left(\frac{\omega}{\omega_H}\right)^n\right] \quad (6)$$

where ω_H is the hopping frequency of the charge carriers and the constant n has the values between 1.5-1.9 (low frequency) and 0.4-0.6 (high frequency). The fitting parameters are provided in Table 9 and 10. The overall conductivity spectra of SYN can be subdivided into three regions [52]. In region A as the frequency is low the electric field does not have any effect on the conduction behaviour of charge particles and the conductivity value is almost

equal to its dc value. In region B when the frequency exceeds a certain critical value the conductivity starts increasing because on increasing the frequency the capacitor admittance becomes larger than the resistor admittance. In region C the conductivity becomes proportional to frequency leading to a constant loss [53]. Region C is absent in the conductivity spectra of SYS.

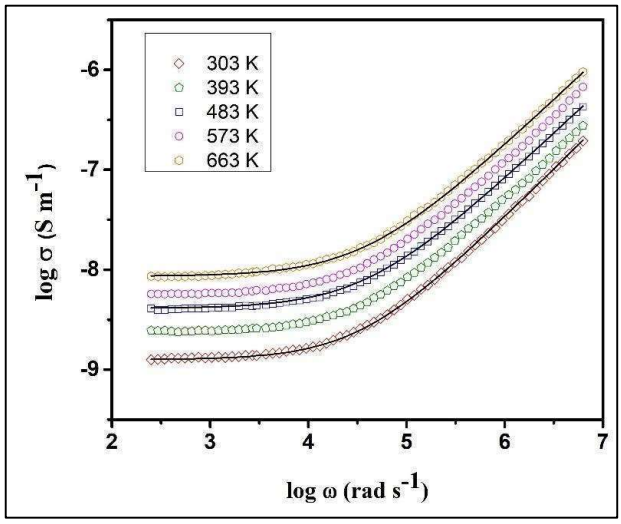

Fig. 17: *The temperature dependence of dc conductivity for SYS.*

Table 9. The power law fitting parameters of the conductivity spectra of SYN.

Temperature (K)	σ_{dc} (Sm^{-1})	ω_H	n
423 (at low frequency)	5.01×10^{-7}	10281.46	1.56
423 (at high frequency)	5.01×10^{-7}	18.1726	0.6
483 (at low frequency)	13.01×10^{-7}	25881.46	1.6
483 (at high frequency)	13.01×10^{-7}	25.1726	0.6

Table 10. The power law fitting parameters of the conductivity spectra of SYS.

Temperature (K)	σ_{dc} (Sm^{-1})	ω_H	n
303	1.2548×10^{-9}	34355	0.97
483	4.1031×10^{-9}	43960	0.98
663	8.6032×10^{-9}	43960	0.99

It has been illustrated in Fig.18 for SYN and Fig. 19 for SYS that the variation of dc conductivity with temperature follows the Arrhenius equation: $\sigma_{dc} = \sigma_0 \exp\left[-\frac{E_\sigma}{K_B T}\right]$, E_σ being the activation energy. The value of E_σ has been obtained to be 0.52 eV for SYN and 0.21 for SYS by linear fitting of the Arrhenius plot. Thus, the conduction mechanism of SYN and SYS is mainly due to the hopping of p type polarons [54,55]. As the presence of grain and grain boundary gives rise to different potentials, the hopping of charge carriers in between these potentials gives rise to the step like nature of the conductivity spectra as seen in SYN [56].

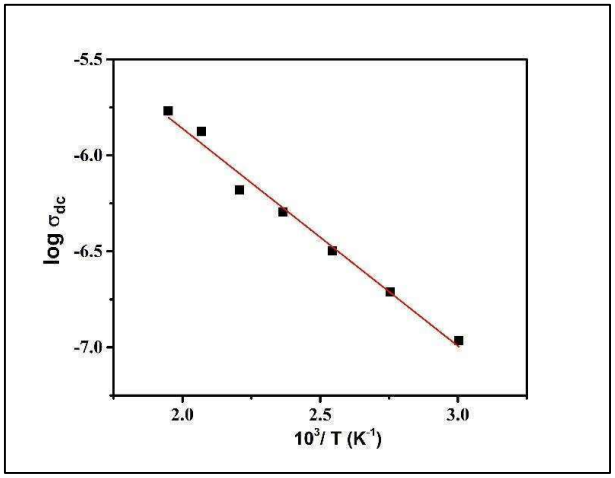

Fig. 18: *The Arrhenius plot for SYN*

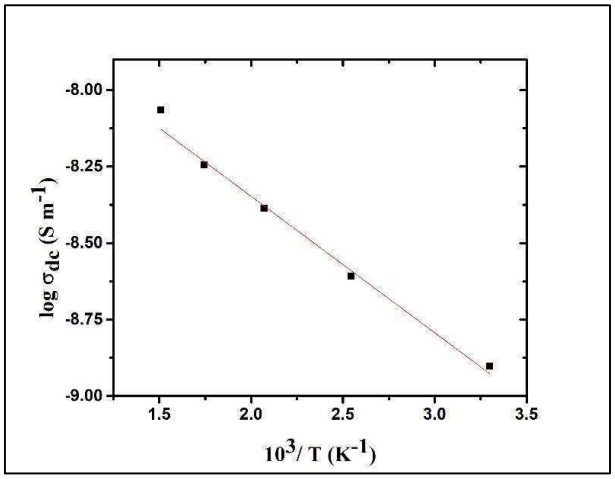

Fig. 19: *The Arrhenius plot for SYS*

5.4. Conclusion:

The double perovskite oxides SYN and SYS has been synthesized using solid-state synthesis technique. Both SYN and SYS possesses monoclinic crystal structure with $P2_1/n$ space group. The samples are polycrystalline in nature with grain size ~ 2.38 μm for SYN and 0.5 to 2.4 μm for SYS. The analysis of the Raman spectrum using Lorentzian peak fitting reveals 24 Raman active modes in SYN and 17 Raman active modes in SYS. The dielectric relaxation in both the samples are polydispersive in nature and has been analysed using the Cole-Cole model. The ε' and ε'' values of SYN is found to be ~ 175 and 23 at 1 KHz. The ε' and tan δ values of SYS is found to be ~ 120 and 0.15 at 1 KHz. The activation energy is 0.52 eV for SYN and 0.21 for SYS as obtained from the Arrhenius plot and the conduction is due to the hopping of p-type polaron.

Dielectric permittivity arises due to the polarization associated with the ionic displacement, electronic displacement and dipole orientation. The permittivity values at any constant temperature decreases with the ionic size of the cations as smaller the electron

orbital radius lower is the electronic displacement polarizability. The ionic displacement polarization also tends to decrease with the decrease in the radius of the associated positive and negative ions [57]. This variation of the permittivity values with the size of the constituent ions can be analysed by comparing the dielectric properties of SYN and SYS with few of their analogous counterpart. The permittivity value and dielectric loss for SYS at 1 KHz is lower than SYN due to the smaller ionic size of Sb as compared to Nb and the permittivity value of Sr_2YbTaO_6 at 1 KHz is ~ 187 which is slightly higher than SYN owing to the larger ionic radii of Ta as compared to Nb [58,59]. The permittivity value of Ba_2YbNbO_6 (BYN) at 1 KHz is ~ 269 which is much greater than SYN due to the larger atomic size of Ba as compared to Sb [60]. The value of ε" for BYN is ~ 80 and for SYN is 23 at 1 KHz. The lower value of loss in SYN is due to the presence of octahedral tilting in the system while no such tilting is observed in case of BYN which possess cubic *Fm3m* structure. The systems having octahedral tilting can absorb thermal energy by reducing the octahedral tilting amplitude whereas for no tilt structure thermal energy is largely absorbed by phonons. The anharmonicity of the restoring forces is increased due to the absorption of thermal energy by phonons. The increase in the anharmonicity of the crystal lattice in no tilt systems is reflected by an increase in the dielectric loss [61]. Even though SYN has lower value of dielectric permittivity as compared to BYN, it would find application in electronic industries where there is requirement of low dielectric loss ceramics. Thus, we can conclude that the dielectric properties of a sample are largely controlled by its crystal structure and the ionic radii of its constituent atoms.

References

[1] A. Jung, V. Ksenofontov, S. Reiman, H.A. Therese, U. Kolb, C. Felser, W. Tremel, Phys. Rev. B 673 (2000) 144414.

[2] I. V. Solovyev, Phys. Rev. B 65 (2002) 144446.

[3] B. Fisher, K.B. Chashka, L. Patlagan, G.M. Reisner, Phys. Rev. B 70 (2004) 205109.

[4] H. Kato, T. Okuda, Y. Okimoto, Y. Tomioka, Phys. Rev. B 69 (2004) 184412.

[5] G. Vaitheeswarana, V. Kanchana, A. Delin, Appl. Phys. Lett. 86 (2005) 032513.

[6] S. Saha, T. P. Sinha, J. Appl. Phys. 99 (2006) 014109.

[7] R. Mukherjee, S. Saha, A. Dutta, T. P. Sinha, J. Alloy Compd. 651 (2015) 222–229.

[8] F. C. Coomer, J. Campbell, N. Giordano, O. M. Collins, E. J. Cussen, J. Solid State Chem. 221 (2015) 411–417.

[9] L. T. Corrodor, J. Velasco Zarate, D. A. Landinez Tellez, F. Fajardo, J. Arbey Rodriguez, M. J. Roa-Rojas, Physica B 404 (2009) 2733.

[10] J. B. Phillip, P. Majewski, L. Alff, A. Erb, and R. Cross, Phys. Rev. B 68 (2003) 144431.

[11] K. A. Muller, H. Burkhard, Phys. Rev. B 19 (1979) 3593.

[12] U. Bianchi, J. Dec, W. Kleemann, J. G. Bednorz, Phys. Rev. B 51 (1995) 8737.

[13] C. Ang, Z. Yu, J. Appl. Phys. 71 (1992) 4451–6025.

[14] C. Ang, Z. Yu, P. Vilarinha, J. L. Baptista, Phys. Rev. B, 57 (1998) 7403.

[15] C. Ang, J. R. Jurado, Z. Yu, M. T. Colomer, J. R. Frade, J. L. Baptista, Phys. Rev. B 57 (1998) 11858.

[16] A. Faik, M. Gateshki, J. M. Igartua, J. L. Pizarro, M. Insausti, R. Kaindi, A. Grzechnik, J. Solid State Chem. 181 (2008) 1759.

[17] A. Faik, E. Ituebe-Zabalo, I. Urcelay, J. M. Igartua, J. Solid State Chem. 182 (2009) 2656.

[18] A. E. Lavat, E. J. Baran, J. Alloy Compd. 460 (2008) 152.

[19] L.A. Reznichenko, G.A. Geguzina, N.V. Dergunova, Inorg. Mater. 34 (1998) 167.

[20] I.P. Raevski, S.A. Prosandeev, J. Phys. Chem. Solids 63 (2002) 1939.

[21] J.M. Haussonne, G. Desgardin, A. Herve, B. Boufrou, J. Eur. Ceram Soc. 10 (1992) 437.

[22] L. A. Reznichenko, N. V. Dergunova, G. A. Geguzina, O. N. Razumovskaya, L. A. Shilkina, L. S. Ivanova, Inorg. Mater. 33 (1997) 1277.

[23] J. H. Yang, W. K. Choo, J. H. Lee, C. H. Lee, Acta Cryst. B55 (1999) 348–354.

[24] M. Takata, K. Kageyama, J. Am. Ceram. Soc., 72 [10] (1989) 1955–59.

[25] A. Dutta, P.K. Mukhopadhyay, T.P. Sinha, S. Shannigrahi, A.K. Himanshu, P. Sen, S. K. Bandyopadhyay, Mater. Chem. Phys. 179 (2016) 55–64.

[26] A. Dutta, P. Kumari, T. P. Sinha, Electron. Mater. Lett., 11[5] (2015) 775–781.

[27] B. Ghosh, S. Halder, T. P. Sinha, J. Am. Ceram. Soc., 97 [8] (2014) 2564–2572.

[28] R. Mukherjee, S. Saha, Alo Dutta, T.P. Sinha, J. Alloy Compd. 651 (2015) 222–229.

[29] B. Ghosh, A. Dutta, T.P. Sinha, Mater. Chem. Phys. 143 (2013) 26–33.

[30] A.E. Lavat, M.C. Grasselli, E.J. Baran, R.C. Mercader, Mater. Lett. 47 (2001) 194.

[31] A.F. Corsmit, H.E. Hoefdraad, G. Blasse, J. Inorg. Nucl. Chem. 34 (1972) 3401.

[32] G. Blasse, A.F. Corsmit, J. Solid State Chem. 6 (1973) 513.

[33] W. Zheng, W. Pang, G. Meng, Mater. Lett. 37 (1998) 276.

[34] A. Dutta, T.P. Sinha, Integr. Ferroelectr. 116 (2010) 41.

[35] J. Tauc, Amorphous and Liquid Semi-conductors, Plenum Press, New York, 1974.

[36] Alo Dutta, T.P. Sinha, Comput. Mater. Sci., 83 (2014) 303–308.

[37] B. Amin, I. Ahmad, M. Maqbool, J. Light. Technol. 28 (2010) 223.

[38] A. Raj, M. Kumar, D. Mishra, A. Anshul, Optical Materials, 101(2020) 109773.

[39] Y. Yamada, Y. Kanemitsu, J. Lumin. 133 (2013) 30–34.

[40] P. Debye, Polar Molecules, Chemical Catalogue Company, New York, 1929.

[41] L. L. Hence, J. K. West, Principles of Electronic Ceramics, Wiley, New York, 1990.

[42] K. S. Cole, R. H. Cole, J. Chem. Phys. 9 (1941) 341–351.

[43] K. S. Cole, R. H. Cole, J. Chem. Phys. 10 (1942) 98–105

[44] Z. Abdelkafi, N. Abdelmoula, H. Khemakhem, O. Bidault, M. Maglione, J. Appl. Phys. 100 (2006) 114111.

[45] D. Ming, J.M. Reau, J. Ravez, J. Gitae, P. Hagenmuller, J. Solid State Chem. 116 (1995) 185.

[46] A. R. von Hippel, Dielectric, Waves, MIT Press, Cambridge, 1954.

[47] C. Park, J. Korean, Phys. Soc. 29 (1996) 327.

[48] P. B. Macedo, C. T. Moynihan, R. Bose, Phys. Chem. Glasses 13 (1972) 171.

[49] A. S. A. Khiar, R. Puteh, A. K. Arof, Physica B 373 (2006) 23–27.

[50] A. K. Jonscher, Dielectric Relaxation in Solids, Chelsea Dielectrics Press, London, 1983.

[51] E. F. Hairetdinov, N. F. Uvarov, H. K. Patel, S. W. Martin, Phys. Rev. B 50 (1994) 13259.

[52] W. Li, R.W. Schwartz, Appl. Phys. Lett. 89 (2006) 242906.

[53] C. Leon, A. Rivera, A. Varez, J. Sanz, J. Santamaria, K.L. Ngai, Phys. Rev. Lett. 86 (2001) 1279.

[54] M. Idrees, M. Nadeem, M. M. Hassan, J. Phys. D Appl. Phys. 43 (2010) 155401.

[55] W. H. Jung, J. Appl. Phys. 90 (2001) 2455.

[56] Y. Tsuji, A. Kan, H. Ogawa, S. Ishihara, J. Eur. Ceram. Soc. 25 (2005) 2883–2887.

[57] Z. Tan, S. Xie, L. Jiang, J. Xing, Y. Chen, J. Zhu, D. Xiao, Q. Wang, J. Materiomics. 5 (2019) 372–384.

[58] A. Barua, S. Maity, R. Mondal, S. Kumar, AIP Conf. Proc. 1942 (2018) 110033.

[59] S. K. Maity, A. Dutta, T. P. Sinha, S. Kumar, AIP Conf. Proc. 1665 (2015) 110044.

[60] S. K. Maity, A. Dutta, S. Kumar, T. P. Sinha, Phys. Scr. 88 (2013) 065702.

[61] M. Valant, D. Suvorov, C. J. Rawn, Jpn. J. Appl. Phys. Vol. 38 (1999) 2820–2826.

Chapter – 6

Structural and dielectric characterization of triple perovskites $Ba_3NiTaNbO_9$ and $Ba_3NiTaSbO_9$

6.1. Introduction

Perovskite oxides have been widely used in the field of microwave communication systems in the form of resonators and filters [1]. They have been widely explored due to their tunable physical properties which are dependent on their composition and their crystal structure. In perovskites having ABO_3 structure, the dielectric properties can be tuned by changing the B-site cation ordering [2]. In recent past a large amount of research have been carried out on triple perovskites having general formula $A(B'_{1/3}B''_{2/3})O_3$ because of their structural diversity and technologically important physical properties. Barium based triple perovskites have been reported to exhibit multiferroicity [3, 4], better dielectric properties [5] and photocatalytic properties [6].

Triple perovskites usually have hexagonal, orthorhombic, monoclinic and trigonal symmetries as they can accommodate varied sized cations in the A-site and any lanthanide or any d-block element in the B′ and B″ sites [7-16]. This structure can easily accommodate different elements, which allows us to substitute different cations in order to obtain the desired physical properties. The dielectric permittivity arises due to the combination of electronic and ionic polarization [17]. The lattice vibrations affect the ionic polarization but the electronic polarization is constant for a specified ion [18, 19]. In our present work we have substituted the B-site with three different cations in order to obtain the $A_3(B'B''B''')O_9$ structure similar to those reported by Mani et al. [20]. We have synthesized two triple perovskites $Ba_3NiTaNbO_9$ and $Ba_3NiTaSbO_9$ having general formula $A_3(B'B''B''')O_9$ and examined their structural, optical and dielectric properties. Dielectric analysis of $Ba(Ni_{1/3}Ta_{2/3})O_3$ has been performed by Hoque et al. [21] but on addition of niobium in the

B‴-site as in case of our BNTN sample has led to a considerable increase in its permittivity value.

6.2. Experimental

The polycrystalline samples of BNTN and BNTS were synthesized by the ceramic method [21]. Reagent grade powders of Ta_2O_5, $BaCO_3$, $NiCO_3$, Sb_2O_5 and Nb_2O_5 were used for the synthesis of the respective samples. The stoichiometric amount of the raw materials was mixed together for 10 h and then calcined at 1325 ºC for 14 h in presence of air. The samples were than brought down to 30º C by cooling at the rate of 2º C/min. The X-ray diffraction (XRD) analysis was performed using Bruker D8 diffractometer in order to verify the phase formation of the prepared samples. Cu-K_α radiation was used and the range was kept in between $10^o \leq 2\theta \leq 120^o$ with scanning step size of 0.02º. The scan rate of the diffractometer was set at 2º min^{-1}. The microstructural analysis of the samples was done using field emission scanning electron microscope (SEM). The FTIR spectrums of the samples were recorded in the room temperature in the transmission mode with wave number between 350 and 1200 cm^{-1}. The Raman measurements were carried out using WITEC alpha 300 R Raman spectrometer.

The calcined powders were than palletized into discs by applying 135 MPa pressure using a hydraulic press. The discs were than sintered at 1375º C for 10 h and then brought down to 30º C by cooling at the rate of 1º C/min. The discs of the samples having thickness and diameter of 1.974 mm and 9.896 mm for BNTS and 1.621 mm and 7.784 mm for BNTN were prepared which were then polished thoroughly using very fine (so called zero) emery paper. The flat surfaces of the discs were coated with fine silver paint and heated at 250º C for 3 h in order to make the electrodes for performing the electrical measurements. Hioki

3532 LCR meter was used for the electrical measurements. The dielectric parameters were measured keeping the oscillation voltage fixed at 1 V and by varying the frequency between 10 Hz to 1 MHz. The dielectric parameters were measured at some discrete temperatures in between 333-573 K. During the measurement each temperature was kept constant with the help of a programmable oven with an accuracy of ±1 K. The samples were heated at the rate of 0.5 K/min in order to study the variations of various dielectric parameters with temperature.

6.3. Results

6.3.1. Structural characterization:

It may be noted that BNTN and BNTS are obtained by partially substituting the Ta^{5+} of $Ba_3NiTa_2O_9$ by Nb^{5+} and Sb^{5+}, respectively. The radii of Nb^{5+} (0.64 Å) is equal to that of Ta^{5+} (0.64 Å) while the radii Sb^{5+} (0.6 Å) is smaller as compared to Ta^{5+} but closer to that of Ir^{5+} (0.57 Å). Thus, the crystal structure of BNTN is likely to be analogous to $Ba_3NiTa_2O_9$, which crystallizes in *P-3m1* space group as reported by Lufaso et al. and Asai et al. [22, 23]. On the other hand, the crystal structure of BNTS is expected to be similar to that of $Ba_3NiIr_2O_9$ [16] and $Ba_3NiSb_2O_9$ [24] where both $Ba_3NiIr_2O_9$ and $Ba_3NiSb_2O_9$ possess *P* $6_3/mmc$ space group of hexagonal symmetry. The XRD patterns of BNTN and BNTS have been analysed by the Rietveld refinement method by using the GSAS program having EXPGUI user interface [25]. The initial input parameters required for analysing the crystal structures of BNTN and BNTS have been obtained from the crystallographic information available for $Ba_3NiTa_2O_9$ and $Ba_3NiIr_2O_9$/$Ba_3NiSb_2O_9$, respectively. The experimentally recorded XRD patterns of both BNTN and BNTS along with their corresponding simulated patterns, obtained after Rietveld refinement, are demonstrated in Fig. 1. The results confirm

that BNTN belongs to trigonal symmetry with *P-3m1* space group and is a structural analogue of $Ba_3NiTa_2O_9$ whereas BNTS belongs to hexagonal symmetry with *P 6₃/mmc* space group and eventually stabilizes adopting the crystal structure of $Ba_3NiIr_2O_9$/$Ba_3NiSb_2O_9$.

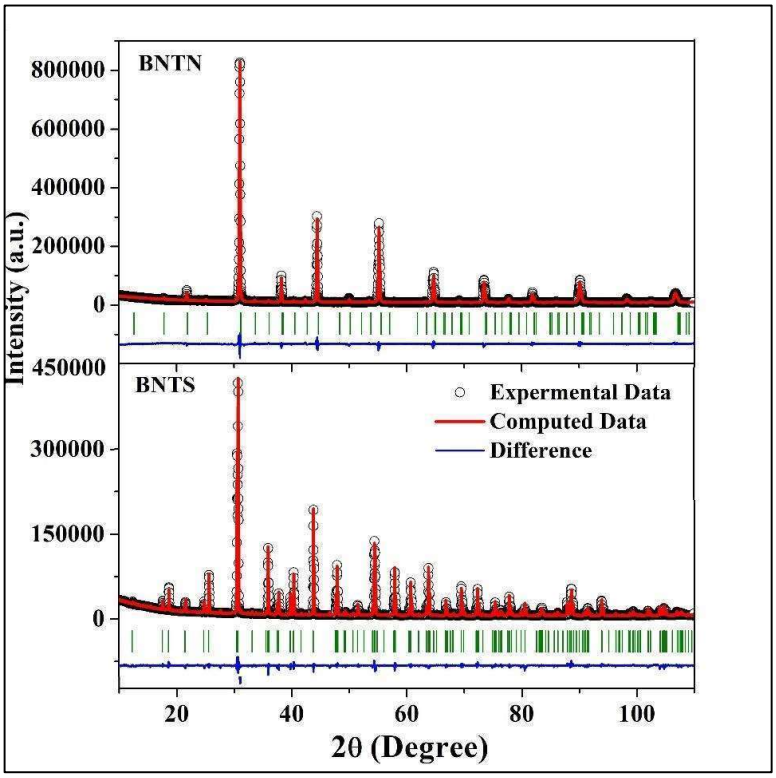

Fig. 1: *Rietveld refinement plots of BNTN and BNTS where the symbols represent the experimental data and the continuous line represents the simulated XRD pattern.*

In order to assess the influence of the ionic radii of A and B-site cations on stabilization of the crystal structures adopted by BNTN and BNTS we have calculated the Goldschmidt tolerance factor $g=(r_A+ r_O)/ [\sqrt{2}\ (r_B+r_O)]$ [26] of the samples, considering the Shannon's ionic radii [27] of different elements present in the A, B and O-sites. We obtained

g=1.03 for BNTN and g=1.04 for BNTS. The g value of BNTN is smaller due to the larger niobium ion in the B′′′- site leading to 2:1 ordered perovskite structure with *P-3m1* space group [22]. The substitution of Sb^{5+} having smaller ionic radii as compared to Nb^{5+} increases the value of g in case of BNTS. Thus, the g value of BNTS being closer to the hexagonal structure, it crystallizes in *P 6₃/mmc* space group [26,28]. Table 1 illustrates the lattice parameters obtained after the refinement. The Wyckoff positions of cations and anions of BNTN and BNTS are tabulated in Table 2 and Table 3, respectively.

Table 1. The refinement and the structural parameters of BNTN and BNTS as obtained from the Rietveld refinement method of powder X-ray data.

Parameters	BNTN	BNTS
Crystal system	Trigonal	Hexagonal
Space group	*P-3m1*	*P 6₃/mmc*
a (Å)	5.75509(2)	5.835973(30)
b (Å)	5.75509(2)	5.835973(30)
c (Å)	7.06650(3)	14.40431(12)
Volume ($Å^3$)	191.34(1)	424.864(4)
α=β(°)	90	90
γ(°)	120	120
R_{wp}	0.069842	0.0458
R_p	0.052798	0.0358
χ^2	1.98	2.4

Table 2. The Wyckoff positions of atoms and the refined atomic coordinates of BNTN.

Atom	Site	*X*	*y*	*z*	Occupancy	*B* (Å^2)
Ba1	1a	0.0	0.0	0.0	1	0.03619
Ni2	1b	0.0	0.0	0.5	1	0.03139
Nb3	2d	0.33333	0.66667	0.180924 (13)	0.5	0.03232
Ta7	2d	0.33333	0.66667	0.180924 (13)	0.5	0.03263
Ba2	2d	0.33333	0.66667	0.659593(6)	1	0.03820
O5	3e	0.5	0.0	0.0	1	0.09264
O6	6i	0.16841(12)	0.30371(14)	0.34922 (6)	1	0.04187

Table 3. The Wyckoff positions of atoms and the refined atomic coordinates of BNTS.

Atom	Site	*x*	*y*	*z*	Occupancy	*B* (Å^2)
Ba1	2b	0	0	0.25	1	0.0247(2)
Ni2	2a	0	0	0	1	0.02143(9)
Sb3	4f	0.33333	0.66667	0.15876	0.5	0.0125(4)
Ta7	4f	0.33333	0.66667	0.15876	0.5	0.02649
Ba2	4f	0.33333	0.66667	0.91349(2)	1	0.0160(2)
O5	6h	0.59722(3)	1.04013(1)	0.25	1	0.0137(3)
O6	12k	0.15148(3)	0.30296	0.42077(1)	1	0.01630(2)

Fig. 2 Depicts the asymmetric unit of BNTN where the Ba^{2+} ions are coordinated with 12 oxygen ions while Ni^{2+}, Nb^{5+} and Ta^{5+} ions are coordinated with 6 oxygen ions. Fig. 3

illustrates the coordination environment of A and B-site atoms Ba, Ni, Ta and Nb. The Ni–O bond length is 1.98 Å whereas Nb/Ta–O2 bond length is 2.016 Å and Nb/Ta–O1 bond length is 2.102 Å for the BNTN sample. The difference in the bond length of Nb/Ta–O indicates off centre distortion of the cation in the octahedra resulting from the second order Jahn-Teller distortion for d^0 cations like Ti^{4+}, Nb^{5+}, Ta^{5+}, W^{6+} [22]. The Nb/Ta^{5+}–O–Nb/Ta^{5+} bond angle is 180º. Fig. 4. depicts the asymmetric unit of BNTS where the Ba^{2+} ions are coordinated with 12 oxygen ions while Ni^{2+}, Sb^{5+} and Ta^{5+} ions are coordinated with 6 oxygen ions and Fig. 5 illustrates the coordination environment of A and B -site atoms Ba, Ni, Ta and Sb. The Ni–O bond length is 1.89 Å whereas Sb/Ta–O2 bond length is 2.183 Å and Sb/Ta–O1 bond length is 2.36 Å for the BNTS sample. The difference in the bond length of Sb/Ta–O results from the cation-cation repulsion between the face sharing Sb_2O_9 groups [28]. The Sb/Ta^{5+}–O–Sb/Ta^{5+} bond angle is 68.9º.

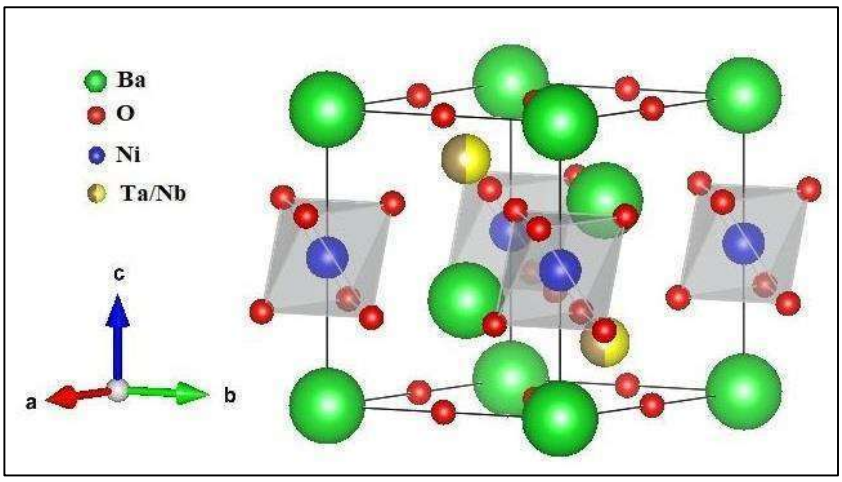

Fig. 2: *Asymmetric unit of BNTN.*

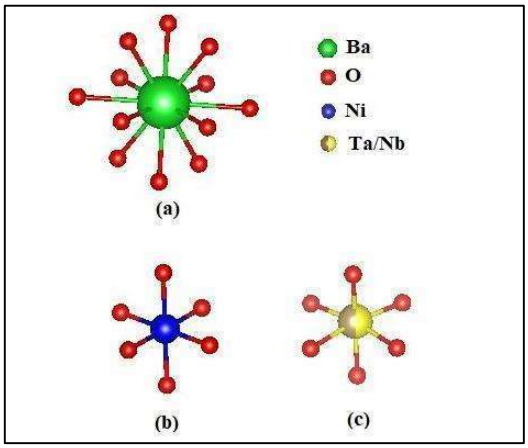

Fig. 3: *Coordination environments of (a) Ba^{2+} (b) Ni^{2+} and (c) Ta/Nb^{5+} for BNTN sample.*

For BNTN the B-site cations are arranged along the (111) planes of the pseudocells with two Nb/Ta layer and one Ni layer as shown in Fig. 6 (a). As both the Ta and Nb ions occupy the *2d* Wyckoff position they are represented by different colours on the same sphere. This arrangement of the B-site atoms is repeated along the crystallographic c axis. On the other hand, the B-site cations of BNTS are arranged along the (111) planes of the pseudocells with two Sb/Ta layer and one Ni layer as shown in Fig.6 (b). As both the Ta and Sb ions occupy the *4f* Wyckoff position they are represented by different colours on the same sphere. This arrangement of the B-site atoms is repeated along the crystallographic c axis.

The difference in the bonding preference of Nb^{5+} having vacant d orbital and Sb^{5+} having filled d orbital and difference in their ionic radii plays a crucial role for the stabilization of BNTN in *P-3m1* space group and BNTS in *P* 6_3*/mmc* space group [28–32].

The vacant d orbitals of Nb^{5+} in BNTN favours the formation of л bond with the p orbitals of oxygen thus resulting in a linear Nb^{5+}–O–Nb^{5+} bond with bond angle ~ 180º which favours the *P-3m1* structure with metal oxygen corner sharing octahedra and cubic stacking of BaO_3 layers [Fig. 2]. The filled d orbitals of Sb^{5+} does not favour the formation of л bond and preferred Sb^{5+}–O–Sb^{5+} bond angle is < 180º, thus BNTS stabilizes in *P 6₃/mmc* structure containing mixed cubic and hexagonal stacking of BaO_3 layers [Fig. 4] with $Ni^{2+}O_6$ octahedra in the vertex and face sharing Sb_2O_9 groups having Sb^{5+}–O– Sb^{5+} bond angle ~ 90º resulting from σ bonding with p orbitals of two different oxygen.

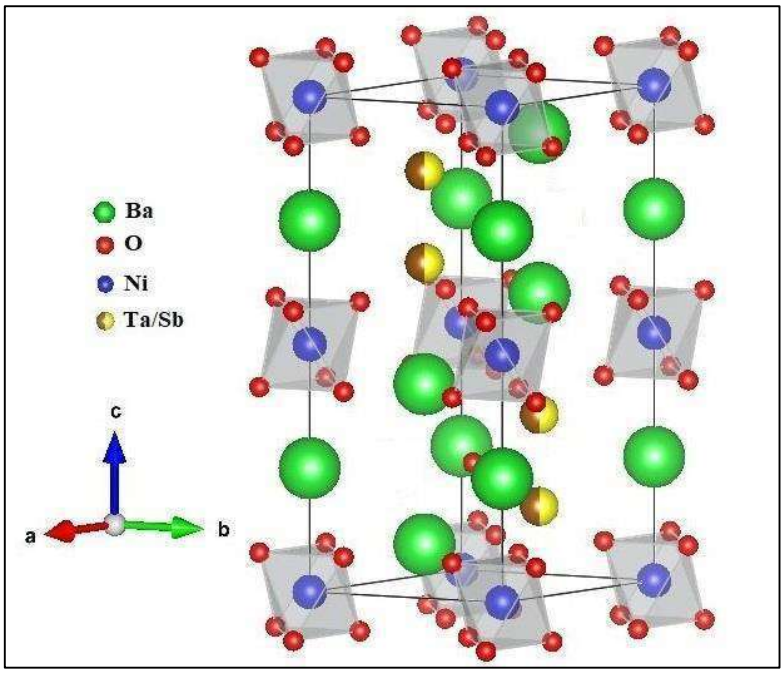

Fig. 4: *Asymmetric unit of BNTS.*

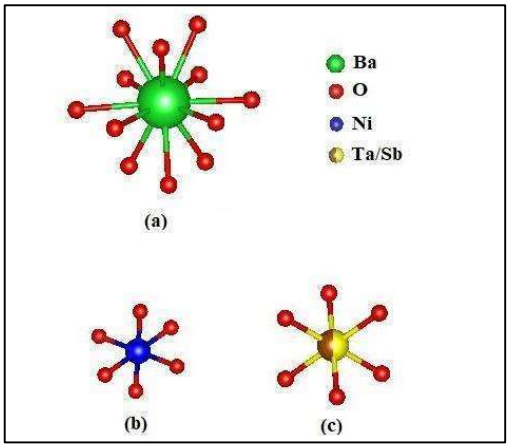

Fig. 5: *Coordination environments of (a) Ba^{2+} (b) Ni^{2+} and (c) Ta/Sb^{5+} for BNTS sample.*

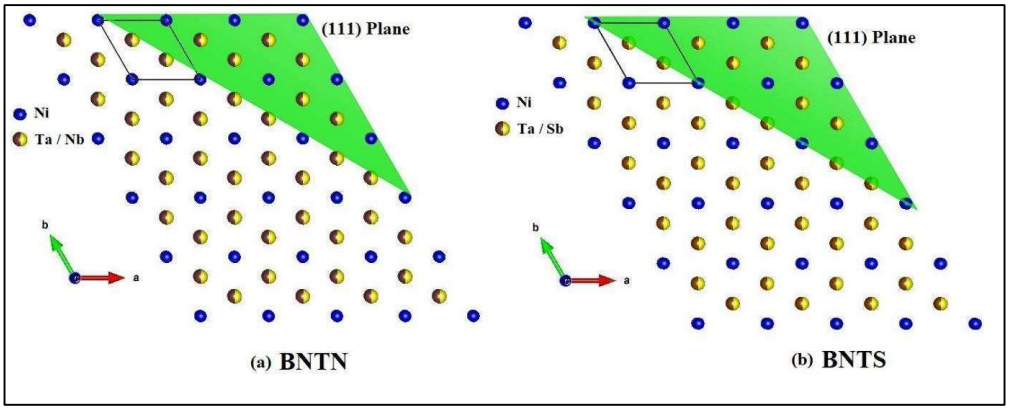

Fig. 6: *Ordering sequences of octahedral B site cations of (a) BNTN and (b) BNTS along the crystallographic c axis.*

The XRD analysis can predict the ordered or disordered nature of the sample depending on the degree of long-range ordering. A perovskite structure is said to be disordered if the B-site cations are randomly distributed along the crystal lattice. Perovskite materials can exhibit partially ordered structure due to their occupational disorder owing to the exchange of their Wykoff site between the B'-B''-B''' ions [33]. It can be seen from Fig. 6 that ordered nature is maintained for both BNTN and BNTS sample however the B''-B''' ions

are indistinguishable due to their identical Wykoff sites. Each *2d* site of BNTN can either be occupied by a Ta^{5+} or Nb^{5+} ion and similarly in case of BNTS the probability that each *4f* site will be filled by a Ta^{5+} or Sb^{5+} ion is equal and this leads to occupational disorder in both the samples. Thus, both BNTN and BNTS fall in the category of partially ordered perovskite having trigonal and hexagonal unit cell respectively.

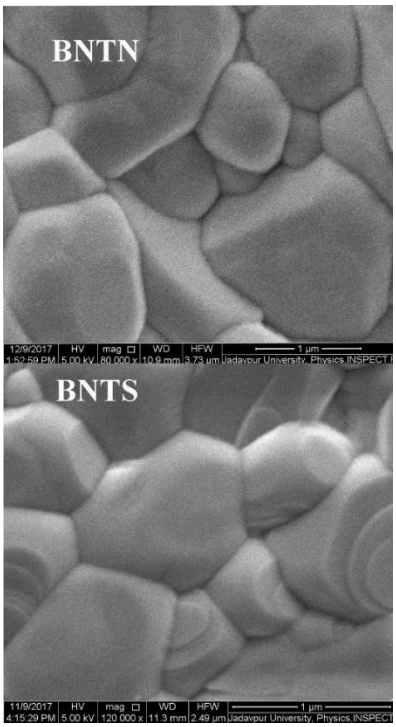

Fig. 7: *The scanning electron micrograph of (a) BNTN and (b) BNTS.*

The theoretical density of BNTN is 8.26 g/cc and for BNTS is 7.53 g/cc. The experimental density of the pellets as measured by the Archimedes principle is 8.01 g/cc for BNTN and 7.29 g/cc for BNTS which indicates that the presence of porosity is negligible. The SEM images of BNTN and BNTS pellets are shown in Fig. 7 from which we can observe that both the samples have well defined grains of asymmetrical shapes and sizes. The grain

size of BNTN ranges from 0.52 μm to 1.83 μm and for BNTS it ranges from 0.25 μm to 1.21 μm.

6.3.2. Raman and FTIR analysis:

The Raman spectra of BNTN and BNTS are illustrated in Fig. 8 and 9, respectively. The spectra are fitted with Lorentzian profile. The peak position and the full width at half maxima of the Raman peaks are provided in Table 4. The group factor analysis can be used to determine the lattice vibration modes of perovskites based on the Wyckoff positions occupied by the atoms [34]. The expected phonon modes for the partially ordered BNTN sample are illustrated in Table 5. Eleven Raman-active modes ($\Gamma_{Raman} = 5\ A_{1g} + 6\ E_g$) are expected in the Raman spectra of the ordered sample with *P-3m1* space group. An increased number of optical active modes can be observed in BNTN for the occupational disorder caused by the exchange of Wyckoff sites between B'-B''-B''' ions [35,36].

For indexing the BNTN crystal structure we have used the D_{3d} cell, but due to the interchange of ions occupying B' and B''/B''' sites additional modes can be observed [33,36,37]. These additional modes can again be predicted by the group factor analysis. The existence of B' ions in *2d* Wyckoff site would give rise to two additional Raman and IR bands each ($\Gamma_{Raman,B'} = A_{1g} + E_g$, $\Gamma_{IR,B'} = A_{2u} + E_u$) and the presence of B''/B''' ions in *1b* Wyckoff site would give rise to two additional IR bands ($\Gamma_{IR,B''/B'''} = A_{2u} + E_u$). The Lorentzian fitting of the BNTN sample indicates the presence of 14 bands. The Raman active bands for the partially ordered BNTN sample are shown in Table 4. Two extra Raman bands occur due to the presence of Ni ions in the *2d* site and an additional Raman band may be attributed to the defect activated modes [36] arising due to the local breakdown of rigid symmetry rules owing to the presence of crystalline defects created during the crystal growth process. Appearance of extra Raman bands due to the presence of such defects in ceramic crystals, developed

during the crystal growth process, are very common [38,39]. Seven prominent bands (1-4, 6, 7, 13) arises due to the vibrations of Ba and O ions and agrees well with those reported by Moreira et al. for sample with *P-3m1* space group [36]. The peaks (12-14) arise due to the vibration of Nb ions and the peaks (8, 9) arises due to the Ta ions occupying their own *2d* site. We propose the peaks (10-11) arises due to the vibrations of Ni ions in the *2d* site. The peak 5 may be attributed to the localized defect activated modes [36].

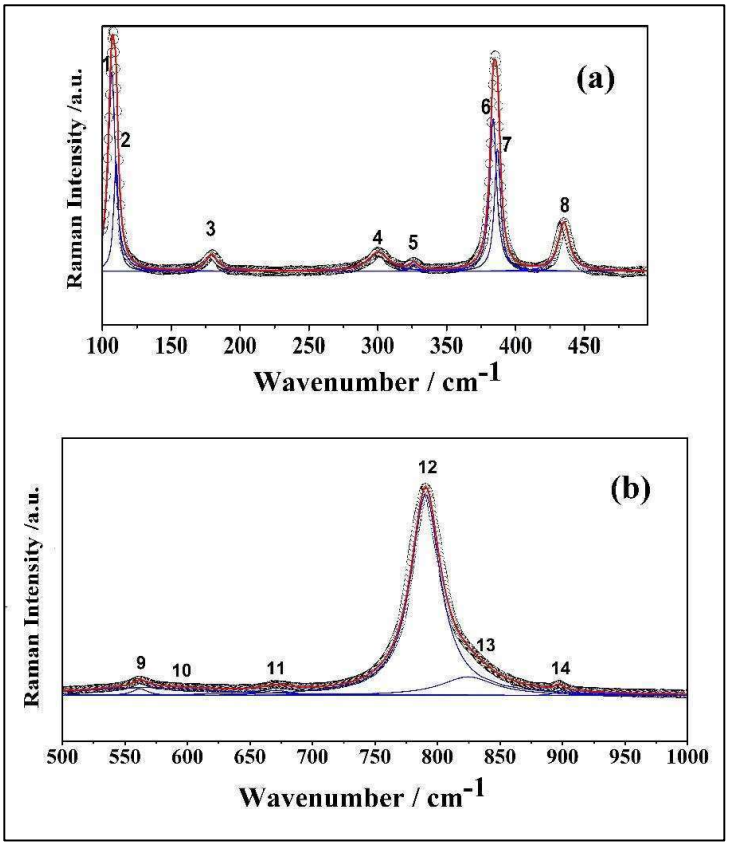

Fig. 8: *The Raman spectra of BNTN where the symbols represent the experimental data and the red line represents the fitted Lorentzian curve.*

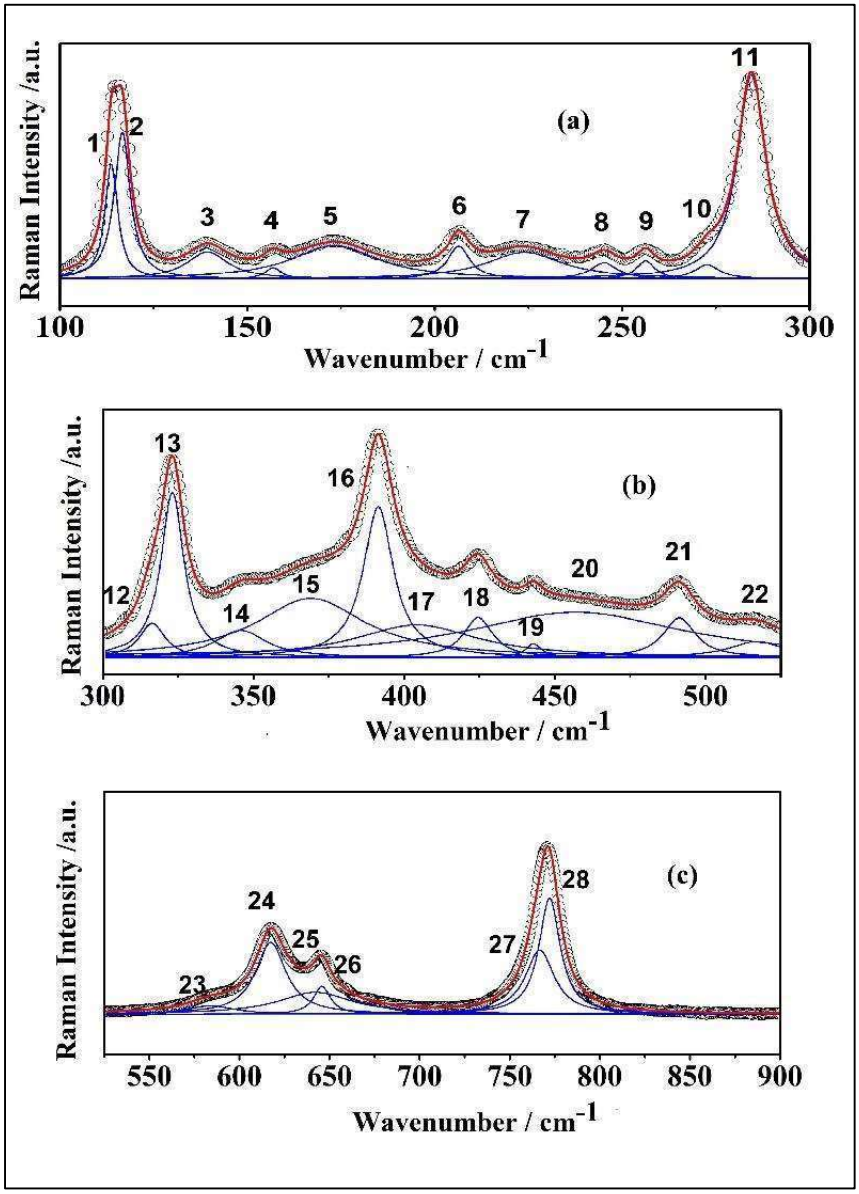

Fig. 9: *The Raman spectra of BNTS where the symbols represent the experimental data and the red line represents the fitted Lorentzian curve*

Table 4. Observed Raman active phonon modes.

Peak No.	BNTN		BNTS	
	Frequency (cm^{-1})	FWHM (cm^{-1})	Frequency (cm^{-1})	FWHM (cm^{-1})
1	106.86061	6.13422	113.73656	4.13635
2	109.94055	4.18384	116.65472	5.2179
3	179.3268	10.63783	139.39437	13.45644
4	300.33057	17.82231	156.93822	5.34014
5	326.35023	6.93163	173.26966	27.89207
6	383.77561	6.09894	206.41028	7.08981
7	386.93194	5.33803	223.90904	24.97306
8	435.17503	9.77481	245.20409	8.69937
9	562.12548	15.33022	256.28441	6.01976
10	568.39212	138.60571	272.66648	8.12174
11	671.08173	28.19654	284.47502	9.19352
12	790.39932	28.85488	316.41858	10.34392
13	824.41936	52.12184	323.12421	9.26482
14	897.29771	9.36599	345.80338	20.57622
15			369.06258	43.86453
16			391.43135	12.07692
17			404.17266	49.40364
18			424.54697	11.75038
19			442.95049	6.69549
20			456.91957	87.35553
21			491.31689	13.0209
22			517.0972	22.39771
23			584.04553	31.63836
24			617.37004	20.5725
25			642.13645	50.53684
26			645.81217	11.43132
27			766.68909	19.4977
28			772.12739	14.3234

Table 5. Distribution of modes for the partially ordered BNTN sample belonging to the trigonal space group *P-3m1*.

Atom	Site	Symmetry	Distribution of modes
Ba1	1a	-3m	$A_{2u} + E_u$
Ba2	2d	3m	$A_{1g} + A_{2u} + E_u + E_g$
Ni2	1b	-3m	$A_{2u} + E_u$
Nb3	2d	3m	$A_{1g} + A_{2u} + E_u + E_g$
Ta7	2d	3m	$A_{1g} + A_{2u} + E_u + E_g$
O5	3e	2/m	$A_{1u} + A_{2u} + E_u$
O6	6i	M	$2A_{1g} + A_{1u} + A_{2g} + 2A_{2u} + 3\ E_u + 3\ E_g$
Modes for the atoms in their own Wykoff site:		Γ_{TOTAL}	$8\ A_{2u} + 9\ E_u + 5\ A_{1g} + 6\ E_g + 2\ A_{1u} + A_{2g}$
		$\Gamma_{ACOUSTIC}$	$A_{2u} + E_u$
		Γ_{RAMAN}	$5\ A_{1g} + 6\ E_g$
		Γ_{IR}	$7A_{2u} + 8\ E_u$
Extra modes for B'-B"-B"' cation disorder:			$\Gamma_{Raman,\ B'} = A_{1g} + E_g$, $\Gamma_{IR,\ B'} = A_{2u} + E_u$ $\Gamma_{IR,\ B''/\ B'''} = A_{2u} + E_u$

According to the charge to mass ratio $[(q_{Ni} / m_{Ni}) / (q_{Nb} / m_{Nb})]^{1/2}$ [36], where q and m denotes the charge and mass of the ion, respectively, the Raman modes for Ni ions occupying the *2d* site would appear at frequency which is 0.796 times of the mode associated with the Nb ions. This ratio is satisfied by peak 10 and 12 (0.719) as well as peak 11 and 14 (0.747). Since the occupation of Ni ions in *2d* site is one of the causes for the partially ordered structure of BNTN leading to extra Raman modes, we can estimate the degree of ordering by the relation $O_{Ni,Nb} = [I_{11,14} /(I_{11} + I_{14})]$ where I_{11} and I_{14} are the intensities of peak 11 and 14

respectively [37]. For ordered structure Ni ions in *2d* site would be absent resulting in no extra peaks ($I_{11} = 0$) and therefore for ordered structure $O_{Ni} = 0$ and $O_{Nb} = 1$. But for our partially ordered sample for the presence of Ni ions in the Nb (*2d*) site, the degree of ordering is found to be $O_{Ni} = 0.517$ and $O_{Nb} = 0.483$. Similarly, according to the charge to mass ratio the Raman modes for Ni ions occupying the Ta (*2d*) site, the peak for Ta would appear at frequencies which are 0.89 times of the mode associated with the Ni ions which is satisfied by peak 9 and 11 (0.83). The degree of ordering for Ni ion in the Ta (*2d*) site can be calculated considering the peak 11 and 9 which is found to be $O_{Ni} = 0.221$ and $O_{Ta} = 0.779$.

The phonon modes of the partially ordered BNTS sample are shown in Table 6. Twenty-two Raman-active modes ($\Gamma_{Raman} = 6\ A_{1g} + 9E_{2g} + 7\ E_{1g}$) are expected in the ordered sample with $P\ 6_3/mmc$ space group and can be indexed using the D_{6h} cell. The increased number of the optical active modes in BNTS can be attributed to the occupational disorder for the exchange of Wyckoff sites between B'-B''-B''' ions. The existence of B' ions in *4f* Wyckoff site would give rise to three additional Raman and two additional IR bands each ($\Gamma_{Raman,B'} = A_{1g} + E_{2g} + E_{1g}$, $\Gamma_{IR,B'} = A_{2u} + E_{1u}$) and the presence of B''/B''' ions in *2a* Wyckoff site would give rise to two additional IR bands ($\Gamma_{IR,\ B''/B'''} = A_{2u} + E_{1u}$). The Lorentzian fitting of the BNTS sample indicates the presence of 28 bands. The Raman active bands for the partially ordered BNTS sample are illustrated in Table 4. Three extra Raman bands occur due to the presence of Ni ions in the *4f* site and three additional Raman band may be attributed to the defect activated modes [36] which might have evolved due to the local breakdown of rigid symmetry rules. The observed Raman modes match well with those reported by Daniel et. al. for sample having $P\ 6_3/mmc$ space group along with few additional peaks for the doping of the B-site cation [40]. The Raman spectra of Barium based hexagonal perovskites as reported by J. Chen et al. can be classified into four frequency ranges (below 200 cm^{-1},

200-400 cm^{-1}, 500-650 cm^{-1} and above 650 cm^{-1}) [41]. The peaks 1-5 which lies below 200 cm^{-1} are associated with the vibration of Ba ions. The peaks lying in the rage of 200-400 cm^{-1} arises due to the rotational and vibrational modes of Ni-O, Ta-O and Sb-O bonds. The peaks lying within 500-650 cm^{-1} are due to the bending and symmetry vibration of NiO_6, TaO_6 and SbO_6 octahedra. The asymmetric stretching vibration of NiO_6, TaO_6 and SbO_6 octahedra are associated with the peaks above 650 cm^{-1}. We propose the peak 26 is for Ta ions, peak 27 is for Ni ions and peak 28 is for Sb ions in accordance with the charge to mass ratio as described above [36]. Considering the ratio $[(q_{Ni} / m_{Ni}) / (q_{Sb} / m_{Sb})]^{1/2}$, the Raman modes for Ni ions occupying the Sb (*4f*) site would appear at frequency which is 0.9113 times of the mode associated with the Sb ions. This ratio is satisfied by peak 27 and 28 (0.99).

Since the occupation of Ni ions in the Sb (*4f*) site is one of the causes for the partially ordered structure of BNTS leading to extra Raman modes, we can estimate the degree of ordering by the relation $O_{Ni,Sb} = [I_{27,28} /(I_{27} + I_{28})]$ where I_{27} and I_{28} are the intensities of peak 27 and 28 respectively. For ordered structure Ni ions in the Sb (*4f*) site would be absent resulting in no extra peaks ($I_{27} = 0$) and therefore for ordered structure $O_{Ni} = 0$ and $O_{Sb} = 1$. But for our partially ordered sample for the presence of Ni ions in the Sb (*4f*) site, the degree of ordering is found to be $O_{Ni} = 0.351$ and $Os_b = 0.649$. Similarly, according to charge to mass ratio the Raman modes for Ni ions occupying the Ta (*4f*) site, the peak for Ta would appear at frequencies which are 0.89 times of the mode associated with the Ni ions which is satisfied by peak 26 and 27 (0.842). The degree of ordering for Ni ion in the Ta (*4f*) site can be calculated considering the peak 26 and 27 which is found to be $O_{Ni} = 0.713$ and $O_{Ta} = 0.2876$.

In summary, the results indicate that both BNTN and BNTS are partially disordered perovskite and in their Raman spectra more than expected number of modes than their ordered form have been obtained due to their B-site (B'-B''-B''') occupational disorder and

localized crystalline defects. It may be noted that it is very difficult to detect very minute amount of occupational disorder and localized defects by powder x-ray diffraction study but for partially ordered perovskites slight amount of such occupational disorder/ localized defects can be detected by Raman spectroscopic technique due to its excellent resolving power [33,35,37].

Table 6. Distribution of modes for the partially ordered BNTS sample belonging to the hexagonal space group *P 6$_3$/mmc*.

Atom	Site	Symmetry	Distribution of modes
Ba1	2b	6m2	$A_{2u} + B_{1g} + E_{2g} + E_{1u}$
Ba2	4f	3m	$A_{1g} + A_{2u} + B_{1g} + B_{2u} + E_{2u} + E_{2g} + E_{1u} + E_{1g}$
Ni2	2a	3m	$A_{2u} + B_{2u} + E_{2u} + E_{1u}$
Sb3	4f	3m	$A_{1g} + A_{2u} + B_{1g} + B_{2u} + E_{2u} + E_{2g} + E_{1u} + E_{1g}$
Ta7	4f	3m	$A_{1g} + A_{2u} + B_{1g} + B_{2u} + E_{2u} + E_{2g} + E_{1u} + E_{1g}$
O5	6h	mm2	$A_{1g} + A_{2g} + A_{2u} + B_{1g} + B_{1u} + B_{2u} + E_{2u} + 2\,E_{2g} + 2\,E_{1u} + E_{1g}$
O6	12k	M	$2\,A_{1g} + A_{1u} + A_{2g} + 2\,A_{2u} + 2\,B_{1g} + B_{1u} + B_{2g} + 2\,B_{2u} + 3\,E_{2u} + 3\,E_{2g} + 3\,E_{1u} + 3\,E_{1g}$
Modes for the atoms in their own Wykoff site:		Γ_{TOTAL}	$6\,A_{1g} + A_{1u} + 2\,A_{2g} + 8\,A_{2u} + 7\,B_{1g} + 2\,B_{1u} + B_{2g} + 7\,B_{2u} + 8\,E_{2u} + 9\,E_{2g} + 10\,E_{1u} + 7\,E_{1g}$
		$\Gamma_{ACOUSTIC}$	$A_{2u} + E_u$
		Γ_{RAMAN}	$6\,A_{1g} + 9\,E_{2g} + 7\,E_{1g}$
		Γ_{IR}	$7A_{2u} + 9\,E_{1u}$
Extra modes for B'-B"-B'" cation disorder:			$\Gamma_{Raman,\,B'} = A_{1g} + E_{2g} + E_{1g}$, $\Gamma_{IR,\,B'} = A_{2u} + E_{1u}$ $\Gamma_{IR,\,B''/\,B'''} = A_{2u} + E_{1u}$

The FTIR spectra of BNTN and BNTS are illustrated in Fig. 10. The bending mode of the BO_6 polyhedra is associated with the energy bands in between 360 and 412 cm^{-1}. The

energy bands for Sb and Nb ions appear in the higher energy side compared to that of TaO_6 octahedra as both Sb and Nb ions are lighter than Ta ion. The asymmetric bending mode of the NbO_6 and SbO_6 octahedra is associated with the band at 410 cm^{-1} for BNTN and 408 cm^{-1} for BNTS. The band at 504 cm^{-1} for BNTN and 494 and 538 cm^{-1} for BNTS are associated with the Ni–O stretching vibrations of the NiO_6 octahedra [42,43]. The asymmetric stretching vibration of NbO_6 and SbO_6 octahedra is related to the broad band at around 614 cm^{-1} for BNTN and 682 cm^{-1} for BNTS, respectively. The asymmetry in the bond lengths of Ni−O, Sb−O and Nb−O gives rise to the broad nature of the observed peaks. The absorption peaks of Nickel, Antimony and Niobium oxides are at nearly same wave numbers which also contributes to the broad nature of the observed peak. The low intensity peak at 692 cm^{-1} for BNTN and 718 and 782 cm^{-1} for BNTS is because of the symmetric stretching vibration of NbO_6 and SbO_6 octahedra.

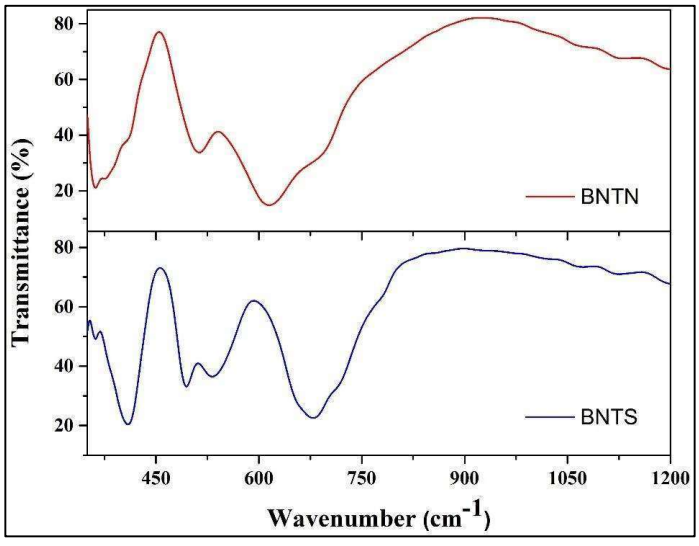

Fig. 10: *The FTIR spectrum of (a) BNTN and (b) BNTS.*

6.3.3. Dielectric analysis:

The dielectric permittivity (ε′) and the loss tangent (tan δ) variations with log of angular frequency (log ω) for BNTS and BNTN is presented in Fig. 11 and 12 respectively. The variation of ε′ with frequency can be roughly classified into three different regions. In the region where the frequency is very low the dipoles start lagging behind the field leading to a slow decrease in ε′. At a certain frequency known as the characteristic frequency the ε′ drops off suddenly pointing towards a relaxation phenomenon. At higher frequencies the dipoles are unable to follow the field resulting in a constant value of ε′. This behaviour of dielectric permittivity can be well explained by the Debye theory [44].

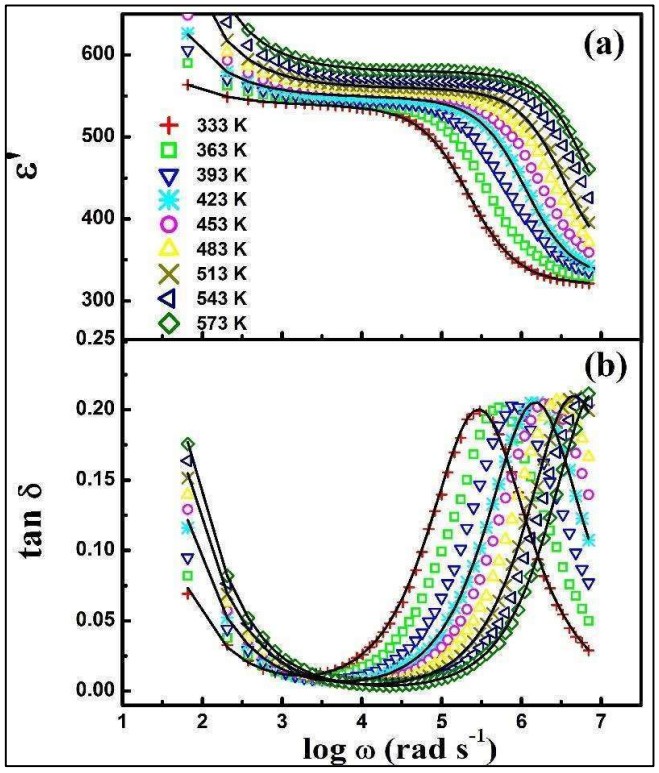

Fig. 11: *Frequency dependence of (a) ε′ and (b) tan δ of BNTN at different temperatures where the Cole-Cole fit of the experimental data are represented by the solid lines.*

A relaxation peak can be observed in the tan δ curve which shifts to the higher frequency side on increasing the temperature as more polarization occurs at high temperatures. The broad nature of the tan δ peaks as observed in Fig. 11 and 12 indicates the polydispersive nature of relaxation times which can be analysed with the help of the Cole-Cole model [45, 46]

$$\varepsilon * = \varepsilon' - i\varepsilon'' = \varepsilon_\infty + \frac{\varepsilon_s - \varepsilon_\infty}{1+(i\omega\tau)^{1-\alpha}} \quad (1)$$

where ε_s and ε_∞ are low and high frequency values of ε′, τ denotes the mean relaxation time and α represents the dispersal of the relaxation time. The value of α is 0 for monodispersive relaxation process and for polydispersive relaxation process α > 0.

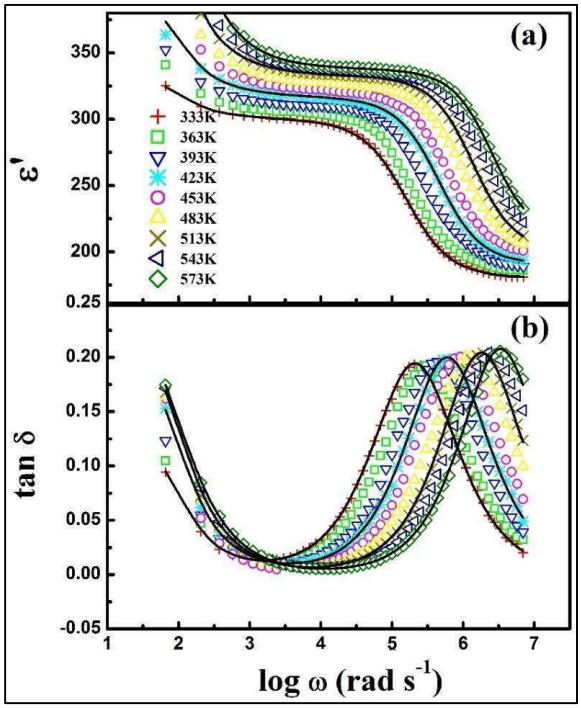

Fig. 12: *Frequency dependence of (a) ε′ and (b) tan δ of BNTS at different temperatures where the Cole-Cole fit of the experimental data are represented by the solid lines.*

In the lower frequency side, tan δ for both the samples increases with the decrease in frequency which may be ascribed due to the effect of dc conductivity. So, a term for the dc electrical conduction is added to equation (1) [47, 48]:

$$\varepsilon * = \varepsilon_\infty + \frac{\varepsilon_S - \varepsilon_\infty}{1+(i\omega\tau)^{1-\alpha}} - i\frac{\sigma*}{\varepsilon_0\omega^n} \quad (2)$$

where the complex conductivity $\sigma^* = (\sigma_1 + i\,\sigma_2)$ with dc conductivity being denoted by σ_1 and conductivity due to localized charges being denoted by σ_2. In the above equation (2) *n* is a dimensionless frequency exponent which lies between 0 to 1. Equation (2) can be written as

$$\varepsilon' = \varepsilon_\infty + \frac{(\varepsilon_S - \varepsilon_\infty)\left[1+(\omega\tau)^{1-\alpha}\sin\frac{1}{2}\alpha\pi\right]}{1+2(\omega\tau)^{1-\alpha}\sin\frac{1}{2}\alpha\pi\ \ (\omega\tau)^{2(1-\alpha)}} - \frac{\sigma_2}{\varepsilon_0\omega^n} \quad (3)$$

$$\varepsilon'' = \frac{(\varepsilon_S - \varepsilon_\infty)(\omega\tau)^{1-\alpha}\cos\frac{1}{2}\alpha\pi}{1+2(\omega\tau)^{1-\alpha}\sin\frac{1}{2}\alpha\pi\ \ (\omega\tau)^{2(1-\alpha)}} + \frac{\sigma_1}{\varepsilon_0\omega^n} \quad (4)$$

and, the dielectric loss can be calculated by: $\tan\delta = \varepsilon''/\varepsilon'$ (5)

The experimental data has been fitted with the help of equations (3), (4) and (5) and is represented by black lines in Fig. 11 and 12. The different fitting parameters are shown in Table 7.

The main factors associated with the dielectric relaxation are the dipole relaxation and the conduction relaxation of the free charge carriers [49]. The value of α which is associated with the dipole relaxation decreases with increase in temperature for both BNTN and BNTS indicating that the dispersal of relaxation time decreases thus the relaxation behaviour in both the samples tends towards monodispersive nature with increase in temperature. The relaxation time τ which is inversely proportional to ω_m decreases with increase in temperature indicating that the rate of polarization and the dipole density increases with temperature. The value of n which is associated with the conduction relaxation of the free charge carriers increases with temperature for both BNTN and BNTS indicating that at higher temperature

the carrier polarization mechanism is less dispersive owing to some barrier height extracted [49,50]. The mobile charge carriers when obstructed by the grain boundaries hinders their charge migration giving rise to space charge polarization [51]. The charges accumulate at the barrier which causes a localized polarization inside the grains. As the temperature increases the density of charges causing the space charge polarization becomes quite large. Thus, with increase in temperature relaxation processes get more and more localized which makes the relaxation process more Debye type or monodispersive as also indicated by the decrease in the α value with increasing temperature.

Table 7. The values of different parameters obtained by fitting the dielectric spectra of BNTN and BNTS by modified Cole-Cole equations.

Temperature(K)	ε_s	ε_∞	ω_m (Hz)	α	n	σ_1 (Sm^{-1})	σ_2 (Sm^{-1})
BNTN							
333	539	319	217532	0.11	0.79	0.1×10^{-7}	6.00×10^{-9}
423	549	325	1113691	0.10	0.81	0.2×10^{-7}	2.00×10^{-8}
513	560	332	3423916	0.09	0.82	0.3×10^{-7}	4.00×10^{-8}
573	580	346	6525959	0.08	0.83	0.4×10^{-7}	6.00×10^{-8}
BNTS							
333	300	180	158018	0.11	0.86	0.1×10^{-7}	8.00×10^{-9}
423	317	190	453625	0.10	0.88	0.2×10^{-7}	2.00×10^{-9}
513	333	200	1375618	0.09	0.9	0.3×10^{-7}	5.00×10^{-9}
573	348	210	2546917	0.08	0.91	0.4×10^{-7}	9.00×10^{-9}

In BNTN and BNTS the existence of long-range migration of free charge carriers (dc conductivity) is evident in the low frequency region thus we can conclude that both the

samples possess some amount of electrical semi conductivity [51]. The hybridization between the vacant d orbitals of B-site cations and the p orbitals of oxygen significantly affects the transport properties of the perovskite oxides [52,53]. The electronegativity of Sb^{5+} being higher than that of Nb^{5+} results in less ionic or more covalent Sb-O bond which in-turn decreases its macroscopic polarizability [52, 54]. The presence of vacant d orbitals in Nb favours higher hybridization with p orbitals of oxygen giving rise to larger polar instabilities and higher permittivity values for BNTN. The presence of vacant 4d orbital of Nb in BNTN sample gives rise to its high dielectric permittivity values as compared to BNTS for which the 4d orbitals of Sb are completely filled. As the permittivity value of BNTN is quite high as compared to BNTS and have almost same low values of dielectric losses, the BNTN sample is more suitable for circuit miniaturization [55].

6.3.4. Complex impedance analysis:

The complex plane impedance plots at temperatures 423 K and 543 K for BNTN and BNTS are illustrated in Fig. 13 and 14 respectively. The contribution of both the grain and grain boundary to the overall impedance has been confirmed by the presence of two deformed circular arcs in both the samples [56]. The centre of the semi-circular arc being below the Z′ axis also confirms the relaxation mechanism of the samples being polydispersive nature. [56–62] The semi-circular arc becomes smaller on increasing the temperature which points towards the thermally activated conduction mechanism of the samples having semiconducting nature. The impedance spectra have been fitted using an equivalent circuit model consisting of two parallel combinations of resistance and capacitance joined together in series. The capacitance term here is replaced by a constant phase element (Q) due to the non-ideal behaviour of the capacitance as a result of more than one relaxation process for a given relaxation time. The capacitance for the constant phase

element is given by $C_p = Q^{1/c} R^{(1-c)/c}$ where c denotes the deviation from the ideal Debye nature. The real and the imaginary part of the impedance have been fitted using equations

$$Z' = \frac{R_g}{1+\left[\omega(R_gQ_g)^{\frac{1}{c_g}}\right]^2} + \frac{R_{gb}}{1+\left[\omega(R_{gb}Q_{gb})^{\frac{1}{c_{gb}}}\right]^2} \quad (6)$$

$$\text{and } Z'' = R_g\left[\frac{\omega(R_gQ_g)^{\frac{1}{c_g}}}{1+\left[\omega(R_gQ_g)^{\frac{1}{c_g}}\right]^2}\right] + R_{gb}\left[\frac{\omega(R_{gb}Q_{gb})^{\frac{1}{c_{gb}}}}{1+\left[\omega(R_{gb}Q_{gb})^{\frac{1}{c_{gb}}}\right]^2}\right] \quad (7)$$

where R_g and R_{gb} denotes the resistance and Q_g and Q_{gb} denotes the constant phase element for the grain and grain boundary respectively. The fitting parameters are given in Table 8. The coincidence of the fitted curve and the experimental data points confirms that both the grain and grain boundary contribute to the total impedance. The high values of R_{gb} indicates that the grain boundaries are more insulating than the grains.

Table 8. The fitted parameters of the impedance circuit for BNTN and BNTS.

	Temp. (K)	R_g (Ω)	Q_g (10^{-8} F/Ω)	c_g	R_{gb} (10^8 Ω)	Q_{gb} (10^{-9} F/Ω)	c_{gb}
BNTN	423	650	3	0.81	28	0.17	0.89
	543	185	1	0.92	11	0.27	0.86
BNTS	423	2800	1.50	0.82	14	0.19	0.86
	543	421	0.98	0.82	5	0.28	0.87

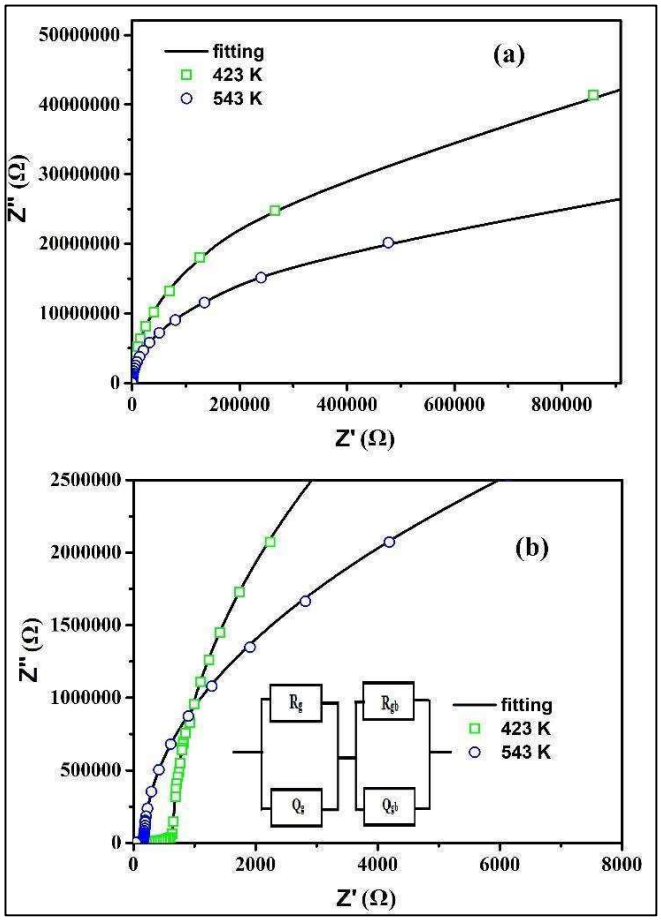

Fig. 13: *(a) Complex impedance plane plots of BNTN and (b) the enlarge view of the high frequency region.*

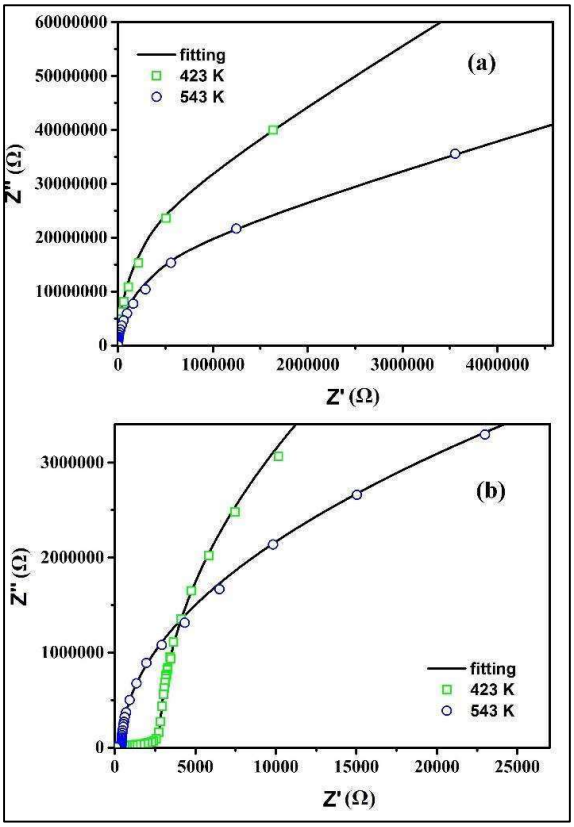

Fig. 14: *(a) Complex impedance plane plots of BNTS and (b) the enlarge view of the high frequency region.*

6.3.5. Conductivity Analysis:

The variation ac conductivity with frequency for BNTN and BNTS at various temperatures is depicted in Fig. 15 and 16 respectively. In the conductivity spectrum two discrete plateaus can be observed. The plateau at the low frequency is associated with the total conductivity whereas the plateau at the higher frequency arises due to the grain's contribution to the total conductivity [63]. Thus, two processes are involved in the bulk conduction mechanism of the samples.

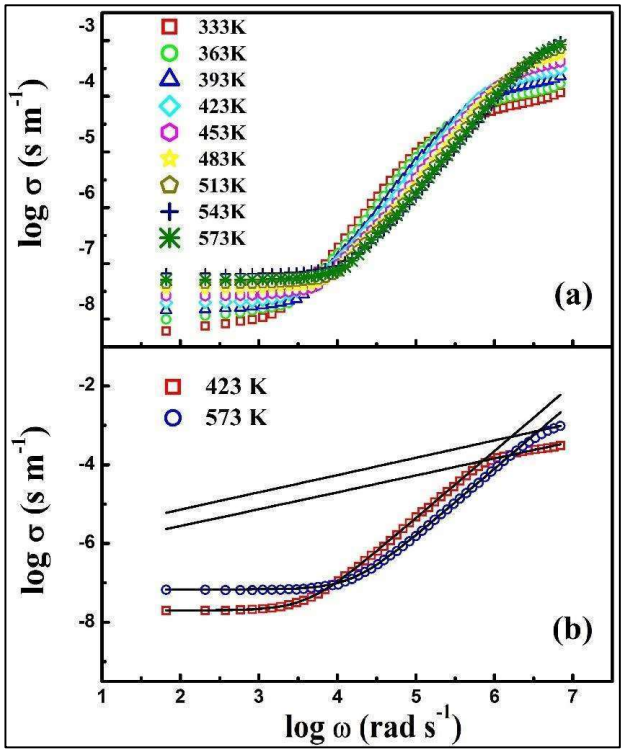

Fig. 15: *(a) Frequency dependence of the ac conductivity of BNTN at different temperatures and (b) the power law fitting of the experimental data as shown by solid lines.*

The total conductivity as stated by the power law is:

$$\sigma(\omega) = \sigma_{dc} + K\,\omega^{n} \quad (8)$$

here σ_{dc} is the dc conductivity and K is a constant dependent on frequency and temperature. In order to fit the conductivity spectra, the basic power law has been used with n values between 1.5-1.9 [64] at lower frequency and 0.4-0.6 at higher frequency [65]. The parameters used for fitting are represented in Table 9. The above equation can also be written as $\sigma(\omega) = \sigma_{dc}[1 + (\omega/\omega_H)^n]$ where the charge carriers' hopping frequency is denoted by ω_H. The value of

ω_H for BNTN is 4158.32 and 15666.79 rads^{-1} at 423 and 573 K respectively and for BNTS the value of ω_H is 3863.92 and 22623.61 rads^{-1} at 423 and 573 K respectively.

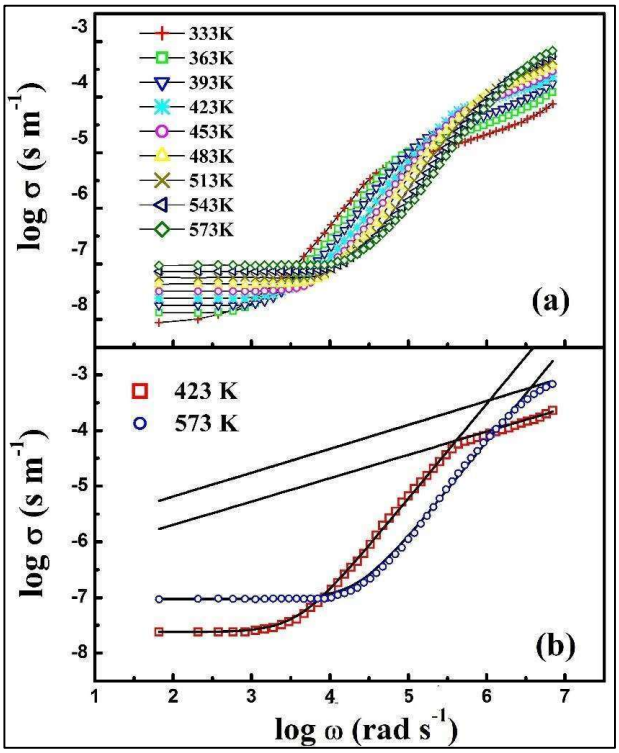

Fig. 16: *(a) Frequency dependence of the ac conductivity of BNTS at different temperatures and (b) the power law fitting of the experimental data as shown by solid lines.*

The variation of the dc conductivity (σ_{dc}) with the inverse of temperature (Fig. 17) is found to follow the Arrhenius Law: $\sigma_{dc} = \sigma_0 \exp\left[-\frac{E_\sigma}{K_B T}\right]$, where E_σ is the activation energy. On increasing the temperature, the dc conductivity value increases. The value of E_σ as deduced from the Arrhenius plot is 0.36 eV for BNTN and 0.37 eV for BNTS. The value of

E_σ suggests that for both BNTN and BNTS the conduction mechanism is governed by p-type polaron hopping [66, 67]. The step like nature of the conductivity spectra is due to the presence of different potentials offered by the grain and grain boundary and the hopping of charge carriers through these potential barriers [54]. As seen from the impedance spectra the grain boundary being more insulating acts as a trap site for the charge carriers taking part in the charge transport.

Table 9. Various fitted parameters of the conductivity spectra for BNTN and BNTS.

Sample	Temperature(K)	σ_{dc} (Sm^{-1})	A	n
BNTN	423 (at low frequency)	1.99×10^{-8}	0.14×10^{-13}	1.7
BNTN	423 (at high frequency)	1.99×10^{-8}	3.8×10^{-7}	0.43
BNTN	573 (at low frequency)	6.81×10^{-8}	0.05×10^{-13}	1.7
BNTN	573 (at high frequency)	6.81×10^{-8}	9.5×10^{-7}	0.44
BNTS	423 (at low frequency)	2.39×10^{-8}	0.19×10^{-13}	1.7
BNTS	423 (at high frequency)	2.39×10^{-8}	2.9×10^{-7}	0.42
BNTS	573 (at low frequency)	9.38×10^{-8}	0.03×10^{-13}	1.72
BNTS	573 (at high frequency)	9.38×10^{-8}	8.9×10^{-7}	0.43

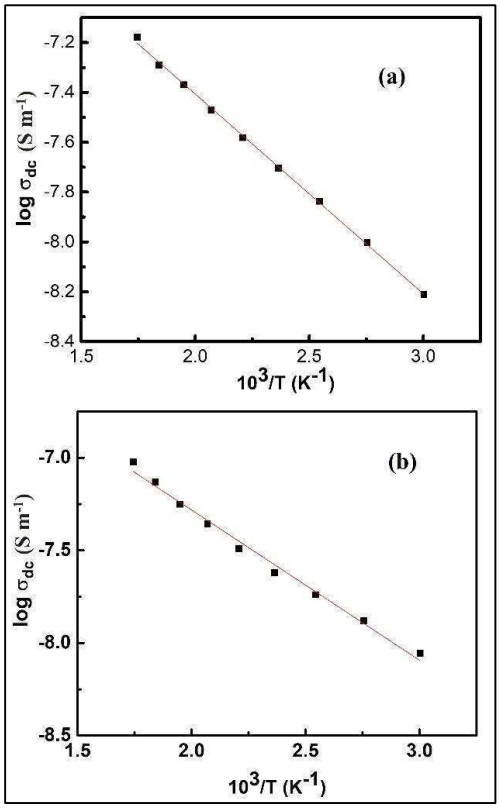

Fig. 17: *Arrhenius plot of dc conductivity for (a) BNTN and (b) BNTS.*

6.4. Conclusion:

We have synthesized the triple perovskites $Ba_3NiTaNbO_9$ (BNTN) and $Ba_3NiTaSbO_9$ (BNTS) by solid state ceramic method and thoroughly investigated their structural, microstructural, optical and dielectric properties. The crystal structure, bonding property and ordering behaviour of BNTN and BNTS are analysed by Rietveld refinement of XRD data and the results are further corroborated by FTIR and Raman studies. It has been shown that both BNTN and BNTS are partially ordered triple perovskite having general formula $A_3(B'B''B''')O_9$. BNTN and BNTS stabilize in *P-3m1* space group of trigonal symmetry and *P*

$6_3/mmc$ space group of hexagonal symmetry, respectively. Both the sample possess cationic disorder due to the site exchange of cations occupying the B', B" and B"' sites. This work will be of immense help in understanding the nature of ordering and probing the presence of occupational disorder evolving due to the exchange of cations between B′, B″, B‴ sites of $A_3(B'B''B''')O_9$ type perovskites. The relaxation nature of the samples has been analysed with the help of the Cole-Cole model. The non-zero values of α for the Cole-Cole model suggests the relaxation phenomena being polydispersive in nature. The activation energy as obtained from the conductivity spectra is 0.36 eV for BNTN and 0.37 eV for BNTS which indicates that the polaron hopping mechanism is responsible for their electrical and dielectric response.

It is noteworthy that at room temperature $Ba_3M^{III}TiM^{V}O_9$ (where, M^{III} = Ga, Y, Lu; M^{V} = Nb, Ta,) and $Ba_3M^{III}TiSbO_9$ (where, M^{III} =Fe, Ga) exhibit dielectric permittivity (ε′) in the range of 20-60 and 20-100, respectively, at frequencies ranging between 1kHz - 1MHz [26]. The values of ε′ for $Ba_3MgTa_{2-x}Nb_xO_9$ (where $0 \leq x \leq 1$) lies in the range of 15-20 at 500 KHz and the dielectric loss (tanδ) is ~ 0.15 for this series of compounds [68]. The value of ε′ and tanδ for the series of compounds with general formula $Ba_3ZnTa_{2-x}Nb_xO_9$ ($0 \leq x \leq 1$) at 500 KHz are ≈ 30 and 0.08, respectively [68]. Further, the dielectric constant and dielectric loss at 500 KHz are 324 and 0.05 for BNTN and 182 and 0.04 for BNTS, respectively. It may be inferred that the chemical property of B-site cations strongly affect the dielectric properties of $A_3(B'B''B''')O_9$ type perovskites and BNTN and BNTS exhibits improved dielectric properties as compared to other triple perovskites of $Ba_3(B'B''B''')O_9$ series. Thus, BNTN and BNTS appears to be very suitable for fabrication of radio frequency devices like dielectric resonator, oscillator and filters and may also find application in the field of electronic device miniaturization.

References

[1] T. A. Vanderah, Science 298 (2002) 1182.

[2] R.J. Cava, J. Mat. Chem. 11 (2001) 54–62.

[3] M. Lee, E. S. Choi, X. Huang, J. Ma, C. R. Dela Cruz, M. Matsuda, W. Tian, Z. L. Dun, S. Dong, H. D. Zhou, Phys. Rev. B 90 (2014) 224402.

[4] J. Hwang, E. S. Choi, F. Ye, C. R. Dela Cruz, Y. Xin, H. D. Zhou, P. Schlottmann, Phys. Rev. Lett. 109 (2012) 257205.

[5] I. Molodetsky, P.K. Davies, J. Euro, Ceram. Soc. 21 (2001) 2587–2591.

[6] B. Xu, F. Zhang, X.Y. Liu, J.H. Ye, W.H. Zhang, L. Shi, X.G. Wan, J. Yin, Z.G. Liu, Phys. Rev. B 76 (2007) 125109.

[7] Y. Doi, Y. Hinatsu, J. Mater. Chem. 12 (2002) 1792–1795.

[8] S. J. Kim, M. D. Smith, J. Darriet, H. C. zur Loye, J. Solid State Chem. 177 (2004) 1493–1500.

[9] Y. Doi, Y. Hinatsu, J. Phys. Condens. Matter 16 (2004) 2849–2860.

[10] J. G. Zhao, L. X. Yang, Y. Yu, F. Y. Li, R. C. Yu, C. Q. Jin, J. Solid State Chem. 182 (2009) 327–330.

[11] V. U. Treiber, S. Kemmler-Sack, A. Ehmann, Z. Anorg. Allg. Chem. 487 (1982) 198.

[12] P. Lightfoot, P. D. Battle, J. Solid State Chem. 89 (1990) 174 –183.

[13] J. C. Albornoz, D. A. Landinez Tellez, J. Roa-Rojas, J. A. Munevar, E. Baggio Saitovich, J. Supercond. Novel Magn. 26 (2013) 2313 – 2317.

[14] P. Beran, S. A. Ivanov, P. Nordblad, S. Middey, A. Nag, D. D. Sarma, S. Ray, R. Mathieu Solid State Sci. 50 (2015) 58 – 64.

[15] F. Casallas, E. Vera, D. Landinez, C. Parra, J. Roa, J. Phys.: Conf. Ser. 687 (2016) 012047.

[16] T. Ferreira, D. Carone, A. Huon, A. Herklotz, S. A. Stoian, S. M. Heald, G. Morrison, M. D. Smith, H. C. zur Loye, Inorg. Chem. 57 (2018) 7362 –7371.

[17] R. D. Shannon, J. Appl. Phys. 73 (1993) 348.

[18] H. Tamura, D. A. Sagala, K. Wakino, Jpn. J. Appl. Phys. 25 (1986) 787.

[19] I. M. Reaney, I. Qazi, W. E. Lee, J. Appl. Phys. 88 (2000) 6708.

[20] R. Mani, P. Selvamani, J. E. Joy, J. Gopalakrishnan, Inorg. Chem. 46 (2007) 6661–6667.

[21] M. M. Hoque, A. Dutta, S. Kumar, T.P. Sinha, Physica B 407 (2012) 3740 – 3748.

[22] M. W. Lufaso, Chem. Mater. 16 (2004) 2148–2156.

[23] S. Asai, M. Soda, K. Kasatani, T. Ono, M. Avdeev, T. Masuda, Phys. Rev. B 93 (2016) 024412.

[24] A. J. Jacobson, A. J. Calvert, J. inorg, nucl. Chem. 40 (1978) 447–449.

[25] Larson AC, Von Dreele RB, General structure analysis system (GSAS). Los Alamos National Laboratory, Report LAUR (2000) 86–784.

[26] J. B. Philipp, P. Majewski, L. Alff, A. Erb, R. Gross, T. Graf, M. S. Brandt, J. Simon, T. Walther, W. Mader, D. Topwal, D. D. Sarma, Phys. Rev. B 68 (2003) 144431.

[27] R.D. Shannon, Acta Cryst. 32 (1976) 751–767.

[28] M.W. Lufaso, E. Hopkins, S.M. Bell, A. Llobet, Chem. Mater. 17 (2005) 4250.

[29] J. E. Joy, E. Atamanik, R. Mani, A. Nag, R.M. Tiwari, V. Thangadurai, J. Gopalakrishnan, Solid State Sci. 12 (2010) 1970–1976.

[30] G. Blasse, J. Inorg. Nucl. Chem. 27 (1965) 993.

[31] J. B. Goodenough, J. A. Kafalas, J. Solid State Chem. 6 (1973) 493.

[32] H. Mizoguchi, P. M. Woodward, S. H. Byeon, J. B. Parise, J. Am. Chem. Soc. 126 (2004) 3175.

[33] J. E. F. S. Rodrigues, E. Moreira, D. M. Bezerra, A. P. Maciel, C. W. A. Paschoal, Mater. Res. Bull. 48 (2013) 3298–3303.

[34] D. L. Rousseau, R. P. Bauman, S. P. S. Porto, J. Raman Spectrosc. 10 (1981) 253.

[35] A. Dias, V. Ciminelli, F. M. Matinaga, R. Moreira, J. Eur. Ceram. Soc. 21 (2001) 2739–2744.

[36] R.L. Moreira, F.M. Matinaga, A. Dias, Appl. Phys. Lett. 78 (2001) 428.

[37] J. E. F. S. Rodrigues, D. M. Bezerra, A. P. Maciel, C. W. A. Paschoal, Ceram. Int. 40 (2014) 5921–5930.

[38] S. A. Prosandeev, U. Waghmare, I. Levin, J. Maslar, Phys. Rev. B 71 (2005) 214307.

[39] V.L. Ginzburg, A.P. Levanyuk, A.A. Sobyanin, Phys. Rep.3 (1980) 151–240.

[40] Ph. Daniel, J. Toulouse, J. Y. Gesland, M. Rousseau, Phys. Rev. B 52 (1995)13.

[41] J. Chen, Y. Tang, J. Li, H. Xiang, C. Li, X. Xing, L. Fang, J. Alloys Compd. 820 (2020) 153159.

[42] A. Dutta, T.P. Sinha, Mater. Res. Bull. 46 (2011) 518–524.

[43] G. V. S. Rao, C. N. R. Rao, J. R. Ferraro, Appl. Spectrosc. 24 (1970) 436.

[44] P. Debye, Polar Molecules, Chemical Catalogue Company, New York, 1929.

[45] K. S. Cole, R. H. Cole, J. Chem. Phys. 9 (1941) 341–351.

[46] K.S. Cole, R.H. Cole,J. Chem. Phys. 10 (1942) 98–105.

[47] R. Coelho, Physics of Dielectrics (New York: Elsevier) 1978.

[48] S. K. Maity, A. Dutta, S. Kumar, T. P. Sinha, Phys. Scr. 88 (2013) 065702.

[49] P. Thongbai, S. Tangwancharoen, T. Yamwong, S. Maensiri, J. Phys. Condens. Matter 20 (2008) 395227.

[50] S. Halder, A. Dutta, T.P. Sinha, J. Phys. Chem. Solids 102 (2017) 79–89.

[51] R. Mukherjee, S. Saha, A. Dutta, T. P. Sinha, J. Alloys Compd. 651 (2015) 222–229.

[52] A. Dutta, T. P. Sinha, D. Das, J. Magn. Magn. Mater. 360 (2014) 211–21.

[53] A.Dutta, T.P. Sinha, Mater. Res. Bull. 46 (2011) 518–524.

[54] Y. Tsuji, A. Kan, H Ogawa, S. Ishihara, J. Eur. Ceram. Soc. 25 (2005) 2883–2887.

[55] Wolfram Wersing, Curr. Opin. Solid State Mater. Sci. 1 (1996) 715–731.

[56] A. Barua, S. Maity, S. Kumar, A. Dutta, T.P. Sinha, Physica B 583 (2020) 412057.

[57] L. Liu, H. Fan, L. Wang, X. Chen, P. Fang, Philosophical Magazine, 88 (2008) 537–545.

[58] L. Liu, H. Fan, P. Fang, L. Jin, Solid State Commun. 142 (2007) 573–576.

[59] L. Liu, H. Fan, P. Fang, X. Chen, Mater. Res. Bull. 43 (2008) 1800–1807.

[60] R. Gerhardt, J. Phys. Chem. Solids. 55 (1994)1491–1506.

[61] M. C. H. Mckubre, J. R. Macdonald, Impedance Spectroscopy Emphasizing Solid Materials and Systems, ed. J. R. Macdonald, Wiley, New York, (1987)191.

[62] M. M. Hoque, A. Barua, A. Dutta, S. K. Dey, T. P. Sinha, S. Kumar, Ionics 23 (2017) 471–483.

[63] A. Dutta, C. Bharti, T. P. Sinha, Mater. Res. Bull. 43 (2008) 1246–1254.

[64] S. Nomura, K. Toyama, K. Kaneta, Jpn. J. Appl. Phys. 21 (1982) 624–626.

[65] C. Bharti, T.P. Sinha, Solid State Sci. 12 (2010) 498–502

[66] M. Idrees, M. Nadeem, M. M. Hassan, J. Phys. D Appl. Phys. 43 (2010) 155401.

[67] W. H. Jung, J. Appl. Phys. 90 (2001) 2455.

Chapter – 7

$BaCo_{1/3}Nb_{2/3}O_3$ and $BaCo_{1/3}Sb_{2/3}O_3$ perovskite oxide: Structural, microstructural, optical and dielectric study

7.1. Introduction:

Perovskite with general formula $A_3B'B''_2O_9$ can accommodate variety of B-site cations having different valences [1, 2]. The difference in the B-site cations leads to the different types of ordering like 1:1 ordering having cubic symmetry or 1:2 ordering having trigonal symmetry. Due to their wide range of technological and industrial applications perovskite oxides have been widely studied [3, 4]. They also have application as photocatalysis, photodetector, photovoltaic cell, microwave devices [5–10]. Thus, perovskite oxides having high efficiency and low cost are of great demand these days.

Ba based perovskite oxides have attracted a lot of research interest in the past few decades [11–15]. The structural and electronic band gap of $Ba_3ZnNb_2O_9$, $Ba_3SrNb_2O_9$, $Ba_3MgTa_2O_9$, and $Ba_3SrTa_2O_9$ have been reported by Mani. et. al. [16]. The structural and magnetic properties of $BaCo_{1/3}Nb_{2/3}O_3$ have been reported by Payen et. al. and its room temperature dielectric property has been reported by Freer et. al. [17, 18]. Theoretical band structure calculation of $BaCo_{1/3}Nb_{2/3}O_3$ has been reported by Berri et. al. [19]. The synthesis procedure and structural characterization of $BaCo_{1/3}Sb_{2/3}O_3$ have been reported by Istomin et al. [20]. To the best of our knowledge the optical and temperature dependent dielectric properties of $BaCo_{1/3}Nb_{2/3}O_3$ and $BaCo_{1/3}Sb_{2/3}O_3$ have not yet been reported. In this context we have performed detailed structural, microstructural, optical and temperature dependent dielectric properties of $BaCo_{1/3}Nb_{2/3}O_3$ and $BaCo_{1/3}Sb_{2/3}O_3$ for better understanding of their structural and electrical properties.

7.2. Experimental:

Solid state ceramic method has been employed in order to synthesize the samples. Stoichiometric amount of reagent grade powders of $BaCO_3$, CoO, Nb_2O_5 and Sb_2O_5 were

mixed together along with acetone with the help of motor pestle for 10 h. Then the samples were calcined at 1400° C for 12 h and cooled down to room temperature under controlled cooling rate of 2° C / min.

The phase formation of both the samples were confirmed using Powder X-ray diffraction analysis using (Bruker D8 advanced X-ray powder diffractometer, XRD). Cu-K_α radiation was used and the scan speed was set at 2º min^{-1}. The range of Bragg angle was taken to be $10º \leq 2\theta \leq 120º$ where the scanning step size was 0.02º. In the XRD patterns only the characteristic diffraction peaks of perovskite structure were obtained which confirmed that both BCN and BCS are single phase perovskite oxides. The samples were than pelletized into discs along with polyvinyl alcohol as a binding agent. Then the discs were sintered at 1450º C for 12 h and cooled down to 30º C with a cooling rate of 1º C min^{-1}. The thickness and the diameter of the discs were 1.5 mm and 10 mm for BCN and 1.6 mm and 10 mm for BCS, respectively. Electrodes were than developed on the flat surfaces of the disc by coating them with fine silver paint followed by heating at 200º C for 2 h.

The microstructural and morphological characterizations of the samples were performed using FEI INSPECT F50 field emission scanning electron microscope (FESEM). The energy dispersive X-ray spectrometer (EDS) was used to determine the chemical constituents of the prepared samples. The Fourier transform infrared (FTIR) spectrum of the samples were recorded using Perkin Elmer spectrometer. WITEC alpha, 300R Raman spectrometer was used to record the Raman spectrum of both the samples. In order to perform the dielectric measurements HIOKI 3532 LCR meter was used in between 110 Hz to 1.1 MHz frequency. The oscillation voltage was kept at 1 V. The dielectric measurements were carried out in the temperature range 333 to 543 K and heating at a rate of 0.5º C min^{-1} with the help of programmable heating-cooling system with an accuracy of ± 1 K.

7.3. Results

7.3.1. Structural characterization:

The XRD patterns of BCN and BCS agrees well with those reported earlier [17, 20]. In order to obtain the structural refinement parameters of BCN and BCS, Rietveld refinement have been performed using GSAS program [21]. The XRD patterns of both BCN and BCS are depicted in Fig. 1. BCN belongs to trigonal symmetry with *P-3m1* space group whereas BCS belongs to hexagonal symmetry with *P 6$_3$/mmc* space group. The crystal lattice parameters and Wyckoff positions of the samples have been tabulated in Table 1 and Table 2, respectively.

Table 1: Structural and refinement parameters of BCN and BCS as obtained from Rietveld X-ray powder structure refinement method.

	BCN	BCS
Crystal system	Trigonal	Hexagonal
Space group	*P-3m1*	*P 63/mmc*
a (Å)	5.75581(11)	5.83744(16)
b (Å)	5.75581(11)	5.83744(16)
c (Å)	7.06833(2)	14.4082(4)
Volume (Å^3)	202.796(10)	425.193(31)
α=β(°)	90	90
γ(°)	120	120
R_{wp}	0.0250	0.0304
R_p	0.0385	0.0458
χ^2	2.90	3.54

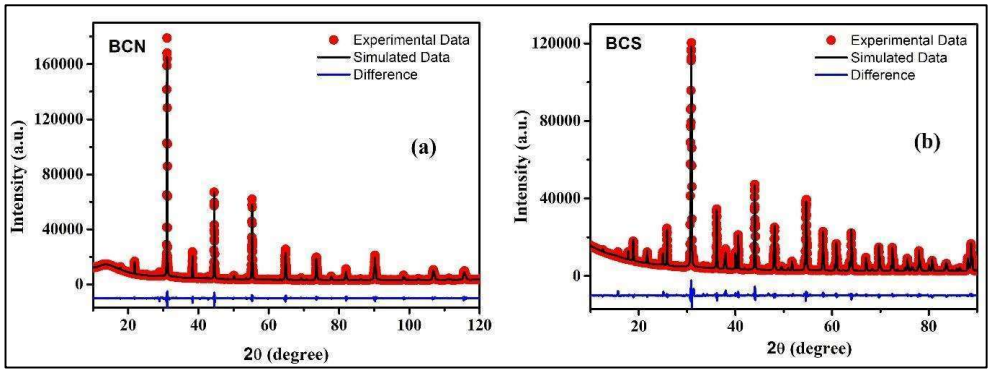

Fig. 1: *The XRD images of (a) BCN and (b) BCS.*

Table 2. Special Wyckoff positions of the atoms and refined values of atomic coordinates of BCN and BCS.

Atom	Site	x (Å)	y (Å)	z (Å)	B (Å^2)
BCN					
Ba1	1a	0.0	0.0	0.0	0.03040
Co1	1b	0.0	0.0	0.5	0.03139
Nb1	2d	0.33333	0.66667	0.1814(4)	0.00501
Ba2	2d	0.33333	0.6667	0.65599(28)	0.03820
O1	3e	0.5	0.0	0.0	0.00864
O2	6i	0.1813(8)	0.3626(17)	0.3213(19)	0.04272
BCS					
Ba1	2b	0	0	0.25	0.0011(2)
Co1	2a	0	0	0	0.0025(9)
Sb1	4f	0.33	0.66	0.15072(7)	0.0017(4)
Ba2	4f	0.33	0.66	0.90997(7)	0.0027(2)
O1	6h	0.4828(8)	0.0344(16)	0.25	0.0046(3)
O2	12k	0.1703(7)	0.3407(14)	0.4180(4)	0.0058(2)

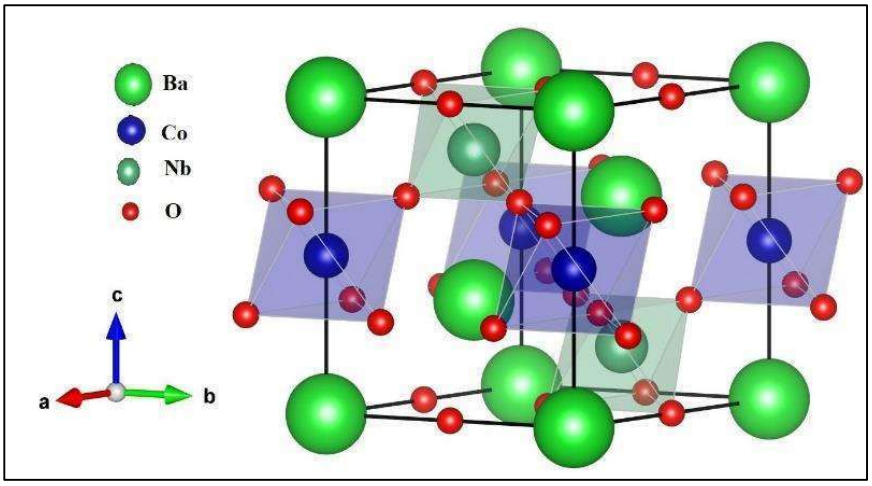

Fig. 2: *The asymmetric unit of BCN.*

In the asymmetric unit of BCN (Fig. 2) it can be observed that the Ba^{2+} ions are coordinated with 12 oxygen ions while Co^{2+} and Nb^{5+} ions are coordinated with 6 oxygen ions. It can be observed from Table 3 that Nb–O bond lengths of BCN are not equal which indicates that there exists an off centre distortion of the cations in the octahedra resulting from the second order Jahn-Teller distortion for d^0 cations like Ti^{4+}, Nb^{5+}, Ta^{5+}, W^{6+} [22]. In the asymmetric unit of BCS (Fig. 3) it can be observed that Ba^{2+} ions are coordinated with 12 oxygen ions while $Co^{2+}$and Sb^{5+} ions are coordinated with 6 oxygen ions. The difference in the bond length of Sb–O (Table 3) results from the cation-cation repulsion between the face sharing Sb_2O_9 groups [23].

The B-site cations of BCN are arranged along the (111) planes of the pseudocells with two Nb layer and one Co layer as shown in Fig.4 (a). This arrangement of the B-site atoms is repeated along the crystallographic c axis. On the other hand, the B-site cations of BCS are arranged along the (111) planes of the pseudocells with two Sb layer and one Co layer as

shown in Fig. 4(b). This arrangement of the B-site atoms is repeated along the crystallographic c axis.

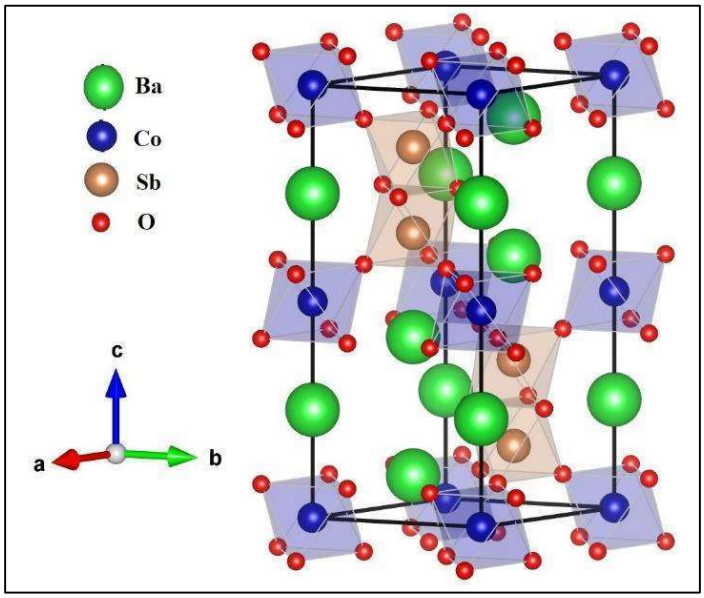

Fig. 3: *The asymmetric unit of BCS.*

Table 3. Cationic bond lengths bond angles of BCN and BCS.

BCN		BCS	
Bonds lengths			
Co–O	2.205 Å	Co–O	2.089 Å
Nb–O1	2.098 Å	Sb–O1	1.922 Å
Nb–O2	1.810 Å	Sb–O2	2.081 Å
Bond angles			
Nb^{5+}–O–Nb^{5+}	180º.	Sb^{5+}–O–Sb^{5+}	86.9º

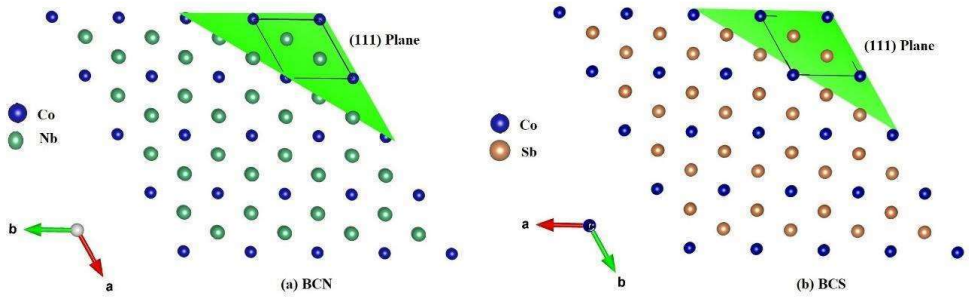

Fig. 4: *The ordering sequence of the B-site atoms in BCN and BCS.*

The vacant d orbital in Nb^{5+} and the filled d orbital in Sb^{5+} effects their bonding preference which along with their ionic radii difference determines the *P-3m1* space group of BCN and *P 6₃/mmc* space group of BCS [23–27]. In BCN the vacant d orbitals of Nb^{5+} favours the formation of л bond with the p orbitals of oxygen thus resulting in a linear Nb^{5+}–O–Nb^{5+} bond with bond angle ~ 180º. This favours the *P-3m1* structure with metal oxygen corner sharing octahedra and cubic stacking of BaO_3 layers as can be seen in Fig. 2. The filled d orbitals of Sb^{5+} does not favour the formation of л bond and preferred Sb^{5+}–O–Sb^{5+} bond angle is < 180º resulting from σ bonding with p orbitals of two different oxygen. Thus, BCS stabilizes in *P 6₃/mmc* structure containing mixed cubic and hexagonal stacking of BaO_3 layers [Fig. 3] with NiO_6 octahedra in the vertex and face sharing Sb_2O_9 groups. Perovskite materials exhibit partially ordered structure due to the exchange of their Wykoff site between the B'-B'' ions [28]. It can be seen from Fig. 4 that ordered nature is maintained for both BCN and BCS sample. Each *2d* site of BCN can either be occupied by a Co^{2+} or Nb^{5+} ion and similarly in case of BCS the probability that each *4f* site to be filled by a Co^{2+} or Sb^{5+} ion is equal and this leads to occupational disorder in both the samples. Thus,

both BCN and BCS fall in the category of partially ordered perovskite. The SEM images of BCN and BCS (Fig. 5) reveal that both the samples have well defined grains of asymmetrical shapes and sizes having grain size 0.6 μm to 2.2 μm for BCN and 0.5 μm to 4.4 μm for BCS.

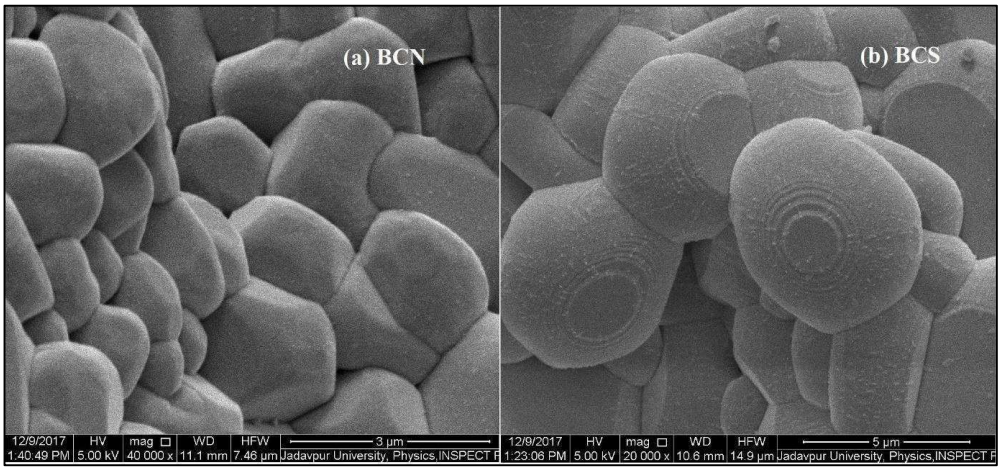

***Fig. 5** The SEM images of BCN and BCS.*

7.3.2. FTIR study

The FTIR spectra of BCN and BCS are shown in Fig. 6 (a) and (b), respectively. In both the spectra the characteristic peaks associated with perovskite phase has been observed. The IR active vibrational modes due to Co–O stretching present in CoO_6 octahedra is associated with the bands around 490 and 531 cm^{-1} for BCN and 511 and 545 cm^{-1} for BCS [29, 30]. The bending mode of the BO_6 polyhedra is associated with the energy bands in between 360 and 412 cm^{-1}. The asymmetric bending mode of the NbO_6 and SbO_6 octahedra is associated with the band at 364 cm^{-1} for BCN and 366 cm^{-1} for BCS. The energy band around 623 cm^{-1} for BCN and 676 cm^{-1} for BCS is associated with the asymmetric stretching vibration of the NbO_6 octahedra and SbO_6 octahedra of BCN and BCS, respectively. The asymmetry in the bond lengths of Co–O, Sb–O and Nb–O bonds and the occurrence of absorption peaks of these bonds at nearly same wave numbers gives rise to the

broad vibrational bands. The symmetric stretching vibration of SbO_6 and NbO_6 octahedra is associated with the peaks around 703 and 756 cm^{-1} for BCN and 780 cm^{-1} for BCS [31].

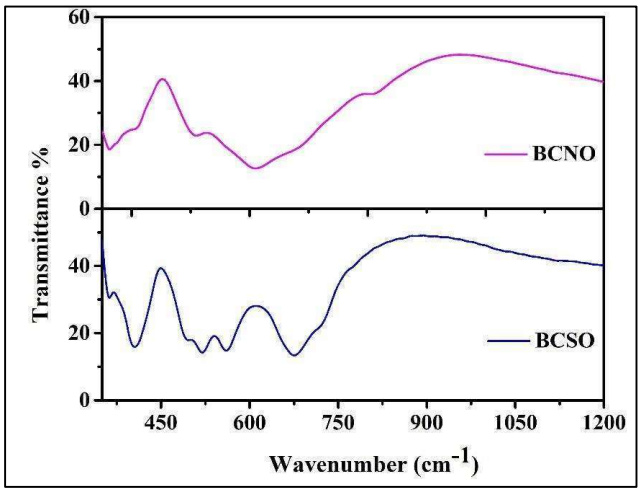

Fig. 6: *The FTIR spectra of BCN and BCS.*

7.3.3. Raman Study

The Raman spectra of BCN are shown in Fig. 7 (a) and (b) whereas for BCS it has been illustrated in Fig. 8 (a), (b) and (c). The Lorentzian peak fitting of the Raman spectra has been performed and the peak positions and their full width half maxima has been tabulated in Table 4. The expected phonon modes for BCN have been determined using group factor analysis and listed in Table 5 [32]. Nine Raman-active modes (Γ_{Raman} = 4 A_{1g} + 5 E_g) are expected for ordered sample with *P-3m1* space group but an increased number of optical active modes arises in BCN due to the occupational disorder caused by the exchange of Wyckoff sites between B'-B'' ions [28, 33–35]. The additional modes due to occupational disorder can also be predicted by the group factor analysis (Table 5). The existence of B' ions in *2d* Wyckoff site would give rise to two additional Raman and IR bands each ($\Gamma_{Raman,B'}$= A_{1g} + E_g, $\Gamma_{IR,B'}$= A_{2u} + E_u) and the presence of B'' ions in *1b* Wyckoff site would give rise to

two additional IR bands ($\Gamma_{IR,B''} = A_{2u} + E_u$). From the Lorentzian fitting of BCN 15 bands are observed where two extra Raman bands occur due to the presence of Co ions in the *2d* site and four additional Raman band may be attributed to the defect activated modes [34]. Appearance of extra Raman bands due to the presence of such defects in ceramic crystals, developed during the crystal growth process, are very common [36, 37]. The bands 1-5, 8, 9, 13 arises due to the vibrations of Ba and O ions and agrees well with those reported by Moreira et al. [34]. The peaks (11, 12) arise due to the vibration of Nb ions occupying their own *2d* site and the peaks (14, 15) arises due to the vibrations of Co ions in the *2d* site. The peak 6, 7 and 10 may be attributed to the localized defect activated modes [34].

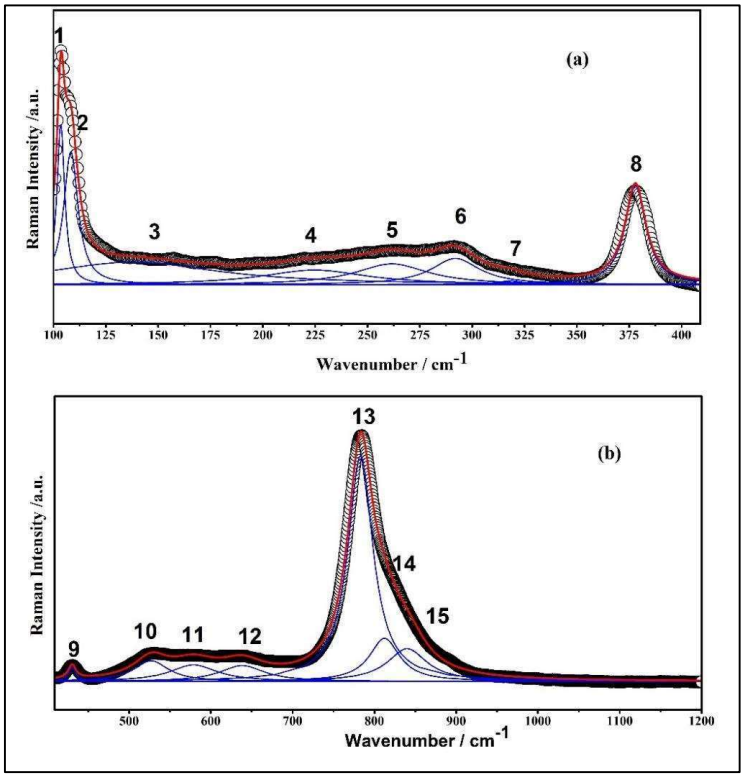

Fig. 7: *The Lorentzian peak fitting of the Raman spectra of BCN where red line represents the fitted curve and the symbols represent the experimental data.*

Table 4. Experimentally observed Raman active phonon modes.

Peak No.	BCN		BCS	
	Frequency (cm^{-1})	FWHM (cm^{-1})	Frequency (cm^{-1})	FWHM (cm^{-1})
1	103.513	4.48856	112.81611	15
2	108.32009	8.26204	140.91587	13.42941
3	137.83902	100.0077	152.79434	21.56576
4	261.68048	42.45575	171.6528	28.22603
5	292.01993	28.1051	187.19805	16.34698
6	318.09595	15.3717	204.71501	17.85759
7	377.98335	12.05426	231.02186	32.67136
8	224.74665	61.69439	253.41388	32.10114
9	430.37708	51.2064	132.63304	7.55846
10	527.07113	70.38416	280.71144	13.05696
11	578.95123	66.42812	321.33789	15.93556
12	638.42673	37.33939	391.87923	14.31787
13	783.0026	44.97352	421.46985	16.93432
14	812.3778	58.41566	483.32363	20.79974
15	840.0624	51.2064	528.62853	92.21762
16			391.87923	100.61716
17			450.29373	46.89063
18			610.00632	14.5296
19			616.5222	31.55602
20			666.55315	15.59623
21			699.20408	12.67554
22			761.46318	24.17309
23			825.03571	17.76318
24			880.07334	62.3557

In accordance with the charge to mass ratio $[(q_{B'} / m_{B'}) / (q_{B''} / m_{B''})]^{1/2}$ [32], where q and m denotes the charge and mass of the ion, respectively, the Raman modes arising due to the exchange of Wyckoff sites can be determined. For Co ions occupying the *2d* site The

Raman modes would appear at frequency which is 0.793 times of the mode associated with the Nb ions. The peaks 11 and 14 (0.713) as well as peak 12 and 15 (0.759) satisfies this ratio. The degree of ordering of BCN can be estimated by the relation $O_{Co,Nb} = [I_{12,15} /(I_{12} +I_{15})]$ where I_{12} and I_{15} are the intensities of peak 12 and 15 respectively [35]. For ordered structure Co ions in *2d* site would be absent resulting in no extra peaks ($I_{15} = 0$) and therefore for ordered structure $O_{Co} = 0$ and $O_{Nb} = 1$. But for the partially ordered BCN sample the presence of Co ions in the Nb (*2d*) site, the degree of ordering is found to be $O_{Co} = 0.67$ and $O_{Nb} = 0.32$.

Table 5. Distribution of modes for the partially ordered BCN sample belonging to the trigonal space group *P-3m1*.

Atom	Site	Symmetry	Distribution of modes
Ba1	1a	-3m	$A_{2u} + E_u$
Ba2	2d	3m	$A_{1g} + A_{2u} + E_u + E_g$
Co1	1b	-3m	$A_{2u} + E_u$
Nb1	2d	3m	$A_{1g} + A_{2u} + E_u + E_g$
O1	3e	2/m	$A_{1u} + A_{2u} + E_u$
O2	6i	M	$2A_{1g} + A_{1u} + A_{2g} + 2A_{2u} + 3\ E_u + 3\ E_g$
Modes for the atoms in their own Wykoff site:		Γ_{TOTAL}	$7\ A_{2u} + 8\ E_u + 4\ A_{1g} + 5\ E_g + 2\ A_{1u} + A_{2g}$
		$\Gamma_{ACOUSTIC}$	$A_{2u} + E_u$
		Γ_{RAMAN}	$4\ A_{1g} + 5\ E_g$
		Γ_{IR}	$6A_{2u} + 7\ E_u$
Extra modes for B'-B" cation disorder:			$\Gamma_{Raman,\ B'} = A_{1g} + E_g$, $\Gamma_{IR,\ B'} = A_{2u} + E_u$ $\Gamma_{IR,\ B''} = A_{2u} + E_u$

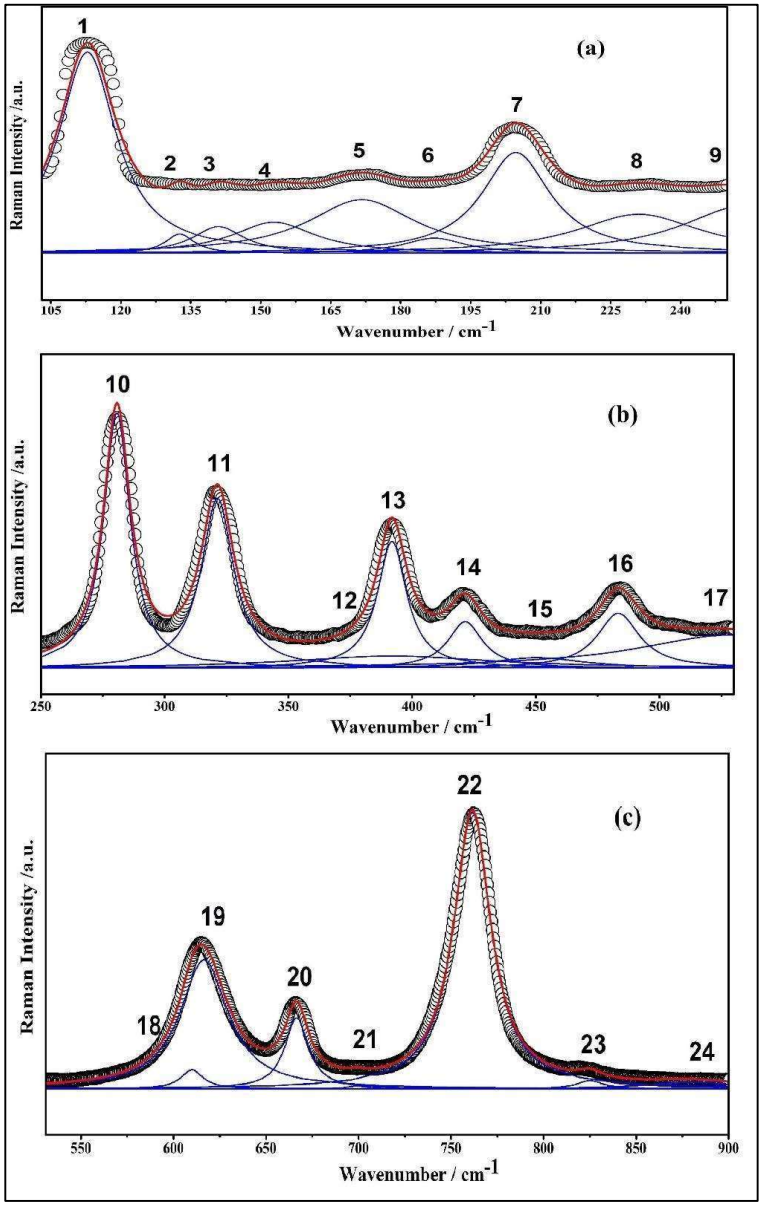

Fig. 8: *The Lorentzian peak fitting of the Raman spectra of BCS where red line represents the fitted curve and the symbols represent the experimental data.*

The expected phonon modes for BCN are listed in Table 6. Nineteen Raman-active modes (Γ_{Raman} = 5 A_{1g} + 8 E_{2g} + 6 E_{1g}) are expected in the ordered sample with *P 6₃/mmc* space group but the increased number of the optical active modes (listed in Table 6) in BCS arises due to the occupational disorder for the exchange of Wyckoff sites between B'-B'' ions. The existence of B' ions in *4f* Wyckoff site would give rise to three additional Raman and two additional IR bands each ($\Gamma_{Raman,B'}$= A_{1g} + E_{2g} + E_{1g}, $\Gamma_{IR,B'}$= A_{2u} + E_{1u}) and the presence of B'' ions in *2a* Wyckoff site would give rise to two additional IR bands ($\Gamma_{IR,\ B''/B'''}$ = A_{2u} + E_{1u}). From the Lorentzian fitting of BCS 24 bands are observed where three extra Raman bands occur due to the presence of Ni ions in the *4f* site and two additional Raman band may be attributed to the defect activated modes [34]. The observed Raman modes match well with those reported by Daniel et. al. along with few additional peaks for the doping of the B-site cation [38].

The Raman spectra of Barium based hexagonal perovskites is divided into four frequency ranges (below 200 cm^{-1}, 200-400 cm^{-1}, 500-650 cm^{-1} and above 650 cm^{-1}) [39]. The peaks below 200 cm^{-1} (1-6) are associated with the vibration of Ba ions. The peaks for the rotational and vibrational modes of Ni-O, Ta-O and Sb-O bonds arises in the rage of 200-400 cm^{-1}. The peaks lying within 500-650 cm^{-1} are associated with the bending vibration of NiO_6, TaO_6 and SbO_6 octahedra. The asymmetric stretching vibration of NiO_6, TaO_6 and SbO_6 octahedra gives rise to the peaks above 650 cm^{-1}. As per the charge to mass ratio the peak 24 is for Co ions and peak 23 is for Sb ions [34]. The Raman modes for Co ions occupying the Sb (*4f*) site would appear at frequency which is 0.92 times of the mode associated with the Sb ions which is satisfied by peaks 23 and 24 (0.93). The degree of ordering of BCS can be estimated by the relation: $O_{Co,Sb}$ = [$I_{23,24}$ /(I_{23} +I_{24})] where I_{23} and I_{24} are the intensities of peak 23 and 24 respectively. For ordered structure Co ions in *4f* site

would be absent resulting in no extra peaks ($I_{24} = 0$) and therefore for ordered structure $O_{Ni} = 0$ and $O_{Sb} = 1$. But for the partially ordered BCS sample the presence of Co ions in the Sb (*4f*) site, the degree of ordering is found to be $O_{Co} = 0.43$ and $Os_b = 0.56$.

Table 6. Distribution of modes for the partially ordered BCS sample belonging to the hexagonal space group *P 6₃/mmc*.

Atom	Site	Symmetry	Distribution of modes
Ba1	2b	6m2	$A_{2u} + B_{1g} + E_{2g} + E_{1u}$
Ba2	4f	3m	$A_{1g} + A_{2u} + B_{1g} + B_{2u} + E_{2u} + E_{2g} + E_{1u} + E_{1g}$
Co1	2a	3m	$A_{2u} + B_{2u} + E_{2u} + E_{1u}$
Sb1	4f	3m	$A_{1g} + A_{2u} + B_{1g} + B_{2u} + E_{2u} + E_{2g} + E_{1u} + E_{1g}$
O1	6h	mm2	$A_{1g} + A_{2g} + A_{2u} + B_{1g} + B_{1u} + B_{2u} + E_{2u} + 2\,E_{2g} + 2\,E_{1u} + E_{1g}$
O2	12k	M	$2\,A_{1g} + A_{1u} + A_{2g} + 2\,A_{2u} + 2\,B_{1g} + B_{1u} + B_{2g} + 2\,B_{2u} + 3\,E_{2u} + 3\,E_{2g} + 3\,E_{1u} + 3\,E_{1g}$
Modes for the atoms in their own Wykoff site:		Γ_{TOTAL}	$5\,A_{1g} + A_{1u} + 2\,A_{2g} + 7\,A_{2u} + 6\,B_{1g} + 2\,B_{1u} + B_{2g} + 6\,B_{2u} + 5\,E_{2u} + 8\,E_{2g} + 9\,E_{1u} + 6\,E_{1g}$
		$\Gamma_{ACOUSTIC}$	$A_{2u} + E_u$
		Γ_{RAMAN}	$5\,A_{1g} + 8\,E_{2g} + 6\,E_{1g}$
		Γ_{IR}	$6\,A_{2u} + 8\,E_{1u}$
Extra modes for B'-B" cation disorder:			$\Gamma_{Raman,\,B'} = A_{1g} + E_{2g} + E_{1g}$, $\Gamma_{IR,\,B'} = A_{2u} + E_{1u}$ $\Gamma_{IR,\,B''} = A_{2u} + E_{1u}$

7.3.4. Dielectric analysis:

The angular frequency (log ω) variation of dielectric permittivity (ε′) and the loss tangent (tan δ) of BCN and BCS is presented in Fig.9 and 10, respectively. When the frequency is very low the dipoles start lagging behind the field leading to a slow decrease in

ε′. As the frequency reaches characteristic frequency the ε′ drops off suddenly pointing towards a relaxation phenomenon. At higher frequencies the dipoles are unable to follow the field resulting in a constant ε′ value. This nature of ε′ can explained by the Debye theory [40]. The relaxation peak in the tan δ curve shifts to higher frequency side on increasing the temperature as more polarization occurs at high temperatures. The broad nature of the tan δ peaks (Fig. 9 and 10) point to the polydispersive nature of relaxation times which can be analysed by the Cole-Cole model [41, 42]

$$\varepsilon * = \varepsilon' - i\varepsilon'' = \varepsilon_\infty + \frac{\varepsilon_s - \varepsilon_\infty}{1+(i\omega\tau)^{1-\alpha}} \quad (1)$$

where ε_s and ε_∞ are low and high frequency values of ε′, τ denotes the mean relaxation time and α represents the dispersal of the relaxation time. The value of α = 0 for monodispersive relaxation process and for polydispersive relaxation process α > 0.

In the lower frequency side, tan δ for both the samples increases with the decrease in frequency due to the effect of dc conductivity. So, a term for the dc electrical conduction is added to equation (1) [43, 44]:

$$\varepsilon * = \varepsilon_\infty + \frac{\varepsilon_s - \varepsilon_\infty}{1+(i\omega\tau)^{1-\alpha}} - i\frac{\sigma*}{\varepsilon_0\omega^n} \quad (2)$$

where the complex conductivity $\sigma^* = (\sigma_1 + i\,\sigma_2)$ with dc conductivity being denoted by σ_1 and conductivity due to localized charges being denoted by σ_2. In the above equation (2) n is a dimensionless frequency exponent which lies between 0 to 1. Equation (2) can be written as,

$$\varepsilon' = \varepsilon_\infty + \frac{(\varepsilon_s - \varepsilon_\infty)\left[1+(\omega\tau)^{1-\alpha}\sin\frac{1}{2}\alpha\pi\right]}{1+2(\omega\tau)^{1-\alpha}\sin\frac{1}{2}\alpha\pi+(\omega\tau)^{2(1-\alpha)}} - \frac{\sigma_2}{\varepsilon_0\omega^n} \quad (3)$$

$$\varepsilon'' = \frac{(\varepsilon_s - \varepsilon_\infty)(\omega\tau)^{1-\alpha}\cos\frac{1}{2}\alpha\pi}{1+2(\omega\tau)^{1-\alpha}\sin\frac{1}{2}\alpha\pi\ \ (\omega\tau)^{2(1-\alpha)}} + \frac{\sigma_1}{\varepsilon_0\omega^n} \quad (4)$$

and, the dielectric loss can be calculated by

$$\tan\delta = \varepsilon''/\varepsilon' \quad (5)$$

The fitting of the experimental data has been performed using equations (3), (4) and (5) and the fitting parameters are given Table 7.

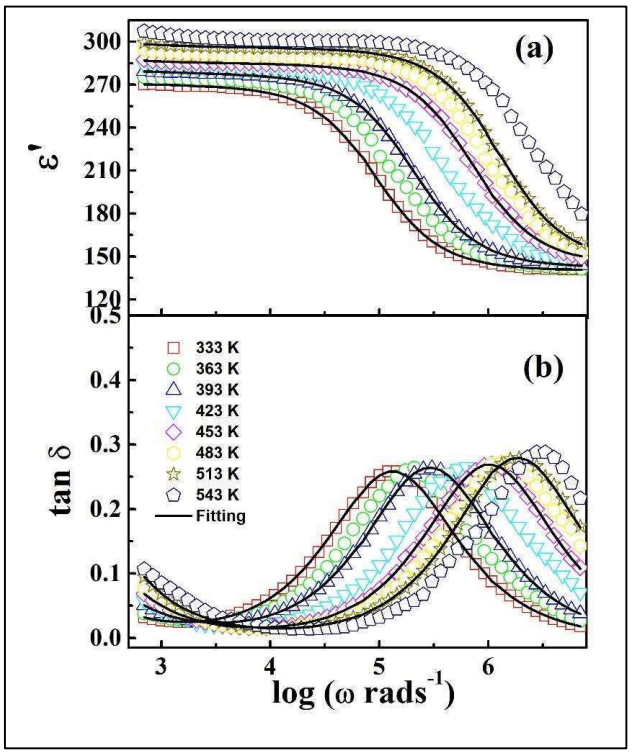

Fig. 9: *The angular frequency (log ω) variation of dielectric permittivity (ε') and the loss tangent (tan δ) of BCN.*

The main factors driving the dielectric relaxation are the dipole relaxation and the conduction relaxation of the free charge carriers [45]. For both BCN and BCS, α which is associated with the dipole relaxation decreases with increase in temperature signifying that the dispersal of relaxation time decreases. The relaxation behaviour in both the samples tends towards monodispersive nature with increase in temperature. The value of ω_m increases with increase in temperature indicating that the rate of polarization and the dipole density increases with temperature. The value of n increases with temperature for both BCN and BCS

indicating that at higher temperature the carrier polarization mechanism is less dispersive owing to some barrier height extracted [45,46]. The mobile charge carriers when obstructed by the grain boundaries hampers their charge migration and they accumulate at the barrier which causes a localized polarization inside the grains [47]. As the temperature increases the density of charges causing the space charge polarization increases and the relaxation processes becomes more localized making the relaxation process more Debye type. In BCN and BCS the existence dc conductivity is evident in the low frequency region indicating that the samples possess some amount of electrical semi conductivity [47].

Table 8. The values of different parameters obtained by fitting the dielectric spectra of BCN and BCS by modified Cole-Cole equations.

Temperature (K)	ε_s	ε_∞	ω_m (Hz)	α	n	σ_1 (Sm^{-1})	σ_2 (Sm^{-1})
BCN							
333	270	140	92222	0.1	0.88	0.2×10^{-7}	0.2×10^{-8}
393	278	142	201111	0.1	0.89	0.4×10^{-7}	0.5×10^{-8}
453	285	144	700000	0.099	0.895	0.6×10^{-7}	0.6×10^{-8}
513	296	146	1255555	0.098	0.9	0.9×10^{-7}	0.8×10^{-8}
BCS							
333	190	95	73333	0.3	0.8	0.05×10^{-7}	0.1×10^{-8}
393	198	98	205555	0.28	0.8	0.1×10^{-7}	0.2×10^{-8}
453	214	102	353235	0.26	0.81	0.2×10^{-7}	0.2×10^{-8}
513	226	107	725114	0.24	0.82	0.3×10^{-7}	0.4×10^{-8}

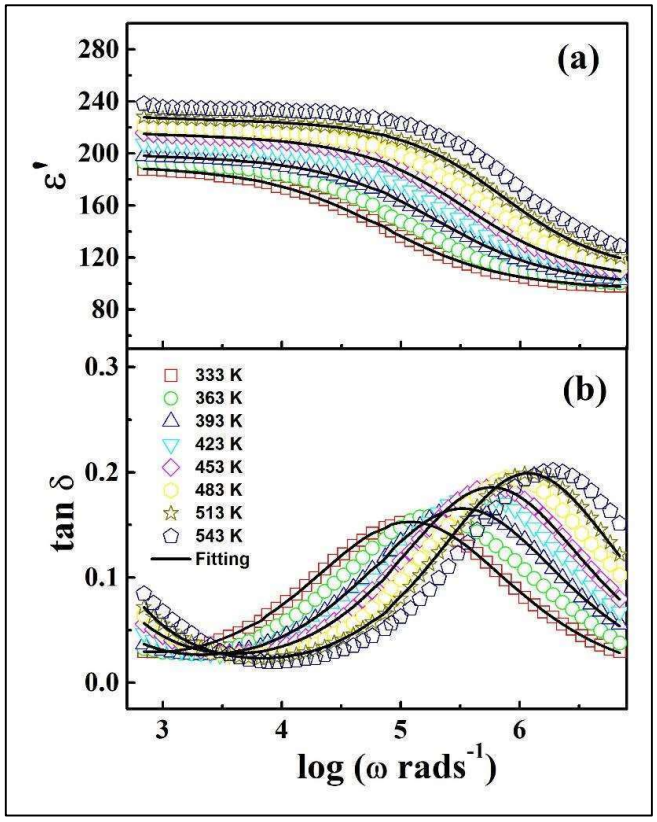

Fig. 10: *The angular frequency (log ω) variation of dielectric permittivity (ε') and the loss tangent (tan δ) of BCS.*

7.3.5. Complex impedance analysis:

The complex impedance plots of BCN and BCS at temperatures 363 K and 423 K are illustrated in Fig. 11 and 12, respectively. The influence of grain and grain boundary to the overall impedance is determined by the presence of two deformed circular arcs which has been observed in case of both the samples [48].

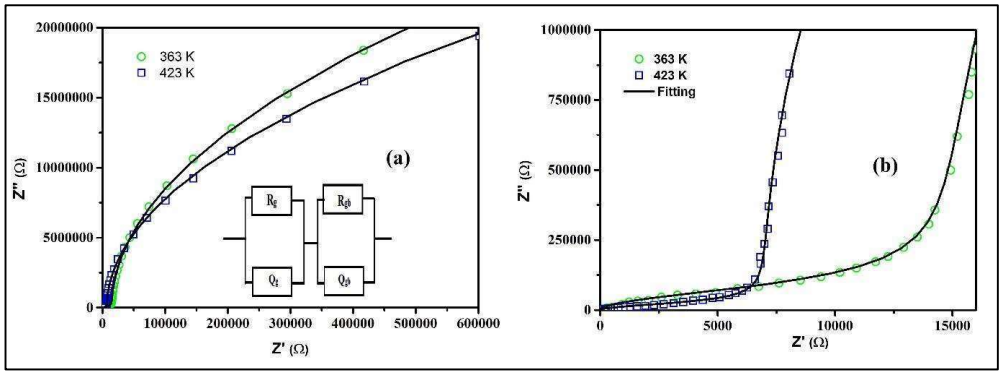

Fig. 11: *The complex impedance plots of BCN.*

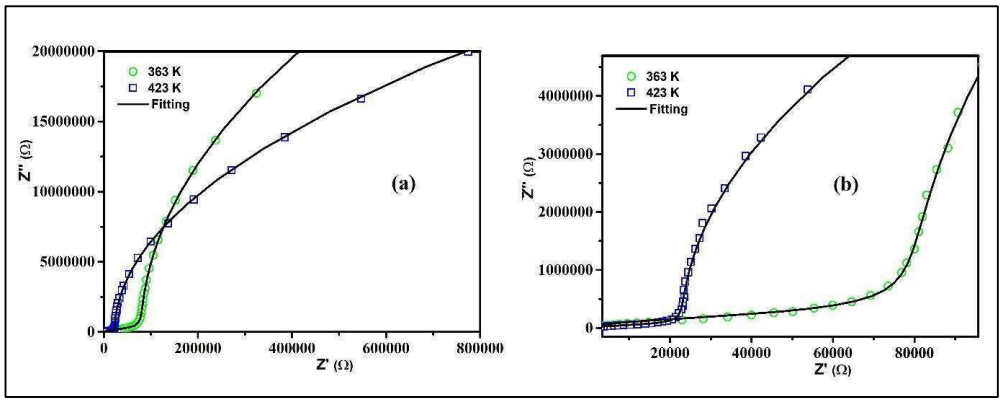

Fig. 12: *The complex impedance plots of BCS.*

The centre of the semi-circular arc lying below the Z′ axis confirms the relaxation mechanism of the samples being polydispersive nature [48-53]. The arcs become smaller with increasing temperature due to the thermally activated conduction mechanism of the samples. The impedance spectra have been fitted using an equivalent circuit model comprising of two parallel combinations of resistance and capacitance joined together in series (Fig. 11). The capacitance term here is replaced by a constant phase element (Q) due to

the non-ideal behaviour of the capacitance as a result of more than one relaxation process for a given relaxation time. The capacitance for the constant phase element is given by $C_p = Q^{1/c} R^{(1-c)/c}$ where c signifies the deviation from ideal Debye nature. For fitting the real and the imaginary part of the impedance the equations used are:

$$Z' = \frac{R_g}{1+\left[\omega(R_g Q_g)^{\frac{1}{c_g}}\right]^2} + \frac{R_{gb}}{1+\left[\omega \quad _{gb} Q_{gb})^{\frac{1}{c_{gb}}}\right]^2} \tag{6}$$

$$\text{and} \quad Z'' = R_g\left[\frac{\omega(R_g Q_g)^{\frac{1}{c_g}}}{1+\left[\omega(R_g Q_g)^{\frac{1}{c_g}}\right]^2}\right] + R_{gb}\left[\frac{\omega(R_{gb} Q_{gb})^{\frac{1}{c_{gb}}}}{1+\left[\omega(R_{gb} Q_{gb})^{\frac{1}{c_{gb}}}\right]^2}\right] \tag{7}$$

where R_g and R_{gb} denotes the resistance and Q_g and Q_{gb} denotes the constant phase element for the grain and grain boundary respectively. The parameters from fitting are given in Table 9 where the high values of R_{gb} indicates that the grain boundaries are more insulating than the grains.

Table 9. The fitted parameters of the impedance circuit for BNTN and BNTS.

	Temp. (K)	R_g (Ω)	Q_g (10^{-8} F/Ω)	c_g	R_{gb} (10^7 Ω)	Q_{gb} (10^{-9} F/Ω)	c_{gb}
BCN	363	15000	0.35	0.82	85	0.1	0.86
	423	7000	0.09	0.89	65	0.09	0.86
BCS	363	80000	0.095	0.85	120	0.098	0.86
	423	23000	0.087	0.84	54	0.08	0.85

7.3.6. Conductivity Analysis:

The frequency (log ω) variation ac conductivity with frequency for BCN and BCS at various temperatures is portrayed in Fig. 13 and 14, respectively where two discrete plateaus can be observed. The plateau at the low frequency is associated with total conductivity whereas the plateau at the higher frequency is associated with grain's contribution to the total conductivity [54]. Hence, two processes dictate the bulk conduction mechanism of the samples. The total conductivity as stated by the power law is:

$$\sigma(\omega) = \sigma_{dc} + K\,\omega^{n} \quad (8)$$

here σ_{dc} is the dc conductivity and K is a constant dependent on frequency and temperature. The conductivity spectra have been fitted using equation 8 with n values between 1.55-1.61 [55] at lower frequency and 0.4-0.45 at higher frequency [56] and the parameters used for fitting are represented in Table 10.

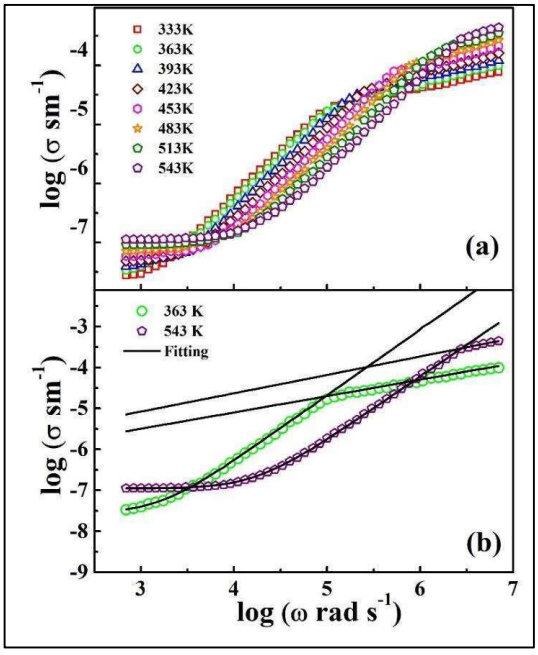

Fig. 13: *The frequency dependent ac conductivity plots for BCN.*

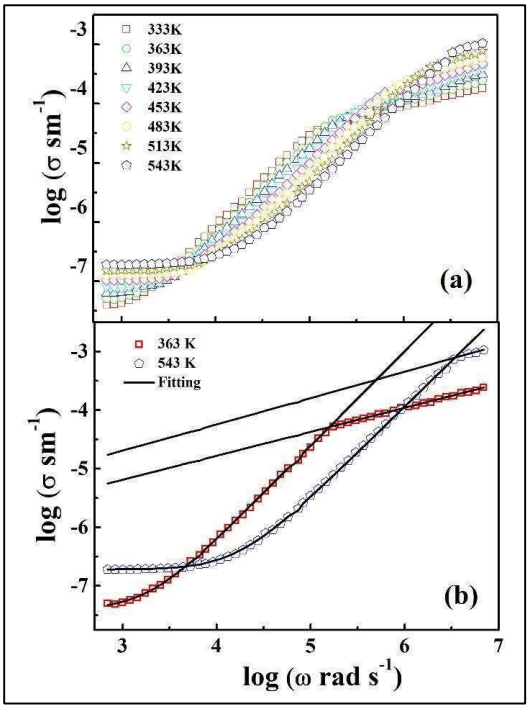

Fig. 14: *The frequency dependent ac conductivity plots for BCS.*

Table 10: Various fitted parameters of the conductivity spectra for BCN and BCS.

Sample	Temperature(K)	σ_{dc} (Sm^{-1})	A	n
BCN	363 (at low frequency)	2.7×10^{-8}	2.1×10^{-13}	1.6
	363 (at high frequency)	2.7×10^{-8}	2×10^{-7}	0.4
	543 (at low frequency)	11×10^{-8}	0.3×10^{-13}	1.55
	543 (at high frequency)	11×10^{-8}	3.7×10^{-7}	0.45
BCS	363 (at low frequency)	3.9×10^{-8}	2.2×10^{-13}	1.61
	363 (at high frequency)	3.9×10^{-8}	3.8×10^{-7}	0.41
	543 (at low frequency)	19×10^{-8}	0.5×10^{-13}	1.56
	543 (at high frequency)	19×10^{-8}	9×10^{-7}	0.45

For both BCN and BCS the variation of the dc conductivity (σ_{dc}) with the inverse of temperature (Fig. 15) is found to follow the Arrhenius Law: $\sigma_{dc} = \sigma_0 \exp\left[-\frac{E_\sigma}{K_B T}\right]$, where E_σ is the activation energy. As temperature increases the dc conductivity value increases. The value of E_σ as deduced from the Arrhenius plot is 0.23 eV and 0.27 eV for BCN and BCS, respectively which suggests that for both the samples the conduction mechanism is governed by p-type polaron hopping [57,58]. The conductivity spectra have step like nature due to the presence of different potentials offered by the grain and grain boundaries and the hopping of charge carriers through these potential barriers [59].

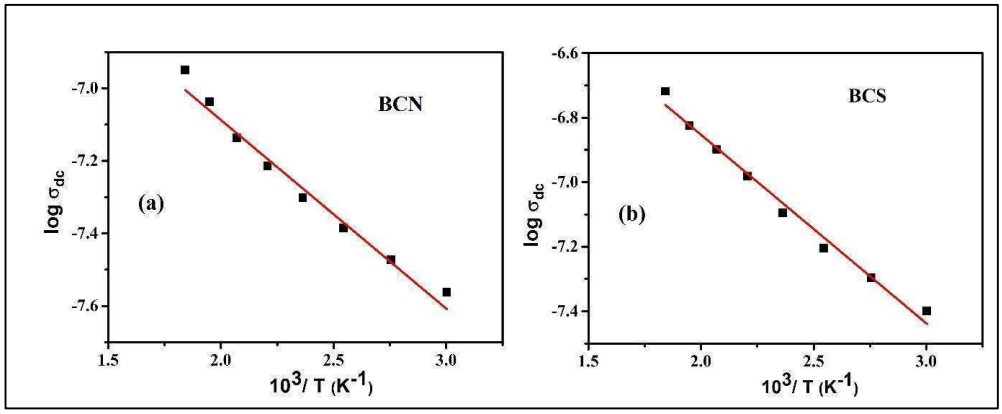

Fig. 15: *The Arrhenius plots for BCN and BCS.*

7.4. Discussion:

It can be observed from Fig 9 and 10 that the room temperature permittivity values of BCN and BCS are 266 and 178, respectively at 1 KHz. Their loss tangent values at 1 KHz are 0.04 for BCN and 0.05 for BCS. The reported permittivity values of analogous 1:2 ordered perovskites are; ε' = 31 for $Ba_3MgNb_2O_9$, ε' = 41 for $Ba_3ZnNb_2O_9$ and ε' = 43 for $Ba_3CaNb_2O_9$ in GHz range [60–62]. Taking into account our previous work on 1:2 ordered

perovskites $Ca_3(MgTa_2)O_9$ (CMT) and $Ca_3(ZnTa_2)O_9$ (CZT), where permittivity values for CMT is ε' ~180 and for CZT ε' ~ 298 at 1 KHz [53]. The tan δ values for CMT and CZT are 0.05 and 0.06, respectively at 1KHz. The permittivity value of BCN is greater than that of CMT and CZT as samples containing Nb^{5+} exhibit larger ionic polarization as compared to Ta^{5+} based perovskites [22]. The permittivity value of BCS is comparable to CMT. The loss tangent value of BCN is lower than that of CMT and CZT.

The hybridization between the vacant d orbitals of B-site cations and the p orbitals of oxygen anion of perovskites effects their transport properties [63,64]. The electronegativity of Sb^{5+} > Nb^{5+} and results in less ionic or more covalent Sb-O bond which decreases its macroscopic polarizability [63, 59]. In BCN the 4d orbital of Nb are vacant whereas in BCS the 4d orbitals of Sb are completely filled. The presence of vacant d orbitals in Nb favours higher hybridization with p orbitals of oxygen leading to larger polar instabilities and higher permittivity values for BCN [65]. Thus, constituent B-site cations in perovskites plays a crucial role in determining their polarizability and hence their dielectric properties.

7.5. Conclusion:

The double perovskites $BaCo_{1/3}Nb_{2/3}O_3$ (BCN) and $BaCo_{1/3}Sb_{2/3}O_3$ (BCS) have been prepared by the ceramic method. The BCN sample crystallizes in trigonal symmetry with *P-3m1* space group and the BCS sample crystallizes in hexagonal symmetry with *P 6₃/mmc* space group and both the samples are possess cationic disorder due to the site exchange of cations occupying the B' and B'' sites. The dielectric loss for both the samples is similar in nature with a broad peak indicating the polydispersive nature of the relaxation phenomena. For both the samples two semi-circular arcs are obtained which indicates that the total impedance is due to the contribution of both grain and grain boundaries. The activation

energy as deduced from the Arrhenius plot is 0.23 eV and 0.27 eV for BCN and BCS respectively, indicating the conduction phenomena is because of the hopping of the polaron of p-type. The dielectric permittivity of BCN is greater than BCS and the dielectric loss for BCN is lower than BCS so BCN will be better option for application in circuit miniaturization

References

[1] P. K. Davies, H. Wu, A. Y. Borisevich, I. E. Molodetsky, L. Farber, Annu. Rev. Mater. Res. 38 (2008) 369–401.

[2] O. V. Ramírez, F. G. García, M. A. C. Lopez, E. R. Trejo, J. Electroceram. 28 (2012) 226–232.

[3] W. Wei, M. Li, Y. H. Hu, Ind. Eng. Chem. Res. 58(20) (2019) 8743.

[4] K. Ke, K. K. Kondamareddy, F. Gao, X. Zhang, X. Yuan, Energy Technol. 7 (2019) 10.

[5] A. Schneider, S. Alon, L. Etgar, Energy Technol. 7 (2019) 7.

[6] A. M. Oo, P. Fan, X. Zhang, J. Yu, Energy Technol. 8 (2020) 3.

[7] S. He, L. Qiu, L. K. Ono, Y. Qi, Mater. Sci. Eng. R Rep. 140 (2020) 100545.

[8] E. V. Péan, C. S. De Castro, S. Dimitrov, Adv. Funct. Mater. 30 (2020) 12.

[9] I. M. Reaney, D. Iddles, J. Am. Ceram. Soc. 89 (2006) 2063.

[10] E. Fabbri, D. Pergolesi, E. Traversa, Chem. Soc. Rev. 39 (2010) 4355–4369.

[11] W. T. Fu, D. J. W. Ijdo, J. Solid State Chem. 178 (2005) 2363.

[12] W. Kockelmann, D. T. Adroja, A. D. Hillier, M. Wakeshima, Y. Izumiyama, Y. Hinatsu, K. S. Knight, D. Visser, B. D. Rainford, Phys. B 378 (2006) 543.

[13] H. Karunadasa, Q. Huang, B. G. Ueland, P. Schiffer, R. J. Cava, Appl. Phys. Sci. 100 (2003) 8097.

[14] S. K. Korchagina, Y. A. Shevchuk, Inorg. Mater. 42 (2006) 64.

[15] K. Henmi, Y. Hinatsu, J. Solid State Chem. 148 (1999) 353.

[16] R. Mani, N. S. P. Bhuvanesh, K. V. Ramanujachary, W. Green, S. E. Lofland, J. Gopalakrishnan, J. Mater. Chem. 17 (2007) 1589.

[17] C. Darie, P. Bordet, M. Viaud, C. Guillot-Deudon, P. Deniard, E. Gautron, C. Colin, F. Porcher, G. Berlanda, F. Bert, P. Mendels, C. Payen, J. Solid State Chem. 317 (2023) 12370.

[18] F. Azough, C. Leach, R. Freer, J. Eur. Ceram. Soc. 26 (2006) 2877–2884.

[19] S. Berri, N. Bouarissa, Potential Energy Solutions (IEEES-12) 46 (2022) 9968–9984.

[20] S. Ya. Istomina, V. A. Koutcenkoa, E.V. Antipova, F. Lindbergb, G. Svensson, Mater. Res. Bull. 39 (2004) 1013–1022.

[21] A. C. Larson, R. B. Von Dreele, General structure analysis system (GSAS). Los Alamos National Laboratory, Report LAUR (2000) 86–784.

[22] M. W. Lufaso, Chem. Mater. 16 (2004) 2148–2156.

[23] M. W. Lufaso, E. Hopkins, S. M. Bell, A. Llobet, Chem. Mater. 17 (2005) 4250.

[24] J. E. Joy, E. Atamanik, R. Mani, A. Nag, R.M. Tiwari, V. Thangadurai, J. Gopalakrishnan, Solid State Sci. 12 (2010) 1970–1976.

[25] G. Blasse, J. Inorg. Nucl. Chem. 27 (1965) 993.

[26] J. B. Goodenough, J. A. Kafalas, J. Solid State Chem. 6 (1973) 493.

[27] H. Mizoguchi, P. M. Woodward, S. H. Byeon, J. B. Parise, J. Am. Chem. Soc. 126 (2004) 3175.

[28] J. E. F. S. Rodrigues, E. Moreira, D. M. Bezerra, A. P. Maciel, C. W. A. Paschoal, Mater. Res. Bull. 48 (2013) 3298–3303.

[29] B. H. Toby, Appl. Cryst. 34 (2001) 210.

[30] R. Gerhardt, J. Phys. Chem. Solids 55 (1994) 1491.

[31] A. Barua, S. K. Dey, S. K. Sabyasachi, S. Kumar, J. Alloys Compd. 854 (2021) 157217.

[32] D. L. Rousseau, R. P. Bauman, S. P. S. Porto, J. Raman Spectrosc. 10 (1981) 253.

[33] A. Dias, V. Ciminelli, F. M. Matinaga, R. Moreira, J. Eur. Ceram. Soc. 21 (2001) 2739–2744.

[34] R. L. Moreira, F. M. Matinaga, A. Dias, Appl. Phys. Lett. 78 (2001) 428.

[35] J. E. F. S. Rodrigues, D. M. Bezerra, A. P. Maciel, C. W. A. Paschoal, Ceram. Int. 40 (2014) 5921–5930.

[36] S. A. Prosandeev, U. Waghmare, I. Levin, J. Maslar, Phys. Rev. B 71 (2005) 214307.

[37] V. L. Ginzburg, A. P. Levanyuk, A. A. Sobyanin, Phys. Rep.3 (1980) 151–240.

[38] Ph. Daniel, J. Toulouse, J. Y. Gesland, M. Rousseau, Phys. Rev. B 52 (1995)13.

[39] J. Chen, Y. Tang, J. Li, H. Xiang, C. Li, X. Xing, L. Fang, J. Alloys Compd. 820 (2020) 153159.

[40] P. Debye, Polar Molecules, Chemical Catalogue Company, New York, 1929.

[41] K. S. Cole, R. H. Cole, J. Chem. Phys. 9 (1941) 341–351.

[42] K. S. Cole, R. H. Cole, J. Chem. Phys. 10 (1942) 98–105.

[43] R. Coelho, Physics of Dielectrics (New York: Elsevier) 1978.

[44] S. K. Maity, A. Dutta, S. Kumar, T. P. Sinha, Phys. Scr. 88 (2013) 065702.

[45] P. Thongbai, S. Tangwancharoen, T. Yamwong, S. Maensiri, J. Phys. Condens. Matter 20 (2008) 395227.

[46] S. Halder, A. Dutta, T.P. Sinha, J. Phys. Chem. Solids 102 (2017) 79–89.

[47] R. Mukherjee, S. Saha, A. Dutta, T. P. Sinha, J. Alloys Compd. 651 (2015) 222–229.

[48] A. Barua, S. Maity, S. Kumar, A. Dutta, T.P. Sinha, Physica B 583 (2020) 412057.

[49] L. Liu, H. Fan, P. Fang, L. Jin, Solid State Commun. 142 (2007) 573–576.

[50] L. Liu, H. Fan, P. Fang, X. Chen, Mater. Res. Bull. 43 (2008) 1800–1807.

[51] R. Gerhardt, J. Phys. Chem. Solids. 55 (1994)1491–1506.

[52] M. C. H. Mckubre, J. R. Macdonald, Impedance Spectroscopy Emphasizing Solid Materials and Systems, ed. J. R. Macdonald, Wiley, New York, (1987)191.

[53] M. M. Hoque, A. Barua, A. Dutta, S. K. Dey, T. P. Sinha, S. Kumar, Ionics 23 (2017) 471–483.

[54] A. Dutta, C. Bharti, T. P. Sinha, Mater. Res. Bull. 43 (2008) 1246–1254.

[55] S. Nomura, K. Toyama, K. Kaneta, Jpn. J. Appl. Phys. 21 (1982) 624–626.

[56] C. Bharti, T.P. Sinha, Solid State Sci. 12 (2010) 498–502

[57] M. Idrees, M. Nadeem, M. M. Hassan, J. Phys. D Appl. Phys. 43 (2010) 155401.

[58] W. H. Jung, J. Appl. Phys. 90 (2001) 2455.

[59] Y. Tsuji, A. Kan, H Ogawa, S. Ishihara, J. Eur. Ceram. Soc. 25 (2005) 2883–2887.

[60] Y. W. Kim, J. H. Park, J. G. Park, J. Eur. Ceram. Soc. 24 (2004) 1775–1779.

[61] S. Nomura, Ferroelectrics. 49 (1983) 61–70.

[62] J. E. F. S. Rodrigues, P. J. Castro, P. S. Pizani, W. R. Correr, A. C. Hernandes, Ceram. Int. 42 (2016) 18087–18093.

[63] A. Dutta, T. P. Sinha, D. Das, J. Magn. Magn. Mater. 360 (2014) 211–21.

[64] A. Dutta, T.P. Sinha, Mater. Res. Bull. 46 (2011) 518–524.

[65] W.Wersing, Curr. Opin. Solid State Mater. Sci. 1 (1996) 715–731.

Chapter – 8

Conclusion and future scope of the work

8.1. Conclusions:

The main objective of this thesis is to develop lead free perovskite oxides having high dielectric constant and low dielectric loss and to study the correlation between their structural and dielectric properties. In this context we have investigated the structural, microstructural, optical and dielectric properties of double (Ba_2YbTaO_6, Ba_2YbSbO_6, Sr_2YbNbO_6 and Sr_2YbSbO_6), and triple ($Ba_3NiTaNbO_9$, $Ba_3NiTaSbO_9$, $BaCo_{1/3}Nb_{2/3}O_3$ and $BaCo_{1/3}Sb_{2/3}O_3$) perovskite oxides; and also a nanocomposite (Ba_2YbSbO_6-CO_3) of perovskite oxides and examined the different types of physical properties exhibited by them. All the samples have been synthesized by solid state ceramic method and the samples obtained are polycrystalline in nature. The crystal structure of the samples has been analyzed using Rietveld analysis. EDS spectroscopy has been used to confirm the sample purity. The optical characteristics of the samples have been investigated using Raman and FTIR spectroscopy. The experimental band gap of the samples has been investigated using UV visible spectroscopy. The dielectric properties of the samples have been investigated at different temperatures to understand their temperature dependent dielectric response. The conclusions of the present work are as follows:

1. The first work (Chapter 3) comprises of the synthesis of a double perovskite Ba_2YbTaO_6 by solid state ceramic method. The Rietveld refinement of the XRD patterns reveals the cubic phase of the sample having $Fm\bar{3}m$ space group with cell parameters: a = b = c = 8.385 Å. The average grain size of the sample is 7.78 μm. The presence of negligible amount of porosity in the sample is confirmed from its density ~ 8.092 g cc^{-1}. The experimental band gap of the sample is 3.95 eV as obtained from the UV-visible Spectroscopy. The cubic phase

of the sample is further confirmed by the three bands (577 cm^{-1}, 1440 cm^{-1} and 1642 cm^{-1}) obtained in the FTIR spectra which is associated with the $Fm\bar{3}m$ space group. In the impedance spectra two deformed semi-circular arcs are obtained confirming the role of both grain boundary and grain in determining the total impedance. The deformed semi-circular arc in the Nyquist plot confirms the non-Debye type relaxation present in the sample. In the region of dispersion for ε′ a relaxation peak is observed in the loss tangent curve and the shifting of its tan δ peak with temperature point towards a temperature dependency of the dielectric relaxation of the sample. The existence of dc conductivity (σ_{dc}) is indicated by the dramatic change in tan δ at low frequencies. The broad nature of its loss tangent peaks indicates the polydispersive behaviour of its dielectric relaxation process. The activation energy E_a = 0.51 eV as calculated from the Arrhenius plot, suggests that the hopping of p-type polaron is responsible for its conduction mechanism. The existence of two plateaus in the conductivity plot indicates that in the bulk conduction behaviour two processes are involved due to the contribution of grain and grain boundary. The dielectric permittivity value at 40 Hz and 363 K for Ba_2YbTaO_6 (ε′ ~ 390) is significantly large as compared to Ba_2YbNbO_6 (ε′ ~ 340) as the Ta-O bond length is weaker than Nb-O bond length and the polarization can be easily achieved. In this way the lattice vibrations associated with the crystal structure strongly affect its dielectric permittivity values.

2. In the second work (Chapter 4) we have scrutinized how the structural, microstructural and surface adsorbed CO_2 influences the dielectric and electrical transport properties of Ba_2YbSbO_6 (BYSB) and Ba_2YbSbO_6-$BaCO_3$ (BYSN). The BYSB sample having grain size ~ 1.92 μm has been prepared by solid state ceramic method. BYSN having particle size ~ 50 nm has been synthesized by high energy ball milling of BYSB. The mechanically activated

nanosized double perovskite Ba_2YbSbO_6 adsorbs atmospheric CO_2 and is converted into a nanocomposite of Ba_2YbSbO_6 and $BaCO_3$ as revealed from the Rietveld refinement of the XRD pattern of BYSN along with spectroscopic evidences. BYSB is a single-phase cubic perovskite oxide with $Fm\bar{3}m$ space group whereas BYSN is a nanocomposite composed of 86.4 % Ba_2YbSbO_6 and 13.6 % $BaCO_3$ phases with surface adsorbed CO_2. Due to the lattice deformation and surface disorder caused by high energy mechanical milling, the BYSN sample adsorbs atmospheric CO_2 and H_2O. The crystalline defects of BYSN acts as active sites prone to chemical reaction and a part of Ba present in BYSN reacts with surface adsorbed CO_2 to form $BaCO_3$. The permittivity value for BYSN at any given temperature is higher than that of BYSB. The loss tangent values of BYSN are comparatively lower than that of BYSB at high frequencies. For both the samples the relaxation mechanism governing the dielectric behaviour is polydispersive in nature and Cole-Cole type. The values of impedance at room temperature for BYSN is higher than that of BYSB. BYSN exhibits anomalous dielectric and electrical properties above 393 K as it releases the surface adsorbed CO_2 above this temperature. In both BYSB and BYSN p-type polaron hopping dictates their electrical transport properties. The formation of secondary $BaCO_3$ phase in case of BYSN sample upon CO_2 adsorption suggests that nanosized Ba_2YbSbO_6 can act as an efficient agent for removing harmful CO_2 from polluted air. The structural and microstructural properties along with surface adsorbed CO_2 plays a key role in determining the dielectric relaxation and electrical transport properties of BYSB and BYSN.

3. In the third work (Chapter 5) we have investigated the structural, microstructural and dielectric properties of double perovskite Sr_2YbNbO_6 (SYN) and Sr_2YbSbO_6 (SYS) synthesized by ceramic method. Both the samples possess monoclinic crystal structure with

$P2_1/n$ space group. The lattice parameters of SYN are: a = 5.79644 (Å), b = 5.76612 (Å), c = 8.15671 (Å), α = γ = 90º and β = 90.5109º. The lattice parameters of SYS are: a=5.79 Å, b=5.79 Å, c=8.19 Å and β = 90.136°. The average size of its polycrystalline grains is 2.38 μm for SYN and 1.45 μm for SYS. The dielectric relaxation of both the sample is polydispersive in nature and has been analysed using the Cole-Cole model. The ε' and ε'' values of SYN is found to be ~ 175 and 23 at 1 KHz. For SYS the values of dielectric permittivity and loss tangent at room temperature are 120 and 0.15, respectively at 1 KHz. The activation energy obtained from the Arrhenius plot is 0.52 eV for SYN and 0.21 eV for SYS. The conduction mechanism of SYN and SYS is mainly due to the hopping of p type polarons. The values of ε' at any constant temperature decreases with ionic size of the cations as smaller the electron orbital radius, lower is its electronic polarizability. The ionic polarization also tends to decrease with the decrease in the radius of the associated ions. The permittivity value of SYS is lower than SYN due to the smaller ionic size of Sb as compared to Nb. Thus, the dielectric properties of a sample are largely controlled by its crystal structure and the radii of its constituent ions.

4. In the fourth work (Chapter 6) we have successfully synthesized two triple perovskites, viz., $Ba_3NiTaNbO_9$ (BNTN) and $Ba_3NiTaSbO_9$ (BNTS) by solid state ceramic method. The crystal structure as obtained from the Rietveld refinement of the XRD patterns reveals that BNTN crystallizes in trigonal symmetry with *P-3m1* space group (a=5.755 Å, b=5.755 Å, c= 7.066 Å and α=β=90º, γ=120º) and BNTS crystallizes in hexagonal symmetry with $P\,6_3/mmc$ space group (a=5.835 Å, b=5.835 Å, c= 14.404 Å and α=β=90º, γ=120º). The experimental density of the pellets is 8.01 g/cc for BNTN and 7.29 g/cc for BNTS which indicates that the presence of porosity is negligible. The grain size of BNTN ranges from 0.52 μm to 1.83 μm

and for BNTS it ranges from 0.25 μm to 1.21 μm. Both BNTN and BNTS are partially disordered perovskite and in their Raman spectra more than expected number of modes than their ordered form has been obtained due to their B-site (B'-B"-B"') occupational disorder and localized crystalline defects. The dielectric loss for both the samples is similar in nature with a broad peak indicating the polydispersive nature of the relaxation phenomena. For both the samples two semi-circular arcs are obtained which indicates that the total impedance is due to the contribution of both grain and grain boundaries. The activation energy as deduced from the Arrhenius plot is 0.36 eV and 0.37 eV for BNTN and BNTS respectively, indicating the conduction is due to the hopping of the polaron of p-type. The room temperature dielectric constant and dielectric loss at 500 KHz are 324 and 0.05 for BNTN and 182 and 0.04 for BNTS, respectively. Both the sample possess cationic disorder due to the site exchange of cations occupying the B', B" and B"' sites. Thus the ordering of $A_3(B'B''B''')O_9$ type perovskites is greatly dependent on the site occupancy of B′, B″ and B‴ cations.

5. In the fifth work (Chapter 7) we have reported the structural properties of $BaCo_{1/3}Nb_{2/3}O_3$ and $BaCo_{1/3}Sb_{2/3}O_3$ synthesized by solid state ceramic method. BCN and BCS are partially ordered perovskite oxide having general formula $A_3(B'B''_2)O_9$. BCN stabilize in *P-3m1* space group (a = 5.75581(Å), b = 5.75581(Å), c = 7.06833 (Å), α = β = 90º and γ = 120 º) of trigonal symmetry and BCS possess *$P6_3/mmc$* space group (a = 5.83744 (Å), b = 5.83744 (Å), c = 14.4082 (Å), α = β = 90º and γ = 120 º) of hexagonal symmetry. Both the sample possess cationic disorder due to the site exchange of cations occupying the B' and B" sites. The Lorentzian fitting of the BCN sample indicates the presence of 15 bands. The Lorentzian fitting of the BCS sample indicates the presence of 24 bands. In BCN and BCS more than expected number of modes arises in the Raman spectra due to their B-site

(B'-B'') occupational disorder and crystalline defects. The loss peaks in BCN and BCS are broad in nature indicating polydispersive nature of the relaxation phenomena. Total impedance in both the samples has the contribution of both grain and grain boundaries. The activation energy as calculated from the Arrhenius plot are 0.23 eV and 0.27 eV for BCN and BCS respectively. The conduction in both the samples is due to the hopping of the polaron of p-type. In BCN the 4d orbital of Nb are vacant whereas in BCS the 4d orbitals of Sb are completely filled. The presence of vacant d orbitals in Nb favours higher hybridization with p orbitals of oxygen leading to larger polar instabilities and higher permittivity values for BCN. Thus, constituent B-site cations in perovskites plays a crucial role in determining their polarizability and hence their dielectric properties.

8.2. Future scope of the work:

1. There is further scope in the synthesis of perovskite oxides having nanometric size in order to show applications in sensing, solid oxide fuel cells and as catalysts. It can also be shown that synthesis procedure strongly effects the physical properties of nano sized perovskite oxides.

2. More nano composites of perovskite oxides can be developed having application in the absorption of toxic atmospheric gases.

3. A and B-sites of the perovskites can be doped with suitable cations in order to enhance their magnetic properties for applications in miniaturized magnetic sensor, magnetic refrigeration and bioprocessing.

4. Dielectric properties of perovskites having more than three B- site cations can be explored.

List of Publications

List of publications in standard refereed journals:

1. Influences of crystal structure, microstructure and adsorbed CO_2 on dielectric properties of Ba_2YbSbO_6-$BaCO_3$ formed by mechanical activation of Ba_2YbSbO_6, **A. Barua**, S.K. Dey, S. Dey, S. Kumar, Physica B 649 (2023) 414449.
2. Structural and dielectric characterization of triple perovskites $Ba_3NiTaNbO_9$ and $Ba_3NiTaSbO_9$, **A. Barua**, S. K. Dey, S. K. Sabyasachi, S. Kumar, Journal of Alloys and Compounds 854 (2021) 157217.
3. Structural, optical and electrical characterization of Ba_2YbTaO_6, **A. Barua**, S. Maity, S. Kumar, A. Dutta, T.P. Sinha, Physica B 583 (2020) 412057.
4. Impedance spectroscopy analysis of complex perovskite Sr_2YbSbO_6, **A. Barua**, S. Maity, R. Mondal, and S. Kumar, AIP Conference Proceedings 1942 (2018) 110033.
5. Study on the structural, spectroscopic, and dielectric properties of 1:2 ordered $Ca_3(B'Ta_2)O_9$ (B′ = Mg and Zn), Md. Monwar Hoque, **A. Barua**, Alo Dutta, Sanjoy Kumar Dey, T. P. Sinha, S. Kumar, Ionics 23 (2017) 471–483.

Seminar, Symposium and Conferences attended

Seminar, symposium and conferences attended:

1. Basic Physics to Contemporary Research, Department of Physics, Jadavpur University, Kolkata, 2015.
2. Some recent trends in research in Physics, Department of Physics, Jadavpur University, Kolkata, 2016.
3. Nanotechnology: Materials and Applications, School of Materials Science and Nanotechnology, Jadavpur University, 2016.
4. Twists and Turns in Physics Research: Special emphasis on condensed Matter and Biophysics, Department of Physics, Jadavpur University, Kolkata, 2017.
5. Semiconductor Materials and Devices, School of Materials Science and Nanotechnology, Jadavpur University, 2017.
6. Advanced Nanomaterials & Nanotechnology, Indian Institute of Technology Guwahati, 2017.
7. Biomedical Device Technology, Center of Nanotechnology, Indian Institute of Technology Guwahati, 2017.
8. Solid state physics symposium, Bhabha Atomic Research Centre, Mumbai, 2017.
9. Recent trend in Frontier Research in Physics, Department of Physics, Jadavpur University, Kolkata, 2018.
10. International Conference on Condensed Matter (ICCM), The Academy of Sciences, Chennai, Tamil Nadu, India, 2021.

Appendix

Reprints of the published papers related to the thesis

Physica B 583 (2020) 412057

Contents lists available at ScienceDirect

Physica B: Physics of Condensed Matter

journal homepage: http://www.elsevier.com/locate/physb

Structural, optical and electrical characterization of Ba_2YbTaO_6

A. Barua [a,*], S. Maity [b], S. Kumar [b], A. Dutta [c], T.P. Sinha [c]

[a] Physics Department, Presidency University, Kolkata, 700073, India
[b] Physics Department, Jadavpur University, Kolkata, 700032, India
[c] Physics Department, Bose Institute, Kolkata, 700009, India

ARTICLE INFO

Keywords:
Double perovskite oxides
X-ray diffraction
Impedance spectroscopy
Dielectric relaxation
Activation energy

ABSTRACT

The double perovskite oxide Ba_2YbTaO_6 (BYT) comprising of a rare earth material was prepared using solid state ceramic route. The structural investigation proposes the cubic phase of BYT with $Fm\bar{3}m$ space group. The optical band gap of BYT is 3.95 eV which was calculated by means of the UV–visible absorption spectrum. The frequency dependent dielectric characterization of BYT was done in between temperatures 303 K and 623 K. The relaxation behavior of BYT was examined utilizing the Cole–Cole model. The frequency reliant conductivity curves were analyzed using the power law. The hopping mechanism responsible for conduction in BYT is due to the p-type polaron hopping which is corroborated by the activation energy value of 0.5 eV.

1. Introduction

Double perovskite oxides are the most promising functional material in the field of electronics as well as electrical technology as they can have different types of chemical composition, various crystal structure and their dependent physical properties [1–3]. Amalgamation of different physical properties in a single material is the most exigent task for material scientists and perovskite oxides have given this opportunity [4]. However, most binary, ternary or quaternary compounds contain lead which is extremely toxic by nature. In the last few decades the progress of electronics as well as electrical technology is based on the continuous effort to develop smart and eco-friendly materials. Lead being a toxic material, other alternatives like lead free dielectric materials are need to be developed [5–9]. The conventional chemical formula of the double perovskite oxides is $A_2B'B''O_6$ [10].

An extensive survey of the literature on ytterbium based double perovskite oxides shows that, the ac electrical properties of very few are reported. The structural properties of Ba_2LnTaO_6 (where Ln is a trivalent lanthanide) in temperature between 82 K and 723 K have been reported by Hammink et al. [11]. Konopka et al. [12] have reported the dielectric permittivity of Ba_2YbTaO_6 in the microwave frequency range and its magnetic susceptibilities and the electron paramagnetic resonance measured between 5 K and room temperature have been reported by Taria et al. [13]. However, the detailed analysis of the variation of the electrical parameters like dielectric permittivity, loss tangent, impedance and conductivity with temperature and frequency of 'Barium Ytterbium Tantalum Oxide' (Ba_2YbTaO_6, BYT) has not yet been reported in the low frequency region. Here we have used the solid-state reaction route to synthesize the BYT sample. The structural, optical, vibrational and electrical properties of BYT have been reported in this paper. Alternating Current Impedance Spectroscopy (ACIS) technique was utilized for measuring the dielectric properties of BYT which was measured using the frequency between 42 Hz and 1 Megahertz and temperatures between 303 K and 623 K.

2. Experimental

Stoichiometric amount of Barium Carbonate (Ba_2CO_3, Loba, Extra pure), Ytterbium oxide (Yb_2O_3, Sigma-Aldrich, 99.9%) and Tantalum Pentoxide (Ta_2O_5, 99.9%) were mixed using acetone (Merck) in an agate motor for 12 h and then placed in a Platinum crucible and calcined at 1500 °C for about 8 h. The mixture was then cooled at a rate of 100 °C/h and brought down to 30 °C. The palletization of the powdered mixture was done after mixing it with a small amount of polyvinyl alcohol which acts as a binding agent. The sintering of the pelletized disc, having 7.46 mm diameter and 1.4 mm thickness, was done at 1550 °C for 12 h. The sintered sample was then brought down to 30 °C by cooling it at a rate of 1 °C/min.

The powder x-ray diffraction (PXRD) pattern was obtained by keeping the Bragg's angle between $10° \leq 2\theta \leq 120°$ and by using Cu-Kα radiation. The PXRD data was recorded at room temperature with step scanning size of 0.02. The surface morphology and homogeneity of BYT

* Corresponding author.
E-mail address: arpita.physics@presiuniv.ac.in (A. Barua).

https://doi.org/10.1016/j.physb.2020.412057
Received 27 June 2019; Received in revised form 3 January 2020; Accepted 29 January 2020
Available online 30 January 2020

was studied with a scanning electron microscope (SEM). For the dielectric measurement, the disc of the sample was polished and a conductive silver electrode on each side of the sample disc were developed and then fired. In order to perform the dielectric measurements LCR meter (HIOKI-3532, Japan) was used.

3. Results

3.1. Structural investigation

The tolerance factor t of BYT has been calculated using $t = \frac{rA+r0}{\sqrt{2}\,(rB+r0)}$, where, r_A, $[r_B = (r_{B'} + r_{B''})/2]$ and r_0 are the ionic radii of the constituent A, B and O site ions, respectively [14]. The calculation has been made considering the Shannon ionic radii [15]. The tolerance factor t for BYT is 0.99. This value of t agrees well with that of the cubic structure which has no driving force to deform them to a lower symmetry thus no octahedral tilt is expected in the system. The Rietveld refinement of the PXRD pattern of BYT (Fig. 1) was performed using the FULLPROF program [16]. The refined PXRD profile has been denoted by the continuous line in Fig. 1 whereas the experimental data are represented by the scattered symbols and their difference is represented by the blue line at the bottom. The Bragg's positions are depicted within first bracket corresponding to each peak position. The flat nature of the difference between the refined XRD profile and the experimental data suggests the phase formation with cubic phase and $Fm\bar{3}m$ (O_h^5) space group.

Fig. 2 shows the crystal structure of BYT with YbO_6 and TaO_6 octahedra being represented in different colors. The XRD fitting, structural parameters and Yb–O–Ta bond angle is given in Table 1. From Fig. 2 it can be clearly seen that no tilt is present in both the YbO_6 and TaO_6 octahedra. For BYT the average grain size is 7.609 μm which has been determined by the Debye-Scherrer's equation: $D_{hkl} = K\lambda/\beta\cos\theta$. The inset of Fig. 1 depicts the SEM image of BYT having average grain size of 7.78 μm. It can thus be concluded that our calculated result agrees well with the experimental data. The compactness of the grains in the SEM image points toward the high density of the prepared sample. The theoretical density of the sample is 8.165 g cc^{-1}. The density of BYT pellet measured using the Archimedes principle is 8.092 g cc^{-1}, indicating negligible amount of porosities present in the sample disc. The chemical constituents of BYT have been depicted in the EDAX spectrum [the inset of Fig. 3].

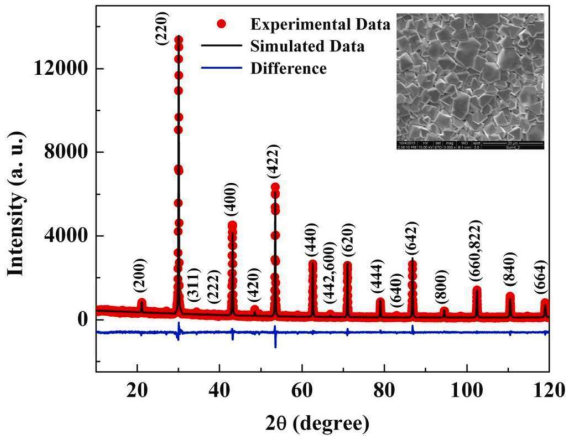

Fig. 1. Rietveld refinement plot of BYT where the experimental points are represented by symbols and the line represents the simulated XRD data. SEM micrograph is in the inset.

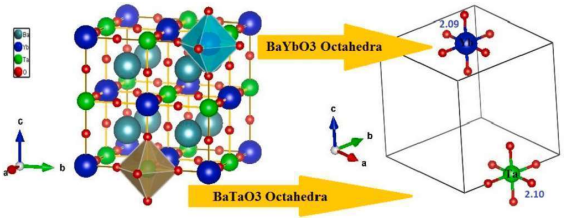

Fig. 2. The structure of BYT obtained from the Rietveld refinement.

Table 1
XRD fitting and structural parameters.

Atom	Wyckoff position	x	y	z	B	Bond length (Å)	BVS
Ba	8c	0.25	0.25	0.25	0.090	Ba–O(x 4) = 2.96463(3)	1.912
Yb	4a	0.0	0.0	0.0	0.074	Ba–O(x 8) = 2.96(7)	1.912
Ta	4b	0.5	0.5	0.5	0.774	Yb–O(x 4) = 2.08789(3)	3.642
O	24e	0.25 (1)	0.0	0.0	1.000	Yb–O(x 2) = 2.09(9) Ta–O(x 4) = 2.10466 Ta–O(x 2) = 2.10(9)	

Cell parameters: a = b = c = 8.38510(14) Å; Rwp = 15.2; Rexp = 8.87; Rp = 15.6; $\chi^2 = 2.95$, (Yb-O-Ta) = 180° (4).

3.2. UV–visible spectroscopic analysis

Fig. 4 demonstrates the UV–visible absorption spectrum of BYT from which the optical band gap (E_g) of BYT has been determined using the Tauc's relation [17]

$$[F(R) * h\upsilon] = C\,[h\upsilon - E_g]^n \quad (1)$$

where the Kubelka-Munk function is represented by F(R), hυ is the incident photon's energy, C is a constant, and n indicates the nature of the sample transition. The optical absorbance of a sample can be calculated from its reflectance by using F(R):

$$F(R) = \frac{(1-R)^2}{2R},$$

where R is the reflectance (%). At the linear absorption edge a tangent is drawn in the graph and from the intersection of the tangent with the abscissa the value of E_g for BYT is calculated to be 3.95 eV.

3.3. Photoluminescence spectroscopic study

The photoluminescence (PL) emission spectra was obtained by keeping the excitation wavelength fixed at 316 nm and is shown in Fig. 5. From the PL spectra we observe a strong, intense peak at around 414 nm which arises due to the direct transition of electron to conduction band (CB) from the valence band (VB). Another shoulder hump at around 438 nm is due to the dangling bonds associated with the BYT microstructure. These dangling bonds may increase the surface states within the band gap of the material. The electrons originating from the bulk BYT fill up the mid-gap states till the Fermi level. The charge accumulation at the surface creates a depletion region resulting in the development of an electric field which causes the bending of the edges of valence band and conduction band. Trap levels are created by these types of band structures and the electron goes from VB to CB via this trap level. The peak at around 438 nm is due to trap related recombination of electron that originates from the structural defects. Photoluminescence

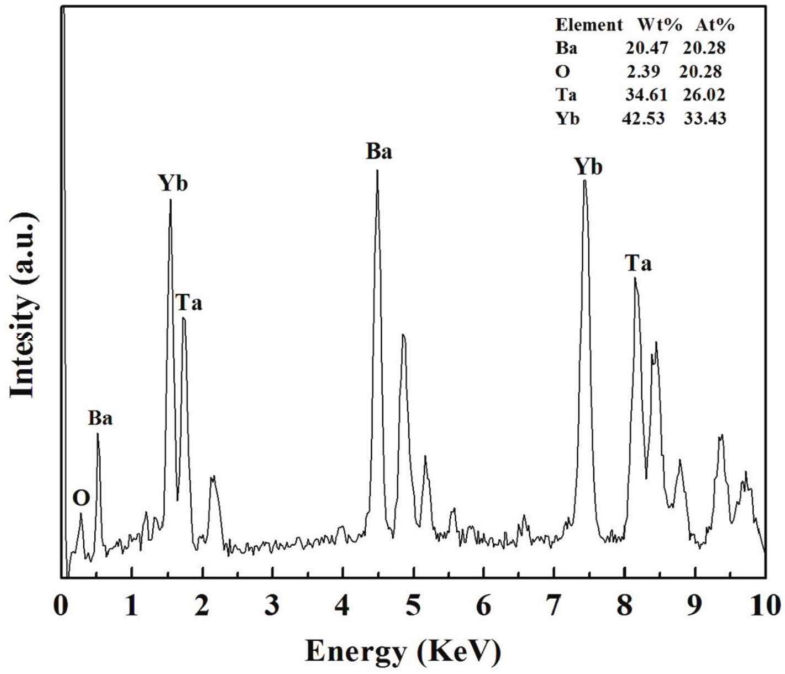

Fig. 3. EDAX spectrum of BYT.

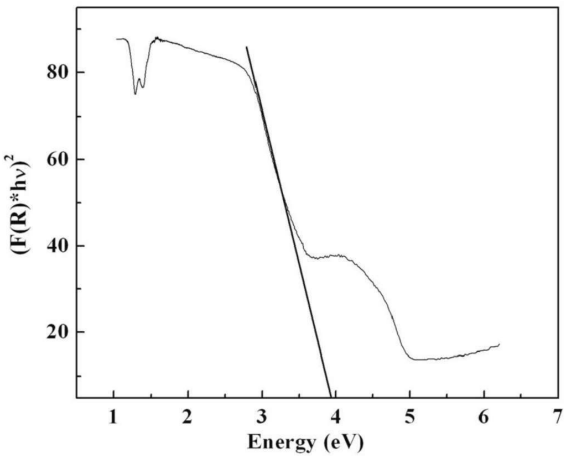

Fig. 4. The UV–visible absorption spectrum of BYT.

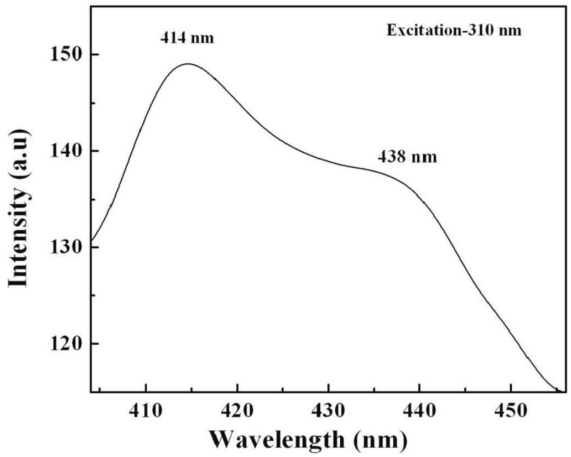

Fig. 5. The photoluminescence emission spectra of BYT.

excitation (PLE) measurement has been performed keeping the emission wavelength fixed at 414 nm, which is shown in Fig. 6. In the PLE spectra it is observed that the excitonic peak is at 316 nm which is very close to the excitonic peak of the UV–Vis spectra.

3.4. FTIR analysis

In order to study the chemical bonding present in BYT we have performed the Fourier transform infrared (FTIR) spectroscopy (Fig. 7) where three bands are detected at 577 cm^{-1}, 1440 cm^{-1} and 1642 cm^{-1}. The results agree well with the predictions of group theory for a cubic perovskite structure [18]. The absorption peaks represent the vibrational coupling between various coordination polyhedral present in BYT. The asymmetric stretching vibration of TaO_6 octahedral is indicated by a strong peak at about 577 cm^{-1} [19]. The IR bands matches well with that reported for cubic $A_2B'B''O_6$ type perovskites [20–24]. The weak band at about 1440 cm^{-1} is due to the overtones of the fundamental vibrations present within BYT and small bands around 1642 cm^{-1} arises because of the carrier KBr $(H_2O)_n$.

3.5. Impedance analysis

Fig. 8 illustrates the impedance formalism at temperatures 453 K and 483 K which has been analyzed for understanding the relaxation

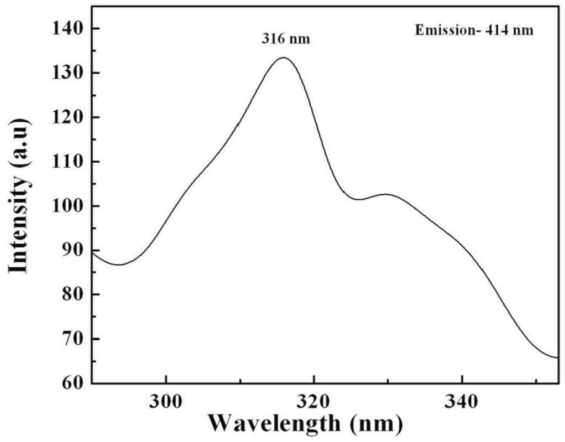

Fig. 6. The photoluminescence excitation spectra of BYT.

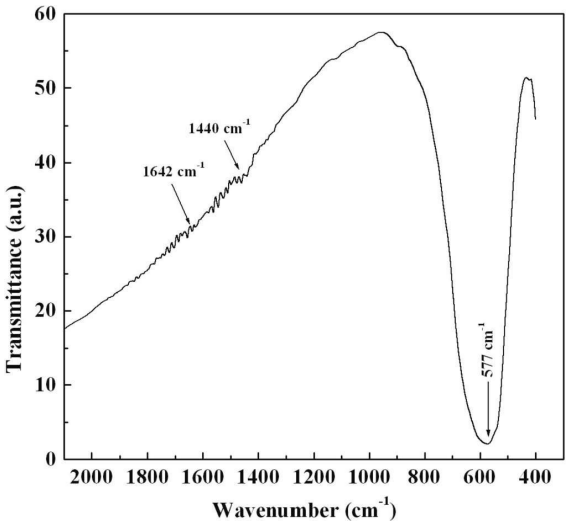

Fig. 7. FTIR spectrum of BYT.

behavior of BYT. Two deformed semicircular arcs are present in the complex impedance plot for each temperature. The smaller semicircular arc is detected in higher frequency side whereas the larger semicircular arc is detected in lower frequency side which point towards the role of both grain boundary (lower frequency side) and grain (higher frequency side) in contributing to the total impedance. The depressed or deformed semicircular arc in the Nyquist plot is due to the non-Debye type relaxation mechanism which is attributed to the possibility of polydispersive nature of BYT. The Debye type relaxation has only one relaxation process with definite relaxation time whereas non-Debye type relaxation involves multiple relaxation processes having different relaxation time, which leads to a distribution in the relaxation times of the dipoles present in the sample. This polydispersive nature can be probed from the Nyquist plot of the sample. In case of Debye type relaxation, the semi-circular arc's center is located in the Z′ axis whereas for the relaxation of non-Debye type as in case of our sample the center lies well below the Z′ axis [25]. Thus, the relaxation phenomena our sample exhibit is polydispersive in nature. Here the non-Debye relaxation process arises due to the charge carriers that are distributed in-homogeneously around grain-boundaries causing local variation of resistances in those regions [26].

The experimental curve has been simulated using a comparable circuit consisting of two parallel resistor-capacitor (RC) components joined together in series. By definition the total impedance consists of real (Z′) and imaginary (Z″) parts which can be written as [27,28]:

$$Z' = \frac{R_g}{1+(\omega R_g C_g)^2} + \frac{R_{gb}}{1+(\omega R_{gb} C_{gb})^2} \quad (2)$$

$$Z'' = R_g\left[\frac{\omega R_g C_g}{1+(\omega R_g C_g)^2}\right] + R_{gb}\left[\frac{\omega R_{gb} C_{gb}}{1+(\omega R_{gb} C_{gb})^2}\right] \quad (3)$$

Here R_g and C_g denotes the grain's contribution to the resistance and the capacitance whereas R_{gb} and C_{gb} denotes the grain-boundary's contribution to the resistance and the capacitance. According to this model the phase angle $\tan\theta = Z''/Z'$, is not constant and is frequency dependent. In the complex Z-plane plot of our sample, it has been observed that at lower frequency side (Fig. 8(b)) it is almost straight line (independent of frequency) which means that the phase is constant. So, there exist a discrepancy between the Cole-Cole model and the Nyquist plot of our present sample and some modification are required in the Cole-Cole model. The pure capacitor cannot explain this vagueness thus in the Cole-Cole equation the pure capacitor has to be substituted using a constant phase element (CPE). From the theory of CPE, the capacitance is written as $C = Q^{1/n} R^{[(1-n)/n]}$, where Q and R are the constant phase element and the resistance associated with the grain boundaries (R_{gb}, Q_{gb}) and the grains (R_g, Q_g). The deviance from ideal capacitive behavior is denoted by n. For $n = 0$ the behavior is purely resistive and for $n = 1$ the behavior is purely capacitive in nature. The modified Cole-

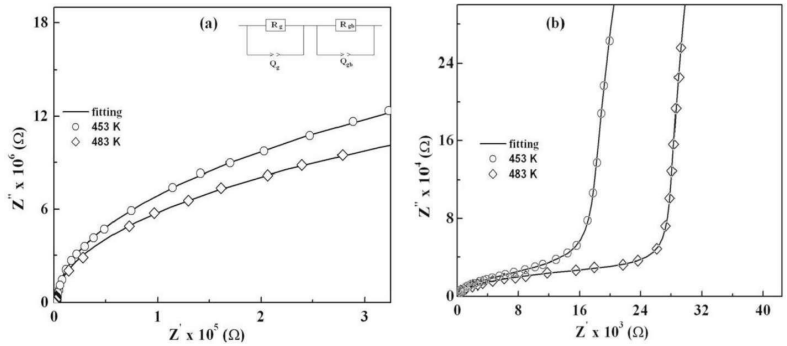

Fig. 8. The complex impedance plane plots between Z″ and Z′ for BYT at temperatures 453 K and 483 K.

Cole equation in terms of CPE is as follows:

$$Z' = \frac{R_g}{1 + \left[\omega(R_g Q_g)^{\frac{1}{n_g}}\right]^2} + \frac{R_{gb}}{1 + \left[\omega(R_{gb} Q_{gb})^{\frac{1}{n_{gb}}}\right]^2} \quad (4)$$

$$Z'' = R_g \left[\frac{\omega(R_g Q_g)^{\frac{1}{n_g}}}{1 + \left[\omega(R_g Q_g)^{\frac{1}{n_g}}\right]^2}\right] + R_{gb} \left[\frac{\omega(R_{gb} Q_{gb})^{\frac{1}{n_{gb}}}}{1 + \left[\omega(R_{gb} Q_{gb})^{\frac{1}{n_{gb}}}\right]^2}\right] \quad (5)$$

The experimental data has been fitted using equations (4) and (5) and is denoted by solid lines as shown in Fig. 8. In Table 2 the different fitting parameters for 453K and 483K are tabulated. The Nyquist plots have been fitted considering CPE instead of pure capacitance of the electrical circuit. The experimental and the fitted curves agrees well with each other confirming the non-ideal nature of the capacitance which results from the multiple relaxation processes for a given relaxation time [29]. The value of 'n' in the fitted parameters as seen in Table 2, indicates the deviation from the ideal Debye process. The RC equivalent circuit for the complex impedance has been shown in the inset of Fig. 8(a). The Nyquist plot of BYT confirms the involvement of both grain boundary and grain to the overall impedance, each having different values of resistances which gives rise to non - Debye type relaxation process. The presence of polycrystalline grains and their grain boundaries are well observed in the SEM image of BYT.

3.6. Dielectric formalism

Fig. 9 (a) & (b) illustrates the angular frequency (ω) dependent dielectric permittivity (ε') and loss tangent (tan δ) curves. The relaxation of ε' is associated with the dipole's oscillation in an ac field which can be examined using Debye theory [30]. From Fig. 9 (a) it has been observed that for ε', two distinct regions of dispersion are present. The interfacial polarization is responsible for dispersion when the frequency is low [31]. Dielectric properties are strongly dependent upon the grain size and the interfacial polarization. In the low frequency region, the dielectric value is dependent upon the conductivity of grain boundaries. If the sizes of the grain boundaries are large, they give rise to large dielectric values. The dielectric permittivity value decreases as the frequency increases as the charge exchange are unable to follow the applied field. The change in dielectric permittivity is almost negligible when the frequency is high as the electronic and the atomic polarization governing the dielectric permittivity values are independent of the variations in temperature and frequency. The dielectric permittivity increases with temperature when the frequency is low as the interfacial and dipolar polarization are dependent on temperature. Thus, the dielectric dispersion in the sample is due to the existence of the grain and grain boundary interface.

It can be seen from Fig. 9 (a), that at lower frequencies the dipoles trail the applied alternating field and $\varepsilon' = \varepsilon_s$ whereas on increasing the frequency the dipoles start lagging behind the field and the ε' value decreases. The characteristic frequency where $\omega = (1/\tau)$, the ε' value suddenly decreases signifying a relaxation process. On increasing the frequency to a very high value the dipoles cannot trail the field and ε' attains a constant value $\varepsilon' \approx \varepsilon_\infty$. At low frequencies the ε' varies considerably with temperature. In the region of dispersion for ε' a relaxation peak is observed in the loss tangent curve. On increasing the temperature, the peak in the loss tangent curve starts shifting towards higher frequency region because more polarization occurs at higher temperature and eventually leading to relaxation at higher frequency. This shifting of tan δ peak with temperature point towards a temperature dependency of the dielectric relaxation of BYT. In our sample the existence of dc conductivity (σ_{dc}) is indicated by the dramatic change in tan δ at the low frequencies. According to ideal Debye relaxation process a kink is expected to appear in tan δ which is attributed to the monodispersive relaxation process. But in our present sample the broad nature of the loss tangent peaks points towards a polydispersive behavior of the relaxation process.

In the loss tangent curve, the peak position gives the value of the relaxation time τ_m (= $1/\omega_m$). It is observed that ω_m satisfies the Arrhenius law,

$$\omega_m = \omega_0 \exp\left[-\frac{E_a}{K_B T}\right] \quad (6)$$

Here E_a represents the activation energy and ω_0 is a constant. The inset of Fig. 9 (b) is a plot between log ω_m and 1000/T, where the experimental data are represented by the symbols and the straight line denotes the least squares fit of the experimental data points. The value of E_a = 0.51 eV as calculated from the Arrhenius plot suggests that the hopping of p-type polaron is responsible for the conduction mechanism of BYT [32–35]. It can be seen from Table 2 for the fitted parameters of the impedance spectra that the resistance for the grain boundaries are very large in comparison to that of the grains. Thus, the grain boundaries provide a barrier to the charge transport acting as a trap for the charge carriers [29]. The oxygen anions surrounding the cations can be considered isolated from one another as the overlapping of the charged clouds is very small. This localization leads to the formation of polaron. The charge transport occurs between the nearest neighbor sites by hopping of charged particles in between the localized sites. The occupancy of the trap centers decreases as the frequency increases endorsing the hopping of the charge carriers which leads to the increase in the conductivity. In our case the behavior of the grain boundaries as the trap centers leads to the conduction process by polaron hopping. The Cole-Cole model has been utilized for examining the polydispersive behavior of the relaxation process of BYT as illustrated in Fig. 10 [36]

$$\varepsilon^* = \varepsilon' - i\varepsilon'' = \varepsilon_\infty + \frac{\varepsilon_s - \varepsilon_\infty}{\left[1 + (i\omega\tau)^{1-\alpha}\right]} \quad (7)$$

Here ε_s denotes the low frequency quasi-static value and ε_∞ denotes the high frequency value of dielectric permittivity, the difference ($\varepsilon_s - \varepsilon_\infty$) gives the dielectric relaxation strength, τ denotes relaxation time and α gives the variation of relaxation times having values amid 0 and 1. When α value is 0 it signifies ideal Debye relaxation and when $\alpha > 0$ it signifies a deviation from ideal Debye relaxation having different relaxation times. Equating real and imaginary parts of equation (7), [37]

$$\varepsilon' = \varepsilon_\infty + \left(\frac{\varepsilon_s - \varepsilon_\infty}{2}\right) \times \left\{1 - \frac{\sinh((1-\alpha)\ln(\omega\tau))}{\left(\cosh((1-\alpha)\ln(\omega\tau)) + \cos\left((1-\alpha)\frac{\pi}{2}\right)\right)}\right\} \quad (8)$$

$$\varepsilon'' = \left(\frac{\varepsilon_s - \varepsilon_\infty}{2}\right) \times \left\{1 - \frac{\left(\sinh\left((1-\alpha)\frac{\pi}{2}\right)\right)}{\left(\cosh((1-\alpha)\ln(\omega\tau)) + \cos\left((1-\alpha)\frac{\pi}{2}\right)\right)}\right\} \quad (9)$$

A sharp increase is observed in both ε' and ε'' at low frequencies which arises due to contribution of electrical conduction. Thus, a contribution term for the electrical conductivity needs to be added to the Cole-Cole equation which becomes

Table 2
The various fitted parameters of the impedance circuit.

Temp. (K)	R_g (10^4 Ω)	Q_g (10^{-10} F/Ω)	n_g	R_{gb} (10^7 Ω)	Q_{gb} (10^{-10} F/Ω)	n_{gb}
453	2.8	29	0.72	5	10	0.64
483	1.8	68	0.65	3.6	7.86	0.57

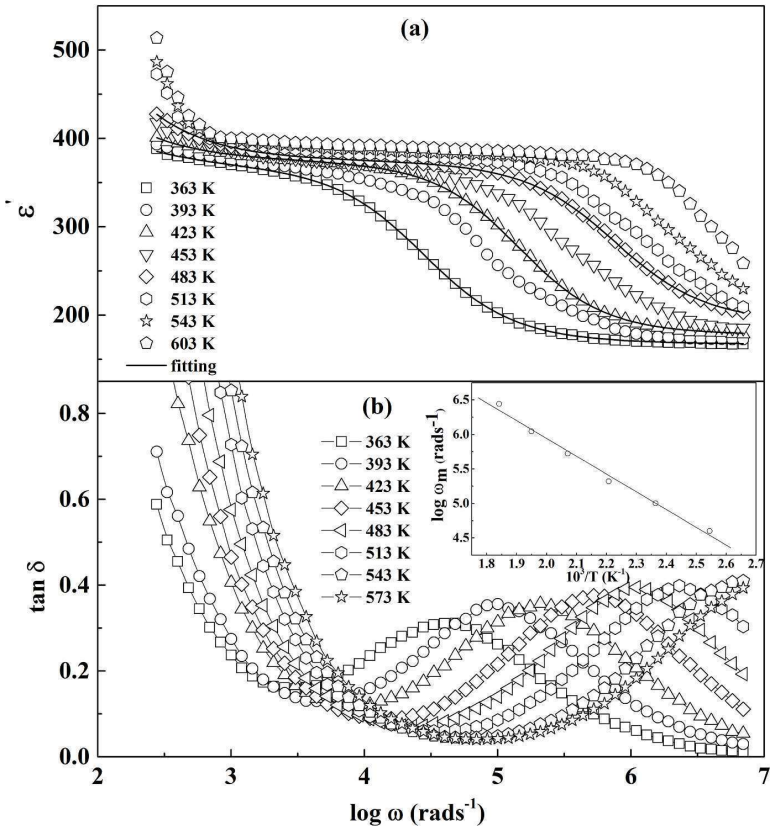

Fig. 9. (a) Frequency dependence of ε' (a) and tan δ (b) of BYT at various temperatures, where the solid lines are the Cole-Cole fit to the experimental data which are represented by symbols. Arrhenius plot of most probable relaxation time is shown in the inset of (b).

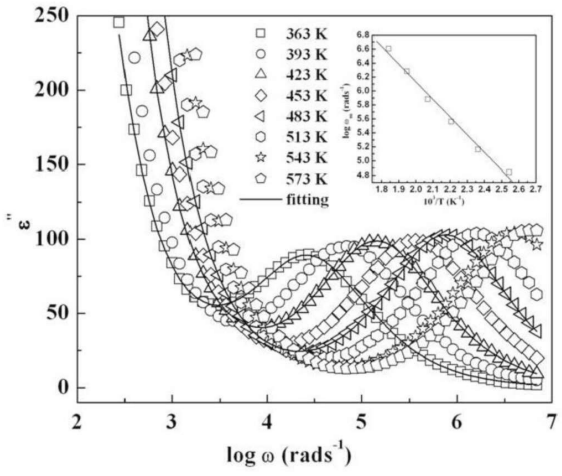

Fig. 10. Frequency dependence of ε'' at various temperatures for BYT where the solid lines are the Cole-Cole fit to the experimental data which are represented by symbols. Arrhenius plot of most probable relaxation time is shown in the inset.

$$\varepsilon^{*} = \varepsilon_{\infty} + \left(\frac{\varepsilon_s - \varepsilon_{\infty}}{1 + (i\omega\tau)^{1-\alpha}}\right) - j\frac{\sigma^{*}}{\varepsilon_0 \omega^{s}} \tag{10}$$

where s represents a constant quantity having values between 0 and 1 and σ* (σ* = σ1+σ2) represents the complex electrical conductivity with σ_1 as dc conductivity and σ_2 as the conductivity for the space charges. Dividing equation (10) into real and imaginary parts,

$$\varepsilon' = \varepsilon_{\infty} + \frac{(\varepsilon_s - \varepsilon_{\infty})\left[1 + (\omega\tau)^{1-\alpha}\sin\left(\alpha\frac{\pi}{2}\right)\right]}{1 + 2(\omega\tau)^{1-\alpha}\sin\left(\alpha\frac{\pi}{2}\right) + (\omega\tau)^{2-2\alpha}} + \frac{\sigma_2}{\varepsilon_0\omega^{s}} \tag{11}$$

$$\varepsilon'' = \varepsilon_{\infty} + \frac{\left[(\varepsilon_s - \varepsilon_{\infty})(\omega\tau)^{1-\alpha}\cos\left(\alpha\frac{\pi}{2}\right)\right]}{1 + 2(\omega\tau)^{1-\alpha}\sin\left(\alpha\frac{\pi}{2}\right) + (\omega\tau)^{2-2\alpha}} + \frac{\sigma_1}{\varepsilon_0\omega^{s}} \tag{12}$$

From equations (11) and (12) it is clear that ε' is associated with the space charge conductivity (σ_2) and ε'' is associated with the dc conductivity (σ_1). In Figs. 9(a) and 10 solid lines represent the fitted curve which has been obtained with the help of equations (11) and (12) for temperatures 363 K, 423 K and 483 K. The parameters utilized for fitting are presented in Table 3. The characteristic relaxation time can be calculated by $\tau_m = \omega_m^{-1}$. The variation of ω_m of ε'' with temperature (inset of Fig. 10) follows the Arrhenius law from which the value of E_a is found to be 0.50 eV, which is nearly equal to that calculated from the Arrhenius plot for tan δ. In Fig. 11 the scaling behavior of ε'' is depicted where ε'' is scaled by ε''_m and ω by ω_m. Here ε''_m is the peak value of the ε'' versus log ω curve. The coinciding curves indicate that same mechanism

Table 3
The various fitting parameters of modified Cole–Cole equation.

Temp. (K)	$\varepsilon_s - \varepsilon_\alpha$	ω_m (KHz)	α	σ_1 (Sm^{-1})	n
363	251	27.54	0.15	4.3×10^{-8}	0.95
393	185	69.38	0.15	5.6×10^{-7}	0.95
423	225	145.21	0.14	8.7×10^{-7}	0.96
453	290	363.65	0.13	1.06×10^{-6}	0.95
483	300	765.50	0.15	1.31×10^{-6}	0.95
513	303	1591.72	0.15	1.67×10^{-9}	0.94
543	299	3999.86	0.14	1.99×10^{-6}	0.95
573	267	5782.51	0.15	2.36×10^{-6}	0.95

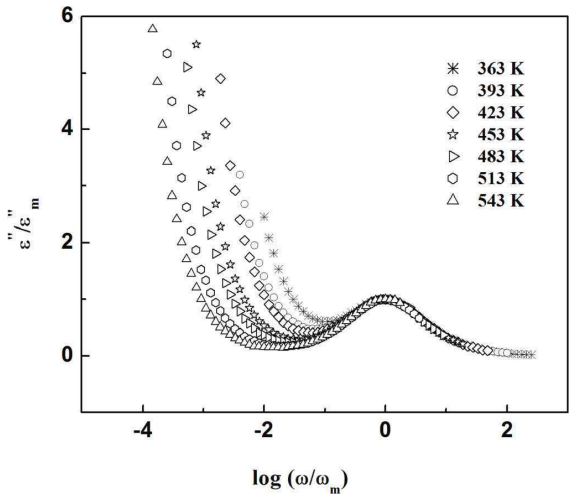

Fig. 11. Scaling behavior of ε'' at various temperatures.

is followed for relaxation process at different temperatures. In the scaled curves the overlapping does not occur at low frequencies because the dipoles can trail the field applied at low frequencies.

Electronic and ionic polarization together plays the key role in determining the dielectric property of the material. For a given ion, electronic polarization is constant but the ionic polarization depends on the crystal structure as ionic polarization occurs due to the lattice vibrations. There exists a correlation between the bond valence sum (BVS) and the dielectric property of a cubic perovskite. The correlation of the dielectric property with the BVS of the B-site cation has been reported by Lufaso et al. [38]. The ions with smaller BVS gives rise to larger ionic polarization as for the ions with longer and weaker bonds polarization can be achieved easily. The BVS values of BYT are mentioned in Table 1. It may be noted that the BVS values of BYT is comparatively smaller than its Niobium based counterpart Ba_2YbNbO_6 as reported by Maity et al. [35] as the Ta–O bond length is comparatively larger than Nb–O bond length. The dielectric permittivity values for BYT are significantly large as compared to that reported by Maity at al. as the Ta–O bond length being weaker; the polarization can be easily achieved. In this way the lattice vibrations associated with the crystal structure strongly affect the dielectric permittivity values.

3.7. Conductivity formalism

Fig. 12 depicts the angular frequency variation of ac conductivity of BYT at several temperatures and it consists of two plateaus indicative of two processes involved in the bulk conduction behavior. It can be observed in Fig. 12 (a) that as the frequency is decreased the conductivity becomes constant at a certain value called the dc conductivity (σ_{dc}). At low frequency the periodicity of the electric field is very low as

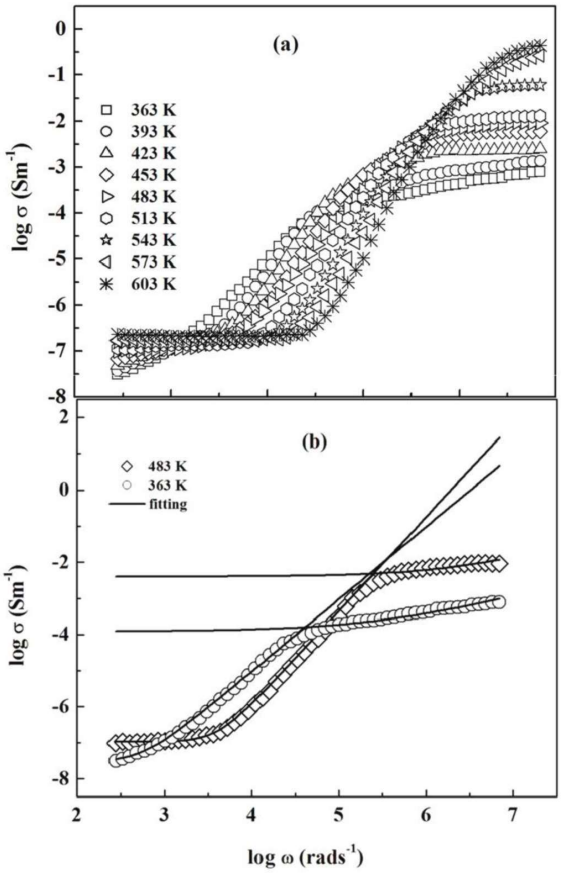

Fig. 12. (a) Frequency dependence of the conductivity (σ) for BYT at various temperature and the fittings (b) of power law for the same at 363 K and 483 K has been shown by solid lines.

a result the accumulation of charge carriers takes place which contributes to the dc conductivity (σ_{dc}) [39]. The spectra of conductivity versus frequency follows Jonscher power law [40]

$$\sigma = \sigma_{dc}\left[1 + \left(\frac{\omega}{\omega_H}\right)^n\right] \quad (13)$$

here ω_H is the frequency of hopping of charge carriers, n is a frequency exponent and σ_{dc} is the dc conductivity. The changeover from the slow rise of conductivity (σ_{dc}) at lower frequency region to sudden change in the conductivity at higher frequency region suggests the onset of conductivity relaxation process. This ac conductivity behavior of the present sample can be easily analyzed using jump relaxation model [41]. When $\omega < \omega_H$ the charge carriers travel very slowly throughout the crystal lattice so they can hop between one site to another resulting in the dc conductivity (σ_{dc}). Again, at high frequency ($\omega > \omega_H$) power law becomes $\sigma(\omega) \alpha \omega^n$ which causes a sharp rise in the conductivity value. Fig. 12 (b) illustrates the fitted conductivity spectra of BYT at 363 K and 483 K which has been fitted using equation (13). The value of n in the low frequency region lies between $1 < n < 2$ whereas n lies between $0 < n < 1$ in the high frequency region (Table 4).

The frequency variation of conductivity results from the hopping of charged particles trough trap sites separated by different potential barriers. The conductivity variation becomes independent of frequency when a charge carrier moves along a lattice comprised of similar

Table 4
The various Fitting parameters of conductivity spectra.

Temp. (K)	Low frequency plateaue			High frequency plateaue		
	σ_{dc} (Sm^{-1})	ω_H (rad s^{-1})	n	σ_{dc} (Sm^{-1})	ω_H (rad s^{-1})	n
363	2.702×10^{-8}	530	1.98	1.21×10^{-4}	268600	0.6
483	10.502×10^{-8}	4000	1.98	4.00×10^{-3}	2563454	0.67

potential well. The conductivity value increases with frequency and finally saturates at high frequency when the charge carrier hops back and forth in a double well having infinite barrier on each side. A system consisting of potential well with different barrier height as in case of our sample, the conductivity spectra shows a step like nature on increasing the temperature. The varied potential barrier heights arise due to the existence of both the grain boundary and the grain.

4. Conclusions

The ceramic method has been employed to synthesize BYT at 1500 °C. The analysis of the PXRD pattern of BYT suggests the cubic structure with $Fm\bar{3}m$ space group. The cubic phase of BYT is further confirmed by the three bands obtained in the FTIR spectra which is associated with the $Fm\bar{3}m$ space group. The average grain size of BYT obtained from SEM is 7.78 μm. EDAX shows the uniformity of the sample. A relaxation behavior is detected in all the temperature region. The presence of two arcs in the Nyquist plot points towards the role of both grain boundary and grain in contributing to the total impedance. The broad nature of the loss tangent peaks points towards the polydispersive nature of the relaxation process. The activation energy value of 0.5 eV as obtained from the Arrhenius plot of the relaxation time indicates that the conductivity and the dielectric relaxation at different temperature is due to the p-type polaron hopping. The existence of two plateaus in the conductivity plot indicates that in the bulk conduction behavior two processes are involved for the contribution of both grain and grain boundary.

CRediT authorship contribution statement

A. Barua: Conceptualization, Methodology, Software, Investigation, Writing - review & editing. **S. Maity:** Data curation, Software, Visualization, Writing - original draft. **S. Kumar:** Supervision, Validation. **A. Dutta:** Software. **T.P. Sinha:** Supervision.

Acknowledgement

We would like to acknowledge the DRDO, New Delhi, Government of India; the UPE program of UGC; FIST and the PURSE program of DST, Govt. of India. We would also like to thank the Presidency University, India for the FRPDF grant.

References

[1] S.N. Putilin, E.V. Antipov, O. Chmaissem, M. Marezio, Nature 362 (1993) 226–228.
[2] S. Jin, T.H. Tiefel, M. McCornack, R.A. Fastnacht, L.H. Chen, Science 264 (1994) 413–415.
[3] C.G. Zhong, J.H. Fang, Q. Jiang, J. Phys. Condens. Matter 16 (2004) 9059–9068.
[4] A.S. Bhalla, R. Guo, R. Roy, Mater. Res. Innovat. 4 (2000) 3–26.
[5] S. Priya, A. Ando, Y. Sakebe, J. Appl. Phys. 94 (2003) 1171.
[6] I. Levin, J.Y. Chan, J.E. Maslar, T.A. Vanderah, J. Appl. Phys. 90 (2001) 904.
[7] R. Zurmuhlen, J. Petzett, S. Kamba, V.V. Voitsekhovskii, E. Colla, N. Setter, J. Appl. Phys. 77 (1995) 5341.
[8] R. Zurmuhlen, J. Petzelt, S. Kamba, G. Kozlov, A. Volkov, B. Gorshunov, D. Dube, A. Tagantsev, N. Setter, J. Appl. Phys. 77 (1995) 5351.
[9] S. Saha, T.P. Sinha, J. Phys. Condens. Matter 14 (2002) 249.
[10] A.W. Sleight, R. Ward, J. Am. Chem. Soc. 83 (1961) 1088–1090.
[11] T.S. Hammink, W.T. Fu, D.J.W. IJdo, J. Solid State Chem. 184 (2011) 848–851.
[12] J. Konopka, R. Jose, M. Wołcyrz, Physica C 435 (2006) 53–58.
[13] N. Taira, Y. Hinatsu, J. Solid State Chem. 150 (2000) 31–35.
[14] V.M. Goldschmidt, Naturwissenschaften 14 (1926) 477–485.
[15] R.D. Shannon, Acta Crystallogr. A 32 (1976) 751–767.
[16] J. Rodriguez-Carvaja, Physica B 192 (1993) 55–69.
[17] J. Tauc, R. Grigorovici, A. Vancu, Physica Status Solidi (b) 15 (1966) 627.
[18] M. Licheron, F. Gervais, J. Coutures, J. Choisnet, Solid State Commun. 75 (1990) 759–763.
[19] R. Ratheesh, H. Sreemoolanadhan, M.T. Sebastian, J. Solid State Chem. 2 (1997) 131.
[20] A.E. Lavat, M.C. Grasselli, E.J. Baran, R.C. Mercader, Mater. Lett. 47 (2001) 194.
[21] A.F. Corsmit, H.E. Hoefdraad, G. Blasse, J. Inorg. Nucl. Chem. 34 (1972) 3401.
[22] G. Blasse, A.F. Corsmit, J. Solid State Chem. 6 (1973) 513.
[23] W. Zheng, W. Pang, G. Meng, Mater. Lett. 37 (1998) 276.
[24] A. Dutta, T.P. Sinha, Integrated Ferroelectrics 116 (2010) 41.
[25] A. Mishra, S.N. Choudhary, R.N.P. Choudhary, V.R.K. Murthy, K. Prasad, J. Mater. Sci. Mater. Electron. 23 (2012) 185–192.
[26] R.C. Da, Y.G. Yan, Electron. Elements Mater. 1 (1982) 25.
[27] M.M. Hoque, A. Barua, A. Dutta, S.K. Dey, T.P. Sinha, S. Kumar, Ionics 23 (2017) 471–483.
[28] R. Gerhardt, J. Phys. Chem. Solid. 55 (1994) 1491.
[29] S. Halder, Md. Seikh, B. Ghosh, T.P. Sinha, Ceram. Int. 43 (2017) 11097–11108.
[30] P. Debye, Polar Molecules, Chemical Catalogue Company, New York, 1929.
[31] D.N. Singh, D.K. Mahato, T.P. Singha, Physica B 550 (2018) 400–406.
[32] A. Barua, S. Maity, R. Mondal, S. Kumar, AIP Conf. Proc. 1942 (2018), 110033.
[33] W.H. Jung, J. Appl. Phys. 90 (2001) 2455.
[34] M. Idrees, M. Nadeem, M.M. Hassan, J. Phys. D 43 (2010), 155401.
[35] S.K. Maity, A. Dutta, S. Kumar, T.P. Sinha, Phys. Scripta 88 (2013), 065702.
[36] K.S. Cole, R.H. Cole, J. Chem. Phys. 9 (1941) 341.
[37] K. Majhi, B.S. Prakash, K.B.R. Varma, J. Phys. D Appl. Phys. 40 (2007) 7128–7135.
[38] Michael W. Lufaso, Chem. Mater. 16 (2004) 2148–2156.
[39] A.S.A. Khiar, R. Puteh, A.K. Arof, Physica B 373 (2006) 23–27.
[40] A.K. Jonscher, Dielectric Relaxation in Solids, Chelsea Dielectrics Press, London, 1983.
[41] K. Funke, Solid State Ionics 94 (1997) 27.

Physica B 649 (2023) 414449

Contents lists available at ScienceDirect

Physica B: Condensed Matter

journal homepage: www.elsevier.com/locate/physb

Influences of crystal structure, microstructure and adsorbed CO_2 on dielectric properties of Ba_2YbSbO_6-$BaCO_3$ formed by mechanical activation of Ba_2YbSbO_6

A. Barua [a], S.K. Dey [b], S. Dey [c], S. Kumar [d,*]

[a] Department of Physics, Presidency University, Kolkata, 700073, India
[b] Purulia Polytechnic, V. Nagar, Purulia, 723147, West Bengal, India
[c] Department of Physics, Swami Vivekananda Institute of Science and Technology, Kolkata, 700145, India
[d] Department of Physics, Jadavpur University, Kolkata, 700032, India

ARTICLE INFO

Keywords:
Double perovskite
Ball milling
Nanocomposite
CO_2 adsorption
Dielectric property

ABSTRACT

Herein, we have reported the structural, microstructural, thermal, optical and temperature dependent dielectric properties (between 40 Hz and 5 MHz) of Ba_2YbSbO_6 (BYSB) synthesized by solid state ceramic method and a nanocomposite of Ba_2YbSbO_6-$BaCO_3$ (BYSN). The samples are characterized by XRD, FESEM, EDS, FTIR and Raman spectroscopy. The nanosized Ba_2YbSbO_6 prepared by ball milling of BYSB adsorbs atmospheric CO_2 leading to the formation of BYSN. The dielectric behaviours of the samples have been examined in the framework of dielectric permittivity, electric modulus and conductivity formalisms. The samples exhibit non-Debye type relaxation governed by polaron hopping. BYSN exhibits better dielectric behaviour than BYSB. It has been shown that crystal structure, grain size, grain boundary contribution and surface adsorbed CO_2 strongly influence the dielectric relaxation dynamics and conduction mechanism of the samples. The dielectric response of these samples is comparable to their analogues counterparts used for fabrication of radio frequency devices.

1. Introduction

Perovskite oxide is one of the fabulous dielectric materials having widespread commercial application in microwave oscillator, radio frequency oscillator, resonator, filter and communication devices [1–8]. However, nowadays there is a huge demand of nanometric materials having high dielectric constant and low dielectric loss for use in high performance miniaturized microwave, radio frequency and energy storage devices. They also have applications in the development of multi-layer capacitors and dynamic random-access memory in smaller structures [9–11]. Research in the area of developing nanometric dielectric materials has been rapidly flourishing in the recent years. In past two decades, the nanometric materials having applications in microwave electronic circuits, optical storage devices, piezoelectric sensors, sonars, transducers and multilayer ceramic capacitors have been developed [9–13]. From application point of view, $BaTiO_3$ is an excellent perovskite oxide. The dielectric properties of nanosized $BaTiO_3$ synthesized by both chemical and high energy ball milling method have been elaborately investigated [9–11,13]. It may be noted that mechanical milling has been largely employed for the production of nanosized counterparts of bulk samples [14–16]. The strain induced by ball milling creates crystalline defects and surface disorder in nanometric samples synthesized by high energy mechanical milling [17–20]. The dielectric properties of nanosized perovskite oxides prepared by high energy ball milling differs from their bulk counterparts [16,21–24]. Very few works have been reported on the dielectric properties of nanocomposites of double perovskite oxides synthesized by high energy ball milling method. In this context, we have reported the dielectric properties of Ba_2YbSbO_6 (BYSB) synthesized by solid state ceramic method and a nanocomposite of Ba_2YbSbO_6-$BaCO_3$ (BYSN) synthesized by high energy ball milling of BYSB. We have shown how the nanocomposite Ba_2YbSbO_6-$BaCO_3$ is formed when Ba_2YbSbO_6 is mechanically activated by high energy ball milling. Further, we have examined the effects of crystalline defects, surface disorder and adsorbed CO_2 present in BYSN on its physical properties.

The nanosized perovskites are known to have applications in the sensing of NO_2 (using $LaFeO_3$), CO (using $LaCoO_3$), alcohols (using $SrFeO_3$), hydrocarbons (using $LnFeO_3$), H_2O_2 and glucose (using

* Corresponding author.
E-mail addresses: sanjay.kumar@jadavpuruniversity.in, kumar_dsa@yahoo.com (S. Kumar).

https://doi.org/10.1016/j.physb.2022.414449
Received 16 August 2022; Received in revised form 15 October 2022; Accepted 23 October 2022
Available online 9 November 2022

$LaNiO_3$). They are also used in dopamine detection (using $LaFeO_3$), solid oxide fuel cells (using $NdFeO_3$) and as catalysts (using $LaFeO_3$) for hydrogen evolution and oxygen reduction reactions [25–33]. In the recent past, the size dependent dielectric properties of nanosized $BaTiO_3$ have been extensively studied due to its high permittivity values and widespread applications in the electronic industry [9–15,21–23]. The rare earth based double perovskites Ba_2RASbO_6 (where RA is a rare earth element) exhibit interesting dielectric properties [34–37]. The nanosized $BaTiO_3$ and $LaCoO_3$ (synthesized by high energy ball milling method) and nanometric $LaFeO_3$ (prepared by sol-gel method) have shown to adsorb gases like CO_2, CO, NO_2 etc. [14,15,25,26]. There are few reports on crystal structure and dielectric properties of Ba_2YbSbO_6 [38–40]. It is may be noted that the dielectric property of this sample has been investigated at room temperature only. The bulk Ba_2YbSbO_6 synthesized by solid state ceramic method: (i) crystalizes in *R-3* space group with lattice parameter a = 5.9104 Å and α = 59.99°, (ii) exhibits semiconducting behaviour with optical band gap of 3.62 eV and electrical band gap of 2.3 eV (theoretical) and (iii) its room temperature dielectric constant is 14 at 10 KHz [40]. On the other hand the values of room temperature dielectric constant and loss tangent of nanosized Ba_2YbSbO_6 (of size 20–50 nm) synthesized by combustion method belonging to $Fm\bar{3}m$ space group (a = 8.4618 Å) are 11.3 and 1.5×10^{-3}, respectively, at 5 MHz [38,39]. It can be seen from the previous reports that room temperature dielectric properties of bulk Ba_2YbSbO_6 and its nanometric counterpart differ drastically [38–40]. In this background, we have studied the physical properties of BYSB and BYSN in order to identify the changes in their dielectric properties arising from mechanically induced crystalline defects and surface disorder. Herein, we have reported the (i) crystal structure of BYSB and BYSN, (ii) relaxation mechanism governing their dielectric behaviour and (iii) influence of adsorbed atmospheric gases in determining the physical character and dielectric property of mechanically activated nanosized Ba_2YbSbO_6.

2. Experimental

BYSB has been synthesized by the solid-state ceramic method following the standard protocol depicted in literature [41], where the reagent grade (~99.9% pure) powders of $BaCO_3$, Yb_2O_3 and Sb_2O_5 were used. The calcination temperature was 1798 K and the sample was heated for 10 h. The calcined powder was then sintered at 1848 K for 12 h to obtain BYSB. The nanosized BYSN sample was prepared at room temperature (300 K) by high energy ball milling of BYSB for 15 h with the help of Fritsch Planetary Mono Mill (pulverisette 6). Tungsten carbide vials and balls were used where ball to mass ratio was 16:1 and the rotational speed of the mill was 330 rpm.

The XRD patterns of the samples have been recorded by using Bruker D8 advanced diffractometer in order to confirm the phase purity and obtain the crystal structure of BYSB and BYSN. Both BYSB and BYSN have been thoroughly characterized by field emission scanning electron microscopy (FSEM, FEI Inspect 50), energy dispersive x-ray spectroscopy (EDS), high resolution transmission electron microscopy (TEM, Jeol 2100), FTIR (PerkinElmer), TGA (Mettler Toledo TG-DTA 85) and Raman spectrometry (WITEC alpha 300 R Raman spectrometer). To carry out the dielectric measurements the pellets of the samples were prepared using hydraulic press with 140 MPa pressure. For BYSB thickness and diameter of the pellets were 11.92 mm and 1.95 mm, respectively. For BYSN thickness and diameter of the pellets were 8.8 mm and 1.50 mm, respectively. Both the pellets were polished and coated with silver paint on each side. The pellets were then heated at 523 K in order to develop the electrodes for the dielectric measurements. The dielectric measurements were performed using LCR meter (Agilent) at discrete temperatures between 303 K and 663 K and in the frequency range of 40 Hz to 5 MHz. The amplitude of the oscillating voltage was kept at 50 mV during the dielectric measurements. The details of sample preparation technique and experimental methodology have been provided in supplementary information file (ESI).

3. Results

3.1. Structural study

The XRD pattern of BYSB (Fig. 1(a)) agrees well with that reported earlier [39]. In the XRD pattern of BYSN (Fig. 1(b)) few extra peaks other than the Ba_2YbSbO_6 phase have been observed. It is noteworthy that some extra XRD peaks other than its perovskite phase may appear in Ba containing nanosized perovskite oxides synthesized by high energy ball milling technique [14,15]. This extra phase arises due to the formation of orthorhombic $BaCO_3$ phase. The extra peaks observed in the XRD patterns of BYSN (Fig. 1(b)) other than that of the Ba_2YbSbO_6 phase matches well with the orthorhombic $BaCO_3$ phase. Thus, the XRD pattern of BYSN (Fig. 1(b)) indicates the presence of an additional orthorhombic $BaCO_3$ phase in it. The Rietveld refinement of the XRD patterns have been performed using the GSAS software [42]. The crystal structure of Ba_2YbSbO_6 [39] has been chosen as model structure for BYSB. The XRD pattern of BYSN has been analysed by superposing the XRD patterns of Ba_2YbSbO_6 [39] and $BaCO_3$ [14] phases. The refined and the experimental patterns of both BYSB and BYSN are shown in Fig. 1(a) and (b), respectively. It can be observed from the figures that the experimental patterns match well with the calculated ones. The abundance (weight %) of Ba_2YbSbO_6 (Phase 1) and $BaCO_3$ (Phase 2) in BYSN sample has been determined with the help X'Pert Highscore Plus software using the crystallographic information file generated by the GSAS program [43]. The crystal structure refinement parameters of both the samples are presented in Table 1. The Wyckoff positions and the atomic coordinates of BYSB and BYSN (both Ba_2YbSbO_6 and $BaCO_3$ phases) are given in Table 2 and Table 3, respectively.

According to the results of the Rietveld refinement, BYSB is single phase cubic perovskite oxide of $Fm\bar{3}m$ space group with structural formula Ba_2YbSbO_6. On the other hand, BYSN is a nanocomposite composed of two phases: 86.4% Ba_2YbSbO_6 belonging to $Fm\bar{3}m$ space group and 13.6% $BaCO_3$ belonging to *Pmcn* space group. The unit cell and the coordination environment of the constituent cations of BYSB sample are pictorially depicted in Fig. 2 (a) and Fig. 2 (b). The unit cell of BYSB consists of 8 Ba^{2+} (at 8c position), 4 Yb^{3+} (at 2a position), 4 Sb^{5+} (at 2 b position) and 24 O^{2-} (at 24e position) ions. In the unit cell of BYSB (Fig. 2 (a)), A sites are occupied by Ba^{2+} ions and B sites are composed of YbO_6 and SbO_6 octahedra. From Fig. 2 (b) it can be seen that Ba cations are coordinated with 12 oxygen anions and Yb and Sb cations are coordinated with 6 oxygen anions, respectively. The unit cell of BYSB is built up with two pseudocells. Further, it is evident from Fig. 2 (c) that the Yb and Sb ions of the B site are distributed along the (101) plane with repetitive stacking arrangement of Yb–Sb–Yb–Sb ions along the crystallographic c-axis. Thus, BYSB is a 1:1 ordered double perovskite. The unit cell and the coordination environment of Ba_2YbSbO_6 phase (Phase 1) of BYSN is similar to that of BYSB (Fig. S1 of ESI). The unit cell and the coordination environment of the Ba^{2+} ion of $BaCO_3$ phase (Phase 2) of BYSN are depicted in Fig. S2 of ESI. Each Ba cations are coordinated with 9 oxygen anions. The unit cell of $BaCO_3$ consists of 4 Ba^{2+} (at 4c position), $4C^{4+}$ (at 4c position) and 12 O^{2-} ions (4 at 4c and 8 at 8d position). The Ba–O1, Ba–O2, C–O1 and C–O2 bond lengths for $BaCO_3$ phase of BYSN are 2.726, 2.904, 1.3989 and 1.2812 Å, respectively. In case of BYSB the Ba–O, Yb–O and Sb–O bond lengths are 2.9593 Å, 2.226 Å and 1.955 Å, respectively. For the Phase 1 of BYSN the Ba–O, Yb–O and Sb–O bond lengths are 2.9623 Å, 2.23 Å and 2.06 Å, respectively (Table 4). It is evident that there is a stretching of bond lengths in case of Ba_2YbSbO_6 phase of BYSN as compared to BYSB resulting in the lattice elongation in BYSN as compared to BYSB.

High energy ball milling reduces particle size significantly, introduces crystalline defects and lattice disorder at the grain boundary of the sample. This leads to the increase in the internal tensile strain in the

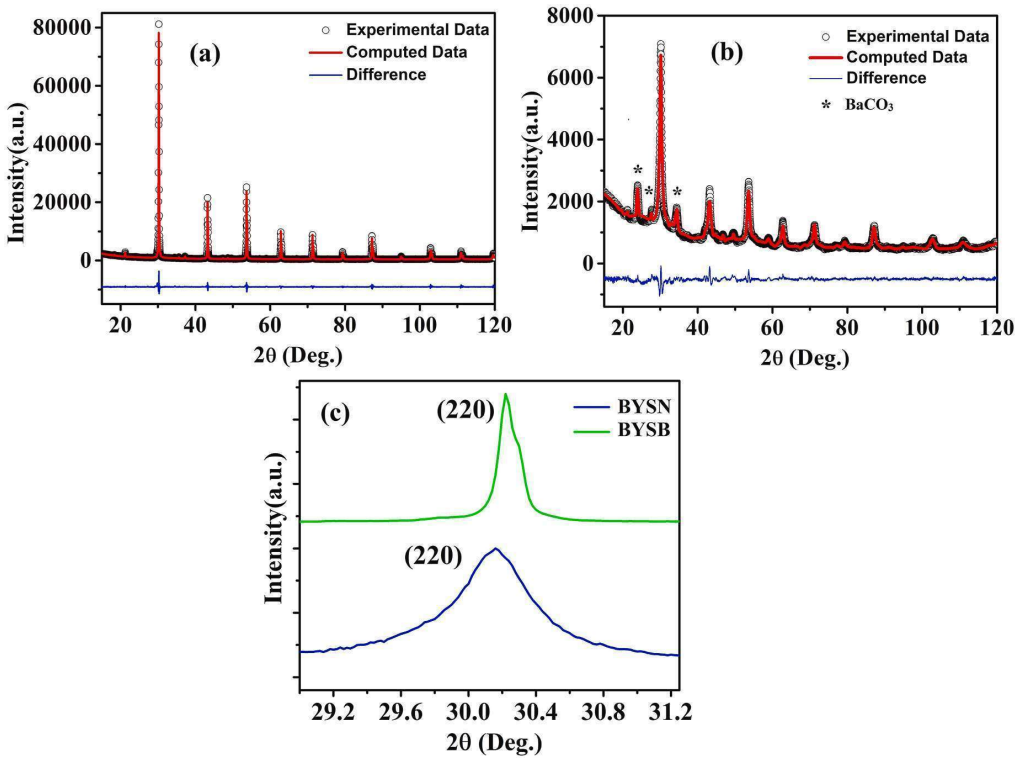

Fig. 1. Rietveld refinement plots of XRD patterns of (a) BYSB, (b) BYSN and (c) the peak broadening and the shift of (220) peak in the BYSN.

Table 1
The Rietveld refinement parameters of BYSB and BYSN.

Parameters	BYSB	BYSN	
		Phase 1 (Ba_2YbSbO_6)	Phase 2 ($BaCO_3$)
Crystal system	Cubic	Cubic	Orthorhombic
Space group	$Fm\bar{3}m$	$Fm\bar{3}m$	*P mcn*
Lattice Parameters (Å)	a = 8.361509 (23)	a = 8.37809(25)	a = 5.3038(11) b = 9.0039(22) c = 6.5136(13)
Volume (Å^3)	584.593(5)	588.08(5)	311.06(11)
α = β = γ(°)	90	90	90
R_{wp}	0.0438	0.0397	
R_p	0.0653	0.0555	
GOF(σ)	2.10	1.71	
Microstrain	2.1800462 × 10^{-5}	1.3066313 × 10^{-4}	
Crystallite size (nm)	201.82	19.16	18.73

Table 2
The Wyckoff positions and atomic coordinates of BYSB.

Atom	site	x (Å)	y (Å)	z (Å)	B (Å^2)
Ba	8c	0.25	0.25	0.25	0.00687
Yb	4a	0.0	0.0	0.0	0.01255
Sb	4b	0.5	0.5	0.5	0.00183
O	24e	0.2662(11)	0.0	0.0	0.01631

sample for the elongation or the contraction of its the crystal lattice [44]. As a result of which the XRD peaks of nanometric samples become broadened and gets shifted as compared to its bulk counterparts [44]. For example, the 220 peak of Ba_2YbSbO_6 phase (Phase 1) of BYSN has

Table 3
The Wyckoff positions and atomic coordinates of BYSN.

Atom	site	x (Å)	y (Å)	z (Å)	B (Å^2)
Phase 1					
Ba	8c	0.25	0.25	0.25	0.00687
Yb	4a	0.0	0.0	0.0	0.01255
Sb	4-b	0.5	0.5	0.5	0.00183
O	24e	0.2542(44)	0.0	0.0	0.01631
Phase 2					
Ba	4c	0.25	0.416	0.756	0.008
C	4c	0.25	0.745	−0.069	0.031
O1	4c	0.25	0.90	−0.076	0.031
O2	8-d	0.46610	0.68140	−0.0779	0.031

been broadened appreciably and has shifted towards lower 2θ angle (from 30.22 to 30.16°) with respect to BYSB (Fig. 1 (c)). This point towards the presence of higher degree of internal tensile strain caused by crystalline defects and surface disorder in Phase 1 of BYSN [44,45]. The peak broadening also indicates that the crystallites of Phase 1 of BYSN are smaller than BYSB. Thus, as a whole the characteristic peak broadening and reduction in intensity of the XRD peaks of BYSN as compared to BYSB can be ascribed to its nanometric size and stress induced enhancement of its lattice strain caused by high energy ball milling. It may be noted that some amount of energy gets transferred during the milling process from the milling balls to the sample being produced. This energy is responsible for the plastic deformation in nanosized samples leading to various crystalline defects like vacancies, stacking defects and dislocations [46]. It may therefore be inferred that in the present case the crystallite size has been reduced and the lattice has been substantially elongated in case of Phase 1 of BYSN (Table 1) as a result of high energy ball milling. This agrees with the results of earlier reports on similar samples [47–49]. Moreover, the higher value of micro strain and

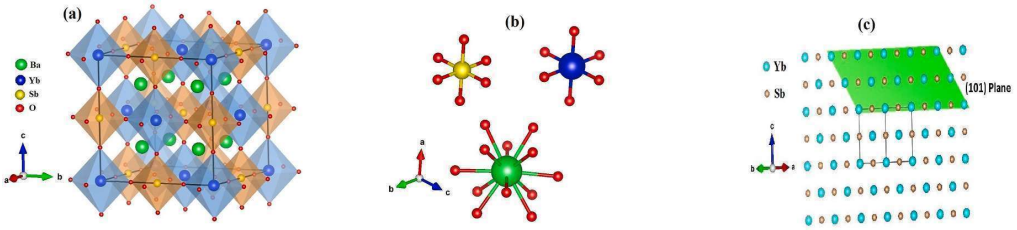

Fig. 2. (a) Unit cell, (b) coordination environments of Ba^{2+}, Yb^{3+} and Sb^{5+} of BYSB sample and (c) ordering sequences of octahedral B site cations of BYSB along the crystallographic c axis.

Table 4
Metal oxygen bond length of BYSB and Ba_2YbSbO_6 phase of BYSN.

Bond	BYSB	BYSN
	Length (Å)	Length (Å)
Ba–O	2.9593(5)	2.9623(5)
Yb–O	2.226(10)	2.13(4)
Sb–O	1.955(10)	2.06(4)

elongation of lattice volume for Phase 1 of BYSN compared to BYSB (Table 1) confirms that in case of BYSN the lattice has been substantially deformed. In Phase 1 of BYSN, atoms in its lattice sites have been dislocated and plastic defects have been created at the surface of its constituent particles due to high energy ball milling [47,48]. Similarly, the large broadening and slight shifting of the XRD peaks of $BaCO_3$ phase (Phase 2) in BYSN compared to bulk $BaCO_3$ suggest that the crystallite size of this phase of BYSN has been reduced and plastic defects has been created at its surface. Thus, the crystallites in BYSN are nanometric in size and have crystalline defects and plastic deformations at its surface.

For Ba containing mechanically activated nanosized perovskite oxide, there is a high chance of $BaCO_3$ formation owing to the spontaneous chemical reaction between the sample and the atmospheric CO_2 adsorbed at its surface [14,15]. In general, the nanometric samples exhibits higher reactivity compared to their bulk counterparts due to their higher surface to volume ratio. Moreover, mechanically activated nanosized sample produced by high energy ball milling tends to exhibit surface phenomena like adsorption of atmospheric gases [15,16]. Formation of high degree of surface defect prone to chemical reaction is the characteristic feature of the mechanically activated nanosized sample [50]. These features are not usually found in nanometric sample prepared by chemical route. It may therefore be concluded that the nanometric Ba_2YbSbO_6 sample synthesized by ball milling, adsorbs atmospheric CO_2. Further, this sample has active sites prone to chemical reactions due to which a part of Ba present in it reacts with surface adsorbed CO_2 and is converted into $BaCO_3$ when kept in normal atmospheric condition.

3.2. Microstructural study

The FESEM images of BYSB and BYSN are shown in Fig. 3 (a) and Fig. 3 (b), respectively. The FESEM image of BYSB (Fig. 3 (a)) indicates that the particles in it are nearly hexagonal in shape with well-defined grain and grain boundaries. The particles in BYSB are of assorted size with average grain size of 1.92 μm. It can be seen from the FESEM image of BYSN (Fig. 3 (b)) that the particles in it are irregular shape and assorted size, which are the characteristic features of mechanically milled nanometric samples [50,51]. The average grain size of BYSN is ~50 nm. It may be noted that we have recorded the TEM (Fig. 4) morphograph of a selective single particle of BYSN in order to visualize the lattice fringes and the presence of surface defects in it. In the TEM morphograph of BYSN the lattice fringes and crystalline defects are clearly visible. The EDS spectra showing the constituent elements of BYSB and BYSN is illustrated in Fig. 5(a) and Fig. 5(b), respectively. The presence of carbon in BYSN is quite evident from Fig. 5 (b) whereas no such peak of carbon has been detected in BYSB. The theoretical mass % of Ba, Yb and Sb in BYSB has been calculated using Ba_2YbSbO_6 as its structural formula (as determined from the results of XRD study) whereas the same for BYSN has been determined considering the ratio of its constituent phases (86.4% Ba_2YbSbO_6 and 13.6% $BaCO_3$ as determined from the results of XRD study). As the quantity of lighter elements

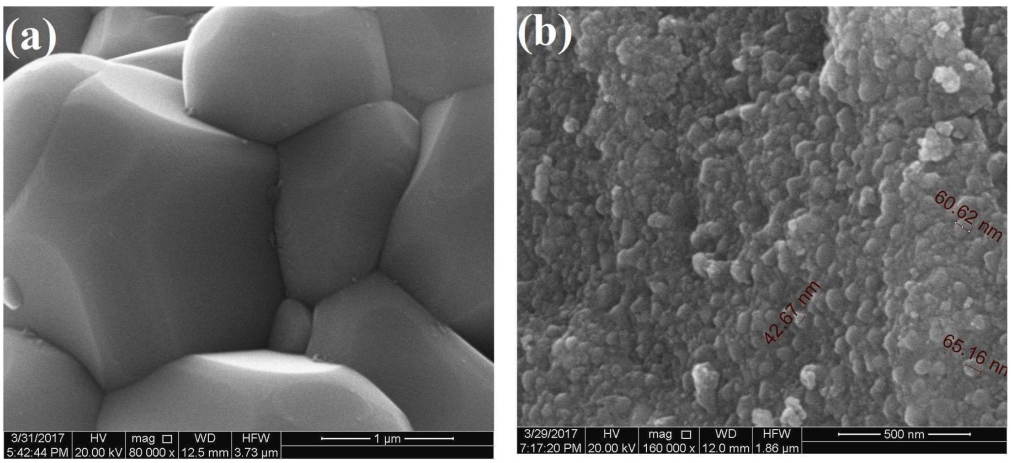

Fig. 3. The scanning electron micrograph of (a) BYSB and (b) BYSN.

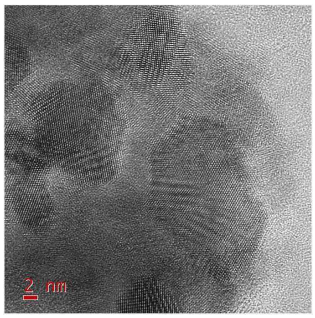

Fig. 4. TEM image of BYSN.

like oxygen and carbon in a species cannot be accurately determined by EDS, therefore we have compared the theoretical and the experimental mass % of Ba, Yb and Sb only. The experimental and the theoretical values of mass % of Ba, Yb and Sb agree well with each other (Table 5).

3.3. FTIR study

The FTIR spectra of both BYSB and BYSN are illustrated in Fig. 6 (a) and Fig. 6 (b), respectively. The FTIR spectrum of BYSB is in consonance with that of Ba_2YbSbO_6 as reported earlier [38]. In the FTIR spectrum of BYSN some additional peaks for $BaCO_3$ phase have been observed along with the peaks for Ba_2YbSbO_6 phase. For both the samples, the bands for the BO_6 octahedra have been obtained in between 400 and 600 cm^{-1}. For both BYSB and BYSN the band obtained at around 460 cm^{-1} is associated with the asymmetric bending modes of the Yb–O and Sb–O bonds belonging to SbO_6 and YbO_6 octahedra, respectively. For both the samples the asymmetric stretching modes of the Yb–O bond of YbO_6 octahedra and Sb–O bond of SbO_6 octahedra gives rise to the intense band at around 614 cm^{-1}. The band centered around 772 cm^{-1} in the spectra of both the samples can be ascribed to the symmetric stretching mode of the SbO_6 octahedra [52]. The six Yb–O bonds of YbO_6 octahedra and six Sb–O bonds of SbO_6 octahedra differ slightly in length due to which the FTIR absorption peaks associated with these bonds appear in close proximity. As a result of this the bands due to Yb–O and Sb–O bonds are broad in nature.

In the FTIR spectrum of BYSN in addition to the bands due to Ba_2YbSbO_6 phase some extra bands have been observed at around 857 (s), 1059 (s), 1422 (s) and 3315 (w) cm^{-1}. It may be noted that the XRD and EDS studies have revealed that BYSN is a nanocomposite of Ba_2YbSbO_6-$BaCO_3$. In the FTIR spectrum of BYSN the wavelength of the extra peaks matches well with those of pure $BaCO_3$ [53]. Further, according to the theoretical calculation $BaCO_3$ gives rise to the peaks at ~892 and 1010 cm^{-1} due to vibrational modes [54]. Therefore, for BYSN the peaks at about 857 and 1059 cm^{-1} can be attributed to the presence of $BaCO_3$ in it. This further corroborates the results of the XRD and EDS studies. The weak and broad band at around 3315 cm^{-1} arises due to the surface adsorbed CO_2 [55]. The band observed at ~1422 cm^{-1} in BYSN can be attributed to the bending mode of the surface adsorbed H_2O and CO_2 [54]. These results indicate that the nanometric

Table 5
EDX results of BYSB and BYSN.

Element	BYSB Theoretical mass %	BYSB Experimental mass %	BYSN Theoretical mass %	BYSN Experimental mass %
Ba	41.27	42.05	45.13	44.40
Yb	26	26.15	22.47	23.02
Sb	18.30	17.50	15.81	16.79

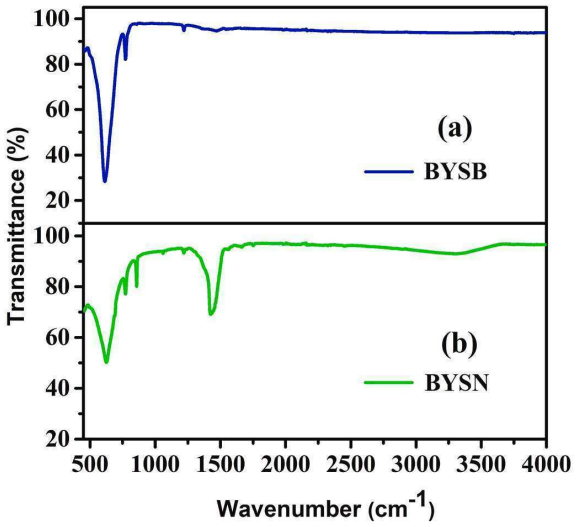

Fig. 6. The FTIR spectrum of (a) BYSB and (b) BYSN.

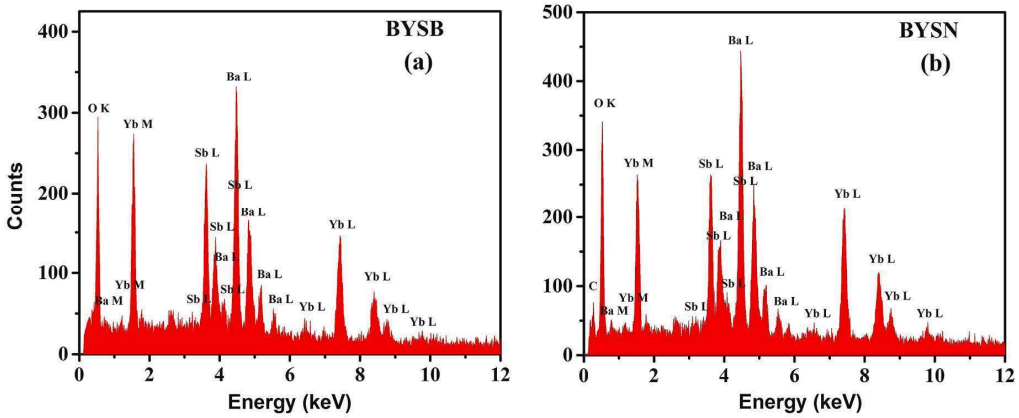

Fig. 5. EDS spectra of (a) BYSB and (b) BYSN.

Ba_2YbSbO_6 prepared by high energy ball milling method adsorbs arial CO_2 and H_2O [54]. Further, the surface adsorbed CO_2 reacts with a part of Ba of nanometric Ba_2YbSbO_6 to form a nanocomposite of Ba_2YbSbO_6 and $BaCO_3$. In the milled nanometric sample the existence of large surface area and active sites favours the formation of $BaCO_3$ [54]. Thus, the results of the FTIR study confirms the formation of a nanocomposite of Ba_2YbSbO_6-$BaCO_3$ from mechanically activated nanosized Ba_2YbSbO_6, which corroborates the results of the XRD study.

3.4. Raman study

The room temperature Raman spectra of BYSB and BYSN are shown in Fig. 7 (a) and Fig. 7 (b), respectively, and their corresponding Lorentzian peak analysis is illustrated in Fig. 8 (a) and Fig. 8 (b), respectively. The peak positions and the full width at half maxima (FWHM) as obtained from the Lorentzian fitting are presented in Table 6. The spectrum of BYSB is dominated by four strong bands centered at 117, 385, 597 and 772 cm^{-1} along with other weaker bands. These four prominent bands of BYSB matches well with those reported for analogous cubic perovskite oxides like Ba_2YbNbO_6, Ba_2ErSbO_6 and Ba_2YbTaO_6 [56–58]. The Raman modes of BYSB as listed in Table 6 are in consonance with the earlier reports on similar systems [56–58]. The lattice vibrational modes of BYSB have been determined with the help of the group factor analysis using the Wykoff sites of the atoms obtained from the XRD study (Table 7). The expected phonon modes for BYSB having $Fm\bar{3}m$ space group (O_h^5) are: $\Gamma = A_{1g}+E_g+F_{1g}+2F_{2g}+5F_{1u}+F_{2u}$, where the four modes viz., A_{1g}, E_g, $2F_{2g}$ are Raman active, four F_{1u} modes are IR active, F_{1u} is acoustic mode and F_{1g} and F_{2u} are silent modes. The intense peaks at 772 cm^{-1} and 597 cm^{-1} appears due to the vibration of O ions along the Yb–O–Sb bond axis. The peak at around 772 cm^{-1} arises due to the symmetric stretching vibration of SbO_6 octahedra and it corresponds to the A_{1g} mode. The antisymmetric stretching vibration of the SbO_6 octahedra gives rise to the E_g mode at 597 cm^{-1}. The symmetric bending vibration of SbO_6 octahedra corresponding to the F_{2g} mode is obtained at ~385 cm^{-1}. The peak at around 117 cm^{-1} corresponds to the F_{2g} mode and arises due to the vibrations of the Ba ions. The weaker bands in the Raman spectra of the samples may be attributed to the second-ordered features [57]. Comparing the obtained Raman modes of BYSB with those of Ba_2YbNbO_6 (BYN) and Ba_2YbTaO_6 (BYT) reported earlier [56,58], it is found that the low frequency modes associated with the vibration of B-site atoms of BYSB are observed at higher wavelength than those of BYT but at lower wavelength than those of BYN. It may be noted that all the B″-site ions of BYSB, BYN and BYT are pentavalent and their ionic mass is in the order

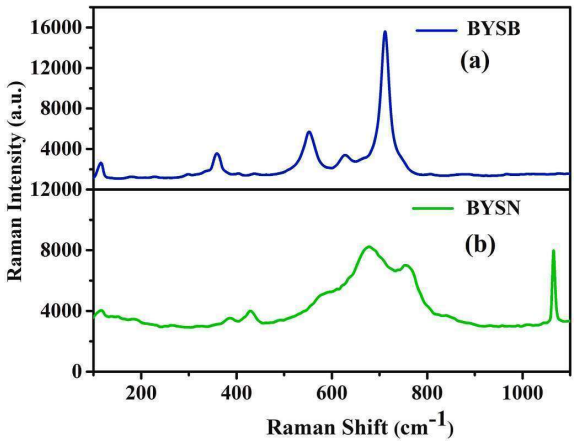

Fig. 7. The Raman spectra of (a) BYSB and (b) BYSN.

Ta > Sb > Nb. Thus, the shifting of Raman modes of these three samples can be attributed to the difference of ionic mass of their B″-site atoms. The difference in the interatomic forces of BYSB, BYN and BYT are also responsible for the difference in the wavelength of the Raman modes of these samples having analogous structure. The cubic double perovskite is usually characterized by the intense A_{1g} mode whereas the lower symmetry perovskites are usually characterized by the splitting of the F_{2g} modes [58]. There is no splitting of the F_{2g} modes of BYSB which confirms its cubic structure.

In the Raman spectrum of BYSN all the characteristic Raman modes of BYSB are present but their intensity has been significantly reduced due to the lowering of crystallite size. In case of BYSN besides the peak for Ba_2YbSbO_6 phase, two extra peaks have been obtained around 630 cm^{-1} and 1065 cm^{-1} due to the presence of $BaCO_3$ in it. The wavelength of these peaks agrees well with the Raman spectra of single phase $BaCO_3$ reported in literature [53]. Thus, the results of Raman spectroscopic study are in full agreement with the findings of XRD, EDS and FTIR studies of BYSB and BYSN.

3.5. Thermogravimetric study

The thermogravimetric analysis of BYSB and BYSN samples have been carried out in the temperature range of 303–973 K in order to study their thermal stability. The TGA curves of BYSB and BYSN are illustrated in Fig. 9(a) and Fig. 9(b), respectively. From the TGA and its derivative curve of BYSB (Fig. 9(a)) it is evident that the sample releases adsorbed atmospheric moisture at 340 K beyond which no appreciable weight loss has been observed up to 973 K (the highest temperature of measurement). This indicates that BYSB remains chemically stable up to 973 K. For BYSN the initial weight loss at 331 K can be attributed to the loss of surface adsorbed moisture and the weight loss in the temperature range of 370–800 K can be ascribed to the release of surface adsorbed CO_2 (Fig. 9(b)). It can be seen from the TGA and its derivative curve of BYSN (Fig. 9(b)) that a significant weight loss has occurred at 926 K due to the decomposition of $BaCO_3$ present in it. It may be noted that decomposition temperature of pillar like nanosized $BaCO_3$ (having diameter 20–40 nm and length 40–80 nm) is ~1073 K [59]. However, the decomposition temperature of $BaCO_3$ in BYSN having 50 nm size and irregular shape differs from its pure pillar like counterpart as they are morphologically different and in case of BYSN it is present in a nanocomposite form. Thus, the results of TGA study commensurate with those of XRD, EDS, FTIR and Raman studies.

3.6. Dielectric study

The variation of the dielectric constant (ε′) and the loss tangent (tan δ) with logarithmic angular frequency (log ω) at different temperatures are plotted in Fig. 10 (a) and Fig. 11 (a) for BYSB and BYSN, respectively. In case of BYSB, the value of ε′ increases with increase in temperature. The ε′ values for both the samples decreases with increase in frequency. The dipoles in the sample direct themselves along the applied field when the frequency is low and contributes to the total polarization. This results in the high value of ε′ at low frequency. At high frequency the dipoles are unable to align themselves along the applied field as the field changes rapidly. Due to this the values of ε′ becomes low and almost independent of temperature at high frequencies. Thus, all the ε′ versus log ω curves of BYSB merges together at higher frequencies (Fig. 10(a)). As shown in Figs. 10 (a) and Fig. 11(a), the value of ε′ decreases with the increase in the frequency and in the dispersion region of the ε′, a relaxation peak in the tan δ (= ε′′/ε′) curve can be observed. In BYSB the value of ε′ increases with temperature indicating that the rate of polarization is higher at higher temperatures (Fig. 10(b)). Thus, the relaxation peaks shift towards higher frequencies with increase in temperature (Fig. 10(a)). The broad nature of the tan δ curve indicates polydispersive nature of the dielectric relaxation in these samples. In the low frequency region, the tan δ values of BYSB shows a slight increasing

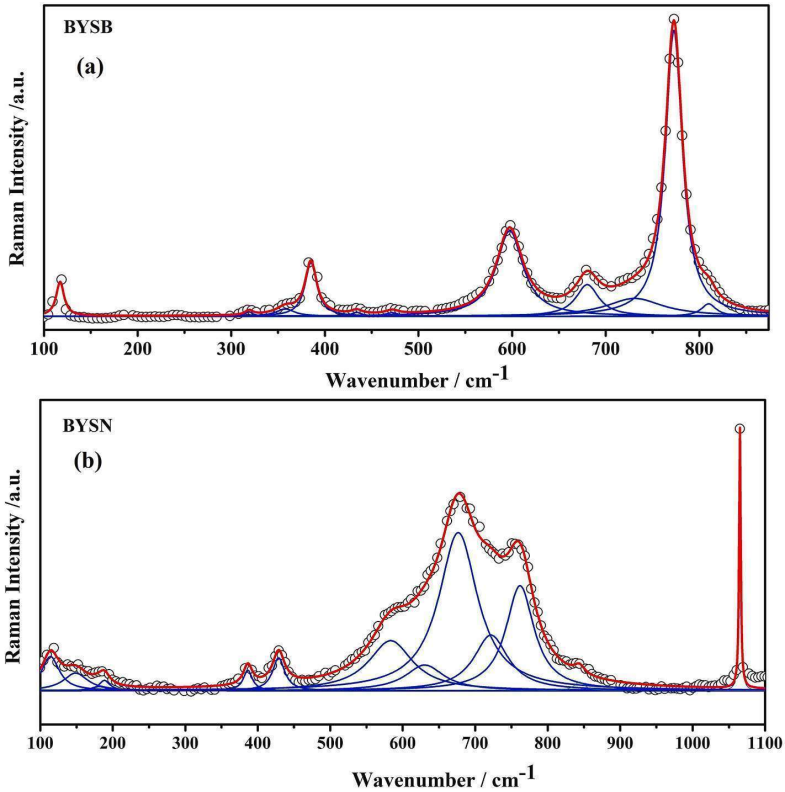

Fig. 8. The Lorentzian fitting profiles of Raman spectra of (a) BYSB and (b) BYSN.

Table 6
Experimental Raman active modes.

	BYSB		BYSN	
	Frequency (cm^{-1})	FWHM (cm^{-1})	Frequency (cm^{-1})	FWHM (cm^{-1})
1	117.19936	10.08201	114.0711	29.41374
2	319.11887	9.98758	148.73972	40.88322
3	357.85036	24.13656	181.42688	25.3368
4	385.07184	15.21006	188.6309	18.22145
5	434.03625	13.78611	386.33556	15.13371
6	471.76312	17.07898	428.76496	20.33834
7	597.44298	34.37726	583.41594	73.40917
8	680.31262	29.60329	630.35296	64.69664
9	730.92477	73.53594	676.55511	65.17666
10	772.8061	22.0445	721.80107	57.66746
11	809.97301	19.43274	761.82933	47.39736
12			843.86522	17.42211
13			1065.16	2.66322

Table 7
Distribution of modes for cubic BYSB.

Atom	Wyckoff Site	Symmetry	Distribution of modes
Ba	8c	T_d	$F_{1u} + F_{2g}$
Yb	4a	O_h	F_{1u}
Sb	4b	O_h	F_{1u}
O	24e	C_{4v}	$A_{1g} + F_{2g} + E_g + 2F_{1u} + F_{2u} + F_{1g}$
Γ_{TOTAL}			$A_{1g} + E_g + F_{1g} + 2F_{2g} + 5F_{1u} + F_{2u}$
$\Gamma_{ACOUSTIC}$			$1F_{1u}$
Γ_{RAMAN}			$A_{1g} + E_g + 2F_{2g}$
Γ_{IR}			$4F_{1u}$
Γ_{SILENT}			$F_{1g} + F_{2u}$

trend while for BYSN the tan δ values increases sharply. This indicates that dc conductivity influences the dielectric response of BYSB (slightly) and BYSN (strongly) [60]. Thus, we have examined the dielectric relaxation process occurring in these samples with the help of the modified Cole-Cole model taking into account the effect of dc conductivity [61–63]. According to modified Cole-Cole model the complex dielectric permittivity (ε^*) is given by:

$$\varepsilon^* = \varepsilon_\infty + \frac{\varepsilon_s - \varepsilon_\infty}{1 + (i\omega\tau)^{1-\alpha}} - i\frac{\sigma*}{\varepsilon_0\omega^n} \tag{1}$$

where σ* is the complex conductivity (σ*= ($\sigma_1 + i\sigma_2$)) with σ_1 denoting the dc conductivity and σ_2 denoting the conductivity for the localized charges. As $\varepsilon^* = \varepsilon' - i\varepsilon''$, the above equation (1) can be written in terms of the real and the imaginary part as,

$$\varepsilon' = \varepsilon_\infty + \frac{(\varepsilon_s - \varepsilon_\infty)\left[1 + (\omega\tau)^{1-\alpha} \sin\frac{1}{2}\alpha\pi\right]}{1 + 2(\omega\tau)^{1-\alpha} \sin\frac{1}{2}\alpha\pi + (\omega\tau)^{2(1-\alpha)}} - \frac{\sigma_2}{\varepsilon_0\omega^n} \tag{2}$$

$$\varepsilon'' = \frac{(\varepsilon_s - \varepsilon_\infty)(\omega\tau)^{1-\alpha} \cos\frac{1}{2}\alpha\pi}{1 + 2(\omega\tau)^{1-\alpha} \sin\frac{1}{2}\alpha\pi + (\omega\tau)^{2(1-\alpha)}} + \frac{\sigma_1}{\varepsilon_0\omega^n} \tag{3}$$

where ε_s and ε_∞ are the low and the high frequency values of the dielectric permittivity, τ represents the relaxation time, the distribution of the relaxation time is represented by the parameter α and the term n denotes the frequency exponent. equation (3) represents dielectric loss where the first term arises due to the relaxation of permanent dipoles and the second term arises due to the losses associated with the movement of charge carriers. equations (2) and (3) have been utilized to fit the experimental ε′ verses log ω and tan δ verses log ω curves of both

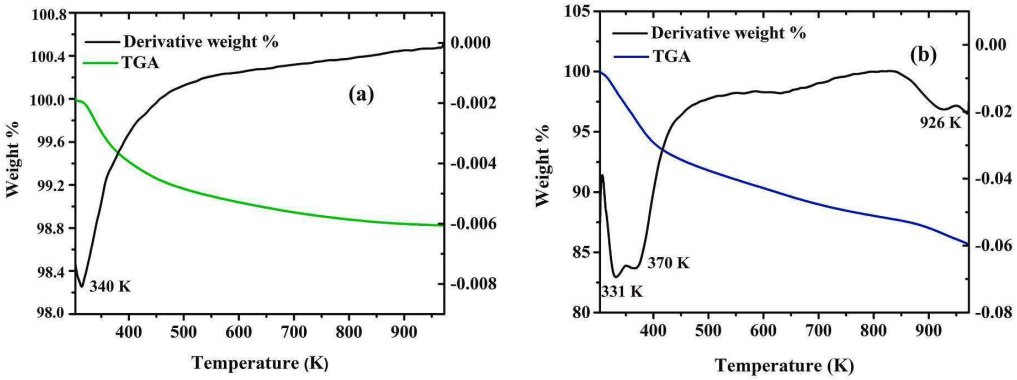

Fig. 9. The TGA curves of (a) BYSB and (b) BYSN.

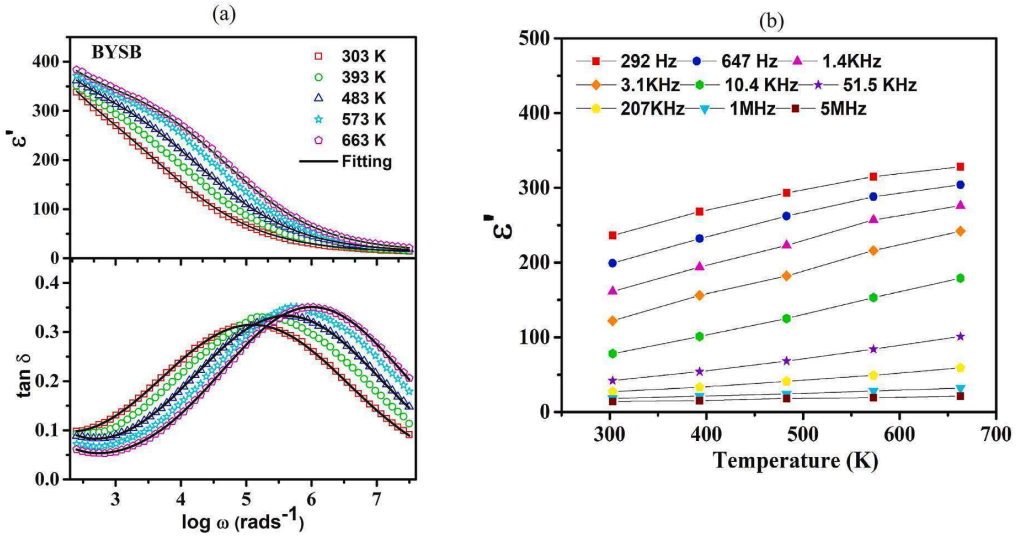

Fig. 10. (a) The variation of ε′ and tan δ with log ω and (b) the variation of ε′ with temperature for BYSB.

BYSB and BYSN. The fitted curves are shown by black lines in Figs. 10 (a) and Fig. 11(a) and the parameters obtained from fitting are given in Table 8. It can be observed from Table 8 that the value of α is non zero indicating a dispersal of the relaxation time. Thus, the relaxation mechanism of both BYSB and BYSN are polydispersive in nature and non-Debye type (α value is zero for Debye type relaxation) [60].

The ε′ verses log ω curves of BYSN exhibits a strong hump at 393 K and above this temperature the values of ε′ values start decreasing as temperature increases (Fig. 11 (a) and Fig. 11 (b)). The peak in the tan δ verses log ω curves of BYSN shifts towards higher frequency region with increase in temperature till 393 K and above it the peak shifts towards lower frequency region with increase in temperature. Thus, BYSN exhibits drastically different dielectric response below and above 393 K. This anomalous behaviour has not been observed for BYSB. It is noteworthy that the results of FTIR study suggests the presence of adsorbed CO_2 in BYSN. The TGA study suggests that BYSN releases adsorbed CO_2 between 370 K and 800 K. Thus, the anomalous dielectric behaviour shown by BYSN above 393 K can be attributed to the continuous release of surface adsorbed atmospheric CO_2 as temperature increases beyond 393 K. This further confirms the presence of CO_2 in BYSN below 393 K while BYSB does not have any trapped CO_2 as has been revealed by their XRD, EDS, FTIR, Raman and TGA studies. The decrease in the ε′ values after 393 K is indicative of the decrease in the amount of the charge carriers in BYSN above this temperature [64]. Thus, it can be inferred that CO_2 present in BYSN contributes to the charge carrier production and with its reduction above 393 K leads to the decrease in ε′ with increase in temperature. Therefore, BYSN exhibits anomalous dielectric behaviour above 393 K as CO_2 adsorbed by it starts escaping above this temperature.

The ε′ verses temperature (T) plots of both BYSB and BYSN at some discrete frequencies are shown in Figs. 10 (b) and Fig.11 (b), respectively. For BYSB it can be observed that as temperature increases ε′ increases (Fig. 10 (b)) and the increase is much more prominent at lower frequencies (between 292 Hz and 207 KHz). In case of BYSB mainly the Maxwell- Wagner polarization around the grain boundaries gives rise to its high value of ε′ at low frequencies [65]. Further, Schottky barrier layer with high contact capacitance and resistance is formed between the sample and electrode where charge accumulation takes place, which may also contribute to the high value of ε′ at low frequencies [65,66]. The capacitance of BYSB becomes almost independent of temperature at higher frequencies and the slight increase in ε′ with increase of temperature between 1 and 5 MHz results from the ion migration [67]. The

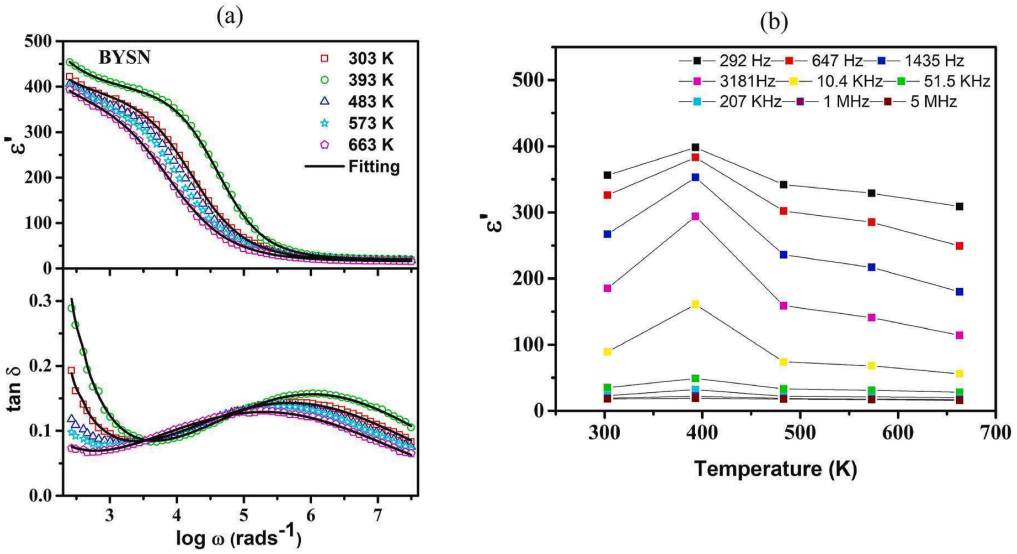

Fig. 11. (a) The variation of ε′ and tan δ with log ω and (b) the variation of ε′ with temperature for BYSN.

Table 8
The Cole-Cole fitting parameters of BYSB and BYSN.

Temperature (K)	ε_s	ε_∞	ω_m (Hz)	α	n	σ_1 (Sm^{-1})	σ_2 (Sm^{-1})
BYSB							
303	350	12	5500	0.46	0.8	0.1×10^{-7}	0.3×10^{-7}
393	358	12.5	19500	0.45	0.85	0.2×10^{-7}	0.3×10^{-7}
663	366	13	51520	0.44	0.9	0.2×10^{-7}	0.4×10^{-7}
BYSN							
303	390	18	16755	0.55	0.94	0.1×10^{-6}	5×10^{-8}
393	400	20	41241	0.54	0.95	0.2×10^{-6}	8×10^{-8}
663	380	16	5522	0.56	0.92	0.2×10^{-7}	4×10^{-8}

ε′ verses T curves of BYSN exhibits a peak at 393 K up to 207 KHz frequency. At higher frequencies (1 and 5 MHz) the ε′ values of BYSN remains almost constant with increase in temperature as observed in case of BYSB. These indicates that BYSN exhibits anamolous dielectric response above 393 K as has been noticed in its frequency dependent dielectric response at discrete temperatures.

For BYSB and BYSN the variation of log ω_m (the frequency at which the peak in the tan δ verses log ω curves have been observed) with the inverse of temperature has been depicted in Fig. 12 (a) and Fig. 12 (b), respectively. We have plotted log ω_m vs. 1000/T curve of BYSN in the temperature range of 303–393 K as it exhibits anomalous dielectric behaviour above this temperature. The log ω_m vs. 1000/T plots of both BYSB and BYSN follows the Arrhenius equation $\omega_m = \omega_0 \exp[-\frac{E_A}{K_B T}]$. The value of activation energy E_A is found to be 0.23 eV for BYSB and 0.21 eV for BYSN. The activation energy values indicates that electrical transport mechanism in both the samples is associated with hopping of p-type polarons [68,69].

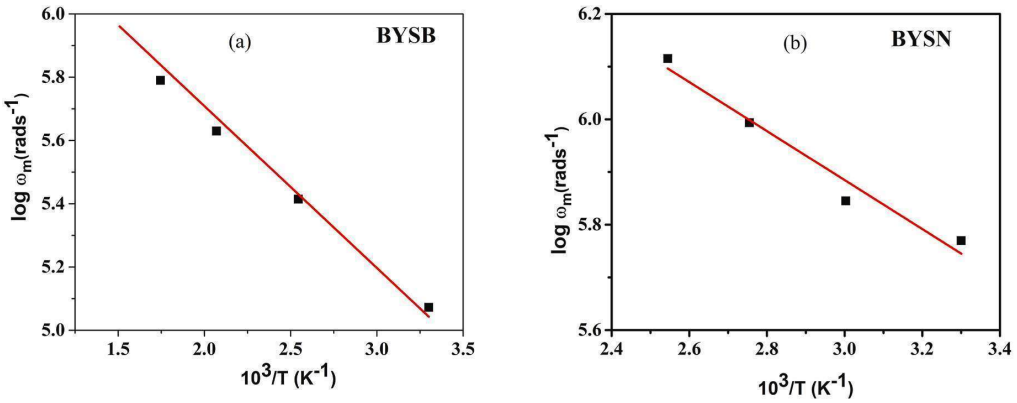

Fig. 12. Arrhenius plot of the most probable relaxation time ω_m for (a) BYSB and (b) BYSN.

3.7. Impedance study

The complex impedance plane plots of both BYSB and BYSN at room temperature have been depicted in Fig. 13 (a) and Fig. 13 (b), respectively. The overall contribution of the grain and the grain boundary to the total impedance is evident from the presence of two distinct depressed semi-circular arc in the Nyquist plots of both BYSB and BYSN [60]. The well-defined grains and the grain boundaries are found in the FESEM images of both BYSB and BYSN. In the impedance plots the grain effect is manifested by the high frequency arc whereas the grain boundary effect is represented by the low frequency arc. The samples possessing polydispersive type of relaxation exhibit deformed semi-circular arc having centre below the Z′ axis as seen in our samples [70–74]. In order to separate the grain and the grain boundary contributions, the experimental impedance plots have been fitted with equivalent electrical circuit comprising of two parallel resistor-capacitor elements connected together in series as shown in the inset of Fig. 13 (a) and Fig. 13 (b). To account for the polydispersive nature of the relaxation process exhibited by the samples we have used a constant phase element (Q) in the model circuit in place of the capacitor element. C_p is the capacitance of constant phase element and is given by $C_p = Q^{1/c} R^{(1-c)/c}$, where the constant c accounts for the non-ideal behaviour of the sample. The value of c is 1 for ideal capacitance and 0 for ideal resistance. The impedance plots have been fitted using the formula:

$$Z' = \frac{R_g}{1+\left[\omega\left(R_g Q_g\right)^{\frac{1}{c_g}}\right]^2} + \frac{R_{gb}}{1+\left[\omega\left(R_{gb} Q_{gb}\right)^{\frac{1}{c_{gb}}}\right]^2} \quad (4)$$

and

$$Z'' = R_g\left[\frac{\omega\left(R_g Q_g\right)^{\frac{1}{c_g}}}{1+\left[\omega\left(R_g Q_g\right)^{\frac{1}{c_g}}\right]^2}\right] + R_{gb}\left[\frac{\omega\left(R_{gb} Q_{gb}\right)^{\frac{1}{c_{gb}}}}{1+\left[\omega\left(R_{gb} Q_{gb}\right)^{\frac{1}{c_{gb}}}\right]^2}\right] \quad (5)$$

where R and Q denotes the resistance and the constant phase element with suffix g and gb for the grain and the grain boundary contributions, respectively. The results have been summarized in Table 9. It can be observed from Table 9 that the grain boundaries are comparatively more insulating than the grains because of the inhomogeneous distribution of the charge carriers around the grain boundaries [75]. The grain boundaries behaving like a trap to the moving charge carriers results in its high impedance values [76]. As BYSN has a greater number of grain boundaries owing to its nanometric size, it offers more barrier to the charge transport. This results in the impedance values of BYSN to be greater than that of BYSB.

Table 9
The fitted parameters for the impedance plots for BYSB and BYSN at room temperature.

	Temp. (K)	R_g (Ω)	Q_g (10^{-10} F/Ω)	c_g	R_{gb} (10^7 Ω)	Q_{gb} (10^{-11} F/Ω)	c_{gb}
BYSB	303	750000	7	0.8	30	9.5	0.85
BYSN	303	1200000	9	0.82	75	6.8	0.88

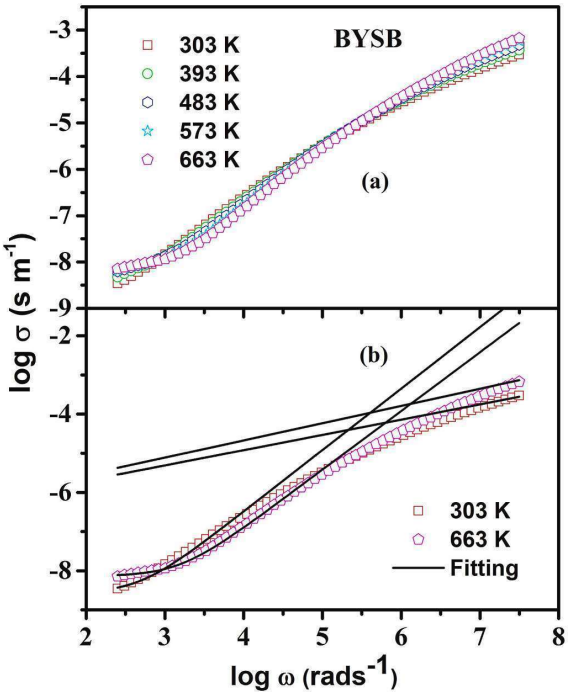

Fig. 14. (a) The variation of ac conductivity with log ω and (b) power law fitting of conductivity spectra for BYSB.

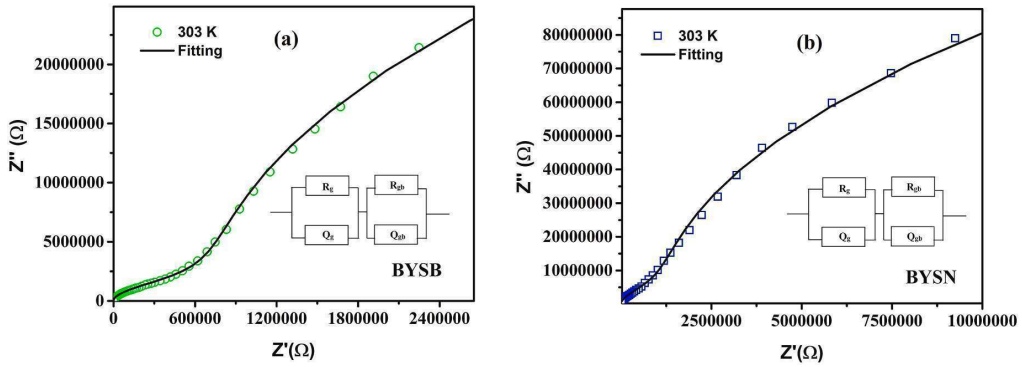

Fig. 13. Complex impedance plane plots of (a) BYSB and (b) BYSN.

3.8. Conductivity study

The frequency dependence of the ac conductivity at different temperatures for both BYSB and BYSN has been illustrated in Fig. 14 (a) and Fig. 15(a), respectively. Two plateaus can be observed in the conductivity plots of both the samples which are representative of two processes responsible for the bulk conduction. At low frequency the conductivity tends towards a constant value which is termed as the dc conductivity (σ_{dc}) [77]. At low frequency the periodicity of the field is low, which causes the accumulation of charge carriers giving rise to the dc conductivity [60]. In the higher frequency region, the rapid change in the conductivity is due to the commencement of conductivity relaxation process. As per the results of the dielectric property study, the p-type polaron hopping caused by electric field governs the dielectric behaviour of the samples. Further, the difference in the potential energies at grains and grain boundaries creates trap sites, which acts as potential barriers towards the charge carriers [60]. Again, the higher value of grain boundary resistance as compared to that of its gain (as has been observed in the impendence study) results in transport of polaron by hopping from one site to another [60]. Thus, the conductivity of the samples increases with increase in frequency. However, in the high frequency region the conductivity value becomes constant as the polarons get trapped in sites having infinite barrier on each side and they start moving back and forth locally [78].

The variation of the conductivity with frequency can be examined with the help of the power law $\sigma(\omega) = \sigma_{dc} + A\,\omega^{n}$, where the A and n are the constants dependent on temperature and frequency [79]. We have fitted the conductivity spectra of both the samples recorded at all the temperatures. However, in Figs. 14 (b) and Fig. 15 (b) we have only shown two representative fitted curves at two distinct temperatures for each of the samples for the sake of clarity. We have provided the fitting parameters for all the temperatures in Table 10. The parameter A corresponds to the strength of polarizability of the sample and n is related to the degree of interaction between the moving charge carriers and its surrounding lattice [80]. The parameters A and n are temperature dependent. The value of n = 0 when the carriers are free to move through the sample. In the low frequency region, the values of n of both BYSB and BYSN are greater than 1 (Table 10) signifying the charge hopping is localized. On the other hand, for both BYSB and BYSN n is less than 1 in high frequency region indicating translational motion of charge carriers [81].

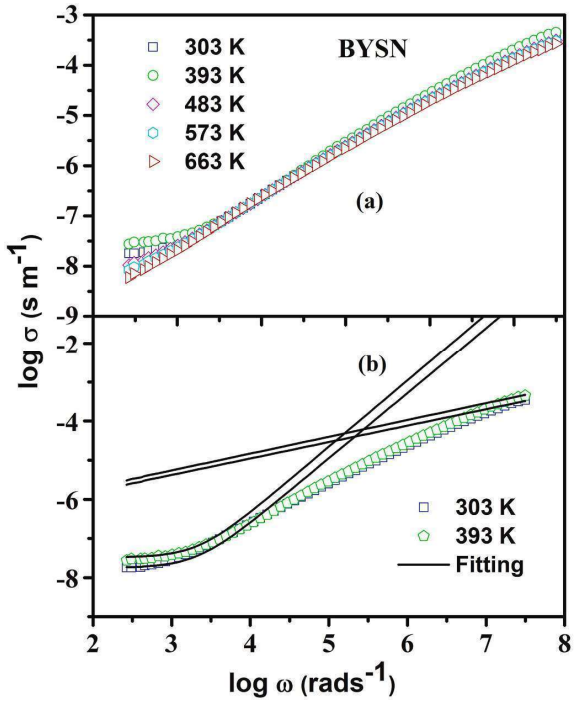

Fig. 15. a) The variation of ac conductivity with log ω and (b) power law fitting of conductivity spectra for BYSN.

The temperature variation of n1 (the values of n at low frequency region) and n2 (the values of n at high frequency region) for both BYSB and BYSN have been shown in Fig. 16 (a) and Fig. 16 (b), respectively. For BYSB, n1 decreases with temperature which agrees with the correlated barrier hopping model (CBH) and n2 increases with temperature which is in agreement with the non-overlapping small polaron tunnelling model (NSPT) [64]. According to CBH model conduction occurs due to the hopping of charge carriers from one defect site to another separated by coulomb barrier [82]. As per NSPT model small polaron formation takes place due to the lattice distortions caused by the accumulation of charge carriers at the lattice site [82]. In BYSN the values n1 and n2 increase initially till 393 K and then they decrease between 393 and 483 K. Such anomalous behaviour of BYSN above 393 K has also been observed in its dielectric response and this can be attributed to the continuous release of CO_2 above 393 K. It may be noted that for BYSN the values of n1 and n2 are independent of temperature beyond 483 K indicating a decrease in the interaction among the charge carriers. This corroborates the finding that amount of charge carrier in BYSN decreases above 393 K as seen in the dielectric study.

The temperature variation of A1 (the values of A in low frequency region) and A2 (the values of A in high frequency region) for BYSB and BYSN have been shown in Fig. 17 (a) and Fig. 17 (b), respectively. For BYSB the values of A1 and A2 increase with increase in temperature indicating an enhancement in its polarizability [83]. For BYSN, A1 increases rapidly up to 483 K and above this temperature it increases very slowly. The A2 verses T curve of BYSN shows a peak at 393 K indicative of maximum polarizability at this temperature. This anomalous behaviour observed for temperature dependence of A1 and A2 of BYSN also corroborates with the results of its dielectric study.

3.9. Electrical modulus study

The linear frequency (f) dependence of M′ and M″ of BYSB are shown in Fig. 18(a) and Fig. 18 (b), respectively. Fig. 19 (a) and Fig. 19 (b) display the linear frequency dependence of M′ and M″ of BYSN, respectively. The value of M′ decreases with decrease in frequency and approaches zero at all temperatures indicating that the electrode polarization is absent in the samples [84]. The dispersion observed in the M′ curves arises due to the conductivity relaxation. The presence of short-range charge carriers is evident from the sigmoid nature of the M′ curves [85]. At high frequencies M′ tends to saturate due to the absence of any restoring force controlling the movement of charge carriers in the induced electric field [86,87]. Under these circumstances, the charge carriers can migrate over long distances indicating existence of long-range charge carriers [88]. The saturation of M′ curves at high frequencies also indicates the discharging of space charge polarization [86].

M″ verses f plots of both the samples exhibit prominent peaks (Figs. 18 (b) and Fig. 19(b)) which are broad and asymmetric in nature pointing towards non-Debye relaxation in the samples [87]. This nature of M″ spectrum also indicates that charge carriers in the samples are transported predominantly by hopping mechanism [88]. This corroborates the results of the dielectric study that charge conduction in the samples takes place by hopping of p type polaron. Further, with increase in temperature the peak in the M″ curves of both the samples shifts towards higher frequency indicating the charge carriers are thermally activated and their relaxation rate increases with increase in temperature.

Table 10
The parameters obtained from the fitting of the conductivity spectra for BYSB and BYSN.

Sample	Temperature (K)	σ_{dc} (Sm-1)	A1 (at low frequency)	n1 (at low frequency)	A2 (at high frequency)	n2 (at high frequency)
BYSB	303	2.7×10^{-9}	1.7×10^{-13}	1.57	3.3×10^{-7}	0.39
	393	4.1×10^{-9}	1.8×10^{-13}	1.55	3.6×10^{-7}	0.40
	483	5.8×10^{-9}	1.9×10^{-13}	1.51	3.8×10^{-7}	0.41
	573	6×10^{-9}	2×10^{-13}	1.49	4×10^{-7}	0.42
	663	6.7×10^{-9}	2.1×10^{-13}	1.45	4.05×10^{-7}	0.43
BYSN	303	1.8×10^{-8}	0.5×10^{-13}	1.67	2.3×10^{-7}	0.42
	393	3.3×10^{-8}	0.7×10^{-13}	1.7	2.8×10^{-7}	0.43
	483	1×10^{-8}	1.9×10^{-13}	1.61	2.5×10^{-7}	0.41
	573	0.7×10^{-8}	2×10^{-13}	1.62	2.4×10^{-7}	0.41
	663	0.5×10^{-8}	2.1×10^{-13}	1.62	2.4×10^{-7}	0.40

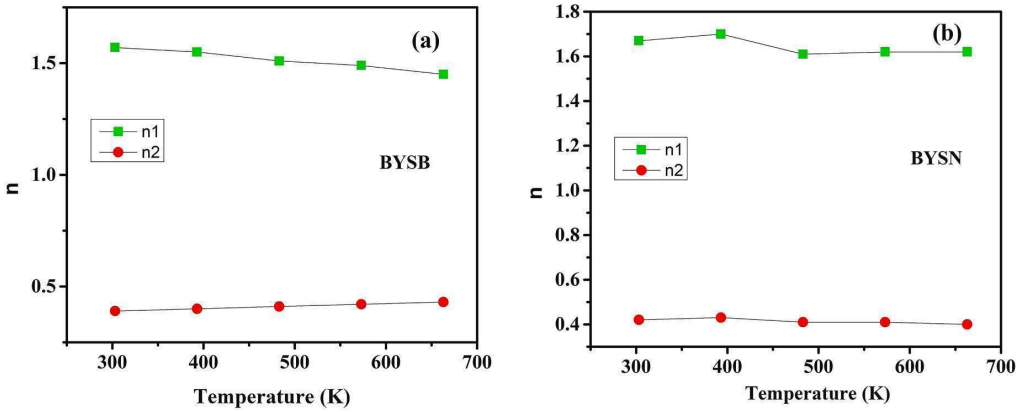

Fig. 16. Temperature dependence of n1 (low frequency) and n2 (high frequency) for (a) BYSB and (b) BYSN.

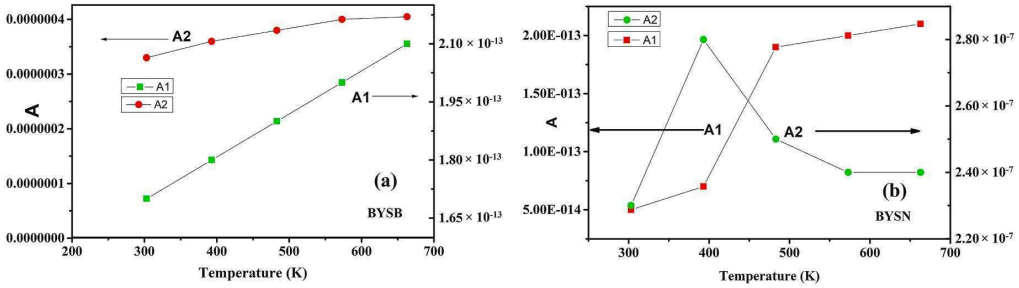

Fig. 17. Temperature dependence of A1 (low frequency) and A2 (high frequency) for (a) BYSB and (b) BYSN.

We have tried to fit the electric modulus spectra of BYSB and BYSN using Cole-Cole model but that lead to unsatisfactory results. On contrary, the dielectric spectra have been successfully analysed by the Cole-Cole model. In this context, it is noteworthy that generally, three angular frequency ($\omega = 2\pi f$) dependent functions viz., complex permittivity: $\varepsilon^*(\omega) = \varepsilon'(\omega) - i\,\varepsilon''(\omega)$, complex electric modulus: $M^*(\omega) = M'(\omega) + i\,M''(\omega)$ and complex conductivity: $\sigma^*(\omega) = \sigma'(\omega) + i\,\sigma''(\omega)$ are used to describe and assess the dielectric behaviour of materials [89]. They are interrelated to each other according to the equation: $M^*(\omega) = 1/\varepsilon^*(f\,\omega) = i\omega\varepsilon_0/\sigma^*(\omega)$ but emphasize different aspects of the same process [89]. Physically, M^* is connected to the electric field (**E**) relaxation inside the material when the dielectric displacement (**D**) remains constant and it describes the actual relaxation. The ε^* is associated with the relaxation of **D** when **E** remains constant and it accounts for the dielectric retardation [90,91]. The details which are not explicitly manifested in one formalism may be noticed in the spectra of other two formalisms [91].

The dc conductivity (σ_{dc}) significantly influences the dielectric and conductivity spectrum but its effect remains masked in the electric modulus spectrum [90,91]. In the dielectric loss spectra, the tan δ tends to increase at low frequency region due the influence of σ_{dc} (as in the present case), which suppresses the structural relaxation process. In such cases, customarily the electric modulus formalism is adopted to examine the dielectric relaxation of the sample. The relaxation time determined from electric modulus corresponds to microscopic relaxation times [89,92]. For non-Debye type relaxation, the relaxation time determined from modulus formalism (τ_m) is supposed to be more accurate than that determined from dielectric permittivity (τ_ε) and $\tau_m > \tau_\varepsilon$ [91].

For the present case tan δ increases (slightly for BYSB and sharply for BYSN) in the low frequency region (Figs. 10 (a) and Fig. 11(a)) due the influence of σ_{dc} whereas in M″ spectrum (Figs. 18 (b) and Fig. 19 (b)) only sharp peaks have been observed. Thus, the above mentioned discussion has insisted us to fit M″ spectra of BYSB and BYSN using

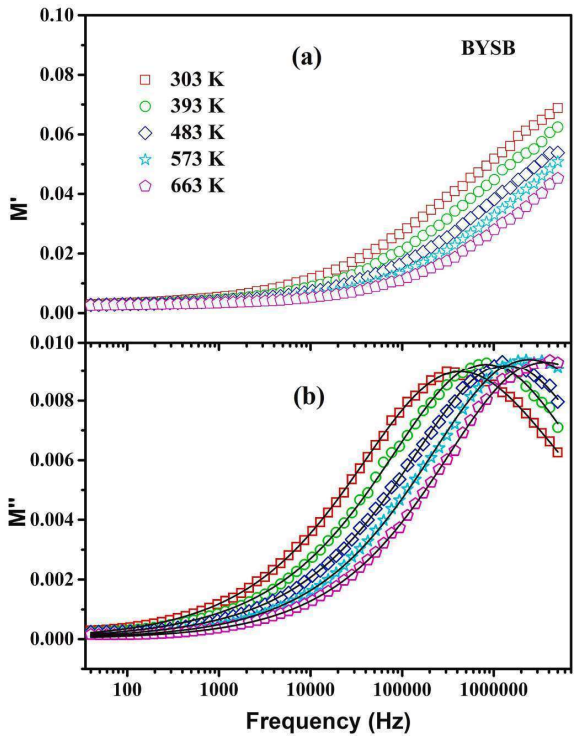

Fig. 18. The variation of (a) M′ and (b) M″ with frequency at different temperatures for BYSB.

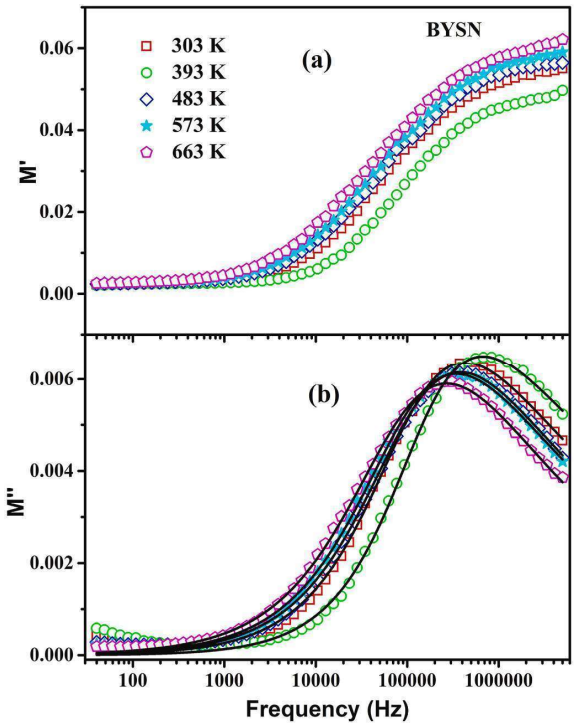

Fig. 19. The variation of (a) M′ and (b) M″ with frequency at different temperatures for BYSN.

Havriliak-Negami (HN) function: $F^{*}_{HN} = \frac{1}{[1+(i\omega\tau_{HN})^{\beta}]^{\gamma}}$, where β and γ are fractional shape parameters representing symmetric and asymmetric broadening of the complex dielectric function. τ_{HN} is the characteristic relaxation time and $\beta\gamma = \beta_{kww}$ is the stretching parameter associated with the relaxation peak. The values of β and γ lies in the range of $0 < \beta \leq 1$ and $0 < \beta\gamma < 1$. At first tan δ verses log ω curves of BYSB and BYSN were fitted using the HN function excluding the low frequency region of those curves. It has been found that for tan δ spectra of both the samples the values of $\gamma \approx 1$, for which the HN function is equivalent to the Cole-Cole function. This justifies the proper fitting of tan δ verses log ω curves of the samples by Cole-Cole model. The M″ spectra are well fitted by HN function and γ lies between 0.58 and 0.95 for BYSB and 0.23–0.39 for BYSN. This reveals that the relaxation peaks of M″ for both the samples is asymmetric in nature and the asymmetry in BYSN is more prominent than BYSB. The effect of σ_{dc} is much more prominent in BYSN than BYSB which can be seen from the sharp increase of tan δ values of BYSN as compared to slow increase of tan δ in BYSB in the low frequency region (Figs. 10 (a) and Fig.11(a)). It can therefore be concluded that the asymmetry masked in the relaxation peak of tan δ due to the presence of σ_{dc} is manifested in the M″ spectra.

The type of relaxation (Debye or non-Debye type) present in the sample can be confirmed using the stretched exponent parameter β_{kww} [93]. The value of $\beta_{kww} = 1$ where there is no interaction among the dipoles and $\beta_{kww} < 1$ where there is a significant interaction among the dipoles. The values of β_{kww} for BYSB lies between 0.45 and 0.81and for BYSN it lies between 0.26 and 0.35 indicating that the relaxation in both the sample is non-Debye type. For BYSN the value β_{kww} is lowest at 393 K which once again confirms the fact that it exhibits anomalous dielectric behaviour above 393 K due to release of surface adsorbed CO_2 by it as has been observed in its dielectric response in other formalisms.

4. Discussion

The reported value of room temperature permittivity of bulk Ba_2YbSbO_6 (same as our BYSB sample) prepared by solid state ceramic method (belonging to *R-3* space group with lattice parameter a = 5.9104 Å and α = 59.99°) is 14 at 10 KHz [40] and the value of the same for BYSB (belonging to $Fm\bar{3}m$ space group with lattice a = 8.361509 and α = β = γ = 90°) is 14 at 5 MHz. To the best of our knowledge there is no report on temperature dependent dielectric response of Ba_2YbSbO_6. It may be noted that for Ba_2YbNbO_6 room temperature dielectric permittivity and loss tangent values are ~250 and ~0.28, respectively at 1.75 KHz [56]. The room temperature the values of dielectric permittivity and loss tangent of Ba_2HoSbO_6 are ~300 and 0.25, respectively, at 1.75 KHz [94]. At room temperature and 1.75 KHz the value of dielectric permittivity of BYSB (~168) is found to be less than that of its analogous systems like Ba_2YbNbO_6 and Ba_2HoSbO_6 but its loss tangent (~0.09) is better than those of its analogous systems. The values of room temperature dielectric permittivity and loss tangent of BYSB matches well with the reported values of these parameters for bulk Ba_2YbSbO_6 sample. On the other hand, the dielectric behaviour of BYSB and its analogous system is significantly different. It may be noted that crystal structure has the direct influence on microscopic structural relaxation of dielectric materials [91]. Thus, the similarity in dielectric behaviour of BYSB with bulk Ba_2YbSbO_6 prepared by ceramic method can be attributed to structural similarity of these two systems. The difference in the microscopic structural relaxation between BYSB and its other analogous systems leads to the change in their dielectric properties. From the above discussion it can be inferred that the crystal structure which determines the microscopic structural relaxation has a key role in determining the dielectric property of perovskite oxides.

The reported values of dielectric constant and loss tangent of nano-sized Ba_2YbSbO_6 (synthesized by combustion method and having

particle size 20–50 nm) are 11.3 and 0.01, respectively, at 5 MHz frequency [38,39]. However, there is no report on dielectric property of Ba_2YbSbO_6-$BaCO_3$ nanocomposite. The values of dielectric constant and loss tangent of BYSN is 18 and 0.08, respectively, at 5 MHz. It is noteworthy that both the single phase Ba_2YbSbO_6 sample mentioned above and the present Ba_2YbSbO_6-$BaCO_3$ nanocomposite are nanometric in size. Due to the difference in the microscopic structural relaxation owing to difference in the crystal structure of nanometric Ba_2YbSbO_6 and the nanocomposite BYSN their microscopic structural relaxation will be different. Moreover, BYSN has surface adsorbed CO_2. It can therefore be inferred that the presence of two crystalline phases and surface adsorbed CO_2 in BYSN is responsible for the difference in the dielectric response of BYSN and nanosized Ba_2YbSbO_6.

The influence of surface adsorbed CO_2 on the dielectric relaxation dynamics and conduction mechanism of BYSN has been discussed elaborately in the 'Results' section of this paper. Apart from this the difference in the crystal structure and microstructure of BYSB and BYSN can influence the dielectric relaxation and conduction mechanism of these samples. At any particular temperature the ε' verses log ω and tan δ verses log ω curves of BYSN (Fig. 11 (a)) follows the same trend as seen in BYSB (Fig. 10 (a)). At any given temperature and frequency, the value of ε' for BYSN is higher than that of BYSB. The values of tan δ of BYSN are comparatively higher than BYSB at low frequency (up to ~1 KHz) owing to the presence of pronounced dc conductivity in it. The values of tan δ of BYSN is less than that of BYSB above 1 KHz. It may be noted that BYSB (Ba_2YbSbO_6) is a single-phase double perovskite while BYSN is a nanocomposite composed of Ba_2YbSbO_6 and $BaCO_3$ phases along with surface adsorbed CO_2. Thus, the difference of microscopic structural relaxation of pure Ba_2YbSbO_6 and Ba_2YbSbO_6-$BaCO_3$ nanocomposite along with the difference of particle size leads to the enhancement of dielectric constant and reduction of loss tangent of BYSN compared to that of BYSB. The dielectric behaviour of a palettized sample is strongly dependent on the presence of grain and grain boundary interface [60]. Due to its nanometric size the number of grains and grain boundary interfaces in the pelletized sample of BYSN are higher than BYSB. The grain size and the grain boundary interface have also contributed to the enhancement of dielectric permittivity and reduction of loss tangent in case of BYSN as compared to BYSB.

If the power law fitting parameter of the conductivity spectra, $n = 0$ then the charge carriers can move freely through the material. When $n \neq 0$, the motion of charge carriers takes place due to conduction as well as polarization [83]. This phenomenon is usually observed for samples with grain boundary disorder creating localized polarons [83]. The motion of the polaron takes place due to induced polarizations [94,95]. Interaction between the mobile charge carriers and the lattice increases as the sample becomes more disordered. If the localized charge states are randomly distributed then hopping of charge carriers becomes faster. This motion of charge carriers increases conduction as well as polarizations. This behaviour has been reported for samples having grain boundary disorder and localized polarons [96,97]. It can be seen that the values of dc conductivity of BYSN at same frequency and temperature is higher than those of BYSB (Table 10). According to power law fitting of conductivity spectra, the values of n1 for BYSB and BYSN lie in the range of 1.45–1.57 and 1.67–1.7, respectively (Table 10). The values of n2 for BYSB and BYSN lie in the range of 0.30–0.43 and 0.40–0.42, respectively (Table 10). Thus, the nonzero values of n1 and n2 reveal the presence of grain boundary disorder (which is usual for palletized sample and has been observed in the FESEM images Fig. 3(a) and (b)) and localized polarons in both BYSB and BYSN. Moreover, the values of n1 for BYSN is greater than those of BYSB, which indicates presence more defects in BYSN. It is well known that mechanical milling induces crystalline defects and disorder mainly at the surface of the samples [17–20]. BYSN has been synthesized by ball milling method and it is nanometric in size while BYSB is synthesized by ceramic method and it is a bulk sample with large particle size. Therefore, BYSN should have more grain boundary disorder than BYSB. Thus, the microstructural (particle size and grain boundary defects) difference between BYSB and BYSN plays a key role in determining their conductivity.

The value of the parameter β_{kww} obtained from analysis of dielectric data in modulus formalism is lower for peaks which are broader and more asymmetric in nature and it also decreases with decrease in particle size [87,91]. Thus, the β_{kww} values of BYSN which are less than those of BYSB [Table 11] results from the particle size effect. Moreover, in BYSN the number of energy barriers arising from the local defects are more owing to its nanometric size resulting in broader distribution of its relaxation time as compared to BYSB [87]. This phenomenon also contributes to the lowering of β_{kww} values of BYSN as compared to those of BYSB. For BYSB β_{kww} value increases with temperature and approaches 1 at higher temperatures. It can therefore be inferred that the relaxation in BYSB tends towards Debye type process at higher temperatures.

5. Conclusion

In this paper we have scrutinized how the structural, microstructural and surface adsorbed CO_2 influences the dielectric and electrical transport properties of BYSB and BYSN. The BYSB sample having grain size ~1.92 μm has been prepared by solid state ceramic method. BYSN having particle size ~50 nm has been synthesized by high energy ball milling of BYSB. Previously, the presence of orthorhombic $BaCO_3$ phase in mechanically activated nanometric $BaTiO_3$ has been detected by Rietveld refinement of XRD pattern only without any supportive spectroscopic evidence [14,15]. In this endeavour, for the first time we have unambiguously shown that the mechanically activated nanosized double perovskite Ba_2YbSbO_6 adsorbs atmospheric CO_2 and is converted into a nanocomposite of Ba_2YbSbO_6 and $BaCO_3$ through Rietveld refinement of XRD pattern of BYSN along with spectroscopic evidences.

In summary, by performing XRD, FESEM, EDS, FTIR, Raman, TGA and impedance spectroscopic studies of BYSB and BYSN we have shown that (i) BYSB is a single phase cubic perovskite oxide with $Fm\bar{3}m$ space group whereas BYSN is a nanocomposite composed of 86.4% Ba_2YbSbO_6 and 13.6% $BaCO_3$ phases with surface adsorbed CO_2, (ii) due to the lattice deformation and surface disorder caused by high energy mechanical milling, the BYSN sample adsorbs atmospheric CO_2 and H_2O, (iii) the crystalline defects of BYSN acts as active sites prone to chemical reaction, (iv) a part of Ba present in BYSN reacts with surface adsorbed CO_2 to form $BaCO_3$, (v) the permittivity value for BYSN at any given temperature is higher than that of BYSB, (vi) the loss tangent values of BYSN is comparatively lower than that of BYSB at high frequencies, (vii) for both the samples the relaxation mechanism governing the dielectric behaviour is polydispersive in nature and Cole-Cole type, (viii) the values of impedance at room temperature of BYSN is higher than BYSB, (ix) the BYSN sample exhibits anomalous dielectric and electrical properties above 393 K as it releases the surface adsorbed CO_2 above this temperature, (x) in both BYSB and BYSN p-type polaron hopping dictates their electrical transport properties, (xi) the structural, microstructural and surface adsorbed CO_2 plays the key role in determining the dielectric relaxation and electrical transport properties of BYSB and BYSN. The formation of secondary $BaCO_3$ phase in case of BYSN sample upon CO_2 adsorption suggests that nanosized Ba_2YbSbO_6 can act as an efficient agent for removing harmful CO_2 from polluted air. Moreover, due to their high dielectric constant and low loss tangent at room

Table 11
The parameters obtained from M″ spectra.

Temperature (K)	BYSB		BYSN	
	β_{kww}	τ_{HN}	β_{kww}	τ_{HN}
303	0.45	4.186×10^{-6}	0.29	9.67×10^{-6}
393	0.57	1.319×10^{-6}	0.26	6.798×10^{-6}
483	0.64	9.027×10^{-7}	0.32	9.758×10^{-6}
573	0.77	8.47×10^{-7}	0.32	1.097×10^{-5}
663	0.81	6.78×10^{-7}	0.35	1.223×10^{-5}

temperature both BYSB and the nanocomposite BYSN may be utilized for fabrication of radio frequency oscillator, resonator, filter and communication devices.

Credit author statement

A. Barua: Sample preparation, recording of experimental data, data analysis, manuscript preparation, S. K. Dey: XRD data analysis, S. Dey: recording and analysis of spectroscopic data, S. Kumar: Overall supervision, mentoring, writing and editing manuscript.

Declaration of competing interest

The authors declare that they have no known competing financial interests or personal relationships that could have appeared to influence the work reported in this paper.

Data availability

Data will be made available on request.

Acknowledgement

I would also like to thank DST, Gov. of India and UGC, Govt. of India for their FIST, PURSE, SAP, UPE program.

Appendix A. Supplementary data

Supplementary data to this article can be found online at https://doi.org/10.1016/j.physb.2022.414449.

References

[1] M.W. Lufaso, Chem. Mater. 16 (2004) 2148.
[2] R. Mani, P. Selvamani, J.E. Joy, J. Gopalakrishnan, Inorg. Chem. 46 (2007) 6661.
[3] I. Levin, J.Y. Chan, R.G. Geyer, J.E. Maslar, T.A. Vanderah, J. Solid State Chem. 156 (2001) 122.
[4] M. Bieringer, S.M. Moussa, L.D. Noailles, A. Burrows, C.J. Kiely, M.J. Rosseinsky, R.M. Ibberson, Chem. Mater. 15 (2003) 586.
[5] Y. Du, A.S. Nowick, J. Am. Ceram. Soc. 78 (1995) 3033.
[6] M. Thirumal, A.K. Ganguli, Bull. Mater. Sci. 25 (2002) 259.
[7] M. Thirumal, A.K. Ganguli, Prog. Cryst. Growth Char. Mater. 44 (2002) 147.
[8] H. Vincent, Ch Perrier, Ph l'heritier, M. Labeyrie, Mater. Res. Bull. 28 (1993) 951.
[9] X. Wang, H. Wen, R. Chen, H. Zhou, L. Li, IEEE Int. Ultrasonics, Ferroelectrics, and Frequency Control Joint 50th Anniversary Conf, Canada, Montreal, August 2004.
[10] T. Hoshina, J. Ceram. Soc. Jpn. 121 (2) (2013) 156.
[11] Y. Kobayashi, A. Nishikata, T. Tanase, M. Konno, J. Sol. Gel Sci. Technol. 29 (2004) 49.
[12] S. Mukherjee, S. Ghosh, C. Ghosh, M.K. Mitra, J. Inst. Eng. India Ser. D 94 (2013) 57.
[13] R. Ashiri, RSC Adv. 6 (2016) 1713.
[14] S. Neogi, U. Chowdhury, A.K. Chakraborty, J. Ghosh, Micro & Nano Lett. 10 (2015) 109.
[15] J. Ghosh, S. Bysakh, S. Mazumder, Phil. Trans. 87 (2014) 325.
[16] V.R. Mudinepalli, L. Feng, W.C. Lin, B.S. Murty, J. Adv. Ceram. 4 (2015) 46.
[17] S.D. Shenoy, P.A. Joy, M.R. Anantharaman, J. Magn. Magn Mater. 269 (2004) 217.
[18] A. Verma, K. Biswas, C.S. Tiwary, A.K. Mondal, K. Chattopadhyay, Metall. Mater. Trans. 42 (2011) 1127.
[19] M.M. Vijatovic Petrovic, J.D. Bobic, A.M. Radojkovic, J. Banys, B.D. Stojanovic, Ceram. Int. 38 (2012) 5347.
[20] O.P. Thakur, A. Feteira, B. Kundys, D.C. Sinclair, J. Eur. Ceram. Soc. 27 (2007) 2577.
[21] M.H. Frey, Z. Xu, P. Han, D.A. Payne, Ferroelectrircs 206 (1998) 337.
[22] M. Vigneswari, K. Sakthipandi, S. Sankarrajan, IJERT 3 (2014) 2278.
[23] V. Buscaglia, C.A. Randall, J. Eur. Ceram. Soc. 40 (2020) 3744.
[24] A. Prasatkhetragarn, S. Kaowphong, R. Yimnirun, Appl. Phys. A 107 (2012) 117.
[25] A. Benali, S. Azizi, M. Bejar, E. Dhahri, M.F.P. Graça, Ceram. Int. 40 (9) (2014), 14367.
[26] M. Ghasdi, H. Alamdari, Sensor. Actuator. B Chem. 148 (2010) 478.
[27] Y. Wang, J. Chen, X. Wu, Mater. Lett. 49 (2001) 361.
[28] H.T. Giang, H.T. Duy, P.Q. Ngan, G.H. Thai, D.T.A. Thu, D.T. Thu, N.N. Toan, Sensor. Actuator. B Chem. 158 (2011) 246.
[29] B. Wang, S. Gu, Y. Ding, Y. Chu, Z. Zhang, X. Ba, Q. Zhang, X. Li, Analyst 138 (2013) 362.
[30] G. Wang, J. Sun, W. Zhang, S. Jiao, B. Fang, Microchim. Acta 164 (2009) 357.
[31] C. Tongyun, S. Liming, L. Feng, Z. Weichang, Z. Qianfeng, C. Xiangfeng, J. Rare Earths 30 (2012) 1138.
[32] A. Galal, N.F. Atta, S.M. Ali, Electrochim. Acta 56 (2011) 5722.
[33] S.M. Ali, Y.M. Abd Al-Rahman, A. Galal, J. Electrochem. Soc. 159 (2012) 600.
[34] W.T. Fu, S. Akerboom, D.J.W. Ijdo, J. Alloys Compd. 476 (2009) 11.
[35] W.T. Fu, D.J.W. Ijdo, J. Solid State Chem. 178 (2005) 2363.
[36] H. Karunadasa, Q. Huang, B.G. Ueland, P. Schiffer, R.J. Cava, Proc. Natl. Acad. Sci. U. S. A 100 (2003) 8097.
[37] P.J. Saines, B.J. Kennedy, M.M. Elcombe, J. Solid State Chem. 180 (2007) 401.
[38] P.R.S. Wariar, V.R. Kumar, V.M. Nair, M.M. Yusoff, R. Jose, J. Koshy, Adv. Mater. Res. 545 (2012) 27.
[39] V. Manikantan Nair, L. Jacob, P.R.S. Wariar, R. Jose, IJESIT 3 (2014) 720.
[40] L.A. Carrero Bermúdez, R. Moreno Mendoza, R. Cardona, D.A. Landínez Téllez, J. Roa-Rojas, J. Exp. Theo. Nanotechnology 3 (2017) 161.
[41] M.M. Hoque, A. Barua, A. Dutta, S.K. Dey, T.P. Sinha, S. Kumar, Ionics 23 (2017) 471.
[42] A.C. Larson, R.B. Von Dreele, General structure analysis system (GSAS), Los Alamos National Laboratory Report LAUR 86 (2004) 748.
[43] B. Panalytical, X'Pert HighScore Plus, Lelyweg, Almelo, Netherlands, 2002, p. 2.
[44] D. Shidqi Khaerudini, Arham, S. Alva, Adv. Nat. Sci. Nanosci. Nanotechnol. 11 (2020), 015013.
[45] B. Amitava, R. Gupta, K. Balani, J. Mater. Sci. 50 (2015) 6349.
[46] A. Banerjee, R. Gupta, K. Balani, J. Mater. Sci. 50 (2015) 6349.
[47] S. Alleg, F.Z. Bentayeb, R. Bensalem, C. Djebbari, L. Bessais, J.M. Greneche, Phys. Status Solidi A 205 (2008) 1641.
[48] N. Bensebaa, S. Alleg, J.M. Greneche, J. Alloys Compd. 393 (2005) 194.
[49] A.S. Bolokang, M. Phasha, Mater. Lett. 64 (2010) 1894.
[50] S. Dey, S.K. Dey, B. Ghosh, V.R. Reddy, S. Kumar, Mater. Chem. Phys. 138 (2013) 833.
[51] R. Mondal, S. Dey, S. Majumder, A. Poddar, P. Dasgupta, S. Kumar, J. Magn. Magn Mater. 448 (2018) 135.
[52] A. Barua, S.K. Dey, S.K. Sabyasachi, S. Kumar, J. Alloys Compd. 854 (2021), 157217.
[53] P. Pasierb, S. Komorniki, M. Rokita, M. Rekas, J. Mol. Struct. 596 (2001) 151.
[54] P. Galhotra, J.G. Navea, S.C. Larsena, V.H. Grassian, Energy Environ. Sci. 2 (2009) 401.
[55] B. Bonelli, B. Civalleri, B. Fubini, P. Ugliengo, C.O. Arean, E. Garrone, J. Phys. Chem. B 104 (2000), 10978.
[56] S.K. Maity, A. Dutta, S. Kumar, T.P. Sinha, Phys. Scripta 88 (2013), 065702.
[57] R. Mukherjee, S. Saha, A. Dutta, T.P. Sinha, J. Alloys Compd. 651 (2015) 222.
[58] D. Rout, G.S. Babu, V. Subramanian, Int. J. Appl. Ceram. Technol. 5 (2008) 522.
[59] C. Zeng, P. Li, H.B. Xu, Z.F. Xu, H.H. Li, Y. Zhang, Ceram. Int. 37 (2011) 1215.
[60] A. Barua, S. Maity, S. Kumar, A. Dutta, T.P. Sinha, Physica B 583 (2020), 412057.
[61] K.S. Cole, R.H. Cole, J. Chem. Phys. 9 (1941) 341.
[62] K.S. Cole, R.H. Cole, J. Chem. Phys. 10 (1942) 98.
[63] R. Coelho, Physics of Dielectrics, Elsevier, New York, 1978.
[64] S. Singha, S.K. Maity, S. Biswas, R. Saha, S. Kumar, Inorg. Chim. Acta. 453 (2016) 321.
[65] S.A. Fatima, R. Shaheen, K. Shahzad, Appl. Phys. A 127 (2021) 466.
[66] I. Ahmad, M.J. Akhtar, M. Younas, J. Solid State Electrochem. 21 (2017) 3093.
[67] U. Ahmadu, S. Tomas, S.A. Jonah, A.O. Musa, N. Rabiu, Adv. Mater. Lett. 4 (2013) 185.
[68] M. Idrees, M. Nadeem, M.M. Hassan, J. Phys. D Appl. Phys. 43 (2010), 155401.
[69] W.H. Jung, J. Appl. Phys. 90 (2001) 2455.
[70] L. Liu, H. Fan, L. Wang, X. Chen, P. Fang, Phil. Mag. 88 (2008) 537.
[71] L. Liu, H. Fan, P. Fang, L. Jin, Solid State Commun. 142 (2007) 573.
[72] L. Liu, H. Fan, P. Fang, X. Chen, Mater. Res. Bull. 43 (2008) 1800.
[73] R. Gerhardt, J. Phys. Chem. Solid. 55 (1994) 1491.
[74] M.C.H. Mckubre, J.R. Macdonald, in: J.R. Macdonald (Ed.), Wiley, New York, 1987, p. 191.
[75] R.C. Da, Y.G. Yan, Electron. Elem. Mater. 1 (1982) 25.
[76] S. Halder, Md Seikh, B. Ghosh, T.P. Sinha, Ceram. Int. 43 (2017), 11097.
[77] A.S.A. Khiar, R. Puteh, A.K. Arof, Physica B 373 (2006) 23.
[78] Y. Tsuji, A. Kan, H. Ogawa, S. Ishihara, J. Eur. Ceram. Soc. 25 (2005) 2883.
[79] A.K. Jonscher, Universal Relaxation Law, Chelsea Dielectrics Press, London, 1996.
[80] A. Dhahri, E. Dhahri, E.K. Hlil, RSC Adv. 8 (2018) 9103.
[81] L. Biswal, P.R. Das, B. Behera, J. Adv. Ceram. 3 (2014) 215.
[82] A. Oueslati, Ionics 23 (2017) 857.
[83] D.K. Pradhan, S. Kumari, V.S. Puli, P.T. Das, D.K. Pradhan, A. Kumar, J.F. Scott, R. S. Katiyar, Phys. Chem. Chem. Phys. 19 (2017) 210.
[84] R.K. Parida, B.N. Parida, R.K. Bhuyan, S.K. Parida, Ferroelectrics 571 (2021) 162.
[85] S. Manzoor, S. Husain, A. Somvanshi, M. Fatem, J. Appl. Phys. 128 (2020), 064101.
[86] S. Mishra, R.N.P. Choudhary, S.K. Parida, J. Mol. Struct. 1265 (2022), 133353.
[87] N.H. Vasoya, P.K. Jha, K.G. Saija, S.N. Dolia, K.B. Zankat, K.B. Modi, J. Electron. Mater. 45 (2016) 2;
[a] S.N. Tripathy, Z. Wojnarowska, J. Knapik, H. Shirota, R. Biswas, M. Paluch, J. Chem. Phys. 142 (2015), 184504.
[88] R. Mukherjee, B. Ghosh, S. Saha, C. Bharti, T.P. Sinha, J. Rare Earths 32 (2014) 334;
[a] S. Sharma, K. Shamim, A. Ranjan, R. Rai, P. Kumari, S. Sinha, Ceram. Int. 41 (2015) 7713.
[89] F. Kremer, A. Schoenhals, Broadband Dielectric Spectroscopy, Springer, Berlin, 2003.
[90] S.N. Tripathy, K.K. Satpathy, R. Palai, D.K. Pradhan, Ferroelectrics 589 (2022) 103.

[91] Z. Wojnarowska, J. Knapik, M. Díaz, A. Ortiz, I. Ortiz, M. Paluch, Macromolecules 47 (2014) 4056.
[92] A. Molak, M. Paluch, S. Pawlus, Phys. Rev. B 78 (2008), 134207.
[93] M.H. Bhat, M. Ganguli, J. Rao, Bull. Mater. Sci. 26 (2003) 407.
[94] D.G. Chen, X.G. Tang, J.B. Wu, W. Zhang, Q.X. Liu, Y.P. Jiang, J. Magn. Magn Mater. 323 (2011) 1717.
[95] H. Zheng, W. Weng, G. Han, P. Du, J. Phys. Chem. C 117 (2013), 12966.
[96] S.R. Elliot, Adv. Phys. 36 (1987) 135.
[97] N. Ortega, A. Kumar, P. Bhattacharya, S.B. Majumder, R.S. Katiyar, Phys. Rev. B Condens. Matter 77 (2008), 014111.

The impedance spectroscopy analysis of complex perovskite Sr_2YbSbO_6

A. Barua, S. Maity, R. Mondal, and S. Kumar

Citation: AIP Conference Proceedings **1942**, 110033 (2018); doi: 10.1063/1.5029016
View online: https://doi.org/10.1063/1.5029016
View Table of Contents: http://aip.scitation.org/toc/apc/1942/1
Published by the American Institute of Physics

The Impedance Spectroscopy Analysis of Complex Perovskite Sr_2YbSbO_6

A. Barua[1], S. Maity[1], R. Mondal[1] and S. Kumar[1, a)]

[1] *Department of Physics, Jadavpur University, Kolkata-700032, India*

[a)]Corresponding author: kumars@phys.jdvu.ac.in

Abstract. Herein, we have reported the dielectric properties of single phase monoclinic double perovskite oxide of Sr_2YbSbO_6 having lattice parameter a=5.79 Å, b=5.79 Å, c=8.19 Å and β = 90.136° with grain size ranging between 0.5 to 2.4 μm. The sample has been synthesized by solid state ceramic method. We have performed the impedence spectroscopic study of the sample in the frequency range of 40 Hz to 5 MHz at various temperatures. The relaxation in the sample is polydispersive in nature and obeys the Cole-Cole model. The values of dielectric permittivity and loss tangent at room temperature are 117.94 and 0.18 respectively. The temperature variation of dc conductivity follows the Arrhenius Law with activation energy 0.2 eV and the conduction mechanism of the sample is governed by p-type polaron hopping. Due to its high dielectric permittivity and low loss tangent the sample can be fruitfully utilized for the fabrication of radio frequency devices.

INTRODUCTION

In the recent years plethora of work has been carried out on the dielectric, structural and microstructural properties of complex perovskite oxides. The development of materials with high dielectric constant and low loss tangent is of utmost interest for the miniaturization of microwave and radio frequency electronic devices. The dielectric and electrical transport properties of double perovskites with general formula $A_2B'B''O_6$, can be easily modified by properly tuning the electron densities at A, B′ and B″-cationic sites. Several reports on structural, microstructural and dielectric properties of Sr_2YbTaO_6 [1] and Sr_2YbNbO_6 [2,3] are available in literature while only the crystal structure of Sr_2YbSbO_6 (SYS) has been thoroughly investigated by using neutron diffraction and powder x-ray diffraction (PXRD) techniques [2]. To the best of our knowledge alternating current impedance spectroscopic study (ACIS) of SYS is yet to be reported. In this background herein we have reported the crystal structure, microstructure and dielectric relaxation property of SYS. We have employed powder x-ray diffractometry, field emission scanning electron microscopy (FESEM) and ACIS technique to fulfill the goal.

EXPERIMENTAL

The polycrystalline Sr_2YbSbO_6 has been synthesized by solid state reaction technique. Analytical grade powders of $SrCO_3$, Yb_2O_3 and Sb_2O_5 were taken as primary raw materials and they were mixed in the presence of acetone for 10 h. The mixture was calcined in a Pt crucible at 1500 ^oC in presence of air for 8 h and brought to room temperature under controlled cooling. The sample was then palletized into circular disc with polyvinyl alcohol as binder and then sintered at 1550 ^oC for 12 h. The PXRD pattern of SYS was recorded at 300 K by Bruker Advanced D8 powder X-ray diffractrometer over a range of Bragg's angle $10^o \leq 2\theta \leq 120^o$ using Cu K_α (λ = 1.54184 Å) radiation. The field emission scanning electron microscope (FESEM) (FEI, INSPECT F50) was used to study the morphological and microstructural characteristics of the sample. For ACIS study a compact finely polished circular disc of thickness and diameter 1.90 and 12.92 mm; respectively, was prepared by pelletizing the sample under uniaxial pressure of 137 MPa using a hydraulic press followed by annealing. The frequency dependence of the

DAE Solid State Physics Symposium 2017
AIP Conf. Proc. 1942, 110033-1–110033-4; https://doi.org/10.1063/1.5029016
Published by AIP Publishing. 978-0-7354-1634-5/$30.00

capacitance (C) and conductance (G) were measured using Agilent Impedance Analyzer in the temperature range of 303 K to 663 K and at the oscillation voltage of 0.5 V. During the data collection the sample was heated at the rate of 0.5 ^{o}C/min.

RESULTS AND DISCUSSION

For perovskite oxides the degree of distortion from cubic lattice can be calculated by using Goldschmidt tolerance factor (T_f) given by the formula $T_f=(r_A + r_0)/\sqrt{2}[(r_B)+ r_0)]$, where, r_A, r_B and r_0 are the ionic radii of A site, B site and O ions, respectively [4]. For cubic perovskites T_f is close to unity, whereas for monoclinic and orthorhombic perovskite T_f is less than 1 [5-7]. The value of T_f for SYS is 0.94 which suggests the structure of SYS should be non-cubic. T_f has been calculated using Shannon effective ionic radii [8]. The structural (lattice parameters) and microstructural parameters (crystallite size and microstrain) of SYS have been extracted by means of PXRD line profile analysis using Rietveld based software package MAUD 2.33.The experimentally obtained and theoretically generated PXRD patterns of SYS along with the residual curve have been presented in Fig.1. The values of Rwp =0.079, Rexp=0.08 and GOF=1.45 (where Rwp, Rexp and GOF are refinement parameters and correspond to the reliability of fitting). The refined values of the lattice parameters are a=5.79 Å, b=5.79 Å, c=8.19 Å and β = 90.136°, crystalline size is 104.7 nm and r.m.s. strain is 6.48× 10^{-4}. The results clearly indicates that SYS is a single phase monoclinic double perovskite oxide of $P2_1/n$ space group and this corroborates with the earlier finding on the same system [2]. The FESEM micrograph (Fig. 2) reveals that the grains are of assorted size with average grain size between 0.5 to 2.4 µm.

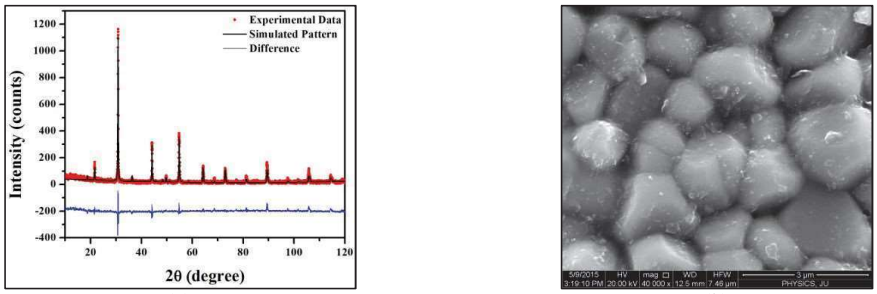

(a) (b)

FIGURE 1. (a) The experimentally observed and theoretically generated PXRD patterns and (b) the FESEM micrograph of SYS.

The logarithmic angular frequency (ω) dependence of the dielectric constant ε' (ω) and the loss tangent tan δ for SYS at different temperatures is shown in Fig. 2. It is observed that the value of ε' decreases with increasing frequency as in the low frequency region ($\omega<<1/\tau$, where τ is the relaxation time), the dipole follows the field. At all the temperatures with the increase in frequency ($\omega<1/\tau$), the dipole starts lagging behind the field and ε_0 starts decreasing and a relaxation peak (loss peak) is observed in tan δ versus log ω curves. As the frequency reaches the characteristic frequency ($\omega=1/\tau$), the relaxation process starts. At very high frequency ($\omega>>1/\tau$), dipoles cannot follow the field and the dielectric constant becomes constant (ε_∞). The large width of the loss peaks indicates that the relaxation cannot be due to monodispersive Debye process but points towards the possibility of the distribution of relaxation times. The polydispersive nature of the dielectric relaxation can be examined by using the Cole- Cole equation which is defined as

$$\varepsilon^* = \varepsilon' - i\varepsilon'' = \varepsilon_\infty + \frac{\varepsilon_s - \varepsilon_\infty}{1+(i\omega\tau)^{1-\alpha}} \quad (1)$$

where, ε_s and ε_∞ are static and high frequency value of relative permittivity respectively, ω is the angular frequency, τ is the mean relaxation time and α gives the nature of distribution of relaxation time. For a mono-dispersive Debye relaxation α=0 and α > 0, implies that there is a distribution of relaxation times, leading to a broader peak than the Debye peak. The real and imaginary parts of the equation (1) can be written as

$$\varepsilon' = \varepsilon_\infty + \frac{(\varepsilon_S - \varepsilon_\infty)\left[1 + (\omega\tau)^{1-\alpha}\sin\frac{1}{2}\alpha\pi\right]}{1 + 2(\omega\tau)^{1-\alpha}\sin\frac{1}{2}\alpha\pi + (\omega\tau)^{2(1-\alpha)}} \quad (2)$$

$$\varepsilon'' = \frac{(\varepsilon_S - \varepsilon_\infty)(\omega\tau)^{1-\alpha}\cos\frac{1}{2}\alpha\pi}{1 + 2(\omega\tau)^{1-\alpha}\sin\frac{1}{2}\alpha\pi + (\omega\tau)^{2(1-\alpha)}} \quad (3)$$

Now, the dielectric loss can be accounted by loss tangent

$$\tan\delta = \varepsilon''/\varepsilon' \quad (4)$$

We have fitted our experimental data using equations (2), (3) and (4). The parameters ε_s, ε_∞, ω_m (value of ω corresponds to the peak value of tan δ) that are obtained from the experimental data for various temperatures is given in the **Table 1** below which are required for the fitting purpose**.** The nonzero value of α discards the possibility of the existence of Debye type monodispersive relaxation process in the sample and indicates that the relaxation process is polydispersive in nature.

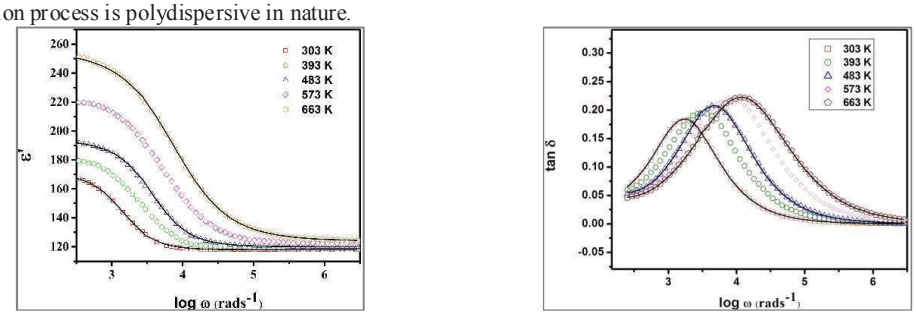

(a) (b)

FIGURE 2. (a) The ε′ versus log ω and (b) tanδ versus log ω curves for SYS at various temperatures, where the solid lines are the fit of the experimental data (shown by symbols) by modified Cole-Cole equations.

TABLE 1. The values of different parameters obtained by fitting the dielectric spectra of SYS by modified Cole-Cole equations.

Temperature(K)	ε_s	ε_∞	ω_m (rads^{-1})	α
303	16.83	11.6	1433	0.02
483	19.22	12	3703	0.06
663	25.14	12.4	7525	0.19

The variation of ac conductivity with frequency for SYS at different temperatures is shown in the Fig. 3. As only the loss part of the complex dielectric permittivity contributes towards the real part of the conductivity therefore the conductivity can be expressed as $\sigma=\omega\varepsilon_0\varepsilon''$; here, σ is the real part of conductivity and ε'' is the imaginary part of the dielectric constant. The real part of conductivity spectra follows the power law defined as

$$\sigma = \sigma_{dc}[1 + (\omega/\omega_H)^n] \quad (5)$$

where, σ_{dc} is the dc conductivity, ω_H is the hopping frequency of the charge carriers, and n is the dimension less exponent. The experimental conductivity spectra are fitted using equation (5). The values of parameter n (n = 0.97, 0.98 and 0.99 at temperatures 303, 483 and 663 K respectively) is weakly temperature dependent. The values of ω_H are 34355, 43960, 48162 rads^{-1} at 303, 483 and 663 K respectively. Thus the conduction mechanism of the sample is governed by carrier hopping process.

It is observed that the value of σ decreases with decreasing frequency and it becomes independent of frequency after a certain value. Extrapolation of the curve toward the low frequency region gives the value of σ_{dc}, the dc conductivity. The values of σ_{dc} at temperatures 303, 393, 483, 573 and 663 K are 1.2548×10^{-9}, 2.4647×10^{-9}, 4.1031×10^{-9}, 5.70374×10^{-9}, 8.6032×10^{-9} Sm^{-1} respectively. It has been found that the temperature variation of σ_{dc}

follows the Arrhenius Law given by $\sigma_{dc} = \sigma_0 \exp (- E_\sigma/K_BT)$ with activation energy E_σ =0.21 eV. The activation energy of p-type polaronic conduction is in the range of 0.2-0.9 eV and for n-type polaronic conduction it is less than 0.2 eV [9-11]. Thus the value of activation energy for SYS indicates that the conduction mechanism is governed by p-type polaron hopping.

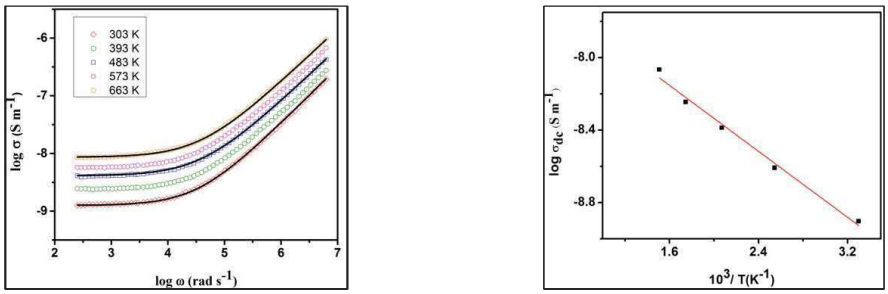

(a) (b)

FIGURE 3. (a) Temperature dependence of dc conductivity of SYS. Symbols represent the experimental data and solid lines are least-squares straight-line fit and (b) The Arrhenius plot of the dc conductivity σ_{dc} for SYS as a function of temperature

CONCLUSION

In this paper we have reported the structural, microstructural and the frequency dependent dielectric and transport properties of SYS synthesized by solid state reaction technique. The analysis of the PXRD pattern of SYS by Rietveld refinement method suggests that the sample possess monoclinic crystal structure of $P2_1/n$ symmetry. A broad peak has been observed in the tan δ verses log ω curves of the sample and therefore the dielectric relaxation of the sample is modelled by Cole-Cole equation. The frequency dependence of the conductivity spectra follows the power law. The temperature dependence of the dc conductivity follows the Arrhenius law having the activation energy of 0.21 eV which indicates the conduction mechanism is governed by p-type polaron hopping.

ACKNOWLEDGMENTS

One of the authors A. Barua (Ref. No: 21/06/2015(ii) EU-V) gratefully acknowledges UGC, New Delhi for junior research fellowship. We also acknowledge the PURSE and FIST program of DST, Government of India and UPE program of UGC, Government of India.

REFERENCES

1. S. K. Maity, A. Dutta, T. P. Sinha and S. Kumar, AIP Conference Proceedings **1665**, 110044 (2015).
2. F. C. Coomer, J. Campbell, N. Giordano, O. M. Collins, E. J. Cussen, J. Solid State Chem. **221**, 411–417 (2015).
3. L. A. Khalam and M. T. Sebastian, Int J. Appl. Ceram. Tecnol. **3[5]**, 364–374 (2006).
4. V. M. Goldschmidt, Naturwissenschaften **14**, 477–485 (1926).
5. M. M. Hoque, A. Dutta, S. Kumar and T. P. Sinha, Physica B **407**, 3740–3748 (2012).
6. M. M. Hoque, A. Dutta, S. Kumar and T. P. Sinha, J. Mater. Sci. Technol. **30**, 311–320 (2014).
7. A. Dutta and T. P. Sinha, Mater. Res. Bull. **46**, 518–524 (2011).
8. R. D. Shannon, Acta.Crystallogr. A. **32**, 751–767 (1976).
9. M. M. Hoque, A. Dutta, S. Kumar and T.P. Sinha, Physica B **468-469**, 85–95 (2015).
10. W. H. Jung, J. Appl. Phys. **90**, 2455 (2001).
11. M. Idrees, M. Nadeem, M.M. Hassan, J. Phys. D **43**, 155401 (2010).

Journal of Alloys and Compounds 854 (2021) 157217

Contents lists available at ScienceDirect

Journal of Alloys and Compounds

journal homepage: http://www.elsevier.com/locate/jalcom

Structural and dielectric characterization of triple perovskites $Ba_3NiTaNbO_9$ and $Ba_3NiTaSbO_9$

A. Barua [a, *], S.K. Dey [b], S.K. Sabyasachi [c], S. Kumar [d]

[a] Physics Department, Presidency University, Kolkata, 700073, India
[b] Purulia Polytechnic, V. Nagar, Purulia, 723147, West Bengal, India
[c] Physics Department, Sundarban Hazi Desarat College, University of Calcutta, Pathankhali, 743611, India
[d] Physics Department, Jadavpur University, Kolkata, 700032, India

ARTICLE INFO

Article history:
Received 30 April 2020
Received in revised form
30 August 2020
Accepted 14 September 2020
Available online 16 September 2020

Keywords:
Triple perovskites
Raman spectra
Dielectric permittivity
Complex impedance
Ac conductivity

ABSTRACT

The perovskites barium nickel tantalum niobium oxide (BNTN) and barium nickel tantalum antimony oxide (BNTS) consisting of two rare earth elements have been prepared by the ceramic method. The BNTN sample crystallizes in trigonal symmetry with *P-3m1* space group and the BNTS sample crystallizes in hexagonal symmetry with *P* $6_3/mmc$ space group, which has been obtained from the analysis of the powder x-ray diffraction pattern (XRD). The results of the structural analysis match well with that of the Raman and Fourier transform infrared spectroscopic studies. For both the samples the dielectric relaxation and ac conductivity were investigated in between temperatures 333 K–573 K and in between 10 Hz and 1 MHz frequency. The relaxation nature of the samples has been analyzed with the help of the Cole-Cole model. The non-zero values of α for the Cole-Cole model suggests the relaxation phenomena being polydispersive in nature. The activation energy as obtained from the conductivity spectra is 0.36 eV for BNTN and 0.37 eV for BNTS which indicates that the polaron hopping mechanism is responsible for their electrical and dielectric response.

1. Introduction

Perovskite oxides have been widely used in the field of microwave communication systems in the form of resonators and filters [1]. They have been widely explored due to their tunable physical properties which are dependent on their composition and their crystal structure. In perovskites having ABO_3 structure, the dielectric properties can be tuned by changing the B-site cation ordering [2]. In recent past a large amount of research have been carried out on triple perovskites having general formula $A(B'_{1/3}B''_{2/3})O_3$ because of their structural diversity and technologically important physical properties. Barium based triple perovskites have been reported to exhibit multiferroicity [3,4], better dielectric properties [5] and photocatalytic properties [6].

Triple perovskites usually have hexagonal, orthorhombic, monoclinic and trigonal symmetries as they can accommodate varied sized cations in the A-site and any lanthanide or any d-block element in the B′ and B″ sites [7–16]. This structure can easily accommodate different elements, which allows us to substitute different cations in order to obtain the desired physical properties. The dielectric permittivity arises due to the combination of electronic and ionic polarization [17]. The lattice vibrations affect the ionic polarization but the electronic polarization is constant for a specified ion [18,19]. In our present work we have substituted the B-site with three different cations in order to obtain the $A_3(B'B''B''')O_9$ structure similar to those reported by Mani et al. [20]. We have synthesized two triple perovskites $Ba_3NiTaNbO_9$ and $Ba_3NiTaSbO_9$ having general formula $A_3(B'B''B''')O_9$ and examined their structural, optical and dielectric properties. Dielectric analysis of $Ba(Ni_{1/3}Ta_{2/3})O_3$ has been performed by Hoque et al. [21] but on addition of niobium in the B‴-site as in case of our BNTN sample has led to a considerable increase in its permittivity value.

2. Experimental

The polycrystalline samples of BNTN and BNTS were synthesized by the ceramic method [21]. Reagent grade powders of Ta_2O_5, $BaCO_3$, $NiCO_3$, Sb_2O_5 and Nb_2O_5 were used for the synthesis of the respective samples. The stoichiometric amount of the raw materials was mixed together for 10 h and then calcined at 1325 °C for 14 h in

* Corresponding author.
E-mail address: arpita.physics@presiuniv.ac.in (A. Barua).

https://doi.org/10.1016/j.jallcom.2020.157217
0925-8388/

presence of air. The samples were than brought down to 30 °C by cooling at the rate of 2 °C/min. The XRD analysis was performed using Bruker D8 diffractometer in order to verify the phase formation of the prepared samples. Cu-K_α radiation was used and the range was kept in between $10° \leq 2\theta \leq 120°$ with scanning step size of 0.02°. The scan rate of the diffractometer was set at 2° min^{-1}. The microstructural analysis of the samples was done using field emission scanning electron microscope (SEM). The FTIR spectrums of the samples were recorded in the room temperature in the transmission mode with wave number between 350 and 1200 cm^{-1}. The Raman measurements were carried out using WITEC alpha 300 R Raman spectrometer.

The calcined powders were than palletized into discs by applying 135 MPa pressure using a hydraulic press. The discs were than sintered at 1375 °C for 10 h and then brought down to 30 °C by cooling at the rate of 1 °C/min. The discs of the samples having thickness and diameter of 1.974 mm and 9.896 mm for BNTS and 1.621 mm and 7.784 mm for BNTN were prepared which were then polished thoroughly using very fine (so called zero) emery paper. The flat surfaces of the discs were coated with fine silver paint and heated at 250 °C for 3 h in order to make the electrodes for performing the electrical measurements. Hioki 3532 LCR meter was used for the electrical measurements. The dielectric parameters were measured keeping the oscillation voltage fixed at 1 V and by varying the frequency between 10 Hz and 1 MHz. The dielectric parameters were measured at some discrete temperatures in between 333 and 573 K. During the measurement each temperature was kept constant with the help of a programmable oven with an accuracy of ±1 K. The samples were heated at the rate of 0.5 K/min in order to study the variations of various dielectric parameters with temperature.

3. Results

3.1. Structural characterization

It may be noted that BNTN and BNTS are obtained by partially substituting the Ta^{5+} of $Ba_3NiTa_2O_9$ by Nb^{5+} and Sb^{5+}, respectively. The radii of Nb^{5+} (0.64 Å) is equal to that of Ta^{5+} (0.64 Å) while the radii Sb^{5+} (0.6 Å) is smaller as compared to Ta^{5+} but closer to that of Ir^{5+} (0.57 Å). Thus, the crystal structure of BNTN is likely to be analogous to $Ba_3NiTa_2O_9$, which crystallizes in *P-3m1* space group as reported by Lufaso et al. and Asai et al. [22,23]. On the other hand, the crystal structure of BNTS is expected to be similar to that of $Ba_3NiIr_2O_9$ [16] and $Ba_3NiSb_2O_9$ [24] where both $Ba_3NiIr_2O_9$ and $Ba_3NiSb_2O_9$ possess *P 6₃/mmc* space group of hexagonal symmetry. The XRD patterns of BNTN and BNTS have been analyzed by the Rietveld refinement method by using the GSAS program having EXPGUI user interface [25]. The initial input parameters required for analysing the crystal structures of BNTN and BNTS have been obtained from the crystallographic information available for $Ba_3NiTa_2O_9$ and $Ba_3NiIr_2O_9$/$Ba_3NiSb_2O_9$, respectively. The experimentally recorded XRD patterns of both BNTN and BNTS along with their corresponding simulated patterns, obtained after Rietveld refinement, are demonstrated in Fig. 1. The results confirm that BNTN belongs to trigonal symmetry with *P-3m1* space group and is a structural analog of $Ba_3NiTa_2O_9$ whereas BNTS belongs to hexagonal symmetry with *P 6₃/mmc* space group and eventually stabilizes adopting the crystal structure of $Ba_3NiIr_2O_9$/$Ba_3NiSb_2O_9$. In order to assess the influence of the ionic radii of A and B -site cations on stabilization of the crystal structures adopted by BNTN and BNTS we have calculated the Goldschmidt tolerance factor $g=(r_A + r_O)/[\sqrt{2}\,(r_B + r_O)]$ [26] of the samples, considering the Shannon's ionic radii [27] of different elements present in the A, B and O -sites. We obtained g = 1.03 for BNTN and g = 1.04 for BNTS. The g value of BNTN is smaller due to the larger niobium ion in the B‴- site leading to 2:1 ordered perovskite structure with *P-3m1* space group [22]. The substitution of Sb^{5+} having smaller ionic radii as compared to Nb^{5+} increases the value of g in case of BNTS. Thus, the g value of BNTS being closer to the hexagonal structure, it crystallizes in *P 6₃/mmc* space group [26,28]. Table 1 illustrates the lattice parameters obtained after the refinement.

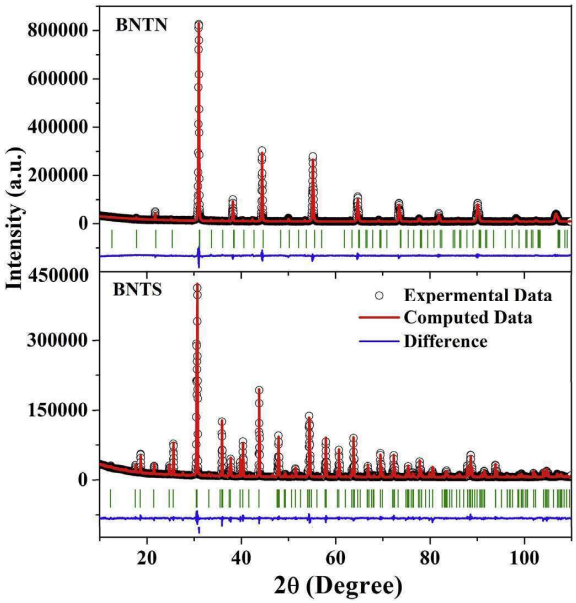

Fig. 1. Rietveld refinement plots of BNTN and BNTS where the symbols represents the experimental data and the continuous line represents the simulated XRD pattern.

The Wyckoff positions of cations and anions of BNTN and BNTS are tabulated in Table 2 and Table 3, respectively. Fig. 2 Depicts the asymmetric unit of BNTN where the Ba^{2+} ions are coordinated with 12 oxygen ions while Ni^{2+}, Nb^{5+} and Ta^{5+} ions are coordinated with 6 oxygen ions. Fig. 3 illustrates the coordination environment of A and B -site atoms Ba, Ni, Ta and Nb. The Ni—O bond length is 1.98 Å whereas Nb/Ta—O2 bond length is 2.016 Å and Nb/Ta—O1 bond length is 2.102 Å for the BNTN sample. The difference in the bond length of Nb/Ta—O indicates off center distortion of the cation in the octahedra resulting from the second order Jahn-Teller distortion for d^0 cations like Ti^{4+}, Nb^{5+}, Ta^{5+}, W^{6+} [22]. The Nb/Ta^{5+}—O—Nb/Ta^{5+} bond angle is 180°. Fig. 4 Depicts the asymmetric unit of BNTS

Table 1
The refinement and the structural parameters of BNTN and BNTS as obtained from the Rietveld refinement method of powder X-ray data.

Parameters	BNTN	BNTS
Crystal system	Trigonal	Hexagonal
Space group	*P-3m1*	*P 6₃/mmc*
a (Å)	5.75509 (2)	5.835973 (30)
b (Å)	5.75509 (2)	5.835973 (30)
c (Å)	7.06650 (3)	14.40431 (12)
Volume (Å^3)	191.34 (1)	424.864 (4)
α = β(°)	90	90
γ(°)	120	120
R_{wp}	0.069842	0.0458
R_p	0.052798	0.0358
χ^2	1.98	2.42

Table 2
The Wyckoff positions of atoms and the refined atomic coordinates of BNTN.

Atom	Site	*x*	*y*	*z*	Occupancy	*B* (Å^2)
Ba1	1a	0.0	0.0	0.0	1	0.03619
Ni2	1 b	0.0	0.0	0.5	1	0.03139
Nb3	2 d	0.33333	0.66667	0.180924 (13)	0.5	0.03232
Ta7	2 d	0.33333	0.66667	0.180924 (13)	0.5	0.03263
Ba2	2 d	0.33333	0.66667	0.659593 (6)	1	0.03820
O5	3e	0.5	0.0	0.0	1	0.09264
O6	6i	0.16841 (12)	0.30371 (14)	0.34922 (6)	1	0.04187

Table 3
The Wyckoff positions of atoms and the refined atomic coordinates of BNTS.

Atom	Site	*x*	*y*	*z*	Occupancy	*B* (Å^2)
Ba1	2 b	0	0	0.25	1	0.0247 (2)
Ni2	2a	0	0	0	1	0.02143 (9)
Sb3	4f	0.33333	0.66667	0.15876	0.5	0.0125 (4)
Ta7	4f	0.33333	0.66667	0.15876	0.5	0.02649
Ba2	4f	0.33333	0.66667	0.91349 (2)	1	0.0160 (2)
O5	6 h	0.59722 (3)	1.04013 (1)	0.25	1	0.0137 (3)
O6	12 k	0.15148 (3)	0.30296	0.42077 (1)	1	0.01630 (2)

where the Ba^{2+} ions are coordinated with 12 oxygen ions while Ni^{2+}, Sb^{5+} and Ta^{5+} ions are coordinated with 6 oxygen ions and Fig. 5 illustrates the coordination environment of A and B -site atoms Ba, Ni, Ta and Sb. The Ni—O bond length is 1.89 Å whereas Sb/Ta—O2 bond length is 2.183 Å and Sb/Ta—O1 bond length is 2.36 Å for the BNTS sample. The difference in the bond length of Sb/Ta—O results from the cation-cation repulsion between the face sharing Sb_2O_9 groups [28]. The Sb/Ta^{5+}—O—Sb/Ta^{5+} bond angle is 68.9°. For BNTN the B-site cations are arranged along the (111) planes of the pseudocells with two Nb/Ta layer and one Ni layer as shown in Fig. 6 (a). As both the Ta and Nb ions occupy the *2d* Wyckoff position they are represented by different colors on the same sphere. This arrangement of the B-site atoms is repeated along the crystallographic c axis. On the other hand, the B-site cations of BNTS are arranged along the (111) planes of the pseudocells with two Sb/Ta layer and one Ni layer as shown in Fig. 6 (b). As both the Ta and Sb ions occupy the *4f* Wyckoff position they are represented by different colors on the same sphere. This arrangement of the B-site atoms is repeated along the crystallographic c axis.

The difference in the bonding preference of Nb^{5+} having vacant d orbital and Sb^{5+} having filled d orbital and difference in their ionic radii plays a crucial role for the stabilization of BNTN in *P-3m1* space group and BNTS in *P* 6_3*/mmc* space group [28–32]. The vacant d orbitals of Nb^{5+} in BNTN favors the formation of л bond with the p orbitals of oxygen thus resulting in a linear Nb^{5+}—O—Nb^{5+} bond with bond angle ~180° which favors the *P-3m1* structure with metal oxygen corner sharing octahedra and cubic stacking of BaO_3 layers [Fig. 2]. The filled d orbitals of Sb^{5+} does not favor the formation of л bond and preferred Sb^{5+}—O—Sb^{5+} bond angle is < 180°, thus BNTS stabilizes in *P* 6_3*/mmc* structure containing mixed cubic and hexagonal stacking of BaO_3 layers [Fig. 4] with $Ni^{2+}O_6$ octahedra in the vertex and face sharing Sb_2O_9 groups having Sb^{5+}—O—Sb^{5+} bond angle ~90° resulting from σ bonding with p orbitals of two different oxygen.

The XRD analysis can predict the ordered or disordered nature of the sample depending on the degree of long-range ordering. A perovskite structure is said to be disordered if the B-site cations are randomly distributed along the crystal lattice. Perovskite materials can exhibit partially ordered structure due to their occupational disorder owing to the exchange of their Wykoff site between the B′-B″-B‴ ions [33]. It can be seen from Fig. 6 that ordered nature is maintained for both BNTN and BNTS sample however the B″-B‴ ions are indistinguishable due to their identical Wykoff sites. Each *2d* site of BNTN can either be occupied by a Ta^{5+} or Nb^{5+} ion and similarly in case of BNTS the probability that each *4f* site will be filled by a Ta^{5+} or Sb^{5+} ion is equal and this leads to occupational disorder in both the samples. Thus, both BNTN and BNTS fall in the category of partially ordered perovskite having trigonal and hexagonal unit cell respectively.

The theoretical density of BNTN is 8.26 g/cc and for BNTS is 7.53 g/cc. The experimental density of the pellets as measured by the Archimedes principle is 8.01 g/cc for BNTN and 7.29 g/cc for

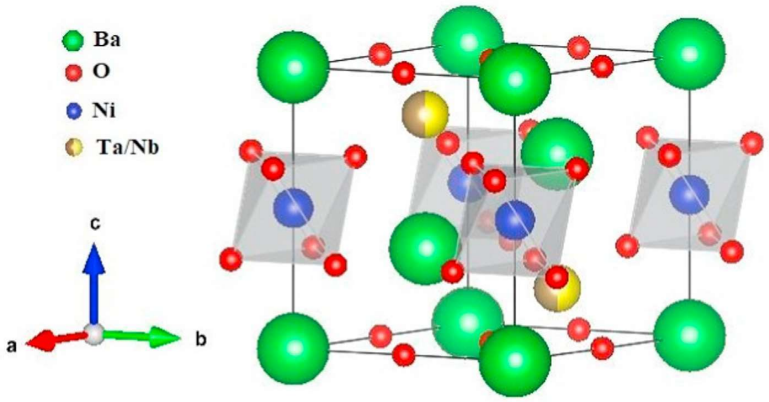

Fig. 2. Asymmetric unit of BNTN.

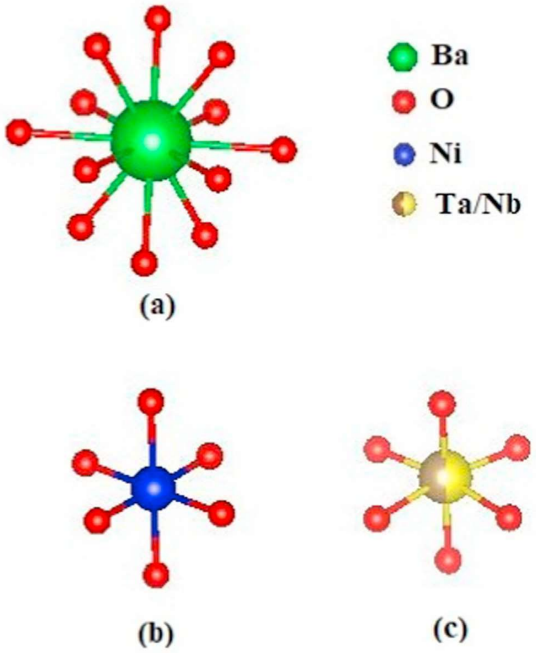

Fig. 3. Coordination environments of (a) Ba^{2+} (b) Ni^{2+} and (c) Ta/Nb^{5+} for BNTN sample.

BNTS which indicates that the presence of porosity is negligible. The SEM images of BNTN and BNTS pellets are shown in Fig. 7 from which we can observe that both the samples have well defined grains of asymmetrical shapes and sizes. The grain size of BNTN ranges from 0.52 μm to 1.83 μm and for BNTS it ranges from 0.25 μm to 1.21 μm.

3.2. Raman and FTIR analysis

The Raman spectra of BNTN and BNTS are illustrated in Figs. 8 and 9, respectively. The spectra are fitted with Lorentzian profile. The peak position and the full width at half maxima of the Raman peaks are provided in Table 4. The group factor analysis can be used to determine the lattice vibration modes of perovskites based on the Wyckoff positions occupied by the atoms [34]. The expected phonon modes for the partially ordered BNTN sample are illustrated in Table 5. Eleven Raman-active modes ($\Gamma_{Raman} = 5\ A_{1g} + 6\ E_g$) are expected in the Raman spectra of the ordered sample with *P-3m1* space group. An increased number of optical active modes can be observed in BNTN for the occupational disorder caused by the exchange of Wyckoff sites between B′-B″-B‴ ions [35,36]. For indexing the BNTN crystal structure we have used the D_{3d} cell, but due to the interchange of ions occupying B′ and B''/B‴ sites additional modes can be observed [33,36,37]. These additional modes can again be predicted by the group factor analysis. The existence of B′ ions in *2d* Wyckoff site would give rise to two additional Raman and IR bands each ($\Gamma_{Raman,B'} = A_{1g} + E_g$, $\Gamma_{IR,B'} = A_{2u} + E_u$) and the presence of B''/B‴ ions in *1b* Wyckoff site would give rise to two additional IR bands ($\Gamma_{IR,B''/B'''} = A_{2u} + E_u$). The Lorentzian fitting of the BNTN sample indicates the presence of 14 bands. The Raman

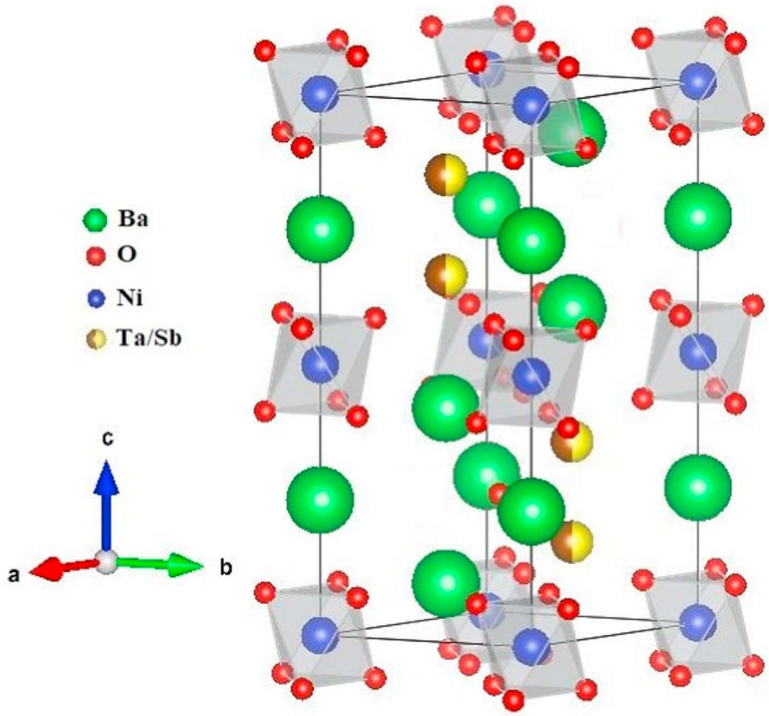

Fig. 4. Asymmetric unit of BNTS.

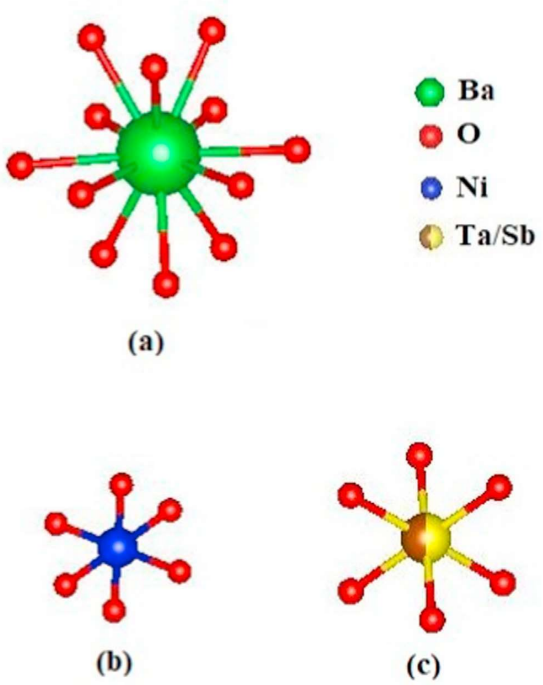

Fig. 5. Coordination environments of (a) Ba^{2+} (b) Ni^{2+} and (c) Ta/Sb^{5+} for BNTS sample.

active bands for the partially ordered BNTN sample are shown in Table 4. Two extra Raman bands occur due to the presence of Ni ions in the *2d* site and an additional Raman band may be attributed to the defect activated modes [36] arising due to the local breakdown of rigid symmetry rules owing to the presence of crystalline defects created during the crystal growth process. Appearance of extra Raman bands due to the presence of such defects in ceramic crystals, developed during the crystal growth process, are very common [38,39]. Seven prominent bands (1–4, 6, 7, 13) arises due to the vibrations of Ba and O ions and agrees well with those reported by Moreira et al. for sample with *P-3m1* space group [36]. The peaks (12–14) arises due to the vibration of Nb ions and the peaks (8, 9) arises due to the Ta ions occupying their own *2d* site. We propose the peaks (10–11) arises due to the vibrations of Ni ions in the *2d* site. The peak 5 may be attributed to the localized defect activated modes [36]. According to the charge to mass ratio $[(q_{Ni}/m_{Ni})/(q_{Nb}/m_{Nb})]^{1/2}$ [36], where q and m denotes the charge and mass of the ion, respectively, the Raman modes for Ni ions occupying the *2d* site would appear at frequency which is 0.796 times of the mode associated with the Nb ions. This ratio is satisfied by peak 10 and 12 (0.719) as well as peak 11 and 14 (0.747). Since the occupation of Ni ions in *2d* site is one of the causes for the partially ordered structure of BNTN leading to extra Raman modes, we can estimate the degree of ordering by the relation $O_{Ni,Nb} = [I_{11,14}/(I_{11} + I_{14})]$ where I_{11} and I_{14} are the intensities of peak 11 and 14 respectively [37]. For ordered structure Ni ions in *2d* site would be absent resulting in no extra peaks ($I_{11} = 0$) and therefore for ordered structure $O_{Ni} = 0$ and $O_{Nb} = 1$. But for our partially ordered sample for the presence of Ni ions in the Nb (*2d*) site, the degree of ordering is found to be $O_{Ni} = 0.517$ and $O_{Nb} = 0.483$. Similarly, according to the charge to mass ratio the Raman modes for Ni ions occupying the Ta (*2d*) site, the peak for Ta would appear at frequencies which are 0.89 times of the mode associated with the Ni ions which is satisfied by peak 9 and 11 (0.83). The degree of ordering for Ni ion in the Ta (*2d*) site can be calculated considering the peak 11 and 9 which is found to be $O_{Ni} = 0.221$ and $O_{Ta} = 0.779$.

The phonon modes of the partially ordered BNTS sample are shown in Table 6. Twenty-two Raman-active modes ($\Gamma_{Raman} = 6\ A_{1g} + 9E_{2g} + 7\ E_{1g}$) are expected in the ordered sample with *P* 6_3/*mmc* space group and can be indexed using the D_{6h} cell. The increased number of the optical active modes in BNTS can be attributed to the occupational disorder for the exchange of Wyckoff sites between B′-B″-B‴ ions. The existence of B′ ions in *4f* Wyckoff site would give rise to three additional Raman and two additional IR bands each ($\Gamma_{Raman,B'} = A_{1g} + E_{2g} + E_{1g}$, $\Gamma_{IR,B'} = A_{2u} + E_{1u}$) and the presence of B"/B‴ ions in *2a* Wyckoff site would give rise to two additional IR bands ($\Gamma_{IR,\ B''/B'''} = A_{2u} + E_{1u}$). The Lorentzian fitting of the BNTS sample indicates the presence of 28 bands. The Raman active bands for the partially ordered BNTS sample are illustrated in Table 4. Three extra Raman bands occur due to the presence of Ni ions in the *4f* site and three additional Raman band may be attributed to the defect activated modes [36] which might have evolved due to the local breakdown of rigid symmetry rules. The observed Raman modes match well with those reported by Daniel et al. for sample having *P* 6_3/*mmc* space group along with few additional peaks for the doping of the B-site cation [40]. The Raman spectra of Barium based hexagonal perovskites as reported by J. Chen et al. can be classified into four frequency ranges (below 200 cm^{-1}, 200-400 cm^{-1}, 500-650 cm^{-1} and above 650 cm^{-1}) [41]. The peaks 1–5 which lies below 200 cm^{-1} are associated with the vibration of Ba ions. The peaks lying in the rage of 200–400 cm^{-1} arises due to the rotational and vibrational modes of Ni–O, Ta–O and Sb–O bonds. The peaks lying within 500–650 cm^{-1} are due

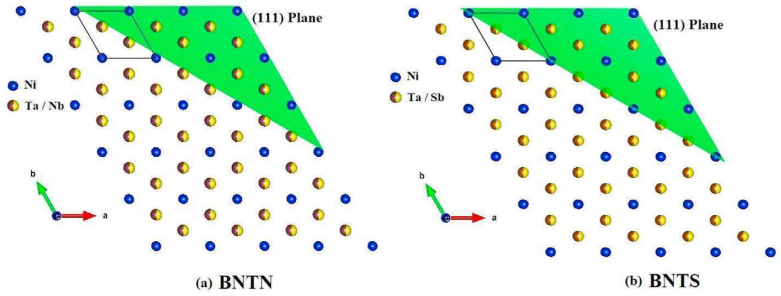

Fig. 6. Ordering sequences of octahedral B site cations of (a) BNTN and (b) BNTS along the crystallographic c axis.

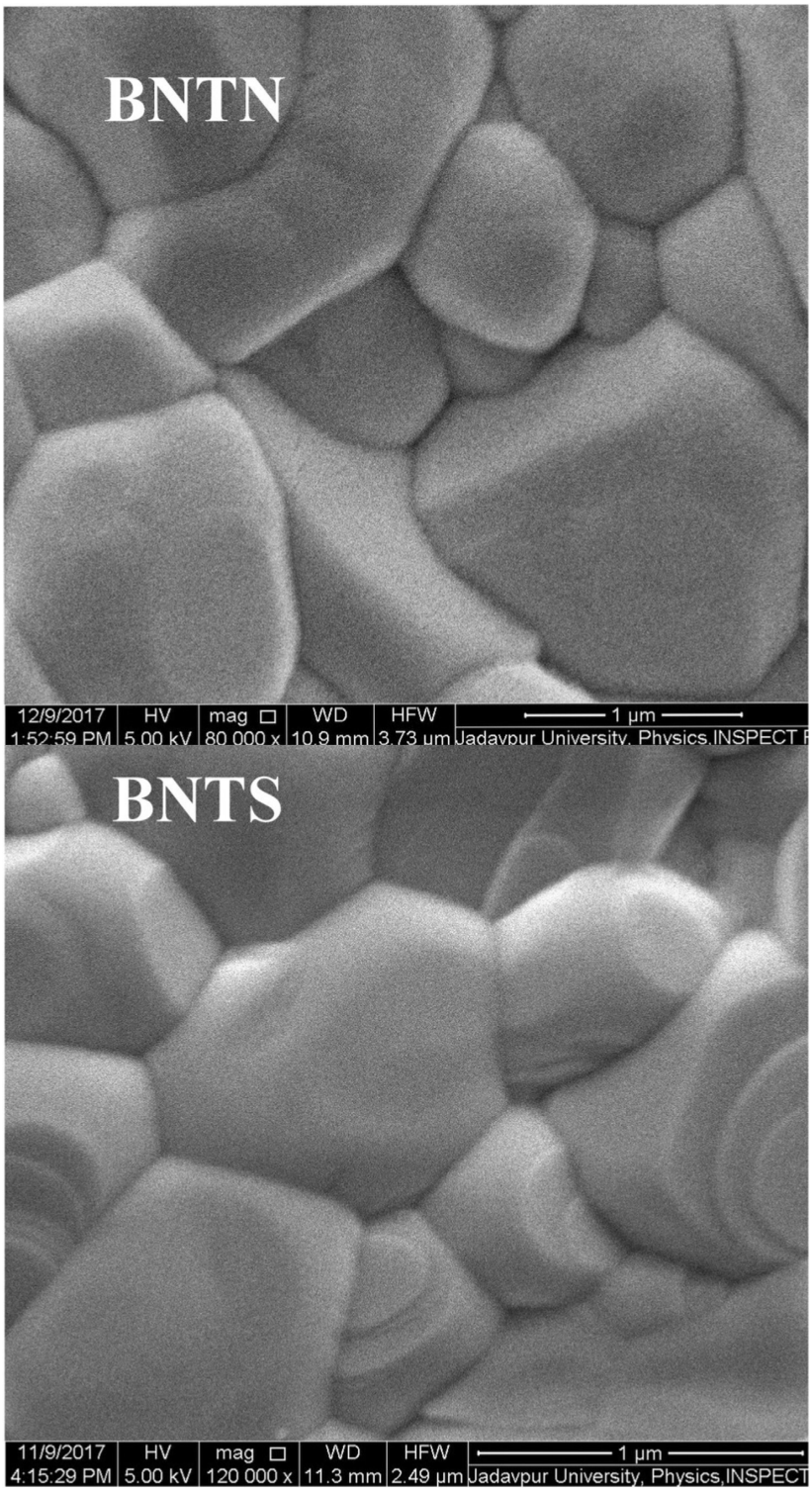

Fig. 7. The scanning electron micrograph of (a) BNTN and (b) BNTS.

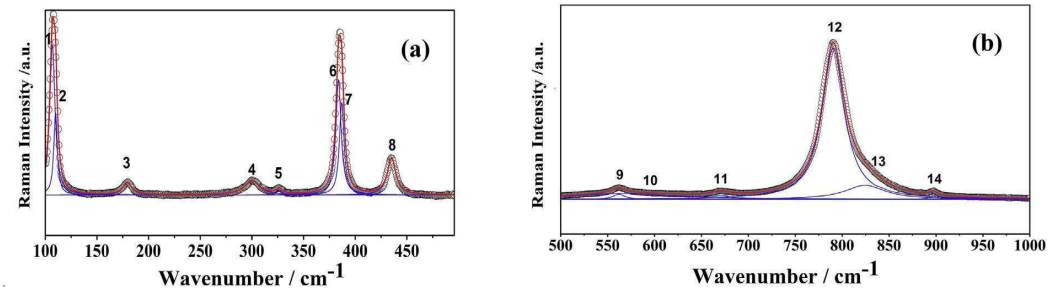

Fig. 8. The Raman spectra of BNTN where the symbols represent the experimental data and the red line represents the fitted Lorentzian curve.

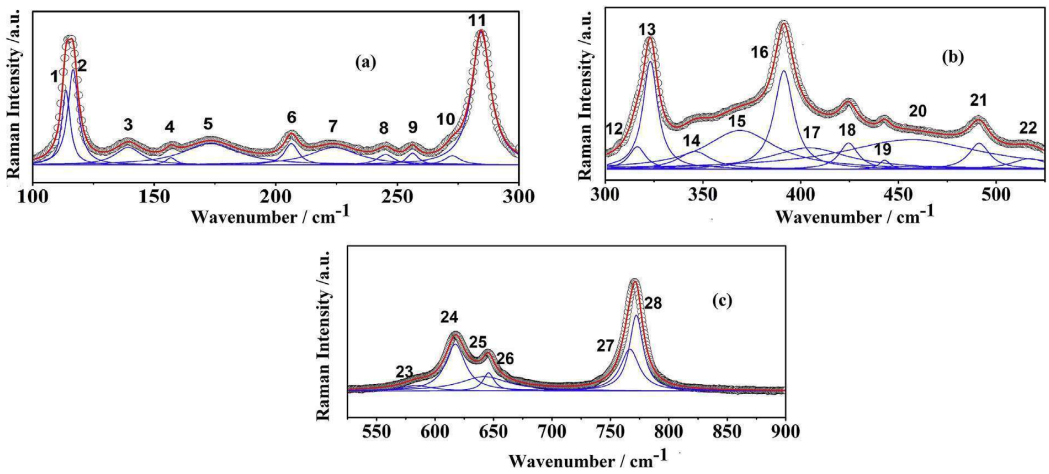

Fig. 9. The Raman spectra of BNTS where the symbols represent the experimental data and the red line represents the fitted Lorentzian curve.

Table 4
Observed Raman active phonon modes.

	BNTN		BNTS	
	Frequency (cm^{-1})	FWHM(cm^{-1})	Frequency (cm^{-1})	FWHM(cm^{-1})
1	106.86061	6.13422	113.73656	4.13635
2	109.94055	4.18384	116.65472	5.2179
3	179.3268	10.63783	139.39437	13.45644
4	300.33057	17.82231	156.93822	5.34014
5	326.35023	6.93163	173.26966	27.89207
6	383.77561	6.09894	206.41028	7.08981
7	386.93194	5.33803	223.90904	24.97306
8	435.17503	9.77481	245.20409	8.69937
9	562.12548	15.33022	256.28441	6.01976
10	568.39212	138.60571	272.66648	8.12174
11	671.08173	28.19654	284.47502	9.19352
12	790.39932	28.85488	316.41858	10.34392
13	824.41936	52.12184	323.12421	9.26482
14	897.29771	9.36599	345.80338	20.57622
15			369.06258	43.86453
16			391.43135	12.07692
17			404.17266	49.40364
18			424.54697	11.75038
19			442.95049	6.69549
20			456.91957	87.35553
21			491.31689	13.0209
22			517.0972	22.39771
23			584.04553	31.63836
24			617.37004	20.5725
25			642.13645	50.53684
26			645.81217	11.43132
27			766.68909	19.4977
28			772.12739	14.3234

to the bending and symmetry vibration of NiO_6, TaO_6 and SbO_6 octahedra. The asymmetric stretching vibration of NiO_6, TaO_6 and SbO_6 octahedra are associated with the peaks above 650 cm^{-1}. We propose the peak 26 is for Ta ions, peak 27 is for Ni ions and peak 28 is for Sb ions in accordance with the charge to mass ratio as described above [36]. Considering the ratio $[(q_{Ni}/m_{Ni})/(q_{Sb}/m_{Sb})]^{1/2}$, the Raman modes for Ni ions occupying the Sb (*4f*) site would appear at frequency which is 0.9113 times of the mode associated with the Sb ions. This ratio is satisfied by peak 27 and 28 (0.99). Since the occupation of Ni ions in the Sb (*4f*) site is one of the causes for the partially ordered structure of BNTS leading to extra Raman modes, we can estimate the degree of ordering by the relation $O_{Ni,Sb} = [I_{27,28}/(I_{27} + I_{28})]$ where I_{27} and I_{28} are the intensities of peak 27 and 28 respectively. For ordered structure Ni ions in the Sb (*4f*) site would be absent resulting in no extra peaks ($I_{27} = 0$) and therefore for ordered structure $O_{Ni} = 0$ and $O_{Sb} = 1$. But for our partially ordered sample for the presence of Ni ions in the Sb (*4f*) site, the degree of ordering is found to be $O_{Ni} = 0.351$ and $Os_b = 0.649$. Similarly, according to charge to mass ratio the Raman modes for Ni ions occupying the Ta (*4f*) site, the peak for Ta would appear at frequencies which are 0.89 times of the mode associated with the Ni ions which is satisfied by peak 26 and 27 (0.842). The degree of ordering for Ni ion in the Ta (*4f*) site can be calculated considering the peak 26 and 27 which is found to be $O_{Ni} = 0.713$ and $O_{Ta} = 0.2876$.

In summary, the results indicate that both BNTN and BNTS are

Table 5
Distribution of modes for the partially ordered BNTN sample belonging to the trigonal space group *P-3m1*.

Atom	Site	Symmetry	Distribution of modes
Ba1	1a	-3m	$A_{2u} + E_u$
Ba2	2 d	3 m	$A_{1g} + A_{2u} + E_u + E_g$
Ni2	1 b	-3m	$A_{2u} + E_u$
Nb3	2 d	3 m	$A_{1g} + A_{2u} + E_u + E_g$
Ta7	2 d	3 m	$A_{1g} + A_{2u} + E_u + E_g$
O5	3e	2/m	$A_{1u} + A_{2u} + E_u$
O6	6i	m	$2A_{1g} + A_{1u} + A_{2g} + 2A_{2u} + 3\,E_u + 3\,E_g$
Modes for the atoms in their own Wykoff site:		Γ_{TOTAL}	$8\,A_{2u} + 9\,E_u + 5\,A_{1g} + 6\,E_g + 2\,A_{1u} + A_{2g}$
		$\Gamma_{ACOUSTIC}$	$A_{2u} + E_u$
		Γ_{RAMAN}	$5\,A_{1g} + 6\,E_g$
		Γ_{IR}	$7A_{2u} + 8\,E_u$
Extra modes for B′-B″-B‴ cation disorder:			$\Gamma_{Raman,\,B'} = A_{1g} + E_g$, $\Gamma_{IR,\,B'} = A_{2u} + E_u$
			$\Gamma_{IR,\,B''/B'''} = A_{2u} + E_u$

Table 6
Distribution of modes for the partially ordered BNTS sample belonging to the hexagonal space group *P 6₃/mmc*.

Atom	Site	Symmetry	Distribution of modes
Ba1	2 b	6m2	$A_{2u} + B_{1g} + E_{2g} + E_{1u}$
Ba2	4f	3 m	$A_{1g} + A_{2u} + B_{1g} + B_{2u} + E_{2u} + E_{2g} + E_{1u} + E_{1g}$
Ni2	2a	3 m	$A_{2u} + B_{2u} + E_{2u} + E_{1u}$
Sb3	4f	3 m	$A_{1g} + A_{2u} + B_{1g} + B_{2u} + E_{2u} + E_{2g} + E_{1u} + E_{1g}$
Ta7	4f	3 m	$A_{1g} + A_{2u} + B_{1g} + B_{2u} + E_{2u} + E_{2g} + E_{1u} + E_{1g}$
O5	6 h	mm2	$A_{1g} + A_{2g} + A_{2u} + B_{1g} + B_{1u} + B_{2u} + E_{2u} + 2\,E_{2g} + 2\,E_{1u} + E_{1g}$
O6	12 k	m	$2\,A_{1g} + A_{1u} + A_{2g} + 2\,A_{2u} + 2\,B_{1g} + B_{1u} + B_{2g} + 2\,B_{2u} + 3\,E_{2u} + 3\,E_{2g} + 3\,E_{1u} + 3\,E_{1g}$
Modes for the atoms in their own Wykoff site:		Γ_{TOTAL}	$6\,A_{1g} + A_{1u} + 2\,A_{2g} + 8\,A_{2u} + 7\,B_{1g} + 2\,B_{1u} + B_{2g} + 7\,B_{2u} + 8\,E_{2u} + 9\,E_{2g} + 10\,E_{1u} + 7\,E_{1g}$
		$\Gamma_{ACOUSTIC}$	$A_{2u} + E_u$
		Γ_{RAMAN}	$6\,A_{1g} + 9\,E_{2g} + 7\,E_{1g}$
		Γ_{IR}	$7A_{2u} + 9\,E_{1u}$
Extra modes for B′-B″-B‴ cation disorder:			$\Gamma_{Raman,\,B'} = A_{1g} + E_{2g} + E_{1g}$, $\Gamma_{IR,\,B'} = A_{2u} + E_{1u}$
			$\Gamma_{IR,\,B''/B'''} = A_{2u} + E_{1u}$

partially disordered perovskite and in their Raman spectra more than expected number of modes than their ordered form have been obtained due to their B-site (B′-B″-B‴) occupational disorder and localized crystalline defects. It may be noted that it is very difficult to detect very minute amount of occupational disorder and localized defects by powder x-ray diffraction study but for partially ordered perovskites slight amount of such occupational disorder/localized defects can be detected by Raman spectroscopic technique due to its excellent resolving power [33,35,37].

The FTIR spectra of BNTN and BNTS are illustrated in Fig. 10. The bending mode of the BO_6 polyhedra is associated with the energy bands in between 360 and 412 cm^{-1}. The energy bands for Sb and Nb ions appear in the higher energy side compared to that of TaO_6 octahedra as both Sb and Nb ions are lighter than Ta ion. The asymmetric bending mode of the NbO_6 and SbO_6 octahedra is associated with the band at 410 cm^{-1} for BNTN and 408 cm^{-1} for BNTS. The band at 504 cm^{-1} for BNTN and 494 and 538 cm^{-1} for BNTS are associated with the Ni–O stretching vibrations of the NiO_6 octahedra [42,43]. The asymmetric stretching vibration of NbO_6 and SbO_6 octahedra is related to the broad band at around 614 cm^{-1} for BNTN and 682 cm^{-1} for BNTS, respectively. The asymmetry in the bond lengths of Ni–O, Sb–O and Nb–O gives rise to the broad nature of the observed peaks. The absorption peaks of Nickel, Antimony and Niobium oxides are at nearly same wave numbers which also contributes to the broad nature of the observed peak. The low intensity peak at 692 cm^{-1} for BNTN and 718 and 782 cm^{-1} for BNTS is because of the symmetric stretching vibration of NbO_6 and SbO_6 octahedra.

3.3. Dielectric analysis

The dielectric permittivity (ε′) and the loss tangent (tan δ) variations with log of angular frequency (log ω) for BNTS and BNTN is presented in Figs. 11 and 12 respectively. The variation of ε′ with frequency can be roughly classified into three different regions. In

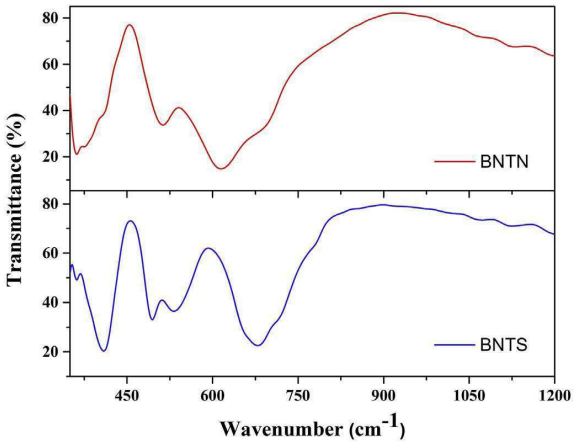

Fig. 10. The FTIR spectrum of (a) BNTN and (b) BNTS.

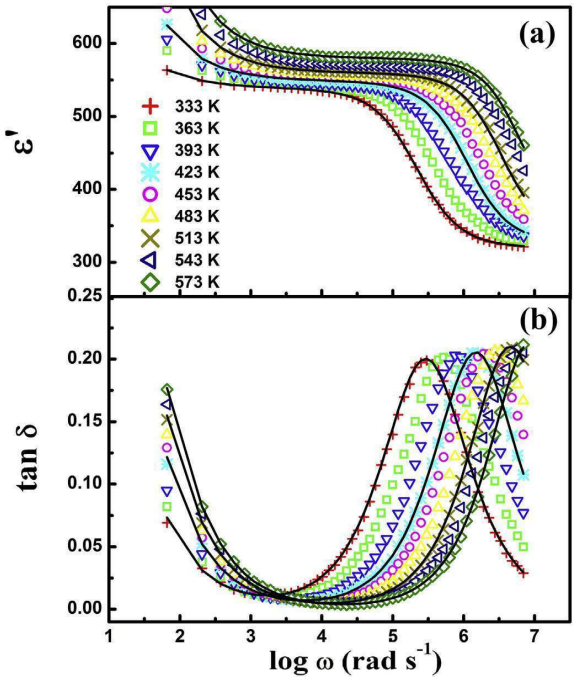

Fig. 11. Frequency dependence of (a) ε' and (b) tan δ of BNTN at different temperatures where the Cole-Cole fit of the experimental data are represented by the solid lines.

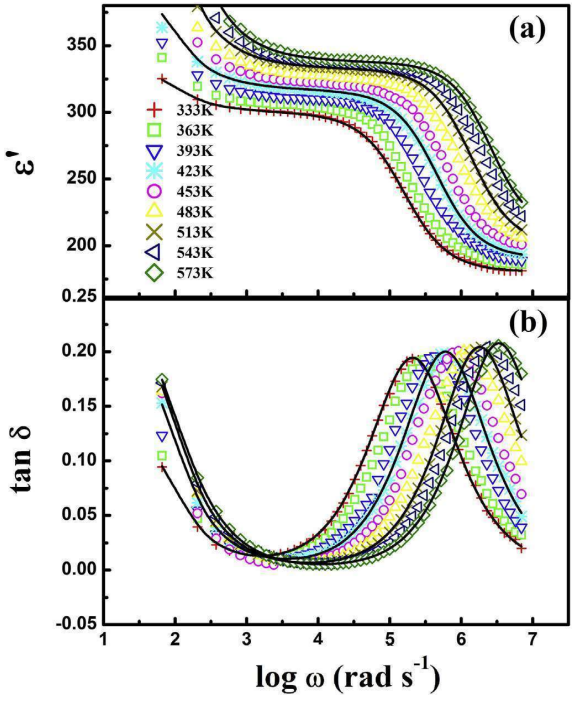

Fig. 12. Frequency dependence of (a) ε' and (b) tan δ of BNTS at different temperatures where the Cole-Cole fit of the experimental data are represented by the solid lines.

the region where the frequency is very low the dipoles starts lagging behind the field leading to a slow decrease in ε'. At a certain frequency known as the characteristic frequency the ε' drops off suddenly pointing towards a relaxation phenomenon. At higher frequencies the dipoles are unable to follow the field resulting in a constant value of ε'. This behavior of dielectric permittivity can be well explained by the Debye theory [44]. A relaxation peak can be observed in the tan δ curve which shifts to the higher frequency side on increasing the temperature as more polarization occurs at high temperatures. The broad nature of the tan δ peaks as observed in Figs. 11 and 12 indicates the polydispersive nature of relaxation times which can be analyzed with the help of the Cole-Cole model [45,46].

$$\varepsilon^* = \varepsilon' - i\varepsilon'' = \varepsilon_\infty + \frac{\varepsilon_s - \varepsilon_\infty}{1 + (i\omega\tau)^{1-\alpha}} \tag{1}$$

where ε_s and ε_∞ are low and high frequency values of ε', τ denotes the mean relaxation time and α represents the dispersal of the relaxation time. The value of α is 0 for monodispersive relaxation process and for polydispersive relaxation process $\alpha > 0$. In the lower frequency side, tan δ for both the samples increases with the decrease in frequency which may be ascribed due to the effect of dc conductivity. So, a term for the dc electrical conduction is added to equation (1) [47,48]:

$$\varepsilon^* = \varepsilon_\infty + \frac{\varepsilon_s - \varepsilon_\infty}{1 + (i\omega\tau)^{1-\alpha}} - i\frac{\sigma^*}{\varepsilon_0\omega^n} \tag{2}$$

where the complex conductivity $\sigma^* = (\sigma_1 + i\,\sigma_2)$ with dc conductivity being denoted by σ_1 and conductivity due to localized charges being denoted by σ_2. In the above equation (2) n is a dimensionless frequency exponent which lies between 0 and 1. Equation (2) can be written as,

$$\varepsilon' = \varepsilon_\infty + \frac{(\varepsilon_s - \varepsilon_\infty)\left[1 + (\omega\tau)^{1-\alpha}\sin\frac{1}{2}\alpha\pi\right]}{1 + 2(\omega\tau)^{1-\alpha}\sin\frac{1}{2}\alpha\pi + (\omega\tau)^{2(1-\alpha)}} - \frac{\sigma_2}{\varepsilon_0\omega^n} \tag{3}$$

$$\varepsilon'' = \frac{(\varepsilon_s - \varepsilon_\infty)(\omega\tau)^{1-\alpha}\cos\frac{1}{2}\alpha\pi}{1 + 2(\omega\tau)^{1-\alpha}\sin\frac{1}{2}\alpha\pi + (\omega\tau)^{2(1-\alpha)}} + \frac{\sigma_1}{\varepsilon_0\omega^n} \tag{4}$$

and, the dielectric loss can be calculated by

$$\tan\delta = \varepsilon''/\varepsilon' \tag{5}$$

The experimental data has been fitted with the help of equations (3)–(5) and is represented by black lines in Figs. 11 and 12. The different fitting parameters are shown in Table 7. The main factors associated with the dielectric relaxation are

Table 7
The values of different parameters obtained by fitting the dielectric spectra of BNTN and BNTS by modified Cole-Cole equations.

Temperature(K)	ε_s	ε_∞	ω_m (Hz)	α	n	σ_1 (Sm^{-1})	σ_2 (Sm^{-1})
BNTN							
333	539	319	217,532	0.11	0.79	0.1×10^{7}	6.00×10^{9}
423	549	325	1,113,691	0.10	0.81	0.2×10^{-7}	2.00×10^{-8}
513	560	332	3,423,916	0.09	0.82	0.3×10^{-7}	4.00×10^{-8}
573	580	346	6,525,959	0.08	0.83	0.4×10^{-7}	6.00×10^{-8}
BNTS							
333	300	180	158,018	0.11	0.86	0.1×10^{-7}	8.00×10^{-9}
423	317	190	453,625	0.10	0.88	0.2×10^{-7}	2.00×10^{-9}
513	333	200	1,375,618	0.09	0.9	0.3×10^{-7}	5.00×10^{-9}
573	348	210	2,546,917	0.08	0.91	0.4×10^{-7}	9.00×10^{-9}

the dipole relaxation and the conduction relaxation of the free charge carriers [49]. The value of α which is associated with the dipole relaxation decreases with increase in temperature for both BNTN and BNTS indicating that the dispersal of relaxation time decreases thus the relaxation behavior in both the samples tends towards monodispersive nature with increase in temperature. The relaxation time τ which is inversely proportional to ω_m decreases with increase in temperature indicating that the rate of polarization and the dipole density increases with temperature. The value of n which is associated with the conduction relaxation of the free charge carriers increases with temperature for both BNTN and BNTS indicating that at higher temperature the carrier polarization mechanism is less dispersive owing to some barrier height extracted [49,50]. The mobile charge carriers when obstructed by the grain boundaries hinders their charge migration giving rise to space charge polarization [51]. The charges accumulate at the barrier which causes a localized polarization inside the grains. As the temperature increases the density of charges causing the space charge polarization becomes quite large. Thus, with increase in temperature relaxation processes get more and more localized which makes the relaxation process more Debye type or monodispersive as also indicated by the decrease in the α value with increasing temperature.

In BNTN and BNTS the existence of long-range migration of free charge carriers (dc conductivity) is evident in the low frequency region thus we can conclude that both the samples possess some amount of electrical semiconductivity [51]. The hybridization between the vacant d orbitals of B-site cations and the p orbitals of oxygen significantly affects the transport properties of the perovskite oxides [52,53]. The electronegativity of Sb^{5+} being higher than that of Nb^{5+} results in less ionic or more covalent Sb–O bond which in-turn decreases its macroscopic polarizability [52,54]. The presence of vacant d orbitals in Nb favors higher hybridization with p orbitals of oxygen giving rise to larger polar instabilities and higher permittivity values for BNTN. The presence of vacant 4 d orbital of Nb in BNTN sample gives rise to its high dielectric permittivity values as compared to BNTS for which the 4 d orbitals of Sb are completely filled. As the permittivity value of BNTN is quite high as compared to BNTS and have almost same low values of dielectric losses, the BNTN sample is more suitable for circuit miniaturization [55].

3.4. Complex impedance analysis

The complex plane impedance plots at temperatures 423 K and 543 K for BNTN and BNTS are illustrated in Figs. 13 and 14 respectively. The contribution of both the grain and grain boundary to the overall impedance has been confirmed by the presence of two deformed circular arcs in both the samples [56]. The center of the semicircular arc being blow the Z′ axis also confirms the relaxation mechanism of the samples being polydispersive nature [56–62]. The semicircular arc becomes smaller on increasing the temperature which points towards the thermally activated conduction mechanism of the samples having semiconducting nature. The impedance spectra have been fitted using an equivalent circuit model consisting of two parallel combination of resistance and capacitance joined together in series. The capacitance term here is replaced by a constant phase element (Q) due to the non-ideal behavior of the capacitance as a result of more than one relaxation process for a given relaxation time. The capacitance for the constant phase element is given by $C_p = Q^{1/c}\ R^{(1-\ c)/c}$ where c denotes the deviation from the ideal Debye nature. The real and the imaginary part of the impedance have been fitted using equations

$$Z' = \frac{R_g}{1+\left[\omega\left(R_gQ_g\right)^{\frac{1}{c_g}}\right]^2} + \frac{R_{gb}}{1+\left[\omega\left(R_{gb}Q_{gb}\right)^{\frac{1}{c_{gb}}}\right]^2} \tag{6}$$

$$\text{and } Z'' = R_g\left[\frac{\omega\left(R_gQ_g\right)^{\frac{1}{c_g}}}{1+\left[\omega\left(R_gQ_g\right)^{\frac{1}{c_g}}\right]^2}\right] + R_{gb}\left[\frac{\omega\left(R_{gb}Q_{gb}\right)^{\frac{1}{c_{gb}}}}{1+\left[\omega\left(R_{gb}Q_{gb}\right)^{\frac{1}{c_{gb}}}\right]^2}\right] \tag{7}$$

where R_g and R_{gb} denotes the resistance and Q_g and Q_{gb} denotes the constant phase element for the grain and grain boundary respectively. The fitting parameters are given in Table 8. The coincidence of the fitted curve and the experimental data points confirms that both the grain and grain boundary contribute to the total impedance. The high values of R_{gb} indicates that the grain boundaries are more insulating than the grains.

3.5. Conductivity analysis

The variation ac conductivity with frequency for BNTN and BNTS at various temperatures is depicted in Figs. 15 and 16 respectively. In the conductivity spectrum two discrete plateaus can be observed. The plateau at the low frequency is associated with the total conductivity whereas the plateau at the higher frequency arises due to the grain's contribution to the total conductivity [63]. Thus, two processes are involved in the bulk conduction mechanism of the samples. The total conductivity as stated by the power law is:

$$\sigma(\omega) = \sigma_{dc} + K\omega^n \tag{8}$$

here σ_{dc} is the dc conductivity and K is a constant dependent on frequency and temperature. In order to fit the conductivity spectra, the basic power law has been used with n values between 1.5 and 1.9 [64] at lower frequency and 0.4–0.6 at higher frequency [65]. The parameters used for fitting are represented in Table 9. The above equation can also be written as $\sigma(\omega) = \sigma_{dc}[1 + (\omega/\omega_H)^n]$ where the charge carriers' hopping frequency is denoted by ω_H. The value of ω_H for BNTN is 4158.32 and 15666.79 rad^{-1} at 423 and 573 K respectively and for BNTS the value of ω_H is 3863.92 and 22623.61 rad^{-1} at 423 and 573 K respectively.

The variation of the dc conductivity (σ_{dc}) with the inverse of temperature (Fig. 17) is found to follow the Arrhenius Law: $\sigma_{dc} = \sigma_0 \exp\left[-\frac{E_\sigma}{K_BT}\right]$, where E_σ is the activation energy. On increasing the temperature, the dc conductivity value increases. The value of E_σ as deduced from the Arrhenius plot is 0.36 eV for BNTN and 0.37 eV for BNTS. The value of E_σ suggests that for both BNTN and BNTS the conduction mechanism is governed by p-type polaron hopping [66,67]. The step like nature of the conductivity spectra is due to the presence of different potentials offered by the grain and grain boundary and the hopping of charge carriers through these potential barriers [54]. As seen from the impedance spectra the grain boundary being more insulating acts as a trap site for the charge carriers taking part in the charge transport.

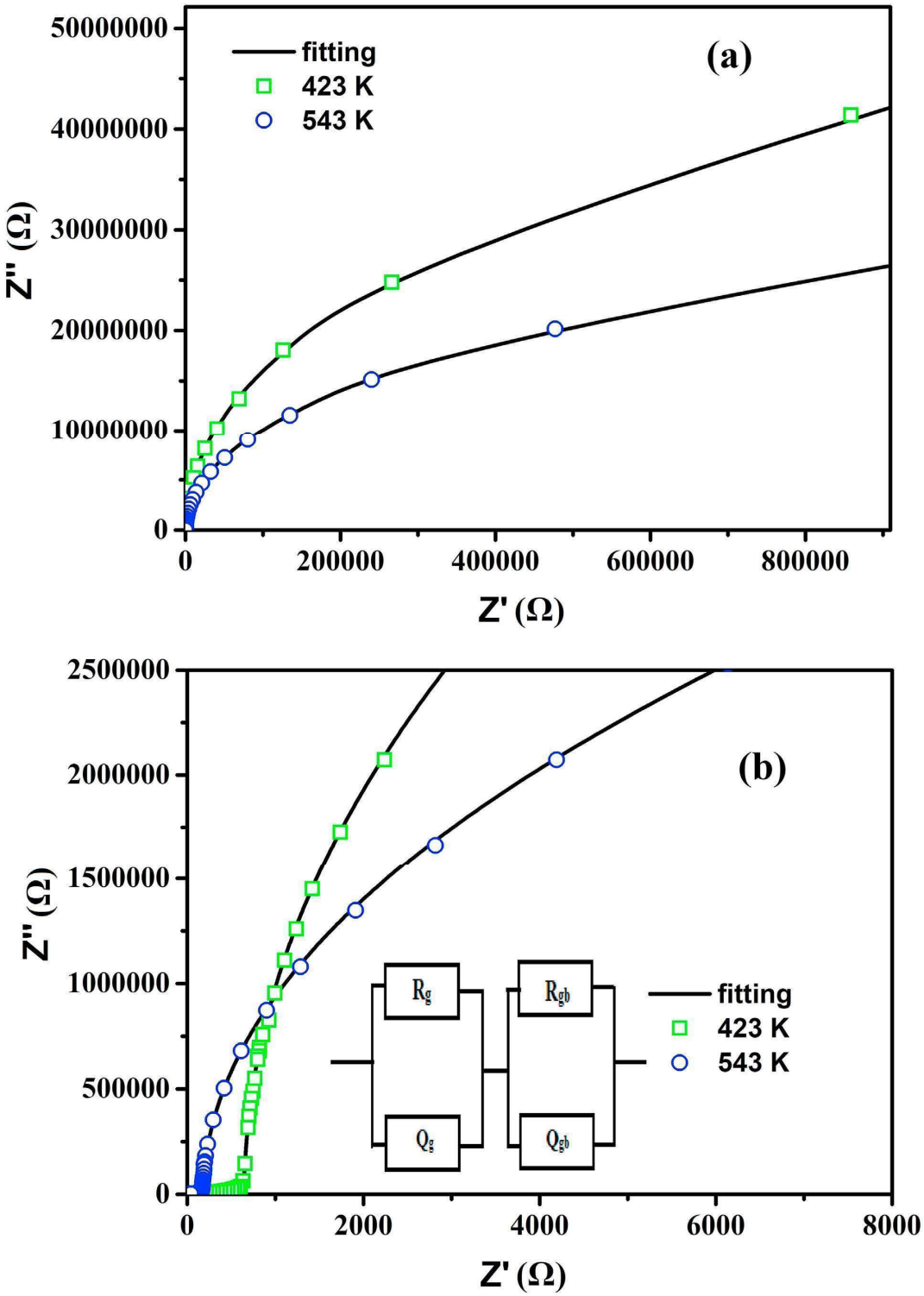

Fig. 13. (a) Complex impedance plane plots of BNTN and (b) the enlarge view of the high frequency region.

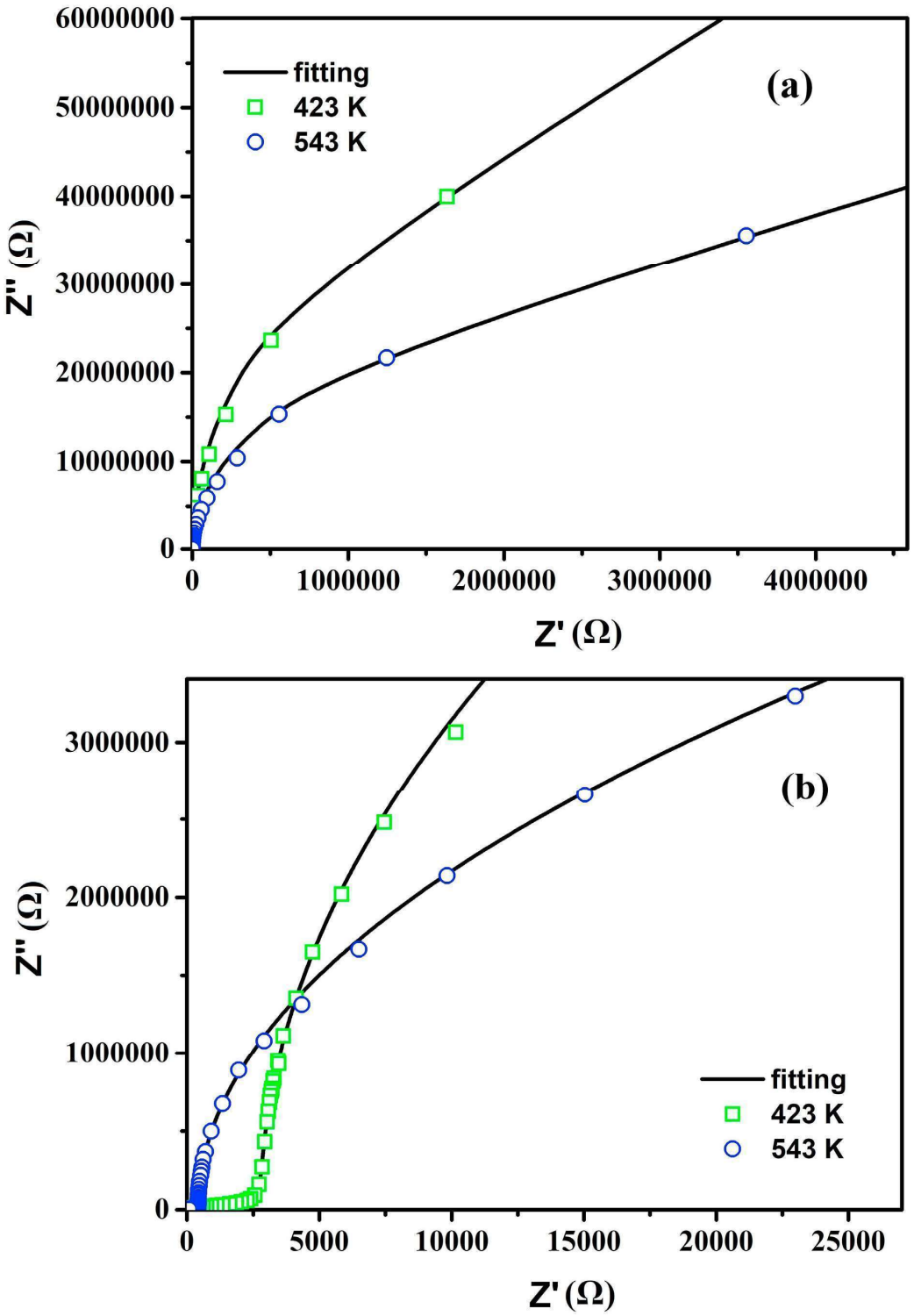

Fig. 14. (a) Complex impedance plane plots of BNTS and (b) the enlarge view of the high frequency region.

Table 8
The fitted parameters of the impedance circuit for BNTN and BNTS.

	Temp.(K)	R_g (Ω)	Q_g (10^{-8} F/Ω)	c_g	R_{gb} (10^8 Ω)	Q_{gb} (10^{-9} F/Ω)	c_{gb}
BNTN	423	650	3	0.81	28	0.17	0.89
	543	185	1	0.92	11	0.27	0.86
BNTS	423	2800	1.50	0.82	14	0.19	0.86
	543	421	0.98	0.82	5	0.28	0.87

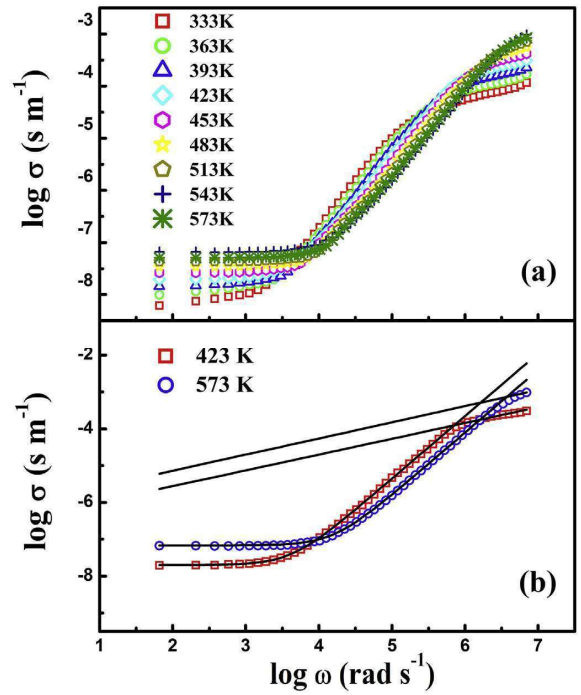

Fig. 15. (a) Frequency dependence of the ac conductivity of BNTN at different temperatures and (b) the power law fitting of the experimental data as shown by solid lines.

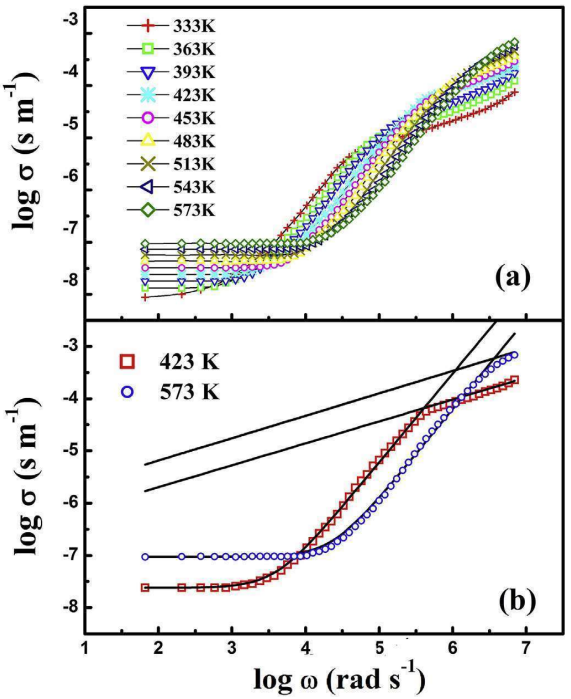

Fig. 16. (a) Frequency dependence of the ac conductivity of BNTS at different temperatures and (b) the power law fitting of the experimental data as shown by solid lines.

4. Conclusion

We have successfully synthesized two triple perovskites, viz., $Ba_3NiTaNbO_9$ (BNTN) and $Ba_3NiTaSbO_9$ (BNTS) by solid state ceramic method and thoroughly investigated their structural, microstructural, optical and dielectric properties. The crystal structure, bonding property and ordering behavior of BNTN and BNTS are analyzed by Rietveld refinement of XRD data and the results are further corroborated by FTIR and Raman studies. It has been shown that both BNTN and BNTS are partially ordered triple perovskite having general formula $A_3(B'B''B''')O_9$. BNTN and BNTS stabilize in *P-3m1* space group of trigonal symmetry and *P* 6_3*/mmc* space group of hexagonal symmetry, respectively. Both the sample possess cationic disorder due to the site exchange of cations occupying the B′, B″ and B‴ sites. This work will be of immense help in understanding the nature of ordering and probing the presence of occupational disorder evolving due to the exchange of cations between B′, B″, B‴ sites of $A_3(B'B''B''')O_9$ type perovskites.

The dielectric loss for both the samples is similar in nature with a broad peak indicating the polydispersive nature of the relaxation phenomena. For both the samples two semicircular arcs are obtained which indicates that the total impedance is due to the contribution of both grain and grain boundaries. The activation energy as deduced from the Arrhenius plot is 0.36 eV and 0.37 eV for BNTN and BNTS respectively, indicating the conduction phenomena is because of the hopping of the polaron of p-type. It is noteworthy that at room temperature $Ba_3M^{III}TiM^{V}O_9$ (where, M^{III} = Ga, Y, Lu; M^{V} = Nb, Ta) and $Ba_3M^{III}TiSbO_9$ (where, M^{III} = Fe, Ga) exhibit dielectric permittivity (ε') in the range of 20–60 and 20–100, respectively, at frequencies ranging between 1 kHz and

Table 9
Various fitted parameters of the conductivity spectra for BNTN and BNTS.

Sample	Temperature(K)	σ_{dc} (Sm^{-1})	A	n
BNTN	423 (at low frequency)	1.99×10^{-8}	0.14×10^{-13}	1.7
BNTN	423 (at high frequency)	1.99×10^{-8}	3.8×10^{-7}	0.43
BNTN	573 (at low frequency)	6.81×10^{-8}	0.05×10^{-13}	1.7
BNTN	573 (at high frequency)	6.81×10^{-8}	9.5×10^{-7}	0.44
BNTS	423 (at low frequency)	2.39×10^{-8}	0.19×10^{-13}	1.7
BNTS	423 (at high frequency)	2.39×10^{-8}	2.9×10^{-7}	0.42
BNTS	573 (at low frequency)	9.38×10^{-8}	0.03×10^{-13}	1.72
BNTS	573 (at high frequency)	9.38×10^{-8}	8.9×10^{-7}	0.43

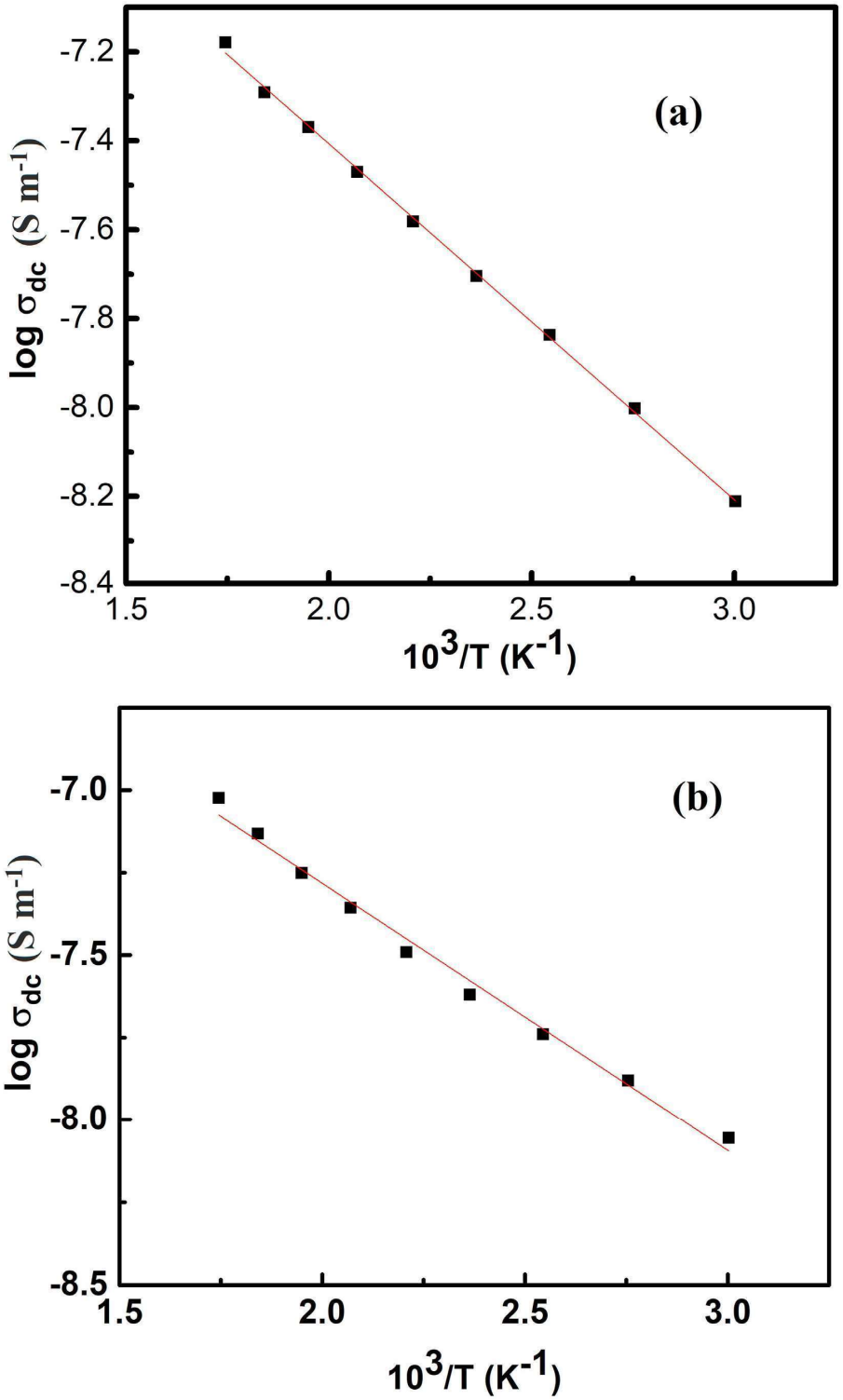

Fig. 17. Arrhenius plot of dc conductivity for (a) BNTN and (b) BNTS.

1MHz [26]. The values of ε' for $Ba_3MgTa_{2-x}Nb_xO_9$ (where $0 \leq x \leq 1$) lies in the range of 15–20 at 500 KHz and the dielectric loss ($\tan\delta$) is ~0.15 for this series of compounds [68]. The value of ε' and $\tan\delta$ for the series of compounds with general formula $Ba_3ZnTa_{2-x}Nb_xO_9$ ($0 \leq x \leq 1$) at 500 KHz are ≈ 30 and 0.08, respectively [68]. Further, the dielectric constant and dielectric loss at 500 KHz are 324 and 0.05 for BNTN and 182 and 0.04 for BNTS, respectively. It may be inferred that the chemical property of B-site cations strongly affect the dielectric properties of $A_3(B'B''B''')O_9$ type perovskites and BNTN and BNTS exhibits improved dielectric properties as compared to other triple perovskites of $Ba_3(B'B''B''')O_9$ series. Thus, BNTN and BNTS appears to be very suitable for fabrication of radio frequency devices like dielectric resonator, oscillator and filters and may also find application in the field of electronic device miniaturization.

CRediT authorship contribution statement

A. Barua: Methodology, Data curation, Software, Investigation, Visualization, Writing - original draft, Writing - review & editing. **S.K. Dey:** Software, Investigation, Visualization. **S.K. Sabyasachi:** Software, Investigation, Visualization. **S. Kumar:** Conceptualization, Supervision, Validation.

Declaration of competing interest

The authors declare that they have no known competing financial interests or personal relationships that could have appeared to influence the work reported in this paper.

Acknowledgement

I would like to acknowledge the FRPDF grant of the Presidency University. I would like to thank the DST, Gov. of India for the FIST and PURSE program. I would also like to acknowledge the SAP and UPE program of UGC, Govt. of India.

References

[1] T.A. Vanderah, Science 298 (2002) 1182.
[2] R.J. Cava, J. Math. Chem. 11 (2001) 54–62.
[3] M. Lee, E.S. Choi, X. Huang, J. Ma, C.R. Dela Cruz, M. Matsuda, W. Tian, Z.L. Dun, S. Dong, H.D. Zhou, Phys. Rev. B 90 (2014) 224402.
[4] J. Hwang, E.S. Choi, F. Ye, C.R. Dela Cruz, Y. Xin, H.D. Zhou, P. Schlottmann, Phys. Rev. Lett. 109 (2012) 257205.
[5] I. Molodetsky, P.K. Davies, J. Eur. Ceram. Soc. 21 (2001) 2587–2591.
[6] B. Xu, F. Zhang, X.Y. Liu, J.H. Ye, W.H. Zhang, L. Shi, X.G. Wan, J. Yin, Z.G. Liu, Phys. Rev. B 76 (2007) 125109.
[7] Y. Doi, Y. Hinatsu, J. Mater. Chem. 12 (2002) 1792–1795.
[8] S.J. Kim, M.D. Smith, J. Darriet, H.C. zur Loye, J. Solid State Chem. 177 (2004) 1493–1500.
[9] Y. Doi, Y. Hinatsu, J. Phys. Condens. Matter 16 (2004) 2849–2860.
[10] J.G. Zhao, L.X. Yang, Y. Yu, F.Y. Li, R.C. Yu, C.Q. Jin, J. Solid State Chem. 182 (2009) 327–330.
[11] V.U. Treiber, S. Kemmler-Sack, A. Ehmann, Z. Anorg, Allg. Chem. 487 (1982) 198.
[12] P. Lightfoot, P.D. Battle, J. Solid State Chem. 89 (1990) 174–183.
[13] J.C. Albornoz, D.A. Landinez Tellez, J. Roa-Rojas, J.A. Munevar, E. Baggio-Saitovich, J. Supercond. Nov. Magnetism 26 (2013) 2313–2317.
[14] P. Beran, S.A. Ivanov, P. Nordblad, S. Middey, A. Nag, D.D. Sarma, S. Ray, R, Mathieu Solid State Sci 50 (2015) 58–64.
[15] F. Casallas, E. Vera, D. Landinez, C. Parra, J. Roa, J. Phys.: Conf. Ser. 687 (2016), 012047.
[16] T. Ferreira, D. Carone, A. Huon, A. Herklotz, S.A. Stoian, S.M. Heald, G. Morrison, M.D. Smith, H.C. zur Loye, Inorg. Chem. 57 (2018) 7362–7371.
[17] R.D. Shannon, J. Appl. Phys. 73 (1993) 348.
[18] H. Tamura, D.A. Sagala, K. Wakino, Jpn. J. Appl. Phys. 25 (1986) 787.
[19] I.M. Reaney, I. Qazi, W.E. Lee, J. Appl. Phys. 88 (2000) 6708.
[20] R. Mani, P. Selvamani, J.E. Joy, J. Gopalakrishnan, Inorg. Chem. 46 (2007) 6661–6667.
[21] M.M. Hoque, A. Dutta, S. Kumar, T.P. Sinha, Physica B 407 (2012) 3740–3748.
[22] M.W. Lufaso, Chem. Mater. 16 (2004) 2148–2156.
[23] S. Asai, M. Soda, K. Kasatani, T. Ono, M. Avdeev, T. Masuda, Phys. Rev. B 93 (2016), 024412.
[24] A.J. Jacobson, A.J. Calvert, J. inorg, nucl. Chem. 40 (1978) 447–449.
[25] A.C. Larson, R.B. Von Dreele, General Structure Analysis System (GSAS), Los Alamos National Laboratory, 2000, pp. 86–784. Report LAUR.
[26] J.B. Philipp, P. Majewski, L. Alff, A. Erb, R. Gross, T. Graf, M.S. Brandt, J. Simon, T. Walther, W. Mader, D. Topwal, D.D. Sarma, Phys. Rev. B 68 (2003) 144431.
[27] R.D. Shannon, Acta Crystallogr. 32 (1976) 751–767.
[28] M.W. Lufaso, E. Hopkins, S.M. Bell, A. Llobet, Chem. Mater. 17 (2005) 4250.
[29] J.E. Joy, E. Atamanik, R. Mani, A. Nag, R.M. Tiwari, V. Thangadurai, J. Gopalakrishnan, Solid State Sci. 12 (2010) 1970–1976.
[30] G. Blasse, J. Inorg. Nucl. Chem. 27 (1965) 993.
[31] J.B. Goodenough, J.A. Kafalas, J. Solid State Chem. 6 (1973) 493.
[32] H. Mizoguchi, P.M. Woodward, S.H. Byeon, J.B. Parise, J. Am. Chem. Soc. 126 (2004) 3175.
[33] J.E.F.S. Rodrigues, E. Moreira, D.M. Bezerra, A.P. Maciel, C.W.A. Paschoal, Mater. Res. Bull. 48 (2013) 3298–3303.
[34] D.L. Rousseau, R.P. Bauman, S.P.S. Porto, J. Raman Spectrosc. 10 (1981) 253.
[35] A. Dias, V. Ciminelli, F.M. Matinaga, R. Moreira, J. Eur. Ceram. Soc. 21 (2001) 2739–2744.
[36] R.L. Moreira, F.M. Matinaga, A. Dias, Appl. Phys. Lett. 78 (2001) 428.
[37] J.E.F.S. Rodrigues, D.M. Bezerra, A.P. Maciel, C.W.A. Paschoal, Ceram. Int. 40 (2014) 5921–5930.
[38] S.A. Prosandeev, U. Waghmare, I. Levin, J. Maslar, Phys. Rev. B 71 (2005) 214307.
[39] V.L. Ginzburg, A.P. Levanyuk, A.A. Sobyanin, Phys. Rep. 3 (1980) 151–240.
[40] Ph Daniel, J. Toulouse, J.Y. Gesland, M. Rousseau, Phys. Rev. B 52 (1995) 13.
[41] J. Chen, Y. Tang, J. Li, H. Xiang, C. Li, X. Xing, L. Fang, J. Alloys Compd. 820 (2020) 153159.
[42] A. Dutta, T.P. Sinha, Mater. Res. Bull. 46 (2011) 518–524.
[43] G.V.S. Rao, C.N.R. Rao, J.R. Ferraro, Appl. Spectrosc. 24 (1970) 436.
[44] P. Debye, Polar Molecules, Chemical Catalogue Company, New York, 1929.
[45] K.S. Cole, R.H. Cole, J. Chem. Phys. 9 (1941) 341–351.
[46] K.S. Cole, R.H. Cole, J. Chem. Phys. 10 (1942) 98–105.
[47] R. Coelho, Physics of Dielectrics, Elsevier, New York, 1978.
[48] S.K. Maity, A. Dutta, S. Kumar, T.P. Sinha, Phys. Scripta 88 (2013), 065702.
[49] P. Thongbai, S. Tangwancharoen, T. Yamwong, S. Maensiri, J. Phys. Condens. Matter 20 (2008) 395227.
[50] S. Halder, A. Dutta, T.P. Sinha, J. Phys. Chem. Solid. 102 (2017) 79–89.
[51] R. Mukherjee, S. Saha, A. Dutta, T.P. Sinha, J. Alloys Compd. 651 (2015) 222–229.
[52] A. Dutta, T.P. Sinha, D. Das, J. Magn. Magn Mater. 360 (2014) 211–221.
[53] A. Dutta, T.P. Sinha, Mater. Res. Bull. 46 (2011) 518–524.
[54] Y. Tsuji, A. Kan, H. Ogawa, S. Ishihara, J. Eur. Ceram. Soc. 25 (2005) 2883–2887.
[55] Wolfram Wersing, Curr. Opin. Solid State Mater. Sci. 1 (1996) 715–731.
[56] A. Barua, S. Maity, S. Kumar, A. Dutta, T.P. Sinha, Physica B 583 (2020) 412057.
[57] L. Liu, H. Fan, L. Wang, X. Chen, P. Fang, Phil. Mag. 88 (2008) 537–545.
[58] L. Liu, H. Fan, P. Fang, L. Jin, Solid State Commun. 142 (2007) 573–576.
[59] L. Liu, H. Fan, P. Fang, X. Chen, Mater. Res. Bull. 43 (2008) 1800–1807.
[60] R. Gerhardt, J. Phys. Chem. Solid. 55 (1994) 1491–1506.
[61] M.C.H. Mckubre, J.R. Macdonald, in: J.R. Macdonald (Ed.), Impedance Spectroscopy Emphasizing Solid Materials and Systems, Wiley, New York, 1987, p. 191.
[62] M.M. Hoque, A. Barua, A. Dutta, S.K. Dey, T.P. Sinha, S. Kumar, Ionics 23 (2017) 471–483.
[63] A. Dutta, C. Bharti, T.P. Sinha, Mater. Res. Bull. 43 (2008) 1246–1254.
[64] S. Nomura, K. Toyama, K. Kaneta, Jpn. J. Appl. Phys. 21 (1982) 624–626.
[65] C. Bharti, T.P. Sinha, Solid State Sci. 12 (2010) 498–502.
[66] M. Idrees, M. Nadeem, M.M. Hassan, J. Phys. D Appl. Phys. 43 (2010) 155401.
[67] W.H. Jung, J. Appl. Phys. 90 (2001) 2455.

Ionics (2017) 23:471–483
DOI 10.1007/s11581-016-1916-6

ORIGINAL PAPER

Study on the structural, spectroscopic, and dielectric properties of 1:2 ordered $Ca_3(B'Ta_2)O_9$ (B′ = Mg and Zn)

Md. Monwar Hoque[1] · A. Barua[1] · Alo Dutta[2] · Sanjoy Kumar Dey[1,3] · T. P. Sinha[2] · S. Kumar[1]

Received: 14 May 2016 /Revised: 19 November 2016 / Accepted: 24 November 2016 /Published online: 21 December 2016

Abstract Herein, we report the structural, bonding, dielectric, and electrical transport properties of $Ca_3(MgTa_2)O_9$ (CMT) and $Ca_3(ZnTa_2)O_9$ (CZT) with the chemical formula $Ca(Mg_{1/3}Ta_{2/3})O_3$ and $Ca(Zn_{1/3}Ta_{2/3})O_3$, respectively, synthesized by the solid-state reaction technique. The Rietveld refinement of powder X-ray diffraction (PXRD) patterns has confirmed that the CMT and CZT are triple perovskites belonging to monoclinic $P2_1/c$ space group with 1:2 B-site ordering. The unit cell contains four formula units of CMT and CZT. The results of the structural study are corroborated by Fourier transform infrared (FTIR) and Raman spectroscopic studies. Comparing the crystal structures of 1:2 ordered perovskites with the chemical formula $Ba(B'_{1/3}B''_{2/3})O_3$ and $Ca(B'_{1/3}B''_{2/3})O_3$, we have predicted that for this group of perovskites, only calcium-based systems exhibit a monoclinic crystal structure of $P2_1/c$ space group due to the smaller ionic radii of Ca^{2+} compared to those of Ba^{2+}. The grain size ranges between 0.38 and 2.66 μm for CMT and 0.11 and 1.60 μm for CZT, respectively. The analysis of the dielectric permittivity in the framework of the modified Cole-Cole model has revealed that the dielectric relaxation in CMT and CZT is strongly temperature dependent and polydispersive in nature. The activation energies associated with dielectric and electrical transport properties are ≈0.35 and 0.33 eV for CMT and CZT, respectively. The polaron hopping governs the electrical and dielectric response of the samples. It has been found that CMT and CZT exhibit enhancement in dielectric properties compared to their niobate counterparts and 1:1 ordered tantalum-based perovskite oxides.

Keywords Dielectric properties · Rietveld refinement · Perovskite · Electrical conductivity · Impedance spectroscopy

✉ S. Kumar
kumars@phys.jdvu.ac.in

[1] Department of Physics, Jadavpur University, Kolkata 700032, India

[2] Department of Physics, Bose Institute, 93/1, A. P. C. Road, Kolkata 700009, India

[3] Department of Physics, NITMAS, 24 Paragana(S) 743368, India

Introduction

Studies on the dielectric, structural, and microstructural properties of complex perovskite oxides have attracted paramount attention in the recent past owing to their widespread technological applications in memory devices (dynamic RAM), wireless communication systems, cellular phones, global positioning systems, etc. in the form of capacitors, filters, and resonators [1–17]. The development of materials with high dielectric constant and low loss tangent has immense importance for miniaturization of electronic devices. The heterovalent perovskites with the general formula $A(B'_xB''_{1-x})O_3$ exhibit various types of cation ordering at B site of the perovskite unit cell [9–17]. Moreover, these materials have high dielectric constant and they have applications in multilayer capacitors and piezoelectric and pyroelectric transducers [9, 10]. For exploring widespread applications, the proper understanding of the structural property and ac electrical behavior of these materials is very crucial. In recent years, the alternating current impedance spectroscopy (ACIS), which probes the electrical phenomena taking place in a system by applying an ac signal, has emerged as an authoritative tool to study the electrical properties of complex perovskite oxides [9–17]. This method also enables us to separate out the intrinsic (bulk) and extrinsic (grain boundary, surface layer, and electrode) contributions of polycrystalline materials.

In case of $A(B'_xB''_{1-x})O_3$-type perovskite oxides, the dielectric property significantly depends upon the B-site ion ordering, atomic radius, and valence of B-site ions as well as on the presence of defect and oxygen vacancies. A large body of work has been carried out on the dielectric property and relaxation mechanism of $A(B'_{1/3}B''_{2/3})O_3$ perovskite oxides where A = Pb, Ba, Sr, Ca; B′ = Mg, Zn, Ni, Sr; and B″ = Nb, Ta [11–18] in the frequency range of 100 Hz to 1 MHz over a wide range of temperature. It may be noted that the dielectric property of perovskite oxides can be indirectly probed by using infrared spectroscopy. The real and imaginary parts of dielectric permittivity, loss tangent, and quality factor of these materials can be estimated using phonon parameters obtained from infrared spectroscopic study. If the experimental error is low, the values of dielectric parameter so obtained match well with the experimentally measured values [19–22]. To the best of our knowledge, there is no such report on the analysis of variation of real and imaginary parts of the dielectric permittivity with frequency of the perovskite systems having the chemical composition $Ca(B'_{1/3}Ta''_{2/3})O_3$ (where B′ = Mg and Zn). In this background, an analysis of the real and imaginary parts of the dielectric permittivity spectra of 1:2 ordered $Ca_3(MgTa_2)O_9$ (CMT) and $Ca_3(ZnTa_2)O_9$ (CZT) with the chemical formula $Ca(Mg_{1/3}Ta_{2/3})O_3$ and $Ca(Zn_{1/3}Ta_{2/3})O_3$ considering the distribution of relaxation time and effect of dc conductivity appears to be very interesting. Further, comparison of the results with other perovskite oxides of the same kind may provide fruitful information regarding the dielectric properties of Ta-based perovskite systems.

The complex perovskite oxides exhibit a wide variety of crystal structure depending on the difference in the radii and valence of B-site cations [23–29]. The $A(B'_{1/3}B''_{2/3})O_3$-type perovskite oxides show hexagonal crystal structure of $Pm\bar{3}1$, $P6_3/mmc$ and monoclinic structure of $P2_1/c$ space groups [30–37], and they exhibit both the 1:1 (e.g., $Pb(Mg_{1/3}Nb_{2/3})O_3$ [23, 24] and 1:2 (e.g., $Ba(Mg_{1/3}Ta_{1/3})O_3$ [29, 38]) B-site ordering patterns. The study on the crystal structure, microstructure, and cation ordering of $Sr(Mg_{1/3}Nb_{2/3})O_3$ and $Ca(Mg_{1/3}Nb_{2/3})O_3$ using X-ray diffractometry, selected area electron diffractometry, and transmission electron microscopy revealed that both samples had 1:2 ordered monoclinic unit cell [28, 29]. However, both Park et al. and Lee et al. did not analyze the powder X-ray diffraction (PXRD) patterns of the samples by the Rietveld refinement method [32, 33]. Relying upon the results of these works, Fu et al. indexed the PXRD pattern of $Ca(Mg_{1/3}Ta_{2/3})O_3$ in monoclinic $P2_1/c$ space group and confirmed the validity of space group assignment by Raman spectroscopic study [34, 35]. Again, Fu et al. did not analyze the PXRD pattern of $Ca(Mg_{1/3}Ta_{2/3})O_3$ by the Rietveld refinement method, although they had shown that the PXRD pattern of the sample matched well with that of $Ca[(Mg_{1/3}Ta_{2/3})_{0.9}Ti_{0.1}]O_3$. The monoclinic $P2_1/c$ symmetry of $Ca(Mg_{1/3}Ta_{2/3})O_3$ was proven by the Rietveld refinement of PXRD pattern and Raman spectroscopic study [34–36]. However, to the best of our knowledge, there is no report on the crystal structure and bonding property of CMT and CZT. In this context, the aim of the present work is to thoroughly investigate the crystal structure, bonding property, and B-site cation ordering of CMT and CZT along with their dielectric behavior in the frequency range of 50 Hz to 1 MHz.

In this paper, we have reported the crystal structure, microstructure, and dielectric relaxation property of CMT and CZT along with the results of dc conductivity measurements. We have employed powder X-ray diffractometry, scanning electron microscopy (SEM), Fourier transform infrared (FTIR) spectroscopy, Raman spectroscopy, and ACIS technique to fulfill the goal. The present study has revealed that the dielectric relaxations in the samples are polydispersive in nature and the polaron hopping mechanism controls the electrical response of the samples. Results also indicate that the dielectric property of perovskite oxides can be tuned by the modification of crystallite size and judicious choice of B-site metal ions.

Experimental

The polycrystalline CMT was synthesized through conventional ceramic method by mixing powders of $CaCO_3$ (reagent grade), Ta_2O_5 (reagent grade), and MgO (reagent grade) in stoichiometric ratio, while for CZT, ZnO (reagent grade) was used instead of MgO. The blended powders were calcined in a Pt crucible at 1623 K in air for 16 h and thereafter cooled down to room temperature at the rate of 100 K h^{-1}. The phase formation was confirmed by recording the powder PXRD patterns of the calcined samples. Finally, the calcined samples were pelletized into a disc using polyvinyl alcohol as binder, and the discs were sintered at 1673 K for 10 h and cooled down to room temperature at the rate of 1 K/min. The thickness and the diameter of these discs were 1.63 and 9.56 mm, respectively, for CMT and 2.87 and 9.72 mm, respectively, for CZT. The structural, morphological, and electrical characterizations were carried out using these discs. For electrical measurements, both the flat surfaces of these discs were polished thoroughly and were coated with silver paste and then heated at 473 K for 2 h. After electrical measurement, the silver paste was thoroughly removed by rubbing these discs by fine emery paper and then cleaned by acetone and distilled water. Afterward, to check whether the porosity will contribute to the dielectric property or not, we had measured the density of these discs using the Archimedes principle. The Archimedes density of CMT is 5.967 g cm^{-3} and CZT is 6.342 g cm^{-3}, while the crystalline densities of CMT and CZT are 5.971 and 6.348 g cm^{-3}, respectively. This indicates that the amount of porosities in the sample discs is negligible.

The PXRD patterns of CMT and CZT were recorded at room temperature by Bruker D8 Advanced Diffractometer

using Cu Kα ($\lambda = 1.54184$ Å) radiation over a range of Bragg angles $10° \leq 2\theta \leq 70°$ with the step size of 0.02° and scan time of 6 s/step. The generator was set at 40 kV and 40 mA. We have determined the space group of the samples by using FINDSPACE of EXPO2009 package [39] through statistical analysis of the PXRD data. The GSAS program with EXPGUI interface was used for Rietveld structural refinement of the PXRD patterns [40]. The background was described by the shifted Chebyshev function of first kind with 36 points regularly distributed over the entire 2θ range. The field emission scanning electron microscope (FESEM) (FEI, INSPECT F50) was used for the morphological and microstructural characterizations. The chemical compositions of the samples were determined by the energy dispersive X-ray spectrometer (EDS, BRUKER) attached with the FESEM equipment.

The FTIR spectra of the samples were recorded in transmission mode within the wavenumber range 400–1300 cm^{-1} at room temperature using Perkin Elmer Spectrum Two FTIR spectrometer. The Raman spectra of CMT and CZT were recorded by WITEC alpha, 300R Raman spectrometer equipped with diode laser source of $\lambda = 532$ nm. To have a good profile, a thin film sample over a glass slide was used instead of a powder sample. For preparing the films, the powders of the sample were dispersed in acetone. Then, the films of the sample were developed on a clean glass slide by the drop cast technique. Afterward, the solvent was removed by drying the films in vacuum at room temperature.

The capacitance (C), conductance (G), impedance (Z), and phase angle (φ) were recorded by an LCR meter (HIOKI 3532) at different temperatures between 393 and 573 K as a function of frequency (50 Hz to 1 MHz) and at the oscillation voltage of 1.0 V. During data collection, the sample was heated at a rate of 0.5 K/min and the measurement temperatures were kept constant with an accuracy of ±0.5 K using a programmable vacuum oven. The dc conductivity of the samples was measured by the four probe method.

Results and discussion

Structural and morphological properties

In case of perovskite oxides, subtle structural variation leads to drastic changes in their physical properties. Thus, determination of the crystal structure of perovskite oxides has immense importance. For many ABO_3-type perovskites, the oxygen octahedra gets tilted due to the misfit of the ionic radii of the A and B cations in the cubic lattice, and in consequence, distortions from ideal cubic structure occur in such systems [41, 42]. The degree of such distortion can be estimated by calculating the Goldschmidt tolerance factor (T_f) using the formula $T_f = \frac{r_A + r_0}{\sqrt{2}(\langle r_B \rangle + r_0)}$, where r_A, r_B, and r_0 are the ionic radii of A site, B site, and O ions, respectively [43]. The cubic structure is obtained if the value of T_f is close to unity, whereas for monoclinic and orthorhombic perovskite, T_f is less than 1 [16–18]. The values of the tolerance factor (T_f) for CMT and CZT are 0.942 and 0.934, respectively. T_f has been calculated by using Shannon effective ionic radii [44] and taking the $r_B = \frac{2r_1 + r_2}{3}$, where r_1 is the radius of Ta^{5+} ion and r_2 is the radius of Mg^{2+} ion for CMT and Zn^{2+} ion for CZT. According to Reaney et al., perovskites with $0.985 < T_f < 1.06$ are expected to have an untilted structure, while perovskites with $0.964 < T_f < 0.985$ exhibit antiphase tilting and those with $T_f < 0.964$ show both inphase and antiphase tilting distortions [45, 46]. Thus, CMT and CZT may possess a monoclinic structure with both inphase and antiphase tilting.

Here, we have determined the crystal structure of CMT and CZT through the Rietveld refinement of PXRD data. It is noteworthy that the PXRD patterns of CMT and CZT (Fig. 1) match very well with that of $Ca(Zn_{1/2}Nb_{2/3})O_3$ [33]. According to the literature, $Ca(Zn_{1/3}Nb_{2/3})O_3$ possesses a monoclinic structure of $P2_1/c$ symmetry, which results from an inphase and antiphase octahedral tilting along the [111] direction and in the basal plane of perovskite pseudocubic cell [33]. It may be noted that the ionic radius of Nb (0.641) ≈ Ta (0.640) and that of Zn(0.74) ≈ Mg(0.72). As the crystal structure of ABO_3 type of perovskite oxide mainly depends upon the ionic radii of A and B cations, it may therefore be inferred that the crystal structure of CMT and CZT may be analogous to that of $Ca(Zn_{1/2}Nb_{2/3})O_3$. Further, the analysis of PXRD data by FINDSPACE indicates that both CMT and CZT possess a monoclinic structure of $P2_1/c$ space group. Given this background, the crystal structures of both CMT and CZT have been refined by the Rietveld-based method by assigning the atomic coordinates using the crystal structure of $Ca(Zn_{1/2}Nb_{2/3})O_3$ [37] as the trial structural model.

To determine the lattice parameters, bond lengths, and bond angles, we have fitted the PXRD patterns of CMT and CZT by the Rietveld refinement package GSAS [40]. The refinement was performed by placing the atoms (Ca, Mg, Zn, Ta, and O) at Wyckoff positions as depicted in Tables 1 and 2. In the refinement process, positions of Mg ions for CMT and Zn ions for CZT are set fixed and the positions of all the other atoms have been refined. After a few cycles, the refinement successfully converges with an excellent agreement between the experimental and calculated patterns (Fig. 1). No trace of any impurity phase has been detected. The refined values of atomic coordinate and isotropic thermal parameter are presented in Tables 1 and 2. The values of lattice, structural, and refinement parameters are listed in Table 3. These values are nearly equal to those reported for $Ca(Zn_{1/3}Nb_{2/3})O_3$. The bond lengths for CMT and CZT are presented in Tables 4 and 5, respectively. The asymmetric units of only CMT along with the coordination environment of different metal ions are shown in Fig. 2 as CMT and CZT

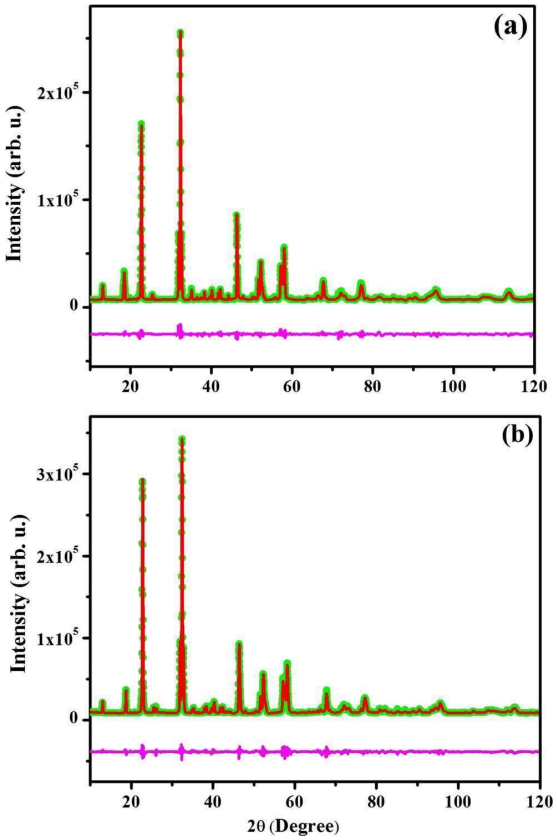

Fig. 1 Rietveld refinement plots of **a** CMT and **b** CZT. The experimental data are represented by *green solid circles* and the *continuous red line* represents the simulated XRD pattern. The difference between the experimental and simulated PXRD patterns is shown by the *continuous pink line*. The magnified view of the highest peaks of CMT and CZT is shown in the insets of the corresponding figures

are isostructural. According to the results of the Rietveld refinement, the crystal structure of both samples is monoclinic, belonging to $P2_1/c$ space group with 60 atoms in the unit cell. The unit cell of CMT and CZT contains four formula units of $Ca_3(Mg_1Nb_2)O_9$ and $Ca_3(Zn_1Nb_2)O_9$, respectively. In the unit cell of CMT, there are two Mg ions at 2a site and two Mg ions at 2d site, while for CZT, there are two Zn ions at 2a site and two Zn ions at 2d site in addition to 12 Ca, 8 Ta, and 36 O ions occupying the 4e Wyckoff positions in the unit cell of both crystal structures.

The A-site Ca^{2+} ions are coordinated with eight nearest neighboring oxygen ions. The A-site cations of perovskite oxides usually exhibit 12 coordination mode, but eight coordination of A cations is unique for perovskites belonging to monoclinic $P2_1/c$ space group and has been observed earlier for $Ca(Zn_{1/3}Nb_{2/3})O_3$ and $Ca(Ca_{1/3}Nb_{2/3})O_3$ [37, 47]. In monoclinic $P2_1/c$ structure, the highly distorted/deformed B-site octahedrons force the A cations at body center position

Table 1 Refined values of the atomic coordinate and thermal parameters for CMT

Atom	Site	*x* (Å)	*y* (Å)	*z* (Å)	U_{ISO}
Ca1	4e	0.24987 (3)	0.46597 (2)	0.05632 (4)	0.004 (15)
Ca2	4e	0.75163 (1)	0.47471 (6)	0.25481 (2)	0.043 (15)
Ca3	4e	0.73970 (7)	−0.02065 (3)	0.09025 (3)	0.039 (14)
Mg1	2a	0	0	0	0.032 (23)
Mg2	2d	0.5	0.5	0.5	0.046 (27)
Ta1	4e	0.00397 (4)	−0.00812 (5)	0.33561 (1)	0.008 (5)
Ta2	4e	0.49580 (3)	0.00792 (9)	0.16230 (4)	0.005 (6)
O1	4e	−0.02348 (2)	0.24214 (5)	0.09425 (6)	0.600 (7)
O2	4e	0.49277 (1)	0.98288 (2)	0.27321 (7)	0.070 (9)
O3	4e	0.06124 (3)	0.81239 (5)	0.25765 (4)	0.120 (5)
O4	4e	0.43494 (9)	0.79102 (2)	0.05723 (1)	0.800 (10)
O5	4e	0.27129 (5)	0.39768 (9)	0.26254 (8)	0.210 (6)
O6	4e	0.76134 (2)	0.61432 (9)	0.07309 (7)	0.130 (4)
O7	4e	0.254329 (6)	0.08543 (4)	0.09654 (3)	0.040 (4)
O8	4e	0.53124 (8)	0.31542 (7)	0.12765 (5)	0.390 (11)
O9	4e	0.06543 (4)	0.70134 (3)	0.09123 (2)	0.010 (5)

U_{ISO} isotropic thermal parameter

with respect to the nearest neighbor oxygen ions, and in turn, eight oxygen ions will be available in the first coordination sphere of A cations. Thus, for perovskite oxides with monoclinic $P2_1/c$ structure, eight oxygen ions are closer to A cations than the next nearest neighbor B cations and therefore the A cations exhibit eight coordination mode. The average bond valence sum (BVS) of Ca^{2+} ion at A site is calculated to be

Table 2 Refined values of the atomic coordinate and thermal parameters for CZT

Atom	Site	*x* (Å)	*y* (Å)	*z* (Å)	U_{ISO}
Ca1	4e	0.25385 (7)	0.50337 (5)	0.06525 (3)	0.011 (6)
Ca2	4e	0.76700 (5)	0.46600 (4)	0.27400 (8)	0.073 (9)
Ca3	4e	0.75000 (3)	0.00500 (2)	0.09530 (2)	0.058 (8)
Zn1	2a	0	0	0	0.037 (7)
Zn2	2d	0.5	0.5	0.5	0.007 (6)
Ta1	4e	0.00390 (8)	−0.00812 (4)	0.33780 (3)	0.034 (18)
Ta2	4e	0.49580 (5)	0.00871 (3)	0.16230 (1)	0.045 (21)
O1	4e	−0.03500 (1)	0.22300 (7)	0.09600 (2)	0.032 (15)
O2	4e	0.46841 (3)	0.71047 (9)	0.23435 (9)	0.005 (18)
O3	4e	0.06354 (4)	0.80231 (3)	0.25714 (1)	0.102 (35)
O4	4e	0.44382 (7)	0.78441 (1)	0.05741 (7)	0.115 (34)
O5	4e	0.27812 (8)	0.39882 (6)	0.26523 (5)	0.030 (20)
O6	4e	0.75643 (9)	0.61421 (4)	0.07328 (4)	0.116 (30)
O7	4e	0.25638 (4)	0.08393 (7)	0.09663 (6)	0.028 (12)
O8	4e	0.53524 (2)	0.31123 (9)	0.12091 (3)	0.180 (5)
O9	4e	0.06414 (1)	0.70128 (8)	0.09137 (7)	0.080 (4)

U_{ISO} isotropic thermal parameter

Table 3 Structural, microstructural, and refinement parameters of CMT and CZT obtained from Rietveld X-ray powder structure refinement method

Parameters	CMT	CZT
Crystal system	Monoclinic	Monoclinic
Space group	$P2_1/c$	$P2_1/c$
a (Å)	9.6210 (6)	9.6397 (3)
b (Å)	5.4835 (2)	5.4844 (2)
c (Å)	16.8097 (6)	16.8782 (5)
β (°)	125.715 (4)	125.822 (3)
Volume (Å^3)	720.04 (7)	723.53 (5)
Crystallite size (μm)	0.85 (7)	0.51 (1)
Microstrain ($\times 10^{-4}$)	8.65 (2)	6.7 (4)
R_{wp}	0.1270	0.1072
R_p	0.0863	0.0737
χ^2	2.63	3.42

equal to 1.86 for CMT and 1.91 for CZT, both of which are less than the ideal BVS value for Ca^{2+} ion. This indicates that the A-site Ca^{2+} ions in both CMT and CZT are underbounded and the stretching of Ca-O bonds has taken place.

Considering the structural similarity of CMT and CZT, the schematic projections of TaO_6 and ZnO_6 octahedra on *ac* plane are illustrated only for CZT (Fig. 3). The TaO_6 and ZnO_6 octahedrons exhibit both inphase and antiphase rotation. Within the crystal structure, six coordinated Ta^{5+} ions and Mg^{2+} ions of CMT/Zn^{2+} ions of CZT are linked with six nearest neighboring oxygen ions in octahedral fashion, and the cavities between the $B'O_6$ (B′ = Mg for CMT and Zn for CZT) and TaO_6 octahedrons are occupied by A-site Ca^{2+} ions located at 4(e) Wyckoff position. Each TaO_6 octahedron is surrounded by two nearest neighbor TaO_6 and two $B'O_6$ octahedra, while each $B'O_6$ octahedron is surrounded by four TaO_6 octahedra. Thus, the octahedra are arranged in sequence {Ta-Ta-B′} and repeat. This suggests that both CZT and CMT exhibit 1:2 cation ordering at B site. In both samples, the B-site metal oxygen bonding network is asymmetric (Tables 4 and 5). Moreover, the BVS calculations suggest that the Ta-O bonds are compressed, while the Zn-O bonds of CZT and Mg-O bonds of CMT are in extension. These indicate that the $B'O_6$ and TaO_6 octahedra are distorted in nature.

The FESEM micrographs of CMT and CZT, which are shown in Fig. 4a, b, respectively, show well-defined particles with irregular shape and assorted size. The grain size for CMT and CZT is between the range of 0.38 to 2.66 μm and 0.11 to 1.60 μm, respectively. Only the characteristic peaks for constituent elements are observed in the EDS spectra (Fig. 5) of the samples. This implies that there is no impurity in the samples.

It is noteworthy that 1:2 ordered perovskites having the general chemical formula $Ba(B'_{1/3}B''_{2/3})O_3$ possess hexagonal crystal structure of either $Pm\bar{3}1$ or $P6_3/mmc$ space group and

Table 4 Metal oxygen bond length for CMT

Bond	Length (Å)	Bond	Length (Å)	Bond	Length (Å)	Bond	Length (Å)
A sites							
Ca1-O1	2.7557 (3)	Ca2-O1	2.7227 (2)	Ca3-O1	2.3297 (6)		
Ca1-O2	2.5383 (1)	Ca2-O2	2.7335 (8)	Ca3-O3	2.9601 (2)		
Ca1-O4	2.8793 (4)	Ca2-O2	2.9801 (6)	Ca3-O3	2.6661 (4)		
Ca1-O5	2.7251 (6)	Ca2-O3	2.3974 (5)	Ca3-O4	2.9116 (1)		
Ca1-O5	2.6178 (4)	Ca2-O4	2.3481 (3)	Ca3-O6	2.8827 (7)		
Ca1-O6	2.4298 (2)	Ca2-O5	2.7217 (1)	Ca3-O6	2.5252 (3)		
Ca1-O8	2.3199 (5)	Ca2-O7	2.3610 (5)	Ca3-O7	2.3873 (9)		
Ca1-O9	2.4338 (7)	Ca2-O9	2.5931 (2)	Ca3-O8	2.1422 (4)		
Avg.	2.5875		2.5916		2.6006		
BVS	1.89		1.88		1.83		
B sites							
Mg1-O1	1.8784 (4)	Mg2-O4	2.2911 (6)	Ta1-O1	2.1039 (7)	Ta2-O2	1.9359 (8)
Mg1-O1	1.8784 (4)	Mg2-O4	2.2911 (6)	Ta1-O3	2.0126 (4)	Ta2-O2	2.2603 (6)
Mg1-O5	2.2756 (5)	Mg2-O6	1.9832 (3)	Ta1-O3	2.0545 (2)	Ta2-O4	1.8345 (3)
Mg1-O5	2.2756 (5)	Mg2-O6	1.9832 (3)	Ta1-O5	1.8259 (9)	Ta2-O6	2.0712 (2)
Mg1-O9	1.9726 (2)	Mg2-O8	1.8254 (7)	Ta1-O7	2.0330 (5)	Ta2-O7	2.0499 (4)
Mg1-O9	1.9726 (2)	Mg2-O8	1.8254 (7)	Ta1-O8	1.9434 (4)	Ta2-O9	1.8751 (5)
Avg.	2.0422		2.0332		1.9955		2.0045
BVS	2.33		2.39		4.89		4.77

BVS bond valance sum

Table 5 Metal oxygen bond length for CZT

Bond	Length (Å)	Bond	Length (Å)	Bond	Length (Å)	Bond	Length (Å)
A sites							
Ca1-O1	2.7265 (7)	Ca2-O1	2.6926 (4)	Ca3-O1	2.9214 (1)		
Ca1-O2	2.5084 (4)	Ca2-O2	2.5671 (2)	Ca3-O3	2.7165 (4)		
Ca1-O4	2.5825 (3)	Ca2-O2	2.5707 (7)	Ca3-O3	2.5741 (7)		
Ca1-O5	2.6494 (8)	Ca2-O3	2.3863 (1)	Ca3-O4	2.5930 (6)		
Ca1-O5	2.7709 (5)	Ca2-O4	2.4682 (9)	Ca3-O6	2.4143 (5)		
Ca1-O6	2.6408 (4)	Ca2-O5	2.4995 (7)	Ca3-O6	2.5857 (9)		
Ca1-O8	2.4957 (2)	Ca2-O7	2.8832 (5)	Ca3-O7	2.4997 (4)		
Ca1-O9	2.3635 (6)	Ca2-O9	2.5753 (8)	Ca3-O8	2.3659 (3)		
Avg.	2.5922		2.5804		2.5838		
BVS	1.87		1.93		1.92		
B sites							
Zn1-O1	1.9851 (8)	Zn2-O4	2.1247 (7)	Ta1-O1	2.0848 (6)	Ta2-O2	1.8272 (9)
Zn1-O1	1.9851 (8)	Zn2-O4	2.1247 (7)	Ta1-O3	2.0759 (5)	Ta2-O2	2.1438 (2)
Zn1-O5	2.3219 (5)	Zn2-O6	1.9624 (3)	Ta1-O3	2.0592 (8)	Ta2-O4	2.0375 (4)
Zn1-O5	2.1219 (5)	Zn2-O6	1.9624 (3)	Ta1-O5	1.9680 (2)	Ta2-O6	2.1018 (1)
Zn1-O9	2.1954 (3)	Zn2-O8	2.3676 (2)	Ta1-O7	1.9981 (1)	Ta2-O7	2.0585 (7)
Zn1-O9	2.1954 (3)	Zn2-O8	2.3676 (2)	Ta1-O8	1.8641 (7)	Ta2-O9	1.9119 (2)
Avg.	2.1675		2.1513		2.0138		2.0135
BVS	1.71		1.79		4.65		4.66

BVS bond valance sum

the value of the tolerance factor for this type of perovskites is ≈1 [29–31, 38]. On the hand, $Ca(Zn_{1/3}Nb_{2/3})O_3$, $Ca(Ca_{1/3}Nb_{2/3})O_3$, $Ca[(Mg_{1/3}Ta_{2/3})_{0.9}Ti_{0.1}]O_3$, and the solid solution of $0.9Ca[(Mg_{1/3}Ta2/3)]O_3/0.1CaTiO_3$ have monoclinic crystal structure of $P2_1/c$ space symmetry [34–37, 47]. To the best of our knowledge, no more example of calcium-based 1:2 ordered perovskite is available in the literature. It may further be noted that the crystal structures of both CMT and CZT belong to monoclinic $P2_1/c$ symmetry. The value of the tolerance factor of perovskites with the general formula

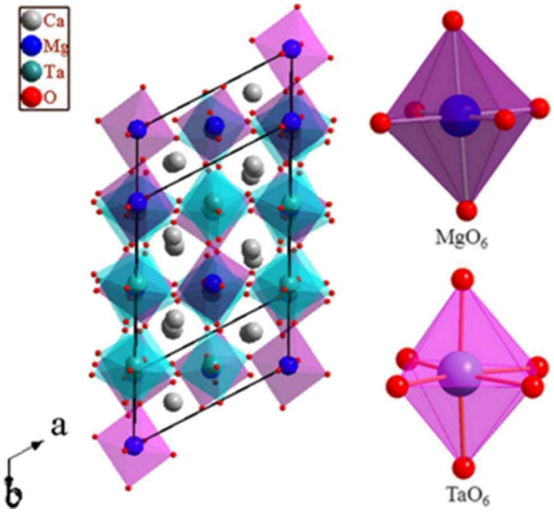

Fig. 2 Unit cell of CMT along with the coordination environment of Mg^{2+} and Ta^{5+} ions

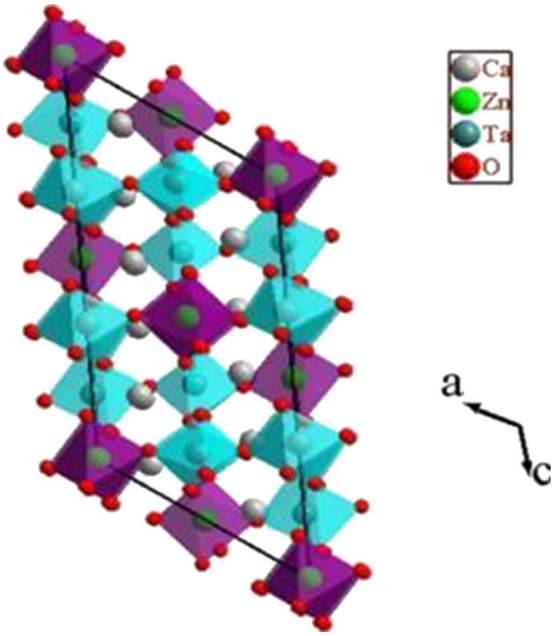

Fig. 3 The schematic projections of TaO_6 and ZnO_6 octahedra of CZT on the *ac* plane

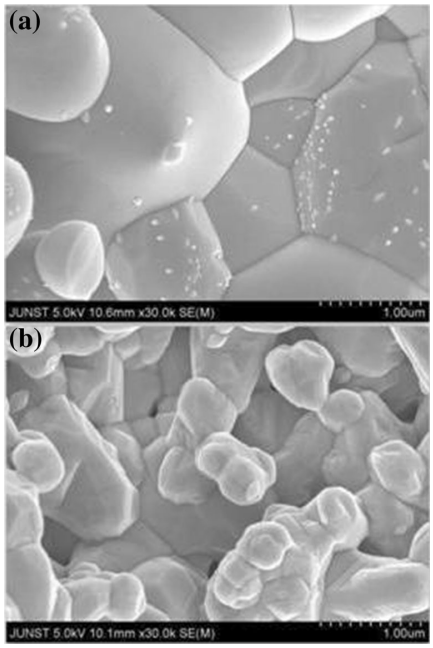

Fig. 4 The FESEM micrographs of **a** CMT and **b** CZT

$Ca(B'_{1/3}B''_{2/3})O_3$ is <0.965. It is well known that the tolerance factor (which depends on the radius of A- and B-site metal cations and oxygen anion) has a strong influence on the crystal structure and physical properties of perovskite oxides. According to previous reports, the crystal symmetry of perovskite oxide reduces as the tolerance factor decreases [45, 46]. The value of the tolerance factor of the members of $Ca(B'_{1/3}B''_{2/3})O_3$ group of perovskites is less than those of perovskites with the general formula $Ba(B'_{1/3}B''_{2/3})O_3$ mainly due to the smaller radius of Ca^{2+} (1.34 Å) ions compared to that of Ba^{2+} (1.61 Å) ions. It may therefore be inferred that 1:2 ordered

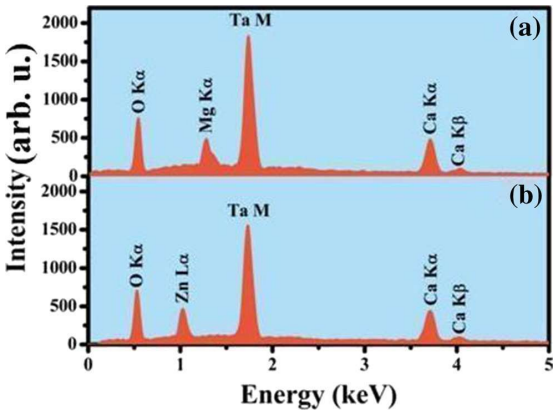

Fig. 5 EDAX spectra of **a** CMT and **b** CZT

$Ca(B'_{1/3}B''_{2/3})O_3$ systems crystallize in monoclinic $P2_1/c$ space group (lower symmetry), while the crystal structure of the members of $Ba(B'_{1/3}B''_{2/3})O_3$ family of perovskites with 1:2 ordering at B site possesses a hexagonal crystal structure of either $Pm\bar{3}1$ or $P6_3/mmc$ space group (higher symmetry) due to the difference in ionic radius of A-site cations.

FTIR and Raman spectroscopic investigation

Several reports on the assignment of the IR and the Raman active modes for 1:2 ordered perovskite oxide with space group $Fm3m$ (O_h^5), $Pm\bar{3}1$ (D_{3d}^3), $Pm3m$ (O_h^1), $Pbnm$ (D_{2h}^{16}), $P21/n$ (C_{2h}^5), and $P2_{1/C}$ (C_{2h}^5) are available in the literature [31, 48–53]. The details of the site symmetry and corresponding modes of vibration for 1:2 ordered perovskites belonging to $P2_{1/C}$ (C_{2h}^5) space group were reported by Fu et al. [35]. According to them, perovskites belonging to this category present 180 normal modes of vibration out of which 3 ($A_u + 2B_u$) are acoustic, 93 ($47\,A_u + 46B_u$) are IR active, and 84 ($42\,A_g + 42B_g$) are Raman active.

The FTIR spectra of CMT and CZT in the wavenumber range of 1300 to 400 cm^{-1} are shown in Fig. 6. Three strong and broad bands are observed in the spectrum of both samples. It may be noted that the IR bands due to symmetric stretching vibration of Mg-O and Zn-O bonds appear at ~436 and 490 cm^{-1}, respectively [54, 55]. Further, asymmetric stretching vibration of Ta-O bonds in 1:2 ordered perovskite oxides having Ta^{5+} ions at B site produces a IR band at ~630 cm^{-1} [18]. The strong and maximum energy band around 636 cm^{-1} for CMT and 627 cm^{-1} CZT can be assigned to the asymmetric stretching mode of Ta-O bonds of TaO_6 octahedra due to higher charge of Ta^{5+} ions [18]. The lowest energy bands around 472 cm^{-1} for CMT and 469 cm^{-1} for CZT are related to the symmetric stretching vibration of Mg-O and Zn-O bonds of the MgO_6 and ZnO_6 octahedra of CMT and CZT, respectively. The broad nature of the IR bands at ~636 and 472 cm^{-1} for CMT and 627 and 469 cm^{-1} for CZT can be attributed to the deformity in the Ta-O, Mg-O, and Zn-O bonding networks due to unequal length of Ta-O, Mg-O, and Zn-O bonds forming TaO_6 and MgO_6 (for CMT) and ZnO_6 (for CZT) octahedra, respectively, as revealed by the structural study (see Tables 4 and 5). The broad medium energy bands at around 554 cm^{-1} for CMT and 555 cm^{-1} for CZT may be allocated to the symmetric stretching vibration of Ta-O and some deformed modes of MgO_6 octahedra for CMT and ZnO_6 octahedra for CZT. The broad nature of these peaks is due to the occurrence of absorption peaks due to symmetric stretching of Ta-O and deformed modes of MgO_6 (for CMT) and ZnO_6 (for CZT) octahedra at nearly the same wavenumbers.

The Raman spectroscopy is regarded as an authentic tool to probe the crystal symmetry and B-site cation ordering of

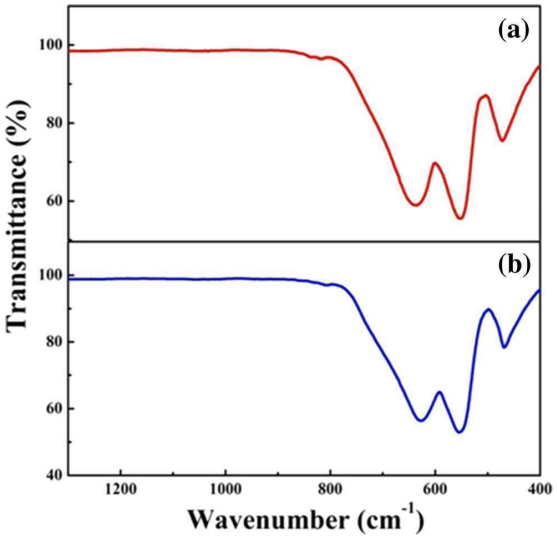

Fig. 6 FTIR spectra of **a** CMT and **b** CZT

perovskite oxides, even when this ordering is confined to the nanoscale level [35, 47, 56, 57]. The Raman spectra of CMT and CZT are displayed in Fig. 7. Eleven distinct Raman modes centered about 143.6, 233.9, 276.3, 318.5, 379.2, 411.2, 480.9, 563.3, 631.3, 725.6, and 832.2 cm^{-1} for CMT and 148.4, 230.5, 276.3, 323.2, 382.5, 410.6, 471.7, 558.7, 629.9, 716.6, and 827.7 cm^{-1} for CZT are observed. In addition, five weak peaks are observed in the Raman spectra of both CMT and CZT. According to the factor group analysis for 1:2 ordered $A(B'_{1/3}B''_{2/3})O_3$ perovskite oxides with monoclinic $P2_1/c$ symmetry, 84 (42 A_g + 42 B_g) Raman active modes are expected out of which only 29 modes are detected experimentally till date[47]. Mode assignment for perovskite oxides with monoclinic $P2_1/c$ symmetry is very difficult due to the presence of a large number of modes in close proximity and serious overlapping of the modes, because the Raman spectrum of such perovskites is analyzed by comparing them with those of other analogous crystal structures [35]. Usually nine to ten Raman active modes are observed for 1:2 ordered perovskite oxides with monoclinic $P2_1/c$ symmetry in the range of 100–1000 cm^{-1} [35, 47]. It is noteworthy that for the perovskite oxides having monoclinic $P2_1/c$ crystal structure with 1:2 ordering at B site and Ca^{2+} ions at A site, a characteristic Raman mode appears at about 408 cm^{-1} [35]. Thus, the Raman mode at about 411.2 cm^{-1} for CMT and 410.6 cm^{-1} for CZT gives evidence in favor of long range 1:2 ordering at B site of the samples. Moreover, the appearance of a large number of (16) Raman modes indicates that both CMT and CZT have a monoclinic crystal structure of $P2_1/c$ space group [35, 47]. The Raman shifts of CZT and CMT match well with that of $Ca[(Mg_{1/3}Ta_{2/3})_{0.9}Ti_{0.1}]O_3$, which also possesses a monoclinic crystal structure of $P2_1/c$ space group [35]. A Raman mode is observed at about 800 cm^{-1} for both 1:1 and 1:2 ordered perovskite oxides, and this nonspecific mode corresponds to short range cation ordering [35]. The strong peak at about 830 cm^{-1} for CMT and 825 cm^{-1} for CZT corresponds to A_g mode and confirms the formation of a complex perovskite phase and the existence of a short range cation ordering in the samples. Thus, the Raman study has confirmed that both samples have crystallized in $P2_1/c$ space group and exhibit 1:2 ordering.

Investigation on dielectric permittivity

The variation of the real (ε') and imaginary (ε'') parts of complex dielectric permittivity (ε^*) with the logarithmic angular frequency ω (=$2\pi\upsilon$) for CMT and CZT at different temperatures is shown in Figs. 8 and 9, respectively. The peak in the ε'' versus log ω curves shifts toward higher frequencies on increasing the temperature (Figs. 8b and 9b), i.e., at higher temperatures, relaxation occurs at higher frequencies. This implies that the relaxation mechanism governing the dielectric properties of the samples is temperature dependent and the rate of polarization formed increases with the increase of temperature.

A close look at Figs. 8 and 9 reveals the presence of a strong dielectric relaxation in CMT and CZT. According to the literature, in perovskite crystals, various relaxation processes with different relaxation times exist simultaneously due to the presence of various types of defects arising in the course of the crystal growth process [18]. The large width of the loss peaks in Figs. 8b and 9b points toward the possibility of participation of a large number of relaxation processes with their own discrete relaxation times. It seems that the dielectric property of CMT and CZT cannot be accounted in terms of the Debye-type monodispersive relaxation process as the dielectric relaxation in the samples is polydispersive in nature. The polydispersive character (distribution of relaxation time) of the dielectric relaxation can be examined by the Cole-Cole model. According to this model, the complex dielectric constant can be expressed as [58, 59]

$$\varepsilon^* = \varepsilon' - i\varepsilon'' = \varepsilon_\infty + \frac{\varepsilon_s - \varepsilon_\infty}{1 + (i\omega\tau)^{1-\alpha}} \quad (1)$$

where ε_s and ε_∞ are low- and high-frequency values of ε', respectively, and α (a constant) is a measure of the distribution of relaxation times. For an ideal Debye-type (monodispersive) relaxation process, $\alpha = 0$, while for polydispersive relaxation, $\alpha > 0$. It may be noted that although the polydispersive nature of dielectric relaxation can be

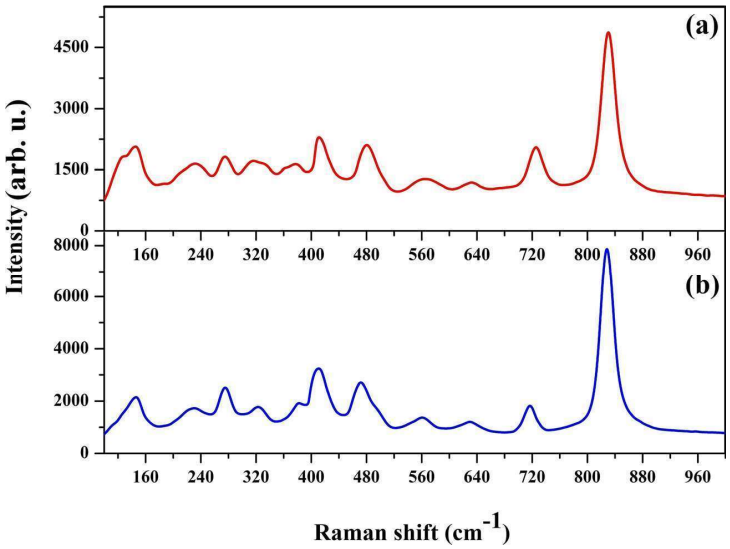

Fig. 7 Raman spectra of **a** CMT and **b** CZT

successfully accounted by the Cole-Cole model, it cannot follow the low-frequency dielectric behavior of the sample when ε'' increases very rapidly with the decrease of frequency due to the influence of dc conductivity [18]. Under such circumstances, a term accounting for the contribution of the dc electrical conductivity is added in the Cole-Cole equation and the

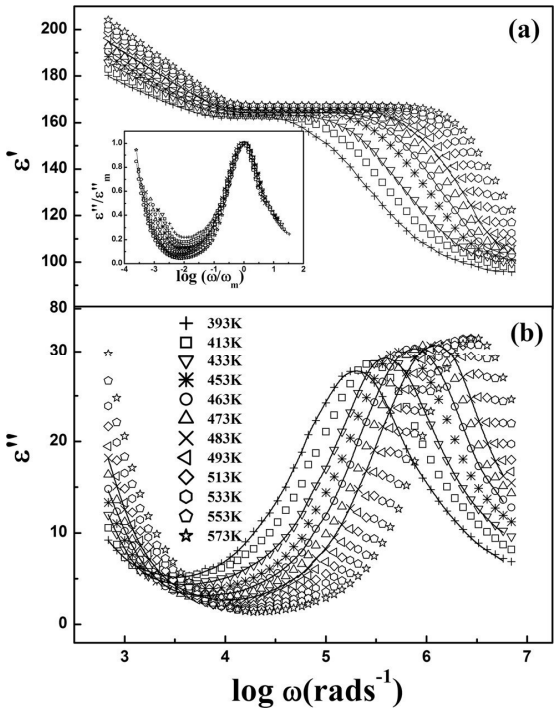

Fig. 8 The **a** ε' versus log ω and **b** ε'' versus log ω curves for CMT at various temperatures, where the *solid lines* are the fit of the experimental data (shown by *symbols*) by the modified Cole-Cole equations

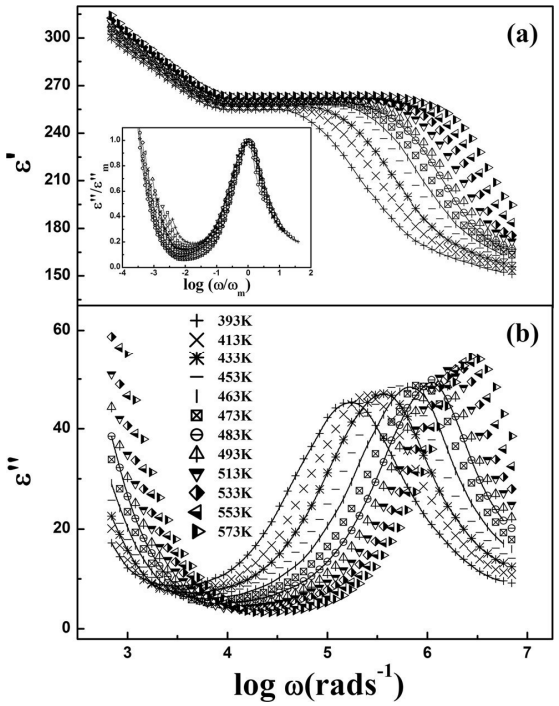

Fig. 9 The **a** ε' versus log ω and **b** ε'' versus log ω curves for CZT at various temperatures, where the *solid lines* are the fit of the experimental data (shown by *symbols*) by the modified Cole-Cole equations

complex dielectric permittivity is described by the empirical equation [60, 61]:

$$\varepsilon^* = \varepsilon_\infty + \frac{\varepsilon_s - \varepsilon_\infty}{1 + (i\omega\tau)^{1-\alpha}} - i\frac{\sigma^*}{\varepsilon_0\omega^n} \quad (2)$$

where n lies in the range between 0 and 1 and σ^* ($\sigma^* = \sigma_1 + i\sigma_2$) is the complex conductivity. Here, σ_1 is the dc conductivity and σ_2 is the conductivity due to localized charges. From Eq. (2), on equating the real and imaginary parts of ε^*, ε' and ε'' can be written as

$$\varepsilon' = \varepsilon_\infty + \frac{(\varepsilon_s - \varepsilon_\infty)\left[1 + (\omega\tau)^{1-\alpha}\sin\frac{1}{2}\alpha\pi\right]}{1 + 2(\omega\tau)^{1-\alpha}\sin\frac{1}{2}\alpha\pi + (\omega\tau)^{2(1-\alpha)}} - \frac{\sigma_2}{\varepsilon_0\omega^n} \quad (3)$$

$$\varepsilon'' = \frac{(\varepsilon_s - \varepsilon_\infty)(\omega\tau)^{1-\alpha}\cos\frac{1}{2}\alpha\pi}{1 + 2(\omega\tau)^{1-\alpha}\sin\frac{1}{2}\alpha\pi + (\omega\tau)^{2(1-\alpha)}} + \frac{\sigma_1}{\varepsilon_0\omega^n} \quad (4)$$

We have fitted the dielectric spectra (ε' versus log ω and ε'' versus log ω curves) obtained at 393, 433, 463, and 480 K using Eqs. (3) and (4). The calculated curves are shown by solid lines in Figs. 8 and 9. The experimentally obtained and calculated ε' versus log ω and ε'' versus log ω curves match very well with each other (see Figs. 8 and 9). The values of the fitting parameters at different temperatures are listed in Table 6. The nonzero value of α discards the possibility of the existence of a Debye-type monodispersive relaxation process in the samples and indicates that the relaxation process is polydispersive in nature. As temperature increases, the value of the Cole-Cole constant α for both CMT and CZT decreases slightly. Thus, for both CMT and CZT, the width of the relaxation time distribution profile decreases with the increase of temperature.

It may be noted that the dielectric permittivity of CZT is higher than that of CMT, whereas the loss component of CMT is less than that of CZT. The value of dielectric permittivity of CZT is higher, while CMT is comparable to that of the 1:2 ordered niobium-based perovskites ($A(B'_{1/3}Nb_{2/3})O_3$, where A = Ba, Ca, and Sr and B′ = Ni, Mg, Sr, Fe, and Zn) perovskites and 1:1 ordered tantalum-based systems reported in the literature [12–18]. The value of loss tangent of CMT is less than that obtained for niobium- and tantalum-based perovskites. Taking into account our recent works on tantalum-based $A(B'_{1/3}B''_{2/3})O_3$-type perovskite oxides [16, 17], it may be concluded that for $Ca(B'_{1/3}Ta_{2/3})O_3$ (where B′ = Ni, Mg, and Zn) series of perovskite oxides, the highest value of dielectric permittivity is obtained for $Ca(Zn_{1/3}Ta_{2/3})O_3$ (CZT), while CMT exhibits the lowest dielectric loss. It is well known that the dielectric property of ABO_3-type perovskite oxides strongly depends on the radii of A- and B-site metal ions and the crystal structure. Thus, the lower dielectric permittivity of CMT compared to CZT can be attributed to the lattice contribution to permittivity.

Investigation on impedance

Figure 10 depicts the complex plane impedance plots of CMT and CZT, where the imaginary part (Z'') of complex impedance is plotted against the real part (Z') of complex impedance at different temperatures. In the complex plane impedance plots of the samples, only one semicircular arc has been observed and there is no signature of any low-frequency arc. It may therefore be inferred that there is no grain boundary (interfacial boundary layer) contribution in the impedance spectrum of the samples [62–64]. The high-frequency semicircular arcs in the complex plane impedance plots are therefore ascribed to the bulk effect and can be modeled by parallel combination of bulk resistance (r_g) and bulk capacitance (c_g) of the material as shown in the insets of Fig. 10a, b. The impedance Z^* for the equivalent circuit is

$$Z^* = Z' - iZ'' = R + \frac{1}{r_g^{-1} + i\omega c_g} \quad (5)$$

where,

$$Z' = R + \frac{r_g}{1 + (\omega r_g c_g)^2} \quad (6)$$

and

$$Z'' = r_b\left[\frac{\omega r_g c_g}{1 + (\omega r_g c_g)^2}\right] \quad (7)$$

We have fitted our experimental data using Eqs. (6) and (7) and the fitted parameters are given in Table 7. A good agreement between the experimental and fitted curves reveals that only the bulk effect contributes to the polarization process in these materials.

Activation energy

In order to estimate the activation energy and to determine the electrical character of CMT and CZT, we have measured the dc conductivity (σ_{dc}) of the samples at different temperatures by the four probe method. The reciprocal temperature dependence of σ_{dc} for CMT and CZT is presented in Fig. 11a. The σ_{dc} versus $10^3/T$ plots of CMT and CZT obey the Arrhenius law, $\sigma_{dc} = \sigma_0 \exp(-E_\sigma/k_BT)$, where σ_0 is the pre-exponential factor and E_σ is the activation energy. According to the numerical fitting, $E_\sigma = 0.35$ and 0.33 eV for CMT and CZT, respectively. Moreover, the value of σ_{dc} for both samples increases with increasing temperature.

The activation energy can also be estimated from the temperature dependence of characteristic relaxation frequency, ω_m (the frequency corresponds to loss peak). The log ω_m versus $10^3/T$ plots of CMT and CZT are presented in Fig. 11b. It

Table 6 The values of different parameters obtained by fitting the dielectric spectra of CMT and CZT by the modified Cole-Cole equations

Temperature (K)	ε_s	ε_∞	ω (KHz)	α	n	σ_1 (Sm^{-1})	σ_2 (Sm^{-1})
CMT							
393	180	096	209,604.21	0.164	0.94	0.53×10^{-7}	4.00×10^{-9}
433	186	099	364,250.37	0.158	0.95	1.28×10^{-7}	2.00×10^{-9}
463	191	101	761,026.88	0.156	0.96	2.33×10^{-7}	0.10×10^{-9}
483	195	104	1,322,513.15	0.154	0.97	3.64×10^{-7}	0.08×10^{-9}
CZT							
393	298	151	174,341.19	0.190	0.96	0.98×10^{-7}	8.20×10^{-9}
433	301	153	364,250.37	0.179	0.95	2.75×10^{-7}	7.80×10^{-9}
463	305	155	632,994.59	0.172	0.94	4.53×10^{-7}	7.20×10^{-9}
483	307	157	1,100,018.53	0.163	0.93	6.2×10^{-7}	6.50×10^{-9}

has been found that log ω_m of both samples follows the Arrhenius law: $\omega_m = \omega_0 \exp(-E_{\varepsilon''}/k_B T)$ (where ω_0 is the pre-exponential factor) with activation energy ($E_{\varepsilon''}$) 0.34 eV for CMT and 0.33 eV for CZT, which are almost equal to the activation energy obtained from temperature dependence of σ_{dc}. For the metallic oxides which are p-type polaronic conductors, the activation energy lies in the range from 0.2 to 0.9 eV [61, 65, 66]. The numerical values of activation energy of CMT and CZT indicate that the electrical conduction process in both samples is governed by the polaron hopping. Further, it may be noted that the values of dc conductivity obtained by fitting the dielectric spectra of CZT and CMT at different temperatures and those obtained experimentally agree well. Good matching of the activation energies obtained from log ω_m versus $10^3/T$ plots and temperature dependence of σ_{dc} along with good agreement between the values of σ_{dc} determined by fitting the dielectric spectra and obtained experimentally suggests that relaxation and conductivity have same microscopic origin (hopping) [67].

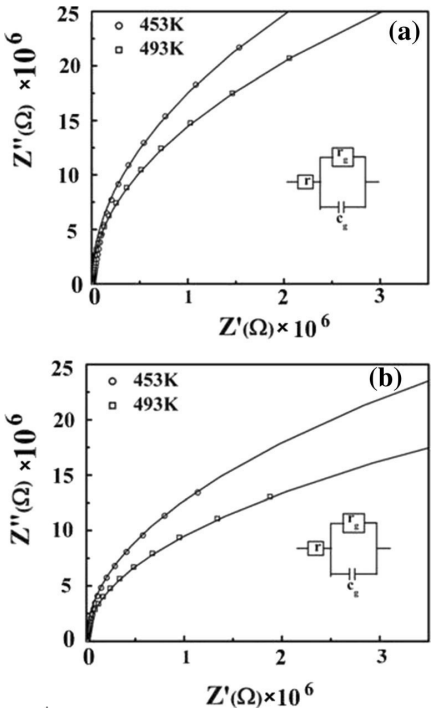

Fig. 10 The complex impedance plane plots of **a** CMT and **b** CZT. The *solid lines* represent the fitted data using the RC equivalent circuit shown in the *inset*

Conclusion

The structural, morphological, dielectric, and electrical transport properties of CMT and CZT with grain size ranging between 0.38 and 2.66 μm and between 0.11 and 1.60 μm, respectively, have been investigated by PXRD, FESEM, and impedance spectroscopic techniques. The compounds have crystallized in monoclinic structure of $P2_1/c$ symmetry. The 1:2 ordering and formation of monoclinic perovskite oxide phase with $P2_1/c$ symmetry are confirmed by FTIR and Raman spectroscopic studies. Comparing the crystal structures of 1:2 ordered $Ba(B'_{1/3}B''_{2/3})O_3$- and $Ca(B'_{1/3}B''_{2/3})O_3$-type perovskite systems, we have shown that for these two classes of perovskites, the calcium-based systems crystallize in monoclinic $P2_1/c$ space group while their barium-based counterparts possess a hexagonal crystal structure of either *Pm*

Table 7 The fitted parameters of the impedance circuit for CMT and CZT

Sample	Temperature (K)	r_g (Ω)	$r_g c_g$ (ΩF)	c_g (F)
CMT	453	3.08×10^8	1.90×10^{-3}	6.17×10^{-12}
CMT	493	2.10×10^8	1.90×10^{-3}	9.05×10^{-12}
CZT	453	1.63×10^8	1.88×10^{-4}	1.15×10^{-12}
CZT	493	0.91×10^8	1.99×10^{-4}	2.19×10^{-12}

r_g grain resistance, c_g grain capacitance

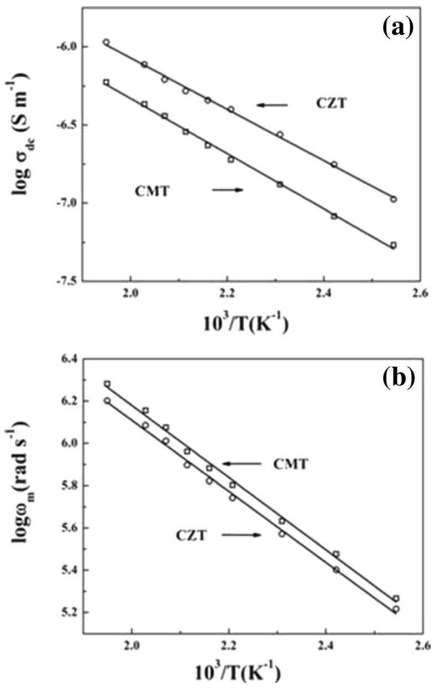

Fig. 11 **a** Temperature dependence of dc conductivity for CMT and CZT. The *symbols* represent the experimental data and *solid lines* are least-square straight-line fit. **b** Temperature dependence of the most probable relaxation frequency obtained from the logarithmic frequency dependent plots of ε'' for CMT and CZT. The *symbols* represent the experimental data and the *solid lines* are the least-square straight-line fit

$\overline{3}1$ or $P6_3/mmc$ due to the smaller ionic radius of Ca^{2+} compared to that of Ba^{2+}.

The variation of ε'' with frequency at different temperatures indicates the presence of dielectric relaxation in the samples, and the characteristic relaxation frequency is strongly temperature dependent. The analysis of the loss component of the dielectric constant in the framework of the modified Cole-Cole model points toward the polydispersive character of the relaxation process. The dielectric and electrical transport properties of the samples are governed by the same mechanism (polaron hopping). It has been shown that the p-type polaron hopping is responsible for the dielectric behavior and electrical response of the samples. Finally, for their high dielectric permittivity and low loss component, CMT and CZT appear to be suitable for various technological applications in capacitors, resonators, filters, and integrated circuits.

Acknowledgments We gratefully acknowledge the financial support of CSIR, New Delhi, Government of India, through grant number 60(0106)/13-EMR-II. The authors gratefully acknowledge the financial support of the Department of Science & Technology, Govt. of India through FIST and PURSE program of the Department of Physics, Jadavpur University. The financial assistance granted by UGC, Govt. of India through SAP and UPE program is also acknowledged. We gratefully acknowledge Prof. R. N. Joardar for helpful discussion.

References

1. Fu MS, Liu XQ, Chen XM, Zeng YW (2010) Effects of Mg substitution on microstructures and microwave dielectric properties of Ba(Zn1/3Nb2/3)O3 perovskite ceramics. J Am Ceram Soc 93:787–795
2. Shah MR, AktherHossain AKM (2013) Structural, dielectric and complex impedance spectroscopy studies of lead free Ca0.5+xNd0.5-x(Ti0.5Fe0.5)O3. J Mater Sci Technol 29:323–329
3. Chen CT, Huang CY, Lin YM, Lee CT (2011) Structure and microwave dielectric property relations in barium cobalt magnesium niobate ceramics. Jpn J Appl Phys 50:091503
4. Belous A, Ovchar O, Kramarenko O, Mischuk D, Jancar B, Spreitzer M, Suvorov D, Annino G, Grebennikov D, Mascher P (2009) Low-loss perovskite niobates Ba(M1/32+Nb2/3)O3: composition, structure, and microwave dielectric properties. Ferroelectrics 387:36–45
5. Ovchar O, Belous A, Kramarenko O, Mischuk D, Jancar B, Spreitzer M, Suvorov D, Annino G, Grebennikov D, Mascher P (2009) The effect of impurity phases on the structure and properties of microwave dielectrics based on complex perovskites Ba(Col/32+Nb2/3)O3. Ferroelectrics 387:189–196
6. Yang Z, Zhang Y, You G, Zhang K, Xiong R, Shi J (2012) Dielectric and electrical transport properties of the Fe3+– doped CaCu3Ti4O12. J Mater Sci Technol 28:1145–1150
7. Hungria T, Alguero M, Castro A (2007) Grain growth control in NaNbO3–SrTiO3 ceramics by mechanosynthesis and spark plasma sintering. J Am Ceram Soc 90:2122–2127
8. Lu H, Zhu L, Kim JP, Son SH, Park JH (2012) Structural, sintering and electrical properties of Cr-doped La06S.r0.4Crx Fe1−xO3 −δ(x=0.10, 0.20) oxides. J Mater Sci Technol 28:654–660
9. Agrawal L, Dutta A, Shannigrahi S, Singh BP, Sinha TP (2011) Impedance spectroscopy study and ground state electronic properties of In(Mg1/2Ti1/2)O3. Physica B 406:1081–1087
10. Prakash V, Dutta A, Choudhary SN, Sinha TP (2007) Dielectric relaxation in perovskite Ba(Zn1/2W1/2)O3. Mater Sci Eng B 142:98–105
11. Bajpai PK, Singh KN (2011) Dielectric relaxation and ac conductivity study of Ba(Sr1/3Nb2/3)O3. Physica B 406:1226–1232
12. Bajpai PK, Pastor M, Singh KN (2011) Relaxor behavior and dielectric relaxation in Pb(Ba1/3Nb2/3)O3: a phase pure new relaxor material. J Appl Phys 109:014114
13. Dutta A, Bharti C, Sinha TP (2008) Dielectric relaxation in Sr(Mg1/3Nb2/3)O3. Physica B 403:3389–3393
14. Dutta A, Sinha TP (2010) Impedance spectroscopy study of BaMg1/3Nb2/3O3: frequency and time domain analyses. Physica B 405:1475–1479
15. Dutta A, Bharti C, Sinha TP (2008) AC conductivity and dielectric relaxation in CaMg1/3Nb2/3O3. Mater Res Bull 43:1246–1254
16. Hoque MM, Dutta A, Kumar S, Sinha TP (2012) The impedance spectroscopic study and dielectric relaxation in A(Ni1/3Ta2/3)O3 [A=Ba, Ca and Sr]. Physica B 407:3740–3748
17. Hoque MM, Dutta A, Kumar S, Sinha TP (2014) Dielectric relaxation and conductivity of Ba(Mg1/3Ta2/3)O3 and Ba(Zn Ta)O. J Mater Sci Technol 30:311–320
18. Dutta A, Sinha TP (2011) Structural and dielectric properties of A(Fe1/2Ta1/2)O3[A = Ba, Sr, Ca]. Mater Res Bull 46:518–524
19. Dias A, Paschoal CWA, Moreira RL (2003) Infrared spectroscopic investigations in ordered barium magnesium niobate ceramics. J Am Ceram Soc 86(11):1985–1987

20. Silva RX, Moreira RL, Almeida RM, Paniago R, Paschoal CWA (2015) Intrinsic dielectric properties of magnetodielectric La CoMnO. J Appl Phys 117:214105
21. Sagala DA, Koyasu S (1993) Infrared reflection of Ba(Mg1/3Ta2/3)O3 ceramics. J Am Ceram Soc 76(10):2433–2436
22. Dias A, Khalam LA, Sebastian MT, Paschoal CWA, Moreira RL (2006) Chemical substitution in Ba (RE1/2Nb1/2) O3(RE= La, Nd, Sm, Gd, Tb, and Y) microwave ceramics and its influence on the crystal structure and phonon modes. Chem Mater 18:214–220
23. Bhalla AS, Guo R, Roy R (2000) The perovskite structure – a review of its role in ceramic science and technology. Mat Res Innov 4:3–26
24. Galasso F (1990) Perovskites and high-Tc superconductors. Gordon and Breach Science, New York, pp 3–58
25. Galasso F, Pyle J (1963) Ordering in compounds of the A(B´ 0.33Ta0.67)O3 type. Inorg Chem 2:482–484
26. Galasso F, Pyle J (1963) Preparation and study of ordering in A(B´ 0.33Nb0.67)O3perovskite-type compounds. J Phys Chem 67: 1561–1562
27. Takahashi J, Fujii T, Shimada S, Kodaira K (1999) Changes in ordered structure and dielectric properties with the A-site and B-site cation ratios of complex perovskites (Sr1-xBax)(Sr0.33Ta0.67)O3. J Eur Ceram Soc 19:1089–1093
28. Lee C, Chou C, Tsai D (1997) Effect of La/K A-site substitutions on the ordering of Ba(Zn1/3Ta2/3)O3. J Am Ceram Soc 80:2885–2890
29. Akbas MA, Davies PK (1998) Cation ordering transformations in the Ba(Zn1/3Nb1/3)O3–La(Zn2/3Nb2/3)O3 system. J Am Ceram Soc 81:1061–1064
30. Lufaso MW (2004) Crystal structures, modeling, and dielectric property relationships of 2:1 ordered Ba3MM′2O9(M=Mg, Ni, Zn; M′ =Nb, Ta) perovskites. Chem Mater 16:2148–2156
31. Mani R, Selvamani P, Joy JE, Gopalakrishnan J (2007) Study of Ba3MIIMIVWO9(MII= Ca, Zn; MIV= Ti, Zr) perovskite oxides: competition between 3C and 6H perovskite structures. Inorg Chem 46:6661–6667
32. Park CS, Paik JH, Nahm S, Lee HJ, Park HM, Kim KY (1999) Crystal structure of A2+(Mg1/3Nb2/3)O3, (A2+=Sr2+and Ca2+) ceramics. J Mater Sci Lett 18:691–694
33. Lee HJ, Park HM, Cho YK, Song YW, Nahm S, Byun JD (2001) Microstructure characterizations in calcium magnesium niobate. J Am Ceram Soc 84:1632–1636
34. Fu MS, Liu XQ, Chen XM, Zeng YW (2008) Microstructure and microwave dielectric properties of (1-x)Ca(Mg1/3Ta2/3)O3/xCaTiO3 ceramics. J Am Ceram Soc 91:1163–1168
35. Fu MS, Liu XQ, Chen XM (2008) Raman spectra analysis for Ca(B′1/3B″2/3)O3-based complex perovskite ceramics. J Appl Phys 104:104108
36. Fu MS, Liu XQ, Chen XM, Zeng YW (2008) Cation ordering and domain boundaries in Ca[(Mg1/3Ta2/3)1-xTi]O3 microwave dielectric ceramics. J Am Ceram Soc 91:2581–2587
37. Chen XM, Liu D, Hou RZ, Hu X, Liu XQ (2004) Microstructures and microwave dielectric characteristics of Ca(Zn1/3Nb2/3)O3complex perovskite ceramics. J Am Ceram Soc 87:2208–2212
38. Akbas MA, Davies PK (1998) Ordering-induced microstructures and microwave dielectric properties of the Ba(Mg1/3Nb2/3)O3–BaZrO3 system. J Am Ceram Soc 81:670–676
39. Altomare A, Caliandro R, Camalli M, Cuocci C, Giacovazzo C, Moliterni AGG, Rizzi R (2004) J Appl Crystallogr 37:1025–1028
40. Larson AC, Von Dreele RB (2000) General structure analysis system (GSAS). Los Alamos National Laboratory, Report LAUR 86-784
41. Glazer AM (1975) Simple ways of determining perovskite structures. Acta Crystallogr A31:756–762
42. Zhou JS, Goodenough JB (2005) Universal octahedral-site distortion in orthorhombic perovskite oxides. Phys Rev Lett 94:065501
43. Goldschmidt VM (1926) Naturwissenschaften 14:477–485
44. Shannon RD (1976) Revised effective ionic radii and systematic studies of interatomic distances in halides and chalcogenides. Acta Crystallogr A 32:751–767
45. Reaney IM, Colla EL, Setter N (1994) Dielectric and structural characteristics of Ba- and Sr-based complex perovskites as a function of tolerance factor. Jpn J Appl Phys 33:3984–3990
46. Woodward DI, Reaney IM (2005) Electron diffraction of tilted perovskites. Acta Crystallogr B61:387–399
47. Levin I, Chan JY, Geyer RG, Maslar JE, Vanderah TA (2001) Cation ordering types and dielectric properties in the complex perovskiteCa(Ca1/3Nb2/3)O3. J Solid State Chem 156:122–134
48. Siny IG, Tao R, Katiyar RS, Bhalla AS, Guo R (1998) Raman spectroscopy of Mg-Ta order–disorder in BaMg1/3Ta2/3O3. J Phys Chem Solids 59(2):181–195
49. Dias A, William C, Paschoal A, Moreira RL (2003) Infrared spectroscopic investigations in ordered barium magnesium niobate ceramics. J Am Ceram Soc 86(11):1985–1987
50. Rodrigues JEFS, Moreira E, Bezerra DM, Maciel AP, Paschoal CWA (2013) Ordering and phonons in Ba3CaNb2O9 complex perovskite. Mater Res Bull 48:3298–3303
51. Moreira RL, Matinaga FM, Dias A (2001) Raman-spectroscopic evaluation of the long-range order in Ba(B′1/3B″2/3)O3 ceramics. Appl Phys Lett 78:428
52. Siny IG, Katiyar RS, Bhalla AS (1998) Cation arrangement in the complex perovskites and vibrational spectra. J Raman Spectrosc 29: 385–390
53. Rodrigues JEFS, Bezerra DM, Maciel AP, Paschoal CWA (2014) Synthesis and structural ordering of nano-sized Ba3B′Nb2O9(B′ = Ca and Zn) powders. Ceram Int 40:5921–5930
54. Li LX, Xu D, Li XQ, Liuc WC, Jia Y (2014) Excellent fluoride removal properties of porous hollow MgO microspheres. New J Chem 38:5445–5452
55. Maensiria S, Laokula P, Promarak V (2006) Synthesis and optical properties of nanocrystalline ZnO powders by a simple method using zinc acetate dihydrate and poly (vinyl pyrrolidone). J Cryst Growth 289:102–106
56. Zheng H, Reaney IM, Csete de Györgyfalva GDC, Ubic R, Seabra MP, Ferreira VM, Yarwood J (2004) Raman spectroscopy of CaTiO3-based perovskite solid solutions. J Mater Res 19:488–495
57. Zheng H, Bagshaw H, Csete de Györgyfalva GDC, Reaney IM, Ubic R, Yarwood J (2003) Raman spectroscopy and microwave properties of CaTiO3-based ceramics. J Appl Phys 94:2948–2956
58. Cole KS, Cole RH (1941) Dispersion and absorption in dielectrics I. Alternating current characteristics. J Chem Phys 9:341–351
59. Cole KS, Cole RH (1942) Dispersion and absorption in dielectrics II. Direct current characteristics. J Chem Phys 10:98–105
60. Coelho R (1978) Physics of dielectrics. Elsevier, New York
61. Maity SK, Dutta A, Kumar S, Sinha TP (2013) Electrical properties of Ba2YbNbO6: an impedance spectroscopy study. Phys Scr 88: 065702
62. Gerhardt R (1994) Impedance and dielectric spectroscopy revisited: distinguishing localized relaxation from long-range conductivity. J Phys Chem Solids 55:1491–1506
63. Mckubre MCH, Macdonald JR (1987) Impedance spectroscopy emphasizing solid materials and systems. In: JR Macdonald (ed.) Wiley, New York, pp 191
64. Bharti C, Sinha TP (2010) Dielectric properties of rare earth double perovskite oxide Sr2CeSbO6. Solid State Sci 12:498–502
65. Idrees M, Nadeem M, Hassan MM (2010) Investigation of conduction and relaxation phenomena in LaFe0.9Ni0.1O3 by impedance spectroscopy. J Phys D Appl Phys 43:155401
66. Jung WH (2001) Dielectric loss anomaly and polaron hopping conduction of Gd1/3Sr2/3FeO3. J Appl Phys 90:2455–2458
67. Schönhals A, Kremer F (2003) Broadband dielectric spectroscopy. Springer, Berlin, pp 59–98

Thesis 13april

ORIGINALITY REPORT

8%
SIMILARITY INDEX

PRIMARY SOURCES

1	www.researchgate.net Internet	198 words	< 1%
2	repository.bose.res.in:8080 Internet	168 words	< 1%
3	Md. M. Hoque, Alo Dutta, S. Kumar, T.P. Sinha. "Structural and dielectric properties of Sr3(MgTa2)O9 and Sr3(ZnTa2)O9", Physica B: Condensed Matter, 2015 Crossref	108 words	< 1%
4	hdl.handle.net Internet	105 words	< 1%
5	Binita Ghosh, Alo Dutta, T.P. Sinha. "Vibrational modes and electrical transport in Sr2GdTaO6", Materials Chemistry and Physics, 2013 Crossref	101 words	< 1%
6	Alo Dutta, Premlata Kumari, T. P. Sinha. "Electrical properties of double perovskite oxide Sr2LaSbO6: An impedance spectroscopic study", Electronic Materials Letters, 2015 Crossref	94 words	< 1%
7	Rodrigues, João Elias Figueiredo Soares, Edvan Moreira, Débora Morais Bezerra, Adeilton Pereira	82 words	< 1%

Maciel, and Carlos William de Araujo Paschoal. "Ordering and phonons in Ba3CaNb2O9 complex perovskite", Materials Research Bulletin, 2013.
Crossref

8 Indrani Das, Sadhan Chanda, Alo Dutta, Sourish Banerjee, T.P. Sinha. "Dielectric relaxation of Y1−xRxFeO3 (R=Dy, Er, x=0, 0.5)", Journal of Alloys and Compounds, 2013 — 75 words — < 1%
Crossref

9 Binita Ghosh, Alo Dutta, T.P. Sinha. "Dielectric relaxation and conduction mechanism in Ba2GdTaO6", Journal of Alloys and Compounds, 2013 — 71 words — < 1%
Crossref

10 Prasit Thongbai. "Dielectric relaxation and dielectric response mechanism in (Li, Ti)-doped NiO ceramics", Journal of Physics Condensed Matter, 10/01/2008 — 63 words — < 1%
Crossref

11 Saswata Halder, Md.Sariful Sheikh, Binita Ghosh, T.P. Sinha. "Electronic structure and electrical conduction by polaron hopping mechanism in A 2 LuTaO 6 (A= Ba, Sr, Ca) double perovskite oxides", Ceramics International, 2017 — 60 words — < 1%
Crossref

12 Halder, Saswata, Alo Dutta, and T.P. Sinha. "Dielectric relaxation and electrical conduction mechanism in A2HoSbO6 (A=Ba, Sr, Ca) Double Perovskite Ceramics: An impedance spectroscopic analysis", Journal of Physics and Chemistry of Solids, 2017. — 59 words — < 1%
Crossref

13 Sumit Kumar Maity, Alo Dutta, Sanjay Kumar, T P Sinha. " Electrical properties of Ba YbNbO : an — 59 words — < 1%

impedance spectroscopy study ", Physica Scripta, 2013
Crossref

14 K.V. Dabre, S.J. Dhoble. "Synthesis and photoluminescence properties of Eu3+, Sm3+ and Pr3+ doped Ca2ZnWO6 phosphors for phosphor converted LED", Journal of Luminescence, 2014 — 57 words — < 1%
Crossref

15 Md M. Hoque, A. Dutta, S. Kumar, T.P. Sinha. "The impedance spectroscopic study and dielectric relaxation in A(Ni1/3Ta2/3)O3 [A=Ba, Ca and Sr]", Physica B: Condensed Matter, 2012 — 54 words — < 1%
Crossref

16 Rajesh Mukherjee, Alo Dutta, T.P. Sinha. "Collective vibrational modes and dielectric relaxation of Ca2ErNbO6", Materials Science in Semiconductor Processing, 2015 — 54 words — < 1%
Crossref

17 Rajesh Mukherjee, Binita Ghosh, Sujoy Saha, Chandrahas Bharti, T.P. Sinha. "Structural and electrical transport properties of a rare earth double perovskite oxide: Ba2ErNbO6", Journal of Rare Earths, 2014 — 53 words — < 1%
Crossref

18 journals.iucr.org — 50 words — < 1%
Internet

19 R. Tripathi. "Dielectric properties of CdS nanoparticles synthesized by soft chemical route", Pramana, 06/2009 — 49 words — < 1%
Crossref

20 Xiaohui Wu, Qin Zhang, Fangyi Huang, Xingyu Huo, Fuyu Li, Jing Yulan, Yuanxun Li, Hua Su. "Low loss Ba3Ti4Nb4O21 microwave dielectric ceramics through — 48 words — < 1%

(Mn1/3Nb2/3)4+ ion control engineering for LTCC applications", Journal of Alloys and Compounds, 2022
Crossref

21 link.springer.com
Internet
47 words — < 1%

22 Binita Ghosh, Saswata Halder, Tripurari Prasad Sinha. " Dielectric Relaxation and Collective Vibrational Modes of Double-Perovskites A SmTaO (A=Ba, Sr and Ca) ", Journal of the American Ceramic Society, 2014
Crossref
42 words — < 1%

23 K. Deshmukh, M. Basheer Ahamed, R.R. Deshmukh, S.K. Khadheer Pasha, P.R. Bhagat, K. Chidambaram. "Biopolymer Composites With High Dielectric Performance: Interface Engineering", Elsevier BV, 2017
Crossref
42 words — < 1%

24 R. Mondal, S. Dey, S. Majumder, A. Poddar, P. Dasgupta, S. Kumar. "Study on magnetic and hyperfine properties of mechanically milled Ni 0.4 Zn 0.6 Fe 2 O 4 nanoparticles", Journal of Magnetism and Magnetic Materials, 2018
Crossref
39 words — < 1%

25 R. Sinha, S. Basu, A.K. Meikap. "The investigation of the electrical transport properties of Gd doped YCrO 3 nanoparticles", Materials Research Bulletin, 2017
Crossref
35 words — < 1%

26 Sanjay Kumar, Soumen Singha, Bhaskar Khanra, Somen Goswami et al. "Structural, optical, dielectric and electrical transport property of a [Mg(H2O)6]2+-templated proton conducting, semiconducting and photoresponsive 3D Hydrogen bonded supramolecular framework", New Journal of Chemistry, 2021
Crossref
35 words — < 1%

27	S. Dey, S. K. Dey, B. Ghosh, P. Dasgupta, A. Poddar, V. R. Reddy, S. Kumar. " Role of inhomogeneous cation distribution in magnetic enhancement of nanosized Ni Zn Fe O : A structural, magnetic, and hyperfine study ", Journal of Applied Physics, 2013 Crossref	33 words —	< 1%
28	Md. Sariful Sheikh, Anup Pradhan Sakhya, Priyabrata Sadhukhan, Alo Dutta, Sachindranath Das, T. P. Sinha. " Dielectric relaxation and Ac conductivity of perovskites CH NH PbX (X = Br, I) ", Ferroelectrics, 2017 Crossref	32 words —	< 1%
29	Wen, Xuejun. "Direct Deposition of c-Axis Textured High-T c YBCO Superconducting Thick Films on Unoriented Metallic Substrates.", University of Cincinnati, 2018 ProQuest	31 words —	< 1%
30	mafiadoc.com Internet	31 words —	< 1%
31	Hoque, Md. M., Alo Dutta, S. Kumar, and T.P. Sinha. "Structural and dielectric properties of Sr3(MgTa2)O9 and Sr3(ZnTa2)O9", Physica B Condensed Matter, 2015. Crossref	29 words —	< 1%
32	Chandrahas Bharti, T.P. Sinha. "Synthesis, crystal structure, dielectric and optical properties of a new rare earth double perovskite: Ca2CeNbO6", Physica B: Condensed Matter, 2012 Crossref	27 words —	< 1%
33	Rohini Mani, P. Selvamani, Joby E. Joy, J. Gopalakrishnan, Tapas Kumar Mandal. " Study of	26 words —	< 1%

Ba M M WO (M = Ca, Zn; M = Ti, Zr) Perovskite Oxides: Competition between 3C and 6H Perovskite Structures ", Inorganic Chemistry, 2007
Crossref

34	eprints.lib.hokudai.ac.jp Internet	26 words — < 1%
35	www.arxiv-vanity.com Internet	26 words — < 1%
36	Rashmi Rekha Sahoo, R.N.P. Choudhary. "Investigation of structural, dielectric, impedance and leakage current behaviour of green phase of yttrium barium copper Oxide:Y2BaCuO5", Physica B: Condensed Matter, 2022 Crossref	25 words — < 1%
37	Sujoy Saha, Sadhan Chanda, Alo Dutta, T. P. Sinha. " Insulator to metal transition in RCoO (R = Pr, Nd) ", Journal of Advanced Dielectrics, 2022 Crossref	25 words — < 1%
38	Rajesh Mukherjee, Sujoy Saha, Alo Dutta, T.P. Sinha. "Dielectric and Raman spectroscopic studies of A 2 ErSbO 6 (A=Ba, Sr and Ca)", Journal of Alloys and Compounds, 2015 Crossref	23 words — < 1%
39	es.scribd.com Internet	23 words — < 1%
40	Bhide, A.. "Sodium ion transport in NaPO"3-Na"2SO"4 glasses", Materials Chemistry & Physics, 20071015 Crossref	22 words — < 1%

41 J. Koaib, N. Bouguila, M. Kraini, I. Halidou, K. Khirouni, C. Vázquez-Vázquez, M. A. López-Quintela, S. Alaya. "Structural and Electrical Properties of Sprayed In2S3 Films on ITO/Glass Substrate", Research Square Platform LLC, 2021
Crossref Posted Content
22 words — < 1%

42 Michael W. Lufaso. " Crystal Structures, Modeling, and Dielectric Property Relationships of 2:1 Ordered Ba MM‘ O (M = Mg, Ni, Zn; M‘ = Nb, Ta) Perovskites ", Chemistry of Materials, 2004
Crossref
22 words — < 1%

43 Yatramohan Jana, Saikat Nandi, Aksar A. Biswas, H.C. Gupta, R. Upadhyay, C. Upadhyay, D. Samanta. " Optical and Magnetic Properties of Cubic Double Perovskites Ba RSbO (R= Dy, Gd) Coordinated to Lattice Dynamical and Crystal - field Computations ", physica status solidi (b), 2021
Crossref
22 words — < 1%

44 www.mdpi.com
Internet
22 words — < 1%

45 Anirban, Sk., T. Paul, Proloy T. Das, T.K. Nath, and A. Dutta. "Microstructure and electrical relaxation studies of chemically derived Gd–Nd co-doped nanocrystalline ceria electrolytes", Solid State Ionics, 2015.
Crossref
21 words — < 1%

46 M. Krichen, M. Megdiche, M. Gargouri, K. Guidara. "Frequency and temperature dependence of the dielectric properties and AC electrical conductivity in mixed pyrophosphate ceramic", Indian Journal of Physics, 2014
Crossref
21 words — < 1%

47	search.ndltd.org Internet	21 words — < 1%
48	www.pure.ed.ac.uk Internet	21 words — < 1%
49	Indrani Das, Sadhan Chanda, Sujoy Saha, Alo Dutta, Sourish Banerjee, Sudipta Bandyopadhyay, T. P. Sinha. " Electronic structure and transport properties of antiferromagnetic double perovskite Y AlCrO ", RSC Advances, 2016 Crossref	20 words — < 1%
50	K. Prasad, Priyanka, K.P. Chandra, A.R. Kulkarni. "Structural and electrical properties of lead-free perovskite ceramic: Ba(In1/2Nb1/2)O3", Journal of Non-Crystalline Solids, 2011 Crossref	20 words — < 1%
51	N.V. Prasad, S. Narendra Babu, A. Siddeshwar, G. Prasad, G.S. Kumar. "Electrical studies on A- and B-site-modified Bi4Ti3O12 ceramic", Ceramics International, 2009 Crossref	20 words — < 1%
52	Pawar, S.S., K.P. Shinde, A.G. Bhosale, R.S. Pawar, and S.H. Pawar. "Studies on role of grain-size on transport properties of Sm0.5Sr0.5CoO3−δ cathodic films", Materials Chemistry and Physics, 2015. Crossref	20 words — < 1%
53	Soumen Singha, Sumit Kumar Maity, Saptarshi Biswas, Rajat Saha, Sanjay Kumar. "A magnesium-based bifunctional MOF: Studies on proton conductivity, gas and water adsorption", Inorganica Chimica Acta, 2016 Crossref	20 words — < 1%

54	Viswarupa Mohanty, G. Govindaraj. "Hydrothermal synthesis, structural, electrical and magnetic studies of cathode material Li2FeZrO4 for lithium ion batteries", Journal of Materials Science: Materials in Electronics, 2017 Crossref	20 words — < 1%
55	ulspace.ul.ac.za Internet	20 words — < 1%
56	Abhinav Yadav, Snigdha Paramita Mantry, Mohd. Fahad, P.M. Sarun. "Temperature dependent dielectric relaxation and ac–conductivity of alkali niobate ceramics studied by impedance spectroscopy", Physica B: Condensed Matter, 2018 Crossref	18 words — < 1%
57	Karandeep, H.C. Gupta, S. Kumar. "First principles study of structural and vibrational properties of Ba2YTaO6 in cubic and tetragonal phases", Journal of Alloys and Compounds, 2013 Crossref	18 words — < 1%
58	dr.iiserpune.ac.in:8080 Internet	18 words — < 1%
59	Navjeet Kaur, Mohan Singh, Anupinder Singh, A.M. Awasthi, Lakhwant Singh. "Dielectric relaxation spectroscopy of phlogopite mica", Physica B: Condensed Matter, 2012 Crossref	17 words — < 1%
60	assets.researchsquare.com Internet	17 words — < 1%
61	Huajun Liu, Yongqi Dong, Dongwei Xu, Evguenia Karapetrova, Sungsik Lee, Liliana Stan, Peter	15 words — < 1%

Zapol, Hua Zhou, Dillon D. Fong. "Dynamic Field Modulation of the Octahedral Framework in Metal Oxide Heterostructures", Advanced Materials, 2018
Crossref

62 Imen Romdhane, Mohamed Ben Bechir, Mohamed Houcine Dhaou. "Impedance spectroscopic study of charge transport and relaxation mechanism in the lead-free hybrid perovskite CH3NH3CuCl3", Physica E: Low-dimensional Systems and Nanostructures, 2021 — 15 words — < 1%
Crossref

63 Sujoy Saha, Sadhan Chanda, Alo Dutta, T. P. Sinha. " Insulator-to-metal transition in RCoO (R = Pr, Nd) ", Journal of Advanced Dielectrics, 2023 — 15 words — < 1%
Crossref

64 espace.library.uq.edu.au — 15 words — < 1%
Internet

65 hal.archives-ouvertes.fr — 15 words — < 1%
Internet

66 www.etro.vub.ac.be — 15 words — < 1%
Internet

67 Alok Kumar Singh, R. N. P. Choudhary. " Study of Ferroelectric Phase Transition in Pb R Ti Nb O (R = Rare Earth Ion) Ceramics ", Ferroelectrics, 2005 — 14 words — < 1%
Crossref

68 B. P. Das, R. N. P. Choudhary, P. K. Mahapatra. " Structural and Electrical Properties of Dy-Modified Pb(SnTi)O Ferroelectric Ceramics ", Ferroelectrics, 2005 — 14 words — < 1%
Crossref

69	Mohd Hashim, Alimuddin, Sagar E. Shirsath, Shalendra Kumar, Ravi Kumar, Aashis S. Roy, Jyoti Shah, R.K. Kotnala. "Preparation and characterization chemistry of nano-crystalline Ni–Cu–Zn ferrite", Journal of Alloys and Compounds, 2013 Crossref	14 words — < 1%
70	Riju Karmakar, Amit Kumar Das, Shubhadip Atta, Ajit Kumar Meikap. "The role of bias voltage in charge carrier transport mechanism of organic semiconductor", Materials Today Communications, 2022 Crossref	14 words — < 1%
71	Sadhan Chanda, Sujoy Saha, Alo Dutta, T.P. Sinha. "Structural and transport properties of double perovskite Dy2NiMnO6", Materials Research Bulletin, 2015 Crossref	14 words — < 1%
72	jultika.oulu.fi Internet	14 words — < 1%
73	www.rsc.org Internet	14 words — < 1%
74	Chandra, B.P., V.K. Chandra, and Piyush Jha. "Luminescence of II-VI Semiconductor Nanoparticles", Solid State Phenomena, 2014. Crossref	13 words — < 1%
75	Dias, Anderson, L. Abdul Khalam, Mailadil T. Sebastian, Carlos William A. Paschoal, and Roberto L. Moreira. "Chemical Substitution in Ba(RE_{1/2}Nb_{1/2})O₃ (RE = La, Nd, Sm, Gd, Tb, and Y) Microwave Ceramics and Its Influence on the Crystal Structure and Phonon Modes", Chemistry of Materials, 2006.	13 words — < 1%

Crossref

76	Jyoti Rani, Varun K. Kushwaha, Jayant Kolte, C.V. Tomy. "Structural, dielectric and magnetoelectric studies of [0.5Ba(Zr 0.2 Ti 0.8)O 3 -0.5(Ba 0.7 Ca 0.3)TiO 3]-Ni 0.8 Zn 0.2 Fe 2 O 4 multiferroic composites", Journal of Alloys and Compounds, 2017 Crossref	13 words — < 1%
77	core.ac.uk Internet	13 words — < 1%
78	curve.carleton.ca Internet	13 words — < 1%
79	scholar.ufs.ac.za Internet	13 words — < 1%
80	tudr.thapar.edu:8080 Internet	13 words — < 1%
81	C.K. Suman, K. Prasad, R.N.P. Choudhary. "Electrical properties of Pb2Bi3NdTi5O18 ceramic", Materials Chemistry and Physics, 2003 Crossref	12 words — < 1%
82	K. BENZERARA. "Scanning transmission X-ray microscopy study of microbial calcification", Geobiology, 10/2004 Crossref	12 words — < 1%
83	Royer, S.. "Mechanism of stearic acid oxidation over nanocrystalline La"1"-"xA^'"xBO"3 (A'=Sr, Ce; B=Co, Mn): The role of oxygen mobility", Applied Catalysis B, Environmental, 20080415 Crossref	12 words — < 1%
84	Springer Series in Materials Science, 2016.	

Crossref

12 words — < 1%

85 V.L. Vilesh, G. Subodh. "Crystal structure and dielectric properties of BaANaTeO 6 (A = Bi, La) double perovskites", Ceramics International, 2017
Crossref

12 words — < 1%

86 Xiaorui Dong, Zuoling Fu, Qian Wang, Guijuan Sun, Zhenwen Dai. "Synthesis and investigation of luminescence properties of Eu3+-doped cubic perovskite Ba3Y2WO9", Optical Materials, 2013
Crossref

12 words — < 1%

87 Y. Ben Taher, A. Oueslati, N. K. Maaloul, K. Khirouni, M. Gargouri. "Conductivity study and correlated barrier hopping (CBH) conduction mechanism in diphosphate compound", Applied Physics A, 2015
Crossref

12 words — < 1%

88 digital.library.ncat.edu
Internet

12 words — < 1%

89 repository.um.edu.my
Internet

12 words — < 1%

90 9lib.net
Internet

11 words — < 1%

91 Dev K. Mahato, Andrzej Molak, Irena Gruszka, Antoni Winiarski, Janusz Koperski. "Low temperature - Dielectric, impedance, and conductivity - Study for lanthanum nickelate-manganate ceramics", Physica B: Condensed Matter, 2022
Crossref

11 words — < 1%

92 Dutta, Alo, P.K. Mukhopadhyay, T.P. Sinha, Dipankar Das, and Santiranjan Shannigrahi. "Structural and magnetic properties of double perovskite oxide Ba2CeSbO6", Solid State Sciences, 2016. — 11 words — < 1%
Crossref

93 Lei Zhang. "Electrode and grain-boundary effects on the conductivity of CaCu[sub 3]Ti[sub 4]O[sub 12]", Applied Physics Letters, 2005 — 11 words — < 1%
Crossref

94 Lingbing Kong, Weiguang Zhu, Ooi Kiang Tan. " Direct formation of nano-sized PbTiO powders by high energy ball milling ", Ferroelectrics, 1999 — 11 words — < 1%
Crossref

95 N. Kumari, A. Ghosh, A. Bhattacharjee. "Investigation of structural and electrical transport mechanism of SnO2 with Al dopants", Indian Journal of Physics, 2014 — 11 words — < 1%
Crossref

96 Omar Oabi, Abdelkrim Maaroufi, Bruno Lucas. "Frequency electrical conductivity dependence and dielectric relaxation of ZnO–P2O5/Co composites", Journal of Materials Science: Materials in Electronics, 2018 — 11 words — < 1%
Crossref

97 Payal Sengupta, Priyabrata Sadhukhan, Apurba Ray, Souvik Mal et al. "Influence of activation energy on charge conduction mechanism and giant dielectric relaxation of sol-gel derived C3H7NH3PbBr3 perovskite; Act as high performing UV photodetector", Journal of Alloys and Compounds, 2022 — 11 words — < 1%
Crossref

98 Sudeep Sarkar, Harish Banda, Sagar Mitra. "High capacity lithium-ion battery cathode using LiV3O8 nanorods", Electrochimica Acta, 2013 — 11 words — < 1%
Crossref

99 V. ISUPOV. "Some Properties of Bismuth-Containing Layered Ferroelectrics", Ferroelectrics Letters Section, 8/1/2006 — 11 words — < 1%
Crossref

100 Y. Suresh Reddy, Y. Markandeya, B. Appa Rao, G. Bhikshamaiah. "Characterization and impedance study of Ba2CeZrO6 double perovskite", Journal of Materials Science: Materials in Electronics, 2017 — 11 words — < 1%
Crossref

101 Zohra Nazir Kayani, Ammara Iqbal, Zainab Bashir, Saira Riaz, Shahzad Naseem. "Effect of K contents on the efficiency of K-doped TiO2 thin films for smart window applications", Inorganic Chemistry Communications, 2023 — 11 words — < 1%
Crossref

102 aip.scitation.org — 11 words — < 1%
Internet

103 backend.orbit.dtu.dk — 11 words — < 1%
Internet

104 dspace.ncl.res.in:8080 — 11 words — < 1%
Internet

105 research-repository.griffith.edu.au — 11 words — < 1%
Internet

106 Alok Singh Verma, Angaraj Singh, Devendra Kumar, Ashutosh Kumar Dubey. "Electro-mechanical and Polarization-Induced Antibacterial Response of — 10 words — < 1%

45S5 Bioglass–Sodium Potassium Niobate Piezoelectric Ceramic Composites", ACS Biomaterials Science & Engineering, 2020
Crossref

107 Amrin R. Kagdi, Robert C. Pullar, Sher Singh Meena, Francisco E. Carvalho et al. "Green synthesis based X-type Ba–Zn Hexaferrites: Their structural, Hysteresis, Mössbauer, dielectric and electrical properties", Materials Chemistry and Physics, 2022 — 10 words — < 1%
Crossref

108 Azam Ali Khan, Anju Ahlawat, Pratik Deshmukh, Dani Dilip, Rashmi Singh, A.K. Karnal, S. Satapathy. "Effect of Sm doping on structure, dielectric and magnetic properties of GdFeO3", Ceramics International, 2020 — 10 words — < 1%
Crossref

109 Azam Ali Khan, S. Satapathy, Anju Ahlawat, Pratik Deshmukh, A.K. Karnal. "Magneto-dielectric coupling in SmFeO 3 : A study on anomalous dielectric, conductivity, impedance at spin reorientation temperature", Ceramics International, 2018 — 10 words — < 1%
Crossref

110 B. B. Arya, S. Nayak, R. N. P. Choudhary. " Structural and Electrical Characteristics of FeTiVO Double Perovskite ", SPIN, 2021 — 10 words — < 1%
Crossref

111 Bhavsar, Shilpaben Narendrabhai. "Modification of Metal Oxide Doped Polymer Nanocomposites Using Ion Beam Irradiation", Maharaja Sayajirao University of Baroda (India), 2021 — 10 words — < 1%
ProQuest

112 Broadband Dielectric Spectroscopy, 2003. — 10 words — < 1%
Crossref

113 Chen, J.C.. "Synthesis, structure and magnetic property of a new mixed-valence copper(I/II) complex derived from 3,5-bis(pyridin-2-yl)-1,2,4-triazole", Journal of Molecular Structure, 20060807
Crossref
10 words — < 1%

114 Deepa Rajendran Lekshmi, Thomas Letang, Kuzhichalil Peethambharan Surendran. "High permittivitty (La 0.5 Sr 0.5)CoO 3-δ - La(Co 0.5 Ti 0.5)O 3-δ ceramic composites for next generation MIM capacitors", Journal of the European Ceramic Society, 2018
Crossref
10 words — < 1%

115 Feng Shi, Helei Dong. "Correlation between vibrational modes and structural characteristics of Ba[(Zn1−xMgx)1/3Ta2/3]O3 solid solutions", CrystEngComm, 2012
Crossref
10 words — < 1%

116 Gotthard Sághi-szabó, Ronald E. Cohen. " Long-range order effects in Pb(Zr Ti)O ", Ferroelectrics, 2011
Crossref
10 words — < 1%

117 Khalid Sultan, M. Ikram, K. Asokan. "Structural, optical and dielectric study of Mn doped PrFeO3 ceramics", Vacuum, 2014
Crossref
10 words — < 1%

118 Khaoula Azouzi, Besma Hamdi, Ridha Zouari, Abdelhamid Ben Salah. "Crystal structure, Hirshfeld surface analysis, vibrational properties, and electrical and dielectric studies of the bis (4-benzylpyridinium) tetrachlorocuprate (II)", Ionics, 2016
Crossref
10 words — < 1%

119 L. Liu, H. Fan, L. Wang, X. Chen, P. Fang. " Dc-bias-field-induced dielectric relaxation and ac conduction in CaCu Ti O ceramics ", Philosophical Magazine, 2008 — 10 words — < 1%
Crossref

120 Ma, Pian Pian, Xiao Qiang Liu, Fa Qiang Zhang, Juan Juan Xing, and Xiang Ming Chen. "Sr(Ga0.5 Nb0.5)1−x Ti x O3 Low-Loss Microwave Dielectric Ceramics with Medium Dielectric Constant", Journal of the American Ceramic Society, 2015. — 10 words — < 1%
Crossref

121 Matjaz Valant, Danilo Suvorov, ClaudiaJ. Rawn. " Intrinsic Reasons for Variations in Dielectric Properties of Ba R Ti O (R=LA–Gd) Solid Solutions ", Japanese Journal of Applied Physics, 1999 — 10 words — < 1%
Crossref

122 Mohd Alam, Labanya Ghosh, Supriyo Majumder, Prajyoti Singh et al. " Multifunctional behaviour in B-site disordered double perovskite EuPrCoMnO ", Journal of Physics D: Applied Physics, 2022 — 10 words — < 1%
Crossref

123 Murli Kumar Manglam, Suman Kumari, Lagen Kumar Pradhan, Sunil Kumar, Manoranjan Kar. "Lattice strain caused magnetism and magnetocrystalline anisotropy in Zn modified barium hexaferrite", Physica B: Condensed Matter, 2020 — 10 words — < 1%
Crossref

124 N Trofimenko. "Transition metal doped lanthanum gallates", Solid State Ionics, 1999 — 10 words — < 1%
Crossref

125	Ortega Achury, Nora Patricia. "Investigations on structural and multiferroic properties of artificially engineered lead zirconate titanate-cobalt iron oxide layered nanostructures", Proquest, 20111004 ProQuest	10 words — < 1%
126	Saswata Halder, Md. Sariful Sheikh, Binita Ghosh, T.P. Sinha. "Octahedral distortion induced phonon vibration and electrical conduction in A 2 NdSbO 6 (A=Ba, Sr, Ca)", Materials Chemistry and Physics, 2017 Crossref	10 words — < 1%
127	Subhojyoti Sinha, Sanat Kumar Chatterjee, Jiten Ghosh, Ajit Kumar Meikap. "Dielectric relaxation and ac conductivity behaviour of polyvinyl alcohol–HgSe quantum dot hybrid films", Journal of Physics D: Applied Physics, 2014 Crossref	10 words — < 1%
128	The DV-Xα Molecular-Orbital Calculation Method, 2015. Crossref	10 words — < 1%
129	Ying Qin, Zhuo Wang, Xiang Ming Chen, Xiao Qiang Liu. "Dielectric and magnetic characteristics of LuFeMgO4 ceramics", Journal of Applied Physics, 2010 Crossref	10 words — < 1%
130	academic.oup.com Internet	10 words — < 1%
131	citeseerx.ist.psu.edu Internet	10 words — < 1%
132	coek.info Internet	10 words — < 1%

133	edoc.hu-berlin.de Internet	10 words — < 1%
134	ir.lib.uwo.ca Internet	10 words — < 1%
135	ja.overleaf.com Internet	10 words — < 1%
136	lib.buet.ac.bd:8080 Internet	10 words — < 1%
137	publications.ub.uni-mainz.de Internet	10 words — < 1%
138	researchspace.ukzn.ac.za Internet	10 words — < 1%
139	www.jmbfs.org Internet	10 words — < 1%
140	www.research-collection.ethz.ch Internet	10 words — < 1%

EXCLUDE QUOTES	ON	EXCLUDE SOURCES	< 6 WORDS
EXCLUDE BIBLIOGRAPHY	ON	EXCLUDE MATCHES	< 10 WORDS